Circulating Tumour Cell Patient-Derived Models To Identify Treatments And Biomarkers Of Response For Small Cell Lung Cancer

A thesis submitted to the University of Manchester for the degree of Doctor of Philosophy in the faculty of Biology, Medicine and Health

2019

Alice Lallo

Cancer Research UK Manchester

Table of contents

Word count: 79,995

List of Figures

List of Tables

Supplementary Data

Supplementary data files can be found in the USB drive provided with the hard copy of this thesis.

Supplementary Data 1. List of the top 488 protein coding genes driving PC3 in Figure 24.

Supplementary Data 2. List of genes differentially expressed between CDX3 +/- ROCKi and CDX4 +/- ROCKi.

Supplementary Data 3. List of genes and pathways differentially expressed between CDX2, CDX3 and CDX4 tumours and the corresponding cultures.

Supplementary Data 4. List of genes differentially expressed between CDX3 tumours and CDX3 cultures after 1-4 weeks *in vitro*.

Supplementary Data 5. List of genes differentially expressed between CDX3 tumours and derived cultures and CDX3 tumours derived from CDX3 cultures.

Supplementary Data 6. List of genes differentially expressed between 'resistant' and 'sensitive' group.

Supplementary Data 7. List of Reactome pathways enriched in the 'resistant' and 'sensitive' CDX.

Supplementary Data 8. Pearson correlation coefficients calculated for each gene for all combinations tested.

List of Abbreviations

Abbreviation	Meaning
AGT	O^6-alkylguanine DNA alkyltransferase
APC	Antigen Presenting Cells
AT1/AT2	Alverolar type I and II
BER	Base Excision Repair
BET	Bromodomain and extra terminal proteins
b.i.d	Twice daily
CDX	CTC-Derived eXplant
CESTA	Cellular Thermal Shift Assay
CEV	Cyclophosphamide Epirubicin Vincristine
CFS	Common Fragile Site
CgA	Chromogranin A
CGRP	Calcitonin gene-related peptide
CIMP	CpG-island methylation phenotype
CIN	Chromosome instability
CK	Cytokeratin
CldU	5-Chloro-2′-deoxyuridine
CNA	Copy Number Alteration
CNV	Copy Number Variants
CRISPR	Clustered Regularly Interspaced Short Palindromic Repeats
CSC	Cancer Stem Cell
CTC	Circulating Tumour Cell
ddH2O	Deionised water
DDR	DNA Damage Response
DDRi	DNA Damage Response inhibitor
NDP	Ribonucleoside diphosphates
dNDP	Deoxyribonucleoside diphosphates
dNTP	Deoxyribonucleoside triphosphate
DSB	Double Strand Break
DSBR	Double Strand Break Repair
ECM	Extracellular Matrix
EdU	2′-Deoxy-5-ethynyluridine
EMA	European Medicines Agency
EMT	Epithelial-Mesenchymal Transition
EP	Etoposide Platinum
ER1	Antigen Retrieval pH 6
ER2	Antigen Retrieval pH 9
ES	Extensive-Stage
FBS	Fetal Bovine Serum
FDA	US Food and Drug Administration
FDR	False Discovery Rate
FFPE	Formalin Fixed Paraffin-Embedded
GEMM	Genetic Engineered Mouse Model

GI_{50}	Dose that produces 50% growth inhibition
GPCR	G protein-coupled receptors
GSH	Glutathione
Gy	Gray
HB	HITES + bombesin
HBRi	HITES + bombesin + ROCK inhibitor
HF	HITES + FBS
HFRi	HITES + FBS + ROCK inhibitor
HITES; H	Hydrocrotisone, Insulin, Transferrin, β-Estradiol, Sodium Selenite
HNSCC	Head and Neck Squamous Cell Carcinoma
HR	Homologous Recombination
HRD	Homologous Recombination Deficiency
HRi	HITES + ROCK inhibitor
IARC	International Agency for Research on Cancer
ICB	Immune Checkpoint Blockade
IdU	5-Iodo-2′-deoxyuridine
IF	Immunofluorescence
IHC	Immunohistochemistry
INSM1	Insulinoma-associated protein 1
IR	Ionising Radiation
ITV	Initial Tumour Volume
LM	Lorvotuzumab Mertansine
LOF	Loss of function
LOH	Loss of heterozygosity
LS	Limited-Stage
LSCC	Squamous Cell Lung Cancer
MDS	Multidimensional Scaling
MMR	Mismatch Repair
MPA	Mycophenolic acid
MT	Metallothionein
N2	Nitrogen
NCAM1	Neural Cell Adhesion Molecule 1
NE	Neuroendocrine
NEB	Neuroendocrine bodies
NER	Nucleotide Excision Repair
NHEJ	Non-Homologous End Joining
NSCLC	Non Small Cell Lung Cancer
NSG	NOD.Cg-*Prkdc*^{scid}*Il2rg*^{tm1Wjl}/SzJ
NT	Non-Targeting
ORR	Overall Response Rate
OS	Overall Survival
p.i.	Intraperitoneal
p.o.	Oral gavage
PAH	Polycyclic Aromatic Hydrocarbons
PBD	Pyrrolobenzodiazepine

PBS	Phosphate-buffered saline
PBST	PBS with Tween20
PCA	Principal Component Analysis
PCI	Palliative Cranial Irradiation
PCR	Polymerase Chain Reaction
PDX	Patient-derived xenograft
PFA	Paraformaldehyde
PFS	Progression Free Survival
PI	Propidium Iodide
PIP_2	Phosphatidylinositol (3,4)-bisphosphate
PIP_3	Phosphatidylinositol (3,4,5)-trisphosphate
PNEC	Pulmonary Neuroendocrine Cells
QIBC	Quantitative Image-Based Cytometry
RNAi	RNA interference
ROCKi	ROCK inhibitor, Y-27632
ROS	Reactive Oxygen Species
RP	$Rb^{flox/flox}$;$p53^{flox/flox}$
RPF	$Rb^{flox/flox}$;$p53^{flox/flox}$;$Nfib^{lox/lox}$
RPKM	Reads Per Kilobase Million
RPM	$Rb1^{flox/flox}$;$Trp53^{flox/flox}$;$Myc^{LSL/LSL}$
RPML	$Rb^{flox/flox}$;$p53^{flox/flox}$;$Mycl^{lox/lox}$
RTK	Tyrosine Kinase Receptor
RTU	Ready To Use
s.c.	Subcutaneous
SCID-*bg*	CDB17.Cg-$Prkdc^{scid}Lyst^{bg-J/}$Crl
SCLC	Small Cell Lung Cancer
SoC	Standard-of-Care
SSA	Single-Strand Annealing
SSB	Single Strand Break
ssDNA	Single stranded DNA
SYP	Synaptophysin
TA	Transactivation
TBS	TBS with Tween20
TIC	Tumour Initiating Cell
TKO	$Rb^{flox/flox}$;$p53^{flox/flox}$;$p130^{flox/flox}$
TLS	Translesion DNA synthesis
TMZ	Temozolomide
TOPcc	Topoisomerase cleavage complex
TRT	Thoracic Radiotherapy
TSA	Tyramide Signal Amplification
VALSG	Veterans Administration Lung Study Group
WES	Whole-exome sequencing
WHO	World Health Organisation
WT	Wild-Type

Abstract

Small cell lung cancer (SCLC) has been defined as a "recalcitrant" disease and better treatments are urgently needed. High mutational burden, oncogene induced replication stress and universal loss of G1 checkpoints in SCLC validate it for treatment with DNA damage response inhibitors (DDRi). I investigated the effects of the PARP inhibitor olaparib and the WEE1 inhibitor AZD1775 on SCLC preclinical models. PARP is a crucial regulator of several DNA damage pathways, whilst WEE1 controls CDK activity and cell cycle progression. Their dual inhibition has emerged as a promising strategy to drive SCLC cells beyond their survival threshold.

In this thesis, I present data that supports the exploitation of circulating tumour cell patient-derived explant models (CDX) as a platform to study the response of SCLC patients to several DDRi and to identify biomarkers of treatment response. I demonstrated that CDX-derived cells can be cultured successfully *ex vivo*, and retain most of the features of the donor CDX tumour. In particular, the majority of CDX cultures I derived were able to predict the original CDX's *in vivo* response to therapies.

I utilised the CDX culture platform to investigate the potential of combining AZD1775 and olaparib. Screening of a panel of 20 CDX cultures demonstrated disparate responses, highlighting the need for predictive biomarkers of response to stratify patients in clinical trials. However, the investigation of cell cycle checkpoints and DNA damage repair pathways revealed a high degree of heterogeneity between individual CDX models. This challenged the identification of a universal response biomarker, and highlighted the need for a better understanding of the molecular mechanisms underpinning these treatment responses.

Ex vivo screens of different DDRi combinations identified a group of CDX resistant to most combinations tested. These models have an intrinsic ability to survive despite the induction of substantial DNA damage. AZD2811, an inhibitor of the mitotic regulator Aurora kinase B, was highly cytotoxic in some of the otherwise resistant cultures, making this drug a promising alternative treatment for chemorefractory SCLC patients. Overall, this thesis shows that CDX cultures are a faithful model to study SCLC and confirms DDRi as a promising therapeutic strategy for SCLC patients.

Declaration

No portion of the work referred to in this thesis has been submitted in support of an application for another degree or qualification of this or any other university or other institute of learning.

Copyright Statement

Acknowledgements

This PhD has been an incredible experience that has led me to grow both from a scientific and personal point of view. During these 5 years, I had the chance to meet wonderful people that, in different ways, have supported and helped me along the path.

First, I would like to thank Caroline. Thanks for giving me the opportunity to work in CEP and, in particular, thanks for always trusting me and for your contagious enthusiasm for research.

Then I would like to thank Kris. It would have been a lot harder without all your useful advices. I am very grateful for all the discussions we had, I will miss them.

To the *in vivo* team, a huge thank you! Thanks for your help with all the animal studies, part of my thesis would not even exist without your support! A special thanks goes to Melanie and Stewart. You have been with me since the beginning, and your advices and teachings have been instrumental for my PhD.

Stuart, we started and finished our adventure in CEP together. You are the first person I have bonded with in CEP and I will never forget all your technical advices in setting up protocols and, mainly, fixing problems. Thank you!

Another big thank you goes to Max, Sarah, James and Alessia. I couldn't have been luckier sharing my experience with PhD students like you! You are funny, you are smart but most of everything you are a team. You have always been ready to share any type of work load without a complain. Thanks a lot! A special thanks to Max, we shared a few tasks together and I am grateful I had to share them with you.

I want to thank Sara for sharing with me 1.5 year of her life! You were there at the beginning, when I was feeling a little bit lost and friendless. Thanks for being there for me!

Fede and Amy, I also have to thank you. You helped me to lighten my days, having lovely chatty dinners and lunches free from any stress or worry.

Maria, thanks for being there, asking how I was and listening to me, when I really needed it.

Alessandra, you infected me with your incredible energy and passion for science, more than once, and I have to thank you for that!

Camilla, Chiara and Cecilia, you were not ‘physically’ with me during these 5 years, but your friendship has been crucial in different moments during my PhD. Camilla, I have to thank you for your chats. After a long day at work, it is always nice to listen to some Turin-gossip! Chiara, you were always there; to laugh, to cry, whatever I needed, you were there, with all your strength and energy! Thank you. And then, Ceci. You are my best friend and probably one of the very few people, who really understand and appreciate my love for science. Thank you for listening every time I had some nerdy stories to tell!

An immense thank you to my family. Thank you to my mum and dad who helped me to achieve this goal. You always believed in me and never missed a chance to cheer me up. Thank you to my sister, who has always had a delicious glass of wine, ready for me, when I was back to Italy.

Finally, I have to thank Renaud, my strictest critic but also my ‘island of freedom’. You made me mad criticising every single experiment I have planned, but at the end your critics helped me to learn, see mistakes and mature scientifically. But most of everything, I want to thank you for all those moments we spent together that allowed me to just stop worrying about work. You gave me peace and support during some of the most challenging years of my life, I will never thank you enough for that.

Chapter 1. Introduction

Lung cancer is the most common cancer diagnosed worldwide, according to the Global Cancer Statistics 2018 (Bray et al., 2018). Estimations made by the International Agency for Research on Cancer (IARC) state that lung cancer killed 1.8 million people in 2018 (18.4% of all cancer-related death), twice the number of deaths caused by colorectal (9.2%), stomach (8.2%) and liver (8.2%) cancers (Bray et al., 2018). The main risk factor for lung cancer is cigarette smoking, however genetic factors, exposure to ionising radiation, air pollution and occupational carcinogens can play an important role in its aetiology (Cogliano et al., 2011; Malhotra et al., 2016). Lung cancers can be subdivided into two major cytological groups: non small cell lung cancer (NSCLC) and small cell lung cancer (SCLC), with the latter accounting for ~15% of all lung cancers (Gazdar et al., 2017). Contrary to NSCLC, SCLC has been defined a "recalcitrant cancer" according to the Recalcitrant Cancer Research Act of 2012 (National Cancer Institute, 2014). The short survival rate of SCLC patients together with the absence of early detection tools, the limitation of treatment options and the lack of tumour material for research, are all aspects of SCLC that highlight the need to better understand this disease and to challenge these poses. Experts from all around the world are working together to fight this disease and with this Thesis I am hoping to partly contribute to the continuous development of SCLC research.

1.1 SCLC biology and genomic landscape

SCLC is an aggressive high-grade neuroendocrine (NE) tumour characterised by dense sheets of small cells with scant cytoplasm, poorly defined cell borders, dispersed and finely granular nuclear chromatin and few or no conspicuous nucleoli (Azzopardi, 1959; Bensch et al., 1968; van Meerbeeck et al., 2011; Travis et al., 2015). In a small subgroup of patients, a mixture of small and large cells with NSCLC features can be identified (combined SCLC, Beasley et al., 2005). SCLC shows rapid proliferation, with extensive necrosis and high mitotic count, and early onset of metastasis. Different markers of neuroendocrine differentiation, such as neural cell

adhesion molecule 1 (NCAM1[1] or CD56), chromogranin A (CHGA), synaptophysin (SYP) and insulinoma-associated protein 1 (INSM1), are used to diagnose SCLC, however a minority of these tumours are negative for all diagnostic markers (Travis et al., 2004). SCLC typically develops in the midlevel bronchioles where the pulmonary neuroendocrine cells (PNEC), the proposed cell of origin for the majority of SCLC, are localized (Figure 1). The tissue surrounding these tumours is highly perturbed with frequent loss of 5q21-22 and 17p13 regions (containing *TP53*) (Wistuba et al., 2000). These alterations probably result from the exposure of the bronchial epithelium to tobacco carcinogens and suggest that SCLC may arise directly from normal and hyperplastic epithelium bypassing a preneoplastic step (Wistuba and Gazdar, 2006; Wistuba et al., 2000). Several studies tried to unravel the mechanisms of SCLC development, with focus on the cell of origin and the molecular landscape, and will be the topic of the next sections.

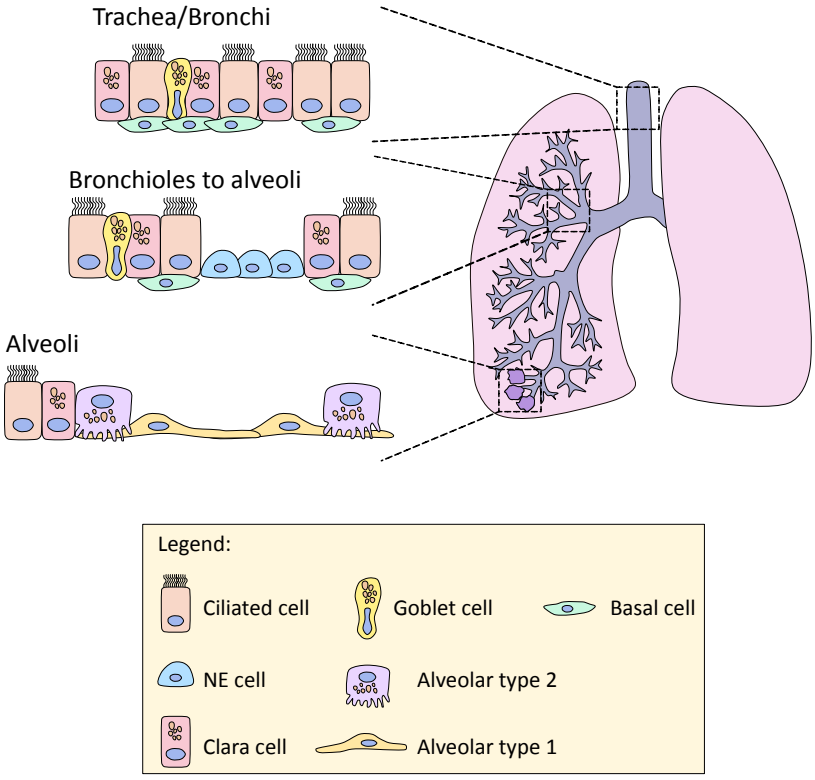

[1] When referring to gene or protein names in this document I will follow guidelines set out by the Human Gene Nomenclature Committee and Mouse Gene Nomenclature Committee (Davisson, 1996; Gray et al., 2012), i.e.
- Capitalised and italicised for human genes (e.g. *KRAS*)
- Capitalised first-letter only and italicised for genes in mice (e.g. *Kras*)
- Capitalised for the protein in either species (e.g. KRAS)

Figure 1. Distribution of the different types of cells in human lung epithelium.

The distribution and localisation of the different components of the lung epithelium change from the trachea to the alveoli. Each cell type plays multiple roles in the maintenance and functions of the lung. AT1 cells participate in the gas exchange in the alveoli, while AT2 cells function in the biosynthesis of pulmonary surfactant. Clara and basal cells have been identified as putative progenitor cells, with the ability to regenerate the epithelium. Ciliated cells participate in the clearance of the mucus produced by the Goblet cells. NE cells are innervated and play different roles, such as oxygen sensing, pulmonary blood flow regulation and maintenance of a stem cell niche. These cells are also the putative cell of origin of SCLC (adapted from Rackley and Stripp, 2012).

1.1.1 SCLC cell of origin

Lungs are formed by a variety of specialized cells with different biological functions (Rackley and Stripp, 2012). The major cell types include basal cells, ciliated cells, Clara cells, NE cells and type I and type II pneumocytes (AT1 and AT2) (Figure 1). PNECs are considered to be the cell of origin of SCLC. They can be found as solitary cells or as clusters (NEB, neuroendocrine bodies) and they are thought to be involved in hypoxia sensing, immunomodulation and lung development (Linnoila, 2006; Rackley and Stripp, 2012). The expression of different NE markers on SCLC cells supports its NE origin encouraging researchers to look into PNECs as the cell of origin of SCLC. The first mouse model of SCLC was generated by Anton Bern's group in 2003 (Meuwissen et al., 2003). Guided by patient genetics (George et al., 2015), they generated $Rb1^{flox/flox}$;$Trp53^{flox/flox}$ (RP) mice in which the deletion of Rb1 and Trp53 was induced via administration of adenovirus particles expressing the Cre recombinase under the control of the CMV promoter (Ad-CMV-Cre) (Meuwissen et al., 2003) (Table 1). These mice developed tumours with NE differentiation and high metastatic potential, mirroring human SCLC, however the exact cell of origin could not be identified because the CMV promoter is not cell specific. Later, Park and colleagues exploited the same mouse model to further characterize the cell of origin of SCLC. They deleted Trp53 and Rb1 specifically in Clara and AT2 cells and neither cell types was able to initiate SCLC (Park et al., 2011a).

Table 1. Genetic engineered mouse models of SCLC.

Name	Alterations	References
RP	*Rb1$^{flox/flox}$;Trp53$^{flox/flox}$*	Meuwissen et al., 2003; Park et al., 2011a; Sutherland and Berns, 2010
TKO	*Rb1$^{flox/flox}$;Trp53$^{flox/flox}$;p130$^{flox/flox}$*	Schaffer et al., 2010
RPF	*Rb1$^{flox/flox}$;Trp53$^{flox/flox}$;Rosa26$^{LSL\text{-}rtTA/LSL\text{-}rtTA}$;TRE-Nfib*	Wu et al., 2016
RPF	*invCAG-Nfib-Luc;Rb1$^{flox/flox}$;Trp53$^{flox/flox}$*	Semenova et al., 2016
RPF	*Rb1$^{flox/flox}$;Trp53$^{flox/flox}$;CAG<Lox66Nfib-LucLox71>*	Böttger et al., 2019
RPP	*Rb1$^{flox/flox}$;Trp53$^{flox/flox}$;Pten$^{flox/+}$*	Cui et al., 2014; McFadden et al., 2014
RPP	*Rb1$^{flox/flox}$;Trp53$^{flox/flox}$;Pten$^{flox/flox}$*	Cui et al., 2014; McFadden et al., 2014
RPM	*Rb1$^{flox/flox}$;Trp53$^{flox/flox}$;Myc$^{LSL/LSL}$*	Mollaoglu et al., 2017
RPML	*invCAG-Mycl1-Luc;Rb1$^{flox/flox}$;Trp53$^{flox/flox}$*	Huijbers et al., 2014; Semenova et al., 2016
RPML	*Rb1$^{flox/flox}$;Trp53$^{flox/flox}$;CAG<Lox66Mycl-LucLox71>*	Böttger et al., 2019

Similarly, Sutherland and colleagues generated cell type-restricted Ad5-Cre virus to induce *Trp53*/*Rb1* loss specifically in Clara cells (Ad5-CC10-Cre), AT2 cells (Ad5-SPC-Cre) and NE cells (Ad5-CGRP-Cre) (Sutherland and Berns, 2010). As expected, SCLC developed mainly from *Trp53$^{-/-}$;Rb1$^{-/-}$* NE cells, however they observed SCLC in half of the mice with *Trp53$^{-/-}$;Rb1$^{-/-}$* in AT2 cells, albeit with delayed tumour latency . Only very few mice with *Trp53$^{-/-}$;Rb1$^{-/-}$* in Clara cells developed SCLC and only after a prolonged latency. Interestingly, independent of the cell of origin, all observed SCLC expressed the typical NE markers (Sutherland and Berns, 2010). More recently, lung injury studies in Ascl1^{CreERT2}Rosa26$^{LSL\text{-}Rainbow}$ mouse model, demonstrated that a rare population of NE cells with stem cell potential can differentiate to different lung epithelial cell types and repopulate the lung after injury. The de-differentiation was regulated by Notch signalling, while the ability to proliferate and migrate to the region of injury was controlled by inhibition of p53 and Rb signalling (Ouadah et al., 2019). Ouadah *et al* suggested that loss of p53 and RB in NE cells could push these cells to uncontrolled proliferation and migration in the presence of a damaged epithelium. All together these data suggest that NE cells are the putative cell of origin of SCLC, even if some non-NE cells have the potential to transform into SCLC after loss of *Trp53* and *Rb1*. This could be explained by the existence of a common cell

progenitor in the epithelium of the lung. Lineage tracing experiments in $CGRP^{CreER/+}$;$Rosa26^{mTmG/+}$ mice demonstrated that eGFP was expressed in PNECs but also in a small fraction of AT1/AT2 cells, suggesting that PNECs may have a common progenitor with alveolar cells (Song et al., 2012). Yang *et al* reinforced the idea of different presumed cells of origin for SCLC studying the metastatic process. They observed that the Ad-CMV-Cre primary tumours had higher expression of different lineage markers, such as club and AT1 and 2 cells, and were localized to both the proximal and distal lung. On the contrary, Ad-CGRP-Cre tumours mainly expressed NE markers and developed in the proximal lung (Yang et al., 2018). This data further indicates that a subpopulation of SCLC can derive from non-NE cells, accounting partly for the high level of heterogeneity observed in this disease.

1.1.2 SCLC subtypes

The presence of more than one cell of origin could be the base of the different SCLC subtypes identified to date. The 2015 World Health Organization Classification of Lung Tumors categorized all SCLC as one disease (Travis et al., 2015). However, recent studies have designated the presence of at least four main subtypes, based on the prevalent expression of one of the four transcription factors described below: ASCL1, NEUROD1, YAP1 and POU2F3 (Rudin et al., 2019). Initially, SCLC was subdivided in classic and variant morphology based on the expression of four markers on SCLC cell lines: L-dopa decarboxylase, bombesin-like immunoreactivity, neutron-specific enolase and brain isozyme of creatine kinase (Carney et al., 1985), however recently this concept has been expanded. The two main and well-established subgroups of SCLC are driven by the expression of the lineage transcription factors ASCL1 (Achaete-Scute Family BHLH Transcription Factor 1) and NEUROD1 (Neuronal differentiation 1). Both transcription factors are involved in the maturation of NE cells in the lung. Mice in which *Ascl1* has been disrupted did not show any NE cells in the lung epithelium and loss of *ASCL1* in human SCLC cell lines decreased the expression of NE markers (Borges et al., 1997). NEUROD1 is involved in the development of the distal lung. Mice with loss of *NeuroD1* showed enlarged alveoli and reduced proliferation as well as alteration of the NE compartment (Neptune et al., 2008). Poirier and co-workers firstly observed that SCLC cell lines with classic morphology

had a higher level of *ASCL1* than the variant subclass, where *NEUROD1* was more expressed (Poirier et al., 2013). This distinction was confirmed in a subsequent study from the same group, where gene expression and methylation profiles of human SCLC primary tumours were segregated in 3 main clusters: the E1 cluster with high *NEUROD1* and low *ASCL1*, the E2 cluster with high *ASCL1* and low *NEUROD1*, and the SQ-P cluster low for both *ASCL1* and *NEUROD1* (Poirier et al., 2015). The double negative subgroup (SQ-P) included SCLC tumours with a non-neuroendocrine phenotype and can be further divided in YAP1- and POU2F3-driven tumours. YAP1 (Yes Associated Protein 1) is a crucial regulator of the Hippo signalling pathway that has been involved in the aetiology of different tumours (Zhao et al., 2010), whereas POU2F3 (POU class 2 homeobox 3) is a transcription factor involved in the development of gastrointestinal and respiratory system and is a master regulator of the tuft cell lineage (Gerbe et al., 2016; Yamaguchi et al., 2014; Yamashita et al., 2017). McColl and co-workers observed that *YAP1* was highly expressed in a subgroup of SCLC cell lines negative for *ASCL1* and *NEUROD1* and this population was confirmed on patient samples (McColl et al., 2017). The POU2F3 subpopulation was identified by Huang and colleagues (Huang et al., 2018b). POU2F3 appeared to be essential for a small group of SCLC cell lines that displayed a variant morphology. The expression of this TF was confirmed on published RNAseq data from primary SCLC samples, where ~18% of the samples expressed this marker (George et al., 2015; Sato et al., 2013). In particular, samples with *POU2F3* expression co-expressed several tuft cell markers, suggesting that POU2F3 distinguishes a SCLC subpopulation with a tuft-like identity (Huang et al., 2018b). These studies show that different subtypes of SCLC exist, which may reflect different cells of origin and/or plasticity. For example, plasticity between NE and non-NE SCLC cells derived from the $Rb1^{flox/flox};Trp53^{flox/flox};p130^{flox/flox}$ (TKO) mice was observed by Lim *et al*. They demonstrated that, *in vitro*, NE cells were able to irreversibly switch to a non-NE phenotype upon activation of the Notch receptors and induction of the transcriptional repressor RE1 silencing transcription factor (REST) (Lim et al., 2017). The ability of the tumour cells to switch from one subtype to the other could be exploited by the tumour cells to support growth and survive treatment.

Examination of whether GEMMs initiated by new TF of lineage-specific Cre develop specific subtypes of SCLC will be of great help to better understand their biological differences, however the lack of the mutational chaos induced by tobacco smoke in these mouse models may mask additional biological aspects. The genomic landscape of SCLC is highly complex and strictly related to the effect of carcinogens present in tobacco smoke (Alexandrov et al., 2016; Pleasance et al., 2010), therefore more patient faithful models of SCLC are necessary to fully understand this disease.

1.1.3 SCLC genomic landscape

SCLC is highly associated with cigarette smoke with 90% of patients been as current or past heavy smokers (van Meerbeeck et al., 2011). Cigarette smoke contains ~10^{10} particles/mL and 4,800 compounds of which over 60 have been confirmed as carcinogens by the International Agency for Research on Cancer (IARC) (Pfeifer et al., 2002). Cytochrome P450 enzymes are involved in the removal of these molecules, however, during the detoxification process, some intermediates can react with DNA to form adducts and other lesions (Hang, 2010). Each lesion can be recognized and repaired by specialised DNA repair mechanisms, of which nucleotide excision repair (NER) and base excision repair (BER) are the most common (Figure 2). Most of the damage caused by these molecules are bulky DNA adducts that thermodynamically destabilise the DNA duplex, and are recognised by NER (Hang, 2010). The XPC-RAD23B complex senses the lesions and recruits the transcription and NER factor, TFIIH. At this point several molecules are recruited and the lesion is excised by ERCC1-XPF, synthesised by DNA polymerase δ, κ or ε and ligate by DNA ligase I, IIIα or XRCC1 (Schärer, 2013) (Figure 2A). The BER pathway is activated when the carcinogens generate small DNA lesions. During BER, specialised glycosylases recognise and remove the damaged base. AP-endonuclease (APE1) cleaves the abasic site, followed by DNA polymerase β (or polymerase δ/ε) that fills the gap and DNA ligase I or III that re-ligates the DNA strands (Krokan and Bjørås, 2013) (Figure 2B). If the lesions are not repaired properly, the presence of DNA adducts during DNA replication can stall the DNA polymerases. This can result in stalled replication forks and activation of translesion DNA synthesis (TLS) to bypass the lesion. TLS polymerases have the ability to accommodate the damaged base and are recruited

at stalled forks to restart replication (Sale, 2013). This process can be error-prone and introduce mutation in the nascent DNA (Figure 2C).

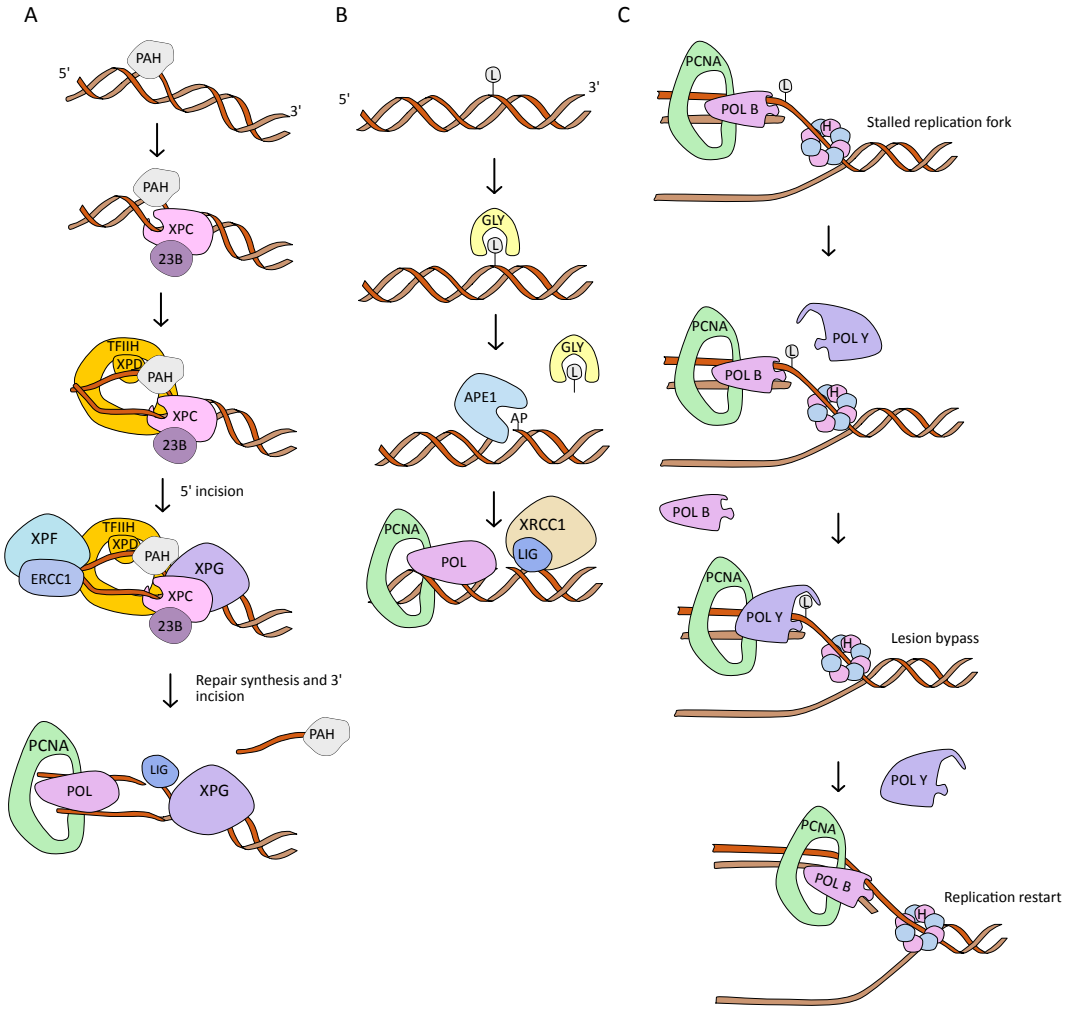

Figure 2. DNA repair pathways activated in the presence of cigarette carcinogens.

A. Schematic of NER. PAH generates a bulky DNA adduct that destabilise the DNA helix. These lesions are recognised by the complex XPC-RAD23B that recruits TFIIH. The XPD subunit of TFIIH acts as un helicase and stops when it encounters the lesion. XPF-ERCC1 are recruited and cut the 5' end near the bulky adduct. This allows the DNA polymerase δ, κ or ε to start the synthesis while XPG cut the 3' end and allows complete removal of the oligo containing the lesion. Several DNA replication factors, including ligases, are recruited at the level of the damage to fill the gap. B. Schematic of BER. Small DNA lesions can be recognised and removed by specialised glycosylases. These enzymes leave an abasic site at the level of the damage that is recognised by APE1. APE1 cuts the 5' end of the abasic site allowing DNA polymerases and ligases to fill the gap. C. Schematic of the general mechanism of TLS. When a lesion is not repaired properly, it can cause the stalling of the replication fork. Common DNA polymerases (B family) cannot accommodate the lesions in their active site pocket. Family Y polymerases and the B-polymerase ζ have larger active site pocket and can accommodate different type of lesions. This allows to bypass the DNA lesions and restart the replication. Polymerases Y are error-prone, especially in the presence of undamaged DNA. Therefore, once the lesion is bypassed, polymerases B, including POL ζ, are required for the extension step. PAH: polycyclic aromatic hydrocarbons; POL: polymerases; POL B: B-family polymerases; POL Y: Y-family polymerases, LIG: ligases; GLY: glycosilases; L: lesions; H: helicase.

The high level of carcinogens present in cigarette smoke together with the continuous activation of error-prone DNA repair pathways induce several mutations in the lung epithelium and can initiate the development of SCLC. Pleasance and co-workers were the first to sequence the genome of a human SCLC cell line. In their study, they identified mutation patterns characteristic of the carcinogens present in cigarette smoke as well as signatures specific of some type of DNA repair (Pleasance et al., 2010). A global analysis of somatic mutations and DNA methylation from more than 5,000 cancers associated with tobacco, confirmed the presence of a mutational signature linked to DNA mis-replication after exposure to tobacco carcinogens (Alexandrov et al., 2016). Comprehensive genomic studies with SCLC patient samples have started to unravel the complexity of the mutational landscape observed in this disease. The most common mutations are the bi-allelic inactivation of the two G1 checkpoint regulators, *TP53* and *RB1,* due to mutations, translocations, homozygous deletions, hemizygous losses, copy-neutral losses of heterozygosity (LOH) and LOH at higher ploidy (George et al., 2015). *TP53* is the most mutated gene in human cancers (Kandoth et al., 2013) and has been widely studied as tumour suppressor protein (Vousden and Lane, 2007). While *RB1* was the first described tumour suppressor gene, frequently lost in retinoblastoma (Dyson, 2016). Combined loss of *TP53* and *RB1* in SCLC is a fundamental step in the aetiology of this tumour, probably because of their role in maintaining a quiescence state in the NE stem cell population (Ouadah et al., 2019). The importance of these two proteins is highlighted by the fact that inactivation of only these two genes is sufficient to induce SCLC in the mouse lung (Meuwissen et al., 2003). Moreover, genomic studies proved that complementary mechanisms of *TP53* and *RB1* inactivation can take place when these genes are wild-type (WT). George *et al* noted that in two patients affected by chromothripsis with WT RB, there was an overexpression of *CCND1* (George et al., 2015). Overexpression of Cyclin D1 is known to hyperphosphorylate RB and inhibit its activity (Resnitzky et al., 1994), therefore becoming an alternative mechanism of RB inactivation in SCLC. Also the RB family member p130 and p107 (*RBL2* and *RBL1,* respectively) can be lost in SCLC (George et al., 2015; Helin et al., 1997). These proteins act by repressing E2F transcription factor in a similar manner than RB (Stengel et al., 2009). Deletion of p130 in $Rb1^{flox/flox};Trp53^{flox/flox}$ mice (TKO) induced

the development of tumours with typical SCLC histopathology but a faster development, suggesting they act as tumour suppressors (Schaffer et al., 2010). p53 is usually inactivated by mutations, however interaction with other member of the p53 family can have suppressive effect. For example, *TP73*, a p53 family member, can produce N-terminally truncated isoforms that lack the TA domain. These isoforms have a dominant-negative effect on p53 (Melino et al., 2002). Somatic aberration in *TP73* have been observed in 13% of SCLC patients. Interestingly, most of those alterations generated N-terminally truncated transcripts that could eventually have oncogenic activities against p53 (George et al., 2015).

Another common genetic feature of SCLC is a non-random deletion of 3p regions with loss of genes like *RASSF1A* (Ras association domain family member 1), *HYAL1* and *2* (hyaluronoglucosaminidase 1 and 2), *SEMA3B* and *3F* (semaphoring 3B and 3F), *FHIT* (fragile histidine triad), *ROBO1* (roundabout guidance receptor 1) and *VHL* (von Hippel-Lindau tumour suppressor) (Gazdar et al., 2017; George et al., 2015). To date, the tumour suppressive role of these genes, if any, remains unclear.

The Notch signalling pathway is involved in the development of the lung, where it regulates NE differentiation (Ito et al., 2000; Morimoto et al., 2012). The Notch ligand Delta Like Canonical Notch Ligand 3 (DLL3) is a direct target of ASCL1. This ligand has an inhibitory effect on the Notch pathway promoting a NE phenotype in ASCL1 expressing cells and is highly express in some SCLC tumours (George et al., 2015; Saunders et al., 2015). The inactivation of this pathway in 25% of SCLC patients, by expression of the Notch inhibitors, DLL3 and DLK1 (Delta Like Non-Canonical Notch Ligand 1) or by inactivating mutations in the extracellular domain of the *NOTCH* members, suggest a tumour suppressive role in SCLC (George et al., 2015). Recent data showed a more complex role of the Notch pathway in SCLC. Lim *et al* demonstrated that the Notch pathway is active in the non-NE subpopulation of SCLC cells and these cells are supportive of their NE counterparts and are relatively more chemoresistant (Lim et al., 2017). This study implies that the Notch pathway may also have an oncogenic potential in specific contexts in SCLC.

Amplification of the three MYC genes, *MYCL1*, *MYCN* and *MYC* has been observed in human SCLC tumours (respectively in 9%, 4% and 6% of the patients, George et al.,

2015). These transcription factors regulate the expression of several genes involved in cell growth, proliferation, differentiation and apoptosis, and have been widely studied as oncogenes (Dang, 2012; Grandori and Eisenman, 1997). Berns and Oliver groups generated SCLC GEMMs by overexpressing *Mycl* (RPML) and *Myc* (RPM) in the RP GEMM, respectively (Huijbers et al., 2014; Mollaoglu et al., 2017; Semenova et al., 2016). In both models, the overexpression of *Mycl* or *Myc* accelerates tumour growth, however, while MYCL-driven tumours expressed NE markers and were $ASCL1^{high}$, the MYC-driven SCLC tumours had lower level of NE markers and expressed a subpopulation of $NEUROD1^{+}$ cells (Mollaoglu et al., 2017; Semenova et al., 2016). Deep genomic analysis of the murine SCLC RP model also demonstrated that *Mycl*-amplified cells had NE features and grew as spheroids on plastic. On the other side, *Mycl* negative cells, derived from the same RP murine SCLC, lost the NE markers and grew adherent to the culture dish, further corroborating the observation that *Mycl* drives a NE phenotype and is always associated with ASCL1 expression (Borromeo et al., 2016; Semenova et al., 2016). *Mycl* amplification has also been recently associated with a different pattern of tumour localisation and these tumours were more intrinsically resistant to cisplatin compared with *Mycl* negative counterpart (Böttger et al., 2019). This work further underscores the heterogeneity of SCLC tumours and the presence of different subtypes with different biology and response to treatment.

Characterisation of the genetic alterations that occur in murine SCLC facilitated identification of a new putative oncogene, the Nuclear factor I/B (NFIB) (Dooley et al., 2011). NFIB is a transcription factor that regulates brain and lung development (Steele-Perkins et al., 2005). NFIB was seen to be highly expressed in 16% of SCLC patients (Dooley et al., 2011) and mouse models with *Nfib* overexpression in the presence of *Trp53* and *Rb1* loss (RPF) showed accelerated tumour initiation and progression compared with RP mice (Semenova et al., 2016; Wu et al., 2016) (Table 1). Other genes altered in SCLC are the acetyltransferases *EP300* and *CREBBP* (in 15% and 13% of patients respectively, (George et al., 2015)), and the lysine methyltransferase, *KMT2D* (8% of the patients, Augert et al., 2017). Alteration of chromatin accessibility is typical in cancers (Hansen et al., 2011) and SCLC has one of

the highest level of methylated CpG islands across all tumours (Poirier et al., 2015). The high methylation instability in SCLC could be an important feature for its progression and the presence of this 'CpG-island methylation phenotype' (CIMP) has been correlated with poorer prognosis in SCLC patients (Saito et al., 2016). Kalari and co-workers observed an enrichment in promoter methylation in genes involved in neuronal fate commitment and neuronal differentiation. They found methylation in regulatory regions of transcription factors like *NEUROD1*, *ZNF423*, *HAND1* and *REST* (Kalari et al., 2013). An additional gene found altered in SCLC is *EZH2*. EZH2, enhancer of zeste homologue 2, is a lysine methyltransferase of the Polycomb repressive complex 2 overexpressed in several cancers (Simon and Lange, 2008). Expression of *EZH2* is higher in SCLC than in any other tumours, and is strictly associated with increased methylation of promoter regions (Byers et al., 2012; Poirier et al., 2015). Multiple studies have demonstrated roles for EZH2 in SCLC. It can repress the TGFβ-SMAD pathway and in turn de-repress *ASCL1* (Murai et al., 2015). EZH2 can also repress *SLFN11*, a protein involved in DNA damage and replication stress (Mu et al., 2016; Murai et al., 2018), induce chemoresistance (Gardner et al., 2017), and promote cell survival by repressing p21 and the pro-apoptotic factors BAD and PUMA (Hubaux et al., 2013).

A small proportion of SCLC patients show alteration in kinase signalling pathways with gain of function mutations in *PIK3CA* (4-6%) and *KIT* (3%), amplification of *FGFR1* (6-10%), *AKT2* (4%), *RICTOR* (14%) and *IRS2* (2%) and loss of function of *PTEN* (~9%), all promoting proliferation and survival (Dowlati et al., 2016; George et al., 2015; Schultheis et al., 2014; Steele-Perkins et al., 2005; Umemura et al., 2014). Mutational analysis of murine RP SCLC showed an enrichment in protein-altering point mutations in the PI3K/PTEN pathways (McFadden et al., 2014). Moreover, deletion of *Pten* in the $Rb1^{flox/flox};Trp53^{flox/flox}$ mouse model exhibited SCLC tumours with shorter latency than the RP mice, bringing attention to the tumour suppressive role of PTEN in these tumours (Cui et al., 2014; McFadden et al., 2014).

Additional oncogenes have been observed in SCLC samples, including BCL-2 and SOX2. BCL-2, a pro-survival protein that antagonizes apoptosis (Edlich, 2018), is frequently overexpressed in SCLC tumour samples (>60%) and has been shown to be

regulated by ASCL1 at the epigenetic level (Ben-Ezra et al., 1994; Byers et al., 2012; Poirier et al., 2015). SOX2 (SRY-high mobility box transcription factor family) is involved in cell reprogramming and regulation of neural differentiation (Zhang and Cui, 2014). This gene is required for proper development of the lung and its overexpression in murine lung epithelium promotes tumorigenesis (Gontan et al., 2008; Lu et al., 2010). This data, together with the observation that *SOX2* is amplified in a subset of SCLC patients, suggests a putative oncogenic role in SCLC (Rudin et al., 2012a).

1.1.4 Conclusions

Although the complex genomic landscape of SCLC is becoming to be unravelled, further effort is required to fully identify the main players as well as elucidate their roles in regulating tumour progression and response to therapies. The presence of SCLC phenotypic subtypes is now generally accepted, with clustering of tumours both at the transcriptional and epigenetic level (Poirier et al., 2015). Gazdar and colleagues recently developed a 50 gene expression classifier for SCLC based on NE status. In both human tumours and cell lines they observed 4 groups: ASCL1 high, NEUROD1 high, dual high and dual low. Genes associated with low NE score were positive for *REST* and *ASCL2*, the Notch family genes, epithelial-mesenchymal transition (EMT) genes (*VIM*, *SNAI2*, *CD44*), *MYC* (but not *MYCL* and *MYCN*), genes in the Hippo pathway including *YAP1* and genes in the TGFβ pathway. On the contrary, *SOX2*, *EZH2* and *NFIB* positively correlated with a positive NE score (Zhang et al., 2018). This classifier partly corroborates the observations made in the past regarding genes involved in NE differentiation status of SCLC tumours (Borromeo et al., 2016; Lim et al., 2017; McColl et al., 2017; Mollaoglu et al., 2017; Poirier et al., 2015; Rudin et al., 2012a; Semenova et al., 2016). It is currently unclear what causes the development of one SCLC subtypes over another one. Epigenetic repression/derepression of specific genomic loci seems to have a role in the different SCLC phenotypes (Poirier et al., 2015), but further studies are needed to define when these modifications take place during tumour evolution. Much of the work mentioned above raises the possibility of exploiting SCLC drivers as candidate targets to stop tumour progression and metastasis. Proof of principle preclinical studies on mouse models and cell lines

have demonstrated the potential of some targets, however more research is needed to translate these findings to the clinic (Byers et al., 2012; Gardner et al., 2014, 2017; Osborne et al., 2013; Poirier et al., 2015; Sato et al., 2013; Saunders et al., 2015). Moreover, further characterisation of the different SCLC subtypes and their molecular alterations may allow stratification of patients to tailor future treatments.

1.2 Clinical management of SCLC patients

SCLC is characterised by a central location, rapid onset of symptoms, high frequency of metastases, and high initial response to chemotherapy (van Meerbeeck et al., 2011). Staging is typically performed with CT scans, PET scans and brain MRI to detect distant metastasis. There are two staging systems for SCLC, the first one was established in the 1957 by the Veterans Administration Lung Study Group (VALSG) and classify SCLC patients depending on whether they have limited-stage (LS) or extensive-stage (ES) disease. Limited-stage disease are tumours confined to one hemithorax with or without extrathoracic diseases which can be encompassed in a single radiation portal, while extensive-stage disease are those cases that cannot be classified as limited-stage (Kalemkerian, 2011). The second staging system was proposed by the IASLC based on the TNM classification for lung cancer (Amin et al., 2017). In the TNM system a tumour is defined according to the size of the primary tumour (T), the presence and number of lymph nodes involved (N), and the presence and number of metastases (M). For SCLC, LS disease is equivalent to TNM stages I-III (T1-3N0-3M0), while ES disease refers to metastatic diseases (stage IV) (Alvarado-Luna and Morales-Espinosa, 2016). Median survival for SCLC patients treated with the chemotherapy standard-of-care (SoC) is of 15-20 months for LS disease and 8-13 months for ES disease. The percentage of patients surviving 2 years drops dramatically in the ES group with only 5% surviving 2 years compared with the 20-40% of LS patients (van Meerbeeck et al., 2011). The SoC chemotherapy for SCLC patients has been defined in the 1980s and has not changed since then. Platinum based chemotherapy in combination with etoposide with or without thoracic irradiation with or without prophylactic cranial irradiation (PCI) are the gold standard of SCLC treatments and are discussed below (Farago and Keane, 2018; van Meerbeeck et al., 2011).

1.2.1 Standard treatment selections for SCLC patients

1.2.1.1 Surgery and adjuvant chemotherapy

Because of the presence of metastasis, surgery with curative intent is performed only on subset of LS disease. Limited-stage diseases account for 30% of all SCLC, of which 5% are considered 'very limited stage' (T1-2N0M0). This small group of patients can undergo lobectomy with mediastinal node resection followed by adjuvant chemotherapy regiments to improve overall survival (OS) (Shepherd et al., 1988; Yang et al., 2016).

1.2.1.2 Combinatorial therapy for limited stage disease patients

Most LS SCLC patients are diagnosed with lymph node involvement and therefore, surgery is not considered as an option. For those patients, SoC consists of a platinum-based agent (cisplatin or carboplatin) in combination with etoposide (VP-16) and concurrent thoracic radiation (Wood et al., 2018). The efficacy of combining platinum-based agents with etoposide (EP treatment) became evident in the 1980s and two meta-analysis confirmed the superiority of EP regimens over other treatments (Mascaux et al., 2000; Pujol et al., 2000). In these studies, a better OS and toxicity profile were obtained with the EP treatment. This work was followed by a randomised study with 436 SCLC patients that directly compared the chemotherapy regimen of cyclophosphamide, epirubicin and vincristine (CEV) with EP treatment. In the LS patients the median OS was 14.5 months *vs* 9.7 months in the EP and CEV groups, respectively. No differences were observed in ES patients (Sundstrøm et al., 2002). All these data led to the approval of platinum-based therapy in combination with etoposide as the SoC for all stage SCLC patients.

The addition of adjuvant thoracic radiotherapy (TRT) to chemotherapy regimens became available in the early 1990s when meta-analysis from Pignon *et al* and Warde *et al* showed an OS benefit at 3 years of 5.4% in the chemotherapy plus radiotherapy arm (Pignon et al., 1992; Warde and Payne, 1992). This combined treatment reduced the recurrence in the chest, however brain metastasis became one of the main sites of relapse (Pignon et al., 1992). For this reason, prophylactic cranial irradiation (PCI) is recommended after chemoradiotherapy. A meta-analysis performed by Auperin and co-workers on 987 SCLC patients with complete remission showed a 5.4%

increase in 3 year survival rate and a reduced incidence of brain metastasis of 54% (Aupérin et al., 1999). The standard dose is now 25 Gy in 10 fractions (Le Péchoux et al., 2009).

1.2.1.3 Clinical care of extensive stage disease patients

First-line treatment of ES disease has only a palliative intent, as these patients are considered incurable with a median OS of 9-11 months. The overall response rate of ES patients to EP treatment is ~70%, showing a high sensitivity of these tumours to chemotherapy. However, virtually all patients inevitably relapse within 6 months (Sabari et al., 2017). Despite the rapid onset of progression, the SoC treatment for these patients has remained unchanged over the past 30 years, mainly because of the lack of benefit of other regimens compared with EP treatment (Farago and Keane, 2018). Carboplatin, another platinum-based agent, can be used in place of cisplatin as the backbone for first-line therapy of ES patients (Rossi et al., 2012). Irinotecan, an alternative to etoposide, is routinely used in Japan to treat patients with SCLC. Only recently, the US Food and Drug Administration (FDA) approved the PDL-1 inhibitor, atezolizumab, in combination with cisplatin and etoposide as new first-line regiment for ES SCLC patients (Horn et al., 2018).

Prophylatic cranial irradiation can be given to ES patients but after careful consideration. A recent trial examined the effect of PCI on ES patients that had no response to chemotherapy and no presence of brain metastasis. They observed that although patients treated with PCI had a reduced incidence of brain metastasis (32.9% *vs* 59% at 12 months in the PCI treated and observation group, respectively), PCI did not lead to an improvement in OS and was associated with toxicities, such as anorexia, malaise and muscle weakness (Takahashi et al., 2017).

Thoracic radiotherapy is routinely proposed to LS patients, however, in the setting of ES disease, chest radiation is usually performed only as palliative treatment upon relapse. A meta-analysis showed an improvement of 20% in OS for the patients who received chemotherapy, PCI and TRT *vs* patients that did not receive TRT. Similar toxicities were observed in both groups (Palma et al., 2016).

1.2.1.4 Second- and third-line treatments

As mentioned before, virtually all SCLC patients with ES disease relapse within 6 months from the end of treatment. Patients that progress after 3 months of completing the first-line treatment are considered 'chemosensitive'. Patient who initially responded to treatment and then relapsed within 3 months of completing the first-line regimen are classified as 'chemoresistant', while patients who never responded to first-line regimen are considered 'chemorefractory' (van Meerbeeck et al., 2011). Second-line treatment following relapse depends on the duration of the initial response and the performance status of the patient with regards to their ability to cope with further cytotoxic challenge (van Meerbeeck et al., 2011). Re-challenge with first-line treatment is an option for chemosensitive SCLC patient, even if the benefits of this treatment are still debated (Giaccone et al., 1987; Vincent et al., 1988; Wakuda et al., 2012). In general, the group of chemosensitive SCLC patients respond better to second-line therapies than chemoresistant or chemorefractory patients (Owonikoko et al., 2012), but still, median OS for all these patients is only 4-5 months (Alvarado-Luna and Morales-Espinosa, 2016). Second-line therapies have the main advantage of improving the quality of life of relapsed SCLC patients, even if with limited gain in their survival. Topotecan is the only FDA and European Medicines Agency (EMA) approved second-line therapy for SCLC. Relapse SCLC patients treated with topotecan have shown improved OS and better quality of life compared with best supportive care (O'Brien et al., 2006), a response that is better or similar to the one obtained with other second-line chemotherapies (Furuse et al., 1996; Masters et al., 2003; Masuda et al., 1992; Smit et al., 1998; Smyth et al., 1994).

Advances in the clinical management of SCLC are needed to identify alternative treatments for relapsing SCLC patients.

1.2.2 Mechanisms of action of chemotherapies

Ninety-five percent of ES SCLC patients progress over first-line treatment and have very limited therapeutic options at progression. The impressive initial response of most SCLC patients to platinum based chemotherapies has made this regimen an inevitable option for these patients. Understanding the mechanisms behind the different responses to SoC is essential to allow better management of these patients

and the identification of alternative effective treatments. A few studies have tried to untangle the mechanisms of resistance to chemotherapies in SCLC preclinical models and are discussed below.

1.2.2.1 Platinum-based agents

Cisplatin

Cisplatin (cis-diamminedichloroplatinum(II)) is a platinum-based drug that works by interacting with DNA (Figure 3A). It is administered intravenously and undergoes an aquation reaction to generate a reactive species. During this reaction, one or both chlorine groups are substituted by a molecule of water generating a reactive species able to interact with several nucleophiles, including antioxidant molecules and the purine bases of DNA (El-Khateeb et al., 1999; Siddik, 2003). In particular, the reaction of the activated platinum (Pt) molecule with the N7-sites of purine bases produces DNA-protein and DNA-DNA interstrand (involving guanines on opposite DNA strands in 2% of cases) and intrastrand (60-65% of 1,2-d(GpG), 20-25% 1,2-d(ApG) and 5-10% 1,3-d(GpNpG)) crosslinks, the main cytotoxic effect of cisplatin (Kartalou and Essigmann, 2001). These DNA adducts cause distinct distortion of the DNA helix that can be recognised by specific proteins (Coste et al., 1999; Garderen and Houte, 1994; Gelasco and Lippard, 1998).

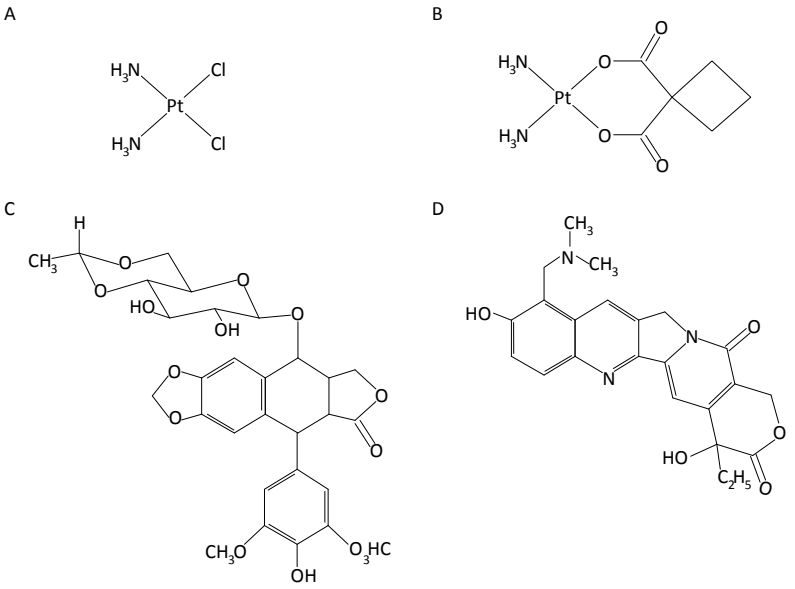

Figure 3. Chemical structure of chemotherapeutic agents.

Chemical structures of cisplatin (A), carboplatin (B), etoposide (C) and topotecan (D) are depicted.

One of the most understood effects of Pt-DNA complexes is their interference with DNA polymerases during replication. This causes stalled replication forks that can be toxic for the cells and are a signal to recruit TLS polymerases. This group of polymerases have a larger active site pocket that allows to accommodate the distorted template and restart replication (Sale, 2013) (Figure 2C, Figure 4).

Other proteins that recognise platinum-induced DNA adducts belong to DNA repair pathways, such as mismatch repair (MMR), NER and BER, high mobility group (HMG) box proteins and transcription factors (Kartalou and Essigmann, 2001) (Figure 4). HMG box proteins are involved in different cellular processes including chromatin structure, DNA replication, DNA repair, transcription and chromatin assembly, and their role in response to cisplatin is controversial. These proteins have the ability to recognise non-canonical DNA structures and can act as sensors of DNA damage activating different downstream pathways (Wang and Lippard, 2005). HMGB1 can bind to DNA adducts and shield them from NER proteins, impeding DNA repair and contributing to the cytotoxic effect of cisplatin (Huang et al., 1994). At the same time, HMGA1 can interact with p53, increase its affinity for damaged DNA and therefore promote p53-dependent DNA repair (Imamura et al., 2001). Other HMG box proteins are involved in RNA synthesis and can interact with cisplatin-induced DNA adducts. Sequestration of these factors at the level of DNA damage reduces their availability for RNA synthesis, accounting for one of the toxic effects of cisplatin (Jordan and Carmo-Fonseca*, 2000) (Figure 4).

The NER pathway is the main repair pathway implicated in the response to cisplatin (Figure 4, Figure 2A). Studies on ovarian, gastric and lung cancers have shown that overexpression of the NER excision protein ERCC1 positively correlates with resistance to cisplatin, underscoring the role of NER in repairing cisplatin-induced DNA adducts (Dabholkar et al., 1994; Lord et al., 2002; Metzger et al., 1998). Moreover, testis tumour cell lines exquisitely sensitive to cisplatin treatment showed a reduced levels of different members of the NER pathway (Welsh et al., 2004).

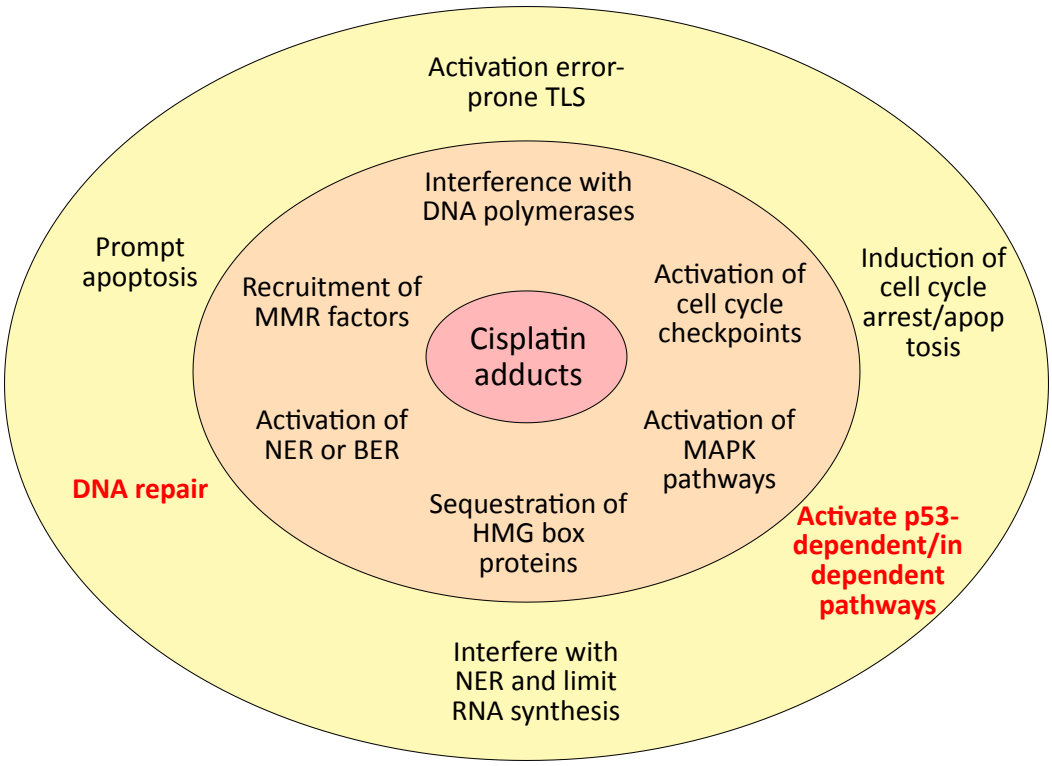

Figure 4. Mechanisms of response to cisplatin-DNA adducts.

The orange circle summarises the responses activated when cisplatin binds the DNA. In the yellow circle are highlighted the consequences of activating specific pathways. In bold red are mechanisms that could impede the cytotoxicity of cisplatin.

Another pathway activated upon cisplatin treatment is the MMR cascade. This pathway plays a role in the removal of base-pair or insertion/deletion mismatches introduced during DNA replication (Li, 2008). Cisplatin adducts cannot be repaired by the MMR pathway, yet these proteins are still recruited at the site of the lesion, where, unable to repair the damage, they prompt the apoptotic cascade (Figure 4).

Cell cycle checkpoints are fundamental to allow the cells to repair the damage before progressing to the next phase of the cell cycle. Main players in the activation of cell cycle checkpoints upon DNA damage are the ataxia-telangiectasia mutated protein, ATM, and its related ataxia-telangiectasia and Rad3 related protein, ATR. These proteins are activated in response to single-strand/double-strand DNA junctions, which can be an intermediate of NER and stalled replication forks (Smith et al., 2010). ATR seems to be the primary sensor induced by cisplatin treatment, triggering p53 activation and cell cycle arrest (Damia et al., 2001). Induction of apoptosis upon cisplatin treatment can be reached also by the activation of a p53-

independent pathway. Gong *et al.* showed that there is a c-ABL/p73 parallel apoptotic pathway, and that the amount of p73 increased in cells treated with cisplatin (Gong et al., 1999). Other p53-independent pathways have been proposed, underlining strong cell-type specificity (Bae et al., 2006). The presence of p53-independent apoptotic pathways could explain the extreme chemosensitivity observed in some SCLC patients, in which p53 is almost universally lost. These differences in how the cells deal with the cytotoxic effect of cisplatin mirror the complexity of this response that depend on the cellular context, as well as the presence of additional genomic alteration or stresses that can prompt a cells towards survival or apoptosis (Figure 4).

Carboplatin

Carboplatin is a cis-diammine (1,1-cyclobutanedicarboxylato)platinum(II) compound. Like cisplatin, it exhibits a Pt^{2+} core and can intercalate with DNA, tubulin and other proteins (Pasqua et al., 2012) (Figure 3B). Whilst the exact mode of action of carboplatin has to be evaluated, carboplatin and cisplatin generate the same cytotoxic effect and therefore can be considered broadly equivalent (Knox et al., 1986). There are many controversies about the real improvements conferred by carboplatin-based therapy in SCLC patients, with the main differences observed in the adverse events produced: carboplatin primarily causes haematological toxicities, and cisplatin nephrotoxicity and neurotoxicity (Rossi et al., 2012). Consideration of these side effects are important during treatment selection.

1.2.2.2 Topoisomerase inhibitors

Etoposide

Etoposide, one of the first-line drugs used for SCLC patients, is an inhibitor of topoisomerase II (Figure 3C). Topoisomerases are enzymes that regulate the coiling of the DNA helix during DNA compaction and when the DNA strands are separated to allow replication or transcription (Champoux, 2001). They do so via a transesterification reaction during which a tyrosyl oxygen of the enzyme covalently binds to the phosphate group at the DNA break and, simultaneously, cleaves the phosphodiester bond between adjacent nucleotides. The reverse reaction is performed to re-join the DNA strand (Wang, 2002). In the absence of

topoisomerases, the double-strand helix of the DNA can produce supercoiling structures that block the process of replication and transcription or cause the formation of abnormal DNA structures (Pommier et al., 2010). There are six different topoisomerases encoded in the human genome that can be grouped into 3 families: type 1A (TOP3α and TOP3β), type 1B (TOP1 and TOP1mt) and type 2A (TOP2α and TOP2β). These three families have different mode of action to cut and re-ligate the DNA, however they all form a topoisomerase cleavage complex (TOPcc) with the altered DNA helix (Pommier et al., 2016a). Etoposide targets the TOP2 cleavage complex (TOP2cc) preventing the re-ligation of the DNA by the enzyme. This causes a trapping of the TOP2cc on the DNA with subsequent inhibition of replication and transcription, as well as the formation of single- and double-strand breaks (SSB and DSB) (Nitiss, 2009). As a result, DNA damage response (DDR) pathways are activated and failure to do so induces programmed cell death. The mechanism of cytotoxicity caused by etoposide is not completely understood. Etoposide, compared with other TOP2 poisons, does not act as DNA intercalating agent. It generates mainly SSB and it traps both TOP2α and TOP2β very effectively (Kerrigan et al., 1987; Long et al., 1985; Willmore et al., 1998). The trapped TOP2cc has to be removed to allow replication and transcription to continue. The repair pathways involved are not completely characterised, but several proteins have been identified that implicate non-homologous end joining (NHEJ) is the pathway of choice to repair this type of damage (Adachi et al., 2003). Homologous recombination (HR) may also be activated upon generation of DSB by TOP2 poisons, while SSB are probably repaired by the single-strand annealing (SSA) pathway (Nitiss, 2009). Activation of the NHEJ pathway upon treatment with etoposide has been linked to the main side effect of this drug: the development of secondary cancers such as treatment-induced acute myelocytic leukemia (t-AML) (Mistry et al., 2005). This effect has been preferentially associated with the binding of etoposide to TOP2β, therefore development of more TOP2α specific drugs is encouraged (Azarova et al., 2007).

Topotecan

In contrast to etoposide, topotecan is a topoisomerase 1B inhibitor, administered as second-line therapy in SCLC. It is a water-soluble derivative of the natural product

camptothecin (CPT) (Pommier et al., 2010). Topotecan binds the TOP1cc and, as etoposide, it inhibits the ability of TOP1 to re-ligate the DNA. The chemical structure of topotecan presents a ring that mimics a DNA base pair, allowing its intercalation in the DNA and interaction with both the upstream and downstream base pairs (Figure 3D). In this way, topotecan acts as a uncompetitive inhibitor of TOP1 (Staker et al., 2002). The crosslink induced by topotecan does not directly damage the DNA but interferes with replication and transcription by causing the collapse of both the replication fork and RNA polymerase. The process to repair the lesions induced by topotecan are similar to the one exploited to repair etoposide-induced lesions (Lin et al., 2009; Yang et al., 1996). Another mechanism involved in the repair of the lesions induced by topotecan is the regression of the replication and transcription complexes. This process is facilitated by the BLM helicase in association with TOP1A (Pommier et al., 2006).

1.2.3 Mechanisms of chemoresistance to chemotherapies

As discussed above, the response of most SCLC patients to first-line chemotherapy is impressive but relapse is inevitable and it is in the second-line setting that there is a clear unmet clinical need. To find new second-line therapeutic options or to improve the existing first-line regimens, it will be crucial to better understand the mechanisms of chemotherapy resistance that frequently develop. Described below are the main mechanisms of resistance to standard chemotherapy identified so far in SCLC (summarised in Figure 5). These mechanisms can be divided in 4 groups, depending on the process in which they are involved as suggested in the review by Galluzzi *et al* (Galluzzi et al., 2012).

1.2.3.1 Pre-target mechanisms of chemoresistance

The most studied potential chemotherapy resistance mechanism in SCLC is the reduced drug accumulation and increased drug efflux caused by the activity of the drug pumps multidrug resistance protein 1 (MDR1, aka ABCB1 or P-glycoprotein 1), multidrug resistance-associated proteins (MRPs) and lung resistance-associated protein (LRP aka MVP). Substrates for these drug pumps include etoposide and cisplatin and different studies have shown a correlation between pump expression and response to these drugs in SCLC patients and PDX (Canitrot et al., 1998; Hsia et

al., 2002; Poupon et al., 1993; Triller et al., 2006, 2006; Yeh et al., 2005). Despite the putative role these pumps have in SCLC chemoresistance, clinical trials with the MDR1 inhibitors verapamil or megesterol acetate in addition to chemotherapy during first-line treatment failed to show improvement in response rate and survival (Milroy, 1993; Stewart, 2010; Wood et al., 1998).

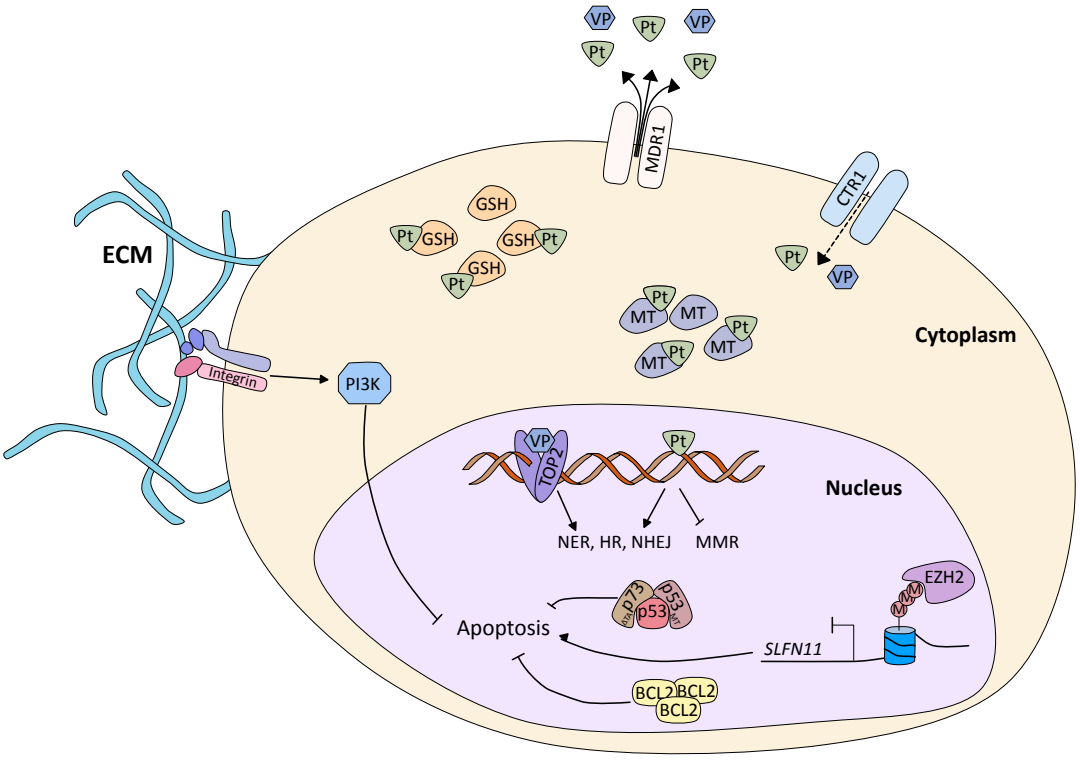

Figure 5. Suggested mechanisms of resistance to cisplatin and etoposide.

The main effect of cisplatin (Pt) and etoposide (VP) resides in their ability to induce DNA damage. Increased efflux of these compounds as well as reduced intake may affect their efficacy. Moreover, interaction of cisplatin with intracellular nucleophiles, like glutathione (GSH) and metallothionein (MT), can sequester it from binding the DNA. Once in the nucleus, cisplatin and etoposide bind to their target (DNA and TOP2, respectively) and trigger different DNA damage repair pathways. Deficiency of the MMR or hyperactivation of NER, NHEJ and HR allow the cells to repair the damage and survive. If the damage cannot be repaired, apoptosis can be induced by p53 or SLFN11. Inactivation of these proteins by mutations or epigenetic silencing render the cells resistance to drug-induced apoptosis. Moreover, overexpression of survival proteins, like BCL-2 or hyperactivation of the PI3K pathway, can compete with induction of apoptosis. For more details, refer to the main text. NER, nucleotide excision repair; HR: homologous recombination; NHEJ: non-homologous end joining; MMR: mismatch repair; ECM: extracellular matrix; MT: metallothionein; GSH: glutathione; Pt: cisplatin; VP: etoposide; p53MT: mutant p53; ΔTAp73: mutant p73; M: methylation.

Another potential mechanism of drug resistance is reduced drug uptake. An important protein for cisplatin uptake is the copper transporter 1 (CTR1), a transmembrane protein involved in the transport of copper in the cells. This transporter has been involved in the uptake of platinum-based agents (Song et al., 2004), and different studies have demonstrated that reduced level of CTR1

correlated with resistance to cisplatin and EP treatment in ovarian carcinoma cell lines and stage III NSCLC patients (Chen et al., 2012; Holzer and Howell, 2006; Holzer et al., 2004). Although this has not yet been observed in SCLC.

As mentioned previously, cisplatin requires aquation to become active. The aquated cisplatin can interact in the cytoplasm with nucleophilic species, such as glutathione (GSH), metallothionein (MT) or other cysteine-rich proteins (El-Khateeb et al., 1999; Siddik, 2003). These cisplatin-protein interactions may play a role in the cytotoxic effect of the drug. The sequestration of GSH molecules by cisplatin decreases their availability for ROS detoxification, contributing partially to the toxic effect of cisplatin. However, the interaction between cisplatin and GSH reduces the amount of drug available to interact with the DNA. Increases in GSH levels or its synthetase activity, or increased levels of metallothionein, have been correlated with resistance to cisplatin in SCLC cell lines (Kasahara et al., 1991; Meijer et al., 1990). Moreover, polymorphisms in the glutathione metabolic pathway were found in SCLC patients and were associated with survival (Sun et al., 2010; Yang et al., 2006).

1.2.3.2 On-target mechanisms of chemoresistance

While cisplatin has a broad activity on several nucleophiles, etoposide specifically targets TOP2 proteins. Therefore, changes in the nuclear availability of these proteins can interfere with the cytotoxic activity of the drug. A few studies on SCLC patients have correlated the expression of TOP2α and TOP2β to the response to chemotherapy. In particular, high level of TOP2α protein or mRNA correlated with worse survival and reduced response to EP treatment (Ceppi et al., 2008; Dingemans et al., 1999; Karachaliou et al., 2013). Mutation in TOP2 genes may also generate isoforms that are not efficiently recognised by the drug. In one study, analysis of *TOP2A* gene sequence before and after treatment with etoposide-containing regimen, showed that one SCLC patient had acquired two missense mutations on *TOP2A* (Kubo et al., 1996). All these data suggest that alterations of TOP2 enzymes can be selected during treatment and generate drug resistant diseases.

Cisplatin lesions have to be repaired for the cells to survive. The NER pathway is the primary response of the cells to cisplatin-induced DNA damage and alterations in some members of the pathway have been associated with cisplatin resistance in

different tumours. A few studies demonstrated that a low level of the NER ssDNA endonuclease, ERCC1, prior to treatment with cisplatin-based regimens was predictive of better OS and PFS in LS patients (Ceppi et al., 2008; Karachaliou et al., 2013; Lee et al., 2008; Sereno et al., 2012). However, more studies are required to assess the role of the different members of the NER pathway in platinum resistance in SCLC.

The MMR pathway is also involved in the recognition of the cisplatin-induced DNA adducts, however, contrary to NER that can repair these types of lesions, MMR fails and triggers the apoptotic response. Therefore, tumours with proficient MMR will be more sensitive to cisplatin than tumours with deficiency in this pathway. Loss of MMR members, such as hMLH1 and hMSH2, have been associated with resistance to cisplatin-based chemotherapy in different tumours (Aebi et al., 1996; Watanabe et al., 2001). However, no work has been published yet where the MMR pathway is assessed in SCLC patients treated with EP regimens.

One study by Hansen *et al* assessed the role of HR in the response to etoposide in SCLC cell lines. They demonstrated that cells with higher level of RAD51 were more resistant to etoposide treatment (p-value < 0.05), suggesting that HR may play a role in repairing etoposide induced DSBs (Hansen et al., 2003). This study fits with other works performed on different tumour types where the roles of the HR and NHEJ pathways in chemoresistance were proposed (Galluzzi et al., 2012; Stewart, 2010). Recently, Cardnell *et al* performed a proteomic profile of SCLC cell lines and generated a DNA repair score based on the average expression of 17 DNA repair proteins. These proteins included MSH2, XRCC1, the MRN complex, phospho-CHK1 and RAD51. Interestingly, SCLC cells with high DNA repair score (and therefore higher expression of these proteins) showed a trend towards increased sensitivity to cisplatin (p-value = 0.046), suggesting that downregulation of some DNA repair proteins could be involved in the resistance to cisplatin (Cardnell et al., 2013). Validation of all these findings in SCLC patients is awaited.

1.2.3.3 Post-target mechanisms of chemoresistance

Platinum-based drugs, as well as topoisomerase inhibitors, act by inducing cell death. Cancer cells can overcome treatment by suppressing this outcome. This can

be achieved through a variety of mechanisms, including direct modulation of the apoptotic cell death cascade. One of the main actors in the induction of apoptosis upon DNA damage is p53 (Roos and Kaina, 2006). As mentioned previously, p53 is almost universally altered in SCLC and seems poorly associated with chemotherapy response (D'Amico et al., 1992; Lohmann et al., 1993). Mutant and WT p53 protein expression has been assessed on several SCLC biopsies, but the correlation with the response to chemotherapy was controversial (Kawasaki et al., 1998; Oshita et al., 2004). A more recent genomic study on ES SCLC patients found that patients with p53 mutations that interfere with the DNA binding domains of p53 or cause a stop-codon had a better response to chemotherapy compared with patients with WT p53 (*p*-value = 0.049), however, PFS and OS were similar between the two groups (Dowlati et al., 2016).

Unrepaired DNA damage after exposure to cisplatin and etoposide activates different apoptotic pathways and strategies to avoid their activation could be exploited by the tumour cells to survive. Overexpression of the anti-apoptotic protein BCL-2 has been observed in almost 60% of SCLC and has been associated with chemoresistance in some studies (Ikegaki et al., 1994; Jiang et al., 1995; Kim et al., 2006; Sartorius and Krammer, 2002; Zangemeister-Wittke et al., 1998). Indeed, inhibition of BCL-2 with *BCL2* antisense oligonucleotides (ODN) showed synergistic effects with cisplatin, etoposide and doxorubicin, while overexpression of *BCL2* in BCL-2 low cells reduced sensitivity to cisplatin *in vitro* (Sartorius and Krammer, 2002; Zangemeister-Wittke et al., 1998). BCL-2 expression correlated with worst survival in an analysis performed on 93 chemonaïve SCLC patients (*p*-value = 0.02), but the same correlation was not observed in a later study (Dingemans et al., 1999; Lee et al., 2008). Biswas and co-workers, demonstrated that the cisplatin resistant variant of the H69 cell line loses BCL-2 expression, arguing that BCL-2 is not the main driver of cisplatin resistance in this cell line (Biswas et al., 2004). Moreover, clinical trials testing BCL-2 inhibitors on unselected ES SCLC patients showed disappointing results because of lack of efficacy (Rudin et al., 2008, 2012b).

Another mechanism of resistance to etoposide-induced apoptosis has been suggested by Pardo *et al*. They showed, in SCLC cell lines, that FGF-2 growth factor can induce the formation of the PKCε-BRAF-S6K2 complex able to upregulate the

anti-apoptotic proteins BCL-xL and XIAP (Pardo et al., 2006). Presence of high serum level of basic FGF has been associated with poor prognosis in chemonaïve SCLC patients, implying a putative mechanism of intrinsic chemoresistance (Ruotsalainen et al., 2002).

Major pathways in cell proliferation and survival are the MAPK/ERK and PI3K/AKT pathways (Downward, 2004; Zhang and Liu, 2002). These pathways are frequently hyperactivated in cancers, underscoring their importance in promoting survival under several other stimuli (Dhillon et al., 2007; Fruman and Rommel, 2014). While alteration of the MAPK/ERK pathways are rare in SCLC, a small percentage of SCLC patients present with activating mutations in *PIK3CA*, *AKT2/3* and *MTOR*, and loss of function of *PTEN* (Dowlati et al., 2016; George et al., 2015; Umemura et al., 2014). AKT can directly phosphorylate the pro-apoptotic protein BAD, preventing BAD from blocking BCL-2 activity. Moreover, AKT can bind and phosphorylate MDM2 and stimulate its inhibitory effect on p53, thus blocking p53-induced apoptosis (Downward, 2004). Krystal *et al* demonstrated that constitutive activation of AKT in SCLC cell lines reduced etoposide-induced apoptosis (Krystal et al., 2002). Moreover, activation of the PI3K/AKT pathway via interaction with the extracellular matrix (ECM) induces drug resistance to chemotherapies, in particular etoposide, in SCLC cell lines (Hartmann et al., 2005; Hodkinson et al., 2006; Kraus et al., 2002; Tripathi et al., 2017; Tsurutani et al., 2005). This effect was mainly driven by integrin−mediated interaction of tumour cells with the ECM. Another association between the activation of the PI3K pathway and response to cisplatin comes from the study of Cardnell *et al* where they observed that SCLC cell lines with greater PI3K/AKT activation (in particular higher phospho-AKT) were more resistant to cisplatin (Cardnell et al., 2013).

1.2.3.4 Off-target mechanisms of chemoresistance

As mentioned before, the classification of SCLC as variant or classic is not comprehensive of the complexity observed in the patients. More phenotypic subgroups are emerging and their role in chemoresistance is not yet understood. Lim and co-workers described a model in which the activation of the Notch pathway generated a subpopulation of non-NE SCLC cells that proliferated slowly and were

chemoresistant. Expression of HES1, a downstream target of NOTCH, in tumours from SCLC patients negatively correlated with survival, suggesting NOCTH activation in SCLC can contribute to chemotherapy resistance (Lim et al., 2017). The MYC-overexpressing RPM GEMM (Mollaoglu et al., 2017) developed SCLC tumours which contained cells with both classic and variant morphologies. Despite having a variant morphology, these tumours were sensitive to cisplatin and etoposide treatment but quickly developed resistance (Mollaoglu et al., 2017). The mechanism underlying resistance to cisplatin/etoposide in the RPM mice was not defined, however it is possible that *Myc* overexpression drives an 'intermediate' phenotype that can rapidly evolve in chemoresistance. The MYC family members are considered proto-oncogenes (Dang, 2012; Grandori and Eisenman, 1997), and initial studies on SCLC cell lines suggested that amplification of the MYC family genes was more common in cell lines derived from patients previously treated with chemotherapies (Johnson et al., 1996).

McColl *et al* identified a new subpopulation of SCLC patients expressing the YAP protein (McColl et al., 2017). In their study, they suggested that the YAP^+ group was more chemoresistant than the YAP^-. This was correlated with the presence of a WT RB, however they did not provide any mechanistic insight into this phenomenon (McColl et al., 2017). The role of RB in SCLC chemoresistance is contradictory, with some preclinical data suggesting that WT RB can induce resistance to cisplatin and etoposide, however evidence in patients is not consistent (Shimizu et al., 1994).

Epigenetic plasticity can also account for the acquisition of resistance during anticancer treatments (Liau et al., 2017; Sharma et al., 2010). Gardner *et al* generated acquired chemoresistance in 10 SCLC PDX models by repeatedly treating chemosensitive PDX with cisplatin/etoposide until resistance occurred (Gardner et al., 2017). Transcriptomic comparison of the chemosensitive *vs* chemoresistant paired PDX showed a recurrent downregulation of Schlafen family member 11 (SLFN11) in the chemoresistant models. The SLFN family has structural similarity with the RNA helicases and SLFN11 has been shown to destabilise the RPA-ssDNA complex, resulting in a lethal replication block and HR repair inhibition (Mu et al., 2016; Murai et al., 2016, 2018). Gardner and co-workers showed that SLFN11 inhibition was driven by epigenetic silencing induced by EZH2, and treatment with

the EZH2 inhibitor, EPZ011989, prevented the emergence of resistance and augmented chemoresponse *in vivo*. Moreover, assessment of SLFN11 protein expression on a tissue microarray (TMA) of SCLC patients showed that SLFN11 was higher in patients who responded to chemotherapy, however no differences in the OS of SLFN11 high and SLFN11 low patients was observed (Gardner et al., 2017).

Very few of the highlighted mechanisms have been tested in the clinic, and where functional testing experiments have been performed, most of them were in established cancer cell lines and GEMMs. Whether any of the mechanisms fully account for resistance to chemotherapies in SCLC seems unlikely. Instead, several mechanisms of resistance probably work in parallel to render SCLC cells insensitive to chemotherapy, and each tumour may utilise a different combination of mechanisms. Recently, Böttger and co-workers demonstrated that different mechanisms of cisplatin resistance can co-exist in the NFIB-amplified RPF GEMM (Böttger et al., 2019). They demonstrated that the resistant phenotype was driven by a population of $CDH1^{high}/CGRP^{high}/NFIB^{low}$ cells. Interestingly, these cells growing in the central compartment of the lung were different from the same population in the alveolar lesions. While resistance in the first population was mainly driven by an AKT-dependent metabolic switch and a more epithelial phenotype, the latter population showed differential expression of proteins involved in drug metabolism (such as cytochrome P450 and glutathione S-transferase) (Böttger et al., 2019). It has to be taken into consideration that the mechanisms of chemoresistance described in SCLC GEMMs may not be the same as the one observed in the patient. However, if the described scenarios do occur in patients, it becomes fundamental to identify biomarkers that could comprehensively define the nature and number of mechanism(s) of resistance present in a tumour to personalise treatment accordingly. Also, it is unclear whether there is a difference between mechanisms of intrinsic and acquired resistance in SCLC, and this will only become apparent as more clinical samples are analysed. The similarity between DNA damage induced by tobacco carcinogens and chemotherapies argues that an analogous selective pressure is applied and could favour the emergence of similar mechanisms of intrinsic and acquired resistance to chemotherapies.

1.2.4 Alternative therapies for SCLC patients

The inevitable relapse of SCLC patients after first-line therapy, the poor response rates, and the short duration of response in the second-line setting highlight the need for new therapies to treat SCLC patients. This could either be a new first-line treatment for a selected population of patients, a maintenance therapy to reduce the probability of relapse after first-line therapy, or an alternative second-line therapy, alone or in combination with topotecan. Several cytotoxic agents have been compared with topotecan in relapsed SCLC patients. For instance, amrubicin (an third generation anthracycline, inhibitor of topoisomerase II) showed an ORR of 44% in the amrubicin arm compared with 15% for the topotecan regimen in previously treated chemosensitive patients (Jotte et al., 2010). In another phase II study, a ORR of 21.3% was also observed in chemoresistant and chemorefractory SCLC patients treated with amrubicin (Ettinger et al., 2010). However, amrubicin failed to replace topotecan as second-line therapy, as a phase III trial showed no significant improvement in the OS of the amrubicin arm compared with the topotecan group (7.5 *vs* 7.8 months, respectively) (von Pawel et al., 2014). Temozolomide (TMZ) is an alkylating agent commonly used in the treatment of glioma patients. TMZ generates methyl adducts on DNA, with the main cytotoxic effect caused by N-7 methylation at the level of 'GGG' motif. These lesions can be recognised and repaired by different pathways including the O^6-alkylguanine DNA alkyltransferase (AGT) encoded by the *MGMT* gene, the MMR and the BER pathways (Newlands et al., 1997). A phase II trial tested the effect of TMZ as second-line therapy for SCLC patients with recurrent disease. The trial did not reach significance for its primary endpoint, however TMZ showed some activity in patients with brain metastasis and patients with methylated *MGMT* promoter showed a greater response than the one with an unmethylated promoter (Pietanza et al., 2012). TMZ has also been tested in combination with the poly(ADP)-ribose polymerase (PARP) inhibitor talazoparib and olaparib on SCLC PDX (Farago et al., 2019; Lok et al., 2017). PARP1 is involved in DNA damage sensing and recruitment of repair proteins during SSB, DSB and replication damage repair (Pommier et al., 2016b). Therefore, inhibition of PARP1 should impair the repairing of the TMZ induced lesions and boost TMZ cytotoxicity. Combination of these inhibitors with TMZ showed some combinatorial efficacy on SCLC PDX, and the

expression of *SLFN11* and inflammatory response genes correlated with a better response, while the EMT regulator *SNAI2* was associated with resistance to this combination (Farago et al., 2019; Lok et al., 2017). A phase II trial to assess the combination of TMZ with the PARP inhibitor veliparib in relapsed SCLC patients showed similar median OS between the TMZ/veliparib and TMZ/placebo (8.2 *vs* 7.0 months, respectively), however the TMZ/veliparib group had a significantly better ORR compared with the TMZ/placebo group (39% *vs* 14%, respectively, *p*-value = 0.016) (Pietanza et al., 2018). Promising initial results were also obtained from a phase I/II trial testing the combination of the PARP inhibitor olaparib with TMZ, where response was observed in 10 out of 19 chemosensitive and 2 out 9 chemoresistant SCLC patients (Farago et al., 2018). The identification of biomarkers of sensitivity to DNA damaging agents is an important step to properly assigned patients to specific treatments. A few studies identified loss of SLFN11 as a predictive biomarker of resistance to PARP inhibition (Lok et al., 2017; Murai et al., 2016; Polley et al., 2016). On this matter, Pietanza and co-workers assessed the role of SLFN11, PARP1 and *MGMT* promoter methylation as predictive biomarkers to TMZ and the PARP inhibitor veliparib in SCLC patients. While no correlation was observed with PARP1 level and *MGMT* methylation, the expression of SLFN11 positively correlated with prolonged OS (*p*-value = 0.014) (Pietanza et al., 2018) (Table 2).

1.2.3.1 Targeted therapies in SCLC

Chemotherapeutic agents have their cytotoxic effect mainly by causing DNA damage that when unrepaired lead to cell cycle arrest and cell death. Targeted therapies developed from the emerging idea that unique features of tumours can be targeted, giving rise to the concept of 'precision medicine'. Genetic and molecular approaches allowed identification of several signalling pathways deregulated in cancer leading researchers to identify means to challenge these alterations (Chae et al., 2017). Unfortunately, despite the emerging information on the molecular alterations in SCLC, no targeted drugs have yet been able to produce significant beneficial effects (Byers and Rudin, 2015) (Table 2).

Table 2. Targeted therapies in SCLC.

Drug	Target	Clinical Trial	Clinical study	Preclinical study	Biomarkers
Amrubicin	TOP2		Ettinger et al., 2010; Jotte et al., 2010; von Pawel et al., 2014		Unknown
Temozolomide	DNA		Farago et al., 2018; Lazzari et al., 2018; Pietanza et al., 2012, 2018	Farago et al., 2019; Lok et al., 2017	*MGMT* methylation
Talazopari	PARP1/2		Bono et al., 2017	Byers et al., 2012; Cardnell et al., 2013	SLFN11
Olaparib	PARP1/2		Farago et al., 2018; Woll et al., 2017	Byers et al., 2012; Cardnell et al., 2013; Farago et al., 2019; Lok et al., 2017; Murai et al., 2014a, 2014b	SLFN11
Rucaparib	PARP1/2			Cardnell et al., 2016; Lok et al., 2017; Murai et al., 2014b	SLFN11
Velipari	PARP1/2		Atrafi et al., 2019; Lazzari et al., 2018; Owonikoko et al., 2018; Pietanza et al., 2018	Lok et al., 2017; Murai et al., 2014a	SLFN11
Ponatinib	pan-RTKs	NCT01935336		Pardo et al., 2006; Sos et al., 2012; Wynes et al., 2014	FGFR1; *FGFR1*
Lucitanib	VEGFR/FGFR	NCT02109016		Pardo et al., 2006; Sos et al., 2012; Wynes et al., 2014	Unknown
				Pardo et al., 2006;	

JNJ-42756493	pan-FGFR	NCT01441297		Sos et al., 2012; Wynes et al., 2014	Unknown
BIBF1120	FGFR/VEGFR /PDGFR	NCT01441297		Pardo et al., 2006; Sos et al., 2012; Wynes et al., 2014	Unknown
Imatinib	BCR-ABL/c-KIT/PDGFR		Krug et al., 2005; Schneider et al., 2010; Spigel et al., 2007	Wang et al., 2000	c-KIT
Crizotinib	MET/HGF			Cañadas et al., 2014	Unknown
Ganitunab	IGF-1R		Glisson et al., 2017; Martínez et al., 2014	Zinn et al., 2013	Unknown
Rilotumumab	IGF-1R		Glisson et al., 2017; Martínez et al., 2014	Zinn et al., 2013	Unknown
Everolimus	PKC/mTOR		Tarhini et al., 2010		Unknown
Temsirolimus	PKC/mTOR		Pandya et al., 2007		Unknown
NVP-LDE225	Smotheened		Pietanza et al., 2016	Park et al., 2011b	SOX2
Vismodegib	Smotheened		Belani et al., 2013		SOX2
Tarexumumab	NOTCH2/3		Daniel et al., 2017		Unknown
ABT737	BCL-2/BCL-xL			Gardner et al., 2014; Hann et al., 2008; Potter et al., 2016	Unknown
ABT263	BCL-2/BCL-xL	NCT03366103	Rudin et al., 2012b	Faber et al., 2015; Potter et al., 2016; Shoemaker et al., 2008	Unknown
vistusertib	mTORC1/2	NCT03366103			Unknown
rapamycin	mTORC1/2			Gardner et al., 2014	Unknown
AZD8055	mTORC1/2			Faber et al., 2015	Unknown
GDC0941	PI3Kα/δ			Potter et al., 2016	Unknown
Rovalpituzumab tesirine	anti DLL3-conjugated antibody	NCT02819999; NCT03033511; NCT03026166; NCT03061812	Carbone et al., 2018; Rudin et al., 2017;	Saunders et al., 2015	DLL3

			TAHOE Trial, 2017		
Lorvotuzumab mertansine	anti CD56-conjugated antibody		Socinski et al., 2017	Whiteman et al., 2014	CD56
Alisertib	AURKA/B		Melichar et al., 2015; Owonikoko et al., 2017	Mollaoglu et al., 2017	MYC
Barasertib/AZD 2811	AURKB	NCT02579226	Burris et al., 2017	Helfrich et al., 2016; Mollaoglu et al., 2017; Oser et al., 2019; Sos et al., 2012	MYC; RB
PF-0384735	AURKA/B			Hook et al., 2012	MYC; MYCN, MYCL
Danusertib hydrochloride	pan-AURK		Schöffski et al., 2015		Unknown
LY3295668	AURKA	NCT03092934		Gong et al., 2019	RB1
ADI-PEG 20	Arginine metabolism	NCT01266018		Chalishazar et al., 2019; Huang et al., 2018a	MYC; ASCL1
Pegzilarginase	Arginine metabolism	NCT03371979			MYC
PF-06821497	EZH2	NCT03460977		Gardner et al., 2017	Unknown
THZ-1	CDK7/CDK12 /CDK13			Christensen et al., 2014	Unknown
Prexasertib	CHK1	NCT02735980		Sen et al., 2017a	MYC; CHK1
PF-477736	CHK1			Doerr et al., 2017	Unknown
AZD7762	CHK1			Doerr et al., 2017	Unknown
VE822	ATR			Doerr et al., 2017	Unknown
AZD6738	ATR			Doerr et al., 2017	Unknown
M6620	ATR	NCT03896503			Unknown
VX-970	ATR	NCT02487095; NCT02589522			Unknown
AZD1775	WEE1	NCT02482311; NCT02937818; NCT02482311; NCT02593019; NCT02511795; NCT02688907	Bauer et al., 2016	Sen et al., 2017b	Unknown

Ipilimumab	CTLA-4		Reck et al., 2013, 2016	Buchbinder and Desai, 2016	Unknown
Pembrolizumab	PD-1		(Gadgeel et al., 2018)		PDL-1
Nivolumab	PD-1	NCT02538666; NCT02481830	Antonia et al., 2016; Owonikoko et al., 2019; Reck et al., 2018		Unknown
Atezolizumab	PDL-1	NCT02763579	Horn et al., 2018		Unknown
Hu5F9-G4	CD47		Sabari et al., 2017	Weiskopf et al., 2016	Unknown

1.2.3.1.1 Tyrosine kinase receptor inhibitors

SCLC depends on several growth factors and paracrine/autocrine signals, such as growth-hormone releasing hormone (GHRH), bombesin (GRP), hepatocyte growth factor (HGF) and fibroblast growth factor 2 (FGF2) (van Meerbeeck et al., 2011). The finding that FGF-2 has an anti-apoptotic effect on SCLC cells (Pardo et al., 2006), the presence of recurrent amplification of FGFR1 in SCLC samples (George et al., 2015; Peifer et al., 2012), and the observed paracrine signalling via Fgf2 and Mapk between non-NE and NE SCLC cells (Kwon et al., 2015), support the hypothesis that inhibition of the FGF receptor may prove efficacious in SCLC. Promising preclinical results were obtained with the FGFR1/3 inhibitor, PD173074 although amplification of *FGFR1* did not always correlate with response (Pardo et al., 2009; Sos et al., 2012). Indeed, subsequent studies demonstrated that mRNA and protein expression of FGFR1 correlated better with sensitivity to the multi RTK inhibitor ponatinib than gene copy number in multiple lung cancer cell lines (Wynes et al., 2014). Clinical trial testing ponatinib (NCT01935336), the VEGFR/FGFR inhibitor lucitanib (NCT02109016), the pan-FGFR inhibitor, JNJ-42756493 (NCT01703481), and the multi-targeted drug BIBF1120 that interferes with FGFR, VEGFR and PDGFR (NCT01441297), are under clinical evaluation in lung cancer patients.

The BCR-ABL, c-KIT and PDGFR inhibitor, imatinib, was the first targeted compound approved for the treatment of chronic myeloid leukemia (Druker et al., 2001), prompting considerable optimism regarding targeted therapies. c-KIT is expressed in a 30-50% of SCLC patients and mutations have been identified in 6% of SCLC patients

(Blackhall et al., 2003; George et al., 2015; Micke et al., 2003). Moreover, SCLC cell lines co-expressing c-KIT and SCF are highly sensitive to imatinib inhibition *in vitro* (Wang et al., 2000). These observations led into the establishment of trials in which SCLC patients were treated with imatinib. Unfortunately, despite the promising results obtained preclinically, none of the phase II trials showed improvement in patient OS and PFS, even when patients were stratified based on c-KIT expression (Krug et al., 2005; Schneider et al., 2010; Spigel et al., 2007). Further negative results were obtained from trials testing the inhibition of the MET/HGF axis, IGF-1R and the PKC/mTOR pathways, despite promising preclinical results (Cañadas et al., 2014; Glisson et al., 2017; Pandya et al., 2007; Tarhini et al., 2010; Zinn et al., 2013).

1.2.3.1.2 NOTCH inhibition

The Hedgehog (Hh) and the NOTCH pathways have been implicated in lung development (Ito et al., 2000; Morimoto et al., 2012; Watkins et al., 2003) and roles for these pathways in SCLC tumorigenesis have been described (Lim et al., 2017; Park et al., 2011b). Constitutive activation of the Hh pathway by adding a constitutively active mutant allele of *Smo* (Smoothened homolog) to RP mice accelerated the formation of SCLC tumours, while loss of *Smo* in the TKO mouse model showed fewer and smaller tumours. Moreover, treatment of a SCLC PDX with the Smo inhibitor, NVP-LDE225, after one cycle of carboplatin/etoposide, prevented tumour recurrence (Park et al., 2011b). In a phase I study, the Smo inhibitor sonidegib (LDE225) was tested on chemonaïve ES SCLC patients in combination with cisplatin/etoposide. Partial responses were observed in 79% of the patients with one durable response in a *SOX2* amplified patient (Pietanza et al., 2016). *SOX2* and *PRKC1* co-amplification in squamous cell lung cancers (LSCC) can activate the Hh pathway by PKCι-mediated SOX2 phosphorylation, posing SOX2 as a putative biomarker of Hh activation (Justilien et al., 2014). Unfortunately, a phase II study comparing the efficacy of the Smo inhibitor vismodegib in combination with cisplatin/etopside on previously untreated ES SCLC patients did not show any improvement in PFS and OS compared with cisplatin/etoposide alone (Belani et al., 2013). In a similar study, the NOTCH2/3 inhibitor tarexumumab in combination with cisplatin/etoposide showed no benefit on the OS and PFS of chemonaïve ES SCLC patients and the drug was discontinued

because of toxicity (Daniel et al., 2017). Again, the absence of response observed in the previous studies could be due to a lack of patient stratification. As suggested by Pietanza and co-workers, *SOX2* amplification may be used to stratify SCLC patients (Pietanza et al., 2016). However, retrospective studies on a larger patient population should be performed in order to confirm the role of SOX2 as predictive biomarker for this treatment.

1.2.3.1.3 Activation of apoptosis

Inhibition of the apoptotic pathway is one of the hallmarks of cancer and can be exploited to evade drug induced cell death (Hanahan and Weinberg, 2011). SCLC can express high levels of the anti-apoptotic protein BCL-2 and therefore various strategies to inhibit BCL-2 have been tested. Initial studies with the *BCL2* antisense oligonucleotides (ODN) were disappointing, probably because of insufficient suppression of BCL-2 *in vivo* (Rudin et al., 2008). ABT737 and the orally bioavailable ABT263 are more specific and more potent inhibitors of BCL-2 and BCL-xL. These molecules are BH3-mimetics that can directly bind BCL-2 and BCL-xL and impede their interaction with BIM (Oltersdorf et al., 2005; Tse et al., 2008). ABT737 and ABT263 have shown promising effects as single agents in some preclinical models of SCLC (Hann et al., 2008; Shoemaker et al., 2008), however the clinical effect of ABT263 in a phase II study for recurrent SCLC patients was underwhelming (Rudin et al., 2012b). To try to improve the apoptotic effect of these molecules, different investigators attempted to identify effective combinatorial treatments. While limited efficacy has been observed with ABT737 in combination with etoposide (Hann et al., 2008), inhibition of the PI3K/AKT/mTOR pathway is more synergistic with BCL-2/BCL-xl inhibition. Gardner and co-workers showed that combination of ABT737 with the mTOR inhibitor rapamycin was synergistic *in vitro* and caused sustained tumour response *in vivo* (Gardner et al., 2014). Faber *et al* combined ABT263 with the mTORC1/2 inhibitor AZD8055 and observed a synergistic effect in SCLC cell lines, GEMM and PDX models. They argued that the observed effect was driven by MCL-1 downregulation (Faber et al., 2015). In a parallel study from our group, Potter *et al* showed that the effect of ABT263 can be increased by the addition of different inhibitors of the PI3K pathway and described BMX, a TEC family member of non-

receptor tyrosine kinase, as a new player in the interplay between PI3K and BCL-2 in SCLC (Potter et al., 2016). Based on all these data a phase I/II trial has been initiated to test the combination of ABT263 with the dual mTORC1/2 inhibitor vistusertib in relapsed SCLC (NCT03366103).

1.2.3.1.4 Inhibition of cell survival signalling

Inhibition of the PI3K/mTOR pathway could be also a promising therapeutic target for a small population of SCLC patients with activating mutations in this pathway (Dowlati et al., 2016; George et al., 2015; Umemura et al., 2014). Based on the results obtained by whole-exome sequencing (WES), Umemura and co-workers tested 4 inhibitors of the PI3K/AKT/mTOR pathway on SCLC cell lines: BEZ235 (PI3K/mTOR inhibitor), BKM120 (PI3K inhibitor), INK128 (mTOR inhibitor) and MK2206 (AKT inhibitor). Interestingly, all cell lines tested were sensitive to these compounds, with a *PIK3CA* mutant cell line the most sensitive (Umemura et al., 2014). A clinical trial testing the PI3K inhibitor BKM120 in combination with cisplatin/etoposide in SCLC patients has been completed (NCT02194049) and another trial testing the effect of the AKT inhibitor, MK2206, in *PIK3CA*-, *AKT*- and *PTEN*-aberrant SCLC is ongoing (NCT01306045). As mentioned before, hyperactivation of the PI3K pathway allows tumour cells to survive and likely promotes resistance to chemotherapies (Cardnell et al., 2013; Kraus et al., 2002; Krystal et al., 2002), suggesting that targeting the chemoresistant subclones with inhibitors of the PI3K/mTOR pathway could help delaying the onset of resistance in SCLC patients. Indeed, in a proof-of-concept study, Kolev and co-workers showed that treatment with the dual PI3K/mTOR inhibitor VS-5584, after response to cisplatin/etoposide, delayed tumour recurrence in SCLC xenografts and PDX (Kolev et al., 2015). They inferred that the delay observed in the arm treated with the VS-5584 was caused by preferentially targeting of cancer stem cells (CSC) dependent on the PI3K/mTOR pathway.

1.2.3.1.5 Targeting tumour initiating cells

Targeting tumour initiating cells (TIC) is an attractive strategy to interfere with the repopulation of a tumour after drug-induced regression (Zhou et al., 2009). SCLC is thought to emerge from the PNECs in the lung and different preclinical studies have demonstrated that targeting mutations present in these NE cells allows the

development of SCLC tumours in mice (Park et al., 2011a; Sutherland and Berns, 2010). Two studies on SCLC have identified a putative subpopulation of TIC with NE characteristic in PDX and GEMM models, respectively. In the first study, Jiang and co-workers identified a population of $ASCL1^{+}/CD133^{high}/ALDH1A^{high}$ SCLC cells with enhanced tumorigenicity (Jiang et al., 2009). Later on, Jahchan *et al* identified a population of cells with $EPCAM^{high}/CD24^{high}/CD44^{low}$ expression in SCLC GEMM (Jahchan et al., 2016). In both studies, the population identified had NE features, was abundant and highly proliferative suggesting that TIC are prevalent in SCLC (~50% of the tumour population). Saunders *et al* developed an antibody-drug conjugate (SC16LD6.5 or rovalpituzumab tesirine) to deliver the cell cycle-independent pyrrolobenzodiazepine (PBD) cytotoxin D6.5 to DLL3 expressing cells only and observed complete and durable responses in DLL3 expressing SCLC PDX. Moreover, SC16LD6.5 treatment of PDX progressing after cisplatin/etoposide, caused a complete tumour response (Saunders et al., 2015). These data suggest that SC16LD6.5 can target a subpopulation of tumour initiating cells unresponsive to SoC. An initial phase I study has been conducted and showed improved PFS in the DLL3 high *vs* DLL3 low SCLC patients (4.5 *vs* 2.3 months) (Rudin et al., 2017). However, a more recent phase III trial testing rovalpituzumab tesirine as second line therapy on advanced SCLC did not show any improvement in the OS of patients treated with rovalpituzumab tesirine compared with topotecan (TAHOE Trial, 2017, NCT03061812). Rovalpituzumab tesirine is under evaluation as frontline or maintenance treatment for SCLC as well as in combination with immune-checkpoint blockade (ICB) (NCT02819999, NCT03033511, NCT03026166).

Another conjugate tested in the clinic is lorvotuzumab mertansine (LM), an anti-CD56 antibody linked to the cytotoxic maytansinoid effector molecule DM1. CD56 is expressed on the majority of SCLC and it is used as diagnostic markers (van Meerbeeck et al., 2011). Maytansinoid is a molecule able to suppress microtubule dynamic (Lopus et al., 2010). LM has been shown to target preferentially $CD56^{+}$ cells *in vitro* and in SCLC xenografts, with durable responses in combination with chemotherapy (Whiteman et al., 2014). In the clinical setting, LM in combination with carboplatin/etoposide did not show any improvement in PFS and OS compared with

carboplatin/etoposide alone, and the incidence of adverse effects was higher in the LM treated group. Therefore the study was discontinued (Socinski et al., 2017).

1.2.3.1.6 Exploiting metabolic dependencies

A recent study by Huang *et al* showed that ASCL1^{high} *vs* ASCL1^{low} human SCLC cell lines had different metabolic profiles (Huang et al., 2018a). In particular, ASCL1^{low} cells expressed high levels of the IMPDH1 and IMPDH2 enzymes involved in *de novo* purine synthesis (Zhao et al., 2015) and were sensitive to inhibition of IMPDH by mycophenolic acid (MPA). In particular, the *Myc*-driven SCLC GEMM was dependent on *de novo* purine synthesis for growth (Huang et al., 2018a). They hypothesised that overexpression of *MYC* accounts for the dependency of some ASCL1^{low} SCLC models on *de novo* purine synthesis, suggesting that targeting of this pathway could be beneficial for *MYC*-amplified SCLC patients (Huang et al., 2018a). Similarly, Chalishazar and co-workers showed that *MYC*-driven but not *MYCL*- and *MYCN*-driven SCLC cells were highly sensitive to arginine depletion (Chalishazar et al., 2019). Depletion of arginine with pegylated arginine deiminase (ADI-PEG 20) *in vivo* reduced tumour growth in both mouse and human MYC-positive SCLC tumours (Chalishazar et al., 2019). ADI-PEG 20 was tested on an unselected population of relapsed SCLC patients and stable disease was observed in 18% of the patients (NCT01266018). Depletion of arginine in ES SCLC patients with pegzilarginase in combination with the anti-PD-1 antibody, pembrolizumab, is ongoing (NCT03371979). Based on the preclinical observation that *MYC*-driven tumours are dependent on arginine to survive, stratification of SCLC patients based on their MYC status is warranted.

The *de novo* pyrimidine biosynthesis pathway has also been shown to be a key vulnerability in SCLC GEMM, PDX and cell lines (Li et al., 2019). In particular, Li *et al* demonstrated that pharmaceutical targeting of DHODH, an enzyme involved in the generation of uridine monophosphate, reduced cell viability and induced tumour regression in mice. Interestingly, the GEMMs used in this study are ASCL1 driven, opening the possibility that while MYC-driven tumours are more dependent on the purine biosynthesis, ASCL1-driven SCLC may be more sensitive to interference with the pyrimidine pathway. Future studies will help dissecting the metabolic

dependencies of the different SCLC subtypes, hopefully, helping the designing of tailored treatment for each patient.

1.2.3.1.7 Downregulation of oncogenes

The main genetic alterations that drive SCLC are the loss of the tumour suppressor *TP53* and *RB1*. Compared with other lung cancers, activating mutations of oncogenes such as *KRAS*, *BRAF*, *PIK3CA* and *EGFR* are rarely identified in SCLC patients (George et al., 2015). On the other hand, SCLC displays the overexpression of different transcription factors (TFs), which regulate neuroendocrine differentiation and proliferation. TFs that regulate cell identity are frequently associated with large, highly active, transcriptional regions called super-enhancers. Inhibition of transcription has been shown to have a strong effect on these regions with particular impact on oncogenic TFs (Hnisz et al., 2013; Lovén et al., 2013). CDK7 is a cyclin dependent kinase involved in the regulation of the RNA polymerase II during transcription and its inhibition reduces the transcriptional activity of several TFs. In SCLC, Christensen *et al* showed that inhibition of CDK7 with the covalent inhibitor THZ-1 delayed tumour growth *in vivo* and caused cell death *in vitro* in different SCLC preclinical models (Christensen et al., 2014). They found that super-enhancers were associated with genes like *MYC*, *MYCN*, *ASCL1*, *NEUROD1* and *SOX2,* and treatment with THZ-1 reduced the expression of these TFs, highlighting their role in the biology of SCLC. (Christensen et al., 2014).

Inhibition of ASCL1 transcription as also been achieved by inhibiting the bromodomain and extra-terminal (BET) proteins. These proteins bind acetylated histones and allow the recruitment of chromatin regulators to start transcription. Lenhart et al observed that SCLC cell lines positive for ASCL1 were more sensitive to the BET inhibitor JQ-1 than ASCL1 negative cells. Indeed, the BET protein BRD4 directly binds the enhancer region of ASCL1 and treatment with JQ1 reduced the expression level of this transcription factor and survival of these cells (Lenhart et al., 2015).

1.2.3.1.8 Re-expression of tumour suppressor genes

As mentioned previously, silencing of *SLFN11* by the EZH2 subunit of the PRC2 is acquired by SCLC tumours during chemotherapy to avoid DNA damage induced cell death (Gardner et al., 2017). Considering the elevated level of EZH2 in SCLC and it is putative role in chemoresistance (Byers et al., 2012; Gardner et al., 2017; Poirier et al., 2015), combination of EZH2 inhibitors with chemotherapies could be a good strategy to prevent or delay the emergence of resistance. A first phase I clinical trial with the EZH2 inhibitor, PF-06821497, for the treatment of relapse/refractory SCLC patients is ongoing (NCT03460977).

1.2.3.1.9 Modulation of DNA damage and replication stress response pathways

As highlighted in a recent review from Thomas and Pommier, the main hallmarks of SCLC are high level of proliferation with unlimited replicative potential, obtained by loss of *RB1* and *TP53,* inhibition of the Notch pathway, upregulation of MYCs and SOX2, and activation of the PI3K pathway; resistance to apoptosis and growth arrest, thanks to *TP53* and *RB1* loss, and overexpression of BCL2; and high genomic instability (Thomas and Pommier, 2016). Because tumours rely on these biological capabilities (hallmarks) to survive, they can be exploited as vulnerabilities. All therapies described above try to target one or more of these vulnerabilities. The impressive initial response of SCLC to platinum and topoisomerase inhibitors suggests that the biggest 'weakness' of this disease lies in its high degree of genomic instability (Alexandrov et al., 2013). Although accumulation of mutations can facilitate tumour evolution, a good balance between genomic alterations and repair is necessary for tumour cell survival. Consistent with this notion, upregulation of several DNA damage repair proteins has been observed in SCLC (Byers et al., 2012). Moreover, the expression of oncogenes, such as MYC, generates a basal level of replication stress (Kotsantis et al., 2018) that needs to be balanced to avoid replication catastrophe and cell death (Toledo et al., 2017). Targeted therapies that preferentially target regulators of DNA damage and replication stress, such as PARP inhibitors, are starting to be investigated in SCLC, with some initially promising results (Foy et al., 2017). Details on the role of different DNA damage repair, replication

stress and cell cycle regulatory pathways in SCLC biology and response to targeted therapies are given in chapter 1.4.

Inhibition of PARPs

Several preclinical studies have demonstrated that PARP can be a valuable target in SCLC. PARP1 and PARP2 are involved in different DNA repair pathways (Pommier et al., 2016b) (Figure 6). They act by catalysing the polymerisation of ADP-ribose units from the enzyme cofactor β nicotine-amide adenine dinucleotide (β-NAD^+) on target proteins. The PAR chains allow recruitment of different effector proteins at the site of the damage and the release of PARP1/2 from the DNA (Ray Chaudhuri and Nussenzweig, 2017). While all PARP inhibitors have the same ability to interfere with the catalytic domain of PARP1/2, they have different capacity to trap PARP to the DNA. Talazoparib is the most potent compound in trapping PARP to the DNA, followed by niraparib, olaparib and rucaparib (with similar trapping potency), and finally veliparib (Pommier et al., 2016b). Trapping of PARP to the DNA happens via two mechanisms: inhibition of PARylation, which impedes the release of PARP from the DNA, and binding of the NAD^+ pocket by the drug, further enhancing the DNA binding of PARP (Murai et al., 2012). Therefore, while inhibition of PARylation directly impair DNA damage repair, PARP-DNA complexes interfere with the replication machinery causing replication fork collapse and DNA damage (Pommier et al., 2016b) (Figure 6). Byers and co-workers assessed the level of different proteins by RPPA on SCLC cell lines and identified PARP1 to have a higher expression in SCLC compared with NSCLC, and SCLC cells were more sensitive to PARP inhibition by treatment with olaparib (AZD2281) or rucaparib (AG014699). Addition of chemotherapy after olaparib treatment further increased the anticancer effect (Byers et al., 2012). Similarly, Cardnell *et al* tested the effect of the more potent PARP1/2 inhibitor, talazoparib (BMN673), on SCLC cell lines. SCLC cells were highly sensitive to this drug, with xenografts showing similar sensitivity to talazoparib and cisplatin treatment. Interestingly, they observed that the SCLC cell lines more sensitive to talazoparib had a higher expression of specific DNA repair proteins (high 'DNA repair score') and a

lower activation of the PI3K pathway (low 'PI3K score'), suggesting that activation of the PI3K pathway could induce resistance to PARP inhibition (Cardnell et al., 2013).

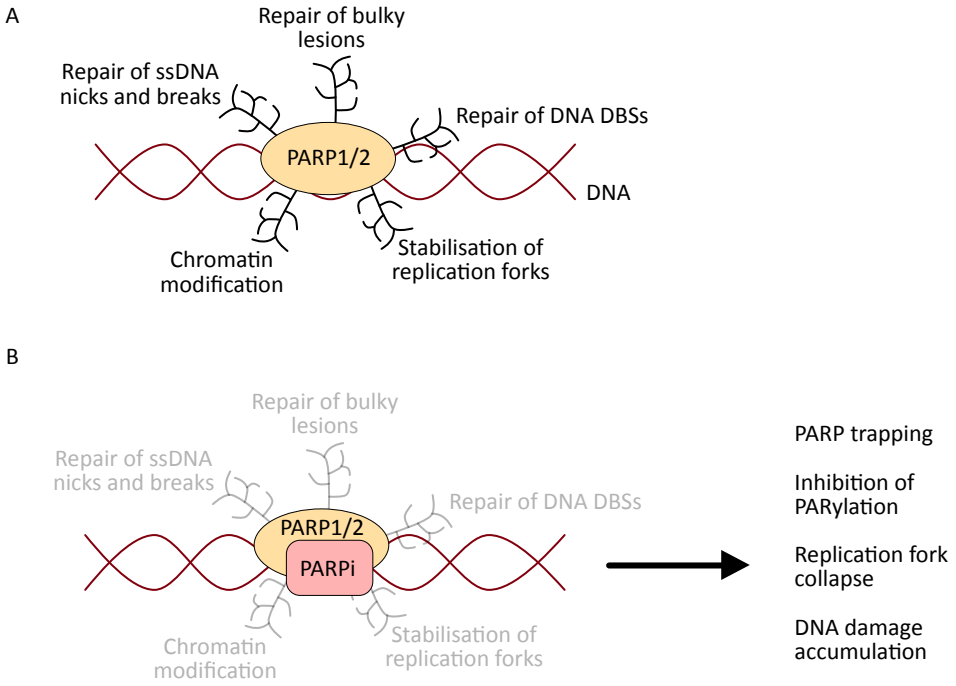

Figure 6. PARP1/2 inhibition.

A. Role of PARP1/2 in different DNA damage processes. B. Inhibition of PARylation by PARPi causes impaired repair of SSBs, DSBs and replication fork damage, while PARP trapping induce replication fork collapse and DNA damage. PARPi: PARP inhibitors.

Both studies hypothesise that the effect of PARP inhibition in SCLC is linked to the role of PARP1 as an E2F1 co-activator (Byers et al., 2012; Cardnell et al., 2013; Simbulan-Rosenthal et al., 2003). E2F1 can regulate the expression of different DNA repair proteins and PARP1 can cooperate with E2F1 in the transcriptional activation of different HR genes in prostate cancer (Biswas and Johnson, 2012; Schiewer et al., 2018). Therefore, inhibition of PARP1 in SCLC may reduce the activity of E2F1 and induce an HR deficient state that renders these cells more sensitive to DSB DNA damage. PARP inhibition has been and is still being tested in several clinical trials involving SCLC patients (Sen et al., 2018). A phase II study with the PARP inhibitor veliparib combined with cisplatin/etoposide in ES SCLC showed a modest increase in PFS and OS in the cisplatin/etoposide plus veliparib group, compared with chemotherapy plus placebo (6.1 *vs* 5.5 months for PFS and 10.3 *vs* 8.9 months for OS, respectively) (Owonikoko et al., 2018). Similarly, a phase I study with veliparib in combination with carboplatin/etoposide for ES SCLC patients showed response at the

recommend phase II dose in 5 out of 6 SCLC patients (Atrafi et al., 2019). A preliminary phase I study testing the PARP inhibitors olaparib as a maintenance therapy on chemosensitive SCLC patients, did not show any improvement in OS and PSF compared with placebo (Woll et al., 2017). Talazoparib is under investigation on previously treated SCLC patients and initial data showed partial response in 6 out of 23 patients (Bono et al., 2017). If different PARP inhibitors can be more effective in specific subgroups of patients is not clear yet and will need further clinical investigation. Combination of PARP inhibitors with chemotherapies or other targeting agents, like PI3K inhibitors (Cardnell et al., 2016), are warranted to improve the ORR and delay the emergence of progressive disease. Moreover, biomarkers to stratify patients that can benefit from this treatment are under investigation (Lord and Ashworth, 2017).

Inhibition of ATR/CHK1 axis

Another important regulator of DNA damage and replication is the ATR-CHK1 axis (Smith et al., 2010). ATR is a sensor of DNA damage and it is recruited to the site of damage by the accumulation of RPA on single stranded DNA (ssDNA). ATR activation leads to the phosphorylation of CHK1. CHK1 in turn phosphorylates several downstream effectors, like the cell cycle regulators CDC25A, CDC25C and WEE1 (Figure 7). ATR-CHK1 activation triggers a cascade of signals to allow cell cycle arrest, fork stabilisation and DNA repair (Smith et al., 2010). Therefore inhibition of this pathway can sensitise SCLC cells to DNA damage and replication stress. In their proteomic profile, Byers *et al* identified different members of the DDR upregulated in SCLC *vs* NSCLC, including PARP1, PCNA, DNA-PKcs and CHK1 (Byers et al., 2012). CHK1 overexpression was confirmed at the protein and mRNA levels in SCLC cell lines and tumours in two independent studies, prompting the possibility of targeting CHK1 in SCLC (Doerr et al., 2017; Sen et al., 2017a). In both studies, Sen *et al* and Doerr *et al* demonstrated that mouse and human SCLC cell lines are highly sensitive to several CHK1 and ATR inhibitors, while NSCLC tumours tend to be more resistant. The effects of these inhibitors was due to an increased level of DNA damage without abrogation of cell cycle progression, leading SCLC cells to accumulate lesions and undergo apoptosis (Doerr et al., 2017; Sen et al., 2017a).

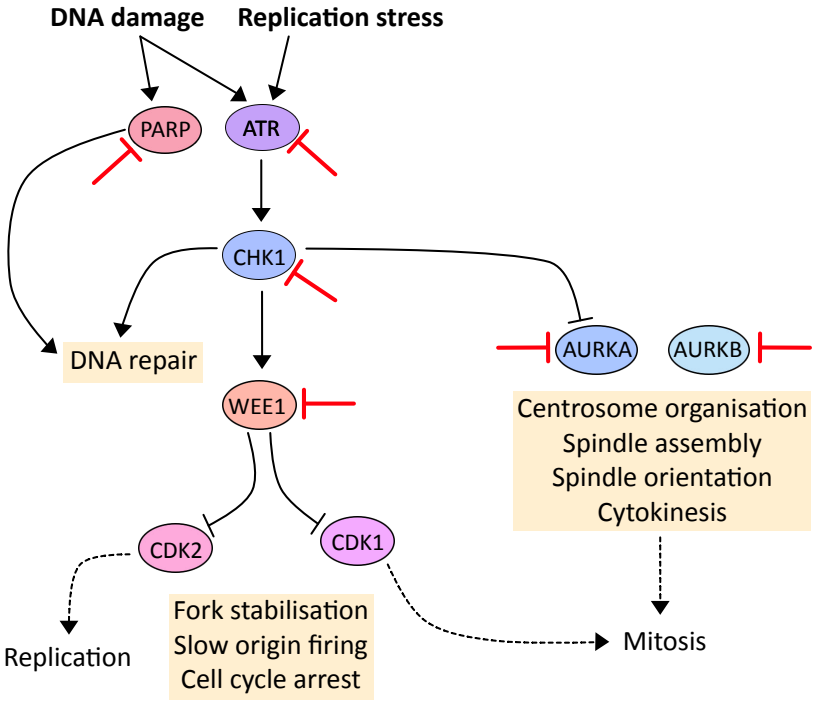

Figure 7. Inhibitors of the DNA damage and cell cycle checkpoint pathways.

Schematic of the main DDR targets currently tested in SCLC clinical trials. A general overview of the pathways and the overall role each target has on cell cycle and DNA repair/replication is shown. Yellow boxes highlight the physiological processes controlled by the proteins. When an inhibitor is administered, these processes are disrupted. Refer to text for more detail.

CHK1 inhibition was highly effective both as single agent and in combination with cisplatin or the PARP inhibitor olaparib in both SCLC GEMM and xenografts. Interestingly, they observed a good synergy between olaparib and the CHK1 inhibitor prexasertib (LY2606368) also in the olaparib-resistant cell lines, probably because of the ability of prexasertib to inhibit the AKT/mTOR pathway (known to induce PARP inhibitor resistance, Cardnell et al., 2013). Sen and co-workers associated expression of MYC with response to prexasertib (Sen et al., 2017a). Similarly, Nagel *et al* demonstrated that *Mycl*-amplified GEMM tumours as well as *MYC* and *MYCL* amplified SCLC cell lines were more sensitive to both CHK1 and ATR inhibition, and combination of the ATR inhibitor VE822 with cisplatin greatly increased the survival of SCLC xenografts (Nagel et al., 2019). The dependency observed in the MYC expressing cells to the ATR/CHK1 checkpoint is an example of how replication stress induced by oncogenes can be exploited to target such tumours, as discussed in chapter 1.4. A phase II study testing prexasertib on ES SCLC patients has been completed and results are awaited (NCT02735980). Trials testing the efficacy of ATR

inhibitors in combination with radiation or chemotherapy are also under evaluation (NCT03896503, NCT02589522, NCT02487095).

1.2.3.1.10 Deregulation of cell cycle progression in SCLC

Aurora Kinases

Aurora kinases are important proteins involved in the regulation of cell division during mitosis. There are 3 paralogues in mammals, Aurora A (AURKA), Aurora B (AURKB) and Aurora C (AURKC) kinases. They have very distinct localisation and functions, however sequence similarities suggest some overlapping functions (Carmena and Earnshaw, 2003). Little is known about AURKC, while AURKA and AURKB have been widely implicated in different process during mitosis: centrosome separation and maturation, spindle assembly and spindle orientation for AURKA, and chromosome bi-orientation, cytokinesis and spindle assembly checkpoint for AURKB (Carmena and Earnshaw, 2003) (Figure 7). The interest for these kinases in SCLC derived from the observation that MYC amplified SCLC tumours showed increased response to both AURKA and AURKB inhibitors. Sos and co-workers performed a large drug screen coupled with genomic characterisation of 60 SCLC cell lines and observed that *MYC* amplified SCLC cells were sensitive to the pan-Aurora kinase inhibitor VX680 and the Aurora B selective inhibitor, AZD1152 (barasertib). This sensitivity was not observed in *MYCL* and *MYCN* amplified SCLC cells (Sos et al., 2012). To corroborate these findings, Helfrich *et al* demonstrated that *MYC* amplified SCLC cells were 16 times more sensitive to barasertib than non-*MYC* amplified cells (including *MYCL* and *MYCN* amplified cells). While barasertib sensitive cells showed polyploidy and endoreduplication after treatment with the compound, these phenotypes were not seen in the resistant cells (Helfrich et al., 2016). Hook and colleagues did not see differences between individual MYC family members and sensitivity to the dual AURKA/B inhibitor PF-0384735, however when they tested the inhibitor *in vivo*, the *MYCN* amplified H69 xenograft had a limited response compared with the *MYC* amplified H82 xenograft (Hook et al., 2012). Moreover, Mollaoglu *et al*. observed that the MYC-driven RPM GEMM was particularly sensitive to alisertib treatment and combination with cisplatin/etoposide generated stable disease in > 60% of the animals with regression in 30% of them (Mollaoglu et al., 2017).

Considering the evidence that *MYC* amplified SCLC cells may be more dependent on AURKB than AURKA (Sos et al., 2012), it would be interesting to see if treatment of RPM mice *in vivo* with the AURKB-selective inhibitor barasertib plus chemotherapy can further improve the benefit observed with alisertib. Clinical trials assessing the effect of Aurora kinase inhibitors in SCLC are under evaluation. A phase II trial testing the effect of alisertib on recurrent SCLC patients showed a ORR of 21% (Melichar et al., 2015). The multikinase Aurora inhibitor danusertib hydrochloride did not show any progression-free survival at 4 months in recurrent SCLC patients (Schöffski et al., 2015). Combination of alisertib with paclitaxel (another inhibitor of spindle function) showed favourable PFS compared with paclitaxel alone in relapse SCLC patients (101 *vs* 66 days, respectively; (Owonikoko et al., 2017). The MYC protein expression was assessed retrospectively in this study, however the results have not yet been published. A further phase I study to assess safety, tolerability and pharmacokinetics of the nanoparticle AZD2811 (previously AZD1152 or barasertib) in advanced solid tumours is ongoing (Burris et al., 2017, NCT02579226). Considering the preclinical data obtained to date, the coming clinical trials should test the role of *MYC* expression as a putative predictive biomarker for the response to Aurora kinase inhibitors. Recently, two parallel studies have been published showing a synthetic lethal effect of AURKA and AURKB inhibition in RB null tumours (Gong et al., 2019; Oser et al., 2019). In both studies, the authors claimed that the high sensitivity of some SCLC preclinical model to inhibition of either AURKA to AURKB correlates with *RB1* status independently to the *MYC* status of the cells. Both studies exploited selective inhibitors of AURKA (LY3295668, Gong et al., 2019) and AURKB (AZD2811, Oser et al., 2019) with similar results. A phase I/II clinical trial to test LY3295668 on *RB1*-deficient solid tumours is ongoing (NCT03092934).

WEE1 Kinase

WEE1 is another protein kinase involved in cell cycle checkpoints. WEE1 inhibits cell cycle progression by phosphorylating Tyr15 resulting in inhibition of CDK1 and prevention of cells from entering mitosis. WEE1 can also phosphorylate Tyr15 on CDK2, controlling entry in S phase and therefore DNA replication (Do et al., 2013) (Figure 7). Inhibition of WEE1 by the ATP-competitive small molecule inhibitor

AZD1775 (previously MK1775) causes loss of the S and G2/M checkpoints leading to uncontrolled mitotic entry, increased replication stress and inhibition of the homologous recombination pathway (Beck et al., 2012; Domínguez-Kelly et al., 2011; Krajewska et al., 2013). It has been demonstrated that AZD1775 is more potent in tumours that have a defective G1 checkpoint (Geenen and Schellens, 2017; Hirai et al., 2009; Rajeshkumar et al., 2011), although the link between p53 loss and response to WEE1 inhibition is controversial (Cuneo et al., 2016; Geenen and Schellens, 2017; Linden et al., 2013). A phase IB clinical trial tested the effect of AZD1775 in different solid tumours including SCLC, showing partial response in 2 out of 4 SCLC patients (Bauer et al., 2016, NCT02482311). Recent work from the Byers' group showed that SCLC cell lines have higher expression of WEE1 than NSCLC cell lines. They observed that SCLC cell lines with high levels of the receptor tyrosine kinases AXL and MET can overcome the inhibition of WEE1 by activating the AKT/mTOR and ERK/p90RSK pathway to stimulate CHK1 (Sen et al., 2017b). At the moment, multiple clinical trials testing AZD1775 alone or in combination with DNA damaging agents are ongoing (NCT02937818, NCT02482311, NCT02593019, NCT02511795, NCT02688907), however based on the data from Sen *et al*, combination with AXL or mTOR inhibitor may be used to prevent or delay the emergence of resistance (Sen et al., 2017b).

1.2.3.1.11 Immunotherapy in SCLC

Suppression of the immune system is a hallmark of cancers (Hanahan and Weinberg, 2011). It is now accepted that the immune system prevents tumour growth. Tumours develop strategies to avoid immunosurveillance and immune cell killing. The general hypothesis is that the acquisition of genetic alterations and the overall transformation that tumour cells undergo cause them to express antigens that are different from those presented by non-transformed cells. This diversity can be recognised by a functional immune system to eliminate tumour cells or create a state of dormancy (Schreiber et al., 2011). However, the genetic chaos present in the tumours allows them to acquire alterations that lead to suppressed immune recognition and/or increased resistance to the cytotoxic effects of the immune system. Immunotherapy approaches attempt to restore immune responses to tumours by increasing the number of immune effector cells, revealing tumour

antigens and/or eliminating cancer-induced immunosuppressive mechanisms (Schreiber et al., 2011). Considering the high mutational burden observed in SCLC (Alexandrov et al., 2013), it has been hypothesised that these patients would express a large number of tumour-specific antigens and therefore they would be responsive to immunotherapy. CTLA-4 is a receptor expressed on the membrane of T cells that competes with CD28 for binding CD80/86 molecules expressed by the antigen-presenting cells (APC). Interaction between CTLA-4 and CD80/86 suppress T-cell activation and can be exploited by tumour cells to elicit immunosuppression. Similarly, PD-1 receptor can reduce T cell activation by binding the PDL-1 molecules on target cells (Buchbinder and Desai, 2016). Antibodies against CTLA-4 and PD-1 have been generated to block the interaction with the corresponding inhibitory molecule (CD80/86 and PDL-1) and stimulate T cell activation against tumour cells (Figure 8). Ipilimumab is an anti-CTLA-4 antibody and it has been tested against different tumour types, including SCLC (Buchbinder and Desai, 2016). Phase II and phase III trials testing the combination of ipilimumab with paclitaxel/carboplatin (phase II) or with cisplatin/etoposide (phase III) as first-line therapy for ES SCLC patients were unable to show any improvement in PFS and OS (Reck et al., 2013, 2016). A maintenance phase II study testing the anti-PD-1 antibody pembrolizumab failed to show an improvement in PFS, however expression of PDL-1 seemed to correlate with better PFS (Gadgeel et al., 2018). Another trial testing the PD-1 inhibitor nivolumab alone or in combination with ipilimumab in recurrent SCLC patients (CheckMate032) showed promising results, with 33% and 43% of the patients reaching 1-year OS on nivolumab monotherapy and combination, respectively (Antonia et al., 2016). In this case, response was observed in both PDL-1 positive and negative patients. Two phase III trials tested nivolumab alone or with ipilimumab as maintenance therapy after first-line chemotherapy in SCLC patients (CheckMate 451, NCT02538666) or nivolumab *vs* single-agent chemotherapy as second-line therapy in SCLC (CheckMate 331, NCT02481830). Both trials were unable to show an improvement in OS, however the increased response observed in some patients suggests that stratification may help selecting patients that can benefit from these treatments (Owonikoko et al., 2019; Reck et al., 2018). In 2019, the U.S. Food and Drug Administration (FDA) has approved the humanized monoclonal anti-PDL-1

antibody, atezolizumab, in combination with carboplatin and etoposide as first-line treatment for ES SCLC patients (U.S. Food and Drug Administration, 2019) (Figure 8). This is the first time in 30 years that a different first-line regiment has been proposed for ES SCLC patients. The approval was based on the IMPower133 phase III clinical trial where it has been shown that patients receiving atezolizumab in combination with carboplatin/etoposide as first-line therapy, had a longer OS compared with the carboplatin/etoposide only group (12.3 *vs* 10.3 months respectively) (Horn et al., 2018).

Immune escape can be reached also by inhibiting the activation of the innate rather than the adaptive immune system. For example, CD47 can bind the SIRPα receptor expressed on the surface of macrophages and inhibit macrophage phagocytosis of tumour cells (Jaiswal et al., 2010) (Figure 8). CD47 has been shown to be overexpressed on SCLC PDX and CDX suggesting a putative immune escape mechanism for these tumours (Weiskopf et al., 2016). Treatment of SCLC tumours with anti-CD47 antibody, Hu5F9-G4, both *in vitro* and *in vivo* showed induction of macrophage-mediated phagocytosis and tumour regression, suggesting the possibility to combine CD47-blocking approaches with other ICB in SCLC (Weiskopf et al., 2016). More clinical trials are under evaluation to assess the efficacy of ICB alone or in combination with other therapies in SCLC (Sabari et al., 2017). Of particular interest, is the recent observation that defects in the DDR can mediate the ICB response in immunocompetent preclinical models, opening the path to new combinatorial treatment with DDR inhibitors and ICB (Hiatt and MacPherson, 2019; Mouw et al., 2017; Sen et al., 2019a, 2019b). One example is the phase II clinical trial testing the combination of the PARP inhibitor, olaparib, in combination with the PDL-1 inhibitor, durvalumab. This trial showed a clinical benefit in 4/20 recurrent ES SCLC patients, however, the pre-set benefit end-point was not met (NCT02484404, Thomas et al., 2019).

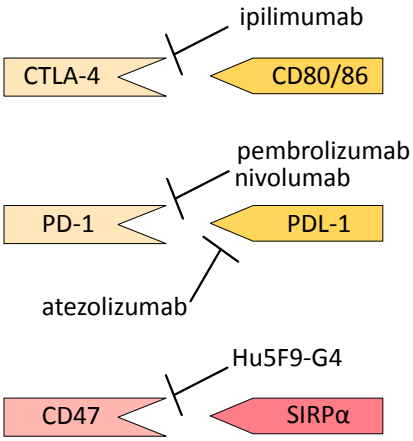

Figure 8. Immunotherapy in SCLC.

List of antibodies and their targets used in SCLC immunotherapy. In yellow are targets that reduce the activity of T cells, while in red are targets that can inhibit the activation of macrophages. The light coloured shapes are receptors, while the dark coloured shapes are the corresponding ligands.

1.3 Preclinical models for SCLC research

The overall failure of clinical trials testing new therapeutic targets in SCLC is in contrast to the promising responses observed in preclinical studies. This lack of clinical success should be a red-flag for researchers and clinicians. One reason for these disappointing results could be related to the lack of patient stratification. Several preclinical studies have demonstrated drug efficacy in specific cellular backgrounds where models expressing a particular biomarker were more or less sensitive to the studied treatment (Table 2). Therefore, clinical trials guided by biomarkers should be preferred when possible. Another factor that limits the efficacy of clinical trials is the lack of preclinical models that can fully recapitulate the patient's tumour. SCLC tumours are rarely resected leaving tissue biopsies as the only options to directly study patient-derived disease. However, these biopsies are usually small, can contain crush artefacts and are prioritised for diagnostic use, limiting the tissue availability for research. This lack of tissue encouraged researchers to establish different models of SCLC. All of the models described below contributed, to some extent, to our knowledge of SCLC pathogenesis. However, it is important to be aware of the advantages and limitations of each preclinical models in order to guide research and the accurate interpretation of results.

1.3.1 Small cell lung cancer cell lines

The most tractable and frequently used preclinical research models are established cancer cell lines, many of which were generated decades ago, and continue to be passaged and survive in *in vitro* culture conditions (Giard et al., 1973). In the field of SCLC, the establishment of human cell lines was initially challenging (Gazdar et al., 1980), but ultimately techniques were developed that allowed the establishment and maintenance of SCLC cell lines (Simms et al., 1980). This led to the generation of a comprehensive database of SCLC cell lines but with limited patient information (Gazdar and Minna, 1996; Phelps et al., 1996). Because resection of primary tumours is rarely performed, most cell lines were established from metastatic sites including pleural effusions and lymph node resections (Gazdar and Minna, 1996). The small size of the sample used to establish cell lines, as well as their metastatic location make these cells representative of only a small population of tumour cells with probably more fitness for culture on plastic and a more aggressive phenotypes. Therefore, SCLC cell lines can be useful tools when studying advanced disease, however they can give little information on the early stage. Nevertheless, established cancer cell lines have the advantages of rapid proliferation and being easy to manipulate, allowing researchers to perform a variety of experimental procedures that are more challenging in other preclinical models. SCLC cell lines were used to identify genomic alterations typical of SCLC, such as loss of *TP53*, *RB1* and chromosome 3p, and amplification of *MYC* (Harbour et al., 1988; Little et al., 1983; Nau et al., 1985; Takahashi et al., 1989; Whang-Peng et al., 1982), and they have been useful to classify SCLC into different phenotypic subtypes (Carney et al., 1985; Gazdar et al., 1985; Rudin et al., 2019). Pleasance *et al* sequenced one SCLC cell line and detected mutation signatures associated with tobacco smoking and identified new putative drivers of SCLC (*CREBBP-BTBD12* fusion, *CHD7* rearrangements), later confirmed in tissue specimens (Peifer et al., 2012; Pleasance et al., 2010; Rudin et al., 2012a). Cell lines can be easily exploited to test large panels of compounds and identify new candidate targets to treat specific tumours (Shoemaker, 2006). This is particularly useful, especially for tumours like SCLC were tumour material is lacking. Sos and co-workers exploited 60 SCLC cell lines to perform a combined genomic and pharmacological vulnerability screen that allowed the identification of a dependency

to Aurora kinases in *MYC*-amplified cell lines (Sos et al., 2012). Byers *et al* performed a reverse-phase protein array (RPPA) to assess 193 total and phospho-proteins in 34 SCLC and 74 NSCLC cell lines and identified PARP1 as a therapeutic target for SCLC patients (Byers et al., 2012). Cell lines are also largely exploited to assess mechanisms of drug response, synthetic lethal dependencies and biological tumour behaviours. Studies of RNA interference, gene knockout and protein expression are possible in cell lines and can help discriminating passenger from driver alterations, or can be used to identify druggable genes and/or players in drug resistance. Huang *et al* performed a CRISPR screening on SCLC cell lines and identified POU2F3 as a master regulator in a subset of SCLC cells with variant morphology (Huang et al., 2018b). Recently, a genome wide CRISPR screen performed on SCLC cells showed a potential vulnerability in the replication stress response that was confirmed by pharmacological inhibition of ATR and CHK1 (Nagel et al., 2019). Another example comes from the work from Oser and colleagues, who forced the expression of RB in *RB1* negative SCLC cells and exploited these isogenic cells to perform synthetic lethal CRISPR screening. They identified *AURKB* loss as synthetic lethal with *RB1* loss and were able to use the isogenic cell lines to mechanistically explain the inter-dependency between RB and AURKB (Oser et al., 2019).

Hence, SCLC cell lines have been fundamental for our initial understanding of SCLC biology, and today they are still necessary when testing large panels of compounds or assessing functional mechanisms. However, cell lines have several disadvantages (Table 3). First, SCLC cell lines are a subpopulation of the original tumour and consequently one cell line cannot really recapitulate the entire complexity of SCLC tumour. Furthermore, the difficulty in establishing SCLC cell lines indicates that only those cells with a more 'robust' phenotype adapt to culture conditions, inevitably selecting for specific clones. Moreover, tumour cells cultured *in vitro* proliferate rapidly, leading to the accumulation of additional molecular changes that could cause genomic drift during culture (Gazdar et al., 2010). Analysing DNA methylation patterns in SCLC primary tumours *vs* PDX *vs* cell lines, Poirier and co-workers observed that cell lines had a different pattern of DNA methylation compared with PDX and primary tumours, probably acquired during long term *ex vivo* culture, and

thus, clustered further apart from the primary tumours (Poirier et al., 2015). Daniel *et al* also demonstrated that during the transition to culture conditions, SCLC cells obtained from a patient-derived xenografts (PDX) changed their gene expression profile. Interestingly, when re-implanted in mice these PDX-derived cells were tumorigenic but could not re-establish the expression profile lost during 6 months of *in vitro* culture. When compared with the primary tissue, only the PDX model closely resembled the donor tumour, while the PDX-derived cell lines presented irreversible changes imposed by the culture conditions (Daniel et al., 2009). This divergence between cell lines and primary tumours as well as the lack of efficacy of novel therapies in the clinical setting can also derive from the lack of interactions with the stroma and the extracellular matrix, with consequent changes in paracrine/autocrine signals, lack of hypoxic regions, as well as metabolic changes (Ertel et al., 2006; Gillet et al., 2011; Stein et al., 2004).

Table 3. Advantages and disadvantages of different SCLC preclinical models.

Preclinical model	Advantages	Disadvantages	Uses
Cell lines	easy to manipulate quick growth cheap less complex background	lack of stromal compartment long-term exposures to culture conditions selection of clones during culture not representative of the complexity of the human disease	genomic manipulation rapid large-scale drug screening biological characterisation of SCLC drivers
GEMM	presence of tumour microenvironment immunocompetent recapitulate human disease	simplified genetic background not patient specific long latency for tumour development expensive difficult to obtain for SCLC patients murine tumour	study tumour pathogenesis allow tumour-immune system interaction studies drug testing in specific genetic background
PDX	patient specific patient stroma at early passages relatively fast growing	selection of clones during passaging mouse stroma at late passage immunodeficient expensive	testing drugs in a patient specific background study patient-derived tumours

		small biopsy not representative of the entire tumour	
CDX	samples are easy to collect (liquid biopsy)	immunodeficient	study mechanisms of resistance acquired by the patient
	patient specific	selection for more aggressive clones	study tumour evolution over time
	may better represent patient's heterogeneity	mostly late stage disease	testing drugs in a patient specific background
	allow longitudinal paired models	mouse stroma	allow studies of metastatic disease
		expensive	study patient-derived tumours
		slow growing	

All together these observations highlight some limitations of established cell lines and potentially explain why, in part, SCLC cell lines are sensitive to drugs that are not effective in the clinic. At the same time, SCLC cell lines are necessary for functional experiments not achievable in *in vivo* settings. Researchers should be aware of the limitations of the cultured cell lines and complement their findings in more complex and clinically relevant models.

1.3.2 Small cell lung cancer genetically engineered mouse models.

Because of the limitations of established cell lines, several studies focused on the development of *in vivo* murine models of cancer, in which autochthonous tumours could grow in the appropriate lung environment and recapitulate the pathogenesis observed in the patient. These models, called genetically engineered mouse models (GEMMs), are immunocompetent mice genetically modified to mimic the pathophysiological and molecular features of human diseases (Jonkers and Berns, 2002). GEMMs are generated via transgenic expression of mutant oncogenes or through conditional deletion of tumour suppressor genes, in specific tissue or in the entire mouse. GEMMs allow development of a tumour in its original microenvironment where stromal interactions and the immune system are maintained, making them particularly relevant and timely models to study novel immunotherapy approaches. Furthermore, the possibility to introduce specific molecular alterations known to be drivers of human cancers allows the study of gene-function causality and tumour progression from the earlier stages (Jonkers and Berns, 2002). The first GEMM of SCLC was generated by Meuwissen *et al,* who

conditionally inactivated *Trp53* and *Rb1* specifically in the epithelium of the lung. They exploited Cre-*LoxP* system to induce the somatic deletion of *Trp53* and *Rb1* in the adult mouse after intra-tracheal instillation of Adeno-Cre (Ad-Cre) virus. The tumours that developed showed SCLC-like morphology, were highly proliferative, expressed NE markers and metastasised to the bone, brain, adrenal glands, ovaries and liver (Meuwissen et al., 2003). With this study, they demonstrated that loss of both *Trp53* and *Rb1* is necessary for the development of SCLC, setting the foundation for the development of future research using SCLC GEMMs. As already mentioned in chapter 1.1.1, different groups developed cell-type specific conditional inactivation of *Trp53*/*Rb1* using Ad-Cre virus under the control of cell-type specific promoters: the CGRP promoter for NE cells, the CC10 promoter for Clara cells and the SPC promoter for AT2 cells (Park et al., 2011a; Sutherland and Berns, 2010). More GEMMs of SCLC have been developed where specific genomic alterations were added to the loss of *Trp53* and *Rb1* in order to characterise their role in promoting SCLC progression. Most of these models and their biological relevance have already been described in the previous sessions (Table 1). These SCLC GEMMs resemble human SCLC, and a pathological analysis demonstrated that they cover a spectrum of high-grade NE tumours of the lungs and can be exploited to study the early stage of these diseases (Gazdar et al., 2015). Despite the utility of GEMMSs to study tumour evolution, they also present some drawbacks (Table 3). Firstly, they are costly and time consuming, with some tumours developing months after induction. Secondly, GEMM tumours derive from a few genetic alterations and cannot completely recapitulate the complexity of a human tumour. Comparison of the murine SCLC genome with human SCLC showed comparable frequency of genomic re-arrangements and copy number alterations, however the murine cancers harboured significantly fewer point mutations (McFadden et al., 2014). This lack of point mutations was associated with the absence of tobacco-associated mutagens in the development of these tumours (McFadden et al., 2014). The lack of this mutational load in SCLC GEMMs reduces the genomic complexity of these cancers and may have an impact in the response to treatments. Moreover, GEMMs develop mouse tumours, and differences in drug metabolism between mice and humans may impact the response to specific compounds (Kersten et al., 2017). To date, there are no studies evaluating the ability

of these models to properly predict clinical therapeutic response in SCLC, however promising data have shown that *Kras*-driven NSCLC and pancreatic carcinoma GEMMs closely modelled the human response (Singh et al., 2010).

1.3.3 Xenograft mouse models

1.3.3.1 Cell line-derived xenografts

The need for human specific models is partially overcome with xenograft mouse models. These models use immunodeficient mice into which established SCLC cell lines are implanted and grown (Morton and Houghton, 2007). There are several immunodeficient mouse models that can be used, like T cell-deficient (nude mice), T and B cell-deficient (*scid* mice) or hybrid strains like NOD-*scid* and the NOD-*scid*-*IL2λ*-receptor null (NSG) mice model in which the immune system is further compromised (Belizário, 2009). The lack of a functional immune system allows the proliferation of human tumour cells in a mouse background. The inoculation of cancer cell lines can be done subcutaneously (heterotopic) or in the original anatomic compartment (orthotopic). Whilst orthotopic models are thought to recapitulate more closely the original tumour, implantation is technically challenging, time consuming, and costly imaging analysis is required to monitor tumour growth (Richmond and Su, 2008). Therefore, subcutaneous injection is the routine method for xenograft implantation, despite the lack of the original microenvironment (Table 3). A further limitation of this model is the lack of a competent immune system, making it impossible to assess its impact on tumour growth and response to therapies. Moreover, xenografts are derived from conventional cell lines with all the limitations previously described (Daniel et al., 2009; Gillet et al., 2011; Poirier et al., 2015) (Table 3). Cell line-derived xenografts have failed to predict response to several cancer therapeutics and hence, should be used cautiously by the scientific community (Johnson et al., 2001). Despite those limitations, the relatively reduced cost of these xenografts compared with other mouse models, and their generally faster tumour growth, make them more tractable to address different biological and translational questions (Day et al., 2015).

1.3.3.2 Patient-derived xenograft using patients' tumour biopsies

Patient-derived xenografts (PDX) have been developed to overcome the limitations imposed by established cell lines. PDX use immunodeficient mice in which

fresh, small tumour fragments of primary or metastatic human cancers are directly implanted subcutaneously or orthotopically (Kim et al., 2009; Morton and Houghton, 2007). This model recapitulates some of the handicaps of the cell line xenograft models, such as the lack of the immune system and the difficulty in monitoring orthotopic engraftments, but they do have several advantages (Table 3). PDX maintain the parental stroma in the early passage, even when implanted subcutaneously and the molecular and histological characteristics of the original tumour are preserved (Hidalgo et al., 2014). Gene expression and genomic analysis have also demonstrated a great concordance between PDX and the paired donor tumours, with relatively minimal PDX-specific alterations (Hidalgo et al., 2014). Several studies on different tumour types have demonstrated the high affinity between PDX and the corresponding patients, with particular emphasis on the ability of PDX to mimic the response to treatment observed in donor patients (Bertotti et al., 2011; DeRose et al., 2011; Dong et al., 2010; Fichtner et al., 2008). Recently, Izumchenko and co-workers sequenced 237 early passage PDX and compared the results with The Cancer Genome Atlas (TCGA) database, showing strong overlap between PDX and primary tumours. Then they looked into the response of 92 PDX models to different therapeutic regimens and demonstrate that PDX can predict the clinical outcome of the patients (Izumchenko et al., 2017). These studies underline the significant opportunity offered by the PDX. These models can be exploited to study specifically the patient's tumour, its mechanisms of response or resistance to therapy, and eventually could be a platform to test personalised treatment for such patients (Hidalgo et al., 2014). As a proof of that, Gao *et al* performed an *in vivo* compound screen in a panel of PDX (~ 1,000 models) with different genetic backgrounds. They created a PDX clinical in which they tested different compounds as single agents or in combination. Not only they were able to recapitulate responses to targeted therapies observed in the clinic, but they have also been able to generate PDX models of resistance and shown the feasibility of using these models to identify and validate biomarkers of response (Gao et al., 2015). Therefore, the generation of large panels of PDX covering several cancers with specific genomic backgrounds can help to identify the best treatment for a given population of patients, to identify biomarkers of response and also to generate paired models of resistance that can be

of enormous help in understanding how tumours evolve and adapt to specific treatments. Because of their ability to predict response to treatment, PDX have also been proposed has 'avatar' models, in which one PDX is generated from a patient's tumour and that PDX is treated at the same time as the patient with the same and other therapies (Hidalgo et al., 2011). In this way, the PDX may predict the emergence of resistance and eventually may show response to a different therapy, allowing clinicians to tailor patients' treatment accordingly. However, despite the good promise of this model, PDX are not perfect and, as for any other model, they show some limitations (Table 3). First, PDX are expensive and although the time to generate these models is shorter compared with some GEMMs, they can often take longer than cell line xenografts to grow. Moreover, generation of PDX requires availability of tumour tissue and this is not always possible, especially in tumours like SCLC where surgery is very rarely performed and biopsies are limited. Additionally, tumour fragments derived from a specific region of the tumour may not properly recapitulate the complex clonal heterogeneity present throughout a patient tumour. It is also possible that propagation of tumour pieces in mice causes a natural selection similar to that observed *in vitro*, where only those clones able to survive these specific *in vivo* conditions proliferate (Hidalgo et al., 2014). A recent analysis of 1,110 PDX demonstrated that during passaging PDX tumours acquired CNA, distinct from those acquired by the patient. These changes can pre-exist in the initial population as low-frequency clones and be selected during passage, but *de novo* events may also appear (Ben-David et al., 2017). This is of particular importance as it may cause divergence in the response to therapies as compared to the donor patients. PDX are grown in immunocompromised mice to avoid rejection from the host, therefore they cannot be used to study the interaction between the tumour and the immune system. Moreover while early passage PDX maintain the patient-derived stroma, this stroma is quickly replaced by the murine counterpart after a few passages *in vivo*, causing changes in the interaction between the tumours and the microenvironment and these changes may also affect the response to therapies (Hidalgo et al., 2014). Despite these limitations, PDX remain one of the most faithful models to recapitulate patient tumours. In the setting of SCLC, the generation of PDX models has been challenging due to the limited availability of tumour tissue, therefore these models

have been frequently excluded from large scale studies. The largest comprehensive characterisation of SCLC PDX has been performed recently by the Farago's group describing 17 PDX derived from SCLC tissue obtained before treatment or after relapse. They demonstrated that SCLC PDX closely resemble the original donor tumour both at the phenotypic and genomic level, and properly mimic the response to EP and olaparib/temozolomide observed in the patient (Drapkin et al., 2018; Farago et al., 2019). Poirier *et al* analysed the DNA methylation profile of 34 primary SCLC tumours, 6 SCLC PDX and 7 SCLC cell lines and showed that SCLC PDX clustered closer to the primary tumours than SCLC cell lines (Poirier et al., 2015). Other studies exploited SCLC PDX to assess the response to novel targeted therapies and associated mechanisms of acquired resistance, underlying the relevance of this model also in SCLC setting (Faber et al., 2015; Gardner et al., 2014, 2017; Park et al., 2011b; Saunders et al., 2015; Weiskopf et al., 2016). Generation of longitudinal PDX models would be the best way to portray how SCLC evolves during treatment in human. Drapkin *et al* were the first one describing the generation of longitudinal PDX derived from the same patient before first-line therapy and after subsequent line of treatment (Drapkin et al., 2018). They did not assess the mechanism of resistance for this particular model, however comparison of the chemonaive PDX *vs* post-treatment PDX can be used to identify patient-specific mechanisms of resistance. The reason why the number of these longitudinal PDX is low is due to the fact that SCLC patients rarely undergo biopsy after diagnosis, because of the invasive and potentially dangerous nature of the procedure (Asano et al., 2012; Eapen et al., 2013) and the poor health of many patients, drastically limiting the availability of tumour tissue after first-line therapies.

1.3.3.3 Circulating-tumour cells derived explants

Tissue biopsies are an impediment to SCLC research. The discovery that cells and molecules derived from the tumour can be detected in the peripheral blood of cancer patients, opened new opportunities. These so called 'liquid biopsies' include circulating tumour cells (CTC), circulating tumour DNA (ctDNA) and other tumour-derived molecules released into the circulation (Siravegna et al., 2017). Liquid biopsies can be used to determine the genomic profile of the tumour, monitor

tumour response to treatment and emergence of resistant clones (Alix-Panabières and Pantel, 2016; Siravegna et al., 2017). In particular, our laboratory showed that CTCs are prevalent in SCLC patients and that the enumeration of $EpCAM^{+}CK^{+}CD45^{-}$ CTC using the FDA approved CellSearch system is an independent prognostic factor for SCLC patients (Hou et al., 2009, 2012). Moreover, recently Carter *et al* sequenced single CTC from pre-treatment SCLC blood patients and generated a CNA based classifier. This classifier was able to pre-assign 83.3% of the patients as chemosensitive or chemorefractory, highlighting the potential of CTC has biomarker of response to standard chemotherapy (Carter et al., 2017). CTCs are released from the primary tumour or the metastatic sites and are representative of the invasive subpopulation of tumour cells (Pantel and Speicher, 2016). They are present in the blood of most patients with malignant carcinoma but rarely identified in healthy individuals (Allard et al., 2004). The molecular characterisation of CTCs demonstrated that they mirror the original tumour (Pantel and Speicher, 2016). Given the aggressive potential of CTCs and their prevalence in SCLC patients, these cells have been exploited by our laboratory to generate new mouse models of SCLC, termed circulating-tumour cell derived explant (CDX). Hodgkinson *et al* demonstrated that CTCs, enriched from the blood of chemonaïve ES SCLC patient are tumourigenic when injected subcutaneously in the flanks of immunocompromised mice. The molecular profiles of these CDX demonstrated broad similarity with the primary tumour and matched single CTC. Most importantly from a pharmacological perspective, the response of CDX to standard chemotherapies mirrored the donor patient's response to the same therapy (Hodgkinson et al., 2014). More recently, Drapkin and co-workers generated and broadly characterised 17 CDX models from both chemonaïve and treated SCLC patients with particular emphasis on their genomic/transcriptomic profile and response to treatments (Drapkin et al., 2018). Similarly, our group generated an extensive characterisation of 39 CDX derived from 32 SCLC patients including pre-treatment and post-treatment models. This study showed heterogeneity across the phenotypes, covering both 'classic' and 'variant' morphologies, with some models showing mixed phenotypes. A comprehensive transcriptomic and protein expression analysis of these models showed that the different SCLC subtypes reviewed by Rudin *et al* (Rudin et al., 2019) were represented

in our biobank of CDX (Simpson et al., 2019). Differential gene expression analysis identified clusters driven by either ASCL1, NEUROD1 or POU2F3, and IHC staining showed that the majority of CDX were $ASCL1^{+}/NEUROD1^{-}$ (58%), 24% were $NEUROD1^{+}/ASCL1^{-}$ and 9% expressed both ASCL1 and NEUROD1. Similarly, and in accordance with the literature, some of our CDX expressed high level of the MYC family member, with *MYCL* been the most frequently expressed (Simpson et al., 2019). This comprehensive study of multiple CDX models highlight their similarity with previously established SCLC preclinical models and strengthen their value as accurate model of SCLC

CDX and PDX share a lot of characteristics with similar advantages and disadvantages (Table 3), with the CDX approach providing an alternative for those patients for whom tumour tissue is not available. Moreover, due to the non-invasive nature of liquid biopsy, CTC can potentially be collected at different time point during patient's treatment and follow up, allowing generation of longitudinal models that can recapitulate tumour evolution and interrogate mechanisms of intrinsic and acquired resistance to therapies. As a proof of concept, we and others have demonstrated the feasibility of generating matched treatment-naïve and post-therapy CDX models demonstrating reduced sensitivity to the selected treatment in the progression model compared with the treatment-naïve CDX (Drapkin et al., 2018; Simpson et al., 2019). Moreover, a recent single-cell analysis of CTC from SCLC patients has demonstrated that most mutations identified in the primary tumour and metastasis were shared with the CTCs, demonstrating that CTCs can fully recapitulate the genomic complexity of this disease (Su et al., 2019). This suggests that CDX models may be more representative of the different subclones present in the patient's tumour than PDX, which derive from a small single biopsy. At the same time, CTC are cells that have acquire the ability to survive in the circulation and invade secondary sites, arguing that CDX may represent a more aggressive population of the original tumour. CDX and PDX should be used as complementary models and where possible generation of both models should be sought.

1.4 DNA damage repair in SCLC

Targeting DNA damage repair and the replication stress response pathways in SCLC may be an effective strategy to treat patients. The high mutational burden induced by tobacco smoke together with the acquisition of specific genomic alterations pushes the level of genomic instability in these cancers (Thomas and Pommier, 2016). But how exactly can SCLC be so sensitive to DNA damage? Is this high level of genomic instability at the base of the exquisite sensitivity to platinum-based treatment observed in patients? And why do these tumours relapse so rapidly? There are no clear answers to these questions. In this section, I would like to examine the known players in SCLC genomic instability, how they can influence DNA damage and replication stress responses and how an inappropriate balance of instability and repair can be exploited to push these cells beyond their survival threshold.

1.4.1 Genomic Instability drives SCLC pathogenesis

Genomic instability characterises most cancers and can stem from different mechanisms: mutations produced during DNA synthesis or defective repair, inappropriate chromosome segregation and failure of mitotic checkpoints (chromosome instability, CIN) or chromosomal rearrangements, copy number variation, hyper-recombination and loss of heterozygosity (Aguilera and García-Muse, 2013). Most of these lesions are generated by failure of the replication process, which leads to the accumulation of ssDNA and DSBs. The type of instability generated depends on the timing (S-, G2- or M-phase) and nature of the breaks (Aguilera and García-Muse, 2013). Indeed, the way cells deal with a specific type of DNA lesion not only depends on the type of damage, but also on the phase of the cell cycle in which the error happens. Cyclin-dependent kinases (CDK) and the checkpoint transducers ATR, ATM and DNA-PK feedback to each other in order to determine which DNA repair pathway should be activated and stop cell cycle progression. During DDR, different DNA lesions recruit specific repair proteins that activate the checkpoint transducers to arrest the cell cycle and promote DNA repair. Which checkpoints are activated depends on which repair proteins have been recruited and this in turn is regulated differently according to the cell cycle phase (Branzei and Foiani, 2008).

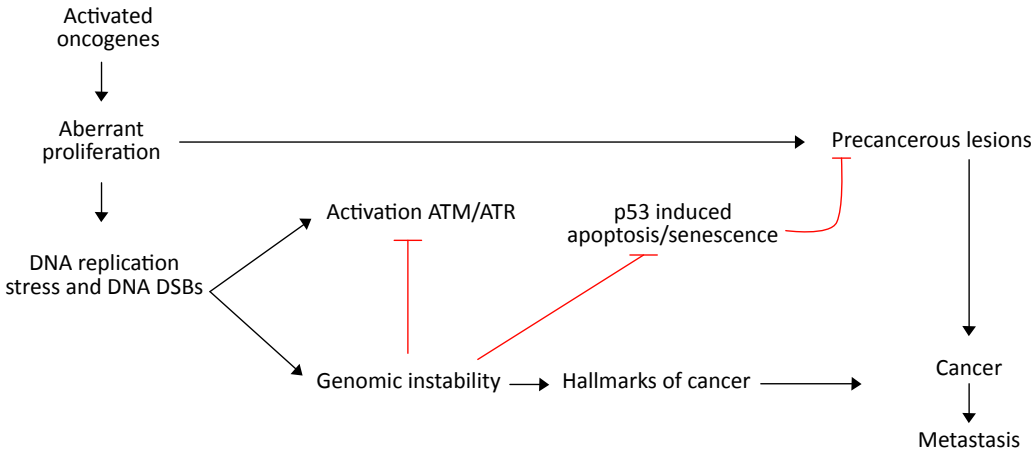

Figure 9. Oncogene-induced DNA damage model for cancer development and progression.

Activated oncogenes induce DNA damage and replication stress that can degenerate in genomic instability. This genetic chaos allows precancerous lesions to acquire hallmarks of cancer and develop in a more aggressive phenotype. Figure was adapted from Halazonetis et al., 2008. Red arrows indicate inhibition of the indicated processes.

In a normal cell, genomic instability is detrimental and activates apoptosis or senescence, however in cancer cells, genomic instability is an 'enabling characteristic' that allows cells to accumulate the multiple hallmarks of cancer and survive in an hostile environment (Hanahan and Weinberg, 2011). Negrini *et al* propose a model in which genomic instability is acquired during tumorigenesis in sporadic cancers (Negrini et al., 2010). The observation that the most frequently mutated genes in human cancers are genes that regulate cell proliferation (oncogenes and tumour suppressors) suggested that these genes may be the cause of genome instability, laying the foundation for the oncogene-induced DNA damage model (Halazonetis et al., 2008). In this model, precancerous lesions with activated oncogenes (or loss of tumour suppressors) show oncogene-induced replication stress that triggers DDR and subsequently apoptosis or senescence. Common fragile sites (CFS) are regions on chromosomes particularly prone to gaps and breaks when DNA synthesis is perturbed (Glover et al., 2017) (Figure 9). Oncogene-induced replication stress can induce CFS breakage and prompt genomic instability. Indeed, incomplete replication of CFS can lead to anaphase bridges, copy number variants (CNV), DSBs and chromosome rearrangements, all of which participate in the acquisition of new oncogenes or loss of tumour suppressors (Glover et al., 2017). These can results in the inactivation of different checkpoints, such as p53 or ATM, allowing cancer cells to avoid DNA

damage-induced apoptosis and cell cycle arrest, and acquire further alterations that increase their fitness and contribute to the development of cancerous lesions (Halazonetis et al., 2008). It is an open question if this process is true for all sporadic cancers. Precancerous lesions are not observed in SCLC, suggesting that these tumours may skip the senescence/apoptotic step (Wistuba and Gazdar, 2006; Wistuba et al., 2000).

In SCLC, genomic instability can be induced by different factors: the high mutational load caused by tobacco carcinogens, the loss of p53 and RB and the expression of oncogenes (Figure 10). During SCLC development some or all of these events may contribute to the high genomic instability observed in these cancers, however, which event starts SCLC progression is not known. Continuous exposure to tobacco carcinogens likely generates an inflammatory response in the lung epithelium that together with the accumulation of DNA lesions can lead to cancer pathogenesis. These initial changes in the lung microenvironment are not recapitulated by current GEMMs, however the fact that loss of *Trp53* and *Rb1* are sufficient to trigger SCLC in these models (Meuwissen et al., 2003), argues that these events are enough to initiate SCLC. Interestingly, loss of *Trp53* only induced the development of adenocarcinoma, but when both alleles of *Rb1* were lost, SCLC-like tumours emerged (Meuwissen et al., 2003). Virtually all SCLC patients have a loss of function of p53 (George et al., 2015); this observation together with the fact that the spectrum of *TP53* mutations in these patients is highly related to the effect of tobacco's carcinogens (Hainaut and Pfeifer, 2001), suggest that tumours develop when the carcinogens hit *TP53* by freeing these cells from the cell cycle and apoptotic controls of p53.

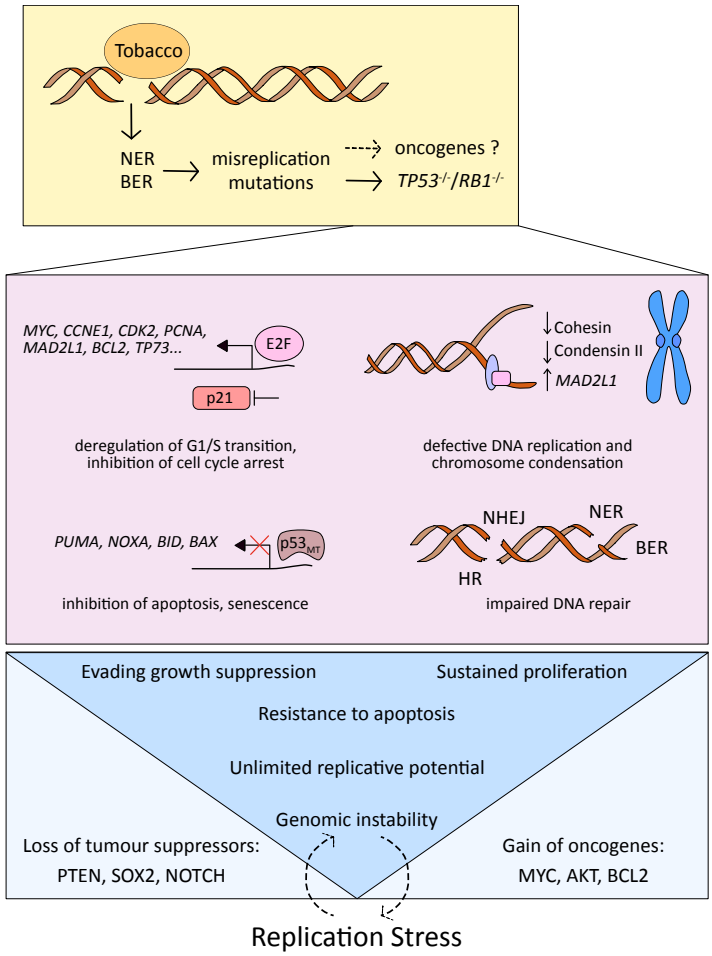

Figure 10. Putative mechanisms behind the increased replication stress observed in SCLC.

Tobacco carcinogens cause DNA lesions that are repaired by the error-prone NER and BER pathways. The mutations acquired can bring to the loss of *TP53* and *RB1* in the early stage of the disease. Gain of oncogenes may follow. Loss of *TP53* and *RB1* prompts to the acquisition of the main hallmarks of SCLC (blue box, (Thomas and Pommier, 2016)) via deregulation of different cellular process (pink box). All together these events bring to high level of replication stress, increased genomic instability and the formation of SCLC.

It is not known whether *TP53* loss occurs concomitantly, before or after *RB1* loss. However, the mouse data suggested that both genes should be deleted to generate SCLC-like tumours. Sequencing analysis of $Rb1^{flox/flox};Trp53^{flox/flox}$ murine SCLC identified similar level of CNA and rearrangements compared with human SCLC (McFadden et al., 2014), further proposing that genomic instability can be triggered by simply deleting *Rb1* and *Trp53*. Addition of oncogenes like *MYC* or *NFIB* accelerates tumour growth in GEMMs (Mollaoglu et al., 2017; Semenova et al., 2016). These events could be acquired, in human tumours, as a consequence of the mutational load of cigarette smoke and the genomic chaos linked to *TP53* and *RB1* loss. These observations suggest that SCLC do not follow the typical multistep pattern

of tumourigenesis and that loss of *TP53* and *RB1* are sufficient to cause a quick accumulation of genomic alterations that bring normal epithelial cells to suddenly transform into an aggressive cancer.

This genomic instability may allow SCLC to acquire de novo alterations, making it a particularly difficult disease to treat. However, the presence of a chaotic genomes could be exploited therapeutically, as discussed in the next sections.

1.4.2 Loss of TP53 and RB, and overexpression of oncogenes can cause genomic instability

Genomic instability is a hallmark of SCLC, and it is probably driven initially by loss of p53 and RB functions. p53 is central in the maintenance of the genome integrity by regulating cell cycle arrest, induction of apoptosis but also by directly acting during DNA repair. Indeed, p53 can modulate BER activity as well as bind several members of the NER pathway and increase lesion detection. These two mechanisms are the main pathways involved in the repair of tobacco induced DNA lesions (Hang, 2010; Williams and Schumacher, 2016). Hence, it is plausible that loss of p53 in SCLC not only allows cells to avoid apoptosis and keep cycling despite the presence of a high DNA damage burden. Loss of p53 may also impair the ability of SCLC cells to repair tobacco-induced lesions, thereby triggering genome instability (Figure 10). RB, as mentioned previously, controls the transition from G1 to the S phase and it is an important cell cycle checkpoint that the cells use to avoid DNA replication initiation in the presence of specific types of DNA damage or stress (Weinberg, 1995). Therefore, loss of RB can further increase genomic instability in SCLC by allowing cells to bypass the G1 checkpoint. Moreover, loss of RB is associated with the CIN phenotype observed in cancers. RB loss deregulates several components of the mitotic checkpoint causing chromosomal aberrations. RB controls *MAD2L1* expression through E2F and loss of RB caused upregulation of MAD2 with subsequent inhibition of APC and increased aneuploidy (Hernando et al., 2004). RB also regulates cohesin functions and its loss has been associated with reduced level of cohesin and subsequent DNA damage, replication defects and chromosomal mis-segregation (Manning et al., 2014a). Moreover, RB forms a complex with E2F1 and condensin II facilitating DNA replication and chromosome condensation. Therefore, loss of RB can

affect proper replication and generate mitotic errors (Coschi et al., 2014) (Figure 10). This role of RB in regulating correct mitotic progression and chromosomal segregation may explain why SCLC cell lines with loss of RB are highly sensitive to Aurora kinases inhibitors (Gong et al., 2019; Oser et al., 2019). Interestingly, high levels of CIN were correlated with both loss of *RB1* and *TP53*, suggesting that while *RB1* loss causes chromosomal aberration, only cells with loss of *TP53* can tolerate these alterations (Manning et al., 2014b).

Another source of genome instability is the overexpression of oncogenes that lead to replication stress and subsequent DNA damage (Halazonetis et al., 2008). Oncogenes can induce replication stress via different mechanisms that involve dysregulation of origin firing, transcription-replication conflicts, alteration in nucleotide metabolism and generation of reactive oxygen species (ROS) (Kotsantis et al., 2018). The role of oncogenes in replication stress has not been assessed for all known oncogenes and most of the studies focused on KRAS, CYCLIN E and MYC overexpressing cells (Kotsantis et al., 2018). MYC is overexpressed in 4% of SCLC (George et al., 2015; Kim et al., 2006) and may contribute to the increased genomic instability. MYC can induce replication stress by deregulating cell cycle via differential expression of CDKs and E2F factors and reducing origin firing (Bretones et al., 2015; Kotsantis et al., 2018). MYC also controls DNA replication by interacting with the pre-replicative complex and overexpression of MYC has been linked to unscheduled origin firing and increased DNA damage (Dominguez-Sola et al., 2007; Srinivasan et al., 2013). Moreover, MYC overexpression shortens the length of G1, causing firing of intragenic origins that are usually inhibited by the transcriptional machinery. These intragenic origins can easily collapse because of replication-transcription conflicts, thus inducing DNA replication stress and DSB (Macheret and Halazonetis, 2018). Overexpression of MYC can also induce ROS, in part due to increased proliferation (Bretones et al., 2015), deoxyribonucleoside triphosphate (dNTP) metabolism (Mannava et al., 2008) and transcription (Macheret and Halazonetis, 2018). When not inactivated, ROS interact with different intracellular molecules, including DNA, and induce lesions (Vafa et al., 2002). All of the above studies have focused on c-MYC, however considering the higher expression of L-MYC in SCLC, it would be interesting

to study the role played by other MYC family members in inducing replication stress and genomic instability in SCLC.

BCL-2 is another oncogene overexpressed in a group of SCLC patients (~60%) (Ben-Ezra et al., 1994; Byers et al., 2012; Poirier et al., 2015). It has been demonstrated that BCL-2 can induce replication stress by interfering with nucleotide metabolism. BCL-2 is able to directly bind to RRM2, the catalytic subunit of the ribonucleotide reductase (RNR), decreasing the conversion from ribonucleoside diphosphates (NDP) to deoxyribonucleoside diphosphates (dNDP). This reaction is necessary to generate dNTPs used during DNA synthesis and DNA repair. Inhibition of RNR by BCL-2 reduces the dNTP pool affecting fork progression and leading to DNA replication stress (Xie et al., 2014).

Of the oncogenes known to have a putative role in genomic instability, *AKT2* is amplified in 4% of SCLC patients (Dowlati et al., 2016). AKT controls energy metabolism and its activation increases oxygen consumption. Therefore, hyperactivation of AKT can generate ROS and cause DNA damage and genomic instability (Nogueira et al., 2008).

Whether oncogene-induced DNA damage has a preponderant role in the genomic instability of SCLC is unknown. It is likely that oncogenes are selected mainly to increase the overall 'fitness' of these cells while their genomic chaos remains a by-product. These 'weapons' are used by the tumours to survive and proliferate, and can be double-edged swords because of the impact oncogenes have on the genome. It is appealing to hypothesise that, independent of the molecular characteristics of a SCLC tumour, we can exploit its genomic instability to push these cells beyond their survival threshold. This may be achievable by interfering with the repair machinery and inducing replication and/or mitotic catastrophe.

1.4.3 Targeting cell cycle and mitotic checkpoint in SCLC

High levels of DNA damage together with increased replication stress in SCLC are features that can potentially be exploited therapeutically. As suggested by O'Connor in 2015, alterations in the DDR during tumourigenesis can be synthetic lethal with pharmacological inhibition of unimpaired DDR pathways (O'Connor, 2015). Indeed,

in SCLC loss of the G1 checkpoint function by lack of p53 and RB generates a dependency in these tumours that rely more on S-phase and G2/M checkpoints to avoid excessive accumulation of DNA lesions. The high level of replication stress in these tumours needs to be tightly regulated in order to avoid replication catastrophe. Replication catastrophe is an irreversible process in which cells exhaust their pool of replication protein A (RPA) (a protein complex that binds ssDNA and protects it from endonucleases), accumulate DSBs and undergo apoptosis or senescence (Toledo et al., 2017). RPA levels are controlled by ATR that, through activation of CHK1 and WEE1, represses the firing of dormant origins and restricts the formation of ssDNA (Toledo et al., 2013). An alternative replication stress-induced cell death has been recently described by Murai *et al*. In their study it is suggested that SLFN11, in the presence of replication stress, can bind RPA and persistently block replication forks independently of ATR-CHK1 signals. In the presence of unscheduled origin firing, like after ATR, CHK1 or WEE1 inhibition, SLFN11 can permanently block all activated forks, thus inducing cell death (Murai et al., 2018). Therefore, inhibition of the S- and/or G2/M-phase checkpoints, and/or induction of further DNA damage/replication stress, can be exploited to drive cells toward replication or mitotic catastrophe. As described in chapter 1.2.4, inhibition of ATR, CHK1 and WEE1 have been tested in SCLC with encouraging preclinical results (Doerr et al., 2017; Nagel et al., 2019; Sen et al., 2017a, 2017b). In these studies, the induction of replication catastrophe and the level of SLFN11 were not assessed. However, the observed induction of DSBs and apoptosis after inhibition of ATR, CHK1 or WEE1 indicate possible replication catastrophe. In some of these studies, the correlation between expression of *MYC* or *MYCL* and a higher sensitivity to ATR and CHK1 inhibitors was observed (Nagel et al., 2019; Sen et al., 2017a), confirming that oncogene-expressing tumour cells have higher levels of replication stress and therefore may rely more on the ATR-CHK1 axis to avoid replication catastrophe (Halazonetis et al., 2008; Toledo et al., 2017).

Another promising strategy to target SCLC genomic instability is the inhibition of the mitotic regulators, Aurora kinase A and B. Treatment with AURKB and AURKA inhibitors induced apoptosis in SCLC preclinical models because they failed to

properly exit mitosis (Gong et al., 2019; Mollaoglu et al., 2017; Oser et al., 2019). While Mollaoglu and co-workers associated the observed phenotype to a synthetic lethal correlation with MYC overexpression, Oser *et al* and Gong *et al* proposed a model in which loss of RB is the main driver for this sensitivity. The synthetic lethality between RB loss and AURKs inhibition seems to be associated with the role RB has during mitotic progression (Coschi et al., 2014; Manning et al., 2014a). It is also possible that the genomic instability and replication stress observed in the RB null cells as well as in the MYC overexpressing cells have deleterious effects when these cells are depleted of their mitotic checkpoints, thus inducing mitotic catastrophe. This alternative hypothesis may explain why some RB null models were not sensitive to AURKB inhibition (Oser et al., 2019). The presence of alternative pathways that can protect these resistant cells from the genomic instability induced by RB loss may account for their reduced sensitivity to AURK inhibition (Figure 11).

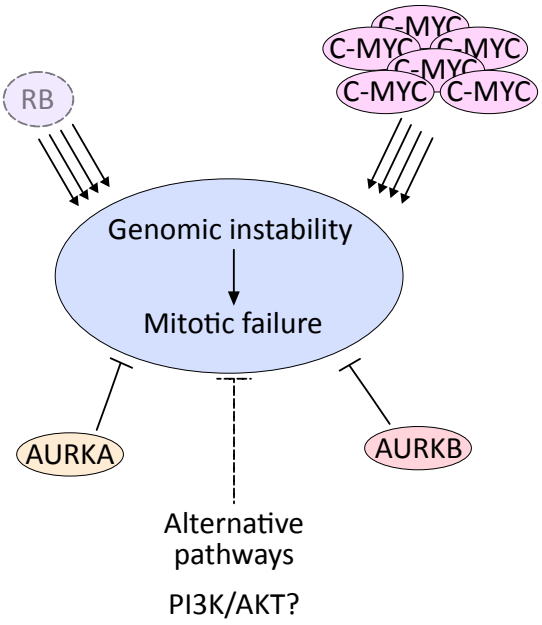

Figure 11. Aurora Kinases and other pathways can protect cancer cells from the mitotic failure induced by RB loss and C-MYC overexpression.

RB loss and C-MYC overexpression increase the level of genomic instability that can degenerate into mitotic failure. Aurora kinases act as mitotic checkpoint protecting the cells from mitotic failure. In the absence of functional Aurora kinases, activation of alternative pathways, such as the PI3K/AKT pathway, could compensate for the loss of this mitotic checkpoints.

This could be the case for the RPP model tested in Mollaoglu *et al*. These mice have a deletion of *Rb1*, however cells derived from this model do not respond to Aurora kinases inhibition *in vitro* (Mollaoglu et al., 2017). If activation of the PI3K/AKT pathway can protect these cells from mitotic catastrophe it is not known, however

roles of AKT/PTEN in regulating mitotic progression have been described (Hemström et al., 2006; Hirose et al., 2005; Leonard et al., 2013). It would be interesting to assess whether co-inhibition of the PI3K pathway and AURKs, would sensitise these cells to this treatment.

The impressive initial response observed in most SCLC patients to first-line EP can stem from the fact that these drugs generate DNA damage and replication stress, thus pushing most SCLC cells beyond their survival limit. Unfortunately, resistance mechanisms inevitably develop (as discussed in chapter 1.2.3). PARP inhibition acts in a similar way, where PARP inhibitors cause DNA breaks by inhibiting PARylation and trapping PARP to the DNA (Pommier et al., 2016b). PARP inhibitors as single agents are synthetic lethal in cancers with deficiencies in the homologous recombination repair pathway (McCabe et al., 2006), however efficacy of these compounds on SCLC preclinical models did not correlate with any known HR deficiency. Byers' group suggests that the activation of E2F1 due to RB loss may cause the overexpression of E2F1 targets, including some DNA repair proteins. They postulate that SCLC relies on these DNA repair proteins to deal with DSB and reduction of their level by inhibition of PARP1 (co-activator of E2F1) make them more sensitive to DNA damage (Byers et al., 2012; Cardnell et al., 2013). At the moment, clinical trials with PARP inhibitors in combination with EP in SCLC have shown very limited efficacy, however none of them stratified patients based on their RB status or expression of DNA repair proteins. Mutations in HR genes are rare in SCLC (Heeke et al., 2018) and genomic scars indicative of HR deficiency did not correlate with the response to different PARP inhibitors in SCLC preclinical models (Lok et al., 2017; Stewart et al., 2017). Both studies reported that high level of SLFN11 correlated with sensitivity to PARP inhibition, and propose SLFN11 as a promising biomarker to stratify SCLC patients prior to treatment with PARP inhibitors. Interestingly, the correlation was stronger for talazoparib treatment, the PARP inhibitor with the strongest trapping ability (Lok et al., 2017; Murai et al., 2014b; Stewart et al., 2017). PARP trapping can block replication fork progression and induce replication stress, explaining why SLFN11 positive cells are more sensitive to talazoparib. Murai *et al* previously showed that DNA damage caused by PARP trapping, is not only repaired

via HR but also via other repair pathways such as the Fanconi Anemia, template switching and BER pathways (Murai et al., 2012). This raises the possibility that deficiencies in other DNA repair pathways could be synthetic lethal with PARP inhibition. Hence, stratification of SCLC patients by SLFN11 protein expression or alterations in DNA repair pathways could be used to identify SCLC patients that may respond to this type of treatment. Moreover, combination of PARP inhibitors with some of the above-mentioned checkpoint inhibitors could be used to induce replication catastrophe in patients which do not express SLFN11.

1.4.4 Conclusions

In conclusion, there is a strong rationale for targeting the DDR and mitotic checkpoints in SCLC. The advantage of these treatments is that they target a common vulnerability of disease, and should demonstrate efficacy in more patients compared with other kinase inhibitors. However, at the moment the beneficial effects observed in SCLC patients have been limited. This is probably due to the high complexity and redundancy of the DDR pathways. Similarly to any other therapy, we need to understand the functional mechanisms underpinning these responses to allow better treatment design. The identification of clinically relevant biomarkers is warranted to stratify patients that would benefit from a selected treatment. Moreover, combination of multiple therapies targeting different aspects of the DDR and mitotic checkpoints should be tested to limit the emergence of resistance and target a broader population of SCLC patients. For example, Murai *et al* showed that resistance to PARP inhibition by loss of *SLFN11* can be overcome by inhibition of ATR (Murai et al., 2016), while Stewart and co-workers demonstrated that ATM inhibition re-sensitised SLFN11-low cells to PARP inhibitors (Stewart et al., 2017). It has also been shown that lesions generated by different DNA damaging agents rely on PARP to varying extent (Murai et al., 2014a), something that should be taken into account when designing clinical trials. Combination of olaparib with EP did not show impressive response in SCLC (Bono et al., 2017; Owonikoko et al., 2018; Woll et al., 2017), while combination of olaparib or veliparib with TMZ was promising and justified further investigation (Farago et al., 2018; Pietanza et al., 2018). This is probably explained by the different lesions generated by these drugs: platinum and

TOP2 inhibitors do not activate PARP or induce PARP trapping, while lesions generated by TMZ are directly recognised by PARP1/2 (Murai et al., 2014a).

Recently, an important link between DDR and immune system function has been drawn in SCLC. Byers' lab observed that olaparib or prexasertib (CHK1 inhibitor) enhanced PD-L1 expression in SCLC cell lines and GEMMs. The immune modulation observed after PARP and CHK1 inhibition was due to the activation of the STING/TBK1/IRF3 innate immune response pathway, and combination of olaparib or prexasertib with PD-L1 blockade potentiated their anti-tumour effect (Sen et al., 2019b). Interestingly, SFLN11-high SCLC patients have an enrichment of type I IFN pathway genes (downstream of the STING pathway) and positively correlated with PD-L1 expression (Stewart et al., 2017), suggesting that the high sensitivity of SLFN11-high SCLC tumours to olaparib could be partly mediated by the activation of the innate immune response.

There is little hope for a universal treatment for all SCLC patients. However, a better understanding of the biology of these tumours and the mechanisms activated in response to their high level of genomic instability can help us to identify treatments and biomarkers to improve the survival of these patients.

1.5 Project Aims

The multitude of mechanisms of resistance identified to date in SCLC preclinical models suggests high intrinsic level of heterogeneity. This heterogeneity may be at the base of the overall failure of recent clinical trials. Even when dealing with a common tumour characteristic, such as genomic instability, highly variable responses have been observed (Byers and Rudin, 2015; Sen et al., 2018). Emergent chemoresistance is the main challenge in the treatment of SCLC patients. The very rapid progression of this tumour, regardless of the treatment applied, is discouraging and challenges the development of novel therapies. Despite the promising results observed in preclinical models, targeting DDR pathways has shown limited efficacy in the clinical setting. Identification of biomarkers of response for these treatments, as well as a better understanding of the mechanisms behind the heterogenous

responses observed in patients, may aid in the design of superior clinical trials that yield the greatest benefit for SCLC patients.

From previous research, we learnt that one preclinical model cannot recapitulate the entire complexity of SCLC. By definition a model is "a simplified or idealised description or conception of a particular system, situation, or process, […], that is put forward as a basis for theoretical or empirical understanding, or for calculations, predictions, etc […]" (OED online, 2019) arguing that a model is inherently unable to entirely recapitulate the real situation. While GEMMs can be extremely useful to dissect the early steps of SCLC pathogenesis, their relative homogeneity limits their use in identifying new predictive biomarkers. Conversely, common cell lines and patient-derived xenografts may be more useful for testing new therapeutics and identify biomarkers of response, although limitations in these models have also to be taken into consideration (Table 3). In our group, we have developed a large panel of SCLC CDX that, at least partly, recapitulates the heterogeneity of SCLC subtypes observed in the literature (Figure 12) (Rudin et al., 2019; Simpson et al., 2019). These models have been the main pillar of my PhD and I have exploited them to address two main questions:

1) Can CDX provide a faithful preclinical model to shape the response to DDR inhibitors?
2) Are there any clinically relevant biomarkers that can predict the response to such inhibitors?

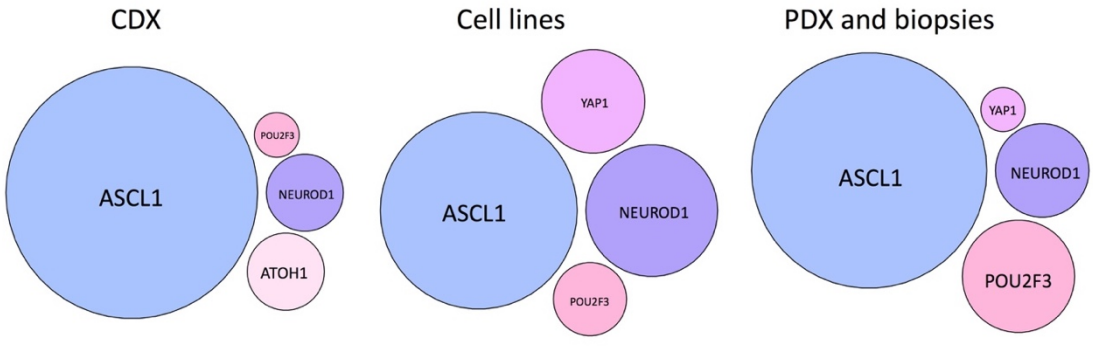

Figure 12. SCLC subtypes observed in different preclinical models.

Circle plots describing the percentage of each SCLC subgroups in the CDX models (Simpson et al., 2019) compared with the frequency of each subtypes in established SCLC cell lines, PDX and patient samples (Rudin et al., 2019). The size of each circle is proportional to the percentage of model in each subgroup.

To answer these questions, my project was divided in two main parts:

a. Development and full characterization of a short-term *ex vivo* culture system of CDX-derived tumour cells in order to functionally test hypotheses and screen novel compounds, bypassing restrictions imposed by *in vivo* models.
b. Identification of putative biomarkers of response and combinatorial treatments of DDR inhibitors with potential implications for SCLC patients.

Chapter 2: Material and Methods

2.1 Culture methods

2.1.1 General culture methods

Different media conditions were used depending on the cell lines (all from ATCC): SCLC cancer cell lines NCI-H524, NCI-H69, NCI-H1694 and NCI-H526, and the osteosarcoma cell line U2OS were grown in RPMI 1640 containing glutamine (GIBCO, Thermo Fisher Scientific, #21875091), supplemented with 10% Fetal Bovine Serum (FBS, Labtech International Ltd). The Lenti-X™ 293T cell line (ClonTech; #632180) was grown in DMEM with 10% FSB and GlutaMAX™ (GIBCO, Thermo Fisher Scientific, #35050061). CDX-derived cells were grown in HITES media (Simms et al., 1980) made up in RPMI 1640 (GIBCO, Thermo Fisher Scientific, #31870-074) with the addition of with 50 µg/mL insulin (Sigma-Aldrich, #I9278), 10 µg/mL human transferrin (Sigma-Aldrich, #T8158), 10 nM ß-estradiol (Sigma-Aldrich, #E2758), 30 nM sodium selenite (Sigma-Aldrich, #S5261) and 10 nM hydrocortisone (Sigma-Aldrich, #H0888), as previously described (Simms et al., 1980). The HITES media was then supplemented with GlutaMAX™, gentamicin (Sigma-Aldrich, #G1272), 5 µM of the ROCK inhibitor Y-27632 (Tocris, Bio-Techne, #1254) and when specified with 2.5% FBS or 50 nM bombesin (Tocris, #1149).

Non-adherent cells were passaged by washing once in PBS then incubating the cell pellet for 5-10 min at 37°C with StemPro Accutase (Thermo Fisher Scientific, #A1110501). After dissociation of the clusters, cells were washed in PBS once and resuspended in fresh media. For CDX-derived cells a 10-15 min treatment with DNase I (STEMCELL technologies, #07469) was also performed before Accutase when a lot

of debris and dead cells were observed in the media. Adherent cells were passaged when they reached 75-90% confluency. Cells were detached using 0.25% Trypsin-EDTA solution (GIBCO, Thermo Fisher Scientific, #25200056) for 5 min at 37°C and then seeded in fresh media.

Cell viability was assessed with trypan blue staining (Sigma-Aldrich, #T8154) and cells were counted with the C-Chip disposable Haemocytometer (LabTech, #DHC-N01). 10 µL of the mixture of cells and trypan blue was loaded on the chip and cells were counted in each main square, as per manufacturer's instructions. The sum of the count obtained in each square was divided by the dilution factor (2) and multiplied by 10^4 to yield the number of cells/mL.

CDX-derived cells were kept in culture for a maximum of five weeks to reduce clonal selection. Similarly, all the other cancer cell lines were maintained in culture for a maximum of ten passages. Human cell line authentication via STR profiling and mycoplasma testing by PCR were routinely performed through the CRUK MI Molecular Biology Core Facility.

2.1.2 Tumour disaggregation

Harvested tumours immediately underwent enzymatic dissociation with the human tumour dissociation kit (Miltenyi Biotec, #130-095-929) according to manufacturer's instructions. Briefly, the tumours were chopped into small pieces and dissociated in media containing a mixture of enzymes (collagenases and DNase) provided with the kit. Dissociation was performed for 1hr at 37°C under continuous rotation. Increased rotation speed to physically dissociate the tissue was performed 3 times for 30 sec during the incubation (program 37C_h_TDK_1 on the gentleMACS Octo Dissociator, Miltenyi Biotec). After dissociation, the cell suspension was passed through a 70 µm cell strainer (VWR, #734-0003) to remove large fragments of tissue and then washed with 20 mL of RPMI media and spun for 10 min at 300 x *g*. The cell pellet was incubated for 5 min at RT with the Red Blood Cell Lysis Buffer (G-Biosciences, #786-672) and then washed with PBS. After lysis of blood red cells, the cell suspension was incubated in Annexin V binding buffer (Miltenyi Biotec, #130-092-820) for 15 min at RT with microbeads conjugated with anti-MHC-I (H-2Kd/H-2Dd) mouse antibody (eBioscience, #14-5998-81 and Miltenyi Biotec, #130-047-202) to

deplete for mouse cells, and the dead cell removal kit (Miltenyi Biotec, #130-090-101) to remove dead cells. After incubation the mixture was passed through a magnetic column (Miltenyi Biotec, #130-042-401), washed 4 times with Annexin V binding buffer and the elute was collected. The final cell suspension was counted with trypan blue and seeded in HITES media with ROCKi without FBS to limit the growth of any mouse fibroblast contamination. FBS was added after 5-7 days in culture.

2.2 Media Optimisation

2.2.1 Identification of the best media conditions

To identify the optimal culture media to grow CDX-derived cells, cell proliferation was assessed by Cell Titer Glo 3D (Promega, G9683) reducing the final concentration of the buffer to 1:10 instead of 1:2 as directed in the manufacturer's instructions. CDX-derived cells were seeded at different densities on 96 well plates and grown for different times in specific media conditions. The conditions tested were:

i. HITES media alone (H)
ii. HITES media with 5 µM ROCK inhibitor (HRi)
iii. HITES media with 2.5% FBS (HF)
iv. HITES media with 2.5% FBS and 5 µM ROCKi (HFRi)
v. HITES media with 50 nM bombesin (Tocris, #1149) (HB)
vi. HITES media with 50 nM bombesin and 5 µM ROCKi (HBRi)

Readout was obtained with the plate reader FLUOstart Omega (BMG LabTech) every other day for a total follow up time of 14 days.

2.3 Drug screening

2.3.1 Drug screening optimisation

Drug screenings were performed to assess the sensitivity of different CDX cultures to a panel of compounds.

2.3.1.1 Low-throughput screenings

Low-throughput screenings were performed on 96 well plates, testing up to 10 different drug concentrations (including untreated control) with three technical replicates. CDX cells were seeded at a density of 10,000-15,000 cells per well and drug treatments were performed 48hr after seeding, in order to allow the cells to settle

after plating and cluster again. CDX cells were incubated with the drugs for a total of 7 days. For Figure 42A,B the concentrations of olaparib and AZD1775 tested ranged from 0 and 30 μM with a 3-fold increment in-between each concentration.

2.3.1.2 Moderate-throughput screening

Moderate-throughput screenings were performed on 384 well plates where a matrix of 6 x 6 drug concentrations of drug 1 and drug 2 was tested. The drugs were dispensed by Mr. Christopher Clark from the CRUK MI Molecular Biology Core Facility using the ECHO® acoustic liquid handler 550 (Labcyte). A total of 108 wells were treated with the two drugs of interest. DMSO was added to each well to reach the same DMSO concentration as in the wells treated with the highest concentration of drugs. Each combination of concentrations was tested in triplicate.

For both low and moderate-throughput screens, readouts were obtained with Cell Titer Glo 3D assay as previously described.

2.3.2 Drug formulation

A list of compounds and formulations used in this thesis is shown below:

Table 4. Compounds and stock concentrations used.

Compound	Other name	Vehicle	Stock (mM)	Main target	Seller	cat. #
Cisplatin		0.9% w/v saline	2	DNA	Sigma-Aldrich	P4394
Etoposide		DMSO	100	TOP2A	Sigma-Aldrich	E1384
AZD1775	WEE1i	DMSO	10	WEE1	AstraZeneca	NA
Olaparib	PARPi	DMSO	10	PARP-1	AstraZeneca	NA
AZD6738	ATRi	DMSO	10	ATR	AstraZeneca	NA
AZD7648	DNAPKi	DMSO	10	DNA-PKcs	AstraZeneca	NA
AZD2811	AURKBi	DMSO	10	AURKB	AstraZeneca	NA
GDC0941		DMSO	9.69	PI3Kα/δ	Selleck Chemicals	S1065
ABT737		DMSO	10	Bcl-2/Bcl-xL	Selleck Chemicals	S1002
TH1579		DMSO	10	MTH1	Thomas Helleday	NA
EdU		PBS	10	DNA	Carbosynth	NE08701
Y-27632	ROCKi	PBS	10	p160ROCK	Tocris	1254
IdU		DMSO	100	DNA	Sigma-Aldrich	I7125
CldU		DMSO	100	DNA	Sigma-Aldrich	C6891

2.4 Biochemical assays

2.4.1 Protein extraction

2.4.1.1 Protein extraction for cell lines

Cell pellets were quickly washed in cold PBS and then solubilised with ice-cold lysis buffer (20 mM Tris-HCl pH 7.5, 150 mM NaCl, 1 mM Na_2EDTA, 1 mM EGTA, 1% Triton, 2.5 mM sodium pyrophosphate, 1 mM β-glycerophosphate, 1 mM Na_3VO_4, 1 µg/mL leupeptin; Cell Signaling technology, #9803S) in the presence of Protease Inhibitor Cocktail (1:100, Sigma-Aldrich, #P8340) and Phosphatase Inhibitor Cocktail II and III (1:100, Sigma-Aldrich, #P5726 and #P0044). Lysis was performed for 30min on ice and the samples were vortexed every 10 min. After incubation in lysis buffer, samples were spun down for 15 min at 4°C at ≥ 16,000 x *g*. The supernatant was collected and stored at -80°C.

2.4.1.2 Protein extraction for tumour tissue

Snap-frozen tumours were homogenised in Fastprep tubes with lysing matrix A (MP Biomedicals, #SKU116910050-CF) using the TissueLyser LT (Qiagen) and ice-cold lysis buffer (Cell Signaling technology, #9803S). Tissue was homogenised for 3 x 1 min at 50 Hz and then the lysate was spun down at ≥ 16,000 x *g* for 15 min at 4°C. Supernatant was collected and stored at -80°C.

2.4.2 Protein quantification

Both protein extractions from cells and tissue were quantified with the Bicinchoninic acid (BCA) assay kit (Thermo Fisher Scientific, #23225) as per manufacturer's instructions. A 1:10 dilution of the protein lysate was used to quantify the protein content from cell lines, while a 1:50 dilution was used for tissue samples. Standards were made up in matched lysis buffer.

2.4.3 Western Blotting

20µg of protein were mixed with 4x NuPAGE LDS buffer (Invitrogen, #NP0007) and 10x NuPAGE reducing agent (Invitrogen, #NP0004) and boiled for 10 min at 70°C before loading on pre-casted NuPAGE 4%-12% Bis-Tris 1.0 mm gel (Invitrogen, #NP0322/0321). Gels were run for 1.5-2hr in MOPS SDS running buffer (Invitrogen, #NP0001) at 120V. Protein were transferred to Amersham Hybond ECL Nitrocellulose

Membrane (GE Healthcare, #RPN203D) for 1hr at 100V in 10% v/v Tris/Glycine/SDS transfer buffer (National Diagnostics, #EC-880) with 5% v/v methanol. Ponceau S staining (Sigma-Aldrich, #P7170) was used to check the quality of the transfer. Membranes were quickly incubated with Ponceau S and then washed with deionised water (ddH2O) before imaging. A final wash with TBS with 0.1% Tween20 (TBST, Sigma-Aldrich, #T2700) was used to completely remove the red dye. Blocking was performed for 2-4hr in TBST with 5% milk at room temperature (RT). Membranes were incubated overnight at 4°C with the appropriate primary antibody diluted in TBST with 5% milk or with 5% BSA when antibodies against phospho-epitopes were used. The only exception was the phospho-RPA2 S33 antibody, which worked better in 5% milk. For a list of antibodies used and their working dilution see Table 5. After incubation with primary antibodies, membranes were washed 3 x 20 min in TBST at RT and then probed with the corresponding horseradish peroxidase-coupled secondary IgG (Dako, Agilent Technologies) in TBST with 5% milk for 1hr at RT. A final 3 washes x 20 min in TBST at RT were performed before detection on Amersham Hyperfilm ECL (GE Healthcare, #28-9068) with the Western Lightning Plus-ECL system (PerkinElmer, #NEL103001EA) or on the ChemiDoc™ XRS+ (BioRad). The acquired images were processed with Affinity Designer v1.7.1 to generate the figures and Fiji (ImageJ v2.0.0) was used to quantify band intensity. Images of the membranes were analysed with the “Gels” tool on ImageJ. Equal squares were drawn around each band and the area under the curve was calculated for each band’s intensity peak. These values were plotted with Graphpad Prism v8.2.0.

For the cellular thermal shift assay (chapter 2.4.4), extracted proteins were mixed with 4 x Laemmli buffer and then heated at 95 °C for 10 min. Samples were run on SDS-PAGE gel followed by protein transfer to nitro-cellulose membranes. Membranes were blocked in TBST and 5 % milk for 1 hour followed by incubation with anti-MTH1 antibody and anti β-actin for 1 hr. Membranes were washed three times in TBST followed by incubation with anti-rabbit-HRP and anti-mouse-HRP antibodies for 1 hr. After washing 3 times in TBST the membranes were analysed using Super signal west femto maximum sensitivity substrate (ThermoFisher

Scientific, #34096) and measurements were performed using Odyssey Li-Cor system. The bands were scanned and normalized to the band of the 25°C sample.

Table 5. List of antibodies used for Western Blot.

Antigen	Vendor	Cat. Number	Clone	Concentration
cleaved caspase 3	Cell Signaling Technology	9661		1:1000
phospho CDC2 Y15	Cell Signaling Technology	4539	10A11	1:1000
CDC2	Cell Signaling Technology	9116	POH1	1:1000
CHK1	Cell Signaling Technology	2360	2G1D5	1:1000
phospho CHK1 S317	Cell Signaling Technology	12302	D12H3	1:1000
phospho CHK1 S345	Cell Signaling Technology	2348	133D3	1:1000
PARP	Cell Signaling Technology	9542		1:1000
pAKT S473	Cell Signaling Technology	9271		1:1000
AKT	Cell Signaling Technology	2920	40D4	1:2000
pS6 S235/236	Cell Signaling Technology	4857	91B2	1:1000
S6	Cell Signaling Technology	2217	5G10	1:1000
α-tubulin	Cell Signaling Technology	2144		1:2000
GAPDH	Cell Signaling Technology	2118	14C10	1:2000
MTH1	Novus	NB100-109		1:500
β-actin	Cell Signaling Technology	3700	8H10D10	1:1000
Histone H3	Cell Signaling Technology	4499	D1H2	1:2000
pHH3 S10	Millipore	05-806	3H10	1:1000
CDK6	Abcam	ab124821	EPR4515	1:1000
pRPA32 S33	Bethyl Laboratories	A300-246A		1:1000
p21	BD Biosciences	556430	SX118	1:200
RB1	Cell Signaling Technology	9309	4H1	1:2000

2.4.4 Cellular thermal shift assay

The cellular thermal shift assay (CESTA) was performed by Thomas Helleday's laboratory and was included in this thesis to complement the described data with the MTH1 inhibitor, TH1579. The preparation of the samples was performed as follow. Tumours from the pharmacodynamic arms (see chapter 2.9.3 for detail) were mashed in liquid nitrogen and homogenized in 300 µL of TBS with protease inhibitor cocktail (Roche, #11697498001). Each tumour suspension was aliquoted in 9 PCR tubes, with 30 µL per tube. Eight of the tubes were heated for 3 min with a temperature-gradient ranging from 48 to 63°C using the Biorad Thermocycler. One tube was kept at room temperature (25°C). Samples were then frozen at -80°C and

thawed three times to lyse the cells. Samples were then centrifugated at 17,000 x *g* for 20 min. The supernatants were processed as described in chapter 2.4.3.

2.4.5 RNA isolation and sequencing

2.4.5.1 RNA extraction for cell cultures

Cells were spun down for 5 min at 300 x *g* and washed once with PBS. If the cells were not processed immediately for RNA extraction, they were pelleted in 1.5 mL eppendorf tube for 5 min at 300 x *g*, snapfrozen in liquid nitrogen and then stored at -80°C. RNA extraction was performed with the RNeasy Mini Kit (Qiagen, #74106), as per manufacturer's instructions. Briefly, samples were defrosted on ice, quickly lysed with RLT buffer and passed through a QIAshredder column, and processed on RNeasy spin columns. Eluted RNA was then quantified with a Nanodrop spectrophotometer (LabTech, #ND-1000) and stored at -80°C until ready for sequencing.

2.4.5.2 RNA extraction for tumour tissue

Total RNA was extracted from snap-frozen or RNA*later®* (Sigma-Aldrich, #R0901) samples with the RNeasy Mini Kit (Qiagen, #74106) according to manufacturer's instructions. Samples were first defrosted on ice and then disrupted and homogenised using Fastprep tubes with lysing matrix A and the RLT buffer with β-mercaptoethanol on the TissueLyser LT. Tissue was homogenised for 3 x 1 min at 50 Hertz and then the lysate was spun down at ≥ 16,000 x *g* for 3 min at 4°C. Subsequent steps were performed the same as for cell cultures.

2.4.5.3 Bulk RNA-sequencing

RNA-sequencing was carried out by John Weightman, Gillian Williams, and Emily Hulme at the CRUK MI Molecular Biology Core Facility. RNA quality checks were performed with the Agilent 2100 Bioanalyser and samples with RNA integrity number > 7.6 were selected for downstream processing. Indexed PolyA libraries were prepared using 200ng of total RNA and 14 or 15 cycles of amplification with the Agilent SureSelect Strand Specific RNA Library Prep Kit for Illumina Sequencing (Agilent, #G9691B). Libraries were quantified by qPCR using a Kapa Library Quantification Kit for Illumina sequencing platforms (Kapa Biosystems Inc., #KK4835).

Paired-end 75 or 150bp sequencing was carried out by clustering 1.8-2.3pM of the pooled libraries on a NextSeq 500 sequencer (Illumina Inc.).

2.4.6 DNA isolation, Sanger sequencing and whole exome sequencing

2.4.6.1 DNA isolation from cell cultures

Genomic DNA was extracted from snap-frozen cell pellets with the QIAmp DNA mini Kit (Qiagen, #51304) according to manufacturer's instructions. Briefly, cell pellets were defrosted on ice, digested in Proteinase and lysed at 56°C for 10 min. Ethanol was added to the mixture and the solution was applied to the QIAmp Mini spin column and processed. The eluted DNA was quantified with a Nanodrop spectrophotometer and stored at -20°C.

2.4.6.2 DNA isolation from tumour tissue

Genomic DNA was extracted from snap-frozen tumours with the QIAmp DNA mini Kit (Qiagen, #51304) according to manufacturer's instructions. Briefly, a small piece of the tumour was placed in 1.5mL Eppendorf and lysed in Proteinase K overnight on a shaker at 300 rpm at 56°C. After lysis, the samples were incubated with RNAse A (100mg/mL) (Qiagen, #1006657) for 2 min at RT. All subsequent steps were the same as described for cell cultures.

2.4.6.3 PCR and primer design

The extracted genomic DNA was amplified by polymerase chain reaction (PCR) using primers flanking relevant regions in the gene of interest. The PCR protocol for Phusion® HighFidelity DNA Polymerase (New England Biolabs Inc, #M0530) was followed as per manufacturer's instructions and run on the Profile PCR system (Applied Biosystems, Life Technologies) with the initial denaturation performed at 98°C for 30 sec, followed by several cycles of denaturation at 98°C for 10 sec, annealing at the melting temperature (58°C for *TP53* and 62°C for *PALB2*) for 30 sec and extension at 72°C for 30 sec. The final extension was also done at 72°C. The sequence of each primer and the PCR protocols are shown in Table 6 and Table 7.

Table 6. List of primers.

Model	Target	forward primers	reverse primers
CDX2	*TP53* A440C	CACTTGTGCCCTGACTTTCA	CTCACAACCTCCGTCATGTG
CDX3	*TP53* A263G	CTCAGATAGCGATGGTGAGC	CCCTTAGCCTCTGTAAGCTT
CDX4	*TP53* G892T	GTGGTTGGGAGTAGATGGAG	TCCCAAGACTTAGTACCTGAAG
CDX3	*PALB2* E178*	AGCTGCCAAGCAGAAGAAAG	TGGTTCTGGAGAATCTGGAAG
CDX4	*PALB2* E178*	AGCTGCCAAGCAGAAGAAAG	TGGTTCTGGAGAATCTGGAAG

Table 7. PCR protocols.

Target	Initial denaturation	Denaturation	Melting Temperature	Initial Extention	Final extention	Hold	Cycles
TP53 A440C	98°C x 30''	98°C x 10''	58°C x 30''	72°C x 30''	72°C x 30''	4°C	x 35
TP53 A263G	98°C x 30''	98°C x 10''	58°C x 30''	72°C x 30''	72°C x 30''	4°C	x 35
TP53 G892T	98°C x 30''	98°C x 10''	58°C x 30''	72°C x 30''	72°C x 30''	4°C	x 35
PALB2 E178*	98°C x 30''	98°C x 10''	62°C x 30''	72°C x 30''	72°C x 2'	4°C	x 28

2.4.6.4 Sanger sequencing

The amplified DNA was Sanger sequenced with an ABI3130xl 16 capillary system by the CRUK MI Molecular Biology Core Facility. Sanger sequencing results were visualised with SnapGene® Viewer v4.3.7 (GSL Biotech; available at snapgene.com).

2.4.6.5 Whole-exome sequencing

For the whole exome sequencing (WES), 300ng of genomic DNA was sheared using the Covaris S2 Ultrasonicator (Covaris Inc.) to an average size of 150-200bp. Indexed libraries were prepared from 50ng of the sheared DNA using the NEB Next Ultra II DNA Library Prep Kit (New England Biolabs, #E7645S) with 4 cycles of amplification. Libraries were quantified by qPCR using a Kapa Library Quantification Kit for Illumina sequencing platforms (Kapa Biosystems Inc., #KK4835). Paired-end 75bp sequencing was carried out by clustering 1.7pM of the pooled libraries on a NextSeq 500 sequencer (Illumina Inc.).

2.5 Irradiation

2.5.1 Irradiation of CDX cultures *ex vivo*

CDX cultures were irradiated with specific amount (Gy) of ionising radiation (IR), as stated in the text and figure legends. After irradiation, cells were kept on ice until the media was refreshed or immediately processed. For the cell viability assay, cells were grown for 5 days after treatment with increasing IR intensities (0, 4, 8 and 12 Gy) and then viability was assessed by Cell Titer Glo (as previously described).

2.6 Immunohistochemistry (IHC) assays

2.6.1 Samples preparation

2.6.1.1 Formalin fixed paraffin-embedded (FFPE) samples

Tumour tissues were collected in cold PBS and immediately cut in small longitudinal sections of ~2 mm depth with a scalpel and fixed in 10% formalin for 24hr. After fixation, tumour pieces were put in 70% ethanol before being embedded in paraffin by Usman Mahmood, Marta Madureira Da Gracia and Vasia Sykioti in the CRUK MI Histology Core Facility. For processing of cell cultures, cells were washed in PBS and then spun for 10 min at 300 x *g*. The cell pellet was fixed with 4% PFA for 30 min at RT and then put in 70% ethanol before embedding in paraffin by Usman Mahmood in the CRUK MI Histology Core Facility.

2.6.1.2 Cytospin samples

CDX cultures were firstly dissociated with accutase for 5-10 min at 37°C, washed twice in PBS and then diluted to 150,000 cells/mL in PBS. 200 µL of the diluted cell suspension were loaded in the cytospin chamber and then spun for 5 min at 500 rpm with the Cytospin 2 (Shadon). After spinning, the slides were fixed with 4% PFA for 20 min at RT and then stored in PBS at 4°C for a maximum of 5 days.

2.6.2 Haematoxylin and Eosin staining

Haematoxylin and Eosin staining was performed by Vasia Sykioti, Usman Mahmood and Marta Madureira Da Gracia in the CRUK MI Histology Core Facility. Sections of 4µm were cut from FFPE blocks and processed in xylene 3 x 5 min to remove paraffin. Slides were then re-hydrated with subsequent washes in decreasing concentrations of ethanol: 3 x 1 min 100% ethanol, followed by 1 x 1 min 90% ethanol

and 1 x 1 min in 70% ethanol. Slides were then washed in water for 1 min before staining the nuclei with Gills 2 Hematoxylin (Thermoshandon, #6765008) for 3 min. After staining, slides were washed in water once for 1 min, then slides were incubated in acetic acid (ThermoFisher Scientific, #10394970) for 30 sec and washed in water once for 1 min. Afterwards, slides were incubated in alkaline water for 1 min, washed in water for another minute and then stained with eosin (Thermoshandon, #6766008) for 1 min. Slides were then washed once in water for 1 min and dehydrated in ethanol: 15 sec in 70% IMS, 15 sec in 90% IMS and 3 times 30 sec in 100% IMS followed by 1 min in xylene. Pertex (CellPath, #SEA-0100-00A) was used to mount coverslips on the slides.

2.6.3 Chromogenic staining

All chromogenic stains were performed on 4 µm slides cut from FFPE tumour tissue or cell pellets on the BondMax/BondRX autostainers (Leica Biosystems) with the Bond polymer refine detection system (Leica Biosystems, #DS9800) or the Ventana Discovery Ultra autostainer and reagents (UltraView Universal DAB Detection Kit, #760-500, Ventana) available at the CRUK MI Histology Core Facility. Briefly, slides were dewaxed in xylene for 3 x 5 min, and re-hydrated in decreasing concentrations of ethanol (3 x 3 min in 100%, 1 x 3 min in 90% and 1 x 3 min in 70%). Slides were then blocked with 3-4% (v/v) hydrogen peroxide for 5 min at RT, washed 3 x 2 min in Bond Wash Solution (Leica Biosystem, #AR9590), incubated 15 min with primary antibody diluted in the Bond Primary Antibody Diluent (Leica Biosystem, #AR9352), washed 3 x 2 min with the Band Wash Solution and then incubated with the rabbit anti-mouse IgG, when needed, for 8 min at RT. Afterwards, slides were washed again 4 x 2 min with the Bond Wash Solution and then incubated with the anti-rabbit poly-HRP-IgG for 8 min at RT and washed again 4 x 2 min with the Bond Wash Solution. Slides were then incubated with the mixed DAB Refine (66 mM 3,3'-Diaminobenzidine tetrahydrochloride hydrate, ≤ 0.1% (v/v) hydrogen peroxide and < 0.1% haematoxylin) for 10 min and washed in ddH2O for 5 min. Afterwards, slides were dehydrated in increasing concentration of ethanol (1 x 1 min 70%, 1 x 1 min 90%, 3 x 1 min 100%) followed by 3 x 1 min washes in xylene. Pertex was used to

mount the coverslip on the slides. A list of all antigens tested and the detection technique used is shown in Table 8.

For 8-oxoguanine (8-oxo-G), slides were stained manually using the UltraVision LP Detection System (ThermoFisher Scientific, #TL-015-HD) according to manufacturer's instructions. The staining was performed by Ioannis S. Pateras in Professor Vassilis G Gorgoulis' lab.

2.6.4 Immunofluorescence stainings

Immunofluorescence was performed on FFPE tissue or cell pellet sections (4 μm) using the BondMax/BondRX autostainer, or alternatively performed manually on cell cytospin or Poly-D-Lysine coated 96 wells plates (VWR, #354640). Poly-D-lysine coated plated were used to allow lying of the cells at the bottom of the plate limiting the number of cells lost during washes and staining.

2.6.4.1 Automated stainings

Two main protocols were performed on the BondMax/RX autostainers. One used Alexa fluorophores and the other one exploited the Opal system with Tyramide Signal Amplification (TSA) (Bobrow et al., 1989, 1991; Pathology et al., 2018). When Alexa fluorophores were used, samples were treated with a specific antigen retrieval buffer (see Table 8) and then permeabilised with 0.5% Triton™ X-100 (Sigma-Aldrich, #T8787) for 15 min at RT. After permeabilisation, samples were blocked with 5% goat serum (Dako, #X090710-8) supplemented with 0.1% Triton™ X-100 for 1 hr at RT and then incubated for 2 hr at RT with one or a cocktail of primary antibodies diluted in the Primary Antibody Diluent BOND (Leica Biosystems, #AR9352). Incubation with one or a cocktail of Alexa fluorophores was performed at RT for 1 hr always in the Primary Antibody Diluent (Table 9). Different washing steps were performed with the Wash Solution 10X Concentrate BOND (Leica Biosystems, #AR9590). DAPI staining was done twice, the first one for 15 min, while the second one for 5 min at RT. Slides were then coverslipped with Prolong™ Diamond Antifade Mountant (ThermoFisher Scientific, #P36965) and air-dried for a few hours. For EdU staining on the Bond autostainers, an additional step of 30 min incubation at RT with the Click Reaction mixture (0.4% 1 M Copper(II) sulphate pentahydrate, Acros #197730010, 0.05% of 10

mM Sulfo-Cyanine 5 Azide, Lumiprobe #B3330, and 10% of 1 M L-ascorbic Acid Sodium Salt, Acros #352685000) was performed before blocking.

Table 8. List of antibodies and detection methods used for IHC.

Antigen	Vendor	Catalogue Number	Clone	Concentration	Antigen Retrieval (min) / Pretreatment	Protocol
Pan-cytokeratins	Dako	M3515	AE1/AE3	1:100	Bond ER1 (20)	Chromogenic
Synaptophysin	Leica Biosystem	NCL-L-SYNAP-299	27G12	RTU	Bond ER2 (20)	Chromogenic
CD56	Leica Biosystem	CD56-1B6-CE	1B6	RTU	Bond ER1 (20)	Chromogenic
Vimentin	Roche	790-2917	V9	RTU	Ventana CC1 (pH 9)	Chromogenic
Cleaved PARP (Asp214)	BD Biosciences	552596	F21-852	RTU	Bond ER1 (20)	Chromogenic
8-oxo-G	Millipore	MAB3560	483.15	1:750	AR 10 mM citric acid (pH 6)	Chromogenic
pS235/236 S6	Cell Signaling Technology	4857	91B2	1:200	Bond ER2 (10)	Chromogenic
phospho Histone H3	Millipore	05-806	3H10	1:1000	Bond ER1 (20)	IF
γH2AX	Biolegend	613402	2F3	1:1000	Bond ER1 (20) / Manual	IF
RAD51	GeneTex	GTX70230	14B4	1:150/1:300	Manual	IF
Geminin	Abcam	ab195047	EPR14637	1:150	Manual	IF
p21	BD Biosciences	556430	SX118	1:200	Bond ER1 (20)	Chromogenic/IF
RPA70	Abcam	ab79398	EPR3472	1:500	Manual / pre-extraction	IF
Cyclin A	Santa Cruz Biotechnology	sc-271682	B-8	1:300	Bond ER1 (20)	IF

For the Opal system, samples followed the same procedure as described above, with a few differences. Blocking was performed at RT with 3% Hydrogen peroxide solution (Sigma-Aldrich, H1009) followed by 10% Casein solution (Vector Laboratories, #SP-5020), 10 min each. Incubation with primary antibodies was performed sequentially: each antibody was left for 30 min, followed by an incubation with the corresponding HRP conjugated secondary antibody (DAKO, #K4003 and K4001) for 30min, followed by incubation with the Tyramide-fluorophore (1:200, PerkinElmer, #NEL821001KT) for 10 min. If more than one epitope was detected, a heat-inactivation step was performed after the Tyramine-fluorophore to allow the binding of the new primary antibody. All steps were then repeated until all primary antibodies were bound. DNA staining was performed with DAPI (two steps of 15 min and 5 min at RT) and slides were coverslipped as described above. Table 8 and Table 10 summarised the antibodies and protocols used.

Table 9. List of Alexa fluorophores and concentrations used.

Antibody	Vendor	Cat. Number	Concentration
Anti-rabbit Alexa488	ThermoFisher Scientific	A11034	1:500
Anti-rabbit Alexa647	ThermoFisher Scientific	A32733	1:400
Anti-rabbit Alexa555	ThermoFisher Scientific	A21430	1:400
Anti-mouse Alexa488	ThermoFisher Scientific	A32723	1:500
Anti-mouse Alexa647	ThermoFisher Scientific	A21235	1:400
Anti-mouse Alexa555	ThermoFisher Scientific	A32727	1:400

Table 10. Protocol used for TSA staining.

Antigen	Concentration	1st(min)/2nd(min) Heat steps	Position
phospho Histone H3	1:2000	Bond ER1(20)/ER1(10)	Second
p21	1:200	Bond ER1(20)/ER1(10)	First

2.6.4.2 On-the-bench stainings

Manual immunofluorescence was performed on samples after they were fixed with 4% PFA (ThermoFisher Scientific, #15424589) for 15 min at RT or 20 min on ice and then permeabilised for 10-15 min with 0.5% Triton™ X-100 (Sigma-Aldrich,

#T8787) at RT. For staining with the chromatin-bound RPA1 antibody, samples underwent a pre-extraction step in 0.2% ice-cold Triton™ X-100 for 1 min prior to fixation. Washes in between steps were performed at RT or on ice with 10% FBS in TBS with 0.2% Tween20 (TBST, Sigma-Aldrich, #T2700). For EdU staining, samples were incubated for 30 min at RT protected from light with the Click Reaction mixture (4mM $CuSO_4$ (Acros, #197730010), 5µM Sulfo-cyanine 5 azide (Lumiprobe, #B3330) and 100mM of sodium ascorbate (Acros, #352685000) in PBS) before incubation in the blocking solution. Blocking was performed with 5% goat serum (Dako, #X090710-8) supplemented with 0.1% Triton™ X-100 for 1 hr at RT. Staining with primary antibodies was performed overnight at 4°C in the blocking solution. After primary, samples were washed 3 x 5 min at RT or on ice with the washing buffer (10% FBS in TBST) and then incubated for 1 hr at RT with the appropriate Alexa secondary antibodies diluted in the blocking solution. Washes were performed as previously described and an additional wash in TBST only was performed before staining with 500 nM of DAPI (ThermoFisher Scientific, #D1306) for 5 min at RT. Samples were washed 2 x 3 min in TBST and then the slides were coverslipped with Prolong™ Diamond Antifade Mountant (ThermoFisher Scientific, #P36965) and air-dried for a few hours.

The same steps were performed for the staining of samples seeded on Poly-D-Lysine coated plates. In between each step, the plates were quickly spun down (450 x *g* for 1 min) to reduce the loss of the cells during washes. Once stained with DAPI, each well was washed twice in TBST and the samples were covered with PBS and stored at 4°C until imaged. Table 8 and Table 9 summarise the antibody dilutions used.

2.6.4.3 Fiber assay

The Fiber assay is divided in three main parts, the labelling, the DNA spreads and the staining. For the labelling, 5-Chloro-2′-deoxyuridine (CldU, Sigma-Aldrich, #C6891) and 5-Iodo-2′-deoxyuridine (IdU, Sigma-Aldrich, #I7125) were dissolved in DMSO at a final concentration of 100 mM. A lysis solution was prepared with 200 mM Tris-HCl (Sigma-Aldrich, #T3253), 50 mM EDTA (ThermoFisher Scientific, #15575020) and 0.5% SDS (VWR, #A0675.0250), pH 7.4 to lyse the cells.

To perform the assay, CDX cells were seeded 48hr before labelling, in order to allow the cells to enter exponential growth. On the day of labelling, media and PBS were pre-warmed at 37°C. The cells were labelled with 50 µM of CldU and incubated at 37°C for 20 or 40 min. After incubation, the cells were washed once in warm PBS and spun for 2 min at 450 x *g*. The cells were then resuspended in fresh warm media with 50 µM of IdU, and incubated at 37°C for another 20 or 40 min. After incubation, the cells were washed once in warm PBS and resuspended in media only for 1hr or 2hr and then exposed to another round of labelling with both thymidine analogues. After labelling, the cells were dissociated with trypsin for 5 min at 37°C, washed and resuspended in cold PBS. Cells were then counted and resuspended in ice cold PBS at 500 cells/µL. For the DNA spread, 2.5 µL of the cell suspension were gently mixed with 7.5 µL of lysis buffer directly on the slide (Superfrost slides precleaned, FisherBrand, #12-550-123). The mixture was pipetted 3 times with a P20 set at 5µL and slides were let to sit horizontally at RT for 8 min. After that, the slides were tilted to 15 degrees and air dried for 1hr. Once dry, the slides were fixed with fresh 3:1 methanol:acetic acid (ThermoFisher Scientific, #10675112 and #10394970) for 10 min. The slides were then dipped in ddH2O to rinse and let air dry for few hours. Once dry, the slides were stored at -20°C overnight. Before staining, the slides were washed twice in PBS for 3 min. A quality check was done, by quickly staining some of the slides with 0.1 µM of YOYO-1 iodide (Invitrogen, #Y3601) diluted in PBS for 5min at RT (Figure 13).

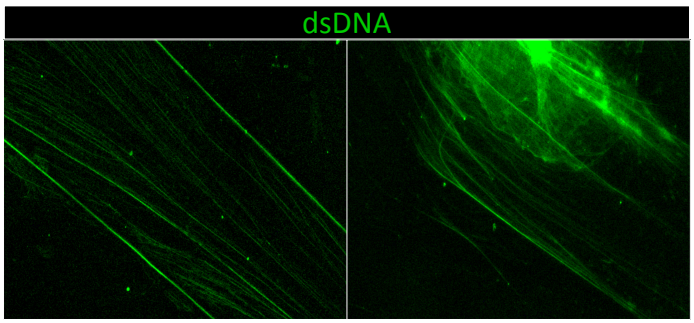

Figure 13. Example of YOYO-1 staining before DNA denaturation.

Slides were checked with a widefield Zeiss 200M Metamorph microscope to assess the quality of the preparation. After washing, the remaining slides were incubated with 2.5 M HCl (ThermoFisher Scientific, #H/1200/PB17) for 1hr to denature the DNA and then washed three times in PBS with 0.05% Tween20 (PBST, Sigma-Aldrich,

#T2700) for 5 min. At this point, the fibers were blocked with a fresh solution of 2% BSA (Sigma-Aldrich, #A7906) and PBST for 40min at RT. After blocking, slides were incubated with the primary antibodies in PBST with 1% BSA. The incubation was performed for 1.5hr at RT (slides inverted on parafilm). Before incubation with the secondary antibodies, the slides were washed three times in PBST, and once in the blocking solution (5 min each wash). Secondary antibodies were diluted 1:300 in 1% BSA/PBST and incubated for 1hr at RT covered by light (inverted on parafilm). Slides were then washed three times in PBST, and once in the blocking solution (5 min each wash). When the ssDNA was stained, the slides were incubated with 100 µL of the primary antibody for ssDNA in 1% BSA/PBST for 45min at RT in the dark (inverted on parafilm). Slides were then washed three times in PBST, and once in the blocking solution (5 min each wash), and incubated with the secondary antibody, BV480 Goat anti-mouse Ig, (1:200, BD Bioscience, #564877) in 1% BSA/PBST for 45min at RT in the dark (inverted on parafilm). Slides were then washed three times in PBST for 5min and then let air dry completely. Coverslips were mounted with prolong Diamond mounting media (ThermoFisher Scientific, #P36961) and stored at -20°C.

Table 11. List of antibodies used for the Fiber assay.

Antibody	Antigen	Vendor	Cat. number	Concentration
YOYO-1 iodide	dsDNA	Invitrogen	Y3601	1:10,000
Anti BrdU	CldU	Novus	NB500-169	1:500
Anti BrdU	IdU	BD Bioscience	347580	1:100
Anti-mouse Alexa647		ThermoFisher Scientific	A11062	1:300
Anti-rat Alexa488		ThermoFisher Scientific	A21470	1:300
Anti-DNA	ssDNA	Millipore	MAB3034	1:200
BV480		BD Bioscience	564877	1:200

2.6.4.4 Comet assay

The Comet assay was performed following the manufacturer's instructions of the CometAssay Kit (Trevigen, #4250-050-K).

Briefly, irradiation was used to induce DNA damage in the CDX cultures, as described in chapter 2.5.1. Once the cells were ready, they were washed once in PBS

and then resuspended at 1 x 10^5 cells/mL in PBS. The obtained cell suspension was then combined with the aliquoted melted LMAgarose in a 1:10 dilution (50 µL of cells in 500 µL of LMAgarose) and spread onto the sample area of the pre-warmed CometSlides. The nuclei were lysed overnight at 4°C and then the slides were placed into the electrophoresis tank and ran at 21V for 45min at 4°C. After the run, slides were immersed in 70% Ethanol for 5 min and then dried at 37°C for 10-15min. SYBR Gold (Invitrogen, #10358492) was used at 1:10,000 in TE buffer, pH 7.5 (10 mM Tris (pH 7.5) (Sigma-Aldrich, #T1503), 1 mM EDTA (ThermoFisher Scientific, #15575020)) to visualise the DNA.

2.8.5 Image acquisition

All IHC slides were imaged with microscopes provided by the CRUK MI Imaging Core Facility thanks to the help of Dr. Isabel Peset, Heather Woodhouse and Kang Zeng. Whole tissue sections of chromogenic stainings were acquired using the Leica SCN400 scanner (Leica Microsystems) using a 20x magnification. For whole slide scanning of immunofluorescent stainings, the Leica Aperio Versa 200 scanner (Leica Microsystems) with either 20x or 40x magnification was used. Single region and DNA fiber images were acquired with the widefield Zeiss 200M Metamorph or the confocal Zeiss LSM880 (Zeiss). Acquisition of 96 well plates was obtained with the Opera Phenix™ High Content Screening System (PerkinElmer). For the comet assay, each region of the slides was scanned using a 10x magnification with the gSTED 2Photon Confocal Leica TCS SP8 microscope.

2.7 Flow cytometry

2.7.1 Flow cytometry with 2'-Deoxy-5-ethynyluridine (EdU)

2.7.1.1 Cell proliferation

Proliferation was assess with EdU using the Click-iT Plus EdU Alexa Fluor 488 or Pacific Blue Flow Cytometry Assay kit (Thermo Fisher Scientific, #C10632 or #C10636) as per manufacturer's instructions. Propidium iodide (PI/RNase, Cell Signaling Technology, #4087) was used to quantify the DNA content. Briefly, CDX cultures were incubated with 2.5 µM of EdU for 14 hours. After incubation, cells were dissociated with accutase for 10 min at 37°C. Cells were then fixed and permeabilised before

staining with the Click-iT™ Plus reaction cocktail. Staining with with 1x PI/RNase staining solution (Cell Signalling Technologies, #4087) was then performed for 30 min at RT protected from light. After staining, cells were immediately run on the flow cytometer (LSRFortessa II) and the percentage of cells in each gate was determined using FlowJo software (v10).

2.7.1.1 Optimisation of thymidine analogues incorporation in CDX cultures

To optimise the fiber assay an in-house protocol for EdU detection was followed. Briefly, CDX cells were incubated with 10µM of EdU for 30 min, 1hr, 2hr or two pulses of 30 min with 2hr incubation in EdU-free media in between pulses. After incubation, cells were dissociated with accutase for 10 min at 37°C and then washed once in cold 2mM EDTA (ThermoFisher Scientific, #15575020) in PBS. After wash, cells were fixed in 4% PFA for 15min at RT. Cells were then washed once with cold 2mM EDTA PBS and then permeabilised with the Click-iT™ fixative and 1X Click-iT™ saponin-based permeabilization and wash reagent (from the Click-iT Plus EdU Flow Cytometry Assay kit: Thermo Fisher Scientific, #C10632) for 15 min at RT. After permeabilisation, cells were stained with the EdU reaction cocktail (4mM $CuSO_4$ (Acros, #197730010), 5µM Sulfo-cyanine 5 azide (Lumiprobe, #B3330) and 100mM of sodium ascorbate (Acros, #352685000) in PBS) for 30min at RT protected from light. The samples were then washed once with 3 mL of 2mM EDTA PBS and then incubated with 3µM of DAPI (Invitrogen, #D1306) for 15min at RT protected from light. Cells were then passed through the flowmi cell strainers (VWR, #734-5950) and analysed with the flow cytometer (LSRFortessa II). The percentage of cells in each gate was determined using FlowJo software (v10).

2.7.2 Flow cytometry to assess WEE1 expression during cell cycle

CDX cells were processed as described in the previous chapter. After permeabilization, cells were washed once with 3 mL of 5% FBS 2mM EDTA PBS. WEE1 antibody (Cell Signaling technology, #13084) was incubated with the cells for 1hr at RT in 5% BSA 2mM EDTA at a dilution of 1:400. After incubation with the primary antibody, cells were washed with 5% FBS 2mM EDTA PBS and then incubated with the secondary antibody for 30min at RT in 5% BSA 2mM EDTA PBS protected from light. Cells were then washed with 5% FBS 2mM EDTA PBS, incubated with DAPI,

filtered and then analysed as previously described. The percentage of cells in each gate was determined using FlowJo software (v10). Samples were gated in order to remove debris and doublets, as shown in Figure 14 Gate 1 to 3, and subsequently the G1 and G2 phase were selected (Gate 4) to quantify the percentage of WEE1 positive and WEE1 negative cells in each phase or in the total population (Gate 5).

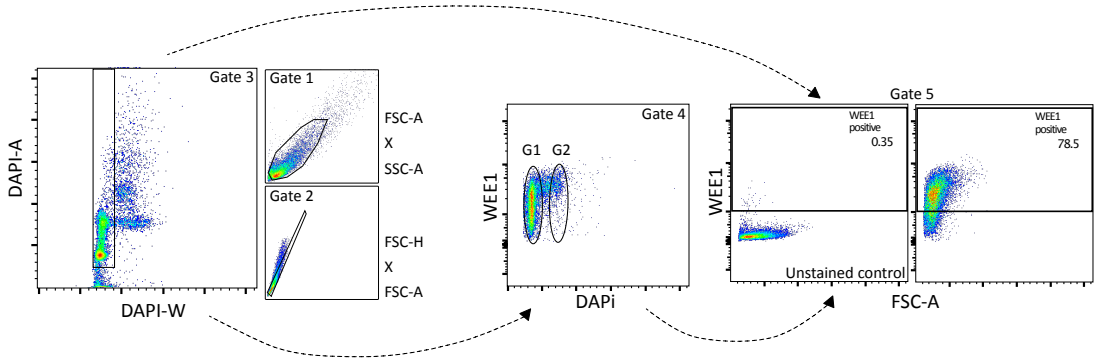

Figure 14. Gating strategy to identify WEE1 positive cells.

Gates were drawn to exclude debris (gate 1) and doublets (gate 2 and 3). Gate 4 allows to identify cells in G1 and G2, while Gate 5 defines the WEE1 positive population based on the unstained control.

2.8 Cloning methods

2.8.1 Cloning of CDKN1A guides into Lentiviral CRISPR plasmid

Guides to target exon 2 of *CDKN1A* were designed using the E-CRISP website (http://www.e-crisp.org/E-CRISP/) where the top 4 ranking guides were selected. The non-targeting guide was obtained from Joung *et al* (Joung et al., 2017). All guide sequences are listed in Table 12. All oligos were designed in order to have the same overhangs after *BsmBI* digestion and were cloned into the lentiviral vector lentiCRISPRv2 following their protocol. LentiCRISPRv2 was a gift from Feng Zhang (Addgene, plasmid #52961) (Figure 15).

Table 12. CRISPR Guides sequences.

Name	Where target?	Sequence
CDKN1A_guide_1	Exon 2/3	GACTGTGATGCGCTAATGGC NGG
CDKN1A_guide_1	Exon 2/3	GGCAGGCCTTGCTGCCGCAT NGG
CDKN1A_guide_1	Exon 2/3	GATGTCCGTCAGAACCCATG NGG
CDKN1A_guide_1	Exon 2/3	GGCGCCATGTCAGAACCGGC NGG
Non-targeting 1 GeCKO A		TAAACAAAAAGGAAATAGTT

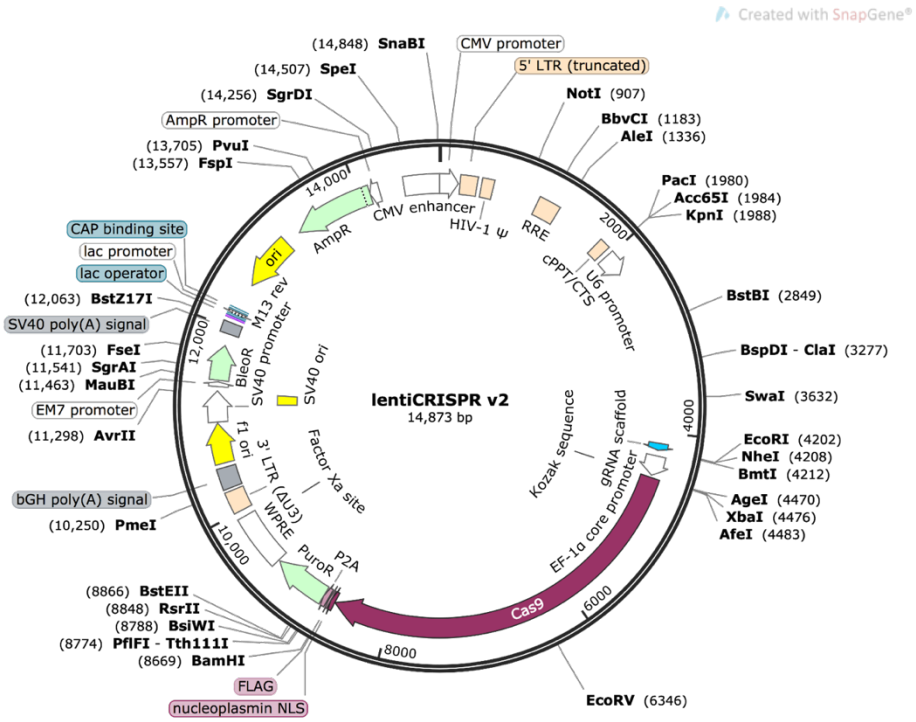

Figure 15. CRISPR targeting of *CDKN1A*.

Map of the lentiviral vector containing the Cas9 (Sanjana et al., 2014).

During digestion with *BsmBI* and dephosphorylation of the lentiviral CRISPR plasmid, each pair of oligos was phosphorylated and annealed. After purification of the lentiviral CRISPR plasmid, a ligation reaction was set to clone the paired oligos in the lentiviral plasmid. All reagents used were the one advised in the protocol:

FastDigest Esp31, ThermoFisher Scientific, #FD0454

FastAP, ThermoFisher Scientific, #EF0654

FastDigest Buffer (10X), ThermoFisher Scientific, #B64

DTT, Sigma-Aldrich, #10197777001

Quick Ligation kit, New England Biolabs, #M2200S

After ligation, the product was transformed into NEB® 5-alpha (New England BioLabs Inc., #C2987U) and 5 colonies from each construct were expanded. DNA was extracted with the NucleoBond® Xtra Maxi EF (Macherey-Nagel, #740424.50) according to manufacturer's instructions. DNA was reconstituted in ddH2O, quantified by Nanodrop and the concentrations adjusted to 1 µg/µL.

2.8.2 Viral production of *CDKN1A* CRISPR knockout

Once good quality DNA was obtained from transformed bacteria, Lenti-X™ 293T cells were transfected to produce the viruses. Lenti-X™ 293T cells were grown to reach > 70% confluence and then transfected with a 3rd generation lentivirus formed by VSVG (envelope, Addgene #12259), pMDL (packaging gag and pol, Addgene #12251) and REV (packaging rev, Addgene #12253) and the CRISPR construct. All reagents were mixed in the presence of FugeneHD transfection reagent (Promega, #E2311, 3:1 Fugene:DNA) and Opti-MEM (ThermoFisher Scientific, #31985062) for 30 min at RT to optimise the transfection. The mixture was added drop by drop in the media of the Lenti-X™ 293T cells and incubated for 36-48hr to allow viral production.

2.8.3 Transduction of CRISPR constructs

Fourty-eight hours after transfection, the supernatants containing the virus were collected. Supernatants were filtered on Acrodisc syringe filters 0.45 µM (VWR, #28144007) and then centrifuged to remove any remaining cell debris. The viral supernatant was then snap frozen in liquid nitrogen (N2) and stored at -80°C or immediately used to transduce cell lines. For transduction, cells were incubated with the viral supernatant (1:1 with media) supplemented with 19.8 µg of Polybrene (Sigma-Aldrich, #TR-1003-G) at 37°C for 6-18 hr. Alternatively, cells were spin-infected at 450 x *g* for 45 minutes in a prewarmed centrifuge (37°C) and then incubated overnight. The day after, the virus-containing media was replaced with fresh media and 48hr after transduction the cells were subjected to selection with 1 µg/mL puromycin (Sigma-Aldrich, #P8833).

2.9. Animal Studies

2.9.1 *In vivo* tumour growth

All procedure were carried out in accordance with the Home Office Regulation (UK) and the UK Coordinating Committee on Cancer Research guidelines using approved protocols (Home Office Project licence no. 70/8252 and Cancer Research UK Manchester Institute Animal Welfare and Ethical Review Advisory Board). The ARRIVE guidelines were followed to report all animal studies (Kilkenny et al., 2010). Tumour pieces (approximately 3 x 3 x 3 mm^3) or 100,000 disaggregated tumour cells

from fresh or cryopreserved tissue were resuspended in a 1:1 mixture of ice-cold Matrigel (VWR, International Ltd, #354130) and RPMI, and were implanted subcutaneously (s.c.) into one or both flanks of 6- to 10-week-old immunocompromised SCID-*bg* (CDB17.Cg-Prkdc^{scid}Lyst$^{bg-J/}$Crl, Harlan, Envigo Laboratories Ltd) or NSG mice (NOD.Cg-*Prkdc*^{scid}*Il2rg*^{tm1Wjl}/SzJ, Harlan, Envigo Laboratories Ltd). Tumour pieces were implanted under general anaesthesia following guidelines of good practice and aseptic technique. Mice were kept under 12 h light/12 h dark environment cycle and maintained at uniform temperature and humidity. They were housed in individually-vented caging systems in groups of five mice per cage. Mice were monitored for signs of tumour growth, and once a palpable tumour was present, this was measured twice a week by callipers. Tumour volume was calculated as 0.5*tumour length*(tumour width)^2, where the length is defined as the longest diameter and the width is the longest diameter that runs perpendicular to the length, and roughly through the middle of the tumour. When the total tumour burden was greater than 600 mm^3 or the animal showed signs of pain, the mice were sacrificed following the Schedule 1 regulation under the Animals Scientific Procedure Act 1986 and the tumours were harvested. Full necropsies were performed to assess the presence of any anomaly when animals were found dead or unhealthy.

When CDX cells were re-implanted after *ex vivo* growth (pCEP237, pCEP276, pCEP289, pCEP321 and pCEP422), 100,000- 150,000 cells from 1-5 week old CDX cultures were resuspended in a 1:1 mixture of ice-cold matrigel and RPMI, and were implanted subcutaneously into one or both flanks of 6-10 week old immunocompromised SCID-*bg* mice. Tumour monitoring was performed as described previously.

2.9.2 *In vivo* tolerance studies for TH1579

All animals were acclimatised for one week before the study started and had free access to water, food and enrichment. Two tolerability studies were performed to optimise the dosing. In both studies, a total of three SCID-*bg* non-tumour bearing mice were used. In the first study (pCEP232), 30 mg/kg TH1579 were administered by oral gavage (p.o.), twice daily (6 hours apart), for 21 consecutive days. The formulation was prepared daily as a 3 mg/mL solution (administering 10 ml/kg), the

vehicle components consisting of 5% v/v DMSO (Sigma-Aldrich, #D4540), 10% w/v Tween®80 (Sigma-Aldrich, #P1754), 10% w/v Kolliphor® ELP (Sigma-Aldrich, #30906) and 75% water. Daily monitoring was performed and weight data collected for each animal to aid in assessment of compound tolerability. Animals were sacrificed via Schedule 1, two weeks after end of treatment or if body weight dropped below 20% of initial body weight or below 15-20% for three consecutive days. A full necropsy was performed to assess the condition of the animal at the conclusion of the study.

The second tolerability study (pCEP247) assessed 90 mg/kg TH1579 p.o., twice daily (6 hours apart) for three cycles consisting of 3 days on and 4 days off. The formulation was prepared daily as a 9 mg/mL solution (administering 10 mL/kg). The formulation was the same as previously described, with the addition of 10% v/v ethanol. Daily monitoring tolerability was performed as above.

2.9.3 *In vivo* efficacy studies

2.9.3.1 Efficacy study with TH1579

Pharmacological assessment of the effect of TH1579 *in vivo* was performed on a total of 20 SCID-*bg* mice bearing CDX3 tumours (pCEP242). When the total tumour burden was between 150-250 mm^3, mice were randomised to either vehicle or TH1579 treatment arm. Mice were dosed twice daily (6 hours apart), 3 days on and 4 days off, for 3 cycles. Details of the dosing and drug formulation are given in Table 13. Mice were monitored as previously described. The endpoint of the study was reached when the tumour burden reached 1,000 mm^3 or when the mice survived 6 months after the first dose if no tumour was present. Upon reaching the endpoint, mice were culled by cardiac puncture under deep non-recoverable anaesthesia in the presence of 0.1M EDTA (Thermo Fisher Scientific, #15575020). Both tumour and plasma were collected and processed as follows: tumour samples were cut into four pieces, one formalin fixed then paraffin embedded (FFPE), one snap frozen, one for DNA analysis stored in CellSave:HBSS (Hyclone, 1:33) at -80°C and one for RNA analysis collected in RNA*later®* solution (Sigma-Aldrich, #R0901) and stored at -80°C; plasma collected from the blood was also stored at -80°C. A total of 10 mice were used to collect pharmacodynamic samples after 3 days of treatment with either compound or vehicle. On the fourth day mice received the last dose and 2h later both

tumour and plasma were collected. Tumours were cut into two pieces, one for FFPE and the second one was snap frozen. Plasma was used to perform pharmacokinetic analysis at the Karolinska Institute in collaboration with Prof. Thomas Helleday.

2.9.3.2 Efficacy study with cisplatin/etoposide on tumours derived from CDX3 cultures

To determine if CDX3 cells grown on plastic maintained the same response as the original CDX3 tumour to the SoC cisplatin/etoposide, 100,000 cells from a 5 weeks CDX3 culture, were injected s.c. single flank into 10 NSG mice (pCEP293). Animals were randomised to either vehicle or cisplatin/etoposide treatment once the tumours reached 200-250 mm^3. Mice were monitored as previously described. The endpoint of the study and the samples collection were performed as described above. The two compounds were administered via intraperitoneal injection (i.p.) with one dose of cisplatin on day 1 and one dose of etoposide on day 1, 2 and 3. 0.9% saline was used as vehicle control. Details of the dosing and drug formulation are given in Table 13.

2.9.3.3 Efficacy study with ABT263 and GDC0941

The efficacy study with ABT263 and GDC0941 was performed by our *in vivo* team. CDX4 bearing mice were treated with the BH3 mimetic, ABT263, and the PI3K inhibitor, GDC0941, to confirm the response observed *ex vivo* (pCEP310). Forty SCID-*bg* mice were injected s.c. with 100,000 cryopreserved CDX4 cells and randomised when the tumours reached 200-250 mm^3 into 4 treatment groups:

1. ABT263 vehicle + GDC0941 vehicle
2. ABT263 + GDC0941 vehicle
3. GDC0941 + ABT263 vehicle
4. GDC0941 + ABT263

The two drugs were given 1 hour apart for 21 consecutive days. Details of the dosing and drug formulation are given in Table 13.

Forty more mice were randomised into eight pharmacodynamic groups once the tumours reached 500-600 mm^3:

5. 1x ABT263 vehicle + GDC0941 vehicle and sacrifice 4 hours later

6. 1x ABT263 + GDC0941 vehicle and sacrifice 4 hours later
7. 1x GDC0941 + ABT263 vehicle and sacrifice 4 hours later
8. 1x GDC0941 + ABT263 and sacrifice 4 hours later
9. 1x ABT263 vehicle + GDC0941 vehicle and sacrifice 24 hours later
10. 1x ABT263 + GDC0941 vehicle and sacrifice 24 hours later
11. 1x GDC0941 + ABT263 vehicle and sacrifice 24 hours later
12. 1x GDC0941 + ABT263 and sacrifice 24 hours later

Mice were monitored as previously described. Body weight was measured daily during the course of the treatment and then twice a week during the recovery period. The endpoint for the efficacy study was achieved when the tumour reached 4 x Initial Tumour Volume (ITV) or when mice approached the severity limit as detailed in the project license. The harvested tumour tissue was half snap frozen and half formalin fixed before paraffin embedding.

For the pharmacodynamic study, mice were culled by cardiac puncture under deep non-recoverable anaesthesia in the presence of 0.1M EDTA. Plasma was extracted from the blood and stored at -80°C. Tumour tissue was half snap frozen and half formalin fixed before paraffin embedding.

2.9.3.4 Efficacy study with AZD1775 and olaparib

The efficacy study to test the response to the WEE1 inhibitor, AZD1775, and the PARP inhibitor, olaparib, were performed by our *in vivo* team. Forty SCID-*bg* mice were injected s.c. with 100,000 cryopreserved CDX cells and randomised when the tumours reached 150-250 mm^3 into 4 treatment groups:

1. AZD1775 + olaparib vehicle
2. Olaparib + AZD1775 vehicle
3. AZD1775 + olaparib
4. AZD1775 vehicle + olaparib vehicle

AZD1775 was given by oral gavage daily, 5 days on and 2 days off, for 3 cycles, while olaparib was given by oral gavage daily for 21 consecutive days. On days when both drugs were administered, olaparib was administered 1hr after AZD1775. Information about the formulation of the drugs are given in Table 13. Mice were monitored as previously described. Body weight was measured daily during the course of the

treatment and then twice a week during the recovery period. The endpoint for the efficacy study was achieved when the tumour reached 4 x ITV or when mice approached the severity limit as detailed in the project license. The harvested tumour tissue was half snap frozen and half formalin fixed before paraffin embedding.

Table 13. Drug dosing and formulation.

pCEP #	Drug(s)	Dose	Formulation
232	TH1579	30mg/kg p.o. b.i.d x 21 days	5% DMSO, 10% Tween80, 10% Kolliphor EPL, 75% water for injection
247; 242	TH1579	90mg/kg p.o. b.i.d 3 days in/4 days off x 3 cycles	5% DMSO, 10% Tween80, 10% Kolliphor EPL, 10% ethanol, 65% water for injection
293;289	Cisplatin	5mg/kg i.p. day 1	0.9% saline
293;289	Etoposide	8mg/kg i.p. day 1, 2, 3	citric acid monohydrate, methyl-2-pyrrolidinone, 0.9% saline
310	GDC0941	75mg/kg p.o. x 21 days	10% DMSO, 5% Tween20, 85% 0.9% saline
310	ABT263	100mg/kg p.o. x 21 days	60% Phosal 50 PG, 30% polyethylene glycol 400, 10% ethanol
223;224;254; 255; 249	AZD1775	120mg/kg p.o. 5 days on/2 days off x 3 cycles	0.5 methycellulose
223;224;254; 255; 249	olaparib	50mg/kg p.o. x 21 days	10% DMSO, 30% KLEPTOSE HPβCD

p.o. = gavage; i.p. = intraperitoneal injection; b.i.d = twice daily

Catalogue numbers:

cisplatin (Sigma-Aldrich, #P4394)

0.9% saline (NaCl 0.9% w/v, VWR, #A1671.0100).

etoposide (Sigma-Aldrich, #E1383)

citric acid monohydrate (Sigma-Aldrich, #C1909)

1-methyl-2-pyrrolidinone (NMP, Sigma-Aldrich, #328634)

60% Phosal 50 PG (American Lecithin Company)

30% polyethylene glycol 400 (Sigma-Aldrich, #807485)

0.5% methylcellulose (Sigma-Aldrich, #M7140)

30% KLEPTOSE HPβCD (60% stock solution prepared in-house by VWR)

2.10 General data analysis

2.10.1 Image analysis

2.10.1.1 Cleaved PARP and phospho-S6 chromogenic staining

For cleaved PARP and phospho-S6 staining, whole slide images were analysed using Definiens Developer XD and the Tissue Studio Portal version 3.51 (Definiens AG). A classifier was generated, training the software to discriminate between tumour, stroma and necrotic regions. Subsequently, a nuclear detection was perform to be able to count the number of single cells in the tissue. In the tumour region only, the percentage of staining positive cells was calculated and plotted with GraphPad Prism v8.1.1.

2.10.1.2 8-oxoguanine chromogenic staining

8-oxoguanine staining was evaluated by Professor Vassilis G Gorgoulis' lab. Three independent observers examined the slides to reduce inter-observer variability. The percentage of positive cells was obtained counting 100 cells in five different field per slides (total number = 500 cells).

2.10.1.3 RAD51 and yH2AX foci immunofluorescent staining

RAD51 and yH2AX foci were quantified using CellProfiler and CellProfiler Analyst (Dao et al., 2016; Lamprecht et al., 2007). A pipeline was optimised on CellProfiler to recognise single cells and yH2AX or RAD51 foci. Single cells were identified by shape and DAPI staining using the Otsu approach to calculate the threshold separating foreground from background (Otsu, 1979), similarly foci were defined as small object inside the nucleus (Figure 16). CellProfiler Analyst was then trained with the 'Fast Gentle Boosting' algorithm to recognise real single cells from cluster and debris. Foci were counted in the single cells only and a cell was considered positive for RAD51 when ≥ 5 foci were observed.

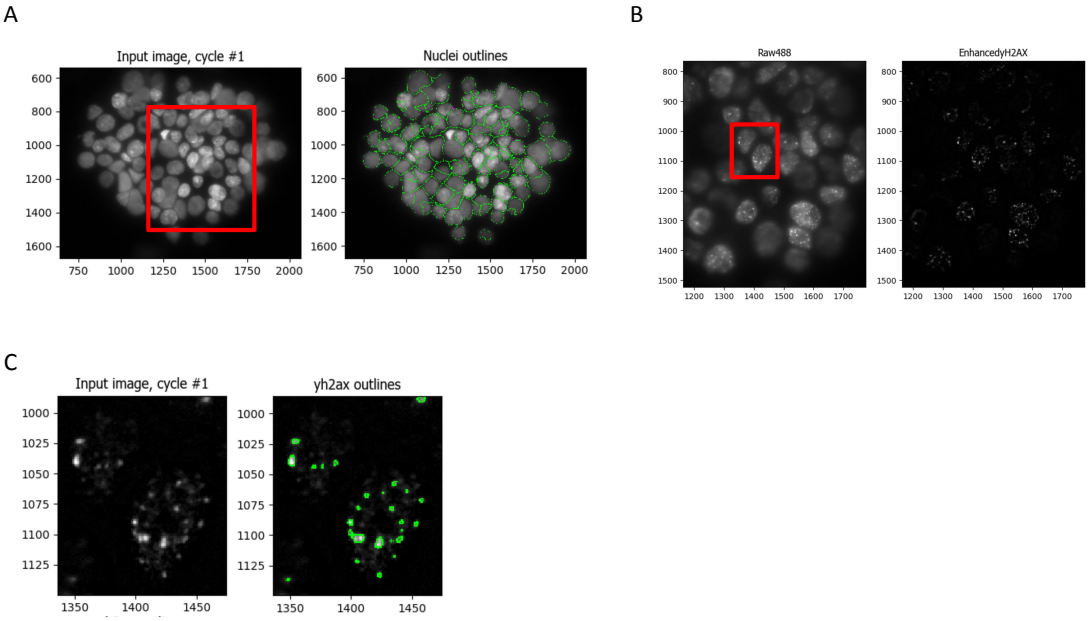

Figure 16. Example of foci detection with CellProfiler.

A. Example of nuclear detection performed with CellProfiler v3.1.5 (Lamprecht et al., 2007). B. Example of the result obtained from applying the EnhanceOrSuppressFeatures in CellProfiler. The feature speckles was used in order to remove the morphological grayscale opening from the image and enhance the foci. C. Example of the foci detection from CellProfiler. The red squares in A and B highlight the region described in B and C.

2.10.1.4 Chromatin-bound RPA, yH2AX and EdU nuclear immunofluorescent staining

Chromatin-bound RPA, yH2AX and EdU nuclear intensity were quantified using CellProfiler and CellProfiler Analyst (Dao et al., 2016; Lamprecht et al., 2007). A pipeline was optimised on CellProfiler to recognise single cells and measure the nuclear intensity of each staining. Single cells were identified by shape and DAPI staining using the Otsu approach to calculate the threshold separating foreground from background (Otsu, 1979). CellProfiler Analyst was then trained with the 'Fast Gentle Boosting' algorithm to recognise real single cells from cluster and debris. The R platform was used to analyse the single cell data and define a cut-off of positivity (R Core Team, 2018). Intensity values were log10 transformed. The Gaussian mixture model was used to identify the negative and positive population making the assumption that the intensity values were normally distributed (Benaglia et al., 2009). The threshold was defined as the intersection of the two Gaussian distributions. It was calculated by subtracting the two Gaussians and identifying where the result was equal to 0 in the interval between the means of the two Gaussian. The uniroot function of the R package 'stats' was used to identify this intersection. Figure 17

shows the distribution of the intensities and the identified thresholds for each staining.

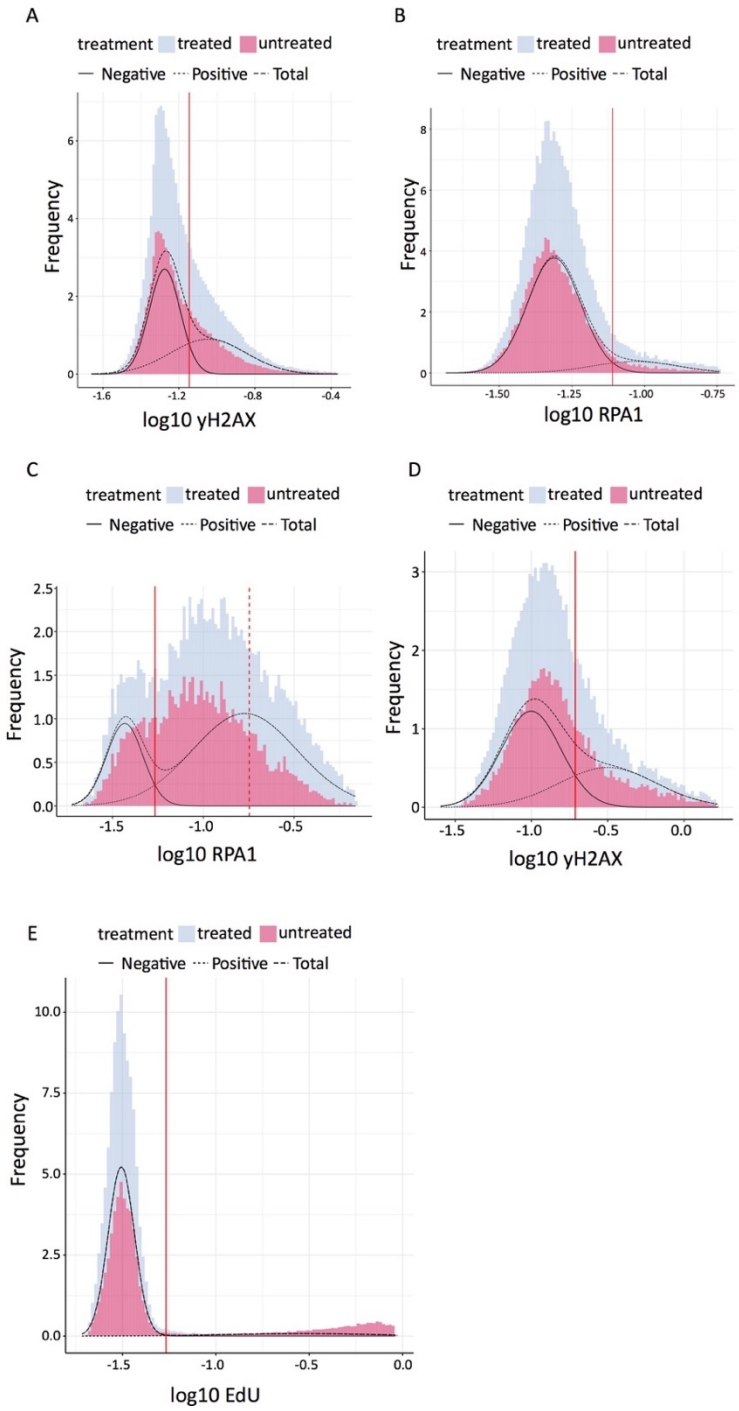

Figure 17. Distribution of chromatin-bound RPA, yH2AX and EdU intensities.

Distribution of chromatin-bound RPA (A,C), yH2AX (B,D) and EdU (E) intensities across all samples before and after treatment with HU (A,B,E) or HU + VE822 (C,D). Vertical red lines delineate the intersection between the positive and negative population. Vertical dotted red line indicate the threshold for chromatin-bound RPA-high defined in Figure 18. Black lines highlight the total (dashed), positive (dotted) and negative (solid) populations calculated by the gaussian mixture model.

To account for the high level of chromatin-bound RPA in the untreated samples, I defined a gate to highlight a population of chromatin-bound RPA high cells, in order to focus the analysis only on cells affected by HU and VE822. The gating was defined looking at the values for chromatin-bound RPA intensity *vs* DAPI intensities (Figure 18). Treatment with VE822 and HU demarcated a clear population with high levels of RPA that were used to set the threshold. The red dotted line in the density plot for RPA distribution shows the location of the threshold used to define this population.

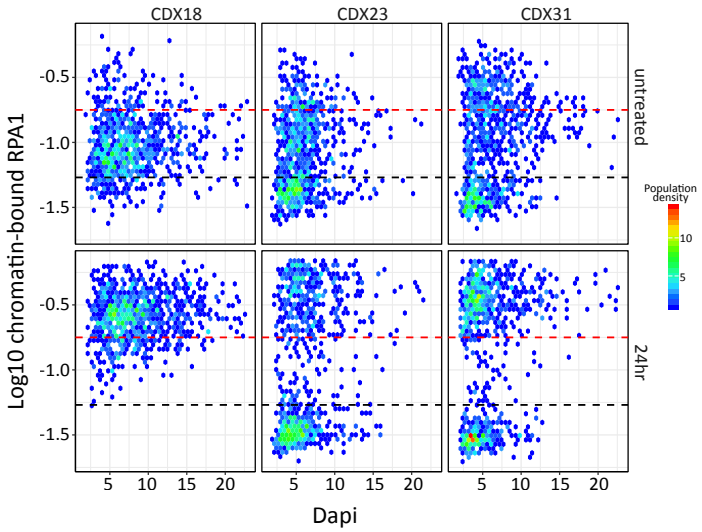

Figure 18. Definition of the chromatin-bound RPA-high population.

Quantitative image-based cytometry single-cell analysis (QIBC) of chromatin-bound RPA against the Dapi before and after treatment with 100 nM VE822 + 2mM HU. 900 random cells were selected from each condition and plotted. Black dotted line define the threshold for chromatin-bound RPA positivity while red dotted lines indicate the threshold to define the population of chromatin-bound RPA-high cells.

2.10.1.5 p21 and pHH3 nuclear immunofluorescent staining with TSA

p21 and pHH3 staining was quantified on whole slide images using QuPath software (Bankhead et al., 2017). Two or three biological replicates were analysed for each model. In this case, nuclear detection was performed before defining a classifier. After nuclear detection with the 'Cell detection' algorithm, DAPI staining and cell shape were used to separate the stroma and necrotic regions form the tumour cells. p21 and pHH3 intensity levels were evaluated in the tumour cells only. The R platform was used to analyse the single cell data and define a cut-off of positivity (R Core Team, 2018). The Gaussian mixture model to identify the thresholds and separate the positive from the negative population was performed as described above. The

Gaussian mixture model was applied to all models tested, excluding the control cell lines. The results were further validated looking at the intensity of p21 in the corresponding slides (Appendix Figure 1A).

Figure 19. Distribution of p21 intensity values.

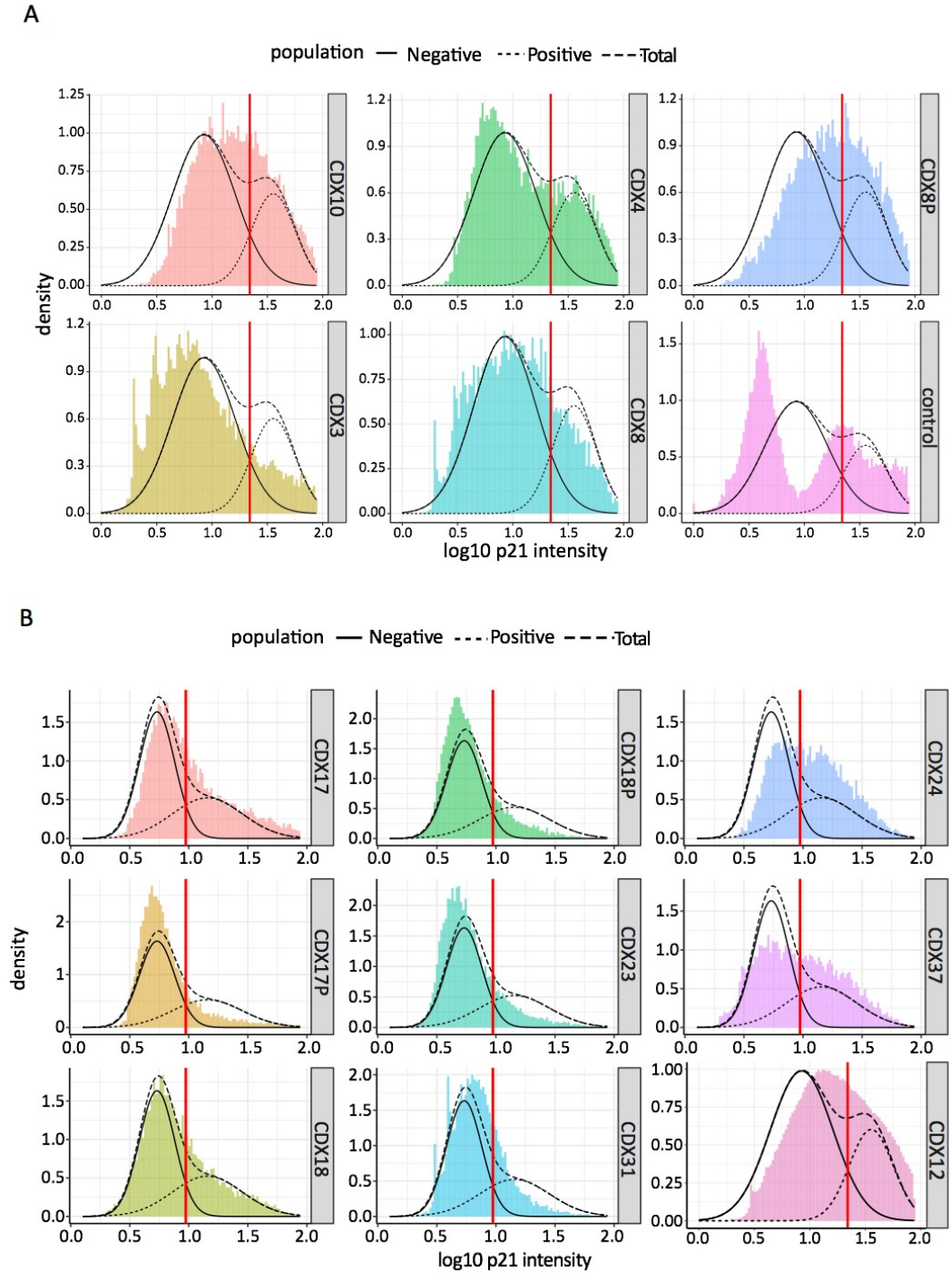

Distribution of p21 intensities across a panel of CDX (batch 1 (A) and batch 2 (B)). Red lines indicate where the thresholds calculated with the Gaussian mixture model fall. Black lines highlight the total (dashed), positive (dotted) and negative (solid) populations calculated by the Gaussian mixture model.

As shown in Figure 19A, the calculated Gaussian distribution partly overlapped with the control populations (where H69 and H524 were combined to highlight the positive and negative peaks), suggesting that the identified distribution were able to separate negative and positive cells. I did not have a positive and negative control for pHH3, however the staining was very clean with limited background, making it easy to identify the real positive cells from false positive ones. Figure 20A shows the gaussian distributions calculated for pHH3 intensities and the calculated threshold for the first batch (equivalent to an intensity of 13.7, red solid line).

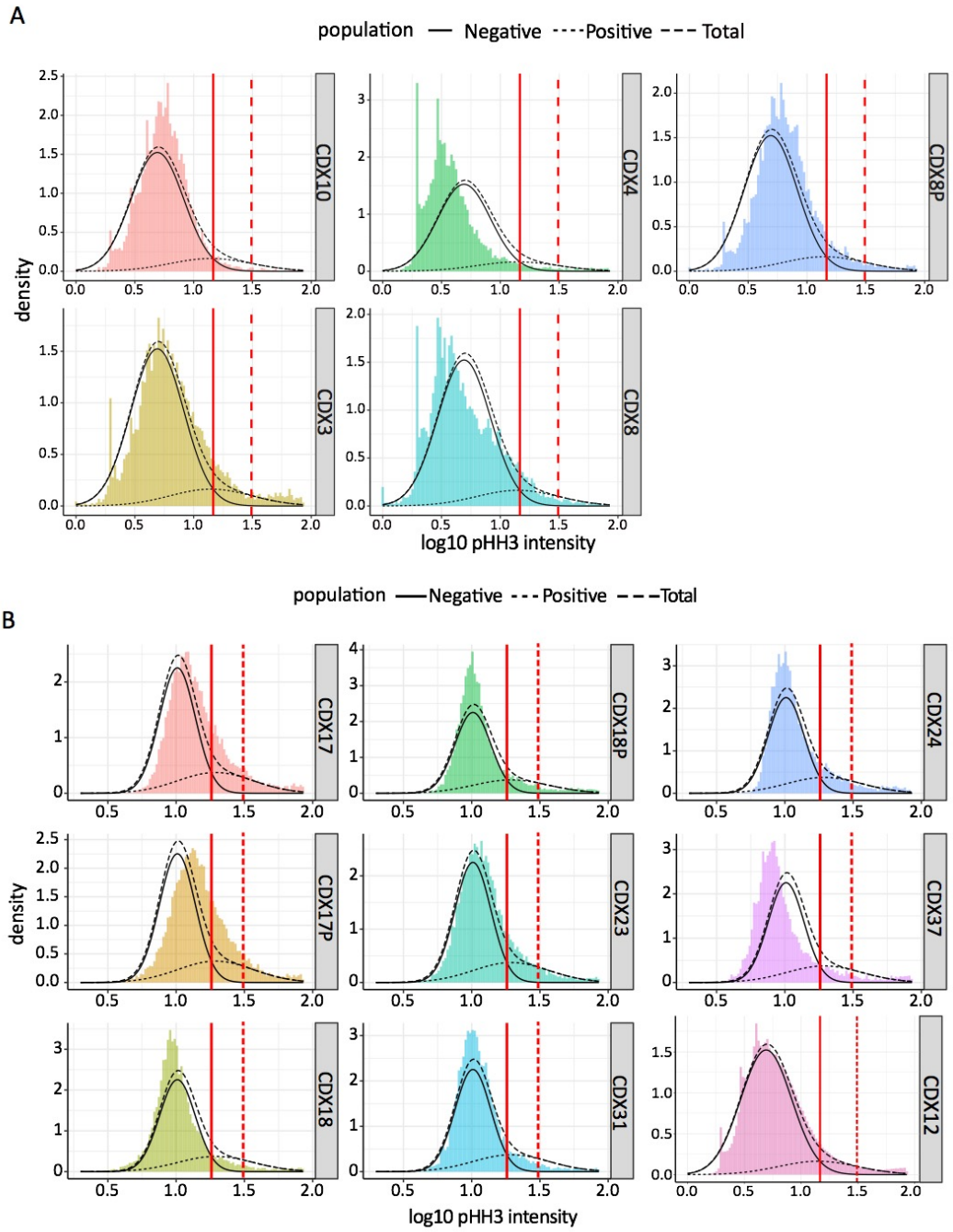

Figure 20. Distribution of pHH3 intensity values.

Distribution of pHH3 intensities across a panel of CDX (batch 1 (A) and batch 2 (B)). Red lines indicate where the thresholds calculated with the Gaussian mixture model fall. Dotted red lines indicate the manually selected threshold. Black lines highlight the total (dashed), positive (dotted) and negative (solid) populations calculated by the Gaussian mixture model.

As shown in Appendix Figure 1A, this threshold caused the inclusion of completely negative cells (white triangle), therefore, based on the analysis of several slides, I have decided to manually set the threshold at 30, to only include weak but not negative cells (Appendix Figure 1A, yellow triangle). The red dotted line in Figure 20A shows the position of the new threshold in the pHH3 distributions. The same approach was used for the second batch of CDX (Figure 19B and 20B).

2.10.1.6 The comet analysis

Each images was processed with the OpenComet plugin in ImageJ (Gyori et al., 2014). Each analysed image was reviewed to exclude the mis-assigned comets and the results were exported for downstream analysis (Figure 21). Of all validated comets, the intensity of the fluorescence was calculated for each tail relative to the intensity of the head (% tail DNA). This parameter correlates with the break frequency and also gives an indication about the shape of the comets (Collins, 2004). The R platform was used to generate the plots summarising the results obtained. In particular, the raincloud plot was used (Allen et al., 2019). This plot permitted the visualisation of the raw data (dot plot), together with the summary statistics (box plot) and the distribution of the probability (half violin plot). The box plots show the median, the vertical size of the boxes are the interquartile range (IQR), and the whiskers are the minimum and maximum values that do not exceed 1.5 x IQR from the middle 50% of the data.

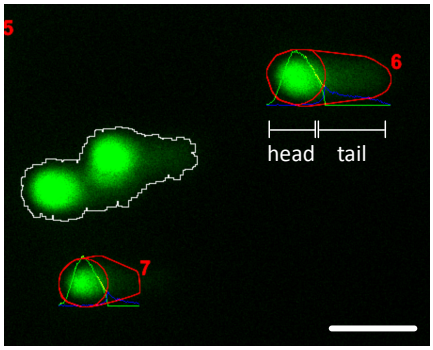

Figure 21. Example of comets identified by OpenComet.

Lines delineate comets accepted (red) or excluded (grey) from the analysis with OpenComet. Scale bar = 100 µm.

2.10.2 Analysis of RNAseq data

Raw sequencing data were processed by Drs. Garima Khandelwal, Sakshi Gulati and Ruth Stoney. Reads were aligned to Genome Reference Consortium Human Build 38 (GRCh38) and Genome Reference Consortium Mouse Build 38 (GRCm38) assembly using Mapsplice (version 2.1.6, (Wang et al., 2010)) and filtered via an in-house algorithm (Khandelwal et al., 2017) to discriminate between human and mouse transcripts. The aligned reads were used to generate count data using the R package 'Rsubread' (version 1.16.1, Liao et al., 2013) and the Ensembl 77 GTF file.

The raw count were analysed with the R package 'DESeq2' by myself (Love et al., 2014). The DESeq object was generated to perform differential gene expression analysis. Protein coding genes with FDR ≤ 0.05, log2 fold change ≥ |1| were selected for gene ontology, pathway overrepresentation and gene set enrichment analyses using the 'ReactomePA', 'clusterProfiler' and 'fgsea' packages in R (Sergushichev, 2016; Yu and He, 2016; Yu et al., 2012). For the network representation shown in Figure 83B, the cluster of drug-resistant CDX (blue, Figure 83A) was compared with the cluster of drug-sensitive CDX (red, Figure 83A). Differentially protein coding genes were identified using 'DESeq2' and sorted by decreasing order (based on log2 fold change) for the downstream analysis. The function 'enrichPathway' from 'ReactomePA' was used to assess if the number of selected genes associated with a reactome pathway was larger than expected. This function returned a list of over-represented reactome pathways. Each pathway had an associated *p*-value calculated based on the hypergeometric model of Boyle *et al* (Boyle et al., 2004). Bonferroni correction was used to control for false positive events during the multiple comparisons. The results obtained were used in the 'emapplot' function in 'ReactomePA' to generate the enrichment network map shown in Figure 83B. This map showed the top 30 over-represented gene sets and their degree of overlap. The function 'cnetplot' in 'ReactomePA' was then used to extract the complex association between the genes of the top 5 reactome pathways identified (Figure 84).

For Figure 85, the specified reactome gene sets were downloaded from the GSEA website (http://software.broadinstitute.org/gsea/msigdb/genesets.jsp). The 'fgsea' R package was used for the analysis. The differentially expressed genes identified

using DESeq2 between drug-resistant CDX and drug-sensitive CDX were used for the gene set enrichment analysis. The function 'fgsea' in the 'fgsea' package was used to perform the analysis. All genes were included with their respective statistical metric value (column 'stat' in the DESeq object), and a total of 1,000 permutation were performed. The function returned a table containing the reactome gene sets analysed, an enriched *p*-value, a Bonferroni adjusted *p*-value, the enrichment score (ES) and the normalised enrichment score (NES). ES are representative of the degree to which each gene set is overrepresented in the list of genes given. NES is calculated to account for differences in the gene set size and allow to compare the results across gene sets. The adjusted *p*-value is computed based on the probability that the NES derived for each gene set is a false positive (Subramanian et al., 2005). The 'ggplot' function was used to plot the NES results for each gene sets. The same workflow was applied to calculate and visualise differential gene expression and pathway enrichment analysis for CDX considered resistant or sensitive to each combination of DDRi tested. For these analyses, a CDX was considered resistant if the average $GI_{50} \geq$ 1 μM, otherwise it was classified as sensitive (Table 16).

Pathway enrichment analsysis was also performed in Figure 26 and 28, using the 'enrichPathway' function from 'ReactomePA' inside the 'compareCluster' function from 'clusterProfiler'. The GeneRatio was used to define the fraction of unique genes in the input list that overlapped with a specific gene set and that overlapped with all the members of the collection of gene sets.

The 'regularised log transformation' or the 'variance stabilizing transformation' from the 'DESeq2' package was used to normalise the data for visualisation and clustering. Both transformations reduce the dependence of the variance on the mean and they account for library size (Love et al., 2014). Normalised data were used to perform the Principal Component Analysis (PCA) using the R packages 'stats' and 'ggplot2' (R Core Team, 2018; Wickham, 2009). Data were scaled and centred during PCA. The multidimensional scaling (MDS) plot was generated with the R package 'limma' (Ritchie et al., 2015). The heatmaps were produced using the R packages 'pheatmap' and 'ComplexHeatmap' (Gu et al., 2016; Kolde R., 2019). For the heatmap shown in Figure 24, the top 5,000 variable genes across all samples were selected using the

'rowVars' function in 'matrixStats'. This function estimates the variance (therefore difference in the expression) for each row (gene) across all columns (samples) in the matrix.

For the heatmap shown in Figure 26, the top 1,000 differentially expressed genes between the original CDX3 tumours and the 4 weeks CDX3 cultures were selected (based FDR ≤ 0.05). These genes were identified extracting the results obtained comparing the gene expression profile of CDX3 tumour vs CDX3 4 weeks culture with 'DESeq2'.

For the heatmap shown in Figure 28, the top 1,000 differentially expressed protein-coding genes between the original CDX3 tumours and CDX3 cultures were selected (based on FDR ≤ 0.05). These genes were identified with 'DESeq2' as described above.

For the heatmap shown in Figure 51 and Appendix Figure 5, the expression of the genes selected in the Peng *et al* HRD signature was assessed across the CDX (Peng et al., 2014). The heatmap in Figure 51 was split in 7 clusters. These clusters were calculated with the 'pam' function of the R package 'cluster'. This function perform a *K*-means clustering around medoids (Maechler M et al., 2019).

The heatmaps shown in Figure 55, 64, 66 depict the expression of the selected genes across the CDX.

In all heatmaps shown, hierarchical clustering with the 'complete linkage' method was applied and Euclidean distances were used to find similar clusters across genes and samples.

The R package 'UpSetR' was used to generate the UpSet plot (Conway et al., 2017). Only genes with *p*-value ≤ 0.05 from the Pearson correlation analysis were included (see chapter 2.10.6 for details).

2.10.3 Visualisation of RNA sequencing reads

The Integrative Genomics Viewer software v2.3 (IGV, Robinson et al., 2011, 2017) was used to visualised RNA sequencing data and confirm the E178* mutation on *PALB2* in CDX3. Aligned BAM files were sorted and indexed with Samtools (Li et al., 2009) and then uploaded on IGV were the human genome reference GRCh38 was uploaded.

2.10.4 Analysis of combinatorial drug screening results

Raw data from the plate readers were quality checked before performing the analysis. The average of the technical replicate for each run was calculated and the data were normalised to the DMSO control (0-100). For visualisation of combinatorial drug screening, the GI_{50} were used to generate the heatmap with the R package 'pheatmap' (Kolde R., 2019). To calculate the GI_{50}, the drm() function in the R package 'drc' was used (Ritz et al., 2015). This function applied a 4-parameter log-logistic distribution to calculate the 50% growth inhibition (GI_{50}). This was performed on every drug as single agent or in combination with a fixed concentration of the second drug. The heatmaps show the log10 transformation of the GI_{50} for each treatment tested. For visualisation, hierarchical clustering using the 'complete linkage' method was applied. This method used the Euclidean distance to find similar clusters. The synergy analysis was performed with the R package 'SynergyFinder' (He et al., 2018). Normalised data were used to define the dose response matrix for each biological replicate and these matrices were used to calculate the synergy with the ZIP reference model (Yadav et al., 2015). Dose response matrices and synergy response landscapes were plotted with the internal functions of the package.

2.10.5 Analysis of WES data

WES data were analysed by Dr. Garima Khandelwal. The data were aligned to Human GRCh37 and Mouse GRCm37 assembly with bwa-mem (version 0.7.12). Deduplication, re-alignment and recalibration were performed on the aligned data using Picard (version 1.96) and GATK tools (version 3.3), as stated in the GATK best practices. The reads aligning the mouse genome were removed using an in-house algorithm (Khandelwal et al., 2017). Somatic mutation calling was done on the filtered reads using Mutect (version 1.1.7), and the mutation calls were annotated using Ensemble Variant Effect Predictor. To visualize the mutations of interest I have used 'oncoprinter' tool on the cBioPortal website (http://www.cbioportal.org/oncoprinter.jsp#).

2.10.6 Statistical Analysis

All statistical analyses were performed using Prism v8.1.1 (GraphPad) or in R (v. 3.5.1) (R Core Team, 2018). All data from the proliferation assay and the low

throughput drug screening are presented as means ± SD of at least three independent experiments, each with three experimental replicates. The only exception are the drug screening of CDX4 culture treated with cisplatin and etoposide or the combination, where only two biological replicates were performed, and the viability assay after irradiation with CDX8p, where only one biological replicate was performed. Doubling times were calculated by non-linear curve fitting of an exponential growth equation. For moderate-throughput drug screenings at least two biological replicates for each combination were analysed, with three internal technical replicates. Plot showing linear correlation were performed with Graphpad using the simple linear regression function with the Pearson correlation algorithm, or with the 'cor' function in the R package 'stats'. Data are presented as means ± SD for the *ex vivo* data and as means ± SEM for the *in vivo* data. For the Pearson correlation of the gene expression with the GI_{50} the 'cor' function in the R package 'stats' was used and the data were plotted with the R package 'ggplot2'. For the quantification of the γH2AX and the RAD51 foci, *p*-values were calculated with the student *t*-test. *In vivo* experimental data points represent individual relative tumour volumes (percentage of change from baseline). Event-free survival was defined as the time for the tumour to reach four times the ITV. Survival analysis was performed with comparison of survival curves by log-rank (Mantle Cox) test with GraphPad. For pharmacodynamics analysis, an unpaired Wilcoxon test was applied to compare the vehicle versus the treated arm. Box and whisker plots were used to show the distribution of the sample. Boxes indicate median, first and third quartiles, while whiskers indicate maximum and minimum values.

Chapter 3: Establishment and characterisation of an *ex vivo* culture of CDX-derived cells

3.1 Introduction

Since 2007, more than 100 clinical trials have investigated new therapeutic targets for SCLC, but positive results have been very limited (Koinis et al., 2016). Unfortunately, SCLC tumour tissues derived from surgery or biopsy are rare and often limited to diagnostic analyses (Koinis et al., 2016), thus making it challenging to

identify candidate biomarkers for patient stratification. We recently demonstrated that the CDX models mimic closely the pathology and response to chemotherapy of the donor patient, and can be passaged to provide a continuous source of tumour material (Hodgkinson et al., 2014). More importantly, CDX can be generated pre-chemotherapy (baseline) and again at different time points during a patient's follow up (Simpson et al., 2019). These paired models are extraordinary patient-derived tools to study differences in the tumour biology before and after treatment. Given the clinical need of identifying new therapeutic options for SCLC patients, we decided to exploit our biobank of CDX as a patient-relevant model to identify potential candidate drugs alone or in combination.

The observation that PARP1 is overexpressed in SCLC compared with NSCLC and the promising responses observed in SCLC cell lines after treatment with different PARP inhibitors (Byers et al., 2012; Cardnell et al., 2013), prompted us to test the effect of PARP1/2 inhibition on our CDX. Considering the universal loss of the G1 checkpoint in SCLC and the resulting high level of genomic instability, we hypothesised that the effect of PARP inhibition could be exacerbated by the concomitant inhibition of the cell cycle checkpoint mediator WEE1.

In collaboration with AstraZeneca, we decided to investigate the effect of the FDA-approved PARP inhibitor, olaparib that shows an intermediate PARP trapping ability. The only clinically available WEE1 inhibitor is the small molecule AZD1775. We hypothesised that the ability of AZD1775 to impair homologous recombination could synergise with PARP inhibition in a cancer where mutation in HR genes are rare (Heeke et al., 2018; Krajewska et al., 2013). Moreover, because WEE1 regulates cell cycle progression downstream of ATR, we speculated that inhibition of this protein in a tumour with high intrinsic level of replication stress, exacerbated by PARP trapping, would induce replication catastrophe (Toledo et al., 2013). We decided to test the efficacy of this combination on 4 CDX models. CDX3 and CDX4 were previously characterised (Hodgkinson et al., 2014). The CTCs that generated these models have been collected at baseline prior to initiation of first-line chemotherapy. CDX3 was derived from a chemosensitive patient that survived 10.5 months, while CDX4 was derived from a chemorefractory patient that never responded to first-line therapies and passed away 1.8 months after the start of the treatment. CDX8 and CDX8p are

paired models, derived from the same chemorefractory patient at different timepoints during disease evolution. CDX8 was derived from CTCs collected before first-line treatment, while CDX8p was developed from CTCs taken following disease progression. Table 14 summarises the clinical history of the patients that generated the CDX used in this thesis. These 4 models mirrored the patient response to EP treatment. CDX3 showed a complete tumour regression after treatment with cisplatin/etoposide, while CDX4 tumours were completely refractory. CDX8 showed an initial partial response with ~50% regression, and as expected, CDX8p was completely resistant to cisplatin/etoposide treatment (Hodgkinson et al., 2014; Lallo et al., 2018). This small panel of CDX allowed us to investigate the effect of PARP1/2 and WEE1 inhibition in both a chemosensitive and a chemorefractory background. In particular, the paired models, CDX8 and CDX8p, helped to assess the differences in response observed when this combination was administered as first-line (CDX8) or second-line (CDX8p) regimen. The dosing schedule for AZD1775 and olaparib was discussed with AstraZeneca prior the start of the study and is described in Chapter 2.9.3.4 and Table 13. These doses were chosen because they have shown to optimally achieve target inhibition, they were tolerated when given in combination, and are clinically relevant (data provided from AstraZeneca). We have initially tested these regimens in a tolerance study in which SCID-*bg* mice were treated with the compounds, as single agents or in combination, for a total of 21 days and subsequently monitored for 2 weeks off-treatment. The study was successful, with only minimal body weight loss in the AZD1775-treated mice (average loss -8.7%, data not shown). The body weight loss in the AZD1775-treated animals was solved by changing the daily dosing to a 5 days on, 2 days off schedule for 3 cycles. This new schedule was applied to the efficacy studies described in the Thesis (Table 13).

Single agent olaparib and AZD1775 showed the best response in CDX3 with complete or modest regression during treatment, but all tumours grew back within 2 months after last dosing. The combination was curative in 5/7 mice with a tumour-free survival of > 100 days in the two mice in which the tumours regrow. Conversely, CDX4 was completely refractory to olaparib and treatment with the AZD1775 either alone or in combination led to tumour stabilization during the treatment window (21 days), suggesting that the main effect was driven by the WEE1 inhibitor. Olaparib

alone had almost no effect on CDX8, while AZD1775 single agent treatment stabilised CDX8 growth. As observed in CDX3, the combination was synergistic with a complete regression in most of the mice, even if all tumours grew back within 75 days. CDX8p did not respond to olaparib and AZD1775 single agents, however the combination slightly delayed tumour growth compared with vehicle. Overall, the combination improved the mice OS compared with cisplatin/etoposide treatment, in all models tested, and has been summarized in Figure 22 (Lallo et al., 2018). Based on these data, I decided to investigate the pathways involved in the response to this combination to understand the range of sensitivities we observed *in vivo*, and identify putative biomarkers of response.

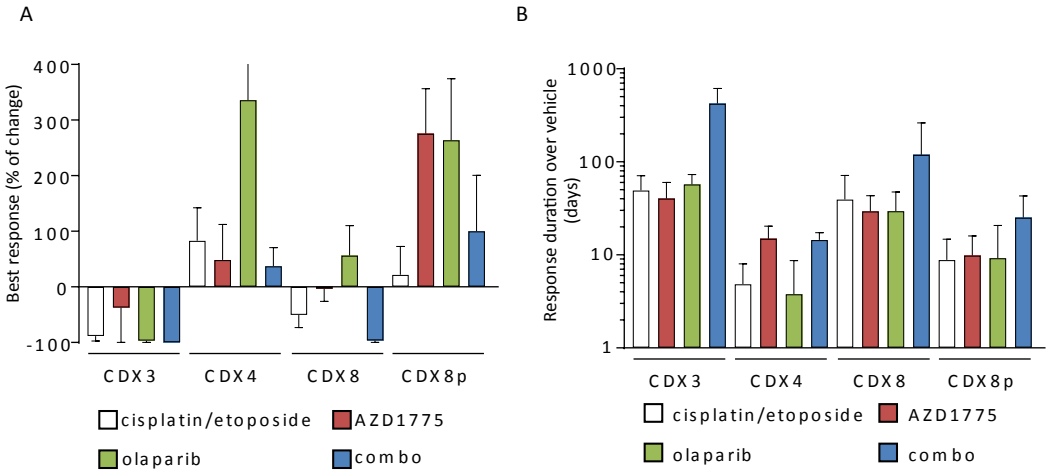

Figure 22. Treatment with olaparib/AZD1775 is effective in SCLC CDX and shows superior activity than cisplatin/etoposide.

A. Barplot showing the average best response (± SD) for cisplatin/etoposide (white), AZD1775 (red), olaparib (green) and AZD1775/olaparib (blue). Best response: percentage of tumour volume change at the end of the treatment (21 days) compared with the tumour volume measured at the start of the treatment. B. Barplot showing the average duration of response for each treatment over the vehicle. Cohort size are ≥ 7 (Lallo et al., 2018).

As mentioned in chapter 1.3, mechanistic analyses are easier to perform *in vitro* on cancer cell lines than directly *in vivo*. Moreover, testing hypotheses *in vitro* utilises fewer mice in accordance with the 3Rs (Russel W.M.S. and Burch R.L., 1959). However, due to the faithfulness of the CDX models for the donor patients compared with common cancer cell lines, I was mainly interested in the mechanisms of response intrinsic to the CDX. Moreover, the continuous lack of drug efficacy in the clinic further highlight the limitation of common SCLC cell lines. Therefore, to overcome the difficulties related to the *in vivo* models and established cell lines, I

established short-term *ex vivo* cultures of CDX-derived cells and this work was recently published (Lallo et al., 2019). Knowing that cell cultures established from SCLC PDX can undergo irreversible changes over time (Daniel et al., 2009), I wanted to fully characterize these cells in order to ascertain the differences and similarities that these cultures have with the original CDX tumour.

3.2 Results

3.2.1 Establishment of a short-term *ex vivo* culture of CDX-derived tumour cells

To optimise culture conditions I selected three distinct CDX models. CDX3 and CDX4 have already been described in the previous paragraph. CDX2 was firstly characterised in Hodgkinson *et al*. Like CDX4, this model was derived from a chemorefractory patient, however CDX2 experienced a partial response to cisplatin/etoposide *in vivo* with 50% regression. This properly recapitulated the differences in survival observed between donor patients 2 and 4, with an OS of 3.9 months for patient 2 *vs* 1.8 months for patient 4 (Hodgkinson et al., 2014, Table 14).

Table 14. Clinical information of the CDX donor patients.

CDX #	Gender	SCLC Stage	Pt Treatment	Time-point	Pt Treatment Response	Chemo-sensitivity	Pt survival (mo)
2	Female	ES	Carbo/etop	baseline	Progressive Disease	refractory	3.9
3	Male	ES	Carbo/etop	baseline	Partial Response	sensitive	10.5
3p	Male	ES	Carbo/etop	progression	Partial Response	N/A	10.5
4	Female	ES	Carbo	baseline	Progressive Disease	refractory	1.8
8	Female	ES	Carbo	baseline	Partial Response	refractory	6.5
8p	Female	ES	Carbo	progression	Partial Response	N/A	6.5
10	Male	ES	Carbo/etop	baseline	Partial Response	sensitive	19.7
12	Male	ES	Carbo/etop	baseline	Partial Response	refractory	5.2
14p	Female	ES	Carbo/etop	relapse	Partial Response	N/A	9.5
15p	Female	LS	Carbo/etop	relapse	Partial Response	N/A	21.2
15p	Female	LS	Carbo/etop	relapse	Partial Response	N/A	21.2
17	Female	ES	Carbo/etop	baseline	Partial Response	N/A	6.3

17p	Female	ES	Carbo/etop	progression	Partial Response	N/A	6.3
18	Male	ES	Carbo/etop	baseline	Partial Response	N/A	6.6
18p	Male	ES	Carbo/etop	follow-up	Partial Response	N/A	6.6
20	Male	ES	Carbo	baseline	Stable Disease	refractory	2.7
20p	Male	ES	Carbo	follow-up	Stable Disease	N/A	2.7
23	Female	ES	Carbo/etop	baseline	Stable Response	refractory	5.1
24	Male	ES	Carbo/etop	baseline	Partial Response	sensitive	13.6
25	Male	ES	Carbo	baseline	Progressive Disease	refractory	2.4
29	Female	LS	Carbo/etop	baseline	Partial Response	sensitive	8.9
31	Female	ES	Carbo/etop	progression	Stable Response	N/A	5.1
37	Male	ES	Carbo/etop	follow-up	Partial Response	N/A	13.6
38	Female	ES	Carbo/etop	baseline	Partial Response	N/A	7.3

mo = months; Pt = patients; ES = extensive stage; LS = limited stage; Carbo = carboplatin; etop = etoposide

To establish the *ex vivo* culture conditions, CDX tumours were collected and immediately processed following an in-house protocol (see chapter 2.1.2). This protocol yielded a single cell suspension enriched with viable human tumour cells that were depleted of mouse stromal cells (Figure 23A). The derived cells were counted and seeded at various densities in different media conditions. All tested media contained the components of the HITES media described by Simms *et al* (Simms et al., 1980), with or without the addition of further supplements included to improve the culture success rate. Bombesin was tested because it has been shown to support SCLC growth both *in vitro* and *in vivo* (Cuttitta et al., 1985). Alternatively, a low concentration of FBS was used (see chapter 2.2.1 for details). All of these combinations were tested with or without the addition of the ROCK inhibitor, Y-27632 to improve cells viability after tissue dissociation (Watanabe et al., 2007). As shown in Figure 23B, CDX2 and CDX4 have a similar proliferation rate in most media tested, while CDX3 proliferated significantly better when FBS was added to the HITES, especially if combined with Y-27632 (with $p = 0.034$ H *vs* HF and $p = 0.0001$ H *vs* HFRi) (Figure 23B).

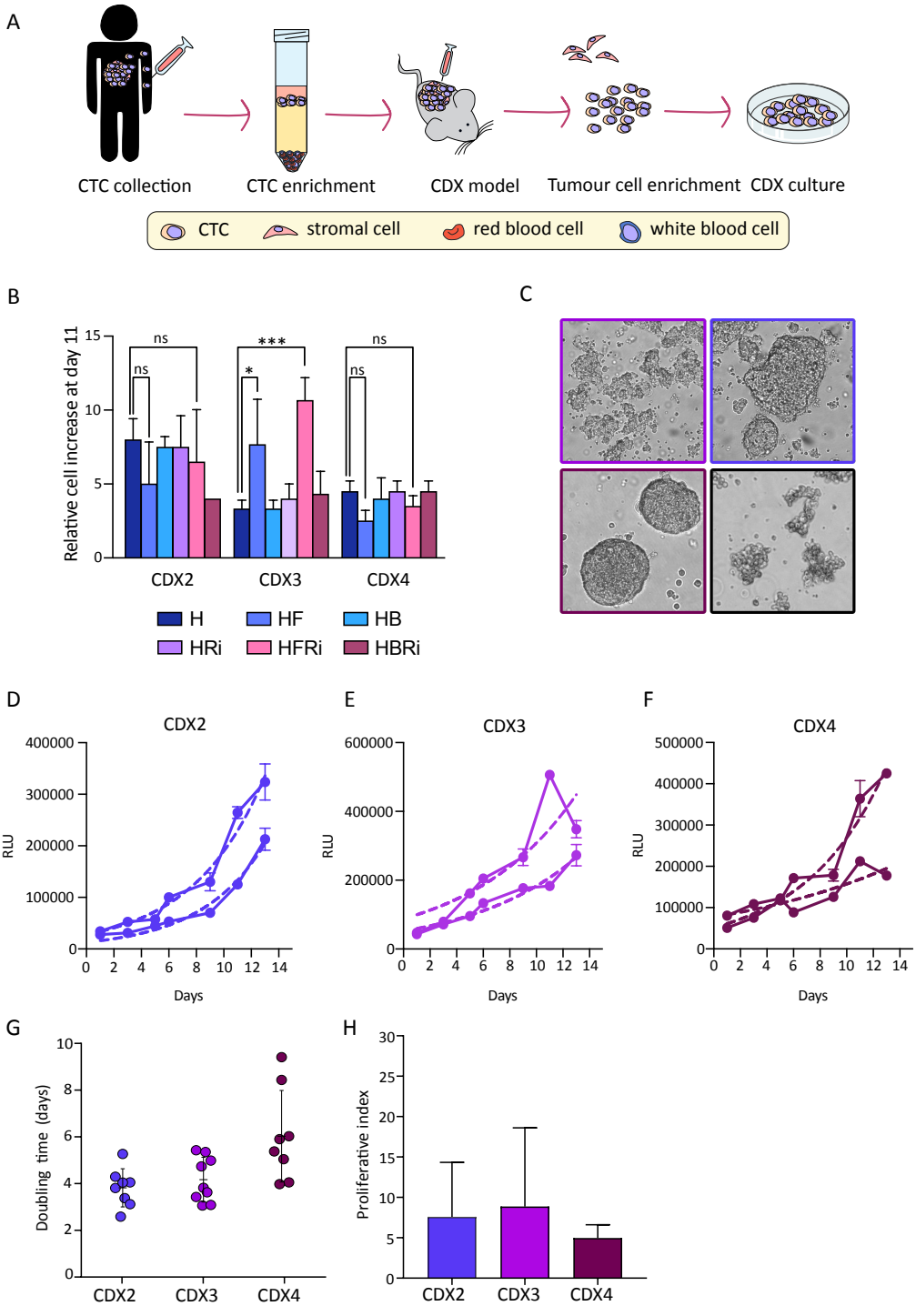

Figure 23. CDX-derived cells can grow *ex vivo.*

A. Schematic of the different steps from CTC to CDX cultures. B. Comparison of the increase in cell number after 11 days in different media conditions. C. Representative picture of CDX3 (light purple), CDX2 (blue) and CDX4 (dark purple) cultures compared with the common SCLC cell line H69 (black). D-F. Representative examples of CDX2 (D), CDX3 (F), CDX4 (G) growth in culture with HFRi media. G. Doubling time of CDX2, 3 and 4 cultures in HFR media. Each data point represent an independent culture. Different plating densities have been included. H. Proliferation of CDX2, 3 and 4 growing in HFR media was assessed by EdU incorporation after 15hr of labelling. The graph depicts the average percentage of EdU positive cells from 3 independent experiments. In all panels, error bars represent

SD. * and *** refer to a *p*-value of 0.034 and 0.0001, respectively. H = HITES, HRi = HITES + Y-27632, HB = HITES + bombesin, HF = HITES + FBS, HFRi = HITES + FBS + Y-27632, HBRi = HITES + bombesin + Y-27632.

Based on these data, HITES media supplemented with FBS and Y-27632 was selected as the condition of choice to grow *ex vivo* CDX tumour cells. In this media, CDX2, CDX3 and CDX4 grew as non-adherent cell clusters of variable size and shape, similar to common SCLC cell lines with classic morphology (Carney et al., 1985) (Figure 23C). Analysis of cellular ATP content at different timepoints in culture over a 2 weeks window showed that CDX-derived cells are metabolically active in HFRi media (Figure 23D-F). Non-linear fitting of exponential curves showed a doubling time of ~ 4 days, consistent with what has been described for classic SCLC cell lines (Gazdar et al., 1985)(Figure 23G).

To further confirm the ability of these cells to replicate in this culture condition, EdU incorporation was assessed. Replicating cells ranged between 8% (CDX4) and 18% (CDX3) of the live cells population (Figure 23H). All experiments described have a high level of variability across biological replicates, as shown by the width of the error bars and the shift in the proliferation profiles observed in Figure 23D-F. This heterogeneity suggested that clones with different fitness could be selected, highlighting the importance of characterising this system thoroughly.

To evaluate the effect of adding the ROCKi in the culture media I examined its effect on RNA expression. CDX3 and CDX4 cultures were grown for 24hr in HITES media with or without the addiction of Y-27632, and RNA was extracted to perform RNA sequencing (Figure 24A). Distance matrix analysis showed a correlation between samples derived from the same CDX model, suggesting that treatment with the ROCK inhibitor had limited impact on the transcriptomic profiles of these cells (Figure 24B). Visualisation of different principal components showed how the cells treated with or without the ROCK inhibitors tended to cluster together, with PC3 displaying the strongest separation between minus and plus Y-27632 across the models (Figure 24C). Analysis of the top 1,000 genes contributing to PC3 identified 488 protein coding genes (Supplementary Data 1). Pathway enrichment analysis with KEGG and Reactome databases only detected one pathway common to 5 of the identified genes (“One carbon pool by folate”/”metabolism of folate and pterines” pathway). GO

terms of these 488 protein coding genes included “tetrahydrofolate interconversion” (x 5 genes), “folic acid-containing compound metabolic process” (x 7 genes), “tetrahtdrofolate metabolic process” (x 6 genes) and “pteridine-containing compound metabolic process” (x 7 genes). Alterations in this metabolic pathway suggested that the CDX cells adapt their metabolism when grown *ex vivo*, as already observed for human stem cells (Vernardis et al., 2017). Overall the very low number of protein coding genes involved in these pathways suggested that inhibition of ROCK at the concentration used in this culture did not affect largely the behaviours of the CDX cells.

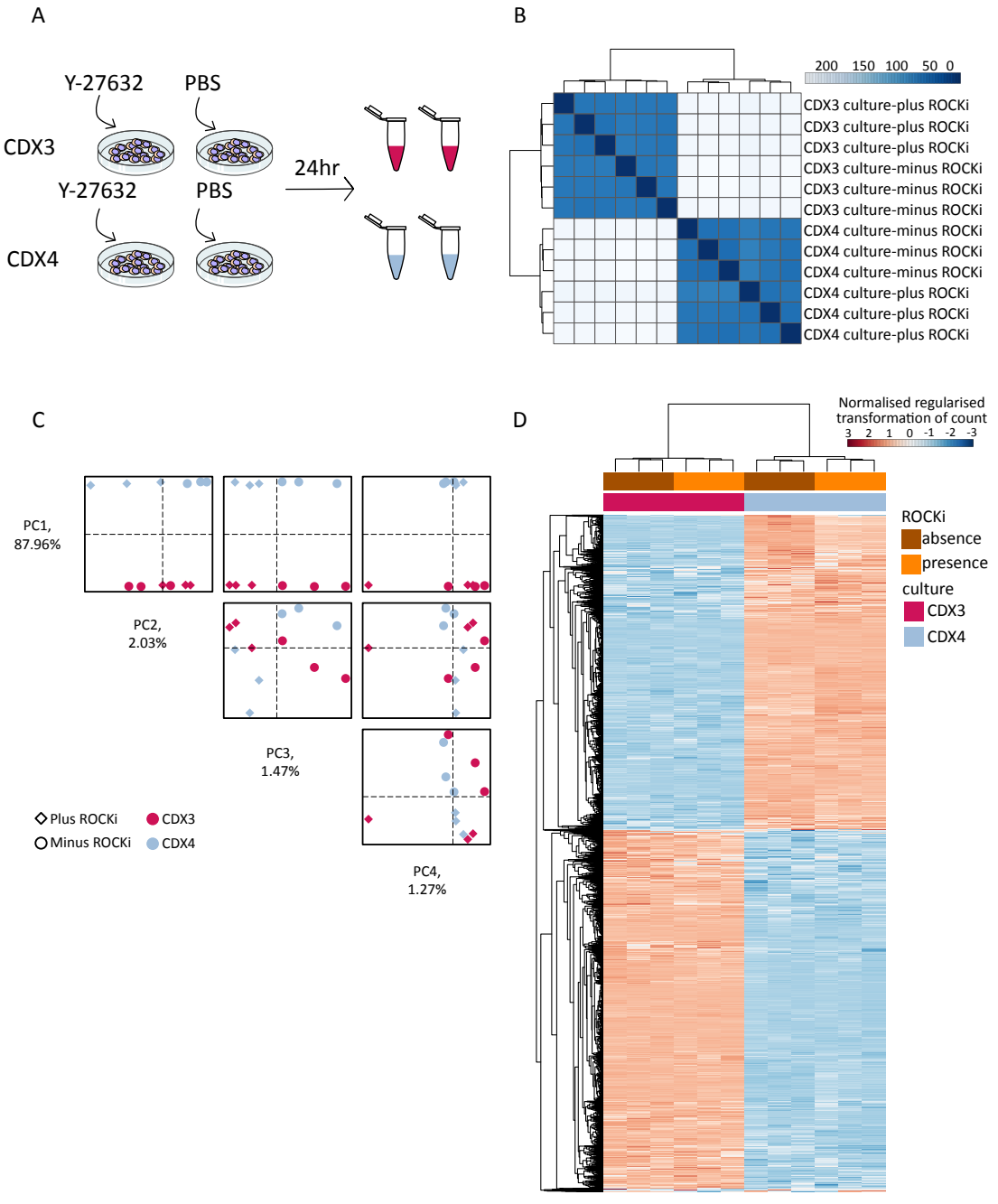

Figure 24. Effect of ROCK inhibition on the transcriptomic profile of CDX cultures.

A. Schematic of the experimental design. B. Distance matrix to correlate each sample with each other. Raw counts were normalised with the regularised transformation function of DESeq2 before calculating the distances. C. Paired PC plots to show the distribution of the samples when different principal components are investigated. D. Unsupervised hierarchical clustering showing the most 5,000 variable genes across all samples. Genes were scaled by row. The colour key represents the regularised transformation of the raw counts. Both CDX3 (dark pink) and CDX4 (light blue) grown in the presence (orange) or absence (brown) of the ROCK inhibitor are shown in the heatmap.

Similarly, plotting of the top 5,000 differentially expressed genes across all the samples did not show any strong variation between each CDX treated with or without the ROCK inhibitor (Figure 24D, Supplementary Data 2). Differential gene expression analysis only identified seven protein-coding genes differentially expressed in CDX3 cultured without Y-27632 compared with CDX3 cultured with Y-27632. Similarly, CDX4 cultures grown in the absence of Y-27632 had only 125 genes differentially expressed compared with CDX4 cells grown in the presence of Y-27632 (Supplementary Table 2). All together these data, validate the use of the HITES media supplemented with FBS and Y-27632 to grow CDX-derived cells *ex vivo*.

3.2.2 CDX *ex vivo* culture show similar phenotypes than the corresponding tumour

Previous work form Prof. Rudin's group showed that tumour cells derived from SCLC PDX accumulated several changes during several months of passage in culture (Daniel et al., 2009). To try to limit the adaptation that cells undergo during 2D growth, I grew the CDX-derived cells for a maximum of 5 weeks in plastic. During this time, cells were collected and processed in multiple ways in order to perform a full characterisation. First, to evaluate if the culture conditions affected the expression of the typical SCLC markers, I collected samples from a 2 weeks culture of each CDX and assess the expression of the epithelial marker, cytokeratins (pan-CK), and the NE markers, synaptophysin (SYP) and CD56 (NCAM). In parallel, tumours from the corresponding models were assessed for the same markers. As already described in Hodgkinson *et al*, CDX2, CDX3 and CDX4 expressed CKs, SYP and CD56, similarly to what was observed in the corresponding patient's biopsy (Hodgkinson et al., 2014). A different set of FFPE blocks for CDX2, CDX3 and CDX4 was used to validate the findings from Hodgkinson *et al* and as direct comparison to the cultures. To increase the panel of markers tested and look at different features of SCLC, I decided to test also vimentin (VIM). Vimentin is usually weakly or not expressed in SCLC and has been associated

with a more variant phenotype (Broers et al., 1986; Zhang et al., 2018). CDX2, CDX3 and CDX4 showed classic morphology *in vivo* with small nuclei (Figure 25A) and grew as non-adherent clusters *ex vivo* (Figure 23C) (Carney et al., 1985), therefore I was expecting low VIM expression. As anticipated, CDX2, CDX3 and CDX4 tumours were positive for CKs, SYP and CD56. CDX2 and CDX3 tumours were negative for VIM, while CDX4 tumour showed a few VIM positive cells suggesting a more mesenchymal phenotype (Figure 25B). In accordance with the *in vivo* data, CDX2, CDX3 and CDX4 cultures were positive for the epithelial and neuroendocrine markers tested. Moreover, while CDX2 and CDX3 cultures were completely negative for VIM, CDX4 cultures showed a mixture of positive and negative cells, suggesting that the culture condition used did not affect the differentiation state of the cells (Figure 25B).

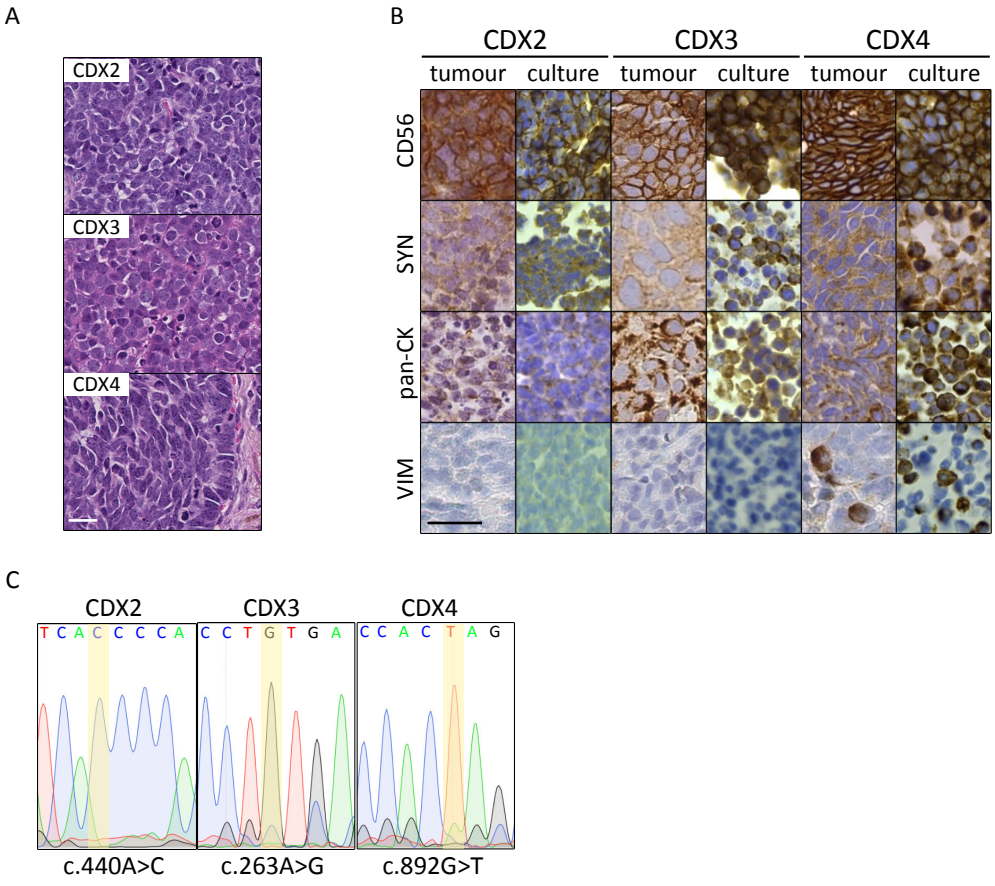

Figure 25. CDX-derived cells mimic the corresponding CDX tumours.

A. Representative H&E pictures of CDX2, CDX3 and CDX4 tumours. Scale bar: 20 µm B. Representative images of chromogenic staining for epithelial (pan-CK), neuroendocrine (SYP and CD56) and mesenchymal (VIM) markers in CDX2, CDX3 and CDX4 cell pellets, derived from 2 weeks cultures, and corresponding CDX tumours. Scale bar: 25 µm. C. Chromatograms highlighting the *TP53* mutations detected on CDX2-, CDX3- and CDX4-derived cultures.

3.2.3 Analysis of transcriptomic changes applied by the culture system

To further characterise the impact of the culture conditions on the CDX-derived cells, I looked at the *TP53* mutational status. p53 is universally inactivated in SCLC (George et al., 2015) and we have previously shown that CDX2 and CDX3 harboured a missense mutation on *TP53* (c.440A>C and c.263A>G, respectively), while CDX4 had a nonsense mutation (c.892G>T) (Hodgkinson et al., 2014). As expected, the same *TP53* mutations were identified in the corresponding cells after 2 weeks of culture (Figure 25C), suggesting that this salient feature of SCLC is not lost during culturing. While I was not expecting any genomic selection after only a few weeks of cultures, I wanted to evaluate if the transcriptomic changes observed by Daniel *et al* were also present at early time points in the CDX cultures (Daniel et al., 2009). First, I wanted to assess overall gene expression differences between each CDX and the derived cultures. CDX2, CDX3 and CDX4 were cultured for 2 weeks and processed for RNA sequencing. Multidimensional scaling was used to look at the similarities between tumour/culture pairs. As shown in Figure 26A, CDX cultures closely resembled the matched CDX tumours. This suggests that two weeks after culture, the derived tumour cells maintained a transcriptomic profile very similar to that of the donor tumours. To look at the changes imposed by the culture, I performed a pathway enrichment analysis focusing on the genes with at least two fold changes of difference between the tumour and the corresponding culture. There were 22 pathways commonly altered across the models. Most of these pathways were involved in synthesis and assembly of collagen and organisation and degradation of the extracellular matrix (Supplementary Data 3), highlighting the effect of growing these cells in an environment that lack interaction with the stromal compartment (Figure 26B). Model-specific changes included alterations in protein biosynthesis in CDX2 and protein-protein interactions at synapses in CDX3 and CDX4.

To understand if the changes observed after 2 weeks of culture were maintained in the short-term, CDX3 was cultured for 4 weeks and samples were collected every week for RNA sequencing. Of a total of 31,652 expressed genes analysed, 35% (equivalent to 11,135 genes) were differentially expressed, of which 4,920 were protein coding genes and 6,215 were non-coding (Supplementary Data 4). To look at the dynamics of these variations, I selected the top 1,000 differentially expressed

genes between CDX3 tumours and the derived cells after 4 weeks of culture and examined how these genes changed overtime. Interestingly, most of the changes appeared by week 2 and were stable up to week 4 in culture, suggesting that, at least in this short time frame, it was possible to limit the strong clonal selection observed by others (Daniel et al., 2009) (Figure 26C-D).

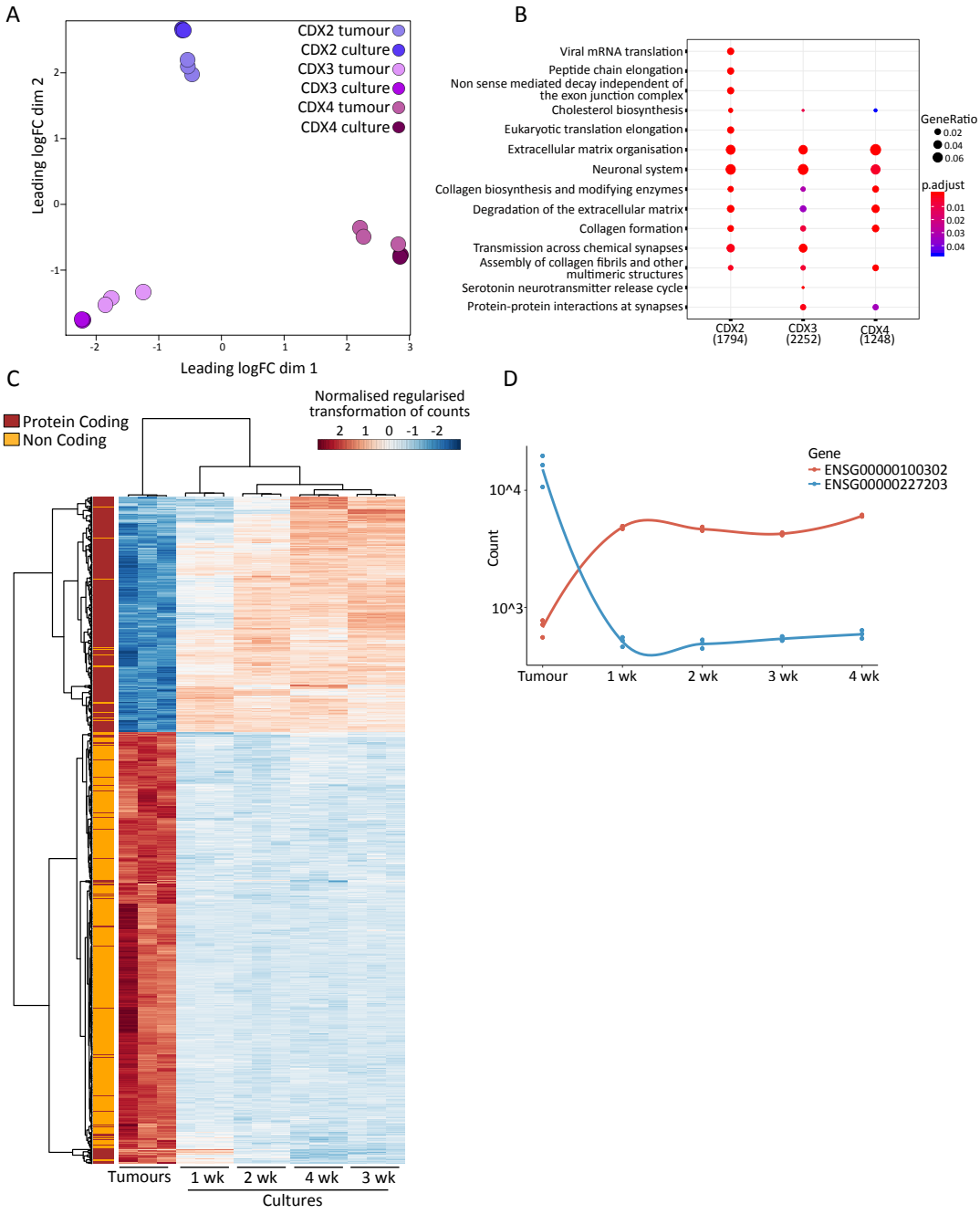

Figure 26. CDX-derived cells adapt to culture by rewiring part of their gene expression.

A. Multidimensional scaling to compare the transcriptomic profile of CDX2-, CDX3- and CDX4-derived cultures with the corresponding tumours. The root mean square of the log2 fold changes between the samples is shown. Dark purple, pink and red dots represent CDX2, CDX3 and CDX4 tumours, respectively, while light-coloured dots represent the corresponding CDX-derived cells after 2 weeks

of culture. B. Pathway enriched in each comparison (CDX tumour *vs* derived culture) for each model tested. Dots are coloured relative to adjusted *p*-value of the enriched pathway and their size depend on the GeneRatio (chapter 2.10.2 for details). The number below each CDX refers to the total number of protein coding genes used in the analysis. C. Unsupervised hierarchical clustering of the top 1,000 differentially expressed genes (FDR ≤ 0.05) between CDX3 tumours and the derived cultures over time. Genes were scaled by row. Both protein-coding (brown) and non-coding (yellow) genes are depicted. D. Example of count variation over time of two of the top 10 differentially expressed genes between the tumours and the cultures. wk: week.

3.2.4 CDX cultures maintain their tumourigenic potential *in vivo*

One of the advantages of commonly used established cell lines is the possibility to easily modify them *in vitro* and then implant them *in vivo* to observe the effect of the modification on tumour growth and response to drugs. While other members of the lab were working on optimizing a way to transduce CDX-derived cells, I wanted to verify that these cells were still tumourigenic *in vivo*. CDX3- and CDX2-derived cells were implanted in immunocompromised mice after 4-5 weeks of culture. Both models were able to repopulate a tumour, with tumours derived from CDX3 cultures growing at a similar rate than CDX3 tumour derived from cells that have never been in culture (average 5.8 *vs* 7 weeks to reach ~ 150mm^3, respectively) (Figure 27A). For CDX2, it took an average of 9.3 weeks to observe tumours at ~150mm^3 in mice implanted with CDX2 cultures, twice the time needed to have tumours at the same size in mice implanted with uncultured CDX2 cells (Figure 27B). Immunohistochemistry analysis of the CDX3 tumours derived from the culture showed similar morphology to the matched original CDX3 as assessed by H&E. Expression of CKs, CD56, SYP and VIM was also maintained in the tumours derived from CDX3 culture, further highlighting the stability of these features *in vivo* and *ex vivo* (Figure 27C). Once confirmed that the cultures can form tumours *in vivo*, I wanted to determine if the transcriptomic changes observed during culture were irreversible and maintained once the cells were re-implanted in immunocompromised mice, as observed by Daniel *et al* (Daniel et al., 2009). To assess this hypothesis, CDX3 cells were cultured for 2 weeks and RNA was extracted. In parallel, RNA was extracted from CDX3 tumours derived from a 5 weeks CDX3 culture (culture-derived CDX tumour). Bulk RNA sequencing was performed on these samples and the raw data were combined with the available RNAseq from the original CDX3 tumours. Differential gene expression analysis was performed between the original CDX3 tumours and the two derived models, as shown in Figure 28A (Supplementary Data 5).

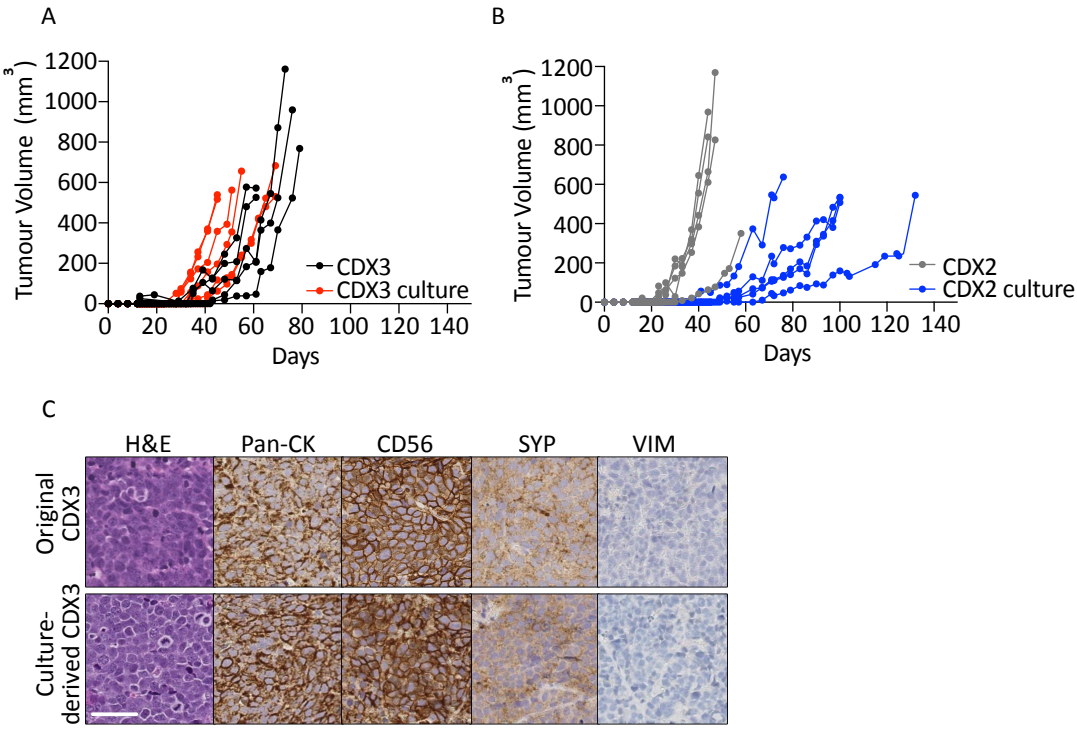

Figure 27. CDX culture are tumourigenic *in vivo.*

A,B. CDX3 (A) and CDX2 (B) cells directly passaged from CDX3 and CDX2 tumours (black and grey, respectively) or maintained in culture for four weeks (red and blue, respectively) were subcutaneously implanted into SCID-*bg* mice. Each line represents an individual tumour. C. Immunohistochemical analysis of SCLC marker expression in both original and culture-derived CDX3 tumours. Pan-CK: pan-cytokeratin, SYN: synaptophysin, VIM: vimentin. Scale bar: 50 µm.

The top 1,000 protein coding genes differentially expressed in CDX3-derived cultures compared with the original CDX3 tumours (comparison 1) were selected to look at how these genes changed in the culture-derived CDX3 tumours compared with the original CDX3 tumours (comparison 2). Interestingly, 51.9% of the top 1,000 protein coding genes differentially expressed in comparison 1 were unchanged in the culture-derived CDX3 tumours, suggesting that some of the changes imposed by the cultures were reversible once the cells were re-implanted in immunocompromised mice (Figure 28B). In total 27.2% of the genes (both protein coding and non-coding) were differentially expressed in comparison 2, while almost twice that number of genes (43.8%) were differentially expressed between the CDX3 cultures and the original CDX3 tumours (comparison 1). Indeed, principal component analysis showed that culture-derived CDX3 tumours clustered closer to the original CDX3 than to CDX3-derived cultures (Figure 28C). Pathway enrichment analysis showed no pathway overlap between the pathways enriched in comparison 1 *vs* comparison 2, suggesting

that the main pathways altered during culture were back to the same level as in the original CDX3 tumours when the cells were re-injected in immunocompromised mice (Figure 28D).

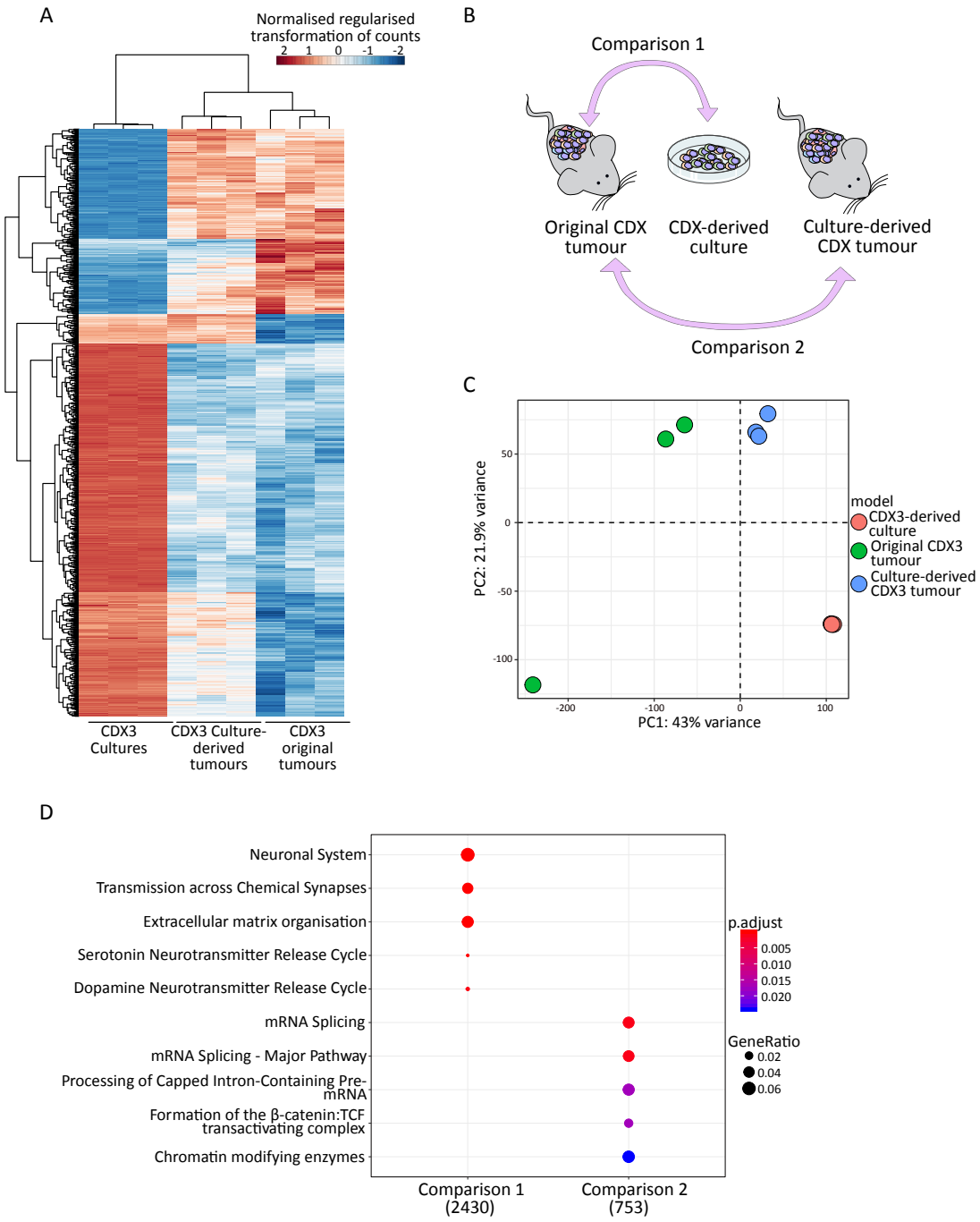

Figure 28. Tumours derived from CDX culture re-acquire some of the features lost *in vitro.*

A. Unsupervised hierarchical clustering of the top 1,000 differentially expressed protein-coding genes (FDR ≤ 0.05) is illustrated in the heatmap. Genes were scaled by row. B. Schematic of the comparison analised in C and D. C. Principal component analysis to compare the transcriptomic profile of the original CDX3, CDX3-derived culture and culture-derived CDX3 tumours. D. Pathway enriched in each comparison 1 and 2. Dots are coloured relative to adjusted *p*-value of the enriched pathway and their

size depends on the GeneRatio (chapter 2.10.2 for details). The number below each comparison refers to the total number of protein coding genes used in the analysis.

3.2.5 CDX cultures show the same response to standard-of-care than the donor CDX

To complete the validation of the CDX *ex vivo* culture, I wanted to assess if these cells were able to maintain a similar response to cisplatin and etoposide. The efficacy of these drugs in CDX2, CDX3 and CDX4 tumours was previously described (Hodgkinson et al., 2014). CDX3 tumours showed almost complete tumour regression (~ 90% maximum regression) after treatment with cisplatin/etoposide. CDX2 tumours partially regressed (~ 50% maximum regression) after treatment, while CDX4 tumours did not respond to cisplatin/etoposide treatment. To initially validate that the response of CDX cultures to cisplatin and etoposide would not change with time in cultures, I treated CDX3 cells with increasing concentrations of cisplatin and etoposide after they had been in culture for 3 days, 1 week or 3 weeks. As shown in Figure 29A and B, CDX3 cells maintained a similar sensitivity to these drugs at all time point tested, suggesting that short-term culture of these cells does not change their response to drugs.

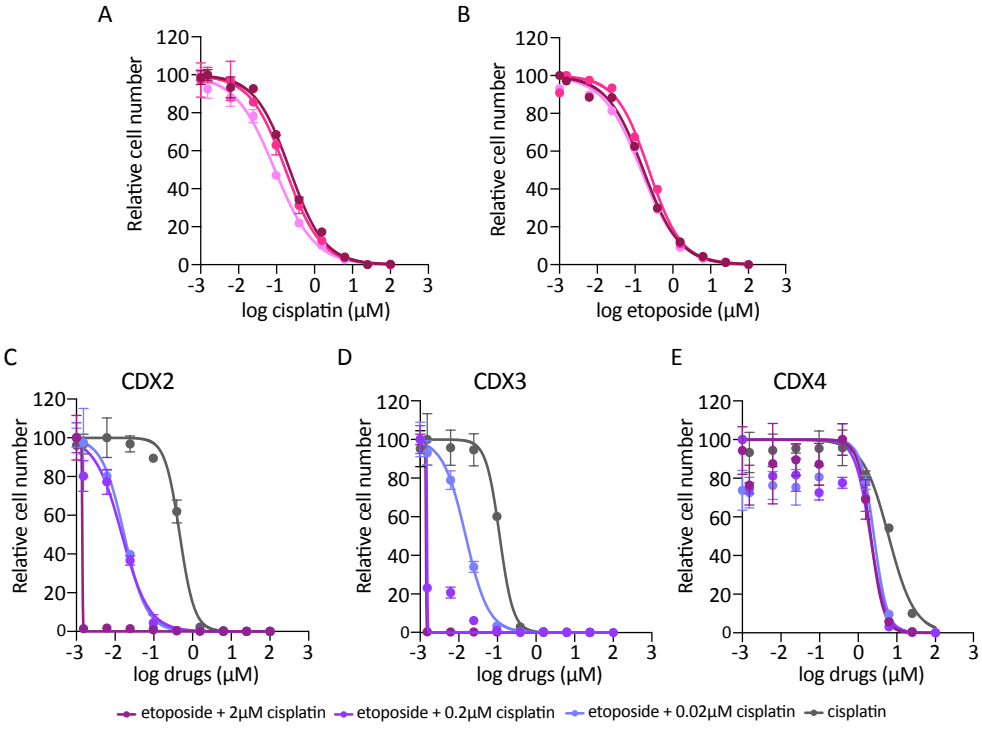

Figure 29. Drug screening on CDX cultures.

A,B. CDX3 *in vitro* response to cisplatin (A) and etoposide (B) after 3 days (dark pink), 1 week (pink) and 3 weeks (light pink) in culture. C-E. Pilot study to determine the best concentration of cisplatin in combination with etoposide. All response curves show the response to increasing concentration of

etoposide (pink, purple and violet lines) or cisplatin (grey line). For the etoposide treatment a fixed concentration of cisplatin was added. The same colour code is applied to the three graphs.

To test if *ex vivo*, CDX-derived cells were able to maintain a similar sensitivity to cisplatin and etoposide compared with the corresponding CDX tumour, two to five weeks CDX cultures were treated with increasing concentrations of cisplatin and etoposide as single agents and in combination. I performed a preliminary pilot study to determine the best concentration of cisplatin to be combined with etoposide in order to obtain a response representative of the *in vivo* data. Three fixed concentrations of cisplatin were selected based on the initial 50% growth inhibition (GI_{50}) obtained with cisplatin treatment alone. CDX2 and CDX3 showed a GI_{50} of 0.5 and 0.12 μM, respectively, while CDX4 showed a GI_{50} of 7.5 μM. Because CDX3 was the most sensitive, I selected a value close to its GI_{50}, and tested one concentration 10 times higher and another one 10 times lower. As shown in Figure 29C-E, etoposide treatment with 2 μM of cisplatin was very toxic in CDX2 and CDX3, while etoposide combined with 0.02 μM of cisplatin showed an intermediate response in both CDX2 and CDX3. Addition of 0.2 μM of cisplatin was more effective in CDX3 than CDX2, while CDX4 was resistant to all conditions tested. Because I knew that CDX2 displayed a more resistant phenotype than CDX3 *in vivo*, I identified 0.2 μM of cisplatin as better representative of the *in vivo* data. When I repeated these experiments focusing on the monotherapies and on etoposide combined with 0.2 μM of cisplatin, CDX2 and CDX3 were more sensitive to both cisplatin and etoposide than CDX4, with CDX3 showing the greatest sensitivity to all treatment conditions (Figure 30A). CDX3 showed an average GI_{50} of 0.09 μM, 0.03 μM and 0.0007 μM for cisplatin, etoposide and the combination respectively. This is consistent with the strong response to cisplatin/etoposide observed in CDX3 tumours *in vivo* and the chemosensitivity observed in patient 3 (Hodgkinson et al., 2014). CDX4-derived cultures, on the other side, were far more resistant to cisplatin, etoposide and the combination, with average GI_{50} of 3.15 μM, 6.54 μM and 4.2 μM, respectively (Figure 30B). CDX2-derived cultures showed an intermediate response to the combination, with average GI_{50} of 0.03 μM. Interestingly, the response of CDX2 cells to the combination was mainly driven by etoposide, with single agent etoposide eliciting a similar effect compared with the combination (average GI_{50} 0.03 μM). This is also shown by the overlap of the

response curves for etoposide and the combination in Figure 30C. Although we have not tested the *in vivo* efficacy of etoposide monotherapy, these data suggest that the initial regression of CDX2 tumours *in vivo* could be related to its sensitivity to etoposide alone rather than the combination of the two drugs.

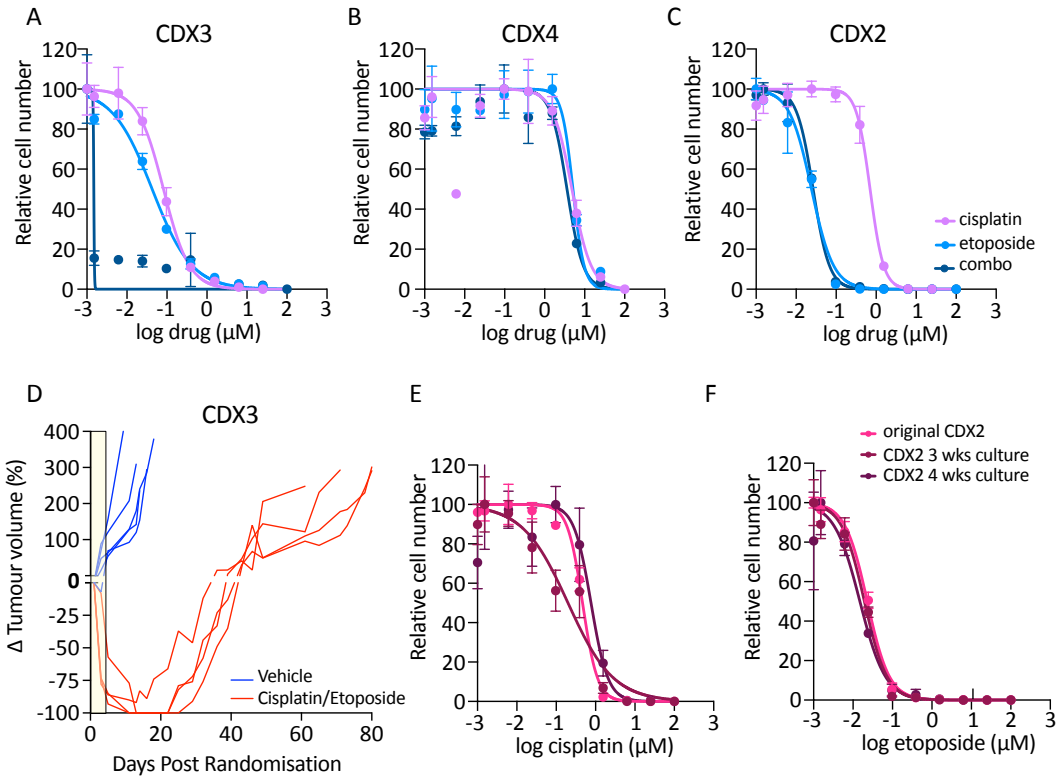

Figure 30. CDX cultures mimic the response to SoC of the corresponding donor tumour.

A-C. *In vitro* response of CDX3 (A), CDX4 (B) and CDX2 (C) cultures to cisplatin (pink), etoposide (light blue) or the combination (blue) after 1 week of treatment. For combination experiments, 0.2 µM cisplatin were added to etoposide. One of at least three representative experiments for each model is shown. D. Culture-derived CDX3 tumours were treated with cisplatin/etoposide (red) or vehicle (blue). Each line represents an individual relative tumour volume. Yellow shaded box demarcates the treatment period. E-F. CDX2 cells were treated with cisplatin (E) or etoposide (F). Both graph are coloured coded as explained in F. See text for details. Wks = weeks.

To further validate the culture system, 5 week CDX3 cultures were re-injected in immunocompromised mice and tumours were treated with one cycle of cisplatin/etoposide or vehicle, as previously performed by Hodgkinson *et al* (Hodgkinson et al., 2014) (see chapter 2.9.3 for details). The culture-derived CDX3 tumours were highly sensitive to cisplatin/etoposide treatment, with complete tumour regression, similar to what was observed with the CDX3 tumours derived from uncultured cells (Figure 30D, Hodgkinson et al., 2014). The drug treatment was not performed on the CDX2 cells re-implanted in mice, however as proof of principle,

I have expanded in culture one of the CDX2 tumours derived from CDX2 culture. These cells were treated with cisplatin or etoposide and the response was compared with the response to cisplatin and etoposide observed on the original CDX2 cells that were not re-implanted in mice. As expected, the response to cisplatin and etoposide was maintained after passaging *in vivo* and over time in culture (Figure 30E,F).

3.3 Conclusions

CDX have been shown to faithfully mirror the donor patient tumour and are representative of the main SCLC subtypes described in the literature (Hodgkinson et al., 2014; Simpson et al., 2019). We exploited the CDX models to test the efficacy of combining the PARP inhibitor olaparib with the WEE1 inhibitor AZD1775 in both chemosensitive and chemorefractory CDX, as well as in paired chemonaïve and chemotreated models (Lallo et al., 2018)(Figure 22). Even if the response to this combination was overall better than the response to cisplatin/etoposide, we observed different patterns of sensitivity, suggesting that each model may have a distinct mechanism of response to these drugs. To investigate this hypothesis, I have developed an *ex vivo* culture system of CDX-derived cells in order to facilitate functional testing and identification of putative biomarkers of response. This short-term cultures maintained most of the salient features of the donor tumours, making them a tractable system to study the response to olaparib/AZD1775. The addition of the ROCK inhibitor and FBS to the original HITES media did not alter the phenotype of these cells which grow as non-adherent clusters similar to most SCLC cell lines (Gazdar and Oie, 1986). These factors rather encouraged the survival of the CDX-derived cells, possibly reducing the induction of anoikis caused by the dissociation of the tumour (Watanabe et al., 2007). The media conditions selected to grow these cells did not affect their NE differentiation and did not seem to select for specific mutant clones in the short-term. Gene expression data showed that culturing of CDX has an effect on ECM organization and collagen biosynthesis probably due to the loss of ECM and stromal compartment. Although these alterations appeared to be reversible when the cultures were re-implanted in mice, they have to be taken into consideration when experiments are performed *ex vivo*. Moreover, the discrepancy between the growth rate of CDX2 tumours and culture-derived CDX2 tumours implies

that some models are more affected than others by the culturing (Figure 27B). Indeed, differently from CDX3 and CDX4, CDX2 cultures showed a major number of pathways altered in the cultures compared with the donor tumour (Figure 26B). Together with changes in the processing of collagens, CDX2 cultures showed alteration in the elongation step during protein translation. These changes could have had an impact on the tumourigenic potential of these cells, explaining the delay observed in tumour growth *in vivo*. Despite the observed differences between the cultures and the tumours, overall these changes did not affect the response these cells had to SoC. Moreover, compared with what has been published for PDX-derived cultures, there were no tumour-related pathways affected by the culturing, arguing that short-term culturing of CDX cells did not affect important hallmarks of cancer (Daniel et al., 2009). One of the advantages of these cultures compared with common cancer cell lines is their vicinity with the *in vivo* model making them a tractable system to assess patient-derived response to drugs. Moreover, because CDX tumours can be continuously generated by passaging the cells in mice, there is no need to passage the CDX culture for long terms. Rather, tumours can be dissociated when needed and the cells can be used for the experiments of interest within 1-2 weeks. This will limit the adaptation imposed by culture conditions. Compared with CDX tumours, the derived cells have the advantage to be relatively easy to manipulate allowing functional characterization of tumour evolution and drug response. The observation that these cells re-acquire some of the features lost in culture when re-implanted in immunocompromise mice, make them particularly interesting to study mechanisms of metastasis formation, tumour evolution and response to therapies. Indeed, these cells could be easily transduced with fluorescent reporters *in vitro* and subsequently grown *in vivo* to follow cell dissemination. Furthermore, these cultures could be genetically modified *in vitro* and then implanted *in vivo* to assess the effect of the modification in a more relevant system. Of particular interest for my project is the fact that these cultures can be used to rapidly screen multiple compounds and initially dissect the mechanisms behind the observed response *in vitro.*

Chapter 4: Drug screening of CDX culture

4.1 Introduction

CDX *ex vivo* cultures maintain the main characteristics of the donor CDX tumours and therefore can be a useful tool to rapidly screen different compounds. The results described in the previous chapter suggested that despite some differences between the culture and the donor tumours, these cells can retain a similar sensitivity to SoC and hence, can be used to predict the response *in vivo*. To further validate this hypothesis and confirm that these cultures can also predict the response to different type of drugs, I have screened the CDX cultures with different compounds and compared the response observed *in vitro* with the one obtained *in vivo*.

It was recently published in our group that CDX2 is sensitive to the combination of the PI3K inhibitor GDC0941 and the BH3 mimetic ABT263, *in vivo*. In this study, Potter *et al* treated CDX2 tumours with GDC0941, ABT263 or the combination of the two. GDC0941 is a class I PI3K inhibitor targeting the p110α and β catalytic subunits of PI3K and suppressing its activity (Salphati et al., 2011). ABT263 targets BCL-2 and BCL-xL and impedes their anti-apoptotic effect (Oltersdorf et al., 2005; Tse et al., 2008). While the PI3K inhibitor alone had barely no effect on CDX2 tumour growth, the BH3 mimetic caused 80% regression during the treatment period and this effect was extended when combined with GDC0941 (Potter et al., 2016).

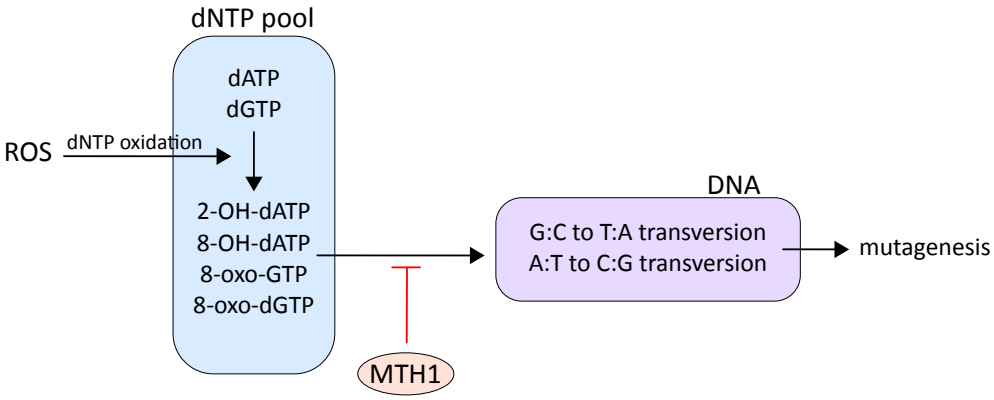

Figure 31. MTH1 role in dNTP sanitation.

ROS can oxidase dNTP that can be mis-incorporated into DNA and induce mutagenesis. MTH1 sanitises the dNTP pool by hydrolysing the oxidised purine nucleoside triphosphates to monophosphates.

Prof. Thomas Helleday developed several inhibitors of MTH1, showing promising results in a panel of cancer cell lines (Gad et al., 2014; Warpman Berglund et al., 2016). MTH1 (or MutT homolog-1) is an 8-oxo-dGTPase that localises in the nucleus and mitochondria. It belongs to the Nudix hydrolase superfamily and acts by sanitising the oxidised dNTP pool (Yoshimura et al., 2003). This pool is highly sensitive to ROS. ROS can oxidise the free bases into 2-OH-dATP, 8-OH-dATP, 8-oxo-dGTP and 8-oxo-GTP, which can be incorporated into DNA and generate specific lesions (Svensson et al., 2011). In particular 8-oxo-GTP tends to form base pairs with cytosine and adenine, causing G:C to T:A transversion, while the 8-oxo-dGTP produces A:T to C:G, as well as G:C to T:A transversion (Tsuzuki et al., 2007) (Figure 31). MTH1 drives the hydrolysis of these oxidised bases into monophosphates, thus preventing their integration into the genome. MTH1 inhibitors act by binding the catalytic pocket of MTH1 as an 8-oxo-GTP analogue. In this way, MTH1 is no longer able to recognise the oxidised dNTPs, causing their accumulation and incorporation into the genome. The MTH1 inhibitors have no effect on untransformed cells, suggesting a higher level of ROS regulation and/or a reduced level of ROS production in this setting (Gad et al., 2014). Cancer cells, instead, showed a strong sensitivity to this drug. This was probably due to the higher metabolic and proliferative rate observed in cancers leading to increased ROS production. Thus, MTH1 acts as an essential checkpoint in cancer cells to balance the level of ROS, explaining why several cancer cell lines do not tolerate its inhibition (Gad et al., 2014).

The BH3 mimetic as well as PI3K and MTH1 inhibitors were used to validate the predictive value of the CDX-derived cultures. I have then optimized an assay to test combination of compounds in order to better characterize the response to AZD1775/olaparib *ex vivo*. In particular, given the patient clinical information, I was able to use cisplatin/etoposide as a reference to assess the cultures ability to recapitulate the patient response to this treatment.

4.2 Results

4.2.1 CDX cultures can recapitulate the response to targeted therapies

Knowing the *in vivo* efficacy of ABT263 and GDC0941 in CDX2, I decided to determine whether CDX2 cultures exhibited a similar response *ex vivo*. CDX2 cultures

were treated with increasing concentrations of GDC0941, ABT737 (the tool compound equivalent to ABT263) or a combination of the two, and viability was measured 7 days after treatment. CDX2 cultures showed a similar trend of response compared with the corresponding CDX2 tumours treated *in vivo* (Figure 32A, Potter et al., 2016). CDX2 cultures were more responsive to ABT737 as single agent than to GDC0941 (average GI_{50} of 0.03 µM *vs* 0.4 µM, respectively) and they showed the highest sensitivity to the combination with an GI_{50} 10,000x lower (average GI_{50} 0.00003 µM) (Figure 32A).

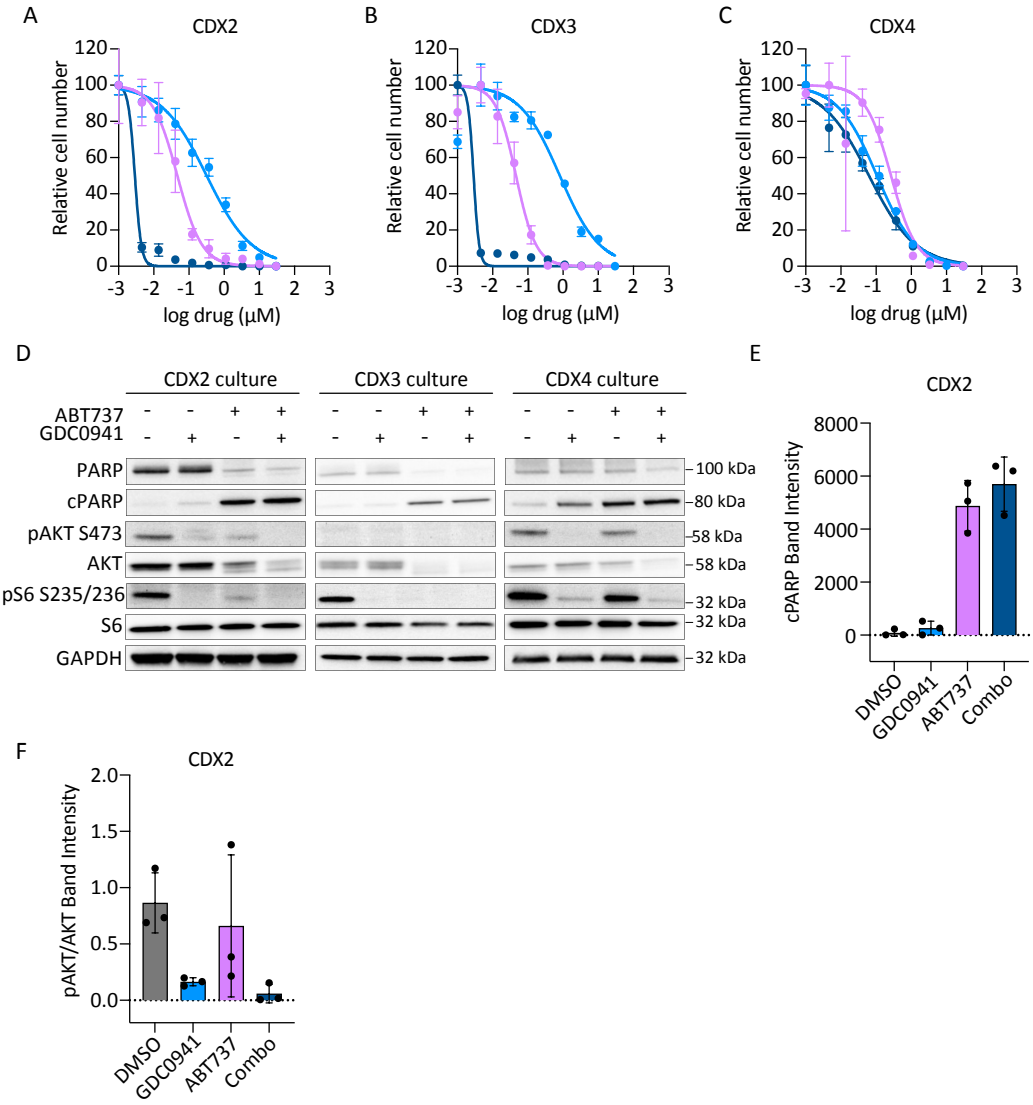

Figure 32. CDX *ex vivo* cultures can predict the response to novel targeted therapies.

A-C. CDX2 (A), CDX3 (B) and CDX4 (C) cultures were treated with increasing concentrations of ABT737 (pink), GDC0941 (light blue) or the combination (dark blue). For the combination, 150 nM of ABT737 were added to increasing concentrations of GDC0941. One of three representative experiments is shown for each culture. D. CDX2, CDX3 and CDX4 cultures were treated with DMSO or 0.5 µM of the indicated compounds for 8 hr. The indicated proteins were probed as biomarkers of ABT737 and

GDC0941 activity. E. cPARP band intensity quantification from CDX2 culture in panel D. F. Ratio of pAKT and AKT band intensities from CDX2 culture in panel D. In all panels, error bars represent SD.

Western blot analysis of CDX2 cultures treated with ABT737, GDC0941 or the combination, confirmed the synergistic effect of ABT737 and GDC0941, as shown by increased levels of cleaved PARP in the combination (Figure 32D left panel, Figure 32E). As expected, inhibition of PI3K strongly reduced the phosphorylation of its downstream targets, AKT and S6 (Figure 32D left panel). Of note, the level of pAKT was also reduced in the presence of ABT737 only (Figure 32D left panel, Figure 32F). AKT has been shown to be a direct target of caspase-3 during apoptosis (Widmann et al., 1998), suggesting that AKT degradation synergizes with the inhibition of PI3K by GDC0941, partially accounting for the increased effect observed with the combination (Figure 32D left panel, Figure 32F). Because the data observed with CDX2 mirrored the response observed *in vivo*, I wanted to test the effects of this combination on CDX3 and CDX4 cultures. While the combination did not have much effect on CDX4 compared with CDX3 and CDX2 cultures (average GI_{50} 0.02 µM *vs* 0.0003 µM *vs* 0.00003 µM, respectively, Figure 32A-C), CDX4 cell viability was greatly reduced compared with the effect elicited by cisplatin/etoposide (GI_{50} of 0.02 µM and 4.2 µM for ABT737/GDC0941 and cisplatin/etoposide, respectively). Of note, CDX3 cultures were the only culture that lacked AKT phosphorylation at baseline and this was translated to a lower dependency on the PI3K pathway as shown by a more resistant phenotype in the presence of the GDC0941 (average GI_{50} 1 µM *vs* 0.4 µM and 0.2µM in CDX3, CDX2 and CDX4 respectively) (Figure 32A-C, Figure 32D mid panel). These results are in accordance with the observation that cisplatin resistant cells, like CDX2 and CDX4, tend to rely more on the PI3K pathway for survival (Cardnell et al., 2013). To further validate the predictive value of the cultures, I have treated CDX4 tumours derived from uncultured cells with GDC0941, ABT263, the combination or vehicle. As expected, the combination did not add much compared with GDC0941 alone with OS of 34.5 *vs* 32 days, respectively (Figure 33A,B). However, GDC0941/ABT263 significantly improved survival compared with vehicle (*p*-value = 0.009) and cisplatin/etoposide treatment (median OS 20 *vs* 34.5 days in the cisplatin/etoposide *vs* ABT263/GDC0941 group, respectively, (Hodgkinson et al., 2014). Immunohistochemistry analysis of cPARP showed increased apoptosis when

CDX4 tumours were treated with ABT263 and the combination (Figure 33C), comparable with what has been observed in culture (Figure 32D, right panel). Similarly, both pS6 and pAKT were reduced after treatment with GDC0941 and the combination, as shown by western blot and immunohistochemistry (Figure 33D,E).

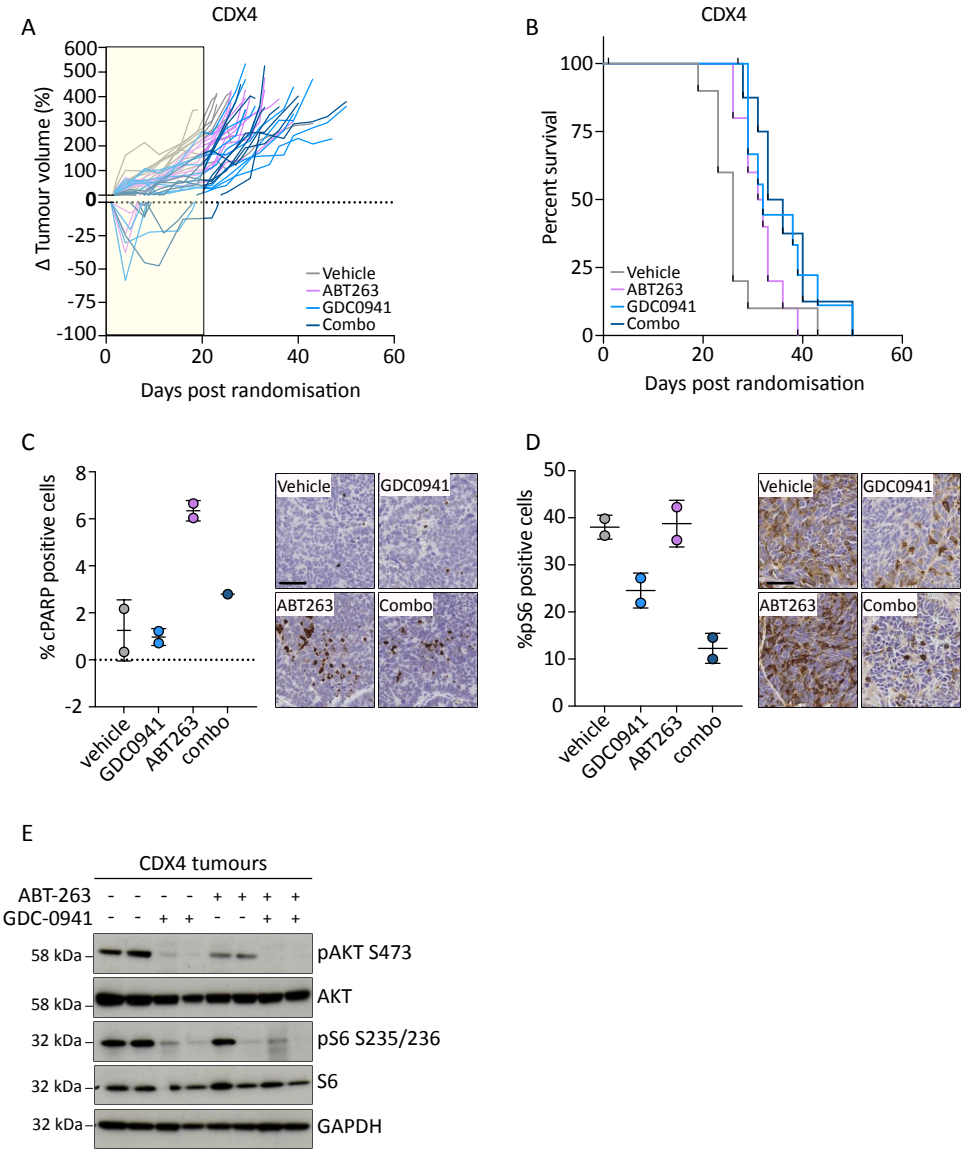

Figure 33. GDC0941 stabilized CDX4 tumour growth during treatment.

A. CDX4 tumours were treated with vehicle (grey), ABT263 (pink), GDC0941 (light blue) or the combination (dark blue) as specified in chapter 2.9.3. Each line represents an individual relative tumour volume. Yellow shaded box demarcates the treatment period. B. Kaplan-Meier analysis comparing the survival of vehicle (grey), GDC0941 and combination treated mice (light and dark blue). C. Immunohistochemistry staining for cPARP on CDX4 tumours treated for 24hr with one dose of vehicle or the indicated compounds. Representative images are shown. Scale bar: 20 µm. Error bars represent SD and each dot is a biological replicate. D. Immunohistochemistry staining for pS6 on CDX4 tumours treated for 4hr with one dose of vehicle or the indicated compounds. Representative images are shown. Scale bar: 20 µm. Error bars represent SD and each dot is a biological replicate. E. Immunoblot analysis of duplicate CDX4 tumour lysates for the indicated proteins. Each tumours was treated with one dose of vehicle or the indicated drugs and collected 4 hr after dosing.

These data, as already shown by others (Cardnell et al., 2013; Faber et al., 2015; Gardner et al., 2014; Potter et al., 2016), highlight the potential of inhibiting the PI3K pathway in chemorefractory SCLC patients to overcome cisplatin resistance. However, PI3K inhibition on its own is not enough to induce tumour regression in CDX4, implying that a combination of drugs targeting different pathways should be tested. Promotion of apoptosis together with inhibition of PI3K is effective in the chemorefractory CDX2 (Potter et al., 2016, Figure 32A), however this is not the case for the chemorefractory CDX4. AKT protein was less affected by ABT737 in CDX4 compared with CDX3 and CDX2 cultures, as shown by reduced AKT degradation and sustained phosphorylation of AKT and S6 in the ABT737 treated cells in CDX4 cultures (Figure 32D). *In vivo*, pAKT was slightly reduced after treatment with the BH3-mimetic, and there was limited effect on total AKT, suggesting that in CDX4 AKT may not be degraded after treatment with the BH3-mimetic, allowing these cells to oppose the pro-apoptotic pathway activated by this drug (Downward, 2004). Overall, the above data supports the feasibility of using CDX cultures to predict the response to novel targeted therapies.

4.2.2 The MTH1 inhibitor, TH1579, as novel treatment for chemosensitive SCLC

In collaboration with Prof. Thomas Helleday, I had the opportunity to test the novel MTH1 inhibitor, TH1579. Considering the high proliferative rate and intrinsic genomic instability of SCLC, we hypothesised that SCLC tumours should have high levels of ROS and therefore should be more dependent on metabolic checkpoints, like MTH1. To test this hypothesis, I have treated CDX2, CDX3 and CDX4 cultures with increasing concentrations of the MTH1 inhibitor, TH1579 (Figure 34A). All three models showed similar sensitivity to TH1579, with CDX4 cultures showing the most variability across replicates (Figure 34B). Before testing the efficacy of this drug *in vivo*, I further investigated the nature of the observed reduced viability *in vitro*. Considering the stronger effect on CDX2 and CDX3, I have select these two models to look at induction of apoptosis. CDX2 and CDX3 cells were treated for 72hr with TH1579 and cleaved PARP was assessed by western blot. Both models showed increased cleaved PARP expression compared with the DMSO treated controls, indicating that TH1579 treatment was cytotoxic on these models (Figure 34C). Before

examining TH1579 *in vivo* efficacy, I first evaluated its tolerability in SCID-*bg* mice. In the first study, three SCID-*bg* non-tumour bearing mice were orally gavaged twice a day with 30 mg/kg for 21 consecutive days (Figure 35A).

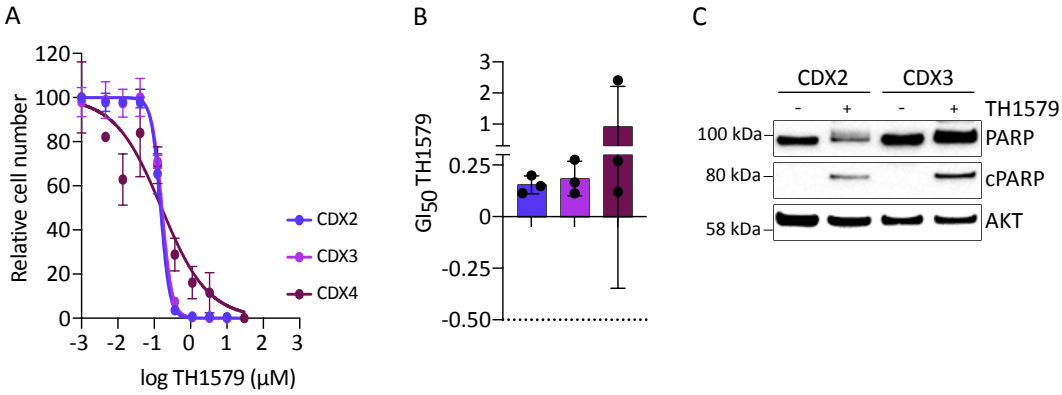

Figure 34. MTH1 inhibition is effective on chemosensitive and chemorefractory CDX.

A. CDX2 (dark blue), CDX3 (purple) and CDX4 (dark red) cultures were treated with increasing concentrations of TH1579. One of three representative experiments is shown for each culture. B. Bar plot of the GI_{50} obtained from treatment of CDX2 (dark blue), CDX3 (purple) and CDX4 (dark red) cultures with TH1579 for 7 consecutive days. Each dot is a biological replicate. C. Immunoblot analysis of CDX3 culture treated with DMSO or 0.5 µM of TH1579 for 72hr. Protein lysates were probed for cleaved PARP as marker of apoptosis and AKT was used as loading control.

This initial dosing caused a pronounced reduction in body weight (less 10%) in the first week that was overcome by introducing a mash diet and a water-based lubricant applied to the gavage tube prior to dose administration. This suggested that the loss of weight was caused by the gavage twice a day and not because of drug toxicity. The second tolerance study employed a 90 mg/kg oral gavage twice-daily dosing, 3 days on and 4 days off. This cycle was repeated three times (Figure 35B). During the second tolerance study the mice did not lose more than 5% of weight, suggesting a better tolerability. Based on this data, the second schedule was applied to test the efficacy of the drug on tumour growth. Treatment of CDX3-bearing mice with TH1579 elicited tumour regression in 8 out of 9 mice, with average maximum tumour regression of 54% (Figure 35C). The mice started to regrow as soon as the treatment was ended, however MTH1 inhibition brought an improvement in overall survival with median OS of 48 days *vs* 30 days in the TH1579 and vehicle treated cohort, respectively (*p*-value = 0.0002, Figure 35D). Immunohistochemical staining demonstrated accumulation of 8-oxo-G and a concomitant increase in apoptosis in the TH1579 treated cohort (Figure 36A,B).

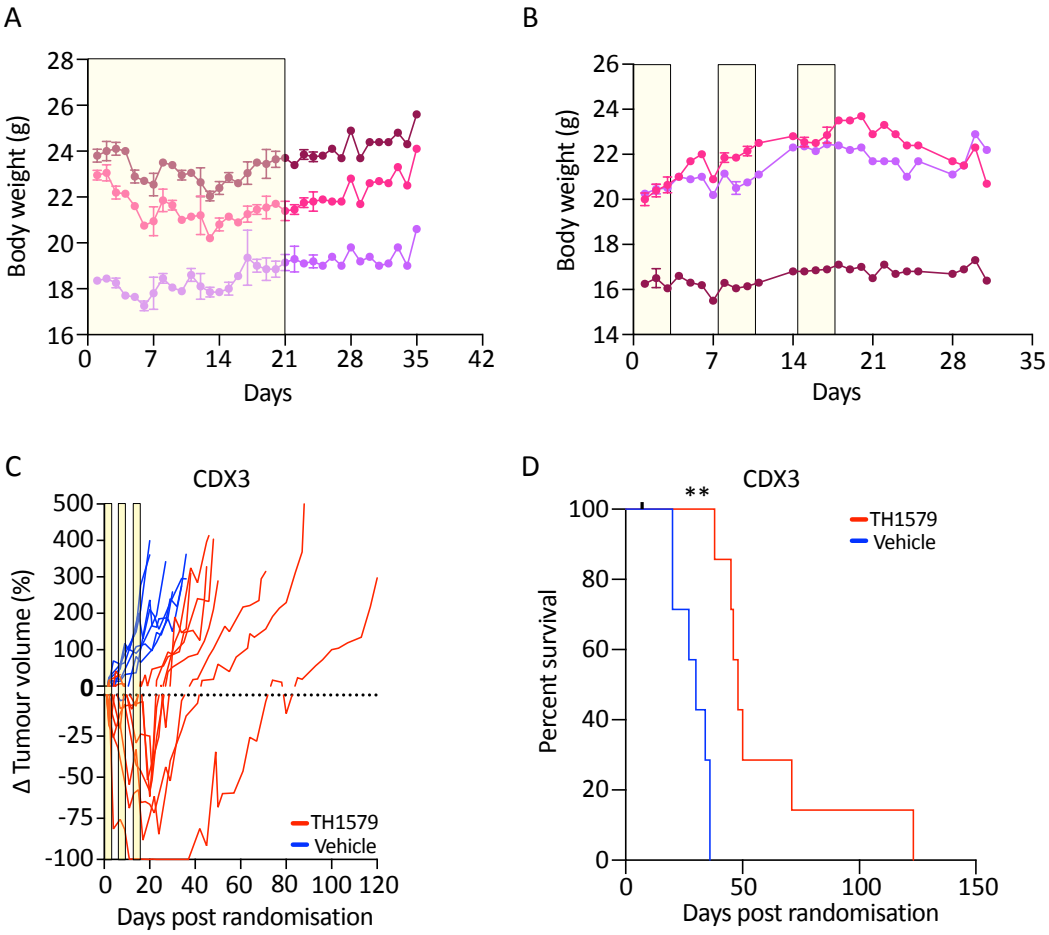

Figure 35. TH1579 efficacy *in vivo.*

A,B Tolerance studies performed to test the toxicity of TH1579 *in vivo*. Yellow shaded boxes indicate the treatment period: 21 consecutive days for pCEP232 (A) and 3 cycles of 3 consecutive days for pCEP247 (B). The treatment schedule is described in chapter 2.9.2. Each line represent a mouse. C. Spider plot showing the percentage of tumour change compared with day 0. CDX3 tumours were treated with TH1579 (red) or vehicle (blue), as specified in chapter 2.9.3. Each line represents an individual relative tumour volume. Yellow shaded boxes demarcate the treatment period. D. Kaplan-Meier analysis showing the time until tumours reached 4 times ITV after treatment with 3 cycles of vehicle (blue) or TH1579 (red).

Moreover, the cellular thermal shift assay performed on the plasma and tumour lysates after treatment with either TH1579 or vehicle, showed that MTH1 was strongly engaged by TH1579, further validating the on-target effect of the inhibitor (Figure 36C,D). These preliminary data showed a promising effect in the chemosensitive model CDX3. The dose used in this study was well tolerated by the mice and therefore studies to increase the treatment window to further delay tumour progression are warranted. Moreover, based on the *in vitro* data, CDX2 should be similarly sensitive to this drug, highlighting the possibility of using this

treatment also on some chemorefractory SCLC patients. CDX4 cells had an heterogeneous response to the TH1579, showing on average GI_{50} of 0.94 µM compared with 0.23 µM and 0.27 µM for CDX3 and CDX2 respectively. Even though CDX4 was more resistant to MTH1 inhibition than CDX2 and CDX3, the response to this compound *in vitro* was greater than the response to cisplatin/etoposide (average GI_{50} 4.2 µM), further suggesting that MTH1 could be a potential therapeutic target for chemorefractory SCLC patients.

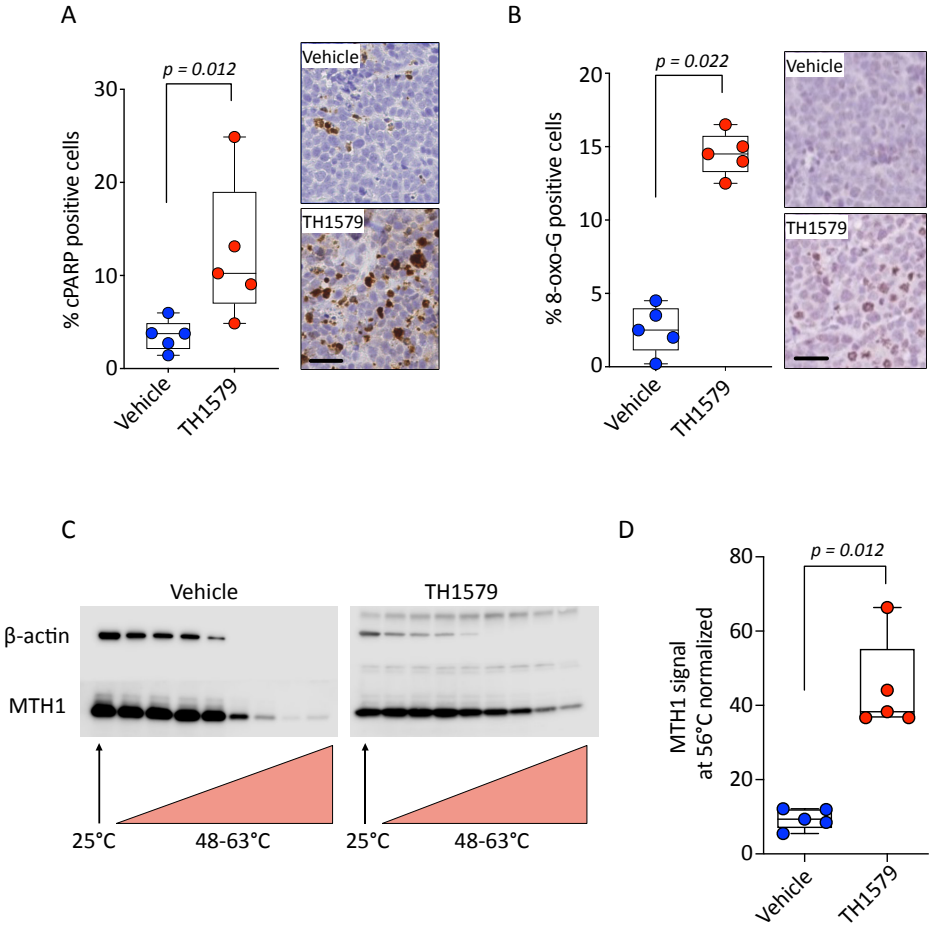

Figure 36. Pharmacodynamic assessment of TH1579 activity.

A. Immunohistochemistry analysis of cleaved PARP on CDX3 tumours treated with one cycle (3 days) of vehicle (blue) or TH1579 (red). Samples were collected 24hr after the last dose. One representative image is shown for each cohort. Scale bar: 25 µm. B. Immunohistochemistry analysis of 8-oxo-G on CDX3 tumours treated with one cycle (3 days) of vehicle (blue) or TH1579 (red). Samples were collected 24hr after the last dose. Samples were stained and quantified by Ioannis S. Pateras in Professor Vassilis G Gorgoulis' lab. One representative chromogenic image is shown for each cohort. Scale bar: 25 µm. C. MTH1 degradation at increasing temperature to assess the target engagement of TH1579 in CDX3. Samples were collected 2hr after the last dose. Helleday's group performed the assay. D. Quantification of MTH1 signal at 56°C from C. In all panel box and whisker plots show median, first and third quartiles and maximum and minimum values. Each dot is a biological replicate. Un-paired Wilcox-test was applied for statistical analysis.

4.2.3 Moderate-throughput drug screening on CDX cultures as a platform to identify candidate drugs

During the treatment history of SCLC, it was demonstrated that combination of chemotherapies were more effective than monotherapies (Evans et al., 1985; Mascaux et al., 2000; Pujol et al., 2000). The rational for combining several drugs is based on two main hypotheses. Initially, combinatorial therapies were developed to exploit drugs with non-overlapping dose-limiting toxicities. With the advent of the genomic era and new targeted therapies, researchers realised that the high heterogeneity observed intra-patients increased the chance of selecting clones that were resistant to a specific compound. This brought the hypothesis that combination of drugs that act on multiple pathways can reduce the ability of cancer cells to develop resistance by activating bypassing pathways (Al-Lazikani et al., 2012). Moreover, combining drugs can also be exploited to address the inter-patient heterogeneity. Indeed, patients resistant to one treatment could have a chance to respond to the second one (Palmer and Sorger, 2017). An important aspect of combinatorial treatment is also linked to the so called 'synthetic lethality'. Synthetic lethality refers to a situation in which a defect in one gene is compatible with cell viability, but can degenerate into cell death when combined with defect in another gene (Lord et al., 2015). In cancer therapy, synthetic lethality can be achieved targeting the dependency generated by the presence of a specific genetic alteration. One example is the synthetic lethal effect of PARP inhibition in the presence of *BRCA1/2* mutations (Lord et al., 2015). BRCA1/2 are main players in the HR pathway and when lost, cells rely on alternative error-prone pathways to repair DNA lesions. Inhibition of PARP in this background leads to reduced DNA repair, uncontrolled accumulation of DNA damage and subsequent apoptosis. Another way to achieve synthetic lethality with therapies is by combining a drug that generates a specific dependency in cancer cells with another drug that targets this addiction and pushes cancer cells beyond their survival limit (Figure 37A). While theoretically we could combine any drugs with each other, the identification of combinatorial treatments that can have real benefit for the patient is challenging. Large drug screens are not always feasible *in vivo*, limiting the discovery to *in vitro* models. One of the main assays to identify promising combinatorial treatments are dose-response matrices.

These matrices are generated by combining multiple concentrations of two drugs of interest, giving information about the effect each drug has as a single agent and in combination. Mathematical models are used to define whether two drugs have a greater (synergistic), equal (additivity) or lower (antagonistic) impact on cell viability than the effect observed with monotherapies (Foucquier and Guedj, 2015) (Figure 37B). A synergistic interaction is what clinicians aim to achieve in the patients. However, there are several challenges in identifying these synergistic effects, including technical difficulties associated with the experimental design, the selection of the proper mathematical model used to define the synergy and the difficulty in translating the results to more complex systems (Foucquier and Guedj, 2015).

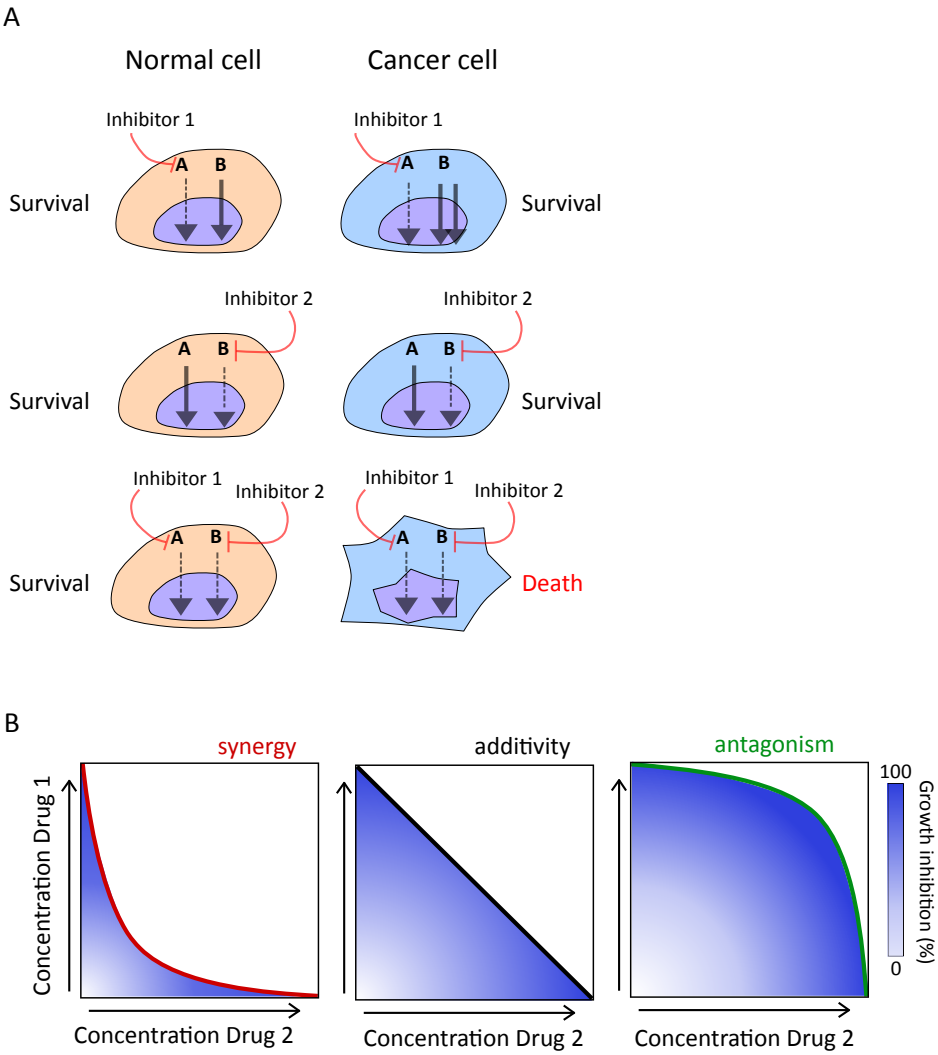

Figure 37. Combinatorial drug screening treatment.

A. Schematic of pharmacological induced synthetic lethality: inhibitor 1 inhibits pathway A (e.g. PARP inhibition) and creates a dependency to pathway B (double arrows) on the cancer cells only. This happens for example when further DNA damage (e.g. by PARP inhibition) is induced in cancer cells

that are already genomic unstable (e.g. by *TP53* and *RB1* loss). These cells will rely more on DNA damage repair pathways and cell cycle checkpoints (pathway B) than normal cells to survive. Inhibition of pathway B (e.g. cell cycle checkpoint) causes only limited effect on both normal and cancer cells. However, when both pathways are inhibited cancer cells will not be able to compensate for pathway B loss anymore and will undergo apoptosis, while normal cells will survive. B. Schematic of the concept of drug synergy, additivity and antagonism. During synergy, the dose of each drug needed to reach the same effect caused by one drug is lower. If antagonism is observed, the two drugs do not interact and higher concentrations of both drugs are needed to reach the same effect as in monotherapy. Additivity is observed when the two drugs together act independently, as they were given as monotherapy. This figure was adapted from Weinstein et al., 2017.

The close relationship between CDX and donor tumours suggests that identification of an effective combination of drugs *in vivo* could be translated into promising candidate treatments for SCLC patients. Short-term cultures of CDX can be exploited to perform preliminary screening of compounds in order to select the most encouraging combinations for further validation *in vivo*. Therefore, I have optimised a dose-response matrix to test a 6 x 6 combination of two compounds on the *ex vivo* CDX cultures. I have initially focused on the combination of cisplatin/etoposide for the validation of the assay. This combination is the SoC for SCLC and it has been already widely studied, making it the perfect control to test the ability of the cultures to predict the response to novel combinatorial treatments.

As shown in Figure 38A and B, the response to single agent cisplatin and etoposide is variable across the models, with 4/7 progression models showing a similar sensitivity compared with baseline models. Indeed, 3/7 progression models, such as CDX18p and CDX20p, were generated from CTCs collected after the patient received the last cycle of chemotherapies but before a relapse was confirmed by CT scan (called follow-up sample, Table 14). Therefore, it is possible that the CTCs collected at this time point were not yet representative of the chemoresistant relapsed tumour. Also, it has been demonstrated that some SCLC patients who had a prolonged response to first-line, can be successfully treated with a second round of first-line chemotherapy (Giaccone et al., 1987; Vincent et al., 1988), suggesting that CTCs collected at relapse may still be sensitive to EP treatment. Figure 38C shows the response to cisplatin of CDX20/CDX20p and CDX8/CDX8p as representative examples. Patient 8 and patient 20 were treated with carboplatin as first line therapy. While patient 8 showed a partial response before relapse (OS 6.5 months), patient 20 did not respond, and experience tumour stabilisation before relapse occurred (OS 2.7 months, Table 14). *In vitro* treatment of CDX20, CDX20p, CDX8 and CDX8p with

cisplatin (equivalent platinum agent of carboplatin) confirmed that CDX8 is more sensitive to cisplatin than CDX20 (average GI_{50} 0.2 *vs* 9.3 µM, respectively). As expected, CDX8p is almost 3 times more resistant than CDX8 (average GI_{50} 0.7 *vs* 0.2 µM, respectively), suggesting acquired resistance to platinum compounds during treatment. CDX20p was more sensitive to cisplatin than CDX20 *ex vivo* (average GI_{50} 1.7 *vs* 9.3 µM), however, both models were > 2 times more resistant than CDX8 and CDX8p (Figure 38D), highlighting the more resistant phenotype of this patient. These data further confirm that single agent chemotherapy *ex vivo* can be used to model the response observed in patients.

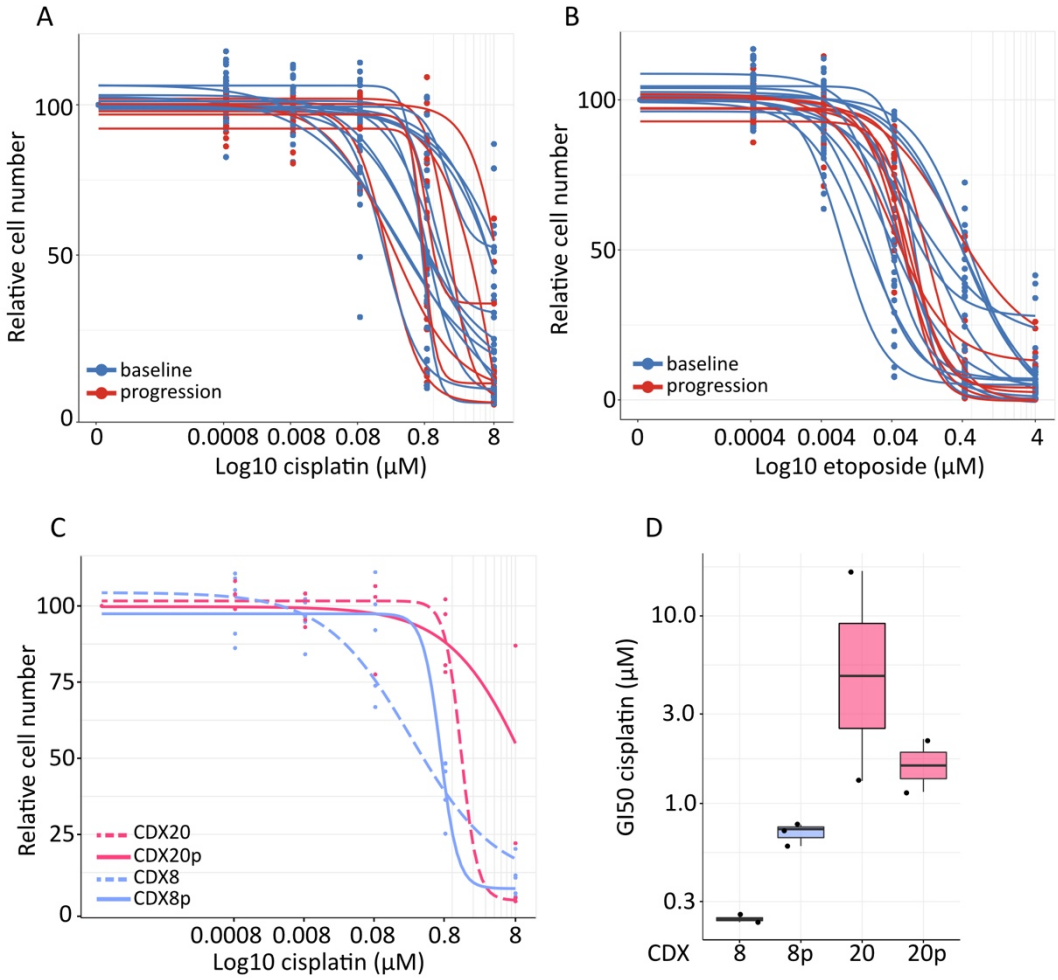

Figure 38. Single agent activity of cisplatin and etoposide on a panel of CDX cultures.

A,B. Dose-response curves for all CDX model tested with increasing concentration of cisplatin (A) or etoposide (B). Each dot represent a biological replicate. Line were colour coded based on whether the CDX was derived from a chemonaïve blood sample (baseline) or after first-line therapy (progression). C. Dose-response curves for CDX20 (dotted pink), CDX20p (pink), CDX8 (dotted blue) and CDX8p (blue) treated with increasing concentration of cisplatin. D. Summary GI_{50} for CDX20, CDX20p, CDX8 and CDX8p from C. Box and whisker plot shows median, first and third quartiles and maximum and minimum values. Each dot is a biological replicate. Dose-response curves were obtained combining

the data from all biological replicates tested. Replicates with values > 0.99 quantiles were considered outliers and removed from the analysis.

Because most SCLC patients are treated with a combination of a platinum-based agent and etoposide (EP treatment), I was interested in assessing the reliability of this assay in predicting the response to cisplatin/etoposide combination *in vitro*. Figure 39A and B show an example of response to cisplatin/etoposide for the chemosensitive CDX3 and the chemorefractory CDX4. To compare the effect each drug had on the different CDX, I have used the GI_{50} (see chapter 2.10.4 for details).

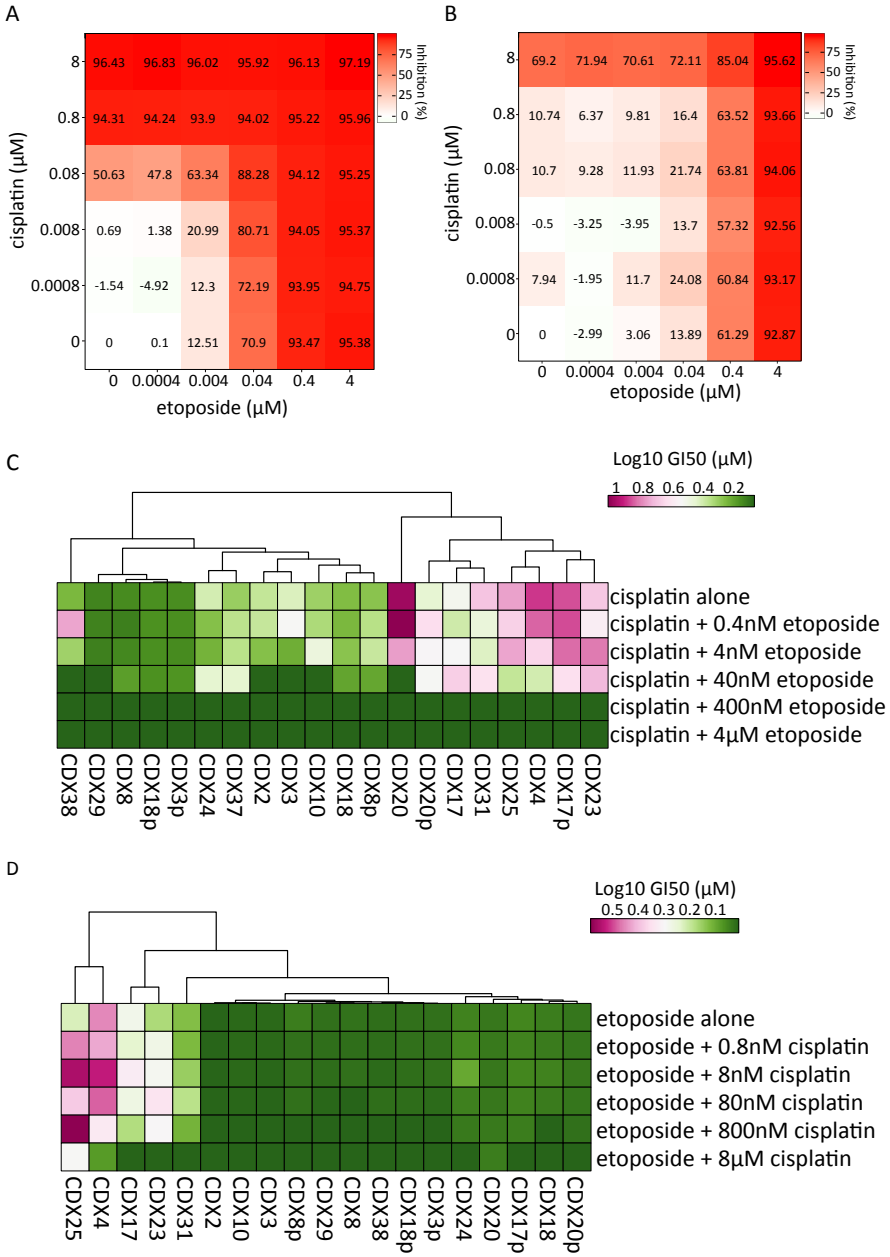

Figure 39. Combination of cisplatin and etoposide on CDX cultures.

A,B. Response matrices for CDX3 (A) and CDX4 (B) cultures treated with increasing concentrations of cisplatin and etoposide. The level of growth inhibition (%) for each combination of drugs compared to

untreated control is shown. One representative biological replicate is shown. C,D. Unsupervised hierarchical clustering of log10 GI_{50} obtained from the panel of CDX cultures treated with increasing concentrations of cisplatin (C) or etoposide (D) with or without a fixed concentration of the other drug.

Etoposide was overall more toxic than cisplatin as shown by the different µM scale in the heatmaps (Figure 39C *vs* D). In both heatmaps, unsupervised hierarchical clustering identified two main groups. The larger group (predominantly green shading) contains models more sensitive to these drugs, while the second smaller group (predominantly pink shading) consisted of CDX cultures less responsive to these combinations. In particular, CDX4 and CDX25 were resistant to almost all combinations tested. Indeed, patient 4 and patient 25 had very short survival with 1.8 and 2.4 months, respectively (Table 14). Both patients received only carboplatin as first-line treatment, however the weak response observed *in vitro* to etoposide treatment alone or in combination with cisplatin suggested that these patients would have been refractory to etoposide as well. On the contrary, patient 20, who also had a survival of less than 3 months and has been treated with carboplatin only, may have benefited from the combination of carboplatin with etoposide. Indeed, CDX20 and CDX20p were much more sensitive to etoposide than cisplatin (Figure 39C,D). As expected, in both conditions (cisplatin combined with fixed concentration of etoposide, or etoposide combined with fixed concentration of cisplatin) the addition of higher concentrations of the fixed drug caused increased cytotoxicity, with both 8 and 4 µM doses having the strongest effect. Platinum-based agents are the backbone of SCLC SoC, therefore the condition with cisplatin combined with fixed concentrations of etoposide should better depict the real situation. Comparison of patient's OS with the GI_{50} of the corresponding CDX culture showed a trend towards a significant negative correlation when low concentrations of etoposide were used, however this correlation was lost with higher concentrations (Figure 40A). The lack of a significant correlation with higher etoposide concentrations could reflect the fact that not all patients received the combination as first-line treatment and therefore the OS may not reflect the response that those patient would have had if they were treated with EP regimen (Table 14). Linear regression analysis was also performed on the data derived from the treatments where etoposide was the main drug and

cisplatin was added at fixed concentrations. None of these conditions showed a significant trend and are described in Appendix Figure 2.

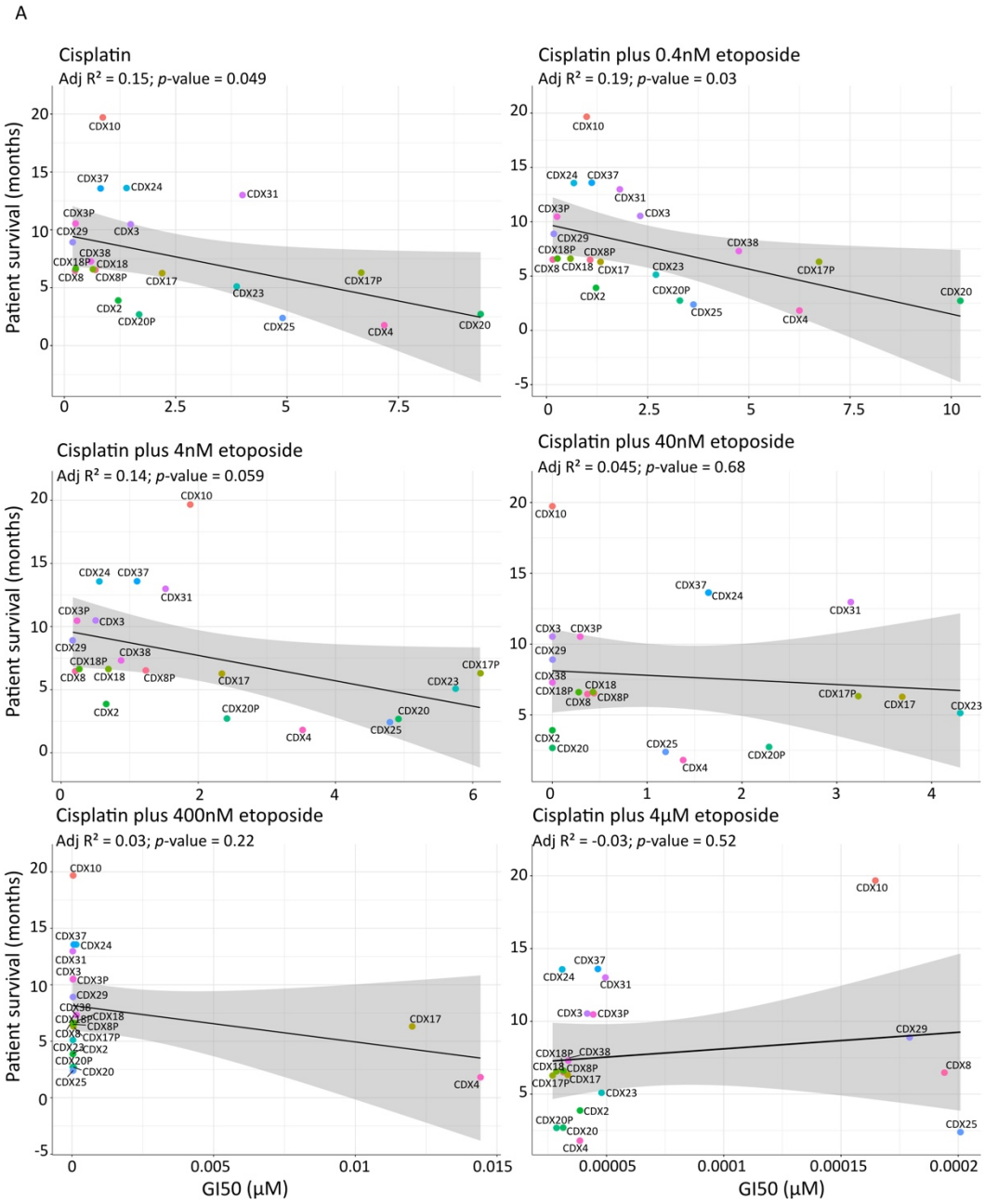

Figure 40. Correlation patient survival and *ex vivo* response to cisplatin/etoposide.

A. Linear modelling to correlate the patient survival (months) with the GI_{50} (µM) of response to cisplatin combined with different concentrations of etoposide *ex vivo*.

As mentioned previously, combinatorial treatments are preferred when the observed effect is greater (synergistic) than the effect expected if the tested drugs were used as monotherapy (non-interaction effect). Synergy can be quantified with different reference models, each of which has a distinct way to describe the non-

interaction effect. The three main models are the Highest Single Agent (HSA), the Loewe additivity and the Bliss Independence models. The HSA assumes that two drugs are interacting when the observed effect is greater than the higher effect of each drug alone. In the Loewe additivity model the non-interaction effect is obtained when one drug is combined with itself, while in the Bliss independence model, drugs are assumed to act independently and do not interfere with each other (Foucquier and Guedj, 2015).

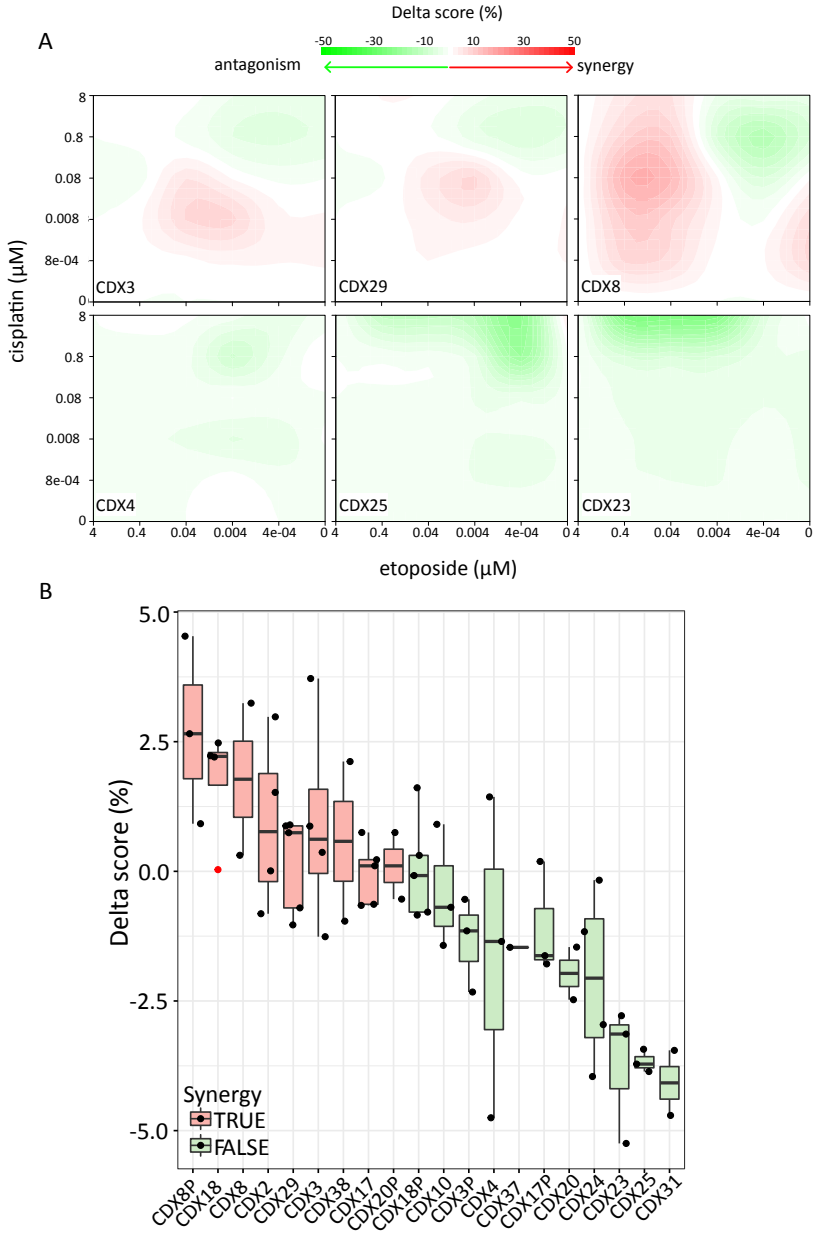

Figure 41. Synergistic interaction between cisplatin and etoposide.

A. Cisplatin-etoposide dose-response landscapes for three responsive and three resistance CDX cultures. Synergy is defined as a positive deviation (positive delta) from the effect expected if the two drugs would not interact. B. Summary of the average delta score for a panel of CDX cultures treated

cisplatin/etoposide. Average delta is the mean of all delta scores obtained for each dose combination in the matrix. The combination is considered synergistic if the median of the average delta score of all biological replicates is > 0 (red coloured). Box and whisker plot shows median, first and third quartiles and maximum and minimum values. Each dot is a biological replicate and red dot indicates an outlier.

Recently a new model has been described, called the zero interaction potency (ZIP), which attempts to combine the advantages of both the Loewe and the Bliss models (Yadav et al., 2015). This model is based on the assumption that two non-interacting drugs will incur minimal changes in their dose-response curves when combined together. The delta score is calculated to identify the deviation from the dose-response curves observed when the drugs are used as single agents. I have applied the ZIP model to cisplatin/etoposide screening in order to assess if their combination was synergistic in the studied models. Figure 41A shows representative interaction landscapes for this combination in sensitive *vs* resistant CDX. Although synergy was observed in several CDX cultures, the level of synergy in the models tested was minimal with a maximum median delta score of 2.6% in CDX8p (Figure 41B). These data suggest that cisplatin and etoposide do not strongly interact *in vitro*, and that their impressive effect in patients may reflect their cytotoxicity profile rather than a mechanistic synergy. This is not surprising considering that both drugs act by inducing DNA damage, and their combination would predominantly increase DNA damage without really causing a synthetic lethal effect. The results obtained also demonstrate that it is possible to perform moderate-throughput drug screening on the CDX cultures maintaining some similarity with the response observed in the patients, and therefore can be used to predict the response to novel compounds.

4.2.4 Effect of PARP and WEE1 inhibition in a panel of CDX *ex vivo*

We have shown that PARP and WEE1 inhibition are promising targets for the treatment of SCLC patients, however not all CDX tumours regressed after treatment with this combination (Figure 22). To better understand which subgroup of patients would benefit from this treatment, I have screened a panel of CDX cultures for their response to AZD1775 and olaparib. Initially, I have tested a range of concentrations between 0 and 30 µM to assess the response of a small panel of CDX cultures to AZD1775 and olaparib single agents. Most CDX cultures showed a GI_{50} < 0.4 µM in response to AZD1775, suggesting that concentration higher than 0.4 µM would have

been highly cytotoxic for the cells (Figure 42A). Therefore I have decided to select a range of AZD1775 concentrations that varies from 0 to 4 µM with a 10-fold increase in-between each concentration for the mid-throughput screen. This range of concentrations also included the AZD1775 clinically relevant doses assessed by AstraZeneca (Table 15). The response to olaparib was weaker with 5/9 models tested showing a GI_{50} > 0.4 µM (Figure 42B). Based on this result, I have decided to double the doses used for olaparib in order to facilitate the separation between sensitive and resistant models. This range included 6 doses that varies between 0 and 8 µM and included the olaparib clinically relevant concentrations assessed by AstraZeneca (Table 15). These concentrations allowed me to obtained sigmoidal dose-response curves for the calculation of GI_{50} (Gadagkar and Call, 2015).

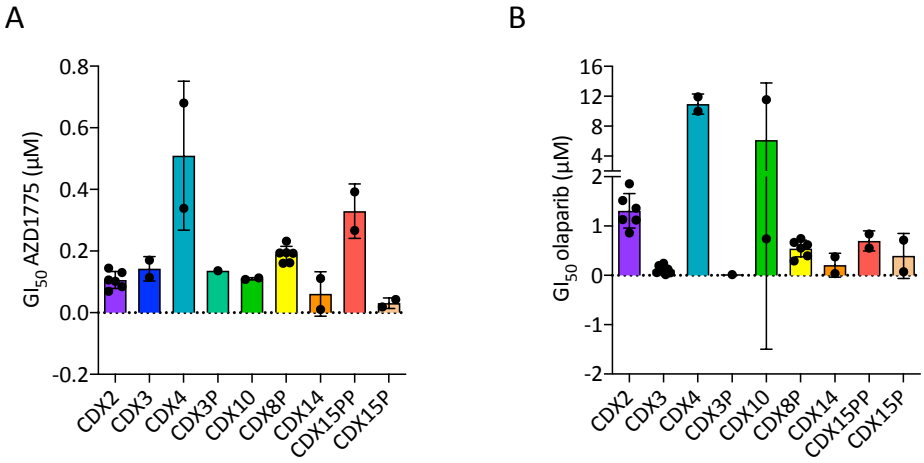

Figure 42. Preliminary drug screening with AZD1775 and olaparib single agents.

A, B. Barplots summarising the GI_{50} obtained from treatment of the stated CDX with AZD1775 (A) or olaparib (B) for 7 consecutive days. Each dot is a biological replicate.

Mid-throughput screen of 20 CDX cultures demonstrated that, as observed in the preliminary screen, AZD1775 alone is generally more cytotoxic than olaparib *in vitro*, as shown by the left shift of AZD1775 response curves compared with olaparib in most models (Figure 43A). As expected from the *in vivo* data, CDX3 was more sensitive than CDX4 to olaparib with average GI_{50} of 0.091 for CDX3 and 4.8 µM for CDX4 (Figure 43B). CDX8p had an intermediate response to olaparib and was ~5x more resistant than CDX8 (average GI_{50} 0.173 *vs* 0.032 µM). Despite the trend of response to olaparib between CDX8 and CDX8p mirrored the response observed *in vivo* (Figure 22), CDX8 and CDX8p showed a GI_{50} similar to CDX3 suggesting that these

two models are particularly sensitive to this combination *ex vivo*. It was possible to observe some modulation in the response to olaparib *ex vivo*, however, this was not true for AZD1775, where all four models had similar GI_{50} *in vitro* (average GI_{50} of 0.27 µM for CDX3, 0.27 µM for CDX4, 0.22 µM for CDX8 and 0.12 µM for CDX8p) (Figure 43B). This made it difficult to directly compare the trends observed *in vitro* with the best response observed *in vivo* to AZD1775.

Table 15. AstraZeneca clinically relevant concentrations of DDRi.

Drug	Concentrations (µM)
Olaparib (PARPi)	0.3, 1, 3
AZD1775 (WEE1i)	0.25, 0.5, 1
AZD6738 (ATRi)	0.1, 0.3, 1
AZD7648 (DNAPKi)	0.1, 0.3, 1
AZD2811 (AURKBi)	0.01, 0.03, 0.1, 0.3

To check if there was a correlation with the single agent responses *in vivo* and *ex vivo*, I have compared the average GI_{50} of AZD1775 and olaparib calculated *ex vivo* with the maximum tumour response at the end of the treatment *in vivo*. CDX10 was added to the analysis to increase the significance of the results. The *in vivo* study looking at the efficacy of AZD1775, olaparib and the combination in CDX10 was performed by our *in vivo* team and the results are summarised in Figure 44. CDX10 was overall resistant to all treatments, with limited tumour growth inhibition after treatment with AZD1775 or the combination (34.4% and 48.2% growth inhibition at day 21, respectively). *Ex vivo*, CDX10 showed a similar response to AZD1775 as the other models tested, but was resistant to olaparib treatment, as observed *in vivo* (Figure 43A,B and Figure 44). Linear regression analysis showed a positive correlation between the olaparib GI_{50} derived *ex vivo* and the maximum tumour regression at day 21, highlighting the ability of the cultures to predict the response observed *in vivo* (R^2 = 0.2264, *p*-value = 0.001, Figure 43C). As expected, the correlation was not predictive for AZD1775 response *in vivo* (R^2 = 0.2355, *p*-value = 0.001, Figure 43D).

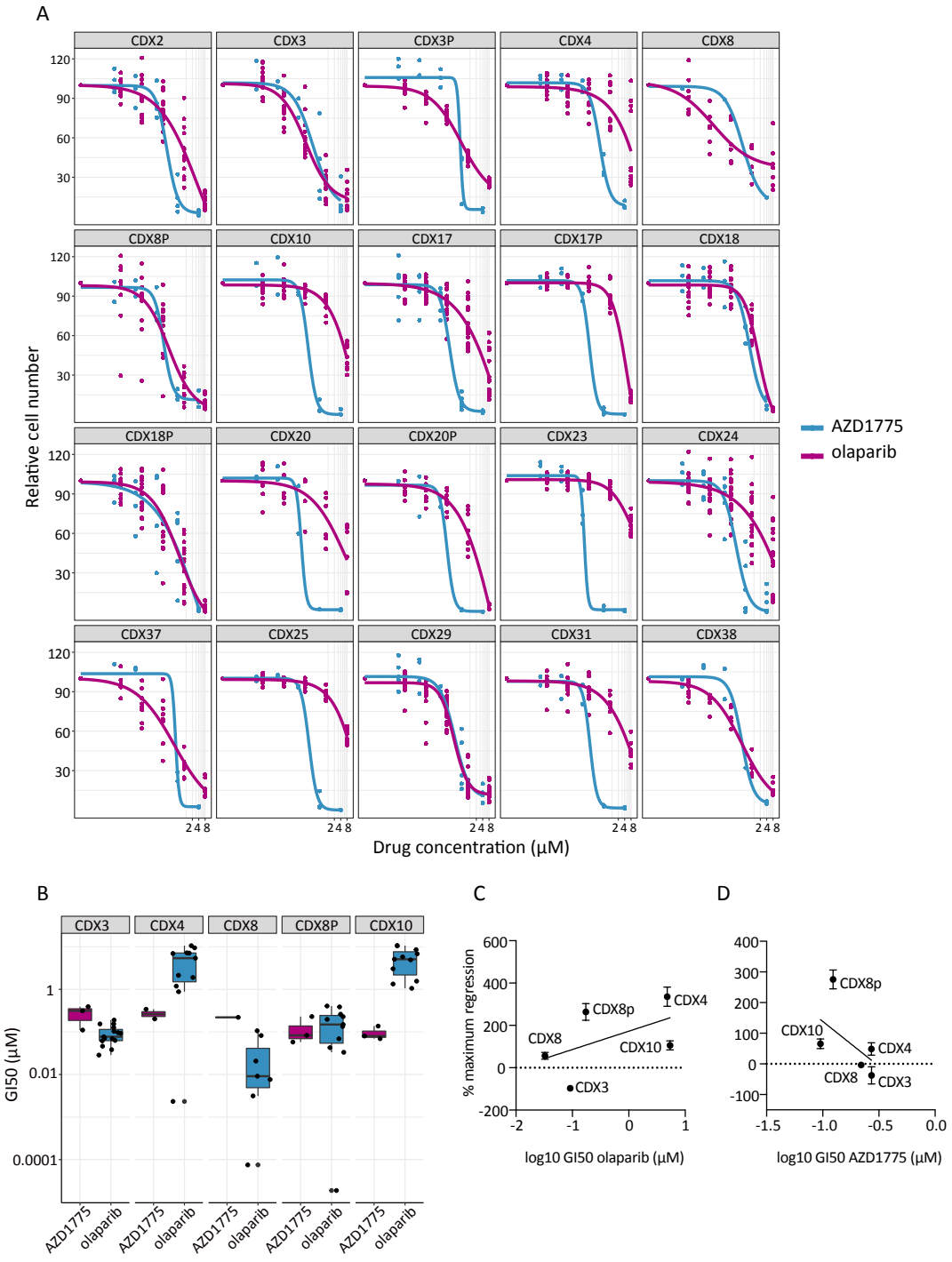

Figure 43. Single agent activity of olaparib and AZD1775 on a panel of CDX cultures.

A. Dose-response curves for all CDX model treated with AZD1775 (dark pink) or olaparib (blue). Each dot represent a biological replicate. Dose-response curves have been fitted combining the data from all biological replicates tested. Replicates with values > 0.99 quantiles were considered outliers and removed from the analysis. B. Summary GI_{50} for CDX3, CDX4, CDX8, CDX8p and CDX10 treated with AZD1775 or olaparib. Box and whisker plot shows median, first and third quartiles and maximum and minimum values. Each dot is a biological replicate. C,D. Linear modelling to correlate the best response *in vivo* to olaparib (C) and AZD1775 (D) with the average GI_{50} (µM).

Despite the cytotoxic effect of AZD1775 *ex vivo*, the trend of response to these two drugs was similar *in vivo* and *ex vivo*. CDX3 and CDX8p had similar level of response to AZD1775 and olaparib, both *in vitro* and *in vivo*, while CDX4 and CDX10 showed a better response to AZD1775 than olaparib in both conditions. The only model that showed a different trend of response was CDX8, which was more responsive to olaparib *in vitro* compared with AZD1775, while *in vivo* CDX8 was more sensitive to AZD1775 than olaparib (Figure 43B, Figure 22A and Figure 44B).

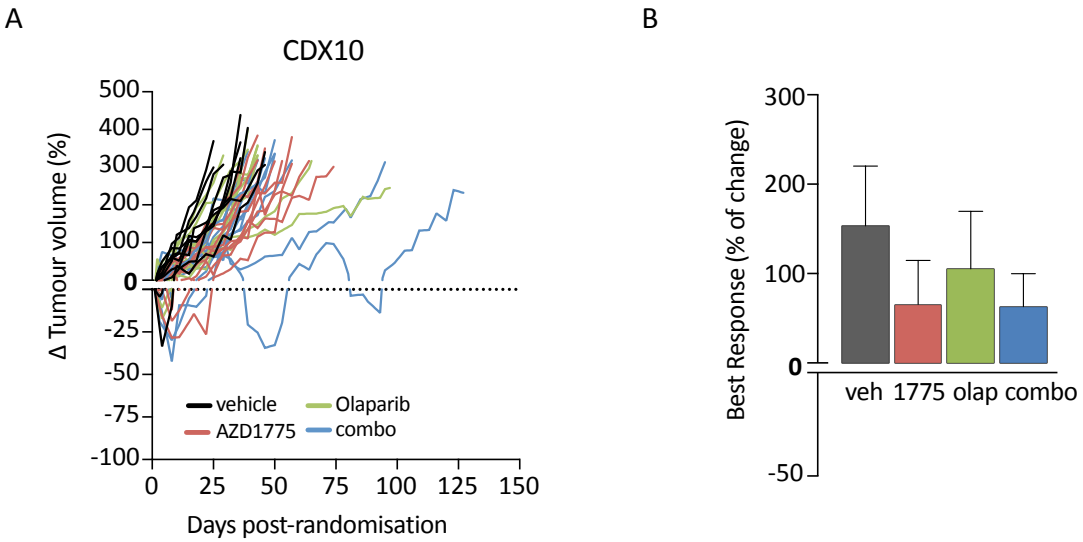

Figure 44. CDX10 response to AZD1775 and olaparib *in vivo.*

A. CDX10 tumours were treated with vehicle (black), AZD1775 (red), olaparib (green) or the combination (blue) as specified in chapter 2.9.3. Each line represents an individual relative tumour volume. Treatment was ended at day 21. B. Barplot showing the average best response (± SD) for vehicle (black), AZD1775 (red), olaparib (green) and AZD1775/olaparib (blue) obtained at day 21. This study was performed by the *in vivo* team in our group.

As mentioned before, combinatorial treatment can be used to delay the onset of resistance and eventually exploit synthetic lethal effects. The GI_{50} generated from AZD1775 treatment with or without the addition of a fixed concentration of olaparib (Figure 45A) showed high level of cytotoxicity, with most CDX showing an average log10 GI_{50} < 0.3 µM (16/20 CDX). On the contrary, only 5/20 CDX had average log10 GI_{50} < 0.3 µM when treated with olaparib alone or with increasing concentration of AZD1775 (Figure 45B). The reduced cytotoxicity of olaparib allowed to determine two main clusters of response. The one on the far left contained CDX that were overall resistant to olaparib as monotherapy or in combination with AZD1775 (magenta).

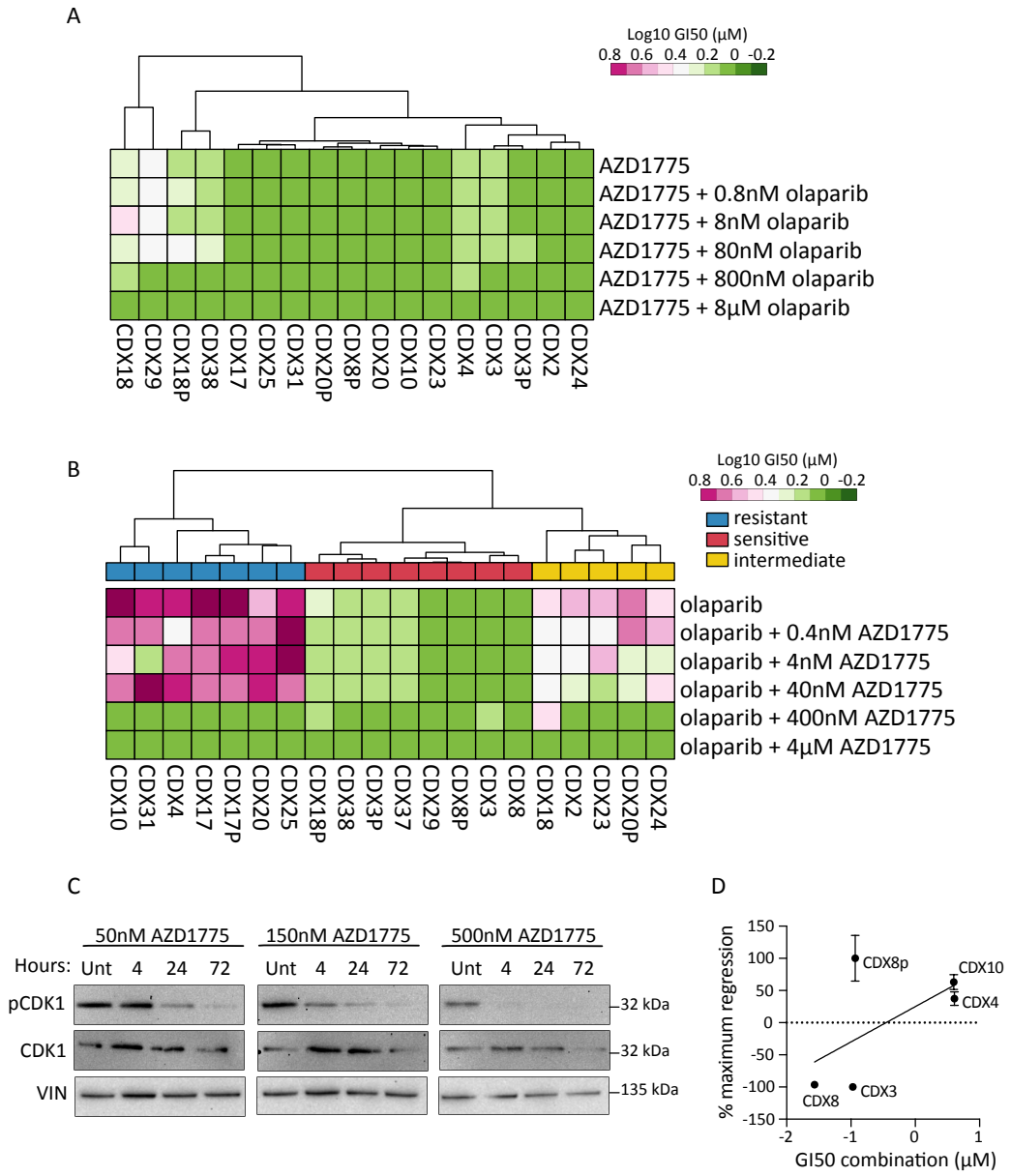

Figure 45. Combination of AZD1775 and olaparib on CDX cultures.

A,B. Unsupervised hierarchical clustering of log10 GI_{50} obtained from the panel of CDX cultures treated with AZD1775 (A) or olaparib (B) with or without a fixed concentration of the other drug. C. Immunoblot of the indicated proteins was performed on H524 protein lysates. Vinculin (VIN) was used as loading control. D. Linear modelling to correlate the best response *in vivo* to olaparib/AZD1775 with the average GI_{50} (μM) of response to olaparib combined with 40 nM AZD1775.

This cluster included CDX4 as expected but did not include CDX8p. Indeed, CDX8p showed a very heterogenous response *in vitro*, and most attempts to culture these cells for more than 10 days failed. This may explain why CDX8p was generally sensitive to all drugs tested despite its very resistant profile *in vivo*. The same was observed for CDX8 and exemplifies the challenges associated with primary cultures rather than established cell lines. In the 'resistant' cluster were present many of the

models that were also resistant to cisplatin/etoposide treatment, such as CDX17p, CDX25 and CDX31. Interestingly, CDX10, a chemosensitive model, was in the 'resistant' cluster. This suggested the presence of an intrinsic mechanism of resistance to PARP inhibition that did not affect the response to EP regimen. The 'sensitive' cluster could be further subdivided into 'sensitive' and 'intermediate' (green and blue, respectively, Figure 45B). In the 'intermediate' group were models partly resistant to olaparib as monotherapy, but that benefited from the addition of AZD1775. On the other hand, the sensitive group included CDX very responsive to olaparib single agent and in combination with AZD1775.

The high cytotoxicity observed with AZD1775 treatment highlighted the need to identify a concentration of this drug that was not too cytotoxic, in order to avoid biasing the data when AZD1775 was combined with olaparib. To assess whether lower concentration of AZD1775 were able to properly inhibit WEE1 *in vitro*, I have treated the H524 cell lines with increasing concentrations of AZD1775 and collected samples at different time point after treatment. CDK1 is phosphorylated by WEE1 during cell cycle and loss of phospho-CDK1 Tyr15 is a direct marker of WEE1 inhibition. As expected, the inhibition of phospho-CDK1 Tyr15 was very effective with high concentration of AZD1775 (500 nM) and the pathway was completely suppressed already 4 hr after treatment. With lower concentration of AZD1775 it took longer to achieve complete WEE1 inhibition, but eventually, 72hr after treatment the level of phosho-CDK1 was strongly reduced (Figure 45C). This happened well before drug efficacy was assessed *ex vivo*, confirming that 150 nM and 50 nM of AZD1775 are enough to affect WEE1 activity. Based on this data, I have selected 40 nM of AZD1775 combined with olaparib as reference for this combination. As validation, I correlated the GI_{50} obtained with olaparib combined with 40 nM of AZD1775 with the *in vivo* best response to the combination and observed a positive linear correlation between the *in vivo* and *ex vivo* response (Figure 45D, R^2 = 0.3, *p*-value = 0.0001). Combinatorial assessment of synergy between AZD1775 and olaparib with the ZIP model showed a stronger synergistic effect in the CDX compared with what has been observed with cisplatin/etoposide (Figure 46A).

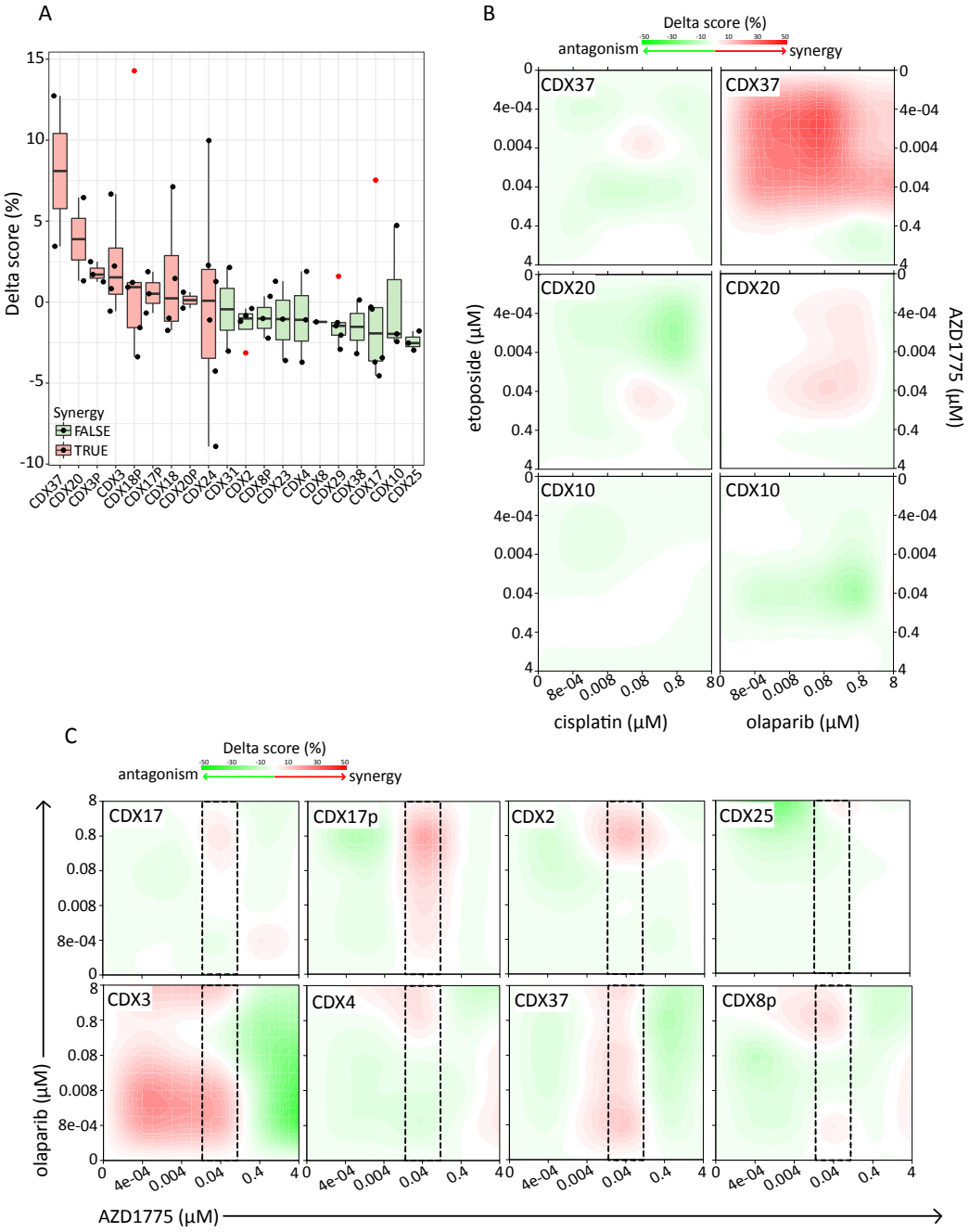

Figure 46. Synergistic interaction between AZD1775 and olaparib.

A. Summary of the average delta scores for the panel of CDX cultures treated with AZD1775/olaparib. Average delta score is the mean of all delta scores obtained for each dose combination in the matrix. The combination is considered synergistic if the median of the average delta score of all biological replicates is > 0 (red coloured). Box and whisker plot shows median, first and third quartiles and maximum and minimum values. Each dot is a biological replicate and red dots indicate outliers. B. AZD1775/olaparib dose-response landscapes for three CDX cultures compared with the corresponding landscapes obtained after treatment with cisplatin/etoposide. C. AZD1775/olaparib dose-response landscapes highlighting the response to 40 nM AZD1775.

In general, there was a high level of variability between biological replicates, highlighting the high heterogeneity of these models. In the CDX in which synergy was

not observed, the overall effect was close to additivity (delta score = 0%) and never showed strong antagonistic effect (lower median delta score = -2.5% for CDX25). Figure 46B shows response landscapes of CDX treated with AZD1775/olaparib or cisplatin/etoposide to highlight the stronger response observed with the first treatment. For both treatments *in vitro*, there was not always a linear correlation between the response (GI_{50}) and the delta score. For example, CDX20, which is mainly resistant to olaparib and AZD1775, had a weak synergistic delta score (median delta = 3.9%) while CDX10 that was relatively sensitive to cisplatin/etoposide, had a median delta score of -0.7%. This discrepancy suggests that the delta score may not be as informative as the GI_{50} to define if a model is sensitive or resistant to a specific combination. However, the response landscape generated by the ZIP model can give a lot of information about the interaction each drug has with each other at a specific concentration. This can be very useful when looking at the lowest concentrations at which two drugs synergise. Looking at the response landscapes to AZD1775/olaparib of the different CDX, it appeared evident that in almost all models, 40 nM of AZD1775 had a synergistic effect when combined with olaparib (Figure 46C). This data corroborates the observation made previously, where I found that 50 nM of AZD1775 are sufficient to inhibit WEE1 and therefore could be used in combination with olaparib to predict the response *in vivo*.

4.3 Conclusions

Identification of the effective drug treatments for cancer patients is one of the main obstacles of clinical care. With the discovery of new gene functions and a better understanding of tumour biology, more and more compounds are developed every year. However, despite this increase very few have shown real benefit when translated in the clinical setting. This is partly due to the fact that most clinical trials have been designed based on results obtained on common cancer cell lines, with only 2 or 3 PDX used to validate the findings. However, the high level of inter- and intra-patient heterogeneity observed in cancers suggests that multiple patient-derived models should be tested to account for this variability. Our biobank of CDX provides the opportunity to test several patient-derived models, covering different SCLC phenotypic subgroups (Simpson et al., 2019).

From the preliminary data with the PI3K inhibitor and the BH3 mimetics, it appeared evident that while chemoresistant tumours may be more sensitive to PI3K inhibition, the mechanisms of response to this drug can be different, as observed with CDX2 and CDX4. This highlights the need to better understand the divergences between chemorefractory patients that would and would not benefit from this treatment. Sustained phosphorylation of AKT and S6 after treatment with the BH3 mimetics in CDX4 cells could be biomarkers of resistance to this treatment. Generally, tumour material is not accessible once the patient has started treatment, but the possibility to track the phosphorylation of AKT or S6 in CTCs after treatment with PI3K inhibitors could be a valuable option for SCLC patients. The MTH1 inhibitor has also shown promising effect on all tested models *ex vivo*, confirming the ability of this drug to reduce cell viability. A few papers have questioned the ability of the MTH1 inhibitors to induce cell death by targeting MTH1, suggesting that the real target of the MTH1 inhibitors developed by Prof. Thomas Helleday was tubulin polymerisation (Kawamura et al., 2016; Kettle et al., 2016; Petrocchi et al., 2016). With the development of TH1579, Helleday's laboratory denied these publications demonstrating that the cytotoxic effects observed with TH588 and TH1579 were driven by MTH1 inhibition and subsequent incorporation of oxidised dNTP into the DNA. TH1579 is able to inhibit MTH1 at nM concentrations and it is highly selective for MTH1 compared with other kinases (Warpman Berglund et al., 2016). The data showed in this chapter demonstrated that TH1579 induced the accumulation of 8-oxo-G in the nucleus of the cells and the CESTA experiment further confirmed the on-target effect of this drug in CDX3 tumours. In particular, the response and the limited adverse effects observed on CDX3 highlighted the possibility to exploit this target in a chemosensitive setting. More experiments are warranted to characterise the mechanism behind the observed response in order to validate this drug as a candidate treatment for SCLC patients.

To facilitate the identification of biomarkers, the feasibility of testing multiple patient-derived tumours can be used to define groups of responders and non-responders. Comparison of the molecular and clinical features of these 2 groups, together with some knowledge of the mechanism of action of the drugs used, can be exploited to scale down the number of candidate biomarkers. Moderate and high-

throughput drug screening can be very useful when testing several models at once and/or when multiple combinatorial treatments are under investigation. Dose-response matrices for cisplatin/etoposide demonstrated the feasibility of performing moderate-throughput screening on panel of CDX recapitulating the patient's response to SoC. The data obtained with olaparib/AZD1775 identified three groups with distinct level of response to this combination. This clustering could be exploited to identify biomarkers of response with focus on what is differentially expressed in one group over the others and will be the focus of chapter 6.

To better characterise these combinations, I have used the ZIP reference model to generate interaction landscapes for both combinations and the results suggested weak synergy for cisplatin/etoposide. For AZD1775/olaparib a good synergistic effect was observed in 5/20 CDX (delta score > 5), however the variability in the delta score implied that distinct molecular backgrounds can have specific influence on the ability of these two drugs to interact. The lack of perfect match between the synergy score and cell viability was not surprising. It has been demonstrated that several combinatorial treatments tested in clinical trials had therapeutic benefit not because of drug additivity or synergy, but mainly because patient that did not respond to one drug had a chance to respond to the other one (Palmer and Sorger, 2017). This could have been the case also for this panel of CDX.

Another important observation derived from these data is that there is not always a perfect correlation between the data observed *in vivo* and *ex vivo*. This is exemplified by CDX8 and CDX8p as described in the results. It is possible to see a difference in drug response between the baseline and progression model, with higher sensitivity in CDX8 compared with CDX8p, however, overall CDX8p is relatively sensitive to all drug tested compared with other CDX. This contrast with the very aggressive phenotype observed *in vivo*. The problem observed with CDX8 and CDX8p exemplifies the challenges associated with primary cultures compared with established cell lines and has to be taken into consideration when designing experiments.

Chapter 5: Validation of biomarkers of response to AZD1775 and olaparib

5.1 Introduction

Combination of olaparib with AZD1775 has been tested in patients with refractory solid tumours, including SCLC, in a phase Ib study (NCT02511795, Hamilton et al., 2019) and showed some anti-tumour activity. However, based on our preclinical data, we would not expect all SCLC tumours to respond to this combination. Therefore stratification based on predictive biomarkers may increase the chance of benefiting patients. I have exploited our panel of CDX models to identify these biomarkers, as they encompass different SCLC subtypes (Simpson et al., 2019) (Figure 12).

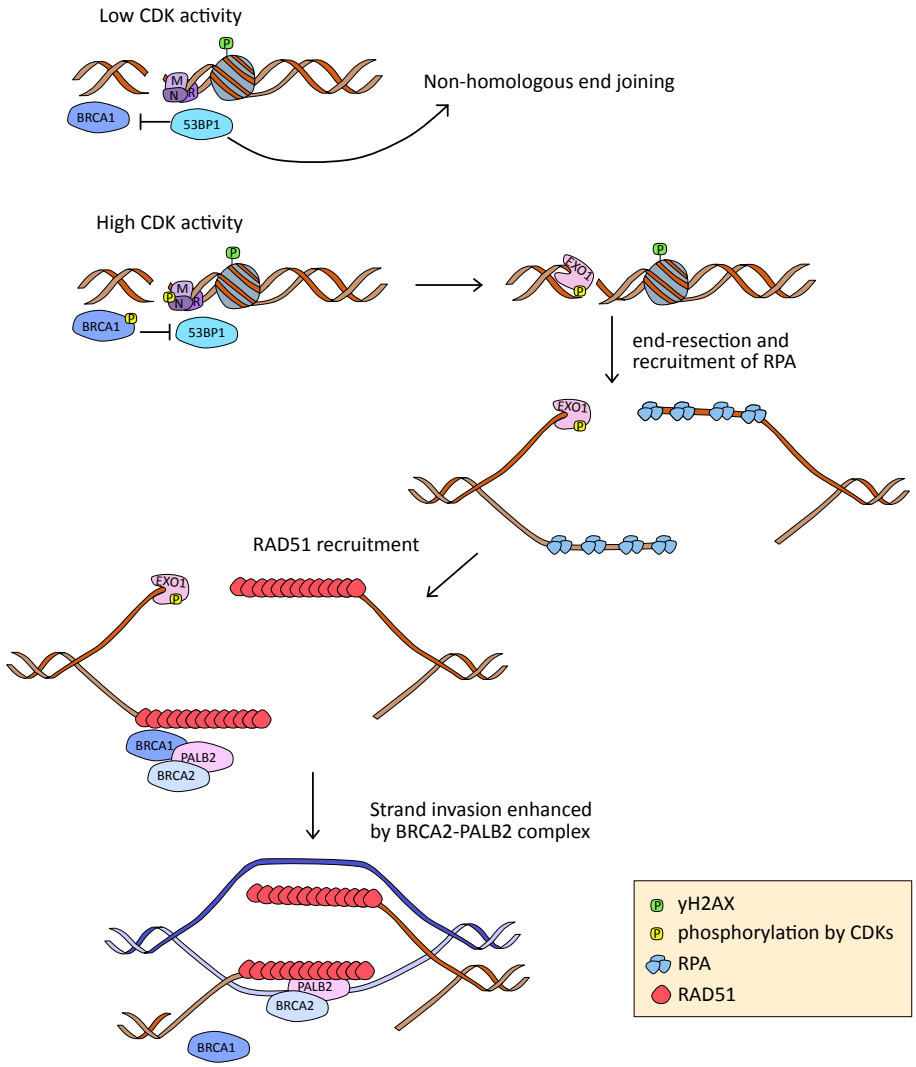

Figure 47. Homologous recombination pathway.

When the CDK activity is low (G1 and early S phases), 53BP1 inhibits BRCA1 and promotes NHEJ to repair DSBs. When the CDK activity increases and sister chromatids are available as template, CDKs phosphorylate the MNR complex and BRCA1 to promote HR over NHEJ. CDKs also phosphorylate multiple repair proteins, including the exonuclease, EXO1, that perform the end-resection. End-resection is the signal to recruit RPA and subsequently RAD51. Together with PALB2 and BRCA2, RAD51 can invade the homologue strands and allow the repair of the DNA damage.

The only clinically approved predictive biomarkers for PARP inhibitors are germline or somatic deleterious mutations in either breast cancer type 1 or type 2 susceptibility protein (BRCA1 or BRCA2). More candidates are under evaluation, such as deleterious mutations in further members of the HR or other DNA repair pathways, as well as the identification of transcriptomic signatures or genomic 'scars' of HR deficiency (Lord and Ashworth, 2017). These biomarkers are based on molecular profiling of the tumours and while they can suggest that the tumour has been defective in HR during its progression, they cannot assess whether the tumour remains HR deficient at the time of treatment (Lord and Ashworth, 2017). Functional assays to measure activation of HR pathways are better suited for this purpose. The most studied functional biomarker of response to PARP inhibition is the formation of RAD51 foci after induction of DNA damage. RAD51 is a crucial regulator of the HR pathway (Figure 47). HR is activated in the presence of DSBs, ssDNA gaps and interstrand crosslinks (Krejci et al., 2012), and competes with the non-homologous end joining (NHEJ) and the single-strand annealing (SSA) pathways for repair. The HR pathway is preferred when sister chromatids are available as template donors. It is tightly regulated throughout the cell cycle and usually occurs in late S, G2 and M phases (Branzei and Foiani, 2008). High level of CDKs promote DSB resection allowing the generation of ssDNA 3' overhangs, the target of RPA. RPA protects ssDNA from endonucleases and is replaced by RAD51 via the help of different mediators, like BRCA2 and RAD51 paralogues. RAD51 forms pre-synaptic filaments, performs a homology search and allows physical interaction between the invading substrate and the homologous template (Krejci et al., 2012) (Figure 47). At this point, DNA can be synthesised via three different pathways: synthesis-dependent strand annealing (SDSA), break-induced replication (BIR) and double-strand break repair (DSBR). Considering the role RAD51 has during HR, its accumulation upon DNA damage is a marker of proficient HR repair, while its loss delineates a situation in which HR cannot

be activated. Deficiency in HR is synthetic lethal with PARP inhibition, making RAD51 loss an ideal functional biomarker of response to this treatment (McCabe et al., 2006; Naipal et al., 2014). Moreover, the increasing number of genes discovered to be involved in the HR pathway, suggest that assessment of functional biomarkers, such as RAD51, would be the best way to define the HR status of a tumour, if clinical samples allowing its measurement are available.

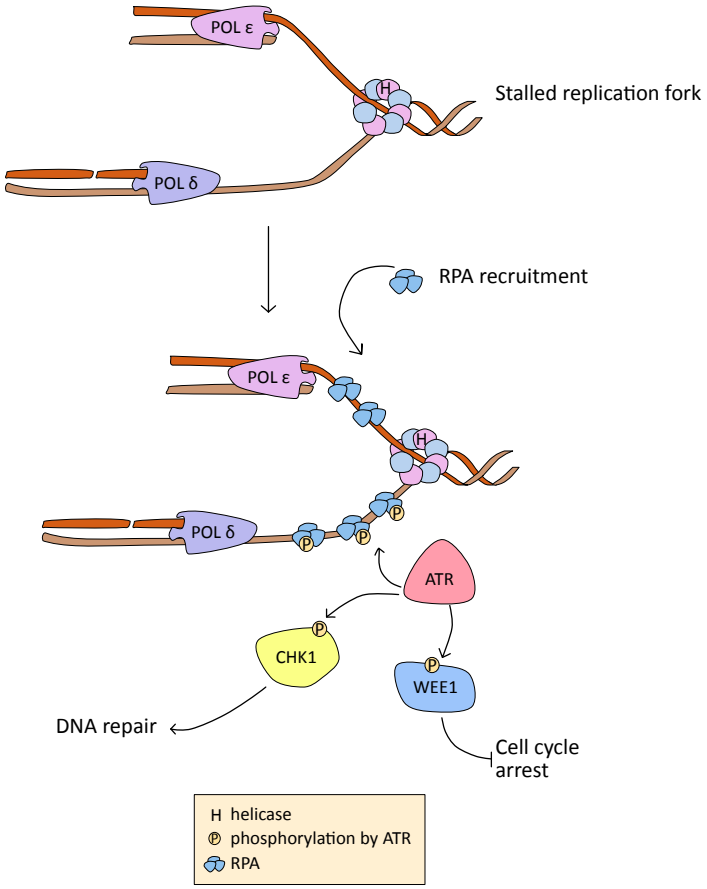

Figure 48. Replication stress response.

When the DNA polymerases encounter a lesion they stop, while the helicase continues to unwind the DNA helix. This cause a stalled replication fork and RPA is recruited to protect the ssDNA exposed by the helicase. Accumulation of RPA activates ATR that in turn phosphorylates multiple downstream targets to arrest cell cycle progression and allow the cells to repair the damage.

There are fewer published studies that focus on the identification of predictive biomarkers of response in the setting of WEE1 inhibition. Loss of the G1-S checkpoint, in particular loss of *TP53,* has generally been associated with a better responses to this compound, albeit not in every case (Cuneo et al., 2016; Geenen and Schellens, 2017; Linden et al., 2013). WEE1 inhibition can cause replication stress by uncontrolled activation of CDK1 and CDK2. Lack of controlled CDK activity induces

increased replication initiation, a shortage of nucleotides, reduced replication fork speed and subsequent DSBs (Beck et al., 2012). Therefore, cells with an intrinsic high level of replication stress are predicted to be more sensitive to WEE1 inhibition. Biomarkers of replication stress may be useful in identifying those patients likely to benefit from this treatment. Replication stress occurs when the replication machinery encounters damaged DNA and temporarily arrests (Figure 48). When this happens, RPA is recruited to stalled replication forks to protect ssDNA. Accumulation of RPA activates the ATR-CHK1 axis leading to cell cycle arrest and activation of DNA repair processes (Dobbelstein and Sørensen, 2015). Therefore, high levels of chromatin-bound RPA and RPA phosphorylation by ATR can be used as biomarkers of replication stress (Liu et al., 2012; Vassin et al., 2009).

To better understand the mechanisms behind the response to olaparib and AZD1775 treatment observed in the CDX models, I have investigated the potential of multiple candidate biomarkers. Although the complex nature of most of these biomarker assays would restrict their use to the preclinical research setting, once properly validated some could be translated into clinical use (Castroviejo-Bermejo et al., 2018).

5.2 Results

5.2.1 HR deficiency is observed in a subset of CDX

As an initial question, I wanted to ask whether HR is functional in our CDX models. First, I assessed the accumulation of RAD51 foci after irradiation of CDX cells. X-rays are known to induce DSBs that are usually repaired via the HR pathway (Vignard et al., 2013). Cell viability of CDX2, CDX3, CDX4, CDX8 and CDX8p cultures was determined five days after treatment with increasing doses of IR. CDX3 and CDX8 were particularly sensitive to IR, with 23% and 39% cell viability following irradiation with 8 Gy (Figure 49A,B). Of note, CDX3 and CDX8 were also very responsive to cisplatin/etoposide and AZD1775/olaparib, suggesting that they may be defective in DNA repair pathway(s). On the contrary, the chemorefractory CDX4 was unaffected by any amount of IR tested, underpinning its very resistant phenotype to different types of DNA damaging agents. Similarly, CDX8p was very resistant to all IR doses tested. CDX2 showed an intermediate response to AZD1775/olaparib and was partly

resistant to olaparib monotherapy (Figure 45B). Despite this result CDX2 cells were very sensitive to IR, suggesting that IR induced DSBs are particularly toxic for these cells. Phosphorylation of the histone H2 variant at serine 139 (γH2AX) is carried out by ATM, ATR and DNA-PKcs to mark DSBs and initiation of the repair (Kinner et al., 2008). Therefore, accumulation of γH2AX in the cell nuclei can be used as biomarker of DSB. Semi-automated quantification of γH2AX foci revealed that CDX2, CDX3 and CDX8 exhibited sustained γH2AX foci 24hr post irradiation, compared with CDX4 that had minimal γH2AX detectable at this time point (Figure 49C,D and Appendix Figure 3A).

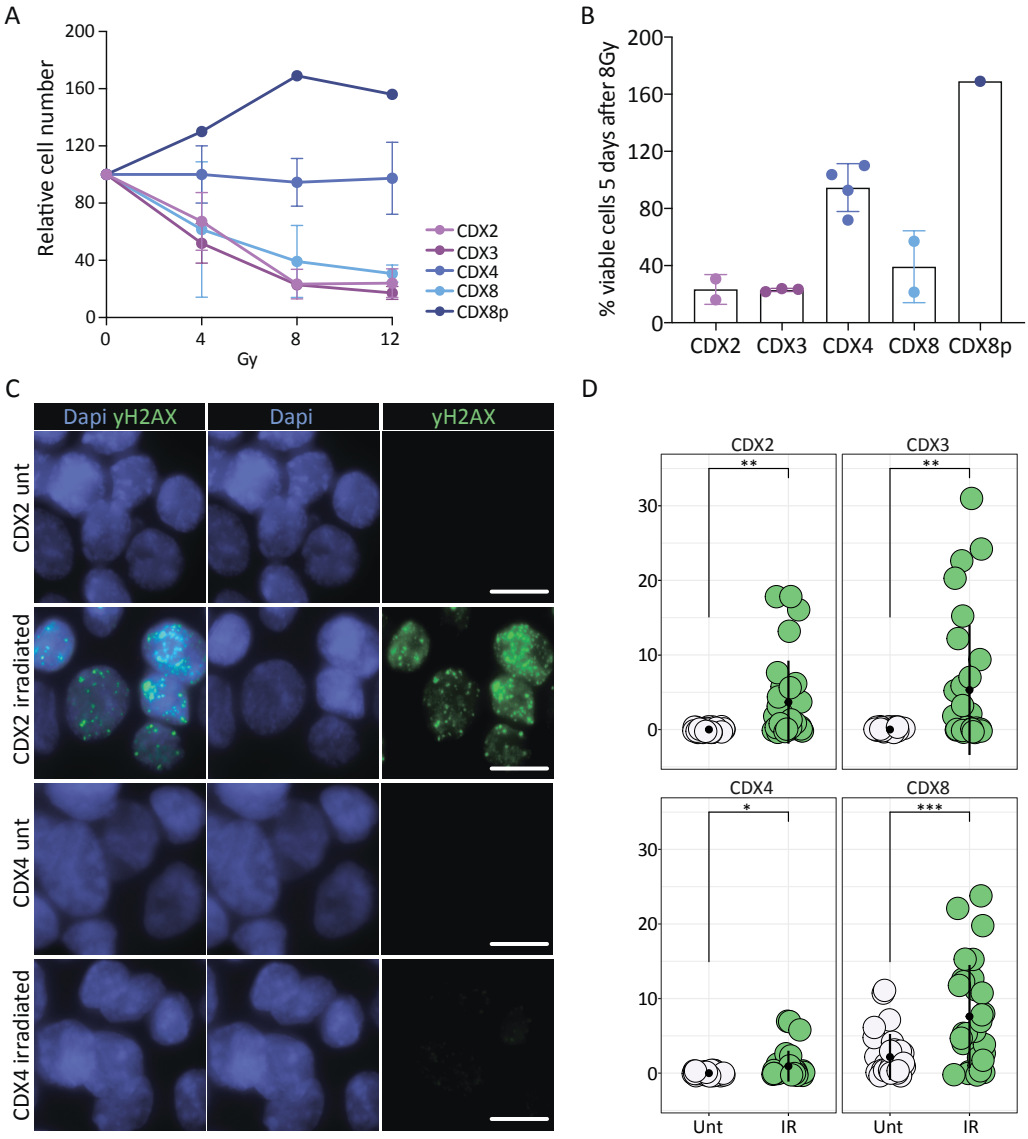

Figure 49. Radiosensitivity in a small panel of CDX cultures.

A. Inhibition of viability 5 days after treatment with increasing level of IR. B. Percentage of viable cells 5 days after 8 Gy irradiation, compared with untreated control. C. Representative images of γH2AX foci formation on CDX2 and CDX4 cells untreated or 24hr after irradiation (10 Gy). Scale bar: 10 µm.

D. γH2AX foci quantification in CDX cultures 24hr post irradiation. A student *t*-test has been performed between untreated and treated samples for each model after 30 random events have been selected from each conditions. SD and mean are shown. *P*-value: * < 0.05, ** < 0.01, *** < 0.001. Unt = untreated.

The maintained phosphorylation of H2AX in CDX2, CDX3 and CDX8 suggests that these cells needed more time to repair the DNA, highlighting the presence of possible deficiency in DSB repair compared with CDX4. The level of γH2AX was intrinsically high in untreated CDX8 cells implying high levels of endogenous DNA damage (Appendix Figure 3A). Having confirmed that irradiation induced DSB in the CDX models, I wanted to assess if these models were able to resolve the lesions activating the HR pathway. Toward this end, I examined RAD51 focus formation in G2/M cells marked by Geminin (or GMNN). As shown in Figure 50A, Geminin-positive CDX4 cells also expressed RAD51 foci following IR. Furthermore, the percentage of RAD51-positive CDX4 cells decreased over time (20% at 24hr *vs* 4.3% at 48hr post IR), suggesting that these cells were able to repair the DNA by activating the HR pathway (Figure 50B). On the contrary, CDX3 and CDX2 cells did not form RAD51 foci after IR, consistent with their inability to resolve γH2AX foci 24hr after IR (Figure 50A,B, Appendix Figure 4A). CDX8 cells had very low levels of RAD51 foci in both untreated and irradiated conditions, with increasing RAD51 positive cells at later time point (1.2%, 0.75% and 7.6% cells at baseline, 24hr and 48hr post IR, respectively) (Figure 50B, Appendix Figure 4B). This observation was consistent with the intrinsically high levels of γH2AX in untreated CDX8 cells. Because the level of RAD51 did not increase following irradiation in CDX8 as much as it did in CDX4, it is difficult to determine whether this model is truly HR-proficient based on this assay. These pilot experiments reveal heterogeneity in the DSBR response to IR, highlighting some discrepancies between olaparib sensitivity, response to IR and HR status. Lack of RAD51 foci in CDX3 correlates with the strong sensitivity to all DNA damaging agents tested, suggesting a lack of HR activation. On the contrary, there was no correlation with the response to olaparib observed with CDX2 and the lack of expression of RAD51. After treatment with olaparib and AZD1775, CDX2 clustered in the intermediate group and showed an average GI_{50} of 2.6 µM in response to olaparib alone, closer to the GI_{50} of the olaparib-resistant CDX4 (average GI_{50} 4.8 µM) than to the olaparib-sensitive CDX3 (average GI_{50} 0.05 µM) (Figure 45B). Therefore, the lack

of RAD51 in CDX2 highlights that in some models, HR deficiency does not synergise with response to PARP inhibition, and therefore, one biomarker is insufficient to predict the response to AZD1775/olaparib.

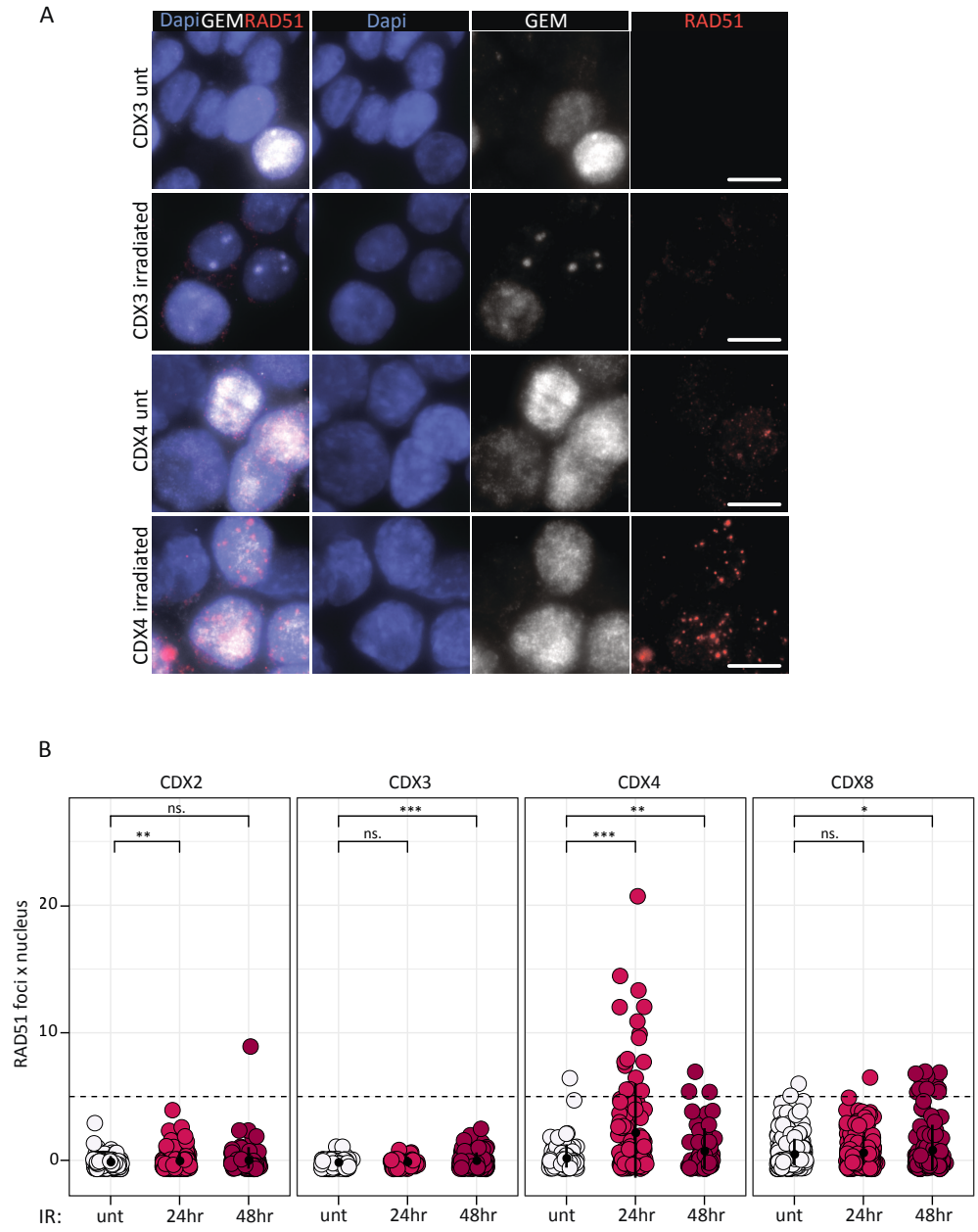

Figure 50. Activation of the homologous recombination pathway in CDX after irradiation.

A. Representative images of RAD51 foci formation on CDX3 and CDX4 cells irradiated with 10 Gy. Geminin staining was used as control to identify cells in late S/G2 phases. Scale bar: 10 µm. B. RAD51 foci quantification in CDX cultures 24hr and 48hr post irradiation. Dotted line indicates the threshold of 5 foci. A student *t*-test has been performed between untreated and treated samples for each model. SD and mean are shown. P-value: * < 0.05, ** < 0.01, *** < 0.001, ns: non significant. Unt = untreated.

5.2.2 Deleterious mutations in genes involved in the HR pathway can be found in SCLC

5Loss of RAD51 focus formation in CDX3 and CDX2 suggested a deficiency in the HR pathway. To better understand the mechanisms behind these results, I looked at the available WES data for 15/45 CDX. Analysis of the mutations detected in CDX3 compared with the germline sample collected from the same patient, revealed a truncating mutation in *PALB2*. PALB2 (Partner And Localizer of BRCA2) is a known member of the HR pathway that promotes RAD51 function (Figure 47).

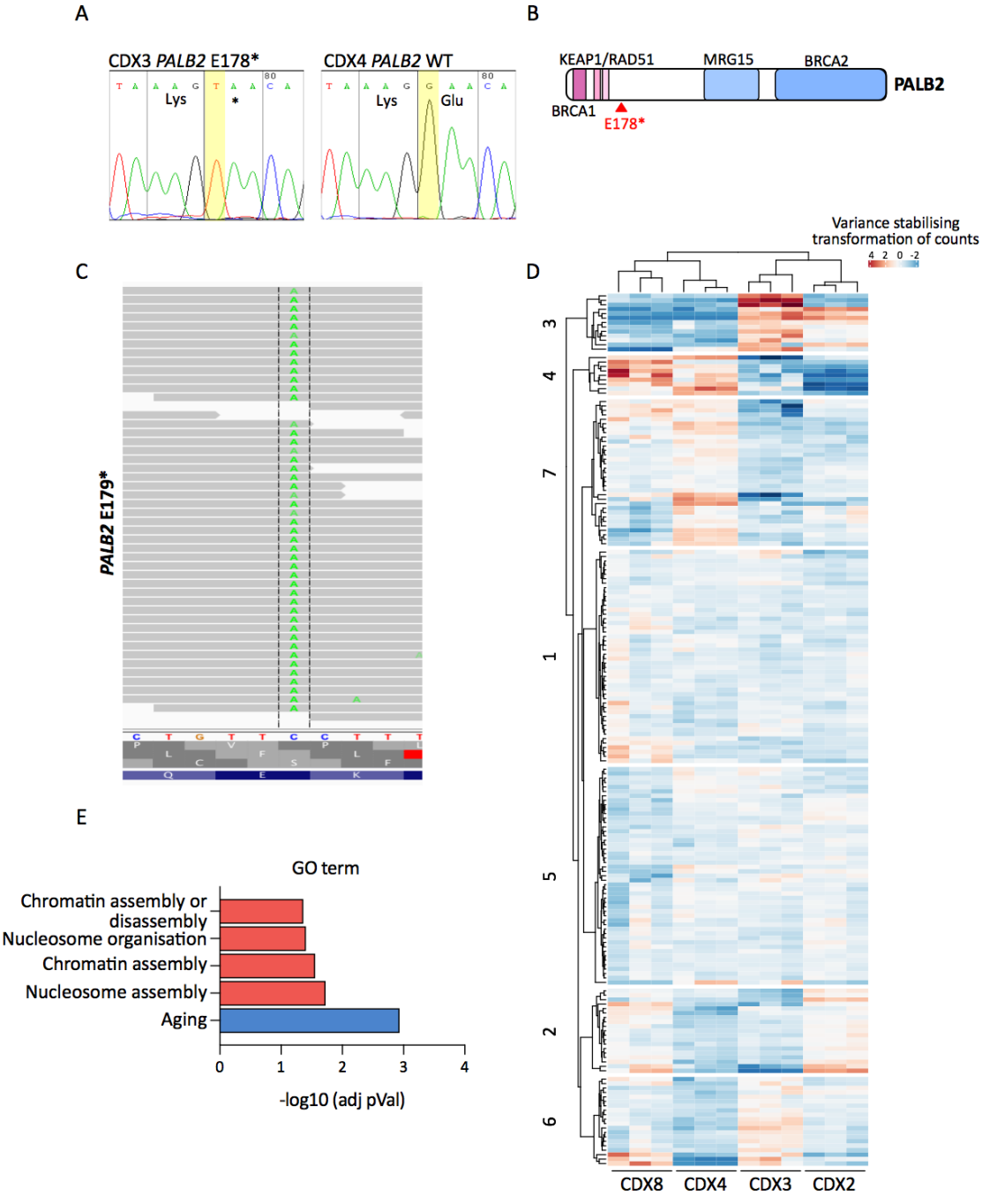

Figure 51. Deficiency in homologous recombination in CDX3.

A. Sanger sequencing for the PALB2 E178* mutation observed in CDX3. CDX4 was used as wild-type control. B. Schematic of the PALB2 protein domains and the region where the stop codon is generated by the E178* mutation in CDX3. C. CDX3 RNA reads covering the region of *PALB2* containing the mutated nucleotides. D. Unsupervised hierarchical clustering of a selected list of published genes (Peng et al., 2014). E. Negative log10 of the adjusted *p*-value for the identified GO terms. Red bars indicate terms from genes that were highly expressed in CDX8 and CDX4 (cluster 4), while the blue bar represent the term from genes highly expressed in CDX3 and CDX2 (cluster 3).

PALB2 enhances RAD51 strand invasion most likely via interaction and stabilization of RAD51 filaments (Buisson et al., 2010). This interaction is supported by the N-terminal 200 amino acids of PALB2 containing a coiled-coil and a DNA binding domain that mediates binding to RAD51 and DNA. The observed *PALB2* mutation in CDX3 creates a stop codon at amino acid 178, disrupting these domains (Figure 51A,B). Therefore, loss of RAD51 foci in CDX3 could be linked to the inability of PALB2 to properly bind both RAD51 and the DNA. PALB2 mutations have already been associated with HR deficiency and sensitivity to PARP inhibitors in pancreatic and ovarian cancers, further validating our hypothesis (Lord and Ashworth, 2016). Moreover, all reads in the RNAseq data harboured this mutation in *PALB2*, suggesting a complete loss of the WT allele (Figure 51C). CDX2 harboured missense mutations in *BARD1* (rs2070094, V507M) and *RAD51C* (rs28363317, T287A), both of which have been implicated in HR, however none of the observed variants were known to correlate with deleterious defects in these genes (Akbari et al., 2010; Capasso et al., 2009). The low level of RAD51 in CDX8 cells suggested that this model may not be completely HR-deficient and cells may need more time to resolve DNA damage. WES did not reveal any alterations in genes known to be involved in the HR pathway. To further assess the presence of HR deficiency in CDX, I have applied a published homologous-recombination deficiency (HRD) signature to the CDX transcriptomic data (Peng et al., 2014). This signature was generated by selecting 230 genes that were differentially expressed between MCF-10A parental or deficient in *BRCA1*, *RAD51* or *BRIT1*. This list included genes involved in cell cycle, DNA replication, recombination and repair (Peng et al., 2014). Despite the lack of RAD51 foci formation in two of the models tested, RNAseq analysis for the HRD signature did not reveal any clear pattern of HR deficiency (Figure 51D). There were some differences between the models and the two RAD51-deficient models clustered together (CDX2

and CDX3). However, the presence of a deleterious mutation on *PALB2* in CDX3 did not seem to correlate with an apparent pattern of expression of the selected genes compared with CDX4. Two clusters were identified that separated HR proficient tumours (CDX4 and CDX8) from the HR deficient (CDX3 and CDX2). Cluster 4 contained genes highly expressed in CDX4 and CDX8, while cluster 3 contained genes highly expressed in CDX3 and CDX2. Three of the nine genes in cluster 4 were involved in nucleosome and chromatin assembly (Figure 51E). Of the genes included in cluster 3, five out of 13 participate in the aging process. The fact that only two small clusters were able to separate the HR deficient from the HR proficient models suggests that in SCLC this list of genes is inadequate to identify tumours with HR deficiency. When tested on a larger panel of models, the signature generated two main groups of CDX (Appendix Figure 5). Group 1 contained CDX4, suggesting that the models present in this group have functional HR and are therefore resistant to olaparib. However, when compared with the response to olaparib observed *ex vivo*, there was no distinct separation between the models that responded (sensitive) and the ones that did not respond (resistant/intermediate). Moreover, CDX2 was included in the same group as CDX4, further suggesting that this signature is not able to separate HR proficient from HR deficient SCLC CDX.

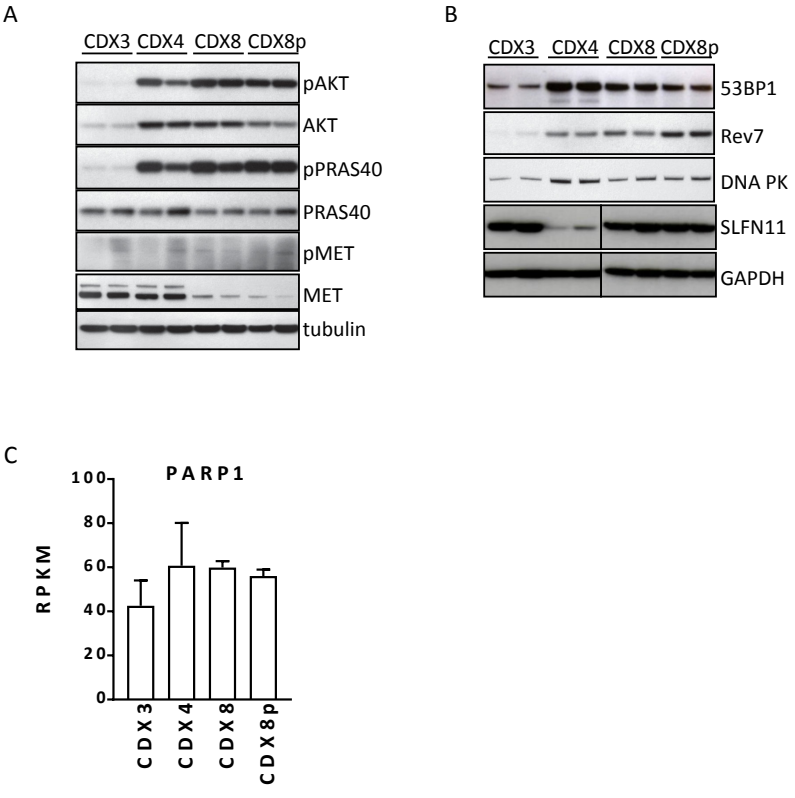

Figure 52. Published mechanisms of olaparib resistance.

A,B. Protein lysates from CDX3, CDX4, CDX8 and CDX8p tumours were probed for the indicated proteins. Tubulin and GAPDH were used as loading control. Biological replicates are shown. C. RPKM value for *PARP1* derived from 3 biological replicates. All three panels were published (Lallo et al., 2018).

Others have demonstrated that there is no correlation between the response to PARP inhibitors and HRD genomic scars in SCLC (Lok et al., 2017), and the HRD mutation frequency in SCLC is lower than in other tumour types (Heeke et al., 2018). These data highlight the possibility that in SCLC, the response to PARP inhibitors is not dependent on the loss of common HR-related genes. In our team, we explored other known biomarkers of response to PARP inhibition, including SLFN11 and PARP1 expression (Lok et al., 2017; Murai et al., 2016; Stewart, 2010, Figure 52A), PI3K or MET pathway activation (Cardnell et al., 2013; Du et al., 2016, Figure 52B), and restoration of DNA end resection (Jaspers et al., 2013; Xu et al., 2015, Figure 52A,C). None of the investigated pathways showed a recurrent pattern in the CDX tested (Lallo et al., 2018).

5.2.3 Loss of the G1 checkpoint does not correlate with response to AZD1775/olaparib

Several studies reported that inhibition of WEE1 can have a synergistic effect with DNA damaging agents in cells lacking the G1-S checkpoint (Geenen and Schellens, 2017; Hirai et al., 2009; Rajeshkumar et al., 2011). Consistent with most SCLC tumours, CDX3, CDX4, CDX8 and CDX8p bear loss of function mutations in *TP53* and *RB1* suggesting that the G1-S checkpoint is not functional in these models (Figure 53A) (the deleterious effect of these mutations was confirmed on the p53 mutations database: http://p53.iarc.fr/). It is well established that many loss-of-function p53 mutants are more stable than WT p53 due to the inability to transactivate MDM2 expression (Gannon et al., 1990). Indeed, CDX3, CDX8 and CDX8p maintain p53 expression (Figure 53B). To further validate that p53 was not functional in these models, I treated CDX3 and CDX10 cultures with doxorubicin to induce DNA damage and activate the p53 checkpoint. CDX10 was used as a positive control for p53 activation, given that this model had *TP53* WT by WES. As expected, doxorubicin induced p53 expression in CDX10 but not in CDX3 and the activation of p53 was confirmed by increased expression of the downstream target, p21 (Figure 53C). This

data confirmed that p53 is not functional in CDX3. Loss of the G1 checkpoint is also accentuated by loss of RB in all models tested, as confirmed by WES and protein expression (Figure 53A,B). Therefore, considering that all models seemed to have an impaired G1 checkpoint but different responses to AZD1775 and olaparib (Figure 22), it seems unlikely that loss of this checkpoint could be used as a predictive biomarker for the response to this combination in SCLC.

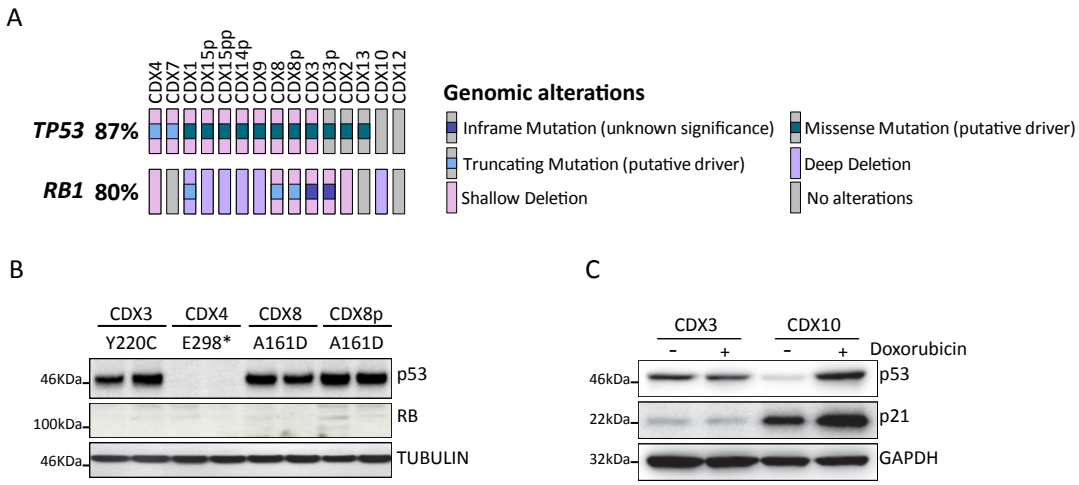

Figure 53. Loss of G1 checkpoint in the CDX models.

A. Summary of the *TP53* and *RB1* mutations identified in a panel of CDX models by WES. B. Immunoblot showing the expression of p53 and RB on tumour lysates form the stated CDX models. Each column is a biological replicate C. Immunoblot depicting the expression of p53 and p21 on protein lysates from CDX3 and CDX10 cultures treated for 15 hr with 1 μM of doxorubicin.

5.2.4 Intrinsic replication stress as predictive biomarker of AZD1775 response

As mentioned previously, WEE1 inhibition triggers an over-activation of CDKs that leads to increased initiation of replication, subsequent nucleotide shortage and replication stress (Beck et al., 2012; Duda et al., 2016) (Figure 54). Therefore, tumours with intrinsic higher level of replication stress are potentially more prone to undergo replication and/or mitotic catastrophe when WEE1 is inhibited. To assess the level of replication stress at baseline in the CDX, I measured phospho-RPA. RPA is a heterotrimer composed of RPA1 (or RPA70), RPA2 (or RPA32) and RPA3 (or RPA14) subunits, which can be phosphorylated on different sites. Increased levels of chromatin-bound RPA activates the ATR-CHK1 axis and ATR starts phosphorylating several downstream effectors, including RPA, to promote cell cycle arrest and DNA

repair (Olson et al., 2006; Zou and Elledge, 2003, Figure 48). The consensus sequences for ATR phosphorylation reside in the N-terminal 33 residues of RPA2, where serine 33 is one of the first sites to be phosphorylated following replication stress and DNA damage (Anantha et al., 2007). Hydroxyurea (HU) is a ribonucleotide reductase inhibitor frequently used to induce replication stress (Alvino et al., 2007).

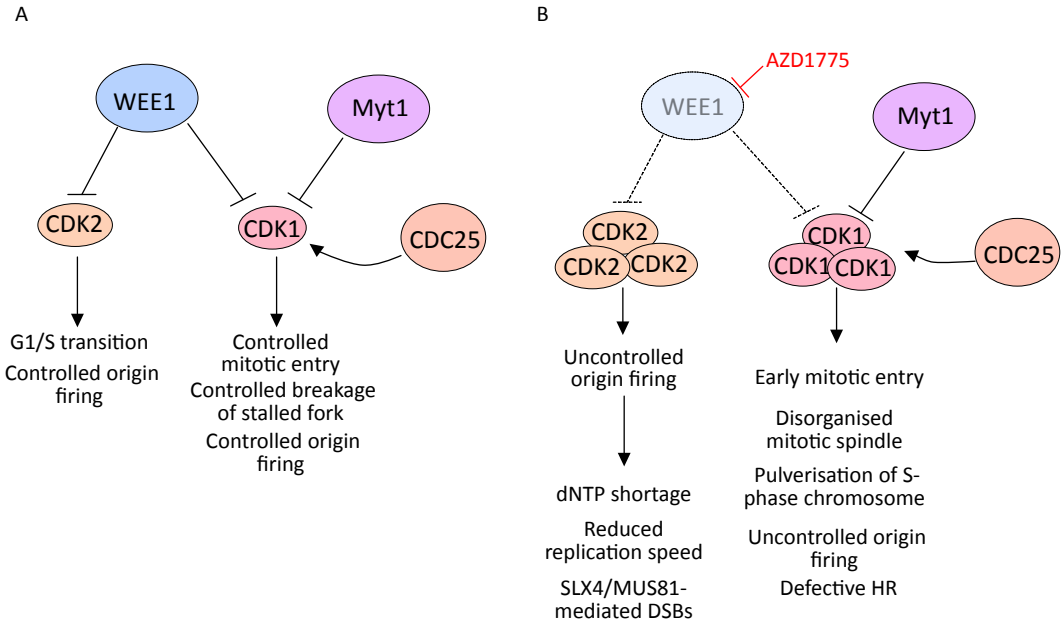

Figure 54. Roles of WEE1 in regulating initiation of replication and mitotic entry.

A. Schematic of the main physiological effects WEE1 has by inhibiting CDK1 and CDK2 during cell cycle. B. Schematic of the effects WEE1 inhibition can have on replication and mitosis (Aarts et al., 2012; Beck et al., 2012; Duda et al., 2016).

HU prevents conversion of ribonucleotides to dNTPs, thereby depleting cells of dNTPs and limiting DNA synthesis. U2OS cell lines have been widely used to look at replication stress (Toledo et al., 2013), therefore to confirm phospho-RPA as good biomarker, I treated these cells with HU and examined RPA phosphorylation by western blot. As expected, phospho-RPA Ser33 was induced after treatment with HU (Figure 55A). I have therefore assessed phospho-RPA Ser33 levels in CDX3, CDX4, CDX8 and CDX8p tumours. Protein lysates from CDX3 showed the highest baseline expression of phospho-RPA Ser33 compared with CDX4, CDX8 and CDX8p tumours (Figure 55B). These data indicate that CDX3 has an intrinsically high level of replication stress. Treatment with AZD1775 further increased phospho-RPA Ser33 levels in CDX3 tumours, while there was almost no effect on CDX4 (Figure 55C). This observation highlights the possibility that the response to AZD1775 observed in CDX3

could be associated with its intrinsic level of replication stress. CDX8 did not show any baseline level of phospho-RPA, and this model was less sensitive to AZD1775 than CDX3 *in vivo*, suggesting that baseline phospho-RPA level can be used to select patients more likely to show a good response to this drug.

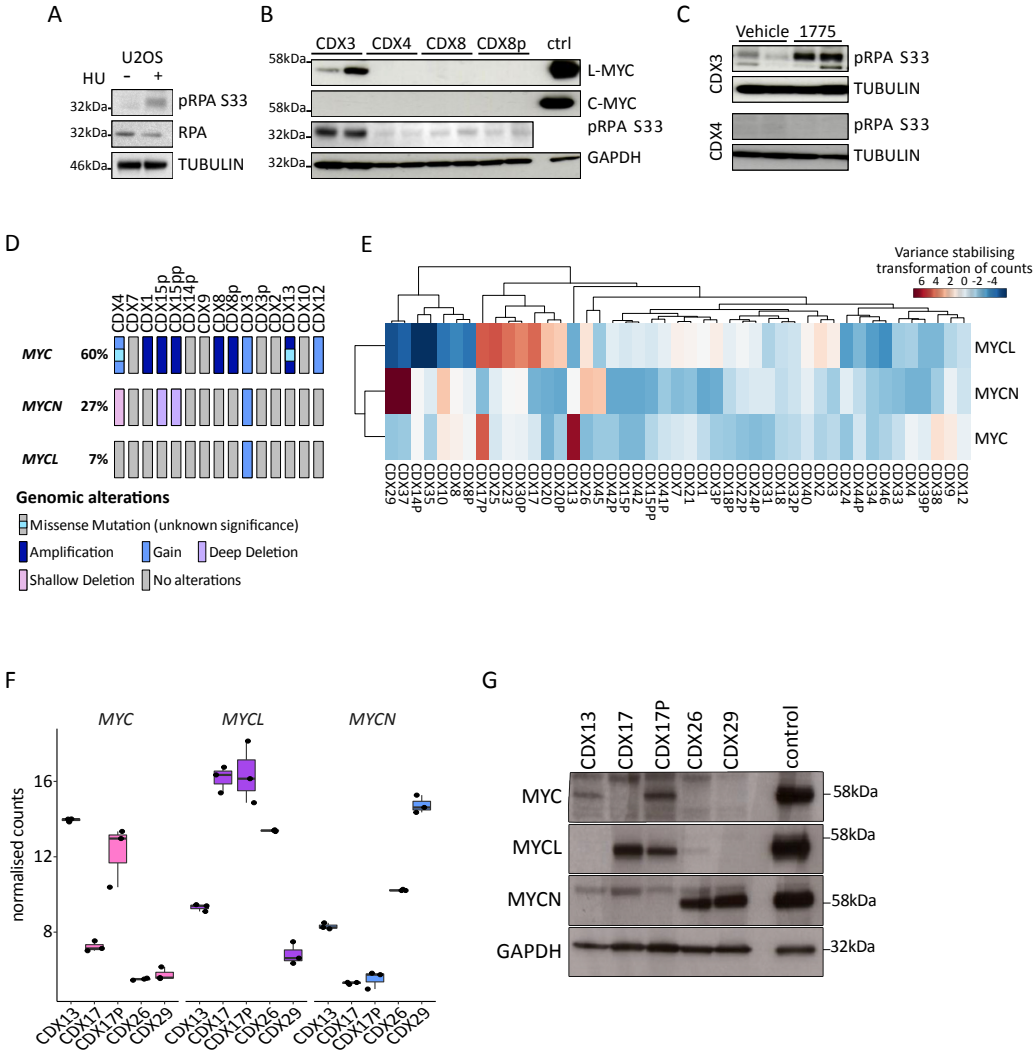

Figure 55. Baseline level of replication stress in the CDX model.

A. Immunoblot showing the induction of phospho-RPA2 at serine 33 after treatment with 2 mM of HU for 80min. B. Characterisation of the protein level of the indicated protein on CDX tumour lysates. Each column represents a biological replicate. C. Assessment of phospho-RPA2 S33 induction 2hr after one dose of AZD1775 on tumour lysates of CDX3 and CDX4. Each column represents a biological replicate. D. Summary of the MYC genes alterations identified in a panel of CDX models by WES. E. Unsupervised hierarchical clustering for each MYC family members in the CDX. F. Boxplot showing the normalized counts for the MYC family members in a selected panel of CDX. G. Western blot to confirm the protein expression of each MYC paralogues. GAPDH was used as loading control. H524 were used as positive control for C-MYC, H526 for N-MYC and H1694 for L-MYC.

Replication stress can be induced via different mechanisms, including expression of oncogenes (Kotsantis et al., 2018; Macheret and Halazonetis, 2018). The MYC

family oncogenes are frequently amplified or overexpressed in SCLC, implying that alterations in one of the MYC genes could be a potential cause of replication stress in SCLC (George et al., 2015; Thomas and Pommier, 2016). Genomic and transcriptomic analysis of our panel of CDX demonstrated that the MYC genes were frequently altered (Figure 55D,E). In particular, *MYC* is amplified (> 3 copies) in CDX8 and CDX8p and it is gained (= 3 copies) in CDX4 and CDX3. As expected, *MYC* expression was higher in CDX8 and CDX8p (normalised count 1.59 *vs* 1.06, respectively) compared with CDX3 and CDX4 (normalised count -0.53 *vs* 0.88, respectively), however none of these models expressed C-MYC at the protein level (Figure 55B). CDX3 showed a gain (= 3 copies) also in the other MYC family members, but had high mRNA levels only for *MYCL* (normalised count 1.65 *vs* -1.02 *vs* -0.53 for *MYCL*, *MYCN* and *MYC*). Indeed, CDX3 was the only model expressing L-MYC by western blot (Figure 55B). Although there are no reports showing that L-MYC overexpression can induce replication stress in tumours, the high level of this oncogene in CDX3 could partly account for the high baseline levels of phosho-RPA Ser33. The lack of correlation between the RNAseq data and C-MYC protein expression in CDX8 and CDX8p warranted further investigation of MYC family member protein levels in the models that expressed the highest transcript levels. CDX13 and CDX17p showed some of the highest levels of *MYC* mRNA (normalised count 6.9 and 5.2, respectively) and expressed C-MYC protein as shown by western blot (Figure 55F,G). Similarly, CDX17p expressed high levels of *MYCL* (normalised count 5.3) and this was confirmed by western blot. Of note, CDX17, the baseline counterpart of CDX17p, expresses L-MYC rather than C-MYC both by western blot and RNAseq (normalised count 4.9 *vs* 0.2). These results suggest that during acquisition of chemoresistance, minor C-MYC clones were positively selected in patient 17. Finally, CDX26 and CDX29 showed intermediate and high levels of *MYCN* transcript and protein (normalised count 3.1 and 7.7) (Figure 55G), respectively. All of these data confirmed that the MYC family members tend to be overexpressed in SCLC patients and therefore could be a source of intrinsic replication stress. Assessment of phospho-RPA in the CDX with overexpression of at least one of the MYC paralogues would support this hypothesis.

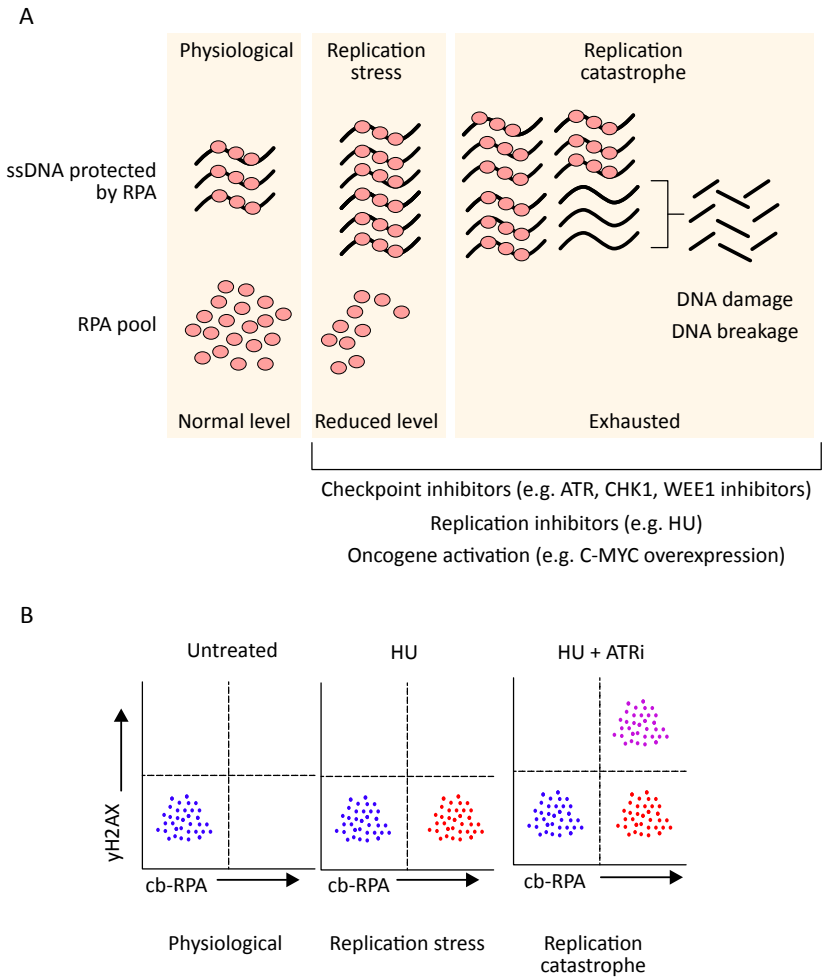

Figure 56. Depletion of the RPA pool causes replication catastrophe.

A. The amount of RPA is fixed in the cells. In physiological conditions, RPA level is sufficient to protect ssDNA generated during normal processes, like replication, R-loops formation and endogenous stress. In the presence of external stressors the amount of ssDNA can increase, exhausting the RPA pool. In the absence of RPA, ssDNA is attacked by endonucleases causing DSBs and replication catastrophe (adapted from Toledo et al., 2017). B. Induction of replication catastrophe can be monitored by the concomitant expression of chromatin-bound RPA and γH2AX. When cells become positive to chromatin-bound RPA only, it indicates that the cells are undergoing replication stress. However, if chromatin-bound RPA positive cells become also positive for γH2AX, it indicates that the pool of RPA has been exhausted inducing DSBs (adapted from Toledo et al., 2017).

Another indicator of replicative stress is the accumulation of chromatin-bound RPA in the nucleus of the cells. Replicative stress generates ssDNA that has to be protected by RPA in order to avoid breakage by endonucleases (Figure 48). When the level of replication stress-induced ssDNA exceeds the amount of RPA, the pool of RPA becomes exhausted, resulting in excessive DNA damage and replication catastrophe (Toledo et al., 2013) (Figure 56A). Cells with high baseline levels of chromatin-bound RPA may undergo a shortage of RPA quicker than cells with no intrinsic replication stress. Similarly, cells with alterations in the DNA damage and replication stress

response pathways can be more sensitive to stress induced by drug treatment and undergo replication catastrophe more easily (Toledo et al., 2017). To assess the level of chromatin-bound RPA in CDX cultures at baseline or at different time points after induction of replication stress, I developed a moderate-throughput screening to evaluate the expression of markers of replication stress and DNA damage using quantitative immunofluorescence. γH2AX was used to mark the cells undergoing DNA damage.

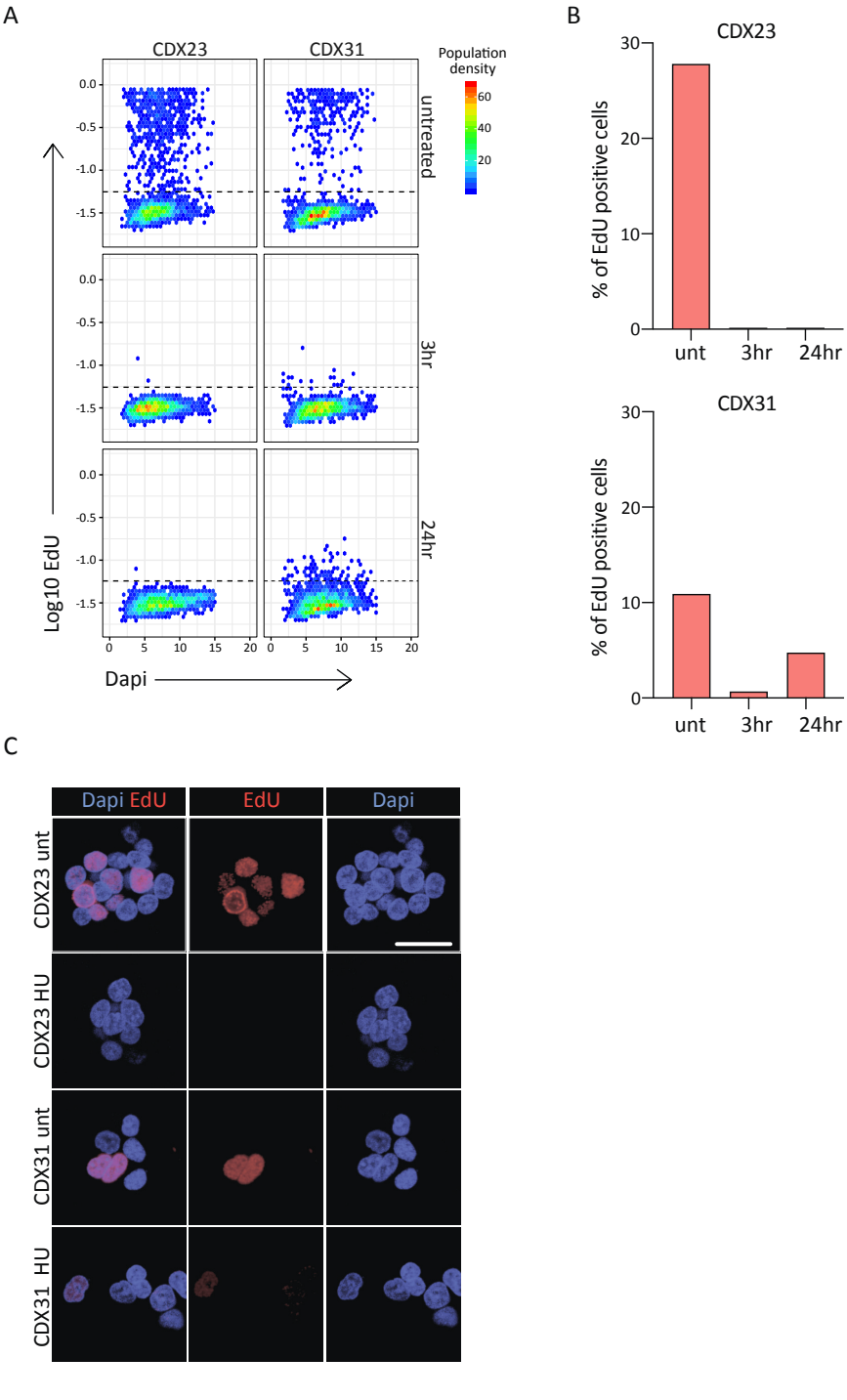

Figure 57. Inhibition of replication stress by hydroxyurea.

A. Quantitative image-based cytometry single-cell analysis (QIBC) of EdU labelled CDX cells before and after treatment with 2mM HU. 1,600 random cells were selected from each condition and plotted. Dotted lines show the threshold for EdU positivity defined in chapter 2.10.1. Only one biological replicate was performed for this assay. B. Quantification of the percentage of EdU positive cells in each condition using the threshold defined in chapter 2.10.1. C. Representative images of EdU^+ cells. Scale bar = 25 µm. Unt = untreated; HU = HU treated for 24hr.

CDX18, CDX23 and CDX31 were used as they were available at the time of the assay optimization. Initially, I treated CDX23 and CDX31 with HU for 3 and 24hr to assess the induction of replication stress. Incorporation of EdU was used to confirm the inhibition of DNA synthesis caused by HU. EdU is a thymidine analogue that can be incorporated in the nascent DNA by the DNA polymerase during replication, and therefore can be used to assess the ability of a cell to properly replicate the DNA (Salic and Mitchison, 2008). Within 3hr of treatment both models stopped replicating, as shown by the reduced amount of EdU labelled cells in the HU treated samples (Figure 57A-C). CDX31 was able to re-activate the replication machinery 24hr after treatment, implying it can overcome the dNTP depletion imposed by HU and recover from replication stress.

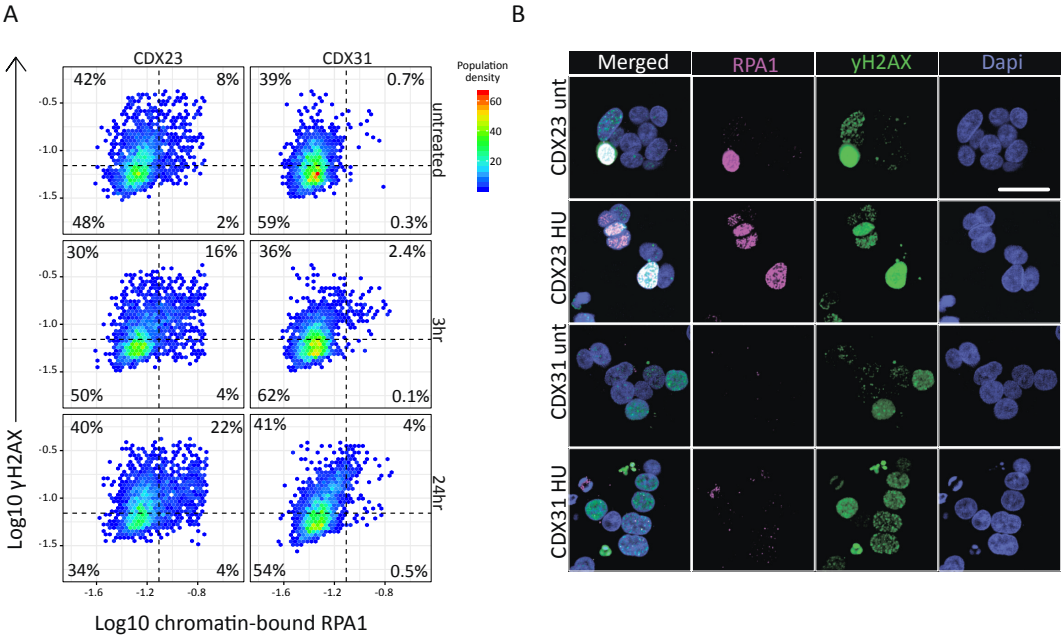

Figure 58. Chromatin-bound RPA as a marker of replication stress in CDX cultures.

A. QIBC of CDX cells stained for chromatin-bound RPA1 and γH2AX before and after treatment with 2mM HU. 2,500 random cells were selected from each condition and plotted. Dotted lines show the thresholds for chromatin-bound RPA1 and γH2AX positivity defined in chapter 2.10.1. Only one biological replicate was performed for this experiment. B. Representative images of single and double positive cells. Scale bar = 25 µm. Unt = untreated; HU = HU treated for 24hr.

Twenty-four hour after treatment with HU, the number of cells positive for chromatin-bound RPA remained low in CDX31 (4.5% of the entire chromatin-bound RPA positive population), while in CDX23 the chromatin-bound RPA positive cells reached 26% (Figure 58A,B). Similarly, CDX31 showed a minimal induction of cells positive for both chromatin-bound RPA and γH2AX (4%), while in CDX23 the double positive population accounted for 22% of the cells. Double positive cells mark a population of cells prone to undergo replication catastrophe (Toledo et al., 2013) (Figure 56B). The observation that cells positive for both chromatin-bound RPA and γH2AX represented a very small percentage in CDX31 is suggesting that the level of replication catastrophe induced by HU in this model was limited compared with CDX23 (Figure 58A).

Toledo and co-workers demonstrated that ATR delays the depletion of RPA during replication stress, limiting its loading onto ssDNA (Toledo et al., 2013). Inhibition of both ATR and the ribonucleotide reductase resulted in a faster depletion of the RPA pool and subsequent formation of DSBs (Figure 56B). To test whether this was also the case in the CDX models, I treated CDX18, CDX23 and CDX31 with HU and the ATR inhibitor, VE822, for different lengths of time. Compared with the results obtained in the previous experiment, CDX23 and CDX31 untreated samples appeared to express higher levels of chromatin-bound RPA at baseline (Figure 59A, Appendix Figure 6B,C). CDX18 cells also expressed relatively high level of chromatin-bound RPA at baseline, as shown in Figure 59A and Appendix Figure 6A. The variability between the baseline level of chromatin-bound RPA in CDX23 and CDX31 could be due to an intrinsic heterogeneity between replicates or a technical variation of the staining. Taking into account this high level of baseline chromatin-bound RPA, I decided to investigate chromatin-bound RPA-high cells only in order to focus the analysis on cells affected by the treatment (threshold defined by the dotted red line in Figure 59A). I observed an increase in the chromatin-bound RPA-high population within 30 min of treatment in all models tested (Figure 59B). At later time points, some of these cells were also positive for γH2AX, suggesting that they were prone to undergo replication catastrophe (Figure 59A,B and Figure 56B). Almost all CDX18 cells became chromatin-bound RPA-high (81%) or double positive (48%) 24hr post-treatment. CDX23 had a response consistent with what was observed with HU treatment only, showing a 2.9x

increase in the chromatin-bound RPA-high compared with the untreated control. However, the double positive population increased of 5x compared to 2.7x in the HU treatment only, suggesting that this treatment induced more replication catastrophe than HU alone. CDX31 had a similar induction of double positive cells after both treatments (5x increase compared with untreated control), however the percentage of double positive cells was higher after HU + ATRi treatment (26% *vs* 4%). Altogether, these results suggest HU combined with ATRi can induced replication catastrophe in the tested models.

Having confirmed the possibility to detect replication catastrophe in the CDX, I wanted to assess if treatment with AZD1775 induced replication catastrophe in these models. CDX23 and CDX31 are particularly sensitive to AZD1775 treatment, with an average GI_{50} of 0.06 and 0.12 μM, respectively. CDX18, in contrast, showed a more resistant phenotype with an average GI_{50} of 0.64 μM. Treatment with 100 nM AZD1775 caused an increased level of chromatin-bound RPA in all models tested reaching a peak 1.5hr after treatment (Figure 59C,D). At this time point, the number of double positive cells increased by almost 3 times in CDX23 and CDX31, but not in CDX18. CDX18 is the less AZD1775 sensitive model suggesting that activation of the replication stress response and subsequent replication catastrophe by AZD1775 could be specific to tumours sensitive to this drug. CDX18 did not exhibit any strong induction of double positive cells, although this model showed the highest increase in the chromatin-bound RPA-high population (from 9% to 32% of positive cells, Figure 59C,D). This observation suggests that WEE1 inhibition induced replication stress in these cells, however, they seemed able to properly deal with the stress and recover before depletion of the RPA pool. CDX31 showed a sustained induction of chromatin-bound RPA and γH2AX 24hr after treatment, while this population decreased in CDX23. Although these experiments require confirmation and extension to additional models, this initial result indicates that AZD1775 induces replication catastrophe in some CDX, partly accounting for their sensitivity to this drug.

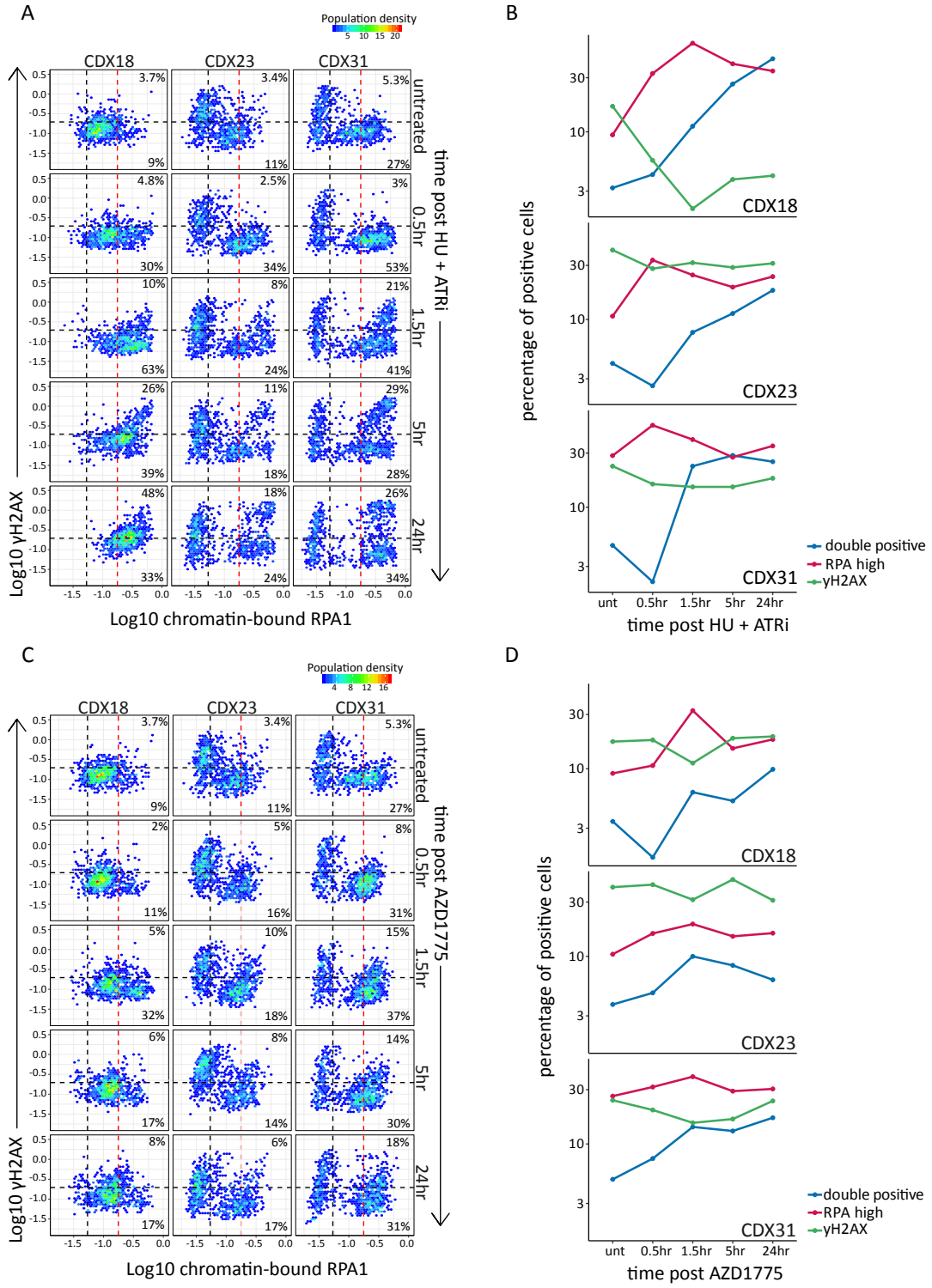

Figure 59. Induction of replication catastrophe after treatment with different inhibitors of the replication stress response.

A. QIBC of CDX cells stained for chromatin-bound RPA1 and γH2AX before and after treatment with 2mM HU + 100nM VE822. 900 random cells were selected from each condition and plotted. Dotted lines show the thresholds for chromatin-bound RPA1 and γH2AX positivity**.** Only one biological replicate was performed for this experiment. B. Line plot showing the evolution of the percentage of cells positive for chromatin-bound RPA (red line), γH2AX (green line) and both markers (blue line) over time as defined in A. C. QIBC of CDX cells stained for chromatin-bound RPA1 and γH2AX before and

after treatment with 100nM AZD1775. 900 random cells were selected from each condition and plotted. Dotted lines show the thresholds for chromatin-bound RPA1 and yH2AX positivity**.** Only one biological replicate was performed for this experiment. D. Line plot showing the evolution of the percentage of cells positive for chromatin-bound RPA (red line), yH2AX (green line) and both markers (blue line) over time as defined in C. All thresholds are computed in chapter 2.10.1.

5.2.5 Optimisation of functional assays to characterise the mechanisms of response to AZD1775/olaparib

In the previous chapters, I have evidenced a certain degree of heterogeneity across the CDX in their ability to respond to AZD1775/olaparib. It is clear that some models have a deficiency in DNA repair pathways and/or have intrinsic high level of replicative stress, however none of the biomarkers tested seemed to be able to completely separate responsive *vs* unresponsive CDX. This is probably due to the fact that the assays performed focused on specific pathways, such as HR and replication stress response, lacking information about the activity of all the other repair mechanisms that can operate in a cell. While it would be ideal to have a panel of biomarkers that cover as many repair pathways as possible, their high redundancy and the lack of detailed knowledge about their mechanisms of action, make this particularly challenging. Nevertheless, there are specific assays that can give general information about the ability of a cell to repair DNA lesions and/or undergo replicative stress, without focusing on specific biomarkers. Unfortunately, these techniques require some *in vitro* manipulation, and therefore they cannot be easily translated as clinical biomarkers. They can, however, be useful to understand the underlying mechanisms of response to this combination.

5.2.5.1 DNA fiber assay

The DNA fiber assay provides information about replication fork dynamics at the single molecule level (Quinet et al., 2017). Understanding the dynamic of replication fork in a specific tumour at baseline can give information about the presence of intrinsic deficiencies that would render these cells more sensitive to induced replication stress. Moreover, replication fork dynamics can be studied after treatment with specific compounds, to assess the ability of a tumour to deal with a defined type of stress (Figure 60). This assay is based on the ability of the cells to incorporate thymidine analogues, which can be specifically detected, into replicating DNA. When a cell is under stress, the stalling or collapse of the replication fork will

impede or slow incorporation of thymidine analogues, creating patterns of incorporation specific to the stress encountered by the fork (Figure 60B). A lot of information can be extrapolated by a thorough analysis of these patterns, such as fork progression, restart, termination and new origin firing (Quinet et al., 2017; Técher et al., 2013).

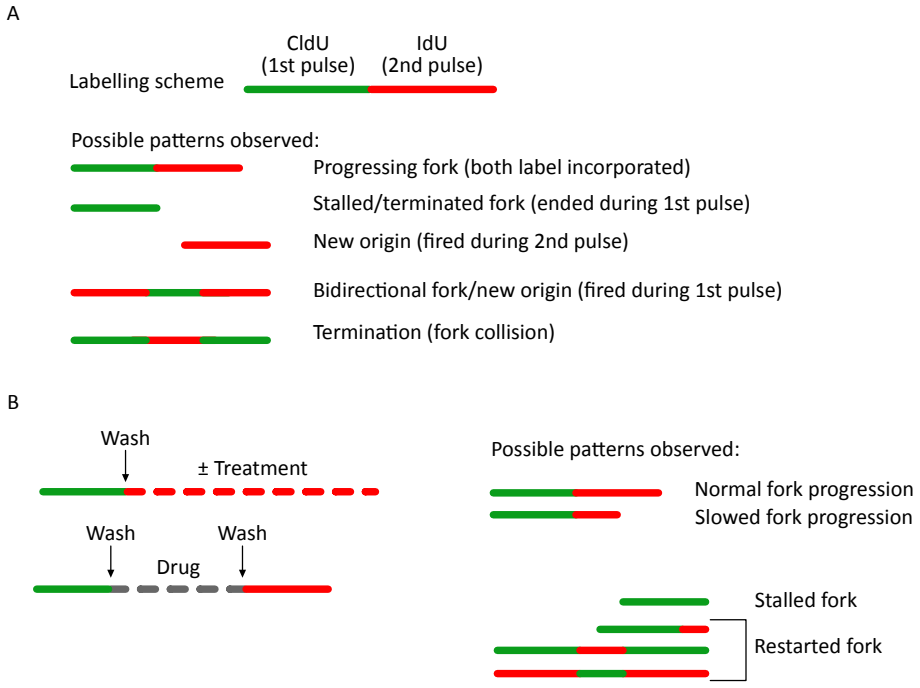

Figure 60. Schematic of different replication events detectable with the DNA fiber assay.

A. Some replication parameters observed with the DNA fiber assay and their interpretations. B. Examples of the effect specific compounds can have on replication dynamic. The panel shows possible experimental designs and putative effects on replication forks. This figure was adapted from Quinet et al., 2017. Green line: CldU pulse; red line: IdU pulse; dotted red line: ± treatment + IdU pulse; dotted grey line: drug only.

To understand if there was any specific replication fork pattern in the CDX that were sensitive or resistant to AZD1775/olaparib treatment, I applied this assay to our CDX models. As an initial experiment, I performed a pilot study to test the ability of the CDX to incorporate EdU, as a surrogate for the thymidine analogues IdU and CldU, after different incubation times (pulse). CDX cultures were labelled with EdU for 30 min, 1hr, 2hr or two pulses of 30 min with a 2hr wash out between pulses (Figure 61A). As expected longer pulses resulted in more EdU incorporation. However, considering that two pulses of 30 min gave better results that one pulse of 30min or 1hr (Figure 61B,C), I have decided to use two short pulses for the assay optimization.

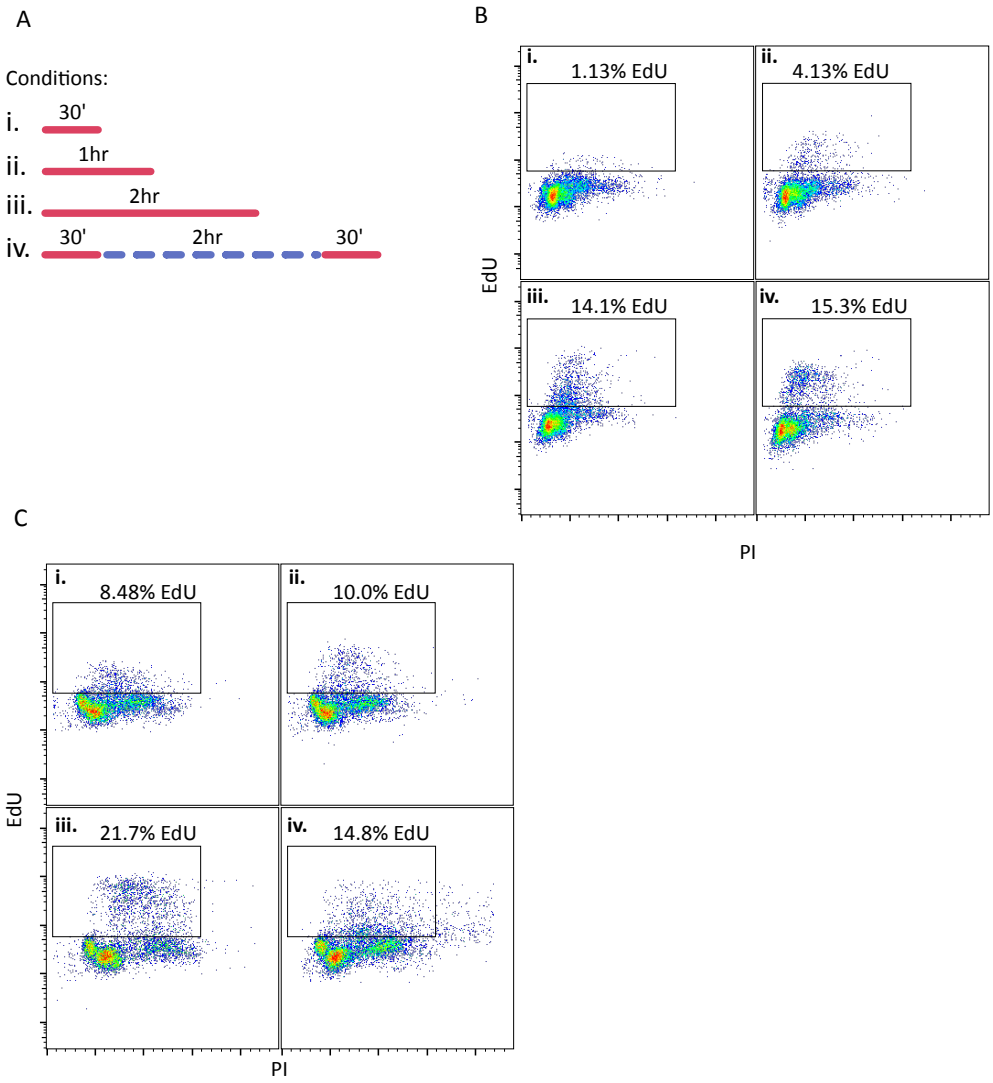

Figure 61. Pilot study to define the ability of CDX culture to incorporate EdU.

A. Schematic to summarise the EdU labelling pulses tested. B,C. CDX10 (B) and CDX29 (C) were tested for EdU incorporation at different time point and assayed by flow cytometry. PI was used to mark DNA content. Percentages are indicative of the amount of EdU positive cells in the designed gate.

Initially, I tested a couple of conditions to assess the quality of the DNA fibers. I pulsed CDX cells with CldU first, followed by a pulse with IdU. The cells were then left in thymidine analogues-free media for 2hr, before repeating the round of labelling (Figure 62A). Twenty minutes pulses (condition a) generated shorter fibers than the 40 min pulses (condition b) (Figure 62B). In both cases the quality of the fibers appeared good, apart from some overlap between IdU and CldU staining, which may be resolved by increasing the concentration of the second thymidine analogue (Quinet et al., 2017).

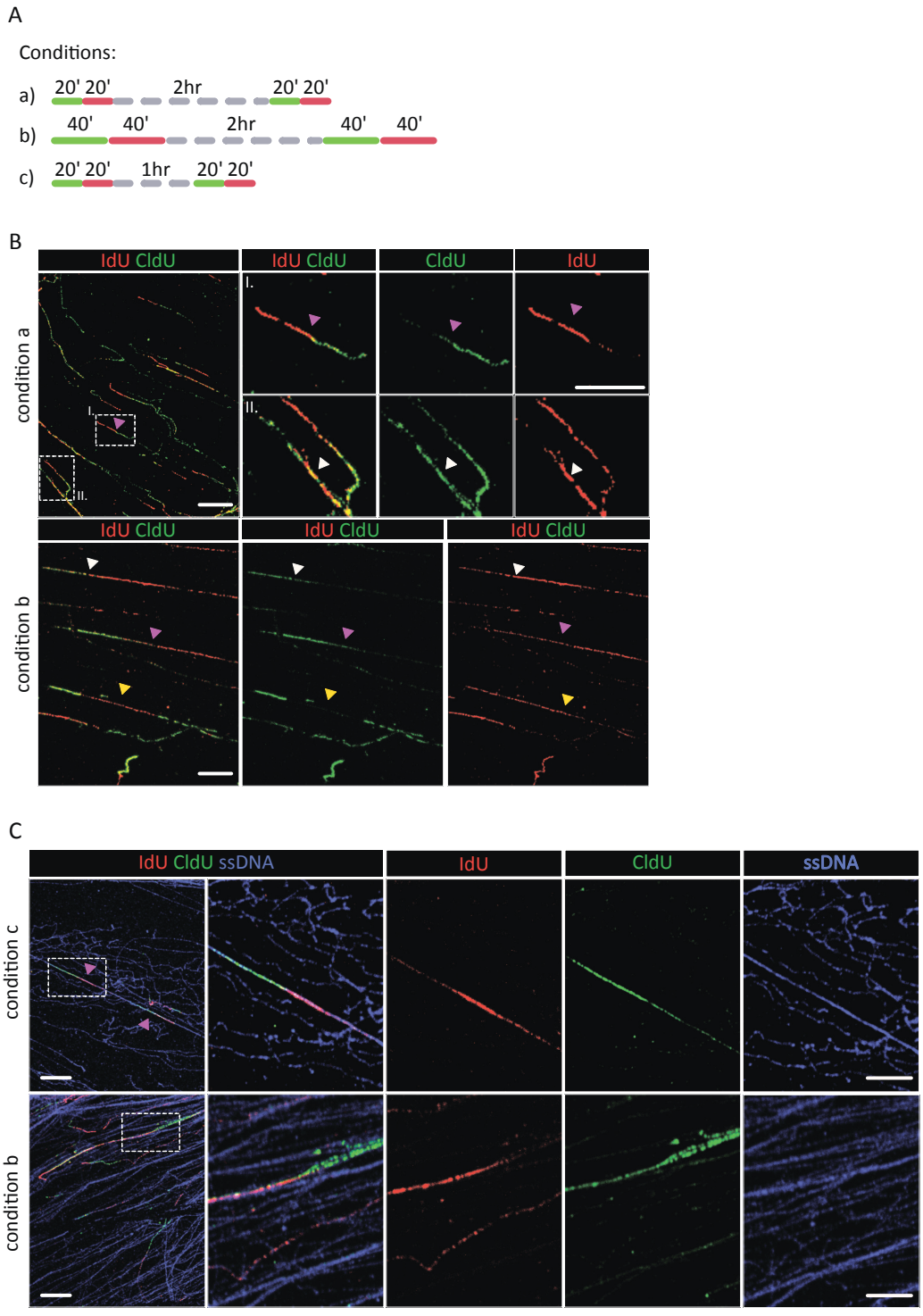

Figure 62. Optimisation of the DNA fiber assay.

A. Schematic to summarise the IdU/CldU labelling pulses tested. Red: IdU; green: CldU; grey: media only. B. Representative images of labelled DNA fiber following the conditions stated in A. Examples of different pattern of replication dynamic are indicated by coloured triangles. Yellow = replication termination, pink = progressing forks. White triangles indicate overlapping staining for IdU and CldU. Scale bar: 10 µm. C. Representative images of labelled DNA fibers, with counterstaining for ssDNA, following the conditions stated in A. An example of progressing forks belonging to the same molecule is highlighted by the pink triangles. Scale bar: 10 µm.

Although the assay may require further optimisation, it was possible to observe aberrant replication dynamics, including termination (probably because of fork collision, yellow triangle), progressing forks (pink triangle) and new origins (fired during the second label, blue triangle) in the sample tested (Figure 62C). Once confirmed that I was able to detect DNA fibers from the CDX cultures, I added a counterstain for ssDNA. Counterstaining is crucial to help understanding if two replication events belong to the same molecule and that the DNA fiber is not broken. ssDNA counterstaining allowed visualization of all DNA fibers making it easier to detect events that belong to the same molecule, as shown in condition c, where two progressing forks are detected on the same fiber (pink triangles) (Figure 62C).

5.2.5.2 Comet assay

The fiber assay specifically examines the dynamics of DNA replication, however the ability of cells to repair specific lesions contributes to the way they respond to AZD1775/olaparib. To investigate DNA repair efficiency of CDX, I performed the comet assay. The comet assay is a single-cell electrophoresis method that detects and quantifies SSB and DSB lesions (Olive and Banáth, 2006). Lysis of undamaged cells frees supercoiled DNA that remains static, whereas presence of breaks releases the supercoils resulting in DNA that migrates toward the anode. This pattern creates comet like configuration, in which the head is representative of the undamaged DNA, while the tail contains all relaxed and broken DNA ends (Collins, 2004) (Figure 63A). All CDX tested showed an increase in the percentage of DNA in the tail straight after IR (10' post IR), with subsequent reduction 3hr post irradiation (Figure 63B). Interestingly, CDX3 and CDX2 were less efficient in repairing the breaks induced by the x-rays compared with the other models, confirming the data showing sustained γH2AX foci 24hr post IR (Figure 63B and 49D). Moreover, both models were unable to form RAD51 foci after IR, suggesting that their impaired ability to repair IR-induced DSBs is linked to their inability to activate the HR pathway. Another characteristic of CDX2 and CDX3 was the presence of higher level of damaged DNA at baseline

(untreated sample) compared with CDX4, CDX8 and CDX8p. This could also be indicative of a deficiency in the ability to repair DNA lesions.

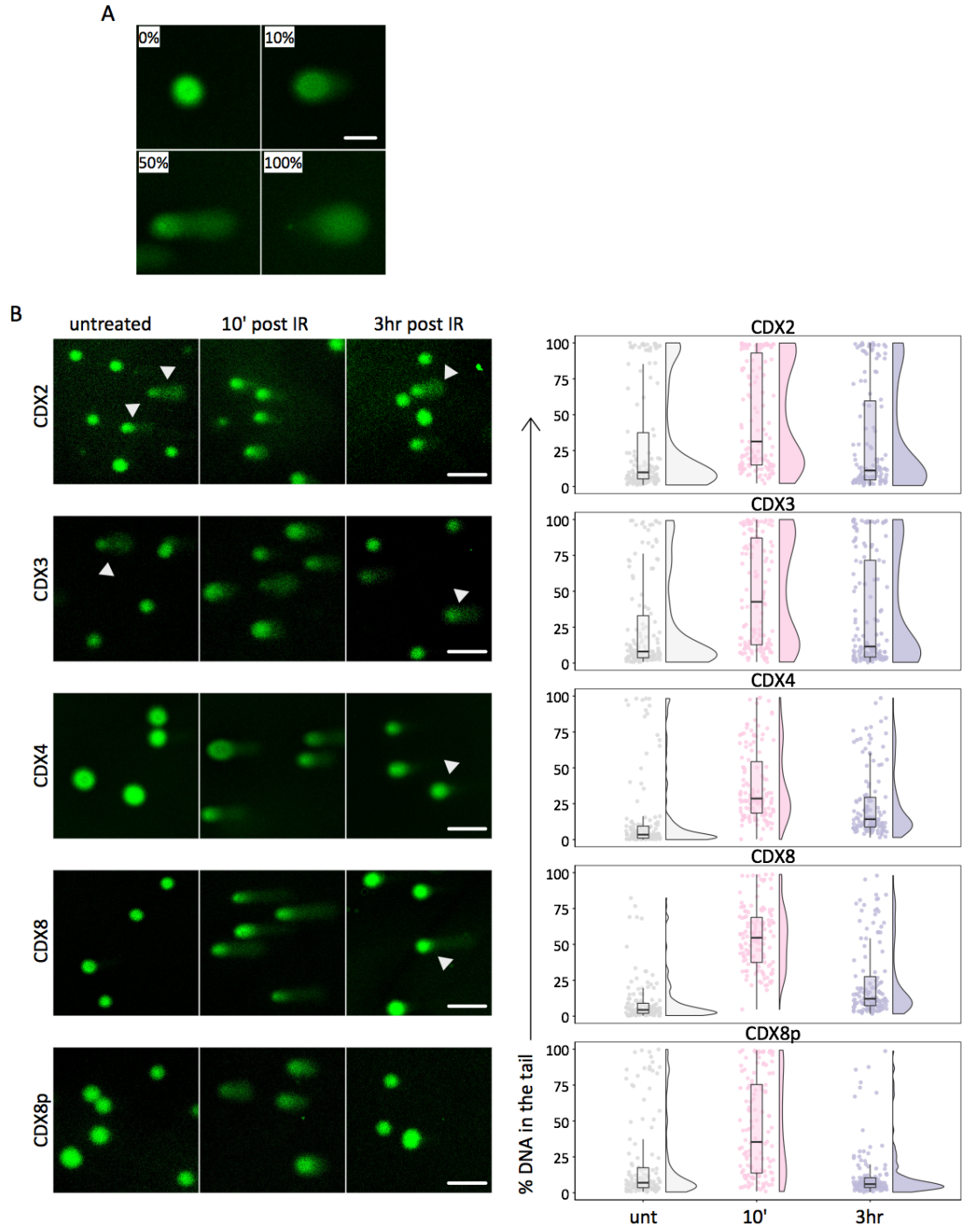

Figure 63. Optimisation of the comet assay.

A. Representative images of comets with different level of DNA damage. Percentages refer to the amount of DNA in the tail (broken DNA) relative to the head (undamaged DNA). Scale bar = 50 µm. B. Representative images of comets at different time points. White triangles mark comets with damaged DNA. The raincloud plots are used to show the percentage of DNA in the tail from 130 randomly selected comets in each sample. For detail see chapter 2.10.1. Scale bar = 100 µm.

The induction of DNA breaks in CDX8 was particularly pronounced, with almost all cells displaying a comet tail. In contrast, CDX8p showed an even distribution of comets, with various level of DNA breaks (Figure 63B). The presence of undamaged cells after IR in CDX8p, but not in the chemosensitive counterpart, CDX8, could represent an IR-resistant population selected in the patient during first-line treatment. However, in both models the repair of the damage was very efficient, with most cells showing intact nuclei 3hr after irradiation (Figure 63B).

This data opposed the observation made previously, where CDX8 appeared to be very sensitive to irradiation and showed an impaired recruitment of RAD51 foci together with high baseline level of γH2AX. These cells may have an intrinsic ability to deal with DNA damage that could explain why the patient has become resistant to chemotherapies. Compared with CDX2, CDX3 and CDX8, CDX4 appeared to be completely insensitive to irradiation and was able to quickly repair most DNA breaks within 3hr of IR. The fact that models with distinct responses to IR had a similar ability to repair the damage, suggests that the differences between the irradiation sensitive CDX8 and the irradiation resistant CDX4 may be very subtle and can be only observed when specific pathways are investigated.

5.2.5.3 WEE1 expression

It is well known that changes in the level of the drug target can affect the drug response observed in tumours. We have shown that mRNA level of *PARP1* were similar in CDX3, CDX4, CDX8 and CDX8p (Figure 52C, Lallo et al., 2018), suggesting that *PARP1* expression does not explain the differences in response to olaparib in the model tested. Recently, it was demonstrated that overexpression of the Protein Kinase Membrane Associated Tyrosine/Threonine 1 (PKMYT1 or Myt1 kinase) is a putative mechanism of acquired resistance to WEE1 inhibition in breast cancer (Lewis et al., 2019). Similar to WEE1, Myt1 kinase inhibits CDK1 activity by phosphorylating Tyr14 and 15 and controlling cell cycle progression (Figure 54A). Lewis *et al* suggested that in the absence of an active WEE1, cells can respond by overexpressing Myt1 kinase in order to keep the level of CDK1 activity under control and avoid mitotic catastrophe (Lewis et al., 2019). Initial analysis of WEE1 and Myt1 kinase expression

levels in our CDX cohort identified 4 groups: tumours expressing both genes, double negative tumours and tumours expressing either one or the other gene (Figure 64A).

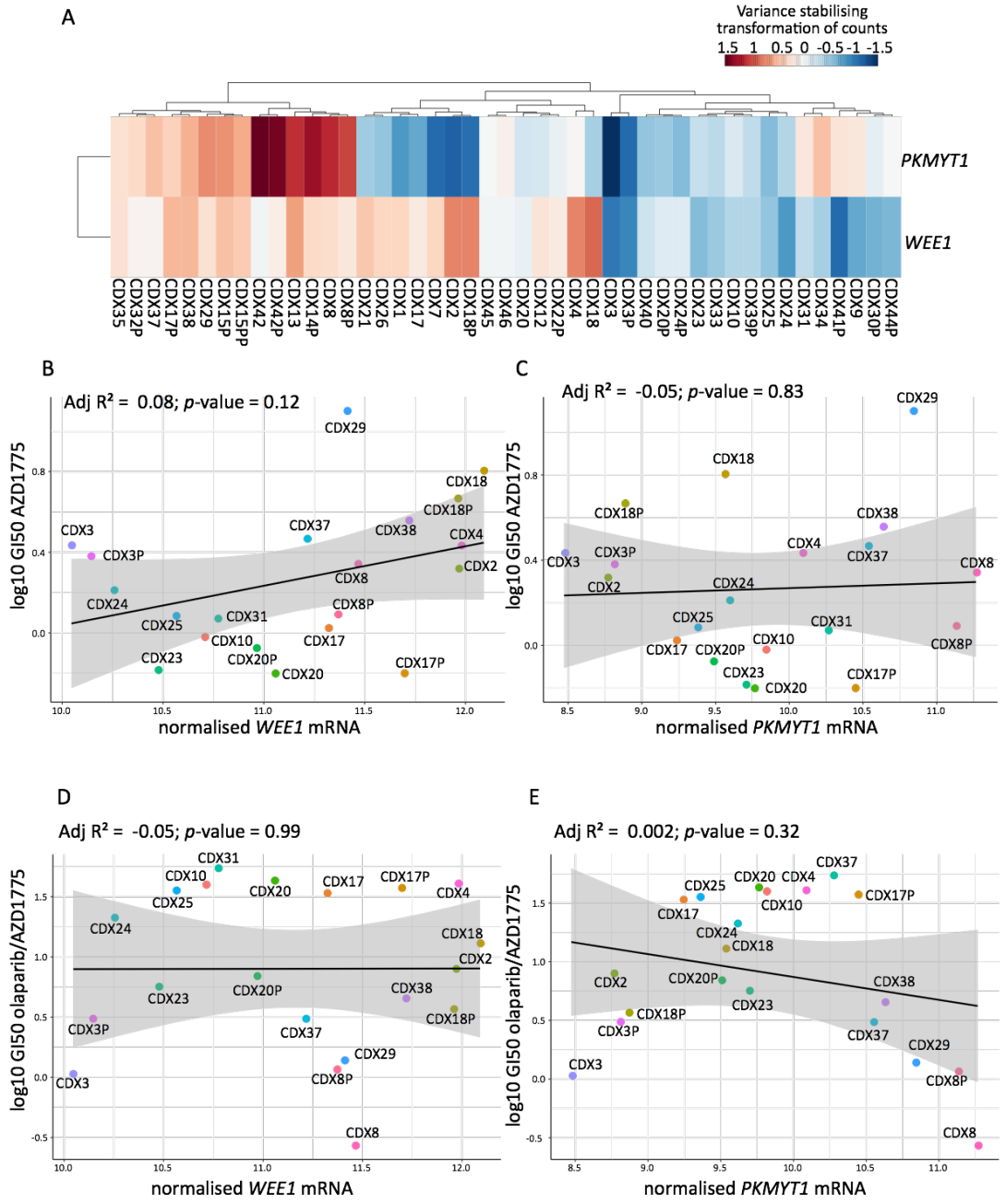

Figure 64. WEE1 and PKMYT1 mRNA expression in the CDX.

A. Unsupervised hierarchical clustering for *WEE1* and *PKMYT1* expression in the CDX. B-E. Linear modelling to correlate the GI_{50} (µM) for AZD1775 (B,C) or olaparib + 40nM AZD1775 (D,E) with the normalized count for *WEE1* (B,D) and *PKMYT1* (C,E).

In vivo, AZD1775 monotherapy induced tumour regression in CDX3 only, it had a stabilizing effect on tumour growth in CDX8 and CDX4 and no effect on CDX8p. *WEE1* expression was higher in CDX8, CDX8p and CDX4 compared with CDX3, suggesting

that the strong response observed in CDX3 could be related to a lower pool of WEE1 protein. Moreover, CDX3 also expressed low level of *PKMYT1* further validating the hypothesis that CDX3 may be more sensitive to WEE1 inhibition because of the low level of these proteins. Reduced expression of these two cell cycle checkpoints could also explain the higher level of replication stress observed in CDX3.

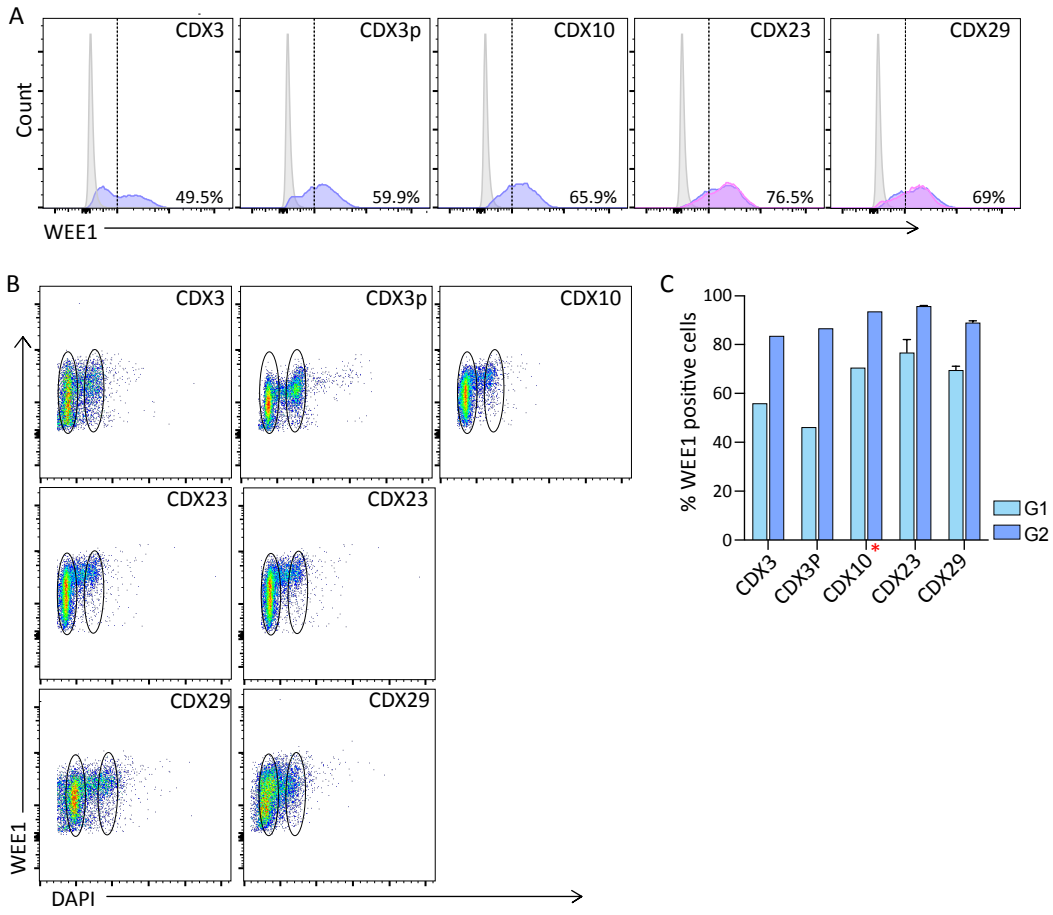

Figure 65. WEE1 protein expression increases at later phase of cell cycle.

A. Percentages are indicative of the amount of WEE1 positive cells in the single cell population. B,C. Expression of WEE1 protein in cells progressing through G1 and G2 assessed by flow cytometry. Barplot summarise the percentage of WEE1 positive cells in the G1 and G2 gates (chapter 2.7.2 for details). Red asterisk indicates CDX resistant to AZD1775/olaparib *ex vivo*. Error bars indicate SD calculated from two biological replicates.

To compare the response to AZD1775 and the relative expression of *WEE1* and *PKMYT1* in the CDX model treated with AZD1775 *ex vivo*, I have correlated the GI_{50} of AZD1775 treatment with the mRNA level of each gene. There was no direct correlation between the response to AZD1775 and the expression of either genes, with just a small trend toward higher level of *WEE1* and a more resistant phenotype (Figure 64B,C). There was also no significant correlation when the expression of *WEE1*

and *PKMYT1* were compared with the response to olaparib/AZD1775 (Figure 64D,E). Because WEE1 is normally regulated during cell cycle, I wanted to assess if changes in the expression of this protein in the different cell cycle phases could correlate with the response to AZD1775 and olaparib. A small panel of CDX was tested for the expression of WEE1 by flow cytometry throughout the cell cycle phase. All models tested expressed a similar level of WEE1 in the total population, with 60-80% of WEE1 positive cells (Figure 65A). When WEE1 expression was plotted against the DNA content, it became clear that WEE1 is more highly expressed at later phases of the cell cycle, with almost 100% of cells in G2 positive for WEE1, compared with an average of 50% WEE1 positive cells in G1 (Figure 65B,C). This is consistent with the role of WEE1 in regulating progression into mitosis. In the tested panel, CDX10 is the less responsive models to AZD1775/olaparib *in vitro*, and yet the distribution of WEE1 expression during cell cycle was very similar to the other CDX. These preliminary data suggest that WEE1 expression does not have any influence on the response to AZD1775/olaparib. It would be interesting to see if a similar trend is observed with Myt1 kinase or if differences in the expression of this protein can predict the response to AZD1775.

5.2.5.4 Heterogenous expression of p21 in the CDX models

One of the mechanisms of action of AZD1775 combined with the DNA damaging agent gemcitabine is the induction of unscheduled mitosis in arrested S-phase cells (Aarts et al., 2012). Gemcitabine inhibits DNA synthesis causing S-phase arrest. In p53 WT cells, p53 can activate the cyclin dependent kinase inhibitor p21 and prevent unscheduled mitosis by inhibiting the expression of mitotic cyclins. In the absence of p53-p21 signaling, cells rely on WEE1 to restrain CDK1 activity and avoid entry into mitosis with damaged DNA (Figure 54). Inhibition of WEE1 in combination with gemcitabine is synergistic in p53 mutant breast cancer cells by causing forced mitotic entry (Aarts et al., 2012). Moreover, AZD1775 also acts by inducing unscheduled firing of replication origins, leading to DNA damage and replication catastrophe (Toledo et al., 2013). p21 can protect p53 WT cell lines from replication stress and DNA damage induced by WEE1 inhibition (Hauge et al., 2019). Although the mechanism for the protective effect of p21 is not completely understood, it seems to play a role during

S phase. On the other side, in a p53-null background, chronic expression of p21 can outcompete PCNA binding cofactors, interfering with the regulation of replication and triggering endoreduplication and genomic instability (Galanos et al., 2016). This dual role of p21, both as an oncogene and a tumour suppressor, has been widely studied (Abbas and Dutta, 2009; Georgakilas et al., 2017) and suggests that p21 could have a p53-independent role in inducing resistance to different DNA damaging agents. Considering the roles of WEE1 and PARP in regulating cell cycle progression, DNA repair and replication, it is possible that overexpression of p21 in the CDX could serve as a biomarker of resistance to AZD1775/olaparib treatment.

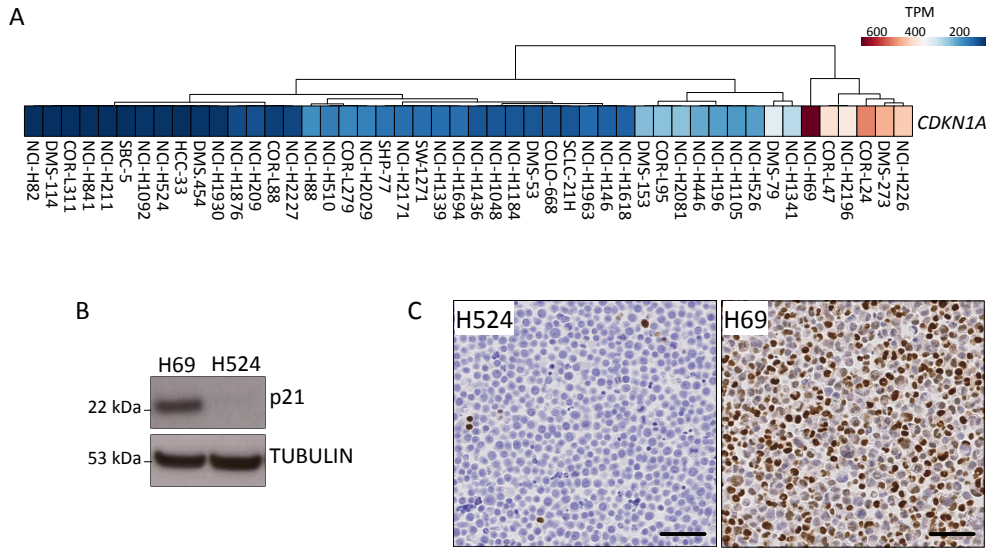

Figure 66. p21 expression in SCLC cell lines.

A. Transcript per Kilobase Million (TPM) values for *CDKN1A* in SCLC cell lines from the Cancer Cell Line Encyclopedia. B,C. Protein expression of p21 in H69 and H524 showed by western blot (B) and immunohistochemistry (C). Scale bar = 50µm.

Before assessing the expression of p21 in the CDX models, I used the Expression Atlas tool from EMBL-EBI to look at the mRNA expression of the p21 gene (*CDKN1A*) in a panel of 48 SCLC cell lines available from the Cancer Cell Line Encyclopedia (Figure 66A). NCI-H69 (H69) expresses the highest level of *CDKN1A*, while NCI-H524 (H524) had one of the lowest values. Based on these data, I selected these two cell lines as positive (H69) and negative (H524) controls for p21 expression. The expression of p21 in these two cell lines was confirmed by western blot and immunohistochemistry (Figure 66B,C). To assess p21 expression in CDX, I optimised an immunofluorescent

assay to look at the expression of both p21 and pHH3. Phosphorylation of Histone H3 on Ser10 was used to assess the percentage of mitotic cells in each model.

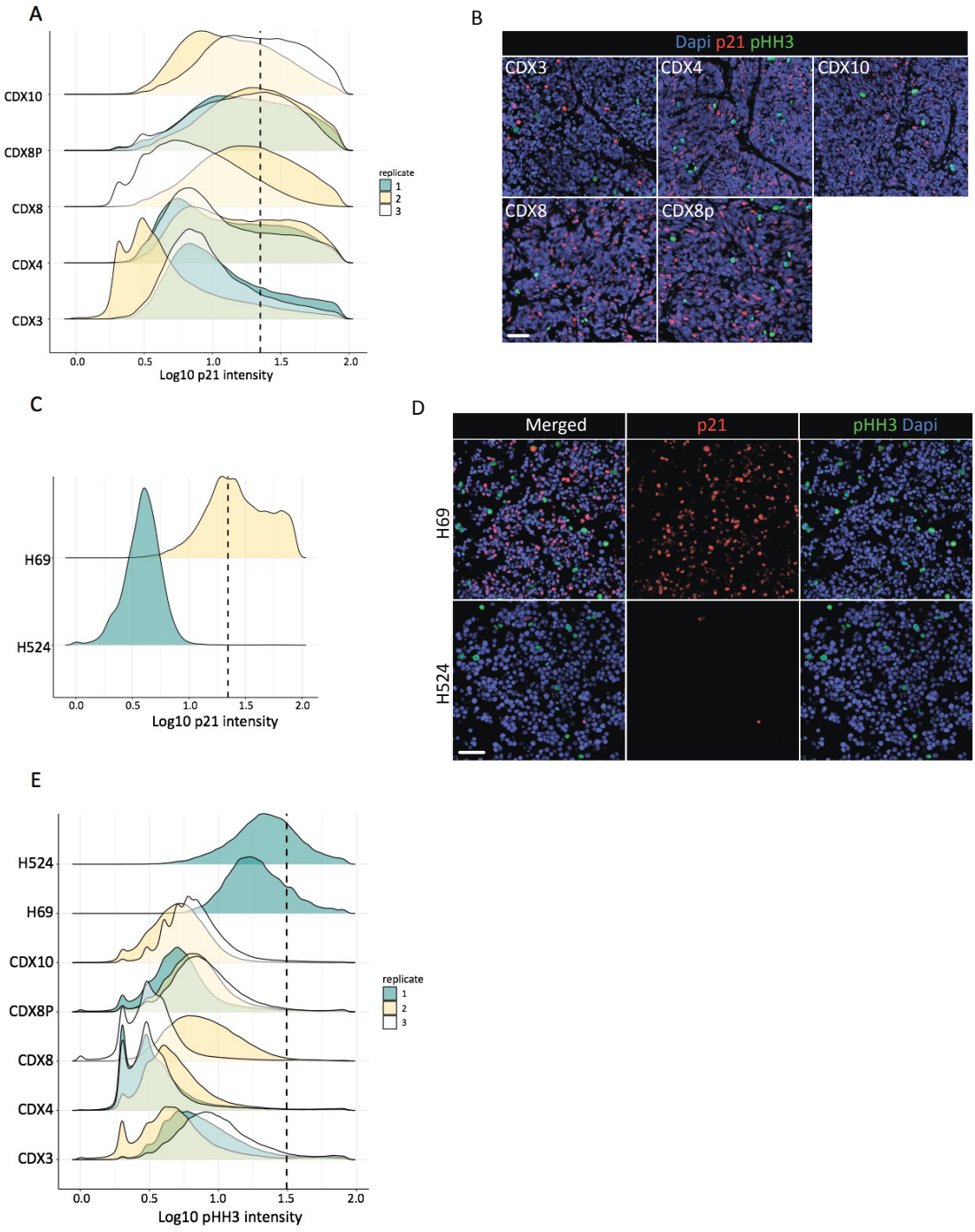

Figure 67. p21 and pHH3 expression in a small panel of CDX.

A. Distribution of p21 intensities in the selected CDX. The dotted black line demarcates the threshold to separate the positive from the negative population. Each distribution represent a biological replicate. B. Representative images of p21 and pHH3 staining on the selected CDX. Scale bar = 50 µm. C. Distribution of p21 intensities in the control cell lines. The dotted black line demarcates the threshold to separate the positive from the negative population. D. Representative images of p21 and pHH3 staining on the control cell lines. Scale bar = 50 µm. E. Distribution of pHH3 intensities in the selected CDX. The dotted black line demarcates the threshold to separate the positive from the

negative population (see Method for detail, chapter 2.10.1).

Figure 67A,C,E shows the distribution of p21 and pHH3 intensities in CDX3, CDX4, CDX8, CDX8p and CDX10, and the control cell lines. A representative image from each sample is shown in Figure 67B,C. Single channel images are shown in Appendix Figure 8. After having defined the percentage of p21 and pHH3 positive cells in each model, I used the percentage of positive cells as well as the average protein intensity level to assess if there was a correlation with the response to AZD1775/olaparib, *in vivo* and *ex vivo*.

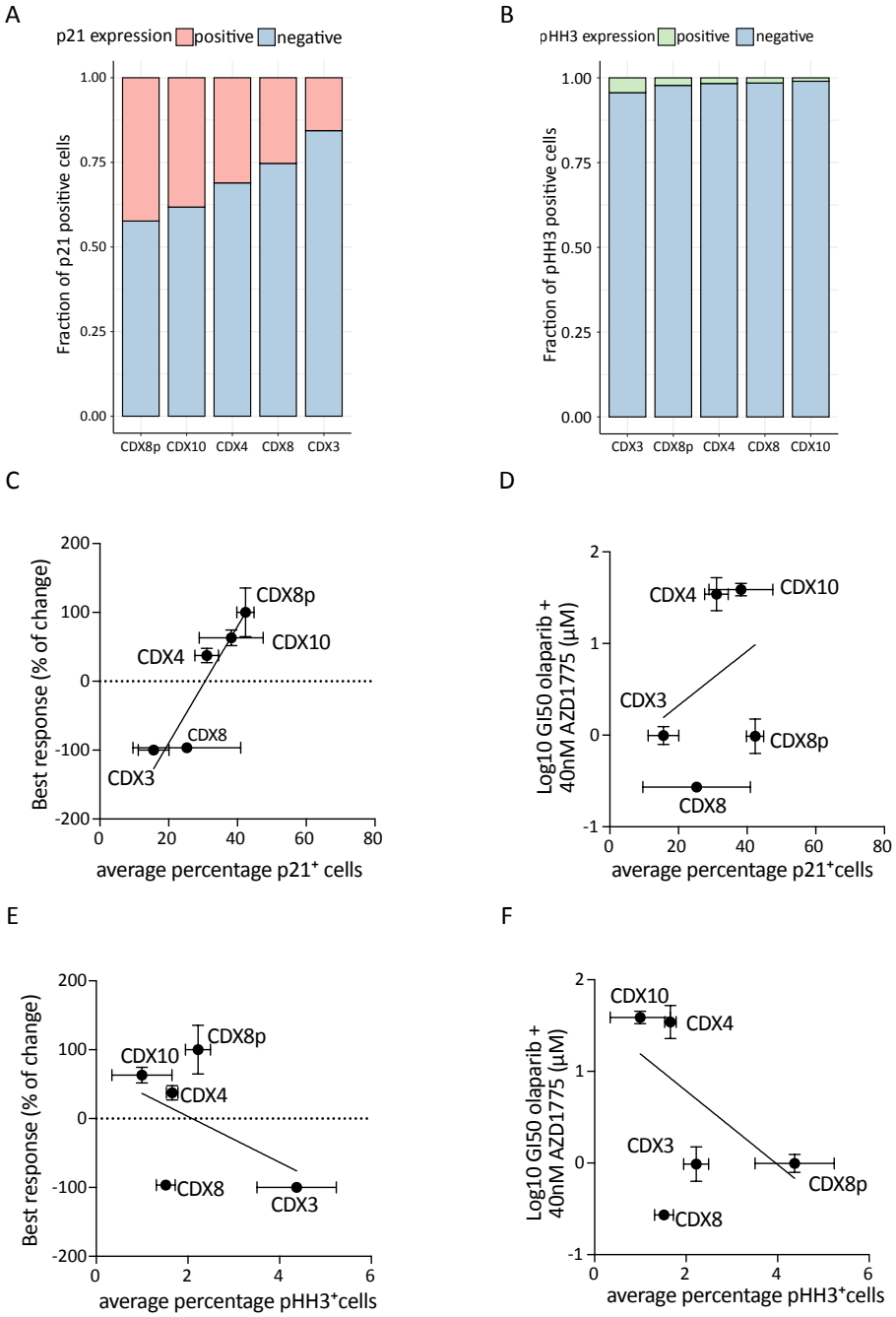

Figure 68. Percentage of p21 and pHH3 positive cells correlate with the response to AZD1775/olaparib.

A,B. Fraction of p21 (A) and pHH3 (B) positive and negative cells for each CDX tested. C,D. Linear modelling to correlate the best tumour response at day 21 *in vivo* (C) or the GI_{50} in response to olaparib with 40nM AZD1775 *ex vivo* (D) with the percentage of p21 positive cells. E,F. Linear modelling to correlate the best tumour response at day 21 *in vivo* (E) or the GI_{50} in response to olaparib with 40nM AZD1775 *ex vivo* (F) with the percentage of pHH3 positive cells.

In general, there was a trend towards increased p21 expression and a more resistant phenotype, while the inverse was observed for pHH3 (Figure 68A,B). There was a positive linear correlation when the percentage of p21 positive cells and the average p21 intensity for each model were plotted against the best response observed *in vivo* (R^2 = 0.65, *p*-value < 0.0001 and R^2 = 0.66, *p*-value < 0.0001, respectively) (Figure 68C, Figure 69A).

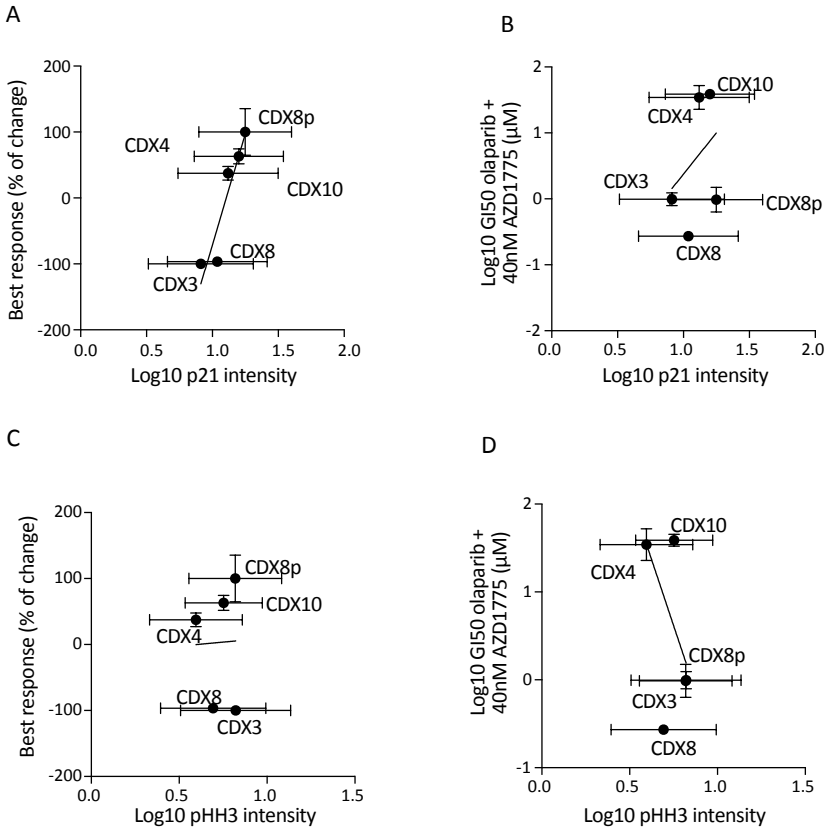

Figure 69. Correlation between the average p21 and pHH3 intensity and the response to AZD1775/olaparib.

A,B. Linear modelling to correlate the best response to AZD1775/olaparib *in vivo* (A) and the GI_{50} in response to olaparib plus 40nM of AZD1775 *ex vivo* (B) with the average p21 intensity. C,D. Linear modelling to correlate the best response to AZD1775/olaparib *in vivo* (C) and the GI_{50} in response to olaparib plus 40nM of AZD1775 *ex vivo* (D) with the average pHH3 intensity.

When compared with the *ex vivo* GI_{50} in response to olaparib/AZD1775, the trend was the same but because of the low GI_{50} of CDX8p compared with its resistant phenotype *in vivo*, the correlation was not statistically significant (R^2 = 0.13, *p*-value = 0.2 and R^2 = 0.15, *p*-value = 0.17 for p21 percentage and average intensity, respectively) (Figure 68D, Figure 69B). On the contrary, there was a statistically significant negative correlation between the GI_{50} and the percentage of cells positive for pHH3 (R^2 = 0.39, *p*-value = 0.017) or the average pHH3 intensity (R^2 = 0.39, *p*-value = 0.017) (Figure 68F, Figure 69D). When the percentage of pHH3 positive cells was compared with the best response observed *in vivo*, the negative correlation was maintained, but not with the average pHH3 intensity (R^2 = 0.15, *p*-value = 0.0081 and R^2 = 0.0005, *p*-value = 0.88, respectively) (Figure 68E, Figure 69C).

A

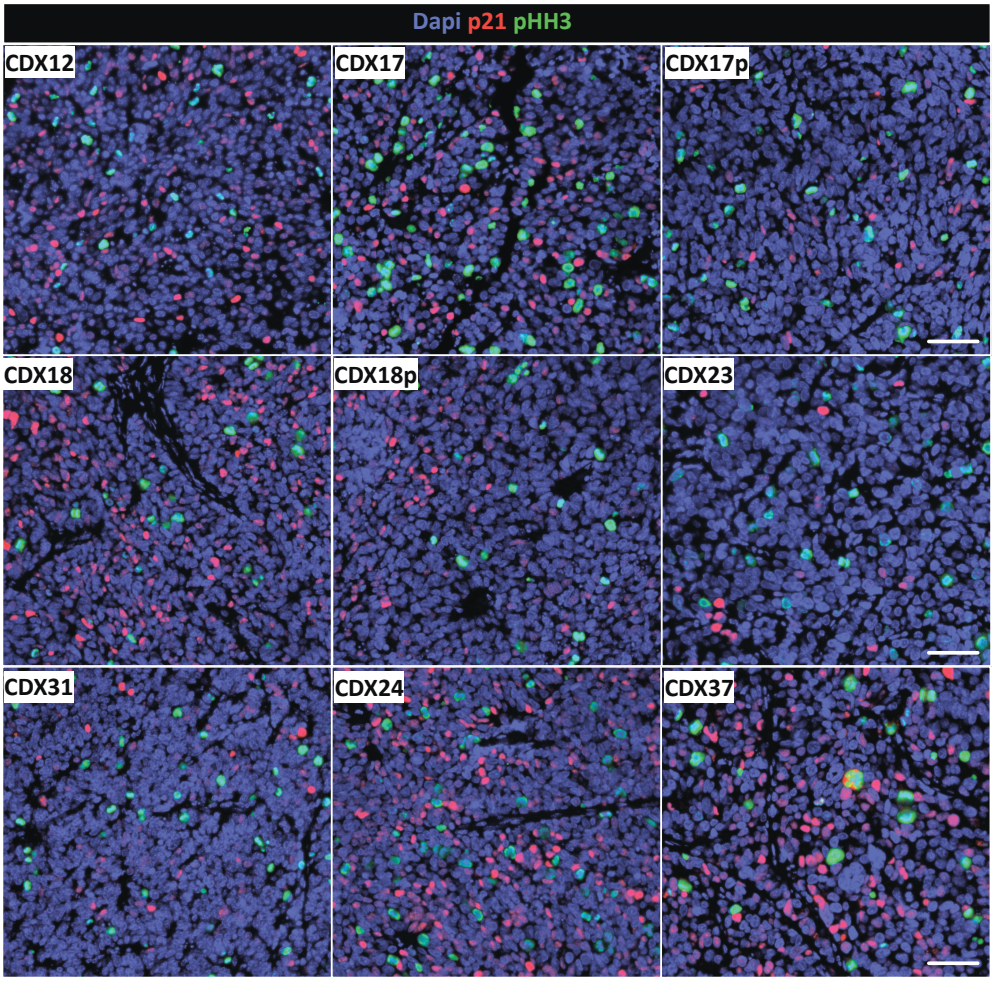

Figure 70. Expression of p21 and pHH3 in a panel of CDX.

A. Representative images of p21 and pHH3 staining on the stated CDX. Scale bar = 50 µm.

Despite the weak correlation between p21 expression and the response to olaparib and AZD1775 *ex vivo*, the presence of a positive trend, confirmed *in vivo*, suggested that higher expression of p21 could confer resistance to this drug combination. To test this hypothesis, I have expanded the panel of CDX tumours stained for both markers. The list of CDX used and the corresponding patient's clinical data are summarized in Table 14. Figure 70A shows representative images for each model. Single colour images are shown in Appendix Figure 8 and 8.1, while Appendix Figure 9 shows the distribution of intensity for each marker in all biological replicates tested. There was a heterogeneous expression of p21 in the models tested, with very high p21 expression in CDX12, CDX17, CDX24 and CDX37, with more than 50% of p21 positive cells in CDX24. The progression models CDX17p and CDX18p expressed lower level of p21 compared with the baseline model (CDX17, CDX18), suggesting that p21 expressing cell clones may have been negatively selected during EP treatment (Figure 71A). High levels of p21 were expected in models like CDX10 and CDX12, where p53 is not mutated and there is a high level of endogenous DNA damage, but it was surprising to see such a strong levels of p21 in several *TP53*/*RB1* deficient models. Phospho-histone H3 expression was limited to a small percentage of cells in all model tested (Figure 71B). The low percentage of cells positive for pHH3 in the CDX could be related to their high level of p21 and its role in cell cycle arrest (Abbas and Dutta, 2009). However, this was not true for all models. 2/8 CDX with the highest percentage of p21 positive cells, also had the highest percentage of pHH3 positive cells (e.g. CDX17 and CDX24), highlighting the possibility that p21 may have distinct roles in SCLC that are not always involved in cell cycle arrest. Moreover, it has to be considered that pHH3 staining is a static measure of a dynamic process, suggesting that distinct levels of pHH3 in the analysed samples may not results in statistically different tumour growth rates.

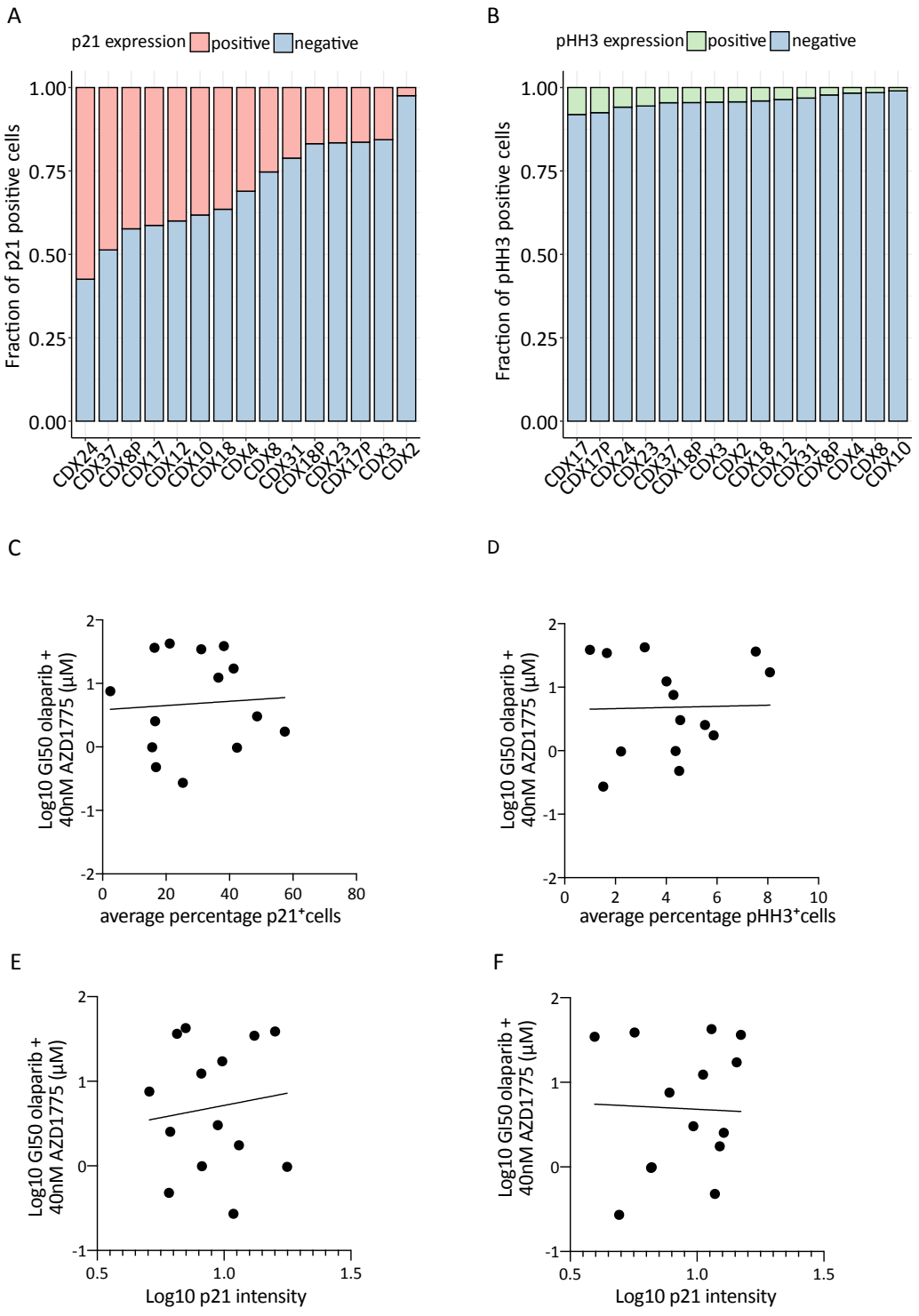

Figure 71. p21 intensity weakly correlates with response to AZD1775/olaparib *ex vivo.*

A,B. Fraction of p21 (A) and pHH3 (B) positive and negative cells for all CDX tested. C,D. Linear modelling to correlate GI_{50} in response to olaparib with 40nM AZD1775 *ex vivo* with the percentage of p21 (C) and pHH3 (D) positive cells. E,F. Linear modelling to correlate the GI_{50} in response to olaparib plus 40nM of AZD1775 *ex vivo* with the average intensity of p21 (E) and pHH3 (F).

To assess whether p21 expression had a role in the *ex vivo* response to AZD1775/olaparib, I correlated GI_{50} in response to olaparib/AZD1775 with the percentage of p21 positive cells in each model. Contrary to what has been observed previously, neither p21 nor pHH3 correlated with the response to this combination *ex vivo* (R^2 = 0.002, *p*-value = 0.75 and R^2 = 0.0003, *p*-value = 0.91 for p21 and pHH3 respectively) (Figure 71C,D). When I looked at the average intensity of p21, a very weak trend was observed. This trend was similar to that observed before, with higher expression of p21 associated with a worse response to this treatment, however this was not the case for every model (Figure 71E, R^2 = 0.006, *p*-value = 0.6). No correlation was observed with the average intensity of pHH3 (Figure 71F, R^2 = 0.0005, *p*-value = 0.9). These data suggest that high p21 may correlate with response to AZD1775/olaparib and/or may play a role in the response to these drugs in only a subset of CDX.

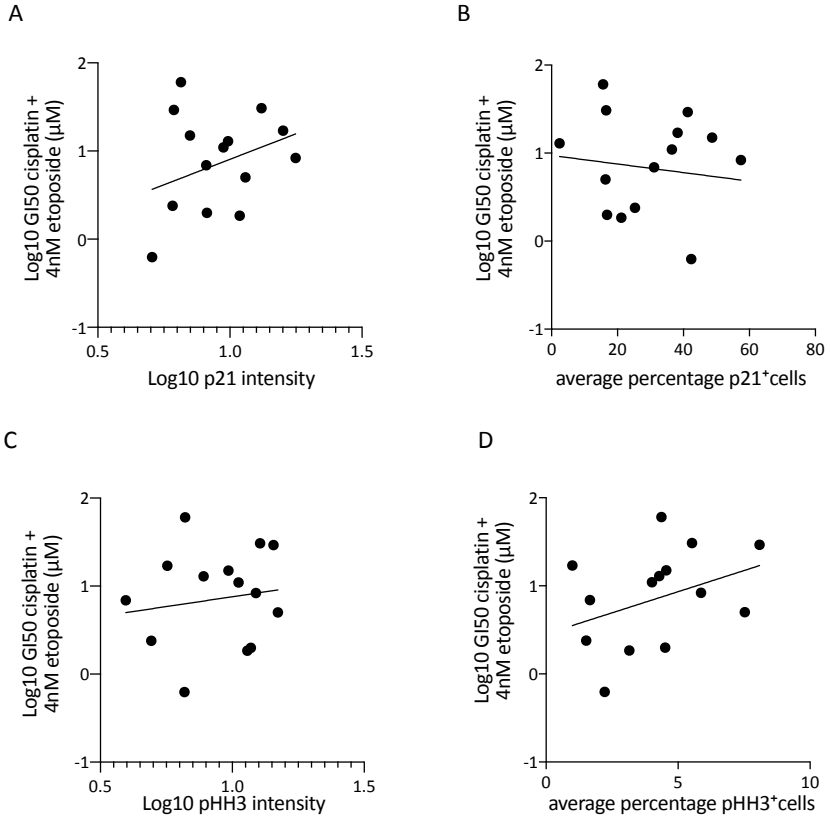

Figure 72. p21 correlates with the response to cisplatin/etoposide *ex vivo.*

A,B. Linear modelling to correlate GI_{50} in response to cisplatin with 4nM etoposide *ex vivo* with the average p21 intensity (A) and the percentage of p21 (B) positive cells. A,B. Linear modelling to correlate GI_{50} in response to cisplatin with 4nM etoposide *ex vivo* with the average pHH3 intensity (A) and the percentage of pHH3 (B) positive cells.

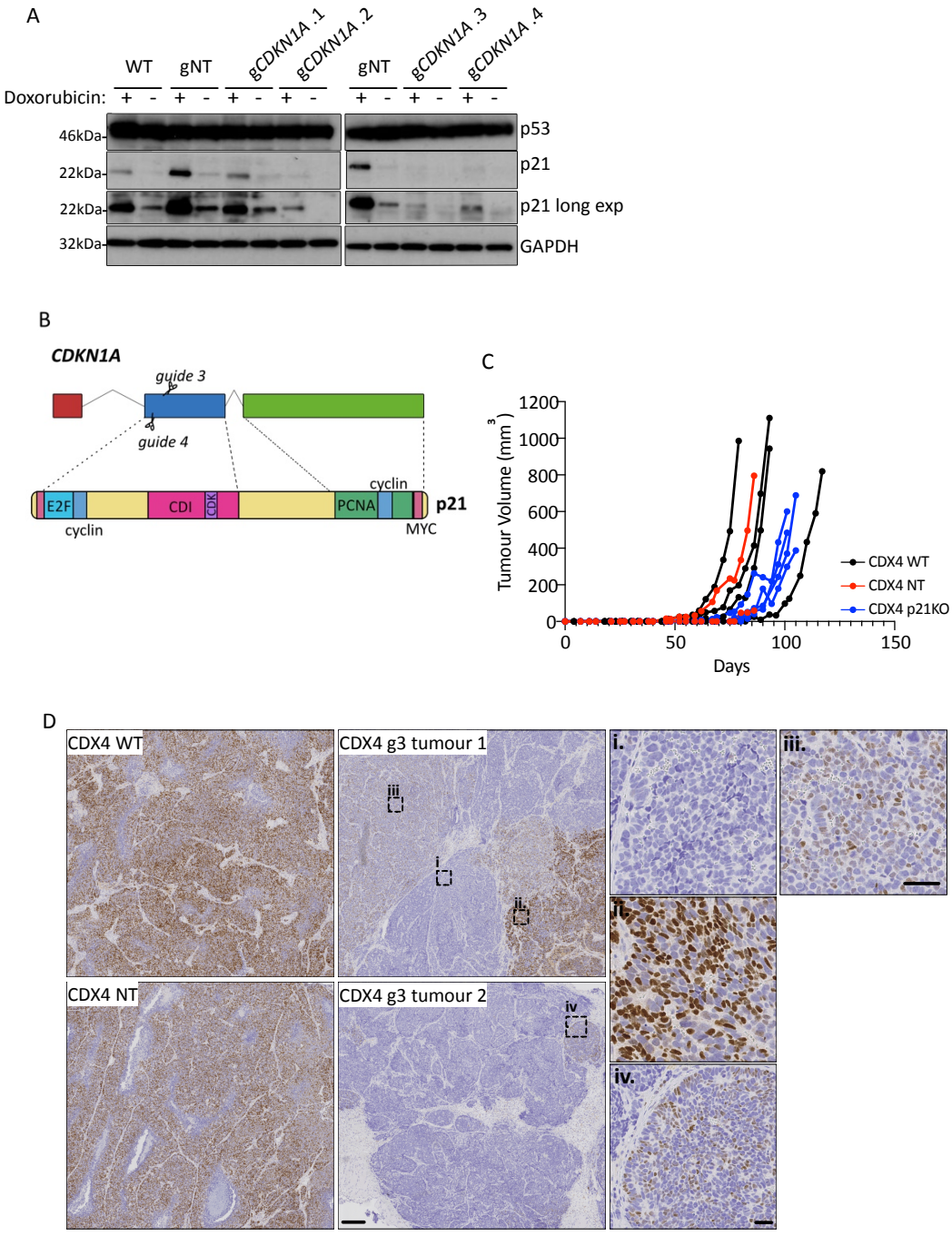

Figure 73. Knock-out of *CDKN1A* in CDX4.

A. Immunoblot showing the expression of p53 and p21 on protein cell lysates from transduced Lenti-X™ 293T treated with or without 1 µM of doxorubicin. GAPDH was used as loading control. B. Schematic of *CDKN1A* gene and p21 protein, highlighting p21 interaction domains. C. CDX4 tumour WT (black lines), infected with *CDKN1A* CRISPR guides (blue lines) or infected with a NT guide (red lines) were subcutaneously implanted into NSG mice. Each line represents an individual tumour. D. Immunohistochemistry for p21 level in CDX4 tumours WT, infected with the NT virus or infected with guide 3 (g3). Dotted squares delineate the region highlighted on the right hand side of the figure. Scale bar for the low magnification images is 250 µm, while for the high magnification images is 50 µm. gNT:

guide non-targeting, g*CDKN1A*: guide against *CDKN1A*; p21KO: tumours infected with g*CDKN1A*.3 and g*CDKN1A*.4; g3: g*CDKN1A*.3.

Because of the differences in p21 expression observed between three paired models (CDX8/CDX8p, CDX17/CDX17p and CDX18/CDX18p), I wanted to determine whether there was any correlation with response to cisplatin/etoposide *ex vivo*. There was a slightly stronger positive correlation, where models responding less well to cisplatin/etoposide, expressed higher levels of p21 (R^2 = 0.05, *p*-value = 0.12, Figure 72A). The correlation was completely lost when the percentage of p21 positive cells was considered (R^2 = 0.008, *p*-value = 0.52, Figure 72B). There was no correlation with pHH3 average expression (R^2 = 0.01, *p*-value = 0.5), although, when looking at the percentage of pHH3 positive cells, there was a trend towards a positive correlation (Figure 72C,D**,** R^2 = 0.07, *p*-value = 0.08).

Despite the lack of correlation with p21 expression and the response to different treatments, I was intrigued by the relatively high level of this protein in several *TP53*/*RB1* mutant CDX. Considering the multiple roles p21 can have in promoting or suppressing tumour growth (Abbas and Dutta, 2009; Georgakilas et al., 2017), I wanted to assess the role of this protein in SCLC utilising CRISPR-Cas9 gene editing (Cong et al., 2013). I lentivirally transduced 293T cells with *CDKN1A* or a non-targeting (NT) guide and the cells were treated with or without 1 µM of doxorubicin for 24hr in order to induce the expression of p21. Guide 3 and 4 generated a better knock-out and therefore were selected to transduce CDX4 cultures (Figure 73A). Both guides targeted exon 2, thus potentially destroying the interaction domains with E2F, cyclins and CDKs (Figure 73B). CDX4 cells were transduced with lentivirus containing the two guides and the NT control. Puromycin-resistant CDX4 cells were subsequently implanted in mice to facilitate cell expansion. CDX4 tumours infected with guides against *CDKN1A* showed a delay in tumour establishment compared with the NT control and WT CDX4 tumours (Figure 73C). Due to the heterogeneity observed in the growth of the WT CDX4 tumours, it was not possible to determine whether the growth rates of the p21 knock-out and the NT control tumours were significantly different. However, if replicated, these data could suggest that p21 plays an oncogenic role in CDX4. Once the tumours reached size, p21 levels were assessed by IHC. Despite the clear lack of p21 in large regions of the tumours, there were some

clones of cells strongly expressing p21 (Figure 73D, Appendix Figure 10A). It is possible that the delay in tumour growth observed in the presence of the knock-out was linked to the time needed for these p21 positive clones to establish in the knock-out population. There were insufficient cells to examine p21 expression in CDX4 cultures before implantation in mice. It is therefore difficult to determine whether the p21 positive cells were pre-existent in the implanted cell population, or if some *CDKN1A* knock-out cells found a way to bypass the mutations induced at exon 2. It is also possible that the mutations induced by the CRISPR system did not result in a deleterious frameshift. Further optimisation of the knock-out and sequencing of the infected CDX4 tumours was not possible because of time constraints, however it would be of real interest to understand whether p21 has a role in the development and/or response to SoC in a subpopulation of SCLC patients.

5.3 Conclusions

In this chapter I sought to identify mechanisms and candidate biomarkers to predict response to AZD1775/olaparib combination. RAD51 focus formation has been extensively validated in the literature as a predictive biomarker to olaparib response (Naipal et al., 2014). This assay was able to predict the response to olaparib in 3 out of 4 models tested and to the combination in 2 out of 4 CDX. More CDX should be tested to reinforce the predictive potential of RAD51 as biomarker of response to AZD1775/olaparib. It is foreseeable that a combination of RAD51 foci with other biomarkers will be needed to improve the predictive potential of RAD51 foci. One of the advantages of RAD51 foci formation is that this assay can be 'easily' translated in the clinical setting. CTCs collected from SCLC patients could be irradiated and subsequently stained to assess their RAD51 status. Moreover, recent publications have demonstrated that RAD51 foci can be detected on FFPE tissue (Castroviejo-Bermejo et al., 2018; Cruz et al., 2018). They showed that RAD51 foci can be observed on baseline samples of breast cancer tumours, without the need of prior induction of DNA damage, and their presence correlated with the response to PARP inhibitors. These data highlight the potential of using baseline patient samples to directly test tumour HR status. It would be of interest to test whether this is true also for SCLC

patients. The information obtained from the ongoing clinical trials testing different PARP inhibitors in SCLC patients could be used for this purpose.

The lack of expression of RAD51 in CDX2 was in contrast with its olaparib-resistant phenotype. I was unable to find reports in the literature showing that other HR deficient models can be resistant to PARP inhibition. Moreover, the sensitivity to irradiation observed with CDX2 and its reduced ability to resolved DSBs, further suggests that this model has a defect in repairing DNA. *BRCA*-deficient tumours can acquire resistance to olaparib by overexpressing drug efflux transporters such as the MDR1/P-gp (Rottenberg et al., 2008), so it would be interesting to assess if high level of these transporters in CDX2 can explain the lack of response to olaparib *ex vivo*.

HR deficiency was confirmed in CDX3, with the deleterious mutation observed on *PALB2*, however no obvious alterations in genes involved in the HR pathway were found in CDX2. The lack of correlation with the HRD genomic scars described by Lok *et al* and the weak expression of most of the genes selected in Peng's signature suggest that in the CDX, the response to PARP inhibitors may not always be linked to HR deficiency (Lok et al., 2017; Peng et al., 2014). To confirm this hypothesis, the results from the randomized, double-blind, phase 3 trial in advanced ovarian cancer patients treated with the PARP inhibitor niraparib after first-line platinum-based chemotherapy, demonstrated that response to niraparib was independent of patient HR status (González-Martín et al., 2019). These data highlight the need to increase the panel of candidate biomarkers in response to olaparib.

Another way to study the ability of a tumour to deal with DNA damage is via the comet assay. Although this assay may be more difficult to translate in the clinic, the small number of cells required make it feasible for CTCs analysis. Development of *ex vivo* CTC cultures is currently ongoing in our group and could be used to expand the CTCs sufficiently to allow testing of multiple conditions. From my pilot experiments on the CDX, CDX2 and CDX3 were less efficient in repairing the damaged DNA compared with CDX8, CDX4 and CDX8p. This is particularly interesting considering the lack of RAD51 focus formation and the sustained γH2AX foci 24hr after irradiation in CDX2 and CDX3. On the contrary, the quick response observed in CDX8 suggests that this model is particularly efficient at repairing DSB and may explain why CDX8 does not respond to olaparib monotherapy *in vivo*. In contrast with these results,

CDX8 cultures seemed sensitive to irradiation, albeit the wide error bars suggested an heterogenous response to this treatment.

While DNA damage repair efficiency may better predict the response to olaparib, the response to WEE1 inhibition can be directly related to the ability of tumour cells to tolerate replication stress. Several of the alterations commonly found in SCLC can interfere with the replication machinery, therefore the increased replication stress imposed by WEE1 inhibition could be lethal (Thomas and Pommier, 2016).

CDX3, the most AZD1775 sensitive model, showed high intrinsic level of replication stress, not observed in CDX8. Single agent activity of AZD1775 on CDX8 was not as effective as in CDX3, however CDX8 responded very well to the combination. This indicates that the presence of intrinsic replication stress could be predictive of the response to AZD1775 monotherapies, but is not enough to anticipate the response to the combination. Despite the lack of response of CDX8 to both monotherapies, the strong effect observed with the combination suggests that something should be defective in this model compared with the resistant CDX8p. Induction of replication catastrophe after treatment with AZD1775/olaparib or the ability of AZD1775 to impair HR could be a possible explanations for the synergy observed *in vivo* in CDX8. Assessment of replication catastrophe can be performed by looking at the accumulation of chromatin-bound RPA and γH2AX in the nuclei of the cells. The results I have described here, suggest that treatment with AZD1775 can induce replication catastrophe in 2/3 models partly contributing to its cytotoxicity. Additional experiments should be performed to properly define the role replication catastrophe has in the response to these drugs. These should particularly focus on studying the accumulation of chromatin-bound RPA and γH2AX after treatment with AZD1775 and olaparib alone or in combination, in a panel of CDX.

The fiber assay can also be used to determine the role of replication in response to AZD1775/olaparib in the CDX models. In this chapter, I have shown that it is possible to label CDX cultures with IdU and CldU and identify DNA fibers. However, the assay still requires further optimisation. The quality of the fibers is frequently reduced by a non-homogenous spread of the fibers on the coverslip. To overcome this problem, the DNA combing assay has been developed. This assay exploit a mechanical device that can comb the DNA onto coverslips at a controlled constant

speed (Quinet et al., 2017; Técher et al., 2013). This allows a proper deposition of DNA fibers on the coverslip, reducing fibers overlap and facilitating the downstream analysis. Another obstacle observed in my pilot study was the very low percentage of replicating cells observed in most CDX cultures. One way to overcome this issue could be to synchronise the cells to enrich for S-phase cells. CDX cells grow in low serum conditions, therefore serum starvation cannot be used for synchronisation. Moreover, the lack of p53 and RB functions are likely to render these tumours insensitive to G1 synchronization with CDK inhibitors. Treatment with nocodazole or induction of thymidine blocks have been successfully exploited to stop the cells in G2/M and G1/S (Harper, 2005), and could be tested on the CDX cultures. The ability to synchronise the cells could also be exploited to properly characterise the cell cycle profile of each model and their ability to progress through the different phases of the cell cycle. Indeed, differences in cell cycle progression could explain the diverse responses to AZD1775/olaparib observed across the CDX *ex vivo.*

Another candidate biomarker tested was p21. p21 roles as a tumour suppressor or an oncogene have been controversial suggesting that it can act differently based on specific background and stimuli. However, p21 expression in the absence of p53 appeared to have more of an oncogenic rather than a tumour suppressive role, suggesting that this may also be the case in SCLC (Abbas and Dutta, 2009; Georgakilas et al., 2017). In the models tested, p21 was higher in two baseline CDX compared with the corresponding progression pairs: CDX18 *vs* CDX18p and CDX17 *vs* CDX17p. This data suggested that expression of p21 was not necessary for the survival of the tumour after first-line treatment. Expression of p21 in a p53-null background has been shown to induce genomic instability and allow the cells to acquire a more aggressive and resistant phenotype (Galanos et al., 2016). It is possible that in tumours with high level of p21 at baseline, p21 plays a role in the establishment of the tumour but became superfluous at later stages, explaining why p21 levels were reduced after treatment in patient 17 and 18. The same could have been true for the chemoresistant model, CDX4. In the pilot study I have performed, *CDKN1A* knock-out in CDX4 cells caused a delay in the establishment of the tumour *in vivo*, suggesting that p21 may be necessary for the early stages of CDX4 development. On the other hand, some tumours may acquire p21 expressing cells as a mechanism of resistance

to EP treatment. This may have been the case for patient 8, whose tumours expressed more p21 at relapse (CDX8p) than before treatment (CDX8). It has been demonstrated that p21 can inhibit apoptosis induced by genotoxic agents (Abbas and Dutta, 2009), and therefore could be exploited by the cells to survive the treatment. Both hypotheses suggest that p21 could have an oncogenic role in SCLC, either by promoting tumour development or resistance to cytotoxic stress. If the above hypotheses are confirmed, assessment of p21 expression on biopsy or CTCs could be used to identify SCLC patients with a reduced chance to respond to EP treatment. Moreover, if p21 can be acquired during treatment, it could be possible to use the emergence of p21 positive CTCs during follow-up sampling as a biomarker of tumour progression.

Within this chapter I wanted to overview several candidate biomarkers and assays that could be used to understand and predict the response to AZD1775/olaparib in SCLC. The challenges encountered during the optimization of these assays were substantial. For most of the described assays, the small number of biological replicates and the limited number of models investigated make it difficult to properly determine whether any of the assays tested could accurately be used to predict the response to this combination. Moreover, the strong heterogeneity of the CDX compared with established cell lines partly contributed to these difficulties. Several of the biomarkers tested in this chapter have been validated on common cell lines and eventually on a few PDX. CDX are derived from a population of cells that has acquired the ability to survive in the circulation. These cells recapitulate the more advanced stages of SCLC and therefore they better mimic the situation observed in the patients enrolled in second or third line clinical trials. This feature of the CDX compared with PDX and SCLC cell lines, may partly explain the inability to identify common biomarkers of response to these treatments. However, considering that most alternative therapies are administered to ES SCLC patients, it becomes even more important to exploit large panel of CDX to identify and validate biomarkers of response that could be effective in this advanced setting.

Chapter 6: Efficacy of multiple DNA damage response inhibitors in SCLC CDX and identification of putative biomarkers of response

6.1 Introduction

Genomic instability is a hallmarks of SCLC (Thomas and Pommier, 2016). The universal loss of *TP53* and *RB1*, together with the acquisition of oncogenes like C-MYC create a perfect storm in which genomic instability and replication stress 'nourish' each other (Figure 10). Our group showed that treatment with PARP and WEE1 inhibitors can be synergistic in some SCLC CDX, such as CDX3 and CDX8, however not all models regressed after treatment. The complexity and redundancy of the DNA repair network suggests that compensatory pathways can be activated when WEE1 and PARP are inhibited. Depending on the molecular background of each tumour, distinct mechanisms can be activated to allow cells to survive in the presence of these drugs. Combinations of different DDR inhibitors (DDRi) could be used to bypass these resistances. In collaboration with AstraZeneca, we initiated a preclinical *in vivo* and *ex vivo* study (termed, Decapus study) to test the effect of several DDRi alone or in combination with olaparib in order to assess the response in our CDX. The response data will be combined with whole-exome sequencing and transcriptomics CDX data to help identify biomarkers of response. *In vivo* efficacy studies are ongoing at the time of writing this thesis, therefore these data will be not discussed. My contribution to the Decapus study was to assess the *ex vivo* responses of a panel of CDX to these drugs as single agents and in selected combinations. As soon as the tumour responses will be available, they could be correlated with the *ex vivo* responses described below to further validate my results.

The Decapus study consists in testing the activity of the WEE1 inhibitor AZD1775, the ATR inhibitor AZD6738, the Aurora Kinase B inhibitor AZD2811, and the DNA-dependent protein kinase catalytic subunit (DNA-PKcs) inhibitor, AZD7648 either alone or in combination with the PARP inhibitor olaparib. In addition to a variety of preclinical data suggesting these inhibitors may work in combination with olaparib (Fang et al., 2019; Fok et al., 2019; Kim et al., 2017; Murai et al., 2016; Parsels et al., 2018; Pilié et al., 2019), PARP inhibitors are the most clinically advanced of these

compounds and therefore the most likely to be tested in combinations in the short term (Pilié et al., 2019). Additionally, we are examining the combination of the ATR inhibitor together with the Aurora Kinase B inhibitor. Figure 74 summarises the main role each drug target has on DNA damage and cell cycle regulation.

A

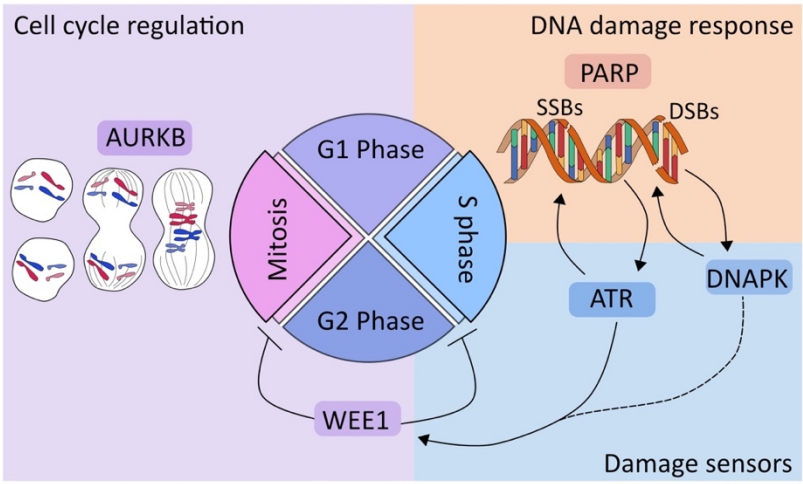

Figure 74. Roles of the different DDR targets.

A. PARP is primarily involved in the recognition of SSBs and regulates the recruitment of multiple DNA repair proteins. DNAPK and ATR are damage sensors. They both recognise different types of DNA damage and activate specific downstream pathways. DNAPK is activated by DSBs and promotes the NHEJ, while ATR can orchestrate several signalling promoting DNA repair and cell cycle arrest. In specific situation, DNAPK can compensate for ATR lack of function. WEE1 regulates cell cycle progression at the level of both S and G2 phases. AURKB plays a role in the proper organisation of chromosomes during mitosis.

PARP and WEE1 have already been extensively described previously. DNA-PKcs is part of the family of phosphoinositide 3-kinase (PI3K)-related kinases (PIKKs), that also includes the ataxia telangiectasia mutated (ATM) and ATR proteins. All three molecules have a distinct and overlapping role in DDR (Blackford and Jackson, 2017). DNA-PK is recruited to DSBs by Ku80 where its main role is to promote the non-homologous end-joining pathway (NHEJ). DNA-PK promotes DNA-end tethering and recruits the endonuclease Artemis to facilitate DNA-end processing, both important steps in NHEJ. Moreover, it has been shown that DNA-PK can activate the stress response pathway by phosphorylating CHK1 in the absence of ATR (Buisson et al., 2015). ATR is activated by the formation of large tracts of ssDNA coated with RPA, therefore ATR is involved in both DNA damage and replication stress response. One of the main activities of ATR is to delay cell cycle progression by phosphorylating and activating CHK1 that in turn inhibits CDKs (Smith et al., 2010). ATR-dependent

inhibition of CDKs is also important to prevent the firing of replication origins in order to avoid exhaustion of replication and repair factors (Toledo et al., 2013), as well as re-replication of origins (Liu et al., 2007) (Figure 7). Moreover, ATR also stimulates RRM2 to increase deoxynucleotide levels during early S-phase and avoid dNTP depletion (Buisson et al., 2015). Aurora kinase B is essential for a number of processes during mitosis. This protein regulates chromosomal condensation, kinetochore function, cytokinesis and the spindle assembly checkpoints. Its activity is enhanced by the co-factors INCENP and survivin (or BIRC5) and dysregulation of this kinase can lead to aneuploidy (Figure 7) (Carmena and Earnshaw, 2003).

All of these proteins work as DDR checkpoints and their inhibition leads to DNA damage accumulation, replication stress and chromosomal aberrations. When combined with PARP inhibition, the loss of any of these checkpoints can have deleterious effects on cell survival. Inhibition of these proteins in tumours that lack functional p53 and RB activities results in intrinsic DNA damage, replication stress and mitotic abnormalities. In particular, replication stress induced by ATR inhibition can degenerate into DNA damage that, in the absence of PARP, will not be repaired efficiently, pushing the cells to accumulate damage and eventually undergo apoptosis. Moreover, PARP-resistance induced by inactivation of SLFN11 can be overcome by ATR inhibition, suggesting that the combination of these two drugs can delay tumour progression compared with single agent treatments (Murai et al., 2016). When Aurora kinase B is inhibited, the accumulation of chromosomal aberrations during mitosis will not be controlled by p53 and RB in G1 and the cells will proceed into S phase where these aberrations can interfere with DNA replication and generate genomic instability. The absence of PARP will impair the repair of these lesions and increase the cytotoxic effect of the Aurora kinase B inhibitor. The combination of olaparib with the DNA-PKcs inhibitor works slightly differently, where both drugs reduce the ability of the cells to repair DNA lesions. In particular, PARP is primarily involved in SSB repair, while DNA-PKcs regulates DSB repair via the NHEJ pathway. Inhibition of both proteins should sensitise the cells to a wider range of DNA lesions. Finally, the rational of combining the Aurora kinase B inhibitor with the ATR inhibitor relies on the fact that when both ATR and Aurora kinase B are lost, the cells undergo mitosis despite the presence of replication errors. This will lead to mitotic

catastrophe and subsequent cell death. PARP, ATR as well as Aurora kinases inhibitors have already been tested in SCLC, with some promising preclinical results (Byers et al., 2012; Cardnell et al., 2013; Doerr et al., 2017; Gong et al., 2019; Mollaoglu et al., 2017; Nagel et al., 2019; Oser et al., 2019; Sen et al., 2017a; Sos et al., 2012) (see Table 2). Based on these data and on our preliminary results obtained with AZD1775/olaparib treatment *in vivo*, we designed Decapus to examine the response of 40 of our CDX to these DDRi.

6.2 Results

The *ex vivo* response to AZD1775 (WEE1i) in combination with olaparib (PARPi) was already described in chapter 4. Here, I report the results obtained combining:

vii. AZD6738 (ATRi) with olaparib or AZD2811 (AURKBi)

viii. AZD2811 (AURKBi) with olaparib

ix. AZD7648 (DNAPKi) with olaparib

To be able to directly compare the CDX response to AZD1775 with the response to the other DDR inhibitors, I have used the same range of concentrations (from 0 to 4 µM) used for AZD1775 in the mid-throughput screen. For simplicity the abbreviations stated above will be used instead of the drug name to describe the results.

6.2.1 CDX models showed heterogenous responses to single agent treatment with DDR inhibitors.

Analysis of the single agent activity of the ATRi, DNAPKi and AURKBi, in comparison with the effect of the WEE1i showed that inhibition of WEE1 and Aurora kinase B were generally more effective than the other inhibitors (Figure 75A).

DNA-PK inhibition seemed to have the weakest effect as shown by the shift on the right of the response curves. This was expected, as DNA-PK is involved in the repair of DSB and in the absence of DNA breakage, inhibition of DNA-PK should not be too toxic for the cells. Based on the GI_{50} values, CDX23, CDX29, CDX17 and CDX10 were the less sensitive to AURKBi (Figure 75B). CDX17 and CDX29 overexpresses L-MYC and N-MYC, respectively (Figure 55G), confirming previous studies that suggested that inhibition of Aurora kinase B is not synergistic in L-MYC and N-MYC expressing tumours (Helfrich et al., 2016; Sos et al., 2012). AURKBi is, however,

synergistic with C-MYC overexpression or loss of RB in SCLC models (Helfrich et al., 2016; Mollaoglu et al., 2017; Oser et al., 2019; Sos et al., 2012). Of note, the CDX17 paired progression model, CDX17p, overexpressed C-MYC (Figure 55G) and was more sensitive to AURKBi than CDX17.

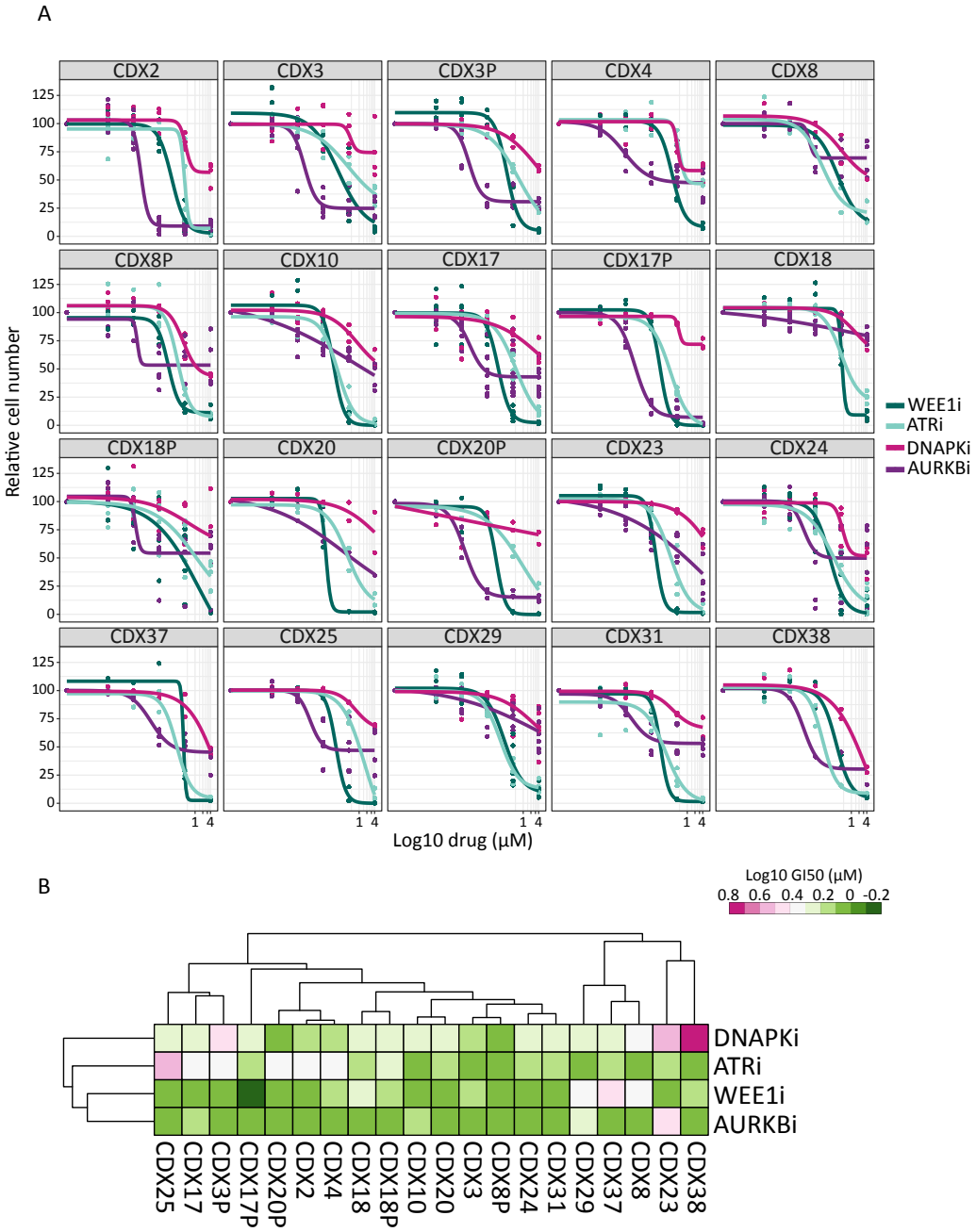

Figure 75. Single agent activity of multiple DDRi on a panel of CDX cultures.

A. Dose-response curves for all CDX models treated for 7 days with increasing concentration of WEE1i (dark blue), ATRi (light blue), DNAPKi (light pink) or AURKBi (dark pink). Each dot represent a biological replicate. Dose-response curves have been fitted with the 4-parametric log-logistic function in the drc package (Ritz et al., 2015), combining the data from all biological replicates tested. Replicates with values > 0.99 quantiles were considered outliers and removed from the analysis. B. Unsupervised hierarchical clustering of log10 GI_{50} obtained from the panel of CDX cultures treated with increasing

concentrations of each drug. WEE1i = AZD1775; ATRi = AZD6738; DNAPKi = AZD7648; AURKBi = AZD2811.

RB loss is almost universal in SCLC and was not expressed in the CDX tested, with the exception of CDX23 and CDX24. CDX23 is one of the most resistant models to this drug suggesting that the reduced effect could be due to a functional RB protein (Figure 76A). At the time of writing, it was not known whether RB in CDX23 and CDX24 was WT and functional, making it difficult to correlate with the observed response.

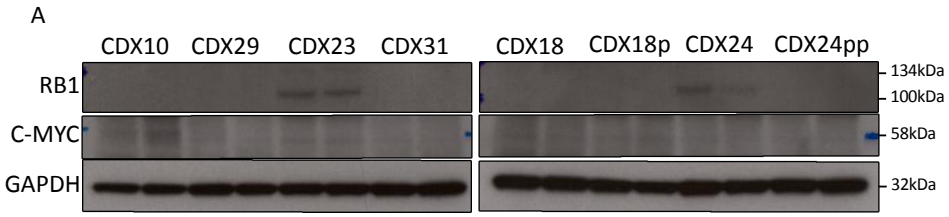

Figure 76. RB protein expression does not always correlate with response to AURKBi.

A. Immunoblot analysis of CDX tumour lysates for the indicated proteins. Each line is a biological replicate. GAPDH was used as loading control.

Although ATR and WEE1 inhibition have a similar effect on the regulation of CDK activity and replication, their effects on DNA damage and cell death have been shown to be different (Young et al., 2019), partly explaining why CDX response to the ATRi was less pronounced than the WEE1i. Models like CDX25, CDX20p, CDX4, CDX2, CDX17 and CDX3p were more resistant to ATR inhibition than the other CDX (Figure 75B), suggesting that these models may be able to bypass ATR loss through activation of complementary pathways (Buisson et al., 2015).

Some of the paired models tested showed a differential response to these inhibitors. CDX3 was more sensitive than CDX3p to ATR and DNA-PK inhibition (Figure 75B), possibly indicating that clones with a better ability to deal with DSB breaks and replication stress were selected during EP treatment. On the contrary, CDX17p appeared to be more responsive to several DDRi compared with CDX17, in particular in response to ATR and WEE1 inhibition. It is appealing to posit that while selection of C-MYC positive clones during first-line therapy has allowed this tumour to adapt and relapse, it may have also led to an increased production of ROS and replication stress, explaining the stronger sensitivity of CDX17p to DDRi. Despite some level of heterogeneity in the response to these DDRi in the CDX, the observation that every

model was responsive to at least two of these inhibitors reinforces the idea that SCLC are dependent on the DNA damage response pathways to survive.

6.2.2 DDR inhibitors synergised with olaparib in the CDX

Afterwards, I determined whether combinations of these DDRi could further improve the observed responses. In almost all tested combinations, high concentrations (≥ 400nM) of the DDRi were highly cytotoxic, suggesting that when used in combination the concentration of these inhibitors should be lowered (Figure 77 and 78). Based on this observation, I focused the analysis on the concentrations that ranged from 0-40 nM or 0-80 nM for the combinations that did not include the AURKBi, while for the AURKBi, I have focused on concentrations ranging from 0 to 4 nM.

As for olaparib and WEE1i, I have divided each combination to evaluate the ability of olaparib to sensitise the cells to the DDRi tested (left hand side of Figure 77 and 78) and to assess if the addiction of any DDRi was able to improve the effect generated by olaparib treatment (right hand side of Figure 77 and 78). Overall, olaparib did not improve significantly the response observed with ATRi and AURKBi single agents (Figure 77A, 78A), however 80 nM treatment with olaparib increased the cytotoxic effect induced by DNAPKi in 9/20 CDX (e.g. CDX37, CDX3p, CDX8, CDX20 and CDX29, Figure 77C). ATRi or DNAPKi enhanced olaparib cytotoxicity only in 4/20 CDX (e.g. CDX20), further highlighting the need to identify biomarkers of response (Figure 77B,D). Of note, 4 nM of the AURKBi synergised with olaparib and improved the response to this drug in almost all olaparib-resistant CDX (Figure 78B). In particular, addition of the AURKBi to olaparib treatment was effective in CDX20 and CDX24 where only 0.4 nM AURKBi reduced cell viability compared to olaparib monotherapy.

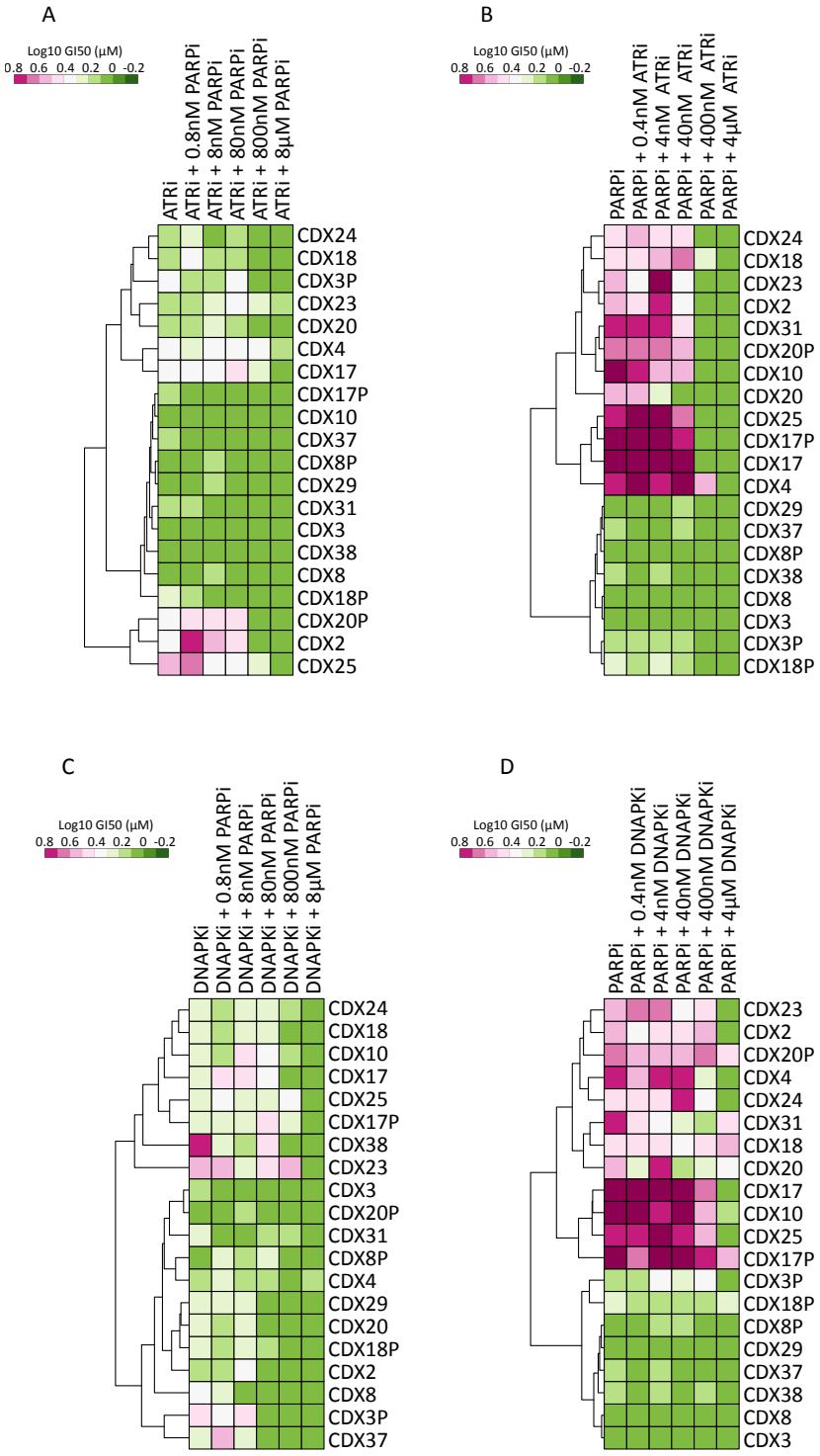

Figure 77. Interaction between PARPi and ATR or DNA-PK inhibition in a panel of CDX cultures.

A-D. Unsupervised hierarchical clustering of log10 GI_{50} obtained from the panel of CDX cultures treated with increasing concentrations ATRi (A) or DNAPKi (C) and fixed concentrations of PARPi. The responses to increasing concentrations of PARPi and fixed concentrations of ATRi (B) or DNAPKi (D) are also shown. ATRi = AZD6738; DNAPKi = AZD7648; PARPi = olaparib.

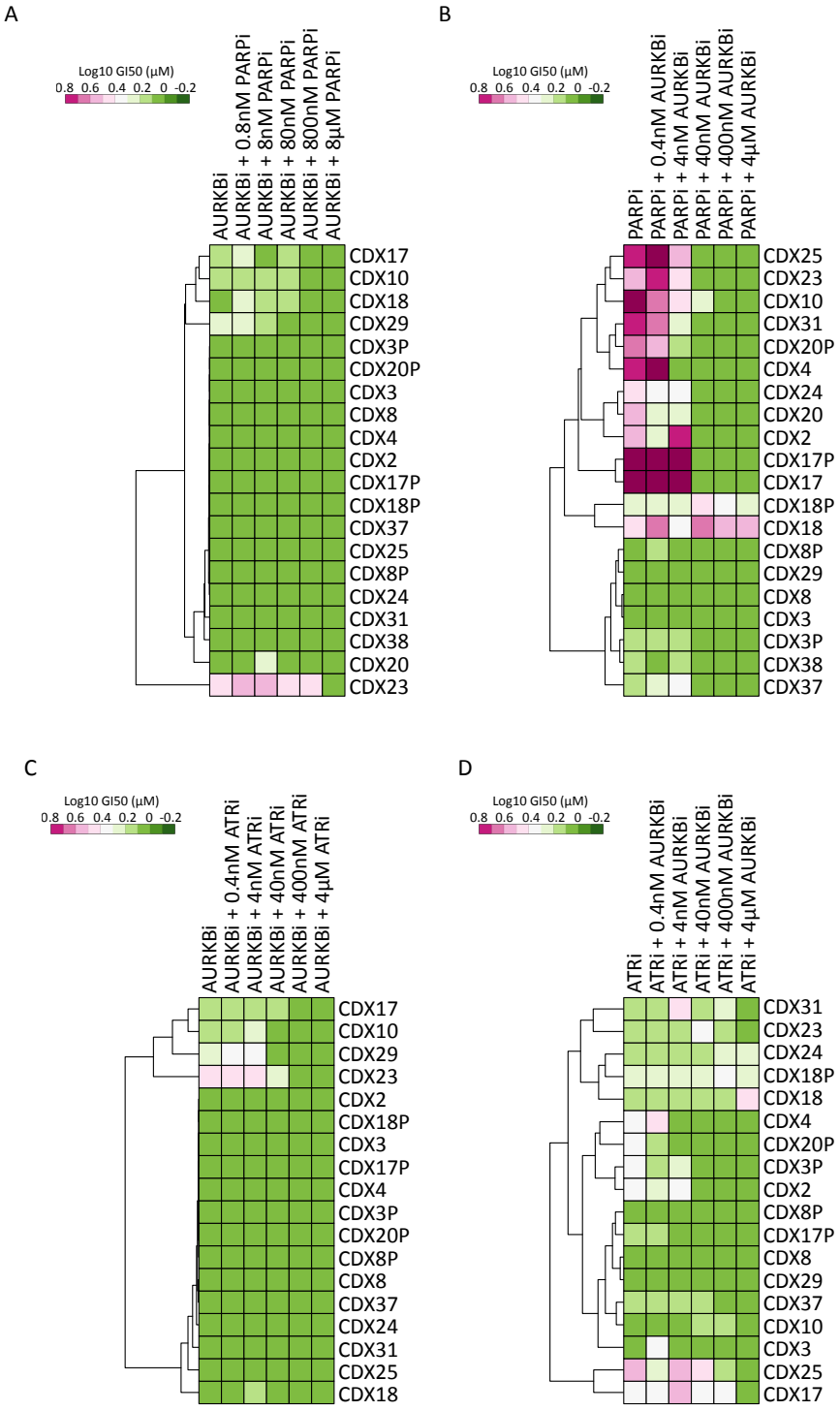

Figure 78. Interaction between PARPi and AURKBi or ATRi and AURKBi in a panel of CDX cultures.

A-D. Unsupervised hierarchical clustering of log10 GI_{50} obtained from the panel of CDX cultures treated with increasing concentrations AURKBi and fixed concentrations of PARPi (A) or ATRi (C). The responses to increasing concentrations of PARPi and fixed concentrations of AURKBi (B) or increasing concentrations of ATRi and fixed concentrations of AURKBi (D) are also shown. ATRi = AZD6738; AURKBi = AZD2811; PARPi = olaparib.

The combination of the AURKBi with the ATRi had overall similar effects than the single drug treatments (Figure 78C,D). However, these results also revealed model

specific sensitivity. For example, CDX23 was resistant to the AURKBi combined with 80 nM olaparib (Figure 78A, GI_{50} 1.8 µM), however combination of AURKBi with 40 nM ATRi reduced CDX23 cell viability (Figure 78C, GI_{50} 0.9 µM). This observation highlights that CDX23 may depend on ATR to repair replication stress induced DNA damage before entering mitosis. Preliminary data with chromatin-bound RPA staining suggested that CDX23 has intrinsic high level of replication stress and may explain the sensitivity to this combination (refer to Figure 59). The cytotoxic effect of the ATRi were partly increased by the combination with the AURKBi (Figure 78D), with an improved benefit compared with the combination of ATRi and olaparib in 4/20 models (Figure 77A, e.g. CDX20p GI_{50} 1.8 µM *vs* 0.04 µM for ATRi + 80 nM olaparib and ATRi + 4 nM AURKBi, respectively). Even though, the monotherapies were particularly effective in several CDX, the advantage of combining multiple drugs together are several. Personal communication from Astrazeneca defined specific concentrations of each DDRi as clinically relevant doses (Table 15). These concentrations are higher than most of the concentrations I used, suggesting that combination of these drugs can be exploited to decrease the final dose administered to patients and reduce the adverse effects. Moreover, combination of drugs can target a wider range of tumour subclones, improving the benefit for the patients (Palmer and Sorger, 2017). Finally, while I was not able to assess the long-term effect of these combinations, it is possible that combination of two different DDRi will delay the onset of resistance, as already shown with PARP and ATR inhibition (Murai et al., 2016).

6.2.3 Identification of synergistic concentrations of DDRi

As mentioned previously, synergy can be used to identify the concentrations at which two drugs interact generating a response greater than the response observed with only one drug. Figure 79A shows representative response landscapes for models that were more resistant (CDX25, CDX2 and CDX17) or more sensitive (CDX38, CDX18p and CDX29) to olaparib/ATRi. The three 'sensitive' models showed a peak of synergy around 40 nM ATRi, whereas the more resistant models showed a peak around 400 nM ATRi, further highlighting the possibility that high concentrations of the ATRi are non-specifically toxic (Figure 79A). The average delta scores for each CDX

showed that these drugs have some weak synergistic activity in 11/20 of the CDX tested (delta score > 0, Figure 79B).

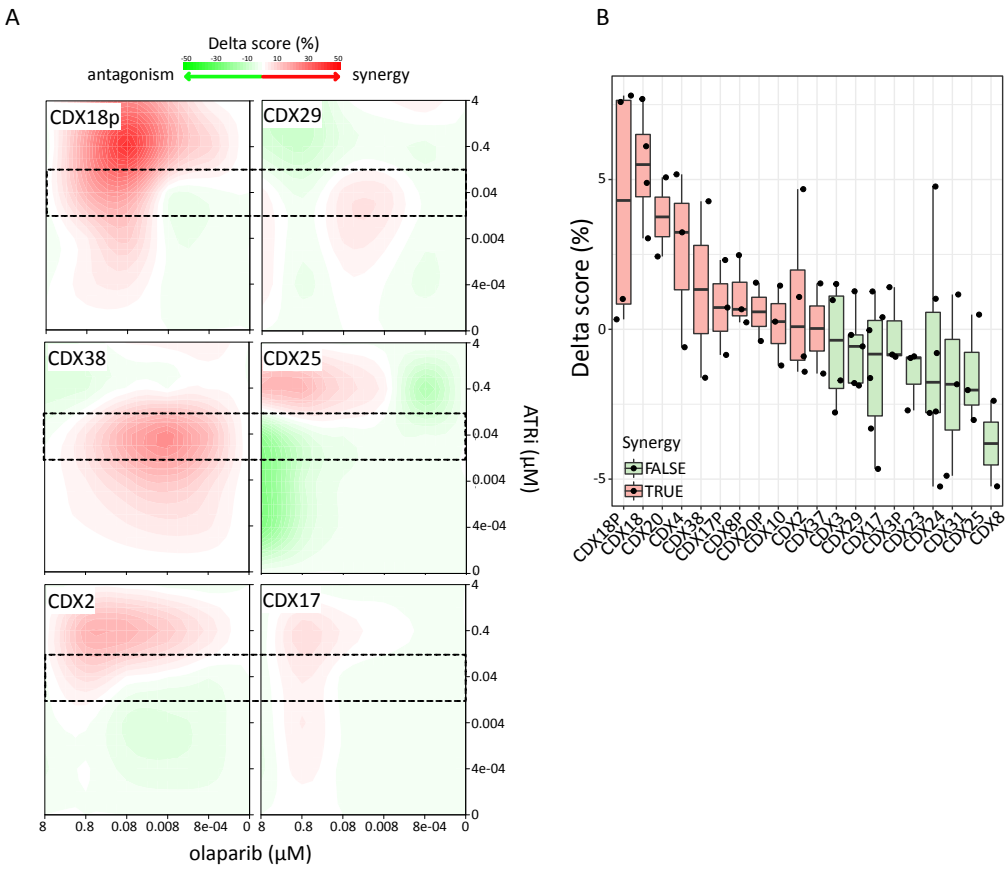

Figure 79. Synergistic interaction between ATRi and olaparib.

A. ATRi-olaparib dose-response landscapes. Dotted squares highlight the concentration of ATRi that creates a peak of synergy. B. Summary of the average delta score for the panel of CDX cultures treated with ATRi and olaparib. Average delta is the mean of all delta scores obtained for each dose combination in the matrix. The combination is considered synergistic if the median the average delta scores of all biological replicates is > 0 (red coloured boxes). Box and whisker plots show median, first and third quartiles and maximum and minimum values. Each dot is a biological replicate and red dots are showing outliers.

Figure 80A shows the response landscapes of three 'sensitive' models (CDX8p, CDX8, CDX37) and three 'resistant' models (CDX20p, CDX23, CDX17p) to olaparib/DNAPKi. The more sensitive models showed a peak of synergy at 40 nM DNAPKi, similar to what has been obtained for the ATRi and the WEE1i. Figure 80B summarises the synergy scores calculated for each biological replicates, highlighting a certain degree of heterogeneity. The average synergy for this combination was lower than the one observed with the ATRi (delta score < 5), even though, some replicates showed a strong synergy score (delta score > 10).

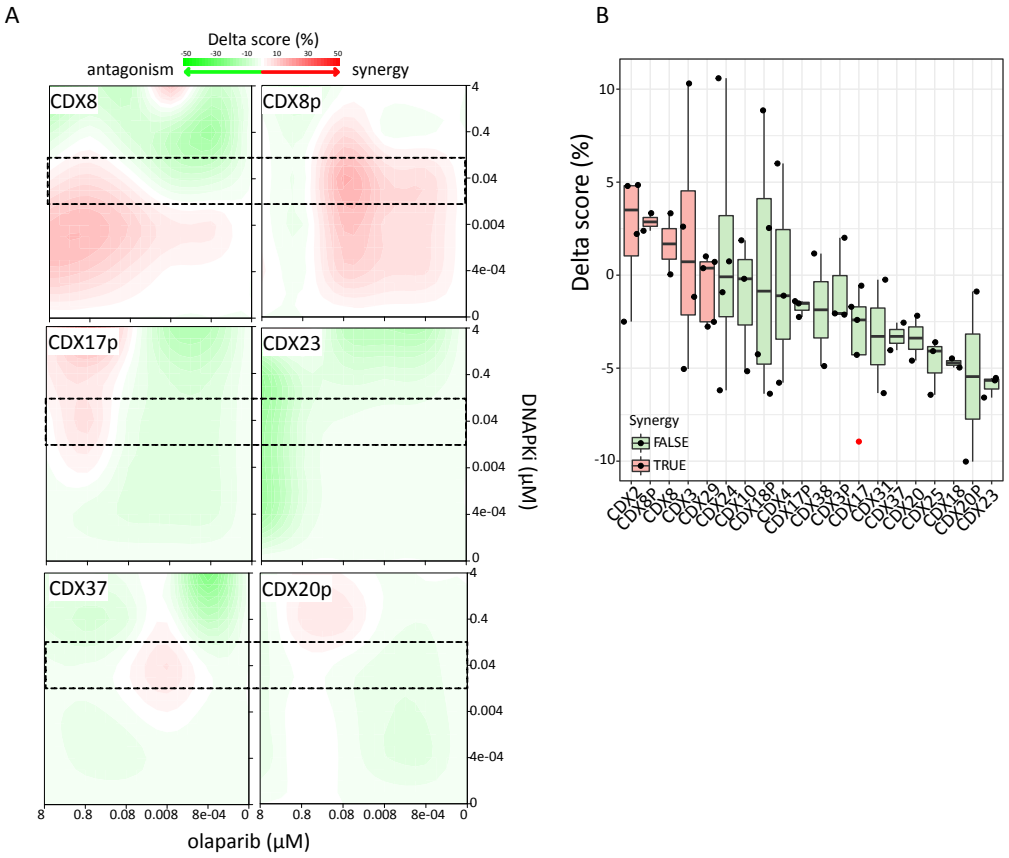

Figure 80. Synergistic interaction between DNAPKi and olaparib.

A. DNAPKi-olaparib dose-response landscapes. Dotted squares highlight the concentration of DNAPKi that creates a peak of synergy. B. Summary of the average delta score for the panel of CDX cultures treated with DNAPKi and olaparib. Average delta is the mean of all delta scores obtained for each dose combination in the matrix. The combination is considered synergistic if the median of the average delta scores of all biological replicates is > 0 (red coloured boxes). Box and whisker plots show median, first and third quartiles and maximum and minimum values. Each dot is a biological replicate and red dots are showing outliers.

The AURKBi was more cytotoxic than any other DDRi tested with peak of synergy observed around 4 nM (Figure 81A). Surprisingly, despite the strong effect observed on cell viability, the combination of olaparib with the AURKBi did not seem to be very synergistic, with average delta score < 3 (Figure 81B). For the last combination, I examined the concentration of AURKBi that synergises with the ATRi. All sensitive models showed a peak of synergy at 0.4 nM AURKBi (Figure 82A). As shown for the combination of the AURKBi with olaparib, the average score for this combination was overall lower than the one observed with the other DDRi, with most models having an average delta score < 3 (Figure 82B). This reduced synergy in the presence of the

AURKBi could be due to a real lack of interaction between the two drugs, or could be caused by putative off-target effects of the AURKBi.

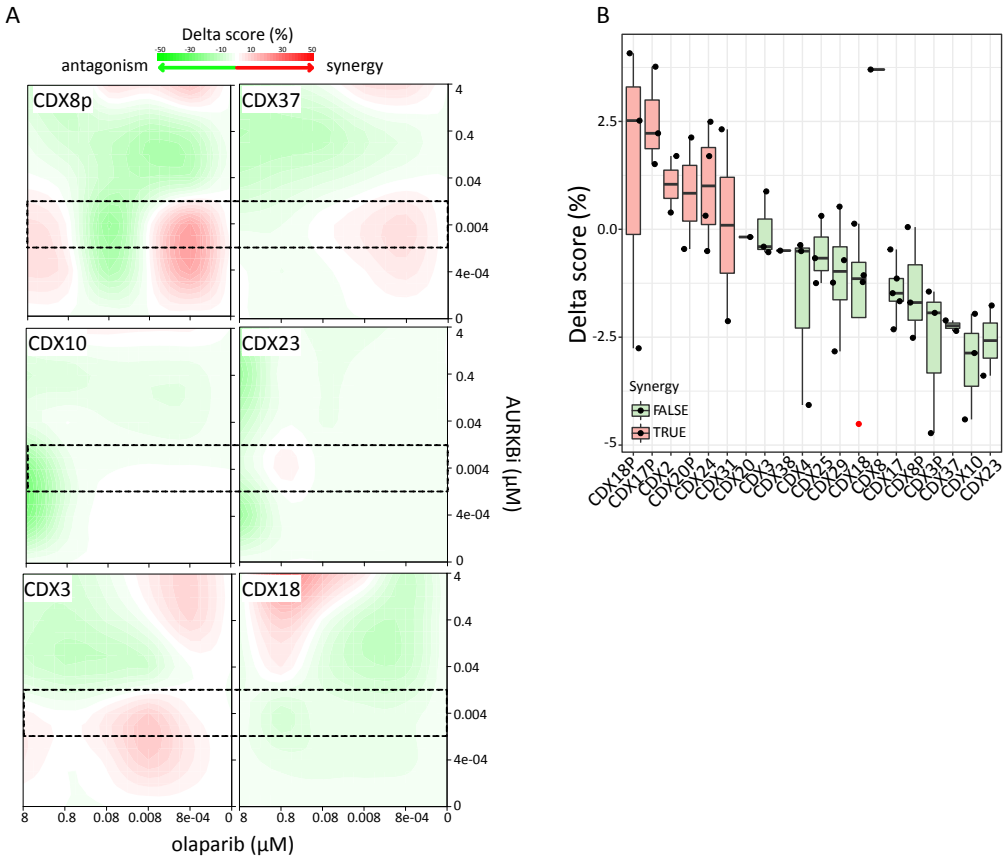

Figure 81. Synergistic interaction between AURKBi and olaparib.

A. AURKBi-olaparib dose-response landscapes. Synergy is defined as a positive deviation (positive Δ) from the expected effect the two drugs would have if they did not interact. Dotted squares highlight the concentration of AURKBi that creates a peak of synergy. B. Summary of the average delta score for the panel of CDX cultures treated with AURKBi and olaparib. Average delta is the mean of all delta scores obtained for each dose combination in the matrix. The combination is considered synergistic if the median of the average delta scores of all biological replicates is > 0 (red coloured boxes). Box and whisker plots show median, first and third quartiles and maximum and minimum values. Each dot is a biological replicate and red dots are showing outliers.

6.2.4 Identification of pathways involved in the response to DDR inhibitors

As for the WEE1i/olaparib treatment, I used the concentrations identified in the synergy landscapes to select one representative combination per drug treatment. For olaparib and the WEE1i, I identified the combination of 40 nM AZD1775 combined with olaparib as a representative condition for this treatment (Figure 46). The same concentration of DNAPKi and ATRi was used to represent the combination of olaparib with the DNAPKi and ATRi. For the AURKBi, 4 nM was used in combination with olaparib, while 0.4 nM was selected for the combination with the ATRi. This allowed me to compare the 5 combinations together (Figure 83A).

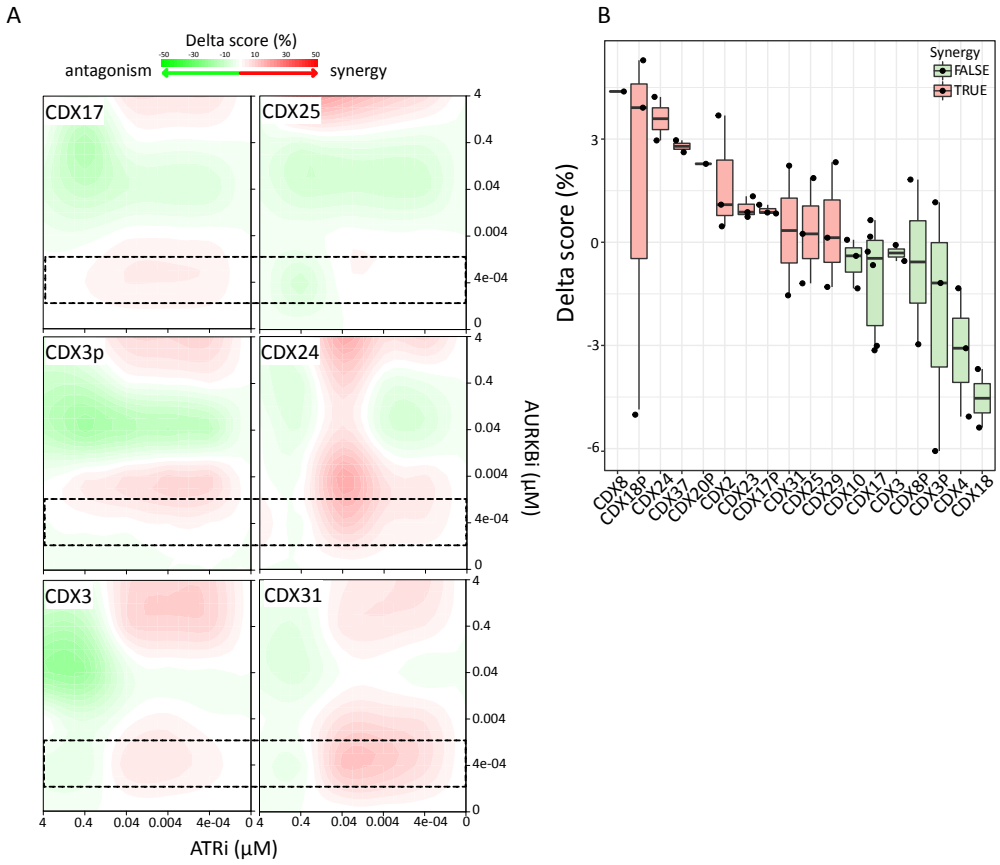

Figure 82. Synergistic interaction between AURKBi and ATRi.

A. AURKBi- ATRi dose-response landscapes. Synergy is defined as a positive deviation (positive Δ) from the expected effect the two drugs would have if they did not interact. Dotted squares highlight the concentration of AURKBi that creates a peak of synergy. B. Summary of the average delta score for the panel of CDX cultures treated with AURKBi and ATRi. Average delta is the mean of all delta scores obtained for each dose combination in the matrix. The combination is considered synergistic if the median of the average delta scores of all biological replicates is > 0 (red coloured boxes). Box and whisker plots show median, first and third quartiles and maximum and minimum values. Each dot is a biological replicate and red dots are showing outliers.

Two main clusters of CDX were identified. The first contained CDX resistant to almost all combinations tested (resistant group: CDX17, CDX17p, CDX4, CDX24, CDX10 and CDX25) and the second cluster contained CDX that were partially sensitive. This second cluster could be further subdivided in a group of CDX sensitive to every combination (sensitive group: CDX37, CDX18p, CDX3p, CDX8, CDX29, CDX8p, CDX3, CDX38) and a group with models resistant to at least one combination (intermediate group: CDX20, CDX31, CDX2, CDX20p, CDX18, CDX23). The presence of models sensitive or resistant to every drug tested suggested the presence of a common mechanism(s) of response to these inhibitors.

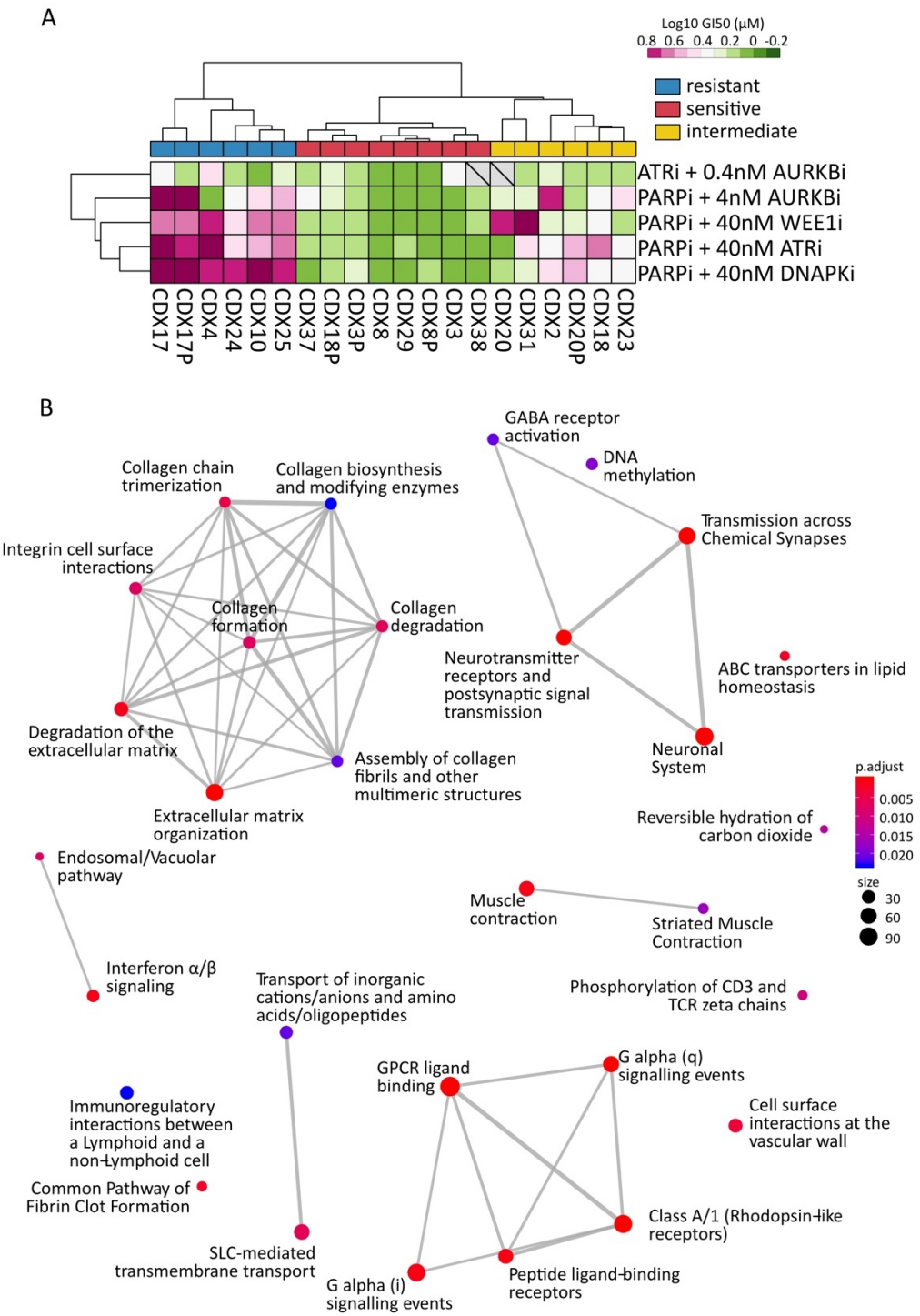

Figure 83. Pathway enrichment analysis between 'resistant' and 'sensitive' CDX.

A. Unsupervised hierarchical clustering of log10 GI_{50} obtained from the panel of CDX cultures treated with increasing concentrations PARPi or ATRi and a fixed concentration of the stated drugs. B. Reactome pathways enriched in the group of 'resistant' *vs* 'sensitive' CDX. Size is relative to the number of mapped genes present in each pathway. P.adjust indicates the adjusted *p*-value to define the probability a pathway has to be randomly identified. Genes with log2 fold change ≥ |1| and FDR ≤ 0.05 were selected (see Chapter 2.10.2 for details).

To try to identify shared alterations in pathways involved in the response to these drugs, I performed differential gene expression analysis comparing the transcriptional profiles of the 'resistant' group with that of the 'sensitive' group. There were 2,646 differentially expressed protein coding genes (Supplementary Data 6). Of these, 1,194 were down regulated and 1,452 were upregulated in the 'resistant' group. Pathway enrichment analysis on all 2,646 protein coding genes identified 53 pathways (Supplementary Data 7). Most pathways converged on 3 main nodes involving the modulation of the ECM, the G protein signalling, and the neuronal system (Figure 83B). Interestingly most of the genes involved in these three groups were upregulated, suggesting that these pathways were enriched in the 'resistant' models (Figure 84A).

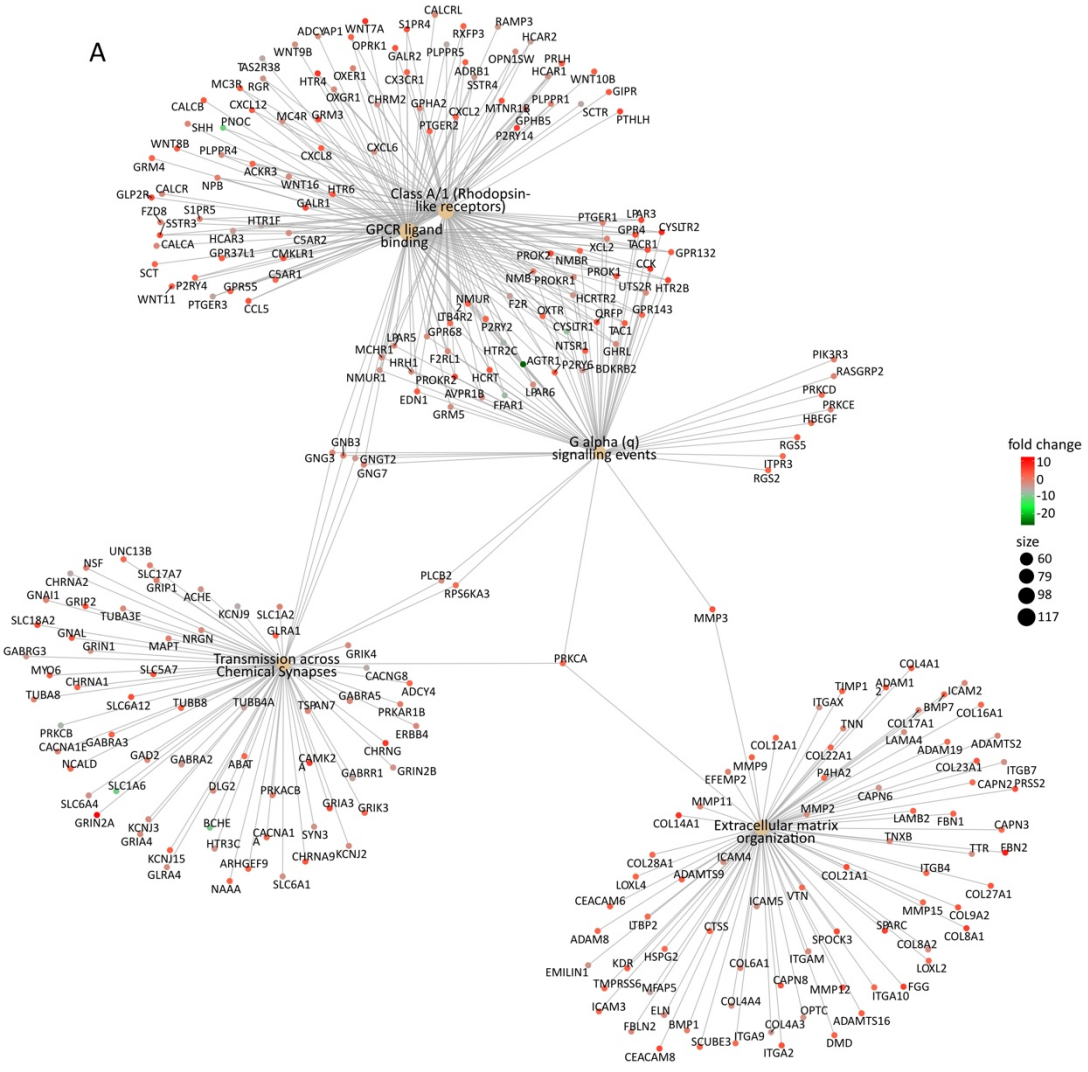

Figure 84. Level of expression and interaction of the genes enriched in the pathway differentially expressed between 'sensitive' and 'resistant' CDX.

A. Network analysis of the main genes differentially expressed between the resistant and sensitive groups. The colour of the dots is relative to the fold change, while the size of the pathway node is related to the number of genes included (see Chapter 2.10.2 for details).

To assess whether any of the main DNA damage repair pathways and cell cycle regulatory networks were altered in the resistant models, I performed gene set enrichment analysis. None of the gene sets tested was statistically enriched in the 'sensitive' or 'resistance' groups, however genes involved in mitosis, cell cycle checkpoint, DNA replication and ATR mediated replication stress response, were mainly downregulated in the 'resistant' group (Figure 85A). The observation that genes involved in these processes are differentially expressed in the CDX suggests that they could participate in the response to these compounds in SCLC, and merits further investigation.

A

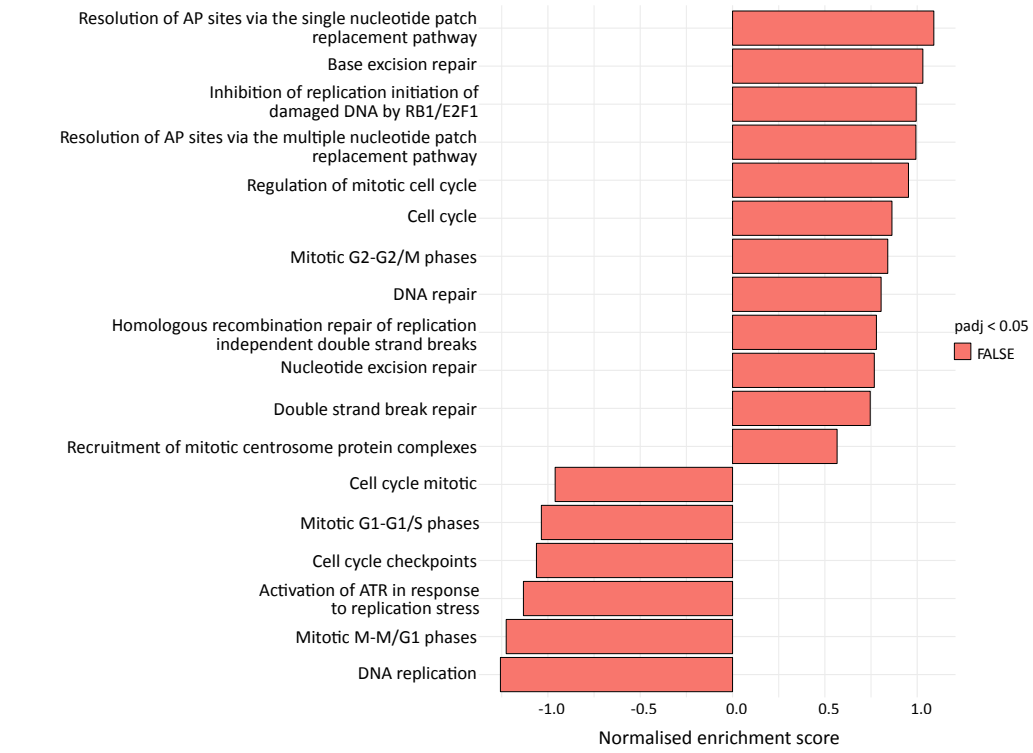

Figure 85. Gene set enrichment analysis between 'resistant' and 'sensitive' CDX.

A. GSEA analysis of different gene sets in the 'resistant' *vs* 'sensitive' CDX. The normalized enrichment score and associated adjusted *p*-value are used to compare the enrichment scores across gene sets (Subramanian et al., 2005) (see Chapter 2.10.2 for details).

6.2.5 Identification of putative biomarkers of response

CDX20, CDX31, CDX2, CDX20p, CDX18 and CDX23 were excluded from the previous analysis because of their variable responses to the different inhibitors. To include these models and increase the power of the analysis, I have examined each combination separately. First, I chose a threshold of 1 µm (equivalent to a log10 GI_{50} of 0.3) to allocate each CDX to the 'resistant' or 'sensitive' group for each combination. Then, I performed multiple analyses to compare gene expression of the resistant *vs* the sensitive groups for each treatment.

6.2.5.1 Olaparib/AZD1775 (WEE1i)

In response to olaparib combined with 40 nM WEE1i, CDX4, CDX10, CDX17, CDX17p, CDX18, CDX20, CDX24, CDX25 and CDX31 showed a $GI_{50} \geq 1$ µM and were therefore included in the 'resistant' group. CDX2, CDX3, CDX3p, CDX8, CDX8p, CDX18p, CDX20p, CDX23, CDX29, CDX37 and CDX38 had an average $GI_{50} < 1$ µM and were allocated to the 'sensitive' group (Table 16). Differential gene expression analysis identified 2,112 differentially expressed protein coding genes, enriched in pathways similar to the one identified with the previous analysis (which was expected considering that only three models were added in each group for this analysis). Supplementary Data 6 and Data 7 list the differentially expressed genes and reactome pathways identified. Gene set enrichment analysis also showed similar results, with no significant enrichment for any of the gene sets tested (Figure 86A).

To identify genes that could be strongly associated with the *ex vivo* response to this combination, I correlated the expression of each gene with the average GI_{50} of each CDX in response to olaparib combined with 40 nM AZD1775. Genes that positively correlated with the GI_{50} were highly expressed in the more resistant models, while a negative correlation identified genes highly expressed in the more sensitive CDX (Figure 86B). Ten percent of the genes that correlated with the GI_{50} had a *p*-value ≤ 0.05 (Supplementary Data 8). Several genes involved in DNA replication, replication fork stabilisation and DNA repairs positively correlated with the GI_{50}.

Table 16. Summary of CDX responses to the tested combination*.

Model	PARPi/WEE1i	PARPi/ATRi	PARPi/DNAPKi	PARPi/AURKBi	ATRi/AURKBi
CDX4	resistant	resistant	resistant	sensitive	resistant
CDX10	resistant	resistant	resistant	resistant	sensitive
CDX17	resistant	resistant	resistant	resistant	resistant
CDX17p	resistant	resistant	resistant	resistant	sensitive
CDX18	resistant	resistant	resistant	resistant	sensitive
CDX20	resistant	sensitive	sensitive	sensitive	sensitive
CDX24	resistant	resistant	resistant	resistant	sensitive
CDX25	resistant	resistant	resistant	resistant	sensitive
CDX31	resistant	resistant	sensitive	sensitive	sensitive
CDX2	sensitive	resistant	resistant	resistant	sensitive
CDX3	sensitive	sensitive	sensitive	sensitive	resistant
CDX3p	sensitive	sensitive	sensitive	sensitive	sensitive
CDX8	sensitive	sensitive	sensitive	sensitive	sensitive
CDX8p	sensitive	sensitive	sensitive	sensitive	sensitive
CDX18p	sensitive	sensitive	sensitive	sensitive	sensitive
CDX20p	sensitive	resistant	resistant	sensitive	sensitive
CDX23	sensitive	resistant	resistant	resistant	sensitive
CDX37	sensitive	sensitive	sensitive	resistant	sensitive
CDX29	sensitive	sensitive	sensitive	sensitive	sensitive
CDX38	sensitive	sensitive	sensitive	sensitive	sensitive

**GI50 ≥ 1 µM was used as cut-off for resistance*

POLI showed the strongest correlation, with $R^2 = 0.80$ and *p*-value < 0.00005. *POLI* encodes for the error-prone DNA polymerase Iota, involved in translesion DNA synthesis (Goodman and Woodgate, 2013). Little is known about this polymerase and it could be involved in the bypass of lesion during replication in a p53-dependent manner (Hampp et al., 2016). More genes involved in the protection and resolution of stalled replication forks appeared to positively correlate with GI_{50}, such as *ATRIP*, the ATR interacting partner ($R^2 = 0.64$ and *p*-value = 0.002), and *RECQL5*, a helicase involved in fork stabilisation ($R^2 = 0.58$ and *p*-value = 0.008) (Kim et al., 2015). *RAD17*, also recruited to stalled replication forks to trigger ATR activity (Smith et al., 2010), as well as the endonuclease *EME2,* the double strand break repair protein *RAD50,* the cyclin-dependent kinase 7 (*CDK7*) and the S-phase cyclin-dependent kinase 3 (*CDK3*), positively correlated with the GI_{50} (Figure 86B,C), further suggesting that resistant

models may have a better ability to regulate the repair of stalled replication forks than the sensitive ones.

A

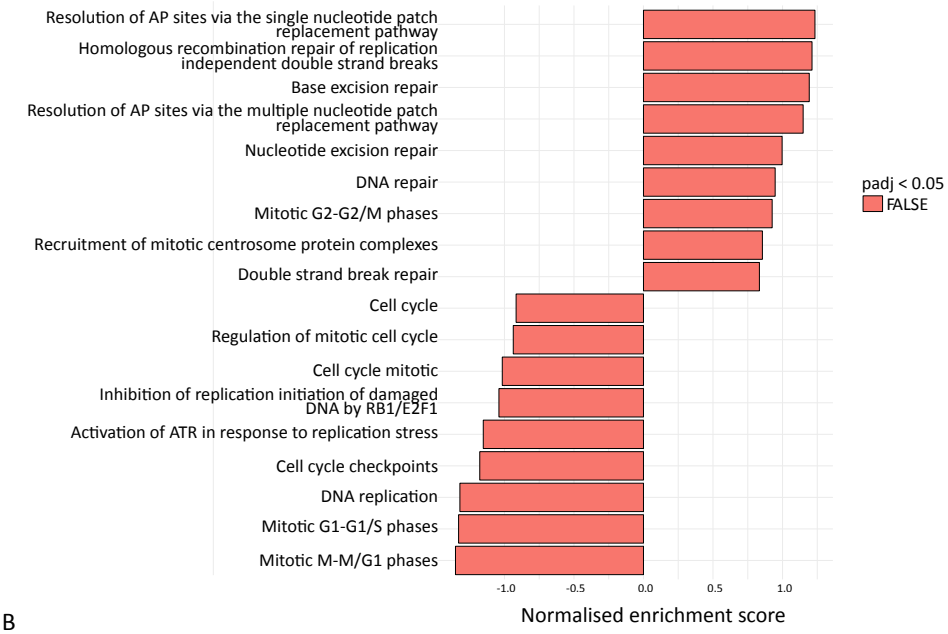

B

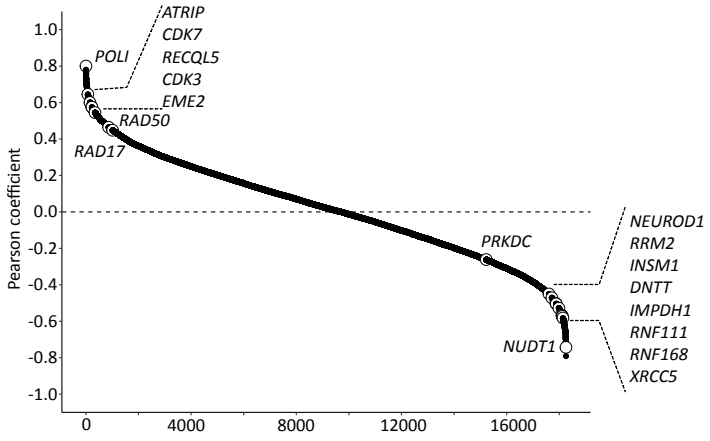

C

genes	cor	pVal
POLI	0.80047946	2.25E-05
ATRIP	0.64597954	0.00209193
CDK7	0.60067972	0.00509938
RECQL5	0.57613493	0.00784506
CDK3	0.57465485	0.00804314
EME2	0.54509302	0.01293635
RAD50	0.46460393	0.03903016
RAD17	0.44809958	0.04754325

genes	cor	pVal
PRKDC	-0.2615068	0.26540305
NEUROD1	-0.4501126	0.04643471
RRM2	-0.4709796	0.03607839
INSM1	-0.5022134	0.02403848
DNTT	-0.5045363	0.02328968
IMPDH1	-0.5281034	0.01668972
RNF111	-0.5676469	0.00903726
RNF168	-0.5728361	0.00829212
XRCC5	-0.5822642	0.00706673
NUDT1	-0.7430852	0.00017417

Figure 86. Identification of genes specifically expressed in CDX resistant/sensitive to olaparib/WEE1i.

A. GSEA analysis of different gene sets in the 'resistant' *vs* 'sensitive' CDX for WEE1i/PARPi. The normalized enrichment score and associated adjusted *p*-value are used to compare the enrichment scores across gene sets (Subramanian et al., 2005) (see Chapter 2.10.2 for details). B. Pearson

coefficients for each gene relative to the GI_{50} in response to olaparib/WEE1i. Big white dots highlight the location of the genes described in the text. C. Table summarizing the Pearson coefficients and the *p*-values of the genes highlighted in B.

While genes involved in stabilisation and repair of stalled replication forks were prevalent in CDX showing a reduced response to this combination, genes like *RRM2*, the inosine monophosphate dehydrogenase 1 (*IMPDH1*) and the nudix hydrolase 1 (*NUDT1*) negatively correlated with GI_{50} (Figure 86B,C). Reduction of *RRM2* has been shown to be a direct consequence of WEE1 inhibition and partially account for the toxic effect of this drug (Pfister et al., 2015). The higher level of *RRM2* in the more sensitive models suggests that these CDX may be more dependent on nucleotide metabolic pathways to survive, and therefore they could be more susceptible to WEE1 inhibition. Increased expression of *IMPDH1* highlights the possibility that these models rely more on the guanosine monophosphate synthesis. A recent publication showed that ASCL1-low/NEUROD1-high SCLC models are more dependent on the purine than pyrimidine synthesis, and these models were sensitive to IMPDH inhibitors (Huang et al., 2018a). In agreement with Huang *et al*, the sensitive models also expressed higher level of *NEUROD1*, further suggesting that ASCL1-low/NEUROD1-high SCLC models are dependent on the purine metabolic pathway. Together with NEUROD1, another neuroendocrine marker, *INSM1*, negatively correlated with the GI_{50}. INSM1 participates in the differentiation of PNECs, particularly by repressing HES1 (Jia et al., 2015). INSM1 is used as diagnostic marker for SCLC and it can coexist with NEUROD1 and/or ASCL1 in SCLC cell lines (McColl et al., 2017; Travis et al., 2004). If this observation is confirmed it may indicate that multiple subpopulations of SCLC, in particular NE tumours, can be more dependent on this metabolic pathway. Moreover, these data suggest that dNTP depletion caused by WEE1 inhibition may have a stronger impact on tumours dependent on the purine metabolism. Finally, another group of genes that seemed to negatively correlate with the GI_{50} included genes involved in DSB repair, in particular the NHEJ pathway. The DNA-PKcs regulatory subunit Ku80 (*XRCC5*) and the NHEJ polymerase, TdT (*DNTT*) (Chang et al., 2017) negatively correlated with the GI_{50}. The catalytic subunit of DNA-PK (*PRKDC*) also negatively correlated with the GI_{50}, although the *p*-value was > 0.05 (Figure 86C). Other genes that strongly inversely correlated with GI_{50} were *RNF168*

and *RNF111*, E3 ubiquitin ligases involved in the repair of DSBs. In particular, RNF168 is required for the recruitment of several DNA repair proteins to DSB (Hustedt and Durocher, 2017), while RNF111 is necessary for the recruitment of RNF168 to DSB and RNF111-mediated neddylation promotes NHEJ over HR repair (Jimeno et al., 2015; Ma et al., 2013). All together, these data suggest that a specific metabolic dependency as well as a preference for the NHEJ pathway may be biomarkers of response to this treatment.

6.2.5.2 Olaparib combined with the other DDR inhibitors

A similar analysis was performed for olaparib combined with 40 nM ATRi, 40 nM DNAPKi and 4 nM AURKBi. As for olaparib/WEE1i, CDX with GI_{50} ≥ 1 μM were classified as 'resistant', while the remaining models were classified as 'sensitive' (Table 16). CDX20 was resistant to olaparib/WEE1i, however it was sensitive to all other combinations tested. The olaparib/WEE1i sensitive, CDX2, CDX20p and CDX23 were resistant to olaparib/ATRi. The response to olaparib/DNAPKi was very similar to that observed with the ATRi, with almost the same models classified as 'resistant' or 'sensitive'. The only exception was CDX31, which was sensitive to the combination with the DNAPKi, while was resistant when treated with the ATRi (Table 16). Similarly, the CDX classified as 'resistant' to the combination of olaparib/AURKBi mostly matched the 'resistant' models observed in response to olaparib/ATRi, with the difference of CDX4, CDX20p and CDX31, which were classified as 'sensitive', and CDX37, which was classified as 'resistant' (Table 16).

The high overlap between the 'resistant' and 'sensitive' models suggests that it will be difficult to identify pathways differentially expressed in a specific combination compared with the others. Pathway enrichment analysis performed comparing the 'resistant' *vs* the 'sensitive' group for each combination tested, detected the same pathways identified for olaparib/WEE1i (Supplementary Data 7). As for the previous analysis, none of the DNA repair and cell cycle gene sets analysed were significantly enriched in the 'resistant' or 'sensitive' groups (Figure 87A,B and Figure 88A). However, the normalized enrichment score (NES) changed for each comparison, with fewer gene sets enriched in the sensitive groups compared with olaparib/WEE1i. For olaparib/ATRi and olaparib/DNAPKi, the gene sets enriched in the sensitive groups

included genes involved in DNA replication, mitosis and G1 phase, while for the olaparib/AURKBi genes involved in cell cycle checkpoints and resolution of AP sites were more enriched.

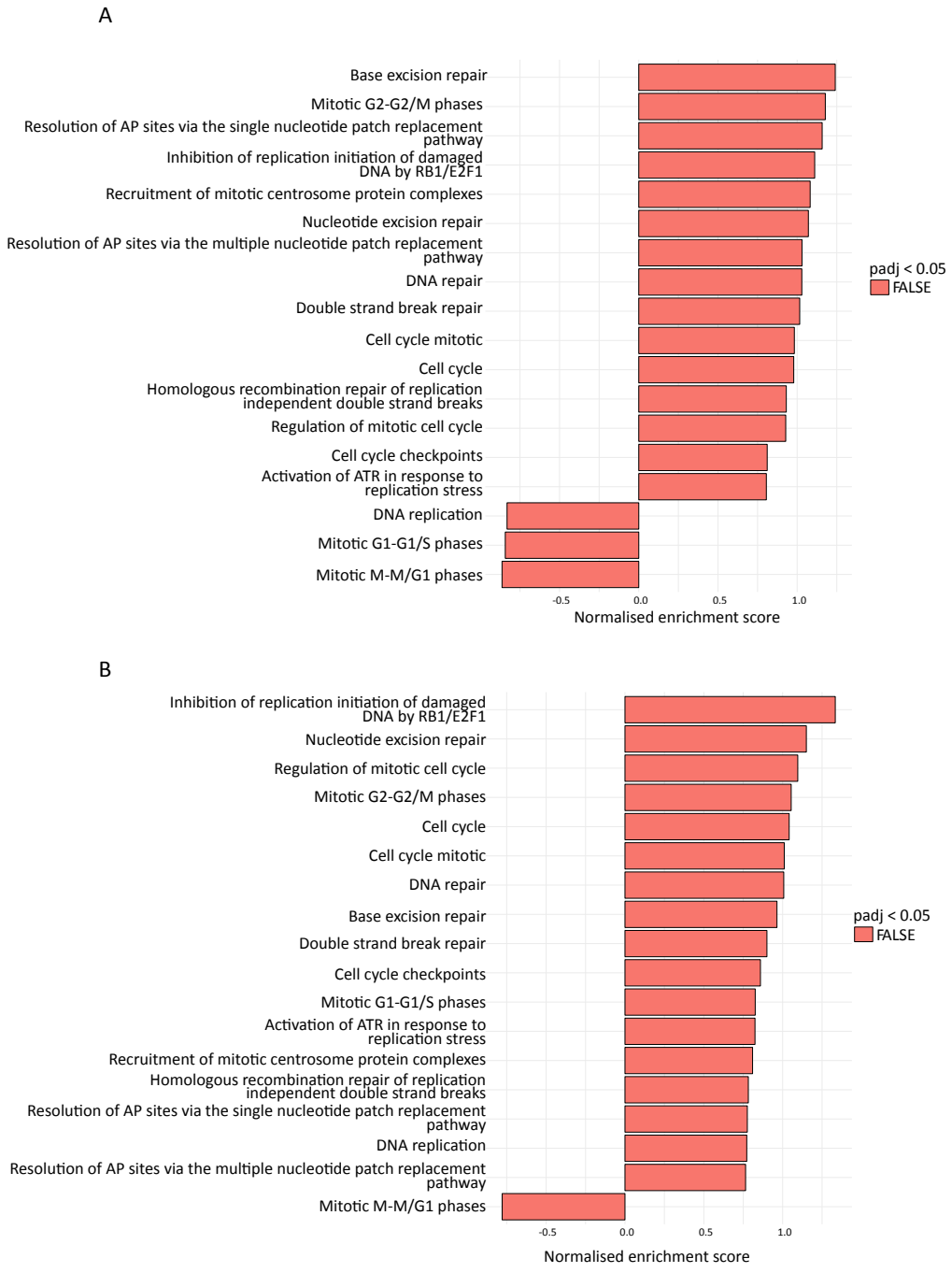

Figure 87. Gene set enrichment analysis of DNA repair and cell cycle pathways in CDX resistant and sensitive to different DDRi.

A,B. GSEA analysis of genes differentially expressed between CDX resistant and sensitive to ATRi/olaparib (A) and DNAPKi/olaparib (B). The normalized enrichment score and associated adjusted *p*-value are used to compare the enrichment scores across gene sets (Subramanian et al., 2005) (see Chapter 2.10.2 for details).

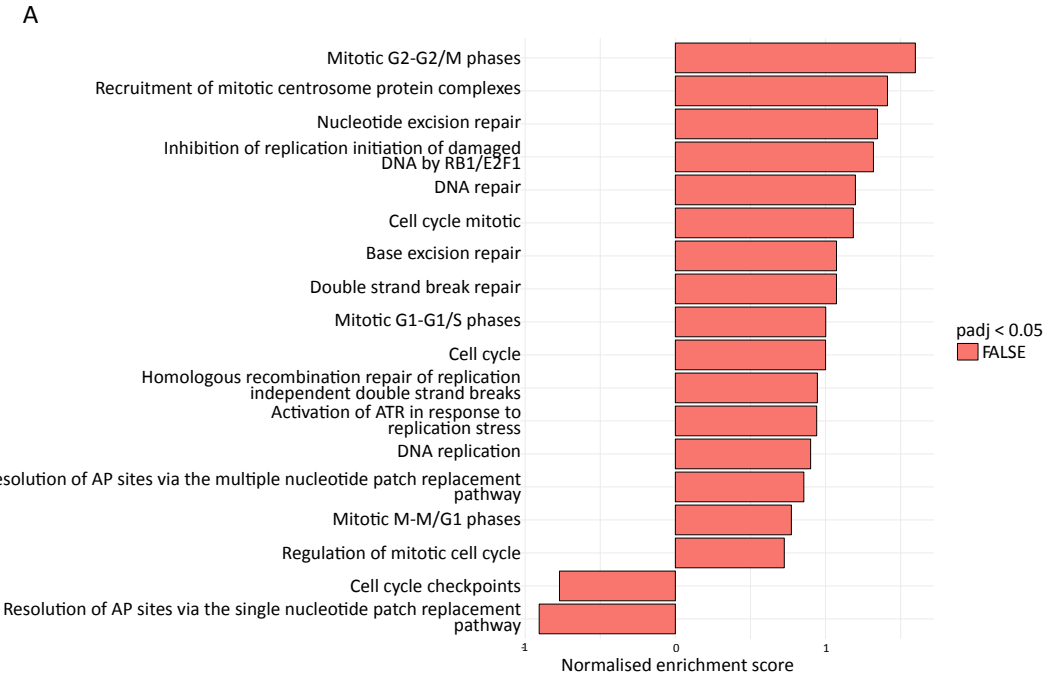

Figure 88. Gene set enrichment analysis of DNA repair and cell cycle pathways in CDX resistant and sensitive to AURKBi and olaparib.

A. GSEA analysis of genes differentially expressed between CDX resistant and sensitive to AURKBi/olaparib. The normalized enrichment score and associated adjusted *p*-value are used to compare the enrichment scores across gene sets (Subramanian et al., 2005) (see Chapter 2.10.2 for details).

When the Pearson correlation between the GI_{50} and gene expression was performed for each combination, a few changes across the different treatments were observed. In response to olaparib/ATRi, 1,383 genes (7.6% of the total) significantly correlated with the GI_{50} (*p*-value ≤ 0.05). There was a positive enrichment of genes involved in the regulation of entry into mitosis. These genes included the APC/C co-activator, fizzy and cell division cycle 20 related 1 (*FZR1*), the cell division cycle 23 (*CDC23*) and the cell division cycle 25B (*CDC25B*) (Figure 89A, Supplementary Data 3). As expected, some genes that positively correlated with the response to olaparib/WEE1i, also positively correlated with the response to olaparib/ATRi, like *ATRIP, POLI* and *CDK7*. Yes associated protein 1 (*YAP1*) correlated with higher GI_{50}, suggesting that the subgroup of $YAP1^{+}$ SCLC patients (Rudin et al., 2019) may be intrinsically resistant to olaparib/ATRi. Similarly, Atonal BHLH Transcription Factor 1 (*ATHO1*), a regulator of neuronal differentiation shown to mark a subset of our CDX (Figure 12, Simpson et al., 2019), positively correlated with the response to this treatment. Several genes

that negatively correlated with the response to olaparib/WEE1i also negatively correlated with the response to olaparib/ATRi, suggesting that NHEJ and dNTP metabolism may also be involved in the response to this combination (Figure 89A).

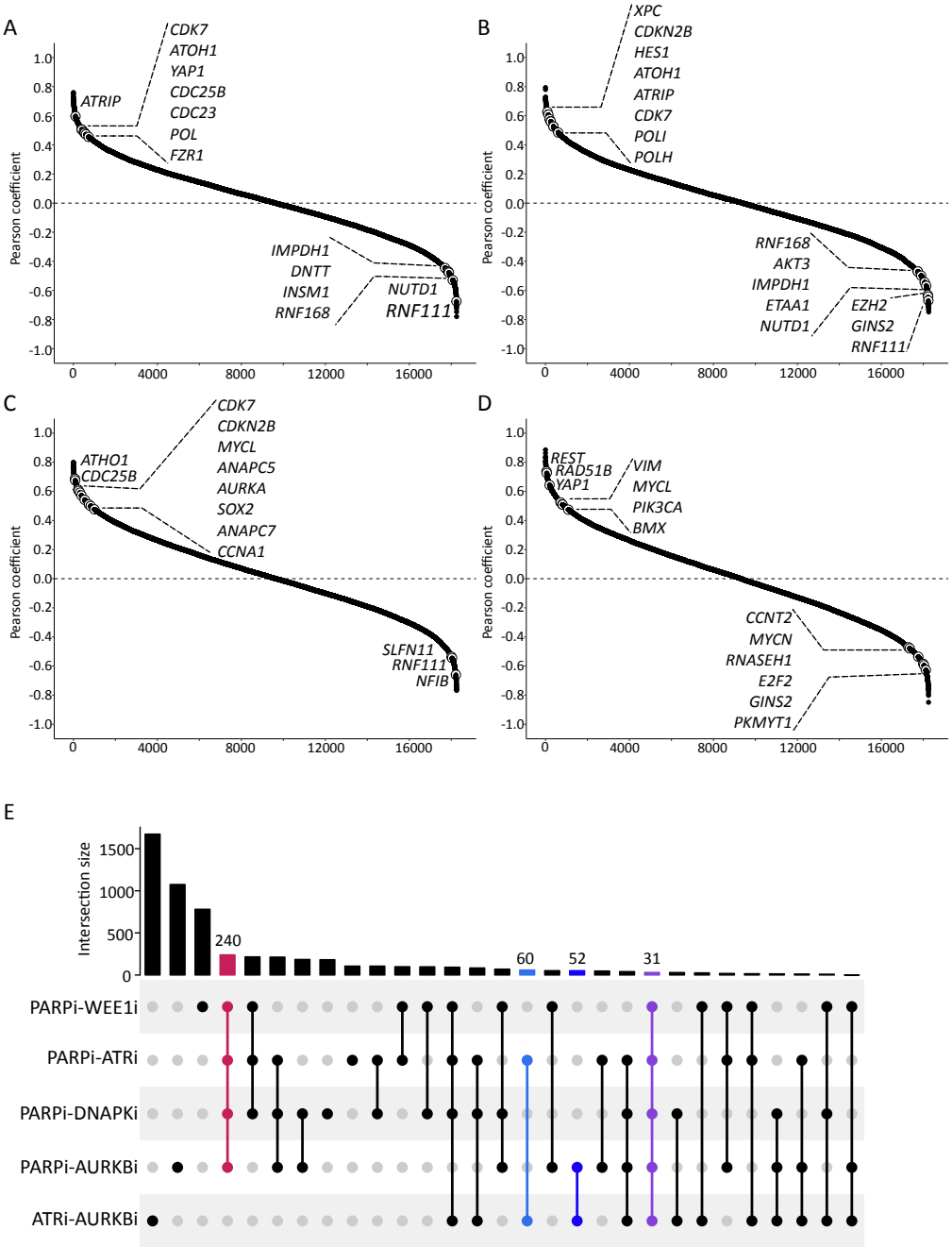

Figure 89. Pearson correlation between RNAseq and GI_{50}.

A-D. Plots showing the Pearson coefficients calculated for each gene relative to the GI_{50} in response to olaparib/ATRi (A), olaparib/DNAPKi (B), olaparib/AURKBi (C) and ATRi/AURKBi (D). Big white dots highlight the location of the genes described in the text. E. UpSet plot showing the intersections of the genes significantly correlating with the GI_{50} for each combination tested. The numbers above the bars indicate the size of the intersection (number of genes included). Intersection of genes shared in all

combinations (dark violet), in all olaparib-containing treatments (pink), in all ATRi-containing combinations (light blue) and in all AURKBi-containing treatments (dark blue) are highlighted.

In the combination with the DNAPKi, 1,612 genes significantly correlated with the GI_{50} (8.8% of the total, *p*-value ≤ 0.05). *ATRIP*, *POLI* and *CDK7* were again some of genes with the strongest positive correlation (Figure 89B, Supplementary Data 8). Also another TLS polymerase, *POLH*, positively correlated with the response to this combination, as well as, the G1 cell cycle regulator, *CDKN2B*, the damage sensor *XPC* involved in NER, *ATOH1* and the NOTCH downstream target, *HES1*. As for the previous combinations, *RNF111* and *RNF168* negatively correlated with the GI_{50}. Members of the DNA replication process also seemed to be involved in the response to olaparib/DNAPKi. The novel ATR activator, *ETAA1* (Feng et al., 2016; Haahr et al., 2016), negatively correlates with the GI_{50} together with the GIN complex subunit 2 (*GINS2*). Similar to the olaparib/WEE1i combination, genes involved in nucleotide metabolism (e.g. *IMPDH1* and *NUDT1*) negatively correlated with the response to olaparib/DNAPKi. Finally, the methyltransferase *EZH2* was more expressed in CDX, which responded better to this treatment (Figure 89B).

The frequency of common genes correlating with the GI_{50} of different combinatorial treatments was not surprising considering that all combinations contained olaparib and that many 'resistant' and 'sensitive' CDX were shared in the different treatments. When the combination of olaparib and AURKBi was correlated with the gene expression, 2,052 genes (11.2% of the total) had a *p*-value ≤ 0.05, similar to the percentage observed with the other combinations. As shown before, *RNF111*, negatively correlated with the GI_{50}, while *ATHO1* showed a positive correlation (Figure 89C, Supplementary Data 8). Specific to the response of this combination were *SLFN11* and *NFB1* that negatively correlated with the GI_{50}, suggesting that SCLC tumours expressing higher level of these genes could be more sensitive to treatment with olaparib/AURKBi. Interestingly, *MYCL* was among the genes that positively correlated with the GI_{50}. This further confirmed that the Aurora B kinase inhibitor is more effective in *MYC* than *MYCL* and *MYCN* expressing SCLC models (Helfrich et al., 2016; Sos et al., 2012). Other genes putatively involved in the resistance to this combination were genes implicated in mitotic entry and mitotic regulation. In particular, *AURKA*, *CDC25B* and the anaphase promoting complex

subunit 5 and 7 (*ANAPC5*, *ANAPC7*). Furthermore, the transcription factor *SOX2* and genes involved in the G1 checkpoint, such as *RBL1*, *CDKN2B* and *CCNA1*, positively correlated with the GI_{50} (Figure 89C).

Finally, for the AURKBi/ATRi combination, I did not perform the differential gene expression and gene set enrichment analyses because most CDX appeared to be particularly sensitive to this combination, limiting the resistant group to only 3 models (Table 16). However, I was able to perform the Pearson correlation analysis because it did not required *a priori* classification of the CDX into 'resistant' or 'sensitive' models. This combination was the only one without the PARP inhibitor and fewer genes that correlate with the GI_{50} were shared with the other combinations (Figure 89D, Supplementary Data 8). 2,143 genes (11.7% of the total) significantly correlate with the GI_{50} (*p*-value ≤ 0.05). Of these, genes associated with a non-NE phenotype positively correlated with the GI_{50}, such as *REST*, *YAP1* and *VIM* (McColl et al., 2017; Simpson et al., 2019). I did not identify any group of genes involved in specific cell cycle checkpoint pathways, however *MYCL*, *PIK3CA* and *BMX* also positively correlated with the GI_{50}. Activation of the PI3K pathway and BMX overexpression has been associated with chemoresistance in SCLC cell lines (Guo et al., 2010; Krystal et al., 2002; Potter et al., 2016), suggesting that it may be associated with a more aggressive phenotype. Lower GI_{50} correlated with higher expression of genes involved in RNA transcription and DNA replication, such as the ribonuclease H1 (*RNASEH1*), *GINS2*, E2F transcription factor 2 (*E2F2*) and cyclin T2 (*CCNT2*). Moreover, the WEE1 paralog *PKMYT1* and *MYCN* inversely correlate with the GI_{50}. If validated on a larger panel of CDX, proteins like Myt1 kinase (*PKMYT1*) and N-MYC (*MYCN*) could be used as biomarkers to select the population of SCLC patient that may better respond to this treatment (Figure 88D).

Overall, these correlations have identified genes that could potentially be used as biomarkers of response. While I have mainly highlighted genes that could have a mechanistic role in the response to these drugs, other genes that correlate with the response to these combination could be used as biomarkers to stratify patients, such as L-MYC, REST, NEUROD1 or genes coding for membranes protein for which antibodies have already been validated. There were 31 genes significantly correlated with the GI_{50} in all combinations tested, 240 genes were shared in all olaparib-

containing combinations, 60 genes significantly correlated in all ATRi-containing combinations, while 52 genes were shared between the AURKBi-containing combinations (Figure 89E). These data highlight the number of candidate biomarkers that could be identified using this analytic strategy. Any of the genes present in these lists could potentially be further validated as a biomarker of response to one or more treatments. It has to be highlighted that the false discovery rate for these correlations is probably high because of the low number of CDX compared with the number of genes tested. Nevertheless, these preliminary analyses suggest several promising genes and pathways for future follow up and functional validation.

6.3 Conclusion

As shown in the literature, treatment of SCLC preclinical models with inhibitors of the DNA damage response pathways are showing some promise. In the panel of CDX I tested, inhibition of WEE1 and Aurora kinase B were the most effective when used as single agents. In combination, most of these DDRi showed a limited level of synergistic activity, with only the olaparib/WEE1i and olaparib/ATRi showing an average delta score ≥ 5 in at least one CDX. Based on the original paper describing the ZIP reference model, combination of drugs with average delta score < 5 were considered insignificant (Yadav et al., 2015). However, despite the low average delta score (< 3) the combinations containing the AURKBi were the most effective in the panel of CDX tested. It is possible that the strong efficacy of AURKBi as single agent hides putative synergistic effect with the other drugs, however it is also possible that the compound (AZD2811) has off-target effects at low concentrations. If this was the case, the observed sensitivity could be biased by the toxicity introduced by the compound rather than a real dependence to Aurora kinase B. Little is known about the putative off-target effects of the AURKBi (AZD2811), although it is highly selective for Aurora Kinase B (Mortlock et al., 2007). Therefore, more experiments should be performed to confirm this hypothesis.

Generally, models sensitive to olaparib monotherapy (e.g. CDX3, CDX8, and CDX29) were also sensitive to all combinations tested. The same applied to some olaparib-resistant CDX (e.g. CDX4, CDX25, CDX17 and CDX17p), in which sensitivity to olaparib only improved when very high concentrations of ATRi or DNAPKi were used

or in the presence of AURKBi. The reduced efficacy of DNAPKi as single agent compared with the other DDRi could be explained by the fact that to rely on DNA-PK, cells need to undergo DSBs, therefore with no further insult, the DNAPKi has only limited cytotoxicity on the cells. The DNA damage induced by PARP inhibition seemed to increase the cytotoxicity of the DNAPKi in 3/4 DNAPKi-resistant CDX (CDX38, CDX3p and CDX8, Figure 77C). However olaparib-resistant CDX did not benefit from the additional inhibition of DNA-PK, suggesting that this combination should only be proposed to patients who are sensitive to PARPi (Figure 77D).

When considering the response to olaparib and ATRi, only CDX20 seemed to benefit from the addition of ATRi to PARP inhibition (Figure 77B). All other models showed improved response only with higher concentrations of the ATRi, suggesting that most of the observed effects could be due to off-target toxicity rather than synergy between the two compounds. Even though a similar pattern of response was observed with the WEE1i, where treatment with ≥400 nM AZD1775 showed very high responses in most models tested, 5/12 of the olaparib-resistant CDX benefited also from lower concentrations of AZD1775 ('intermediate' group in Figure 45B). Therefore, in these models, WEE1i synergises with olaparib better than the ATRi. In particular, the CDX included in the 'intermediate' group showed a slight improvement when treated with olaparib combined with 40 nM ATRi (1.2-2.4x decrease in the GI_{50} compared with olaparib single agents, Figure 77B), suggesting that the effects of inhibiting ATR partly overlapped with the one induced by WEE1 inhibition, but were not enough to trigger the same level of response as with olaparib/WEE1i treatment (1.7-4.6x decrease in the GI_{50} compared with olaparib single agents, Figure 45B).

Differential gene expression analysis of 'resistant' *vs* 'sensitive' CDX identified genes involved in the organization of the ECM, GPCR signalling and neuronal system to be more enriched in the resistant models. The higher expression of genes involved in differential processing of the ECM suggests that the resistant CDX may have a more aggressive phenotype and the ability to interact with the surrounding ECM to migrate or promote angiogenesis (Lu et al., 2011). G protein-coupled receptors (GPCRs) are integral membrane proteins involved in a variety of cellular processing. Once activated by their ligands, these receptors interact with the G proteins to promote GTP loading. The G_{α} subunit binds to GTP, dissociates from $G_{\beta\gamma}$ and activates

downstream effectors (Weis and Kobilka, 2018). In particular, $G_{\alpha q}$ proteins stimulate the β-subunit of the phospholipase C (PLC) leading to intracellular Ca^{+} mobilisation, activation of the protein kinase C (Mizuno and Itoh, 2009). This signalling triggers multiple cellular responses, including integrin and RhoA activation and inhibition of PI3K. $G_{\alpha i}$ proteins counteract the stimulatory effect of $G_{\alpha s}$ protein by inhibiting the adenylate cyclase, leading to a decrease in the activity of cAMP dependent kinases (Dessauer et al., 2002). Moreover, $G_{\alpha i}$ can interact with the catalytic domain of c-Src facilitating the access of the c-Src ligands and it has been demonstrated that activated mutant $G_{\alpha i}$ proteins are oncogenic and can activate the MAPK pathway (Ma et al., 2000; Pace et al., 1995). The complexity of the signalling regulated by the G proteins make it difficult to assess which, if any, of the downstream pathways is involved in the resistance to these inhibitors. While there is no clear direct role for these pathways in the response to the tested combinations, it is possible that they are involved in the establishment of a more aggressive phenotype, making these tumours overall more resistant to different type of treatments. The lack of enrichment of genes significantly associated with different DNA repair and cell cycle checkpoint pathways does not mean that this pathways do not participate in the response to these combinations. The degree of genes expression, measured at the mRNA level, involved in DNA repair and cell cycle related pathways may not be the best indicator of their activation or inhibition, which highlights further the importance of developing functional assays to study these processes. Moreover, changes in the expression of these genes after treatment with DDRi may better highlight deficiency in DNA repair and cell cycle regulation compared with their baseline expression.

To help selecting putative biomarkers of response, I have performed a Pearson correlation across each gene, in respect to the response (GI_{50}) each CDX had to the different combinations. This analysis allowed to point out genes that directly correlated with the response, and when possible extrapolate putative mechanisms of response. In particular, in the response to olaparib/WEE1i, it was interesting to observe that genes involved in the resolution of stalled replication forks positively correlated with a lower response to this treatment. Similarly, the result obtained suggested that tumours with a dependency for the purine metabolism could be more responsive to this combination. Because of the effect that inhibition of WEE1 has on

DNA replication and the dNTPs pool (Beck et al., 2012; Pfister et al., 2015), it was reassuring to identify these group of genes in the analysis. Genes involved in the NHEJ pathway were also recurrently expressed in the more sensitive models. Some of these genes were also negatively correlated with the response to the other olaparib-containing treatments. These intriguing observations could lead to speculate that the increased expression of genes implicated in the NHEJ pathway in the olaparib-sensitive models, could be a surrogate of HR-deficiency, explaining the better response observed with these combinations. There were more than 1,000 genes significantly correlating with the GI_{50} in each combination (*p*-value ≤ 0.05, R^2 < -0.4 and R^2 > 0.4), suggesting that several putative biomarkers of response could be identified. For reason that could be completely independent from mechanisms of response, these genes can be exploited as biomarkers for subpopulation of cells sensitive or resistant to the specified treatment. For example, *POLI* and *CDK7* are recurrently positively correlated with the response to olaparib-containing combinations. This suggests that if the corresponding proteins are also more expressed in the resistant CDX, antibodies against these two proteins could be exploited to select SCLC patients resistant to these treatments. *YAP1* positively correlated with the GI_{50} derived from both combination that contained the ATRi, suggesting that YAP1 could mark a subpopulation of cells resistant to ATR inhibition. Similarly, *NEUROD1* for the olaparib/WEE1i combination and *MYCL* for the AURKBi-containing combinations could be exploited as candidate biomarkers of response.

As soon as the results from the Decapus *in vivo* efficacy studies become available, further testing of the selected biomarkers is warranted to evaluate if they can robustly discriminate between sensitive and resistant models. Once validated, these biomarkers could be translated in the clinic and measured on serial CTCs in order to select the best treatment option for the patient.

Chapter 7. Final Discussion and Future Directions

SCLC was defined a 'recalcitrant' tumour by the US National Cancer Institute in 2014. The lack of tumour tissues for clinical and preclinical studies, together with the rapid onset of resistance to SoC are two of the major obstacles in fighting this disease (National Cancer Institute, 2014). Our laboratory discovered that SCLC CTCs are

tumourigenic in mice, which provides an approach that bypasses the limitation of tumour biopsies and increases the chance to expand patient-derived tumours for research purposes (Drapkin et al., 2018; Hodgkinson et al., 2014; Simpson et al., 2019). The recent FDA approval of an anti-PDL-1 inhibitor as first-line treatment for ES SCLC patients was a great advance in the treatment of these tumours (Horn et al., 2018), however all other novel therapies tested in clinical trials have failed (Koinis et al., 2016). There is an urgent need to identify novel combinatorial treatments together with biomarkers of response in order to improve the clinical care of SCLC patients. Multiple hallmarks of SCLC development can result in replication stress, suggesting that targeting the DDR in these tumours could have promising benefit for the patients (Thomas and Pommier, 2016). We have demonstrated that some SCLC CDX are sensitive to the inhibition of both PARP1/2 and WEE1 (Lallo et al., 2018). During my PhD, I attempted to understand mechanisms underpinning the observed responses and identify candidate predictive biomarkers. My goal was to develop research on CDX towards optimising multiple promising assays interrogating different aspects of the DDR. Here, I will discuss the main findings of my research and highlight areas of future focus.

7.1 Understanding the advantages and limitations of the CDX *ex vivo* cultures

To facilitate the screening of multiple combinatorial treatments and the identification of biomarkers of response, I developed and characterised *ex vivo* culture of cells derived from SCLC CDX models. In this thesis, I have shown that CDX can be cultured *ex vivo*, and retain, in the short-term, many features of the donor tumour. Contradictory to previously published data (Daniel et al., 2009), I have shown that transcriptional changes induced by short-term culture of these cells are reversible when the cells were re-implanted subcutaneously into immunocompromised mice. This observation is crucial when planning to manipulate CDX cells *in vitro* and then study the associated phenotype(s) *in vivo*. Another important feature of CDX cultures is their ability to qualitatively reproduce the response observed *in vivo* to different compounds. These characteristics allowed me to exploit the system I developed to test multiple inhibitors involved in the DDR and

begin to investigate putative predictive biomarkers of response. I have shown that CDX8 and CDX8p do not mimic perfectly the response observed *in vivo* to cisplatin/etoposide and AZD1775/olaparib, with CDX8p *ex vivo* cultures being particularly more sensitive to all treatments tested. The reason for this discrepancy could be linked to an inability of these cells to thrive in culture or the imposition of drastic molecular changes when these cells are grown on plastic. While I cannot exclude the latter hypothesis, the lack of strong transcriptional drift when CDX2, CDX3 and CDX4 were cultured for a few weeks suggests that the difficulty in adapting to the culture conditions could be the main reason for the sensitive phenotype of CDX8p. CDX8 and CDX8p have a high stromal component that is lost during *ex vivo* culturing. The lack of this important feature may explain the differences in response to therapies observed *ex vivo*. Several studies have demonstrated that the tumour microenvironment can contribute to drug resistance phenotypes in different tumour types (Gilbert and Hemann, 2010; Müerköster et al., 2004; Nakasone et al., 2012). Co-culture of CDX with stromal cells should be performed to assess if the response to therapies *ex vivo* would better mimic the response observed *in vivo*. Although there are not yet any *in vivo* data reporting the response of these two models to the different DDRi tested here, I decided to include them in all the analysis performed in this thesis. However, if the discrepancy between the response observed *in vivo* and the response observed *ex vivo* is recapitulated in all the combinations tested, these models should be excluded from the downstream analysis to avoid mis-interpretation of the results.

7.2 Future work to better understand the DNA damage repair pathways involved in the response to DDRi

Part of my thesis focused on the identification of deficiencies in specific DNA damage repair pathways. I have exploited an immunofluorescence assay to look at the formation of RAD51 and γH2AX foci after irradiation on CDX cultures. The lack of RAD51 foci in CDX3 helped explaining its high sensitivity to both cisplatin/etoposide and AZD1775/olaparib, and the presence of a *PALB2* mutation confirmed the HR deficiency in this model. None of the other CDX tested harboured any known mutations in genes involved in the HR pathways, confirming previous studies showing

HRD genomic scars do not correlate with the response to PARP inhibitors in SCLC (Lok et al., 2017).

CDX3, CDX4, CDX8 and CDX8p have shown a differential response to AZD1775 and olaparib *in vivo*, both as single agents and in combination, inferring that multiple mechanisms of response could be implicated in these phenotypes. While the RAD51/γH2AX assay, together with the comet assay, have helped elucidating how these models could manage the DNA damage imposed by these drugs, I could not identify a common predictive biomarker of response to this combination. These assays can now be used to assess the HR status on a larger panel of CDX and increase the robustness of the data. The comet assay can be exploited to look at the ability of the different models to repair DNA damage after treatment with olaparib/AZD1775, or any of the other combinations tested in this thesis. This experiment would allow to distinguish which CDX are able or not to resolve the damage induced by these drugs. These results, together with the ability to form RAD51 foci after irradiation, will aid in understanding the responses to AZD1775/olaparib and facilitate the identification of responsive/refractory patients.

During my PhD, I have mainly focused on trying to dissect intrinsic mechanisms of resistance to olaparib, however it would be interesting to understand also acquired resistance to this inhibitor. For example, despite the strong response to olaparib single agent observed in CDX3 tumours, all mice inevitably relapsed. Similarly, CDX8 tumours responded very well to olaparib/AZD1775, however most tumours progressed after termination of treatment (Lallo et al., 2018). Several mechanisms of acquired resistance to PARP inhibitors have been published already, even though most of them have been described in *BRCA*-deficient backgrounds (Table 17, Noordermeer and Attikum, 2019). None of the CDX tested harbour a deleterious mutation in *BRCA1* or *BRCA2*, yet, it would be interesting to assess if the proposed mechanisms of acquired resistance also apply to *BRCA*-proficient SCLC tumours. It has been shown that reversion mutations in *BRCA1* and *BRCA2* enable the reactivation of these genes, restoring HR and therefore causing resistance to PARP inhibitors (Edwards et al., 2008; Lheureux et al., 2017). Reversion mutations have been described also in other HR genes (Kondrashova et al., 2017), suggesting that *PALB2* could be affected by these mutations. It would be interesting to determine the

mutational status of *PALB2* in the CDX3 tumours that grew back after olaparib treatment. Similarly, once the RAD51 assay for FFPE tissue is optimised in our laboratory, it could be used to assess the restoration of HR in models that have become resistant to olaparib treatment. This assay would provide a general idea of the HR status of a tumour before and after olaparib treatment, without the need to know the underlying mechanism of HR deficiency.

Table 17. Mechanisms of acquired resistance to PARP inhibitors*.

Resistance mechanisms	Cause of resistance
Increased drug efflux	Upregulation of ABC transporters
Decreased PARP trapping	Loss or decreased trapping of PARP1 Loss of PARG
Restoration of HR	Reactivation of BRCA1/2 Loss of 53BP1 Loss of Shieldin factors Loss of CTC/Polα Loss of DYNLL1/ATMIN
Stabilisation of stalled replication forks	Loss of PTIP Loss of EZH2

**Table adapted from* Noordermeer and Attikum, 2019

Finally, another consideration comes from the key observation that genes involved in the NHEJ pathways negatively correlated with the response to olaparib combined with WEE1i, ATRi and DNAPKi. This analysis is based on gene expression and therefore cannot give information about the actual activation of the NHEJ pathway in the sensitive CDX. However, *BRCA1*-deficient PDX that are resistant to PARP inhibition have reduced expression of NHEJ genes (Dev et al., 2018), highlighting the strong connection between HR, NHEJ and PARP inhibitors response. Because of the lack of alterations in genes known to be involved in the HR pathway in the CDX tested, it is difficult to speculate whether the reduced expression of NHEJ genes in the resistant CDX models is linked to HR restoration. Nevertheless, the role of the NHEJ in the sensitivity/resistance to olaparib cannot be excluded. A recent study performed in advanced ovarian cancer demonstrated that the response to the PARP inhibitor niraparib was independent from the HR status of the patients, further suggesting the possibility that alterations in other DNA repair pathways can synergise with this drug (González-Martín et al., 2019). WES data together with the

establishment of RAD51 foci formation in a larger panel of CDX, and the assessment of the NHEJ status (Bindra et al., 2013; McCormick et al., 2017; Pastwa et al., 2009), could help answering these questions.

7.3 Implementation of biomarker assays to investigate the replication stress response in the CDX

During my PhD, I also focused on replication stress response. In particular, I assessed the presence of replication stress by studying the expression of phospho-RPA Ser33 and chromatin-bound RPA. The presence of phospho-RPA in CDX3 tumours suggested a high intrinsic level of replication stress in this model, which may account for its exquisite sensitivity to AZD1775. One of the causes for this intrinsic replication stress could be the expression of the oncogene L-MYC (Kotsantis et al., 2018). Data obtained from the *ex vivo* drug screening suggests that if overexpression of the MYC genes induces replication stress in SCLC, it may correlate with the response to AZD1775 alone, but does not always correlate with sensitivity to AZD1775/olaparib. The olaparib-resistant CDX17 and CDX17p express high levels of L-MYC and C-MYC and, while they are sensitive to AZD1775 single agent, AZD1775 was not able to sensitise these models to olaparib (Figure 45A,B). Chromatin-bound RPA combined with a marker of DSB (i.e. double positive cells) can be used as a marker of replication catastrophe. I have generated preliminary data showing that treatment with HU and the ATRi VE822 induced a population of double positive cells in CDX18, CDX23 and CDX31 cultures, demonstrating that it is possible to detect cells undergoing replication catastrophe with this assay. Despite these promising initial results, the detection of chromatin-bound RPA and γH2AX double positive cells in CDX cultures was particularly challenging due to the non-adherent nature of SCLC cells. Moreover, I uncovered high heterogeneity across biological replicates which precluded robust data interpretation and will necessitate careful experimental design in the future. In theory this assay could be used to concomitantly test the induction of replication catastrophe in multiple CDX before and after treatment with different drugs. The presence of double positive cells at baseline or after treatment could be used to predict treatment response or better understand molecular mechanisms, respectively. Other markers of DNA damage and replication stress, including

phospho-RPA, phospho-CHK1, phospho-CHK2, 53BP1 or phospho-DNAPKcs, could be added to the screening to provide a more comprehensive overview of the pathways activated in any given model before and after treatment.

To further study the replication potential of the CDX, I also began to optimise the DNA fiber assay. This assay can be used to understand the dynamics of DNA replication under normal and stress-induced conditions. Hill *et al* demonstrated that assessment of defects in the replication fork protection with the DNA fiber assay was predictive of carboplatin, CHK1 and ATR inhibitors response in patient-derived ovarian cancer organoids (Hill et al., 2018). Because most of the drugs used in this thesis can induce replication stress, it would be interesting to characterise the replication dynamics of each CDX before and after treatment in order to evaluate whether certain models can be classified as sensitive or resistant based on the way they deal with replication stress. This could be particularly useful to help design better combinatorial treatments and identify proper biomarkers of response. Genes involved in DNA replication and repair of stalled replication forks are enriched in AZD1775/olaparib sensitive and resistant models, respectively, further suggesting that understanding the dynamics of these complicated processes in the CDX could help deciphering their response to this therapeutic combination.

7.4 Molecular validation of the on-target effect of AZD1775 and olaparib in SCLC CDX cultures

Drugs can have several off-target effects. A recent CRISP-Cas9 screen demonstrated how different cancer drugs used in clinical trials kill cells via off-target effects, highlighting the importance of fully characterise the mechanism of action of each tested drug (Lin et al., 2019). PARP proteins consist of 17 members in humans. These proteins may have different cellular roles, most of which are unknown. In 2012, Wahlberg and colleagues demonstrated that different PARP inhibitors, including olaparib, can bind to multiple PARP proteins and therefore can have distinct cytotoxic effects (Wahlberg et al., 2012). More recently, Knezevic *et al* performed a proteome-wide profiling of clinical PARP inhibitors and identified 17 novel drug targets beyond the PARP protein family (Knezevic et al., 2016). Similarly, some studies have shown that AZD1775 can efficiently bind to both WEE1 and the Polo-like Kinase 1 (PLK1)

(Wright et al., 2017), suggesting that WEE1 inhibition may not be the only effect responsible for the AZD1775 cytotoxicity observed in tumours. All together, these data highlight the importance of performing genetic validation of the mechanism of action of the drugs under study. During my PhD, I have focused my studies in defining the overall effects of DDR inhibitors on our CDX cultures. However, I did not study whether the observed responses were caused by on-target or off-target effects. Genetic silencing or knock-out of PARP1 or WEE1 should be used to validate whether the effects observed with these drugs are triggered by their ability to inhibit WEE1/PARP1 or off-target proteins. There are currently multiple genetic approaches that could be used to perform such validations. These approaches can be based on RNA interference (RNAi) or on genetic editing by the CRISPR-Cas9 system (Aagaard and Rossi, 2007; Mali et al., 2013; Qi et al., 2013). Both approaches can efficiently interfere with the expression of specific genes, however, they have some limitations. As with drugs, both RNAi and CRISPR-Cas9 can introduce off-target effects (Aagaard and Rossi, 2007; Fu et al., 2013). This is usually linked to the design of the RNA that may have low affinity for several regions of the genome and therefore silence off-target genes. To reduce the risk of off-target effects, several small interfering RNA or guides per target are normally used. This allows validation of the on-target effect of the genetic manipulation. Other limitations have been described, including activation of compensatory mechanisms to bypass the silencing of the gene of interest or the technical challenges observed with some transfection-resistant cell types (Chen et al., 2016; El-Brolosy et al., 2019). It is also important to note that, although genetic validation is often beneficial, it is not equivalent to pharmacological inhibition and the phenotypic consequences can diverge (Pettitt et al., 2018).

Overall, all methods have advantages and disadvantages and a multi-modal approach should be used to cross-validate each findings. Genetic manipulation can also be exploited to overexpress a protein of interest. These approaches can be exploited as complementary rescue experiments to assess for off-target effects and further confirm the role played by the target protein in the phenotype investigated (Oser et al., 2019). Going forward, it will be very important to exploit these techniques to fully characterise how the DDR inhibitors act on the CDX models and better understand their role in SCLC.

7.5 DDR inhibitors as promising targets for SCLC

As suggested in the analysis comparing *in vitro* efficacy and RNAseq data, multiple genes and pathways could be involved in the response to the DDRi tested. I focused on the role of p21 in the CDX because of published data showing that p21 can have p53-independent roles in cancers, including modulation of DNA repair and DNA replication (Georgakilas et al., 2017). Interestingly, p21 is heterogeneously expressed across the CDX, with 8/15 models showing more than 30% of cells positive for p21. I was not able to functionally assess the role of p21 in the CDX due to the outgrowth of $p21^{+}$ clones in CDX4 tumours infected with CRISPR guides against *CDKN1A*. However, these data suggest that p21 may be necessary for tumour development. Galanos *et al* demonstrated that constitutive expression of p21 in the absence of p53 triggers replication stress. This was caused by an up-regulation of the licensing factors CDT1 and CDC6 that elicited endoreduplication and consequent genomic instability. They suggested that this p21-driven genomic instability allowed the tumour to acquire more aggressive features (Galanos et al., 2016). If this is also the case in SCLC, it could explain why some tumours displayed high level of p21 at baseline. However, I was unable to find any correlation between the level of p21 and the response to cisplatin/etoposide or AZD1775/olaparib, suggesting that if p21 is involved in the evolution of some SCLC tumours, it does not seem to influence the response to treatments. Similarly, pHH3 did not correlate with the response to AZD1775/olaparib and a weak positive correlation was observed with the response to cisplatin/etoposide. It has to be taken into consideration that I have compared the levels of p21 and pHH3 proteins observed in tumours versus the response of the corresponding cultures. Therefore, the lack of correlation could be linked to differences in the level of these markers between the *in vivo* models and the cultures.

More putative predictive biomarkers were identified via transcriptomic analyses conducted using RNAseq data available in our group. However, because the complete analysis was only generated at the end of my PhD, I have not been able to perform validation studies. Genes like *NEUROD1* and *YAP1* are particularly interesting because they have already been validated as biomarkers to classify SCLC to different phenotypic subgroups, but there is little research so far that look at whether these

subgroups show different responses to treatments (Rudin et al., 2019). One weakness of this analytical strategy lies in the fact that RNAseq data were derived from tumour samples, while the GI_{50} were derived from the cultures. While I consider that most of the data obtained from the cultures are representative of what is observed *in vivo*, the lack of correlation observed with CDX8/8p flags that these cultures have some limitations that could have biased the results.

In conclusion, I have optimised several assays for CDX cultures that can now be used to address specific biological questions. With the completion of the *in vivo* Decapus study, there will soon be plentiful data to mine and validate the predictive value of the cultures. It will also be possible to identify those models that do not behave *ex vivo* as the donor tumours. Independently of the results from this comparison, the *ex vivo* cultures are a new and reliable model that can complement the preclinical tools currently available to study SCLC. While both the inter- and intra-heterogeneity observed in the CDX may have challenged some of the analyses conducted, it may also be seen as a strong advantage of these models. It is likely that this heterogeneity constitutes a true representation of the tumour complexity observed in patients, which may be overlooked when using established SCLC cell lines or GEMMs.

The combination of AZD1775 with olaparib has shown to be very promising in a specific subgroup of SCLC CDX and the identification of biomarkers of response merits further investigation. Furthermore, the response to the AURKB inhibitor observed *ex vivo* was impressive. If the results obtained are shown to be a consequence of on-target effects of the drug, it would be worth prioritizing this inhibitor and test it in combination with additional drugs. It is also necessary to investigate further the role these DDRi have in SCLC, not only to understand why these tumours seems to be so sensitive to these drugs, but also to predict the inevitable mechanism(s) of relapse.

Finally, all biomarkers and drugs validated with the CDX have the potential to be translated directly on the CTCs. This could allow to use these biomarkers to monitor individual patient tumour responses to specific treatments over time, without the need to access tumour biopsy specimens. Moreover, once the CTC cultures will be fully validated, they could be used as ‘avatar’ models to test multiple

biomarkers/drugs in real time, and help inform clinicians in the selection of the most promising treatment for the patient.

With this thesis I have confirmed the use of CDX as a wonderful resource for SCLC research. At the time of writing, our laboratory has developed 45 SCLC models, which cover a wide clinical spectrum of SCLC patients. However, their complexity adds challenges to biomarkers discovery and development. It seems likely that simple predictive biomarkers (e.g. EGFR mutations for EGFR inhibitors, Su et al., 2012) will not be sufficient for DDRi-based therapeutic strategies, and a combination of gene expression profiles and functional assays will be required to stratify SCLC patients.

Appendix Figures

A

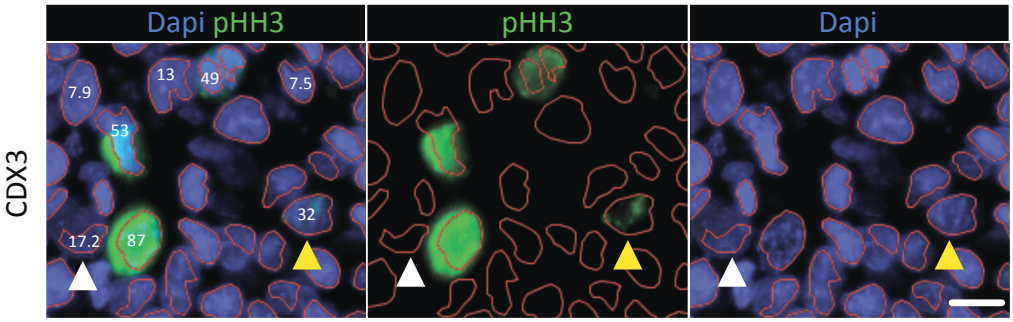

Appendix Figure 1 related to Figure 18. A. Image of CDX3 tumour showing different level of pHH3 intensities. The white triangle indicates a pHH3 negative cell included in the positive population by the threshold set by the Gaussian mixture model, while the yellow triangle indicates a cell weakly positive for pHH3. Red lines demarcate the nuclei. Scale bar = 10 µm.

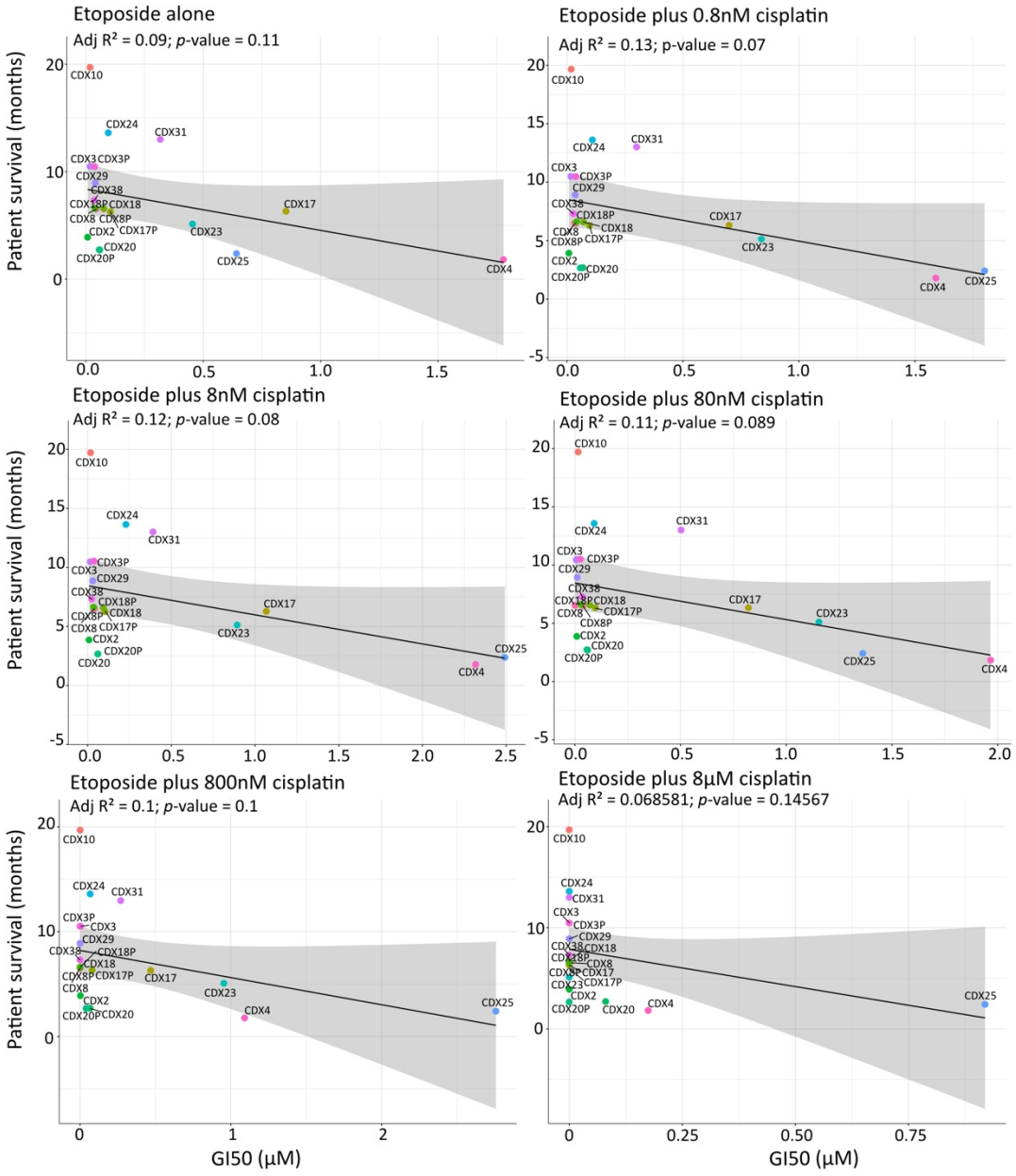

Appendix Figure 2 related to Figure 40. Linear modelling to correlate the patient survival in months with the GI_{50} (µM) of response to etoposide combined with different concentrations of cisplatin.

A

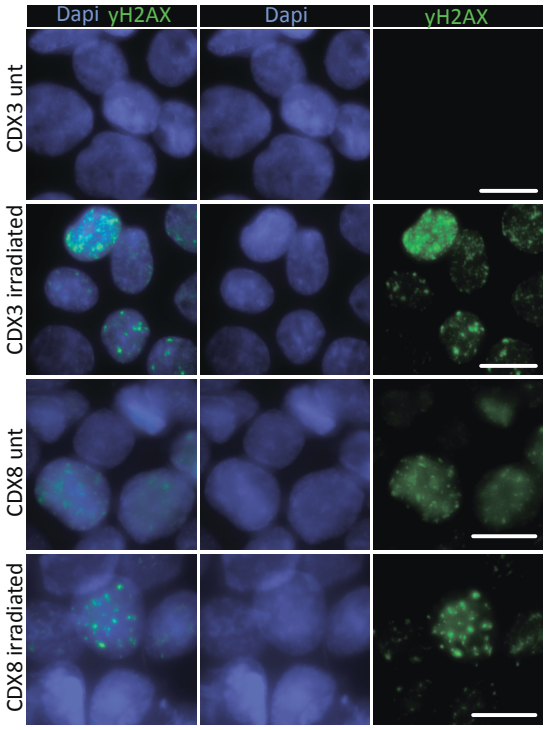

Appendix Figure 3 related to Figure 49. A. Representative images of yH2AX foci formation on CDX3 and CDX8 cells untreated or 24hr after irradiation (10 Gy). Scale bar: 10 µm. Unt: untreated.

A

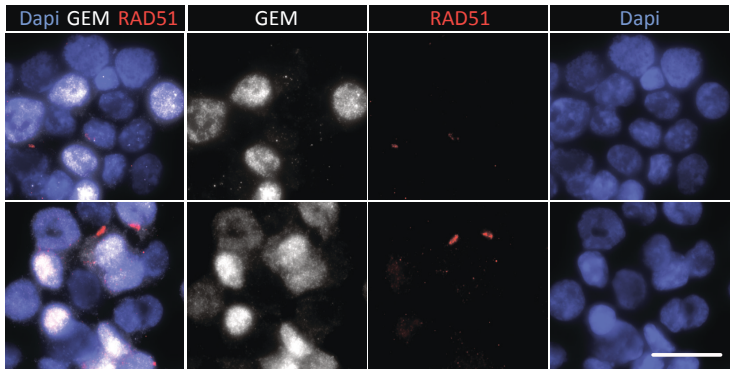

B

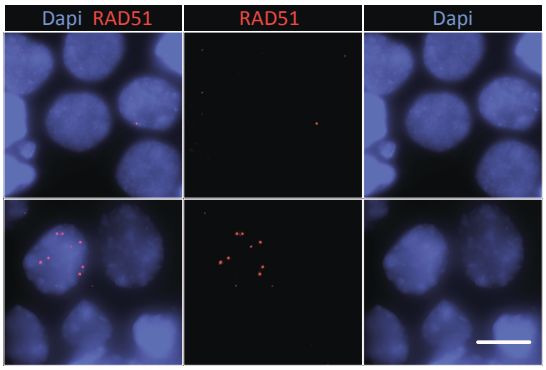

Appendix Figure 4 related to Figure 50. A,B. Representative images of RAD51 foci formation on CDX2 (A) and CDX8 (B) cells irradiated with 10 Gy. Scale bar: 10 µm.

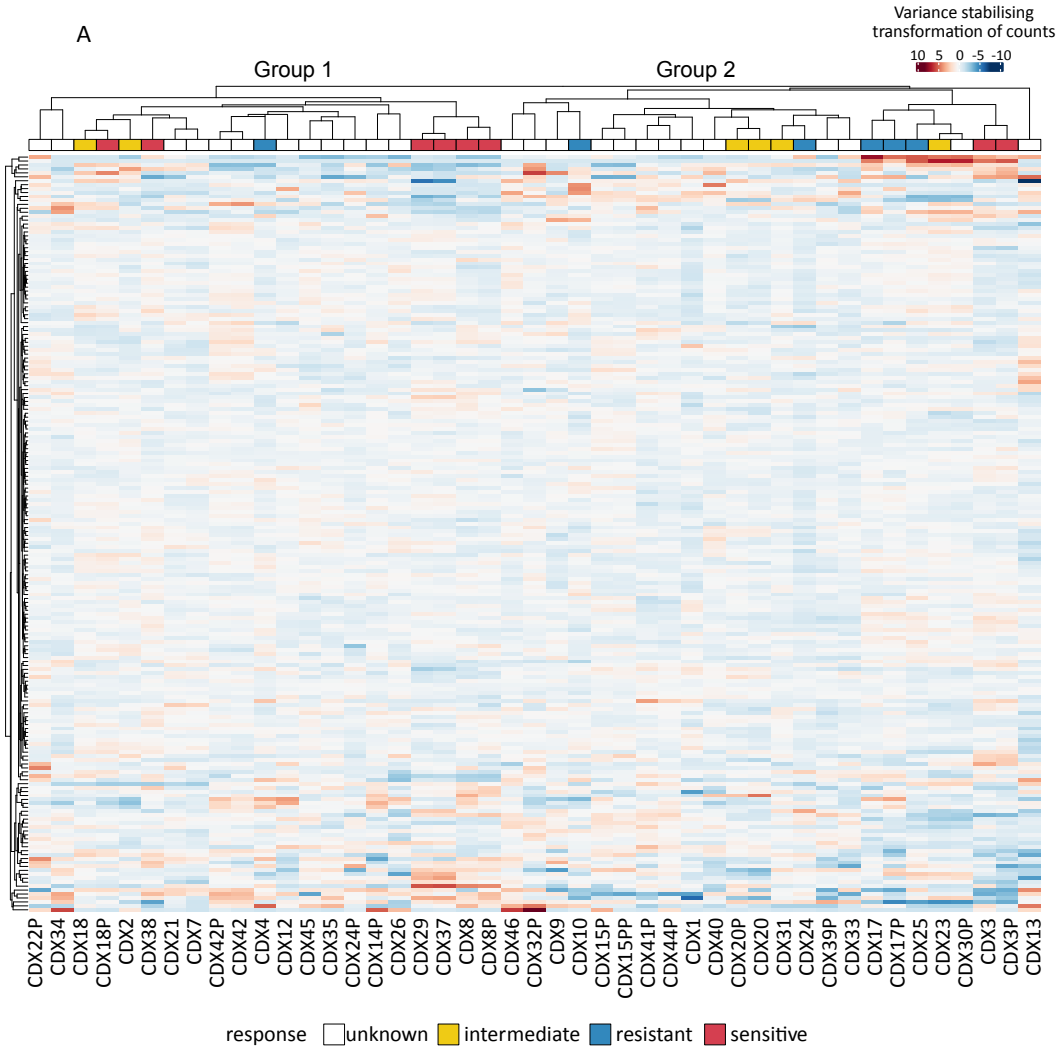

Appendix Figure 5 related to Figure 51. A. Unsupervised hierarchical clustering of a selected list of genes to discriminate tumours with HR deficiency (Peng et al., 2014). Coloured annotations were based on the cluster of response to olaparib *ex vivo* described in chapter 4.2.4 (Figure 44B).

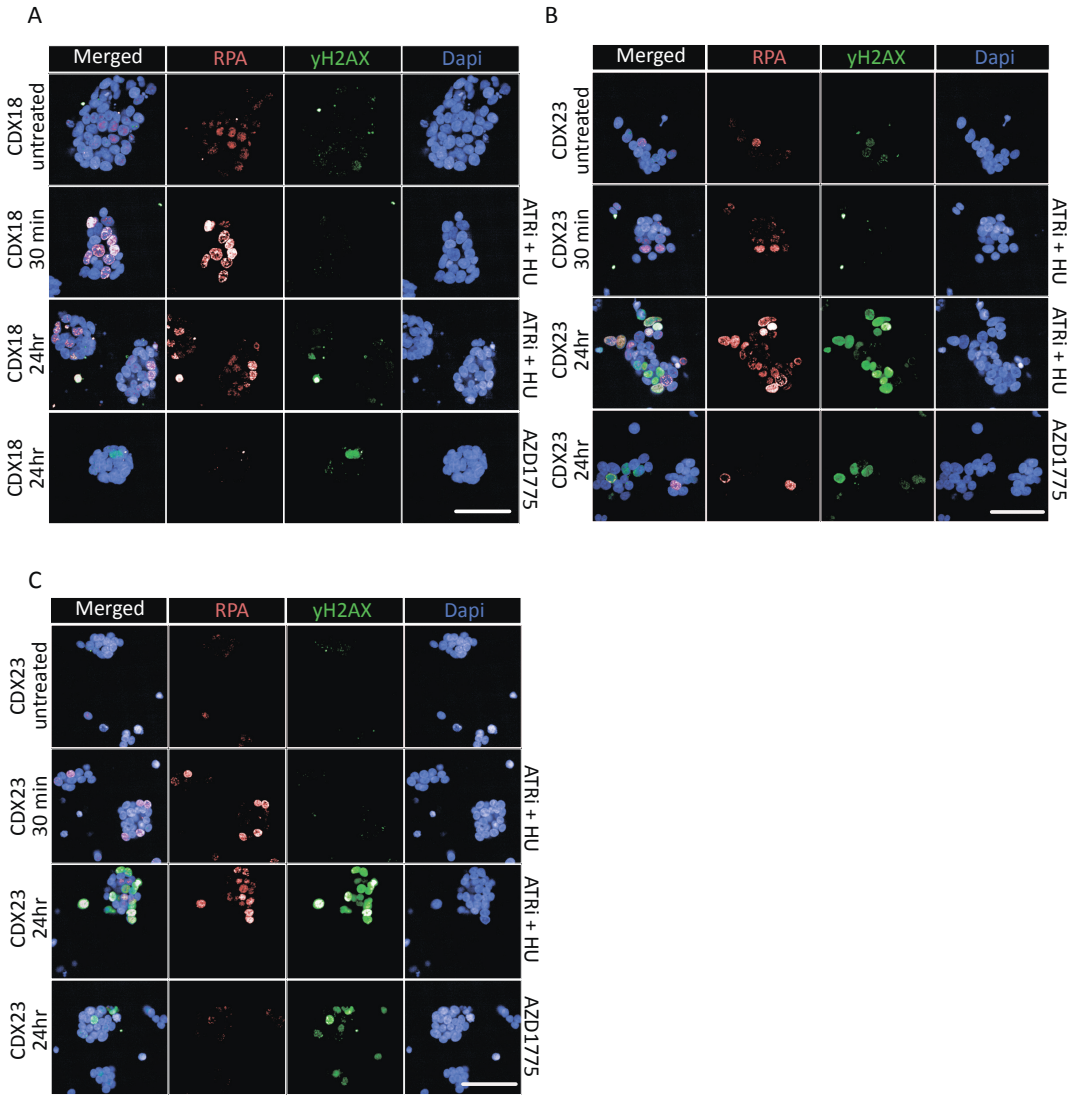

Appendix Figure 6 related to Figure 59. A-C. Representative images of CDX18 (A), CDX23 (B) and CDX31 (C) before and after treatment with 100 nM VE822 + 1 mM HU or 100 nM AZD1775. Scale bar = 50 µm.

A

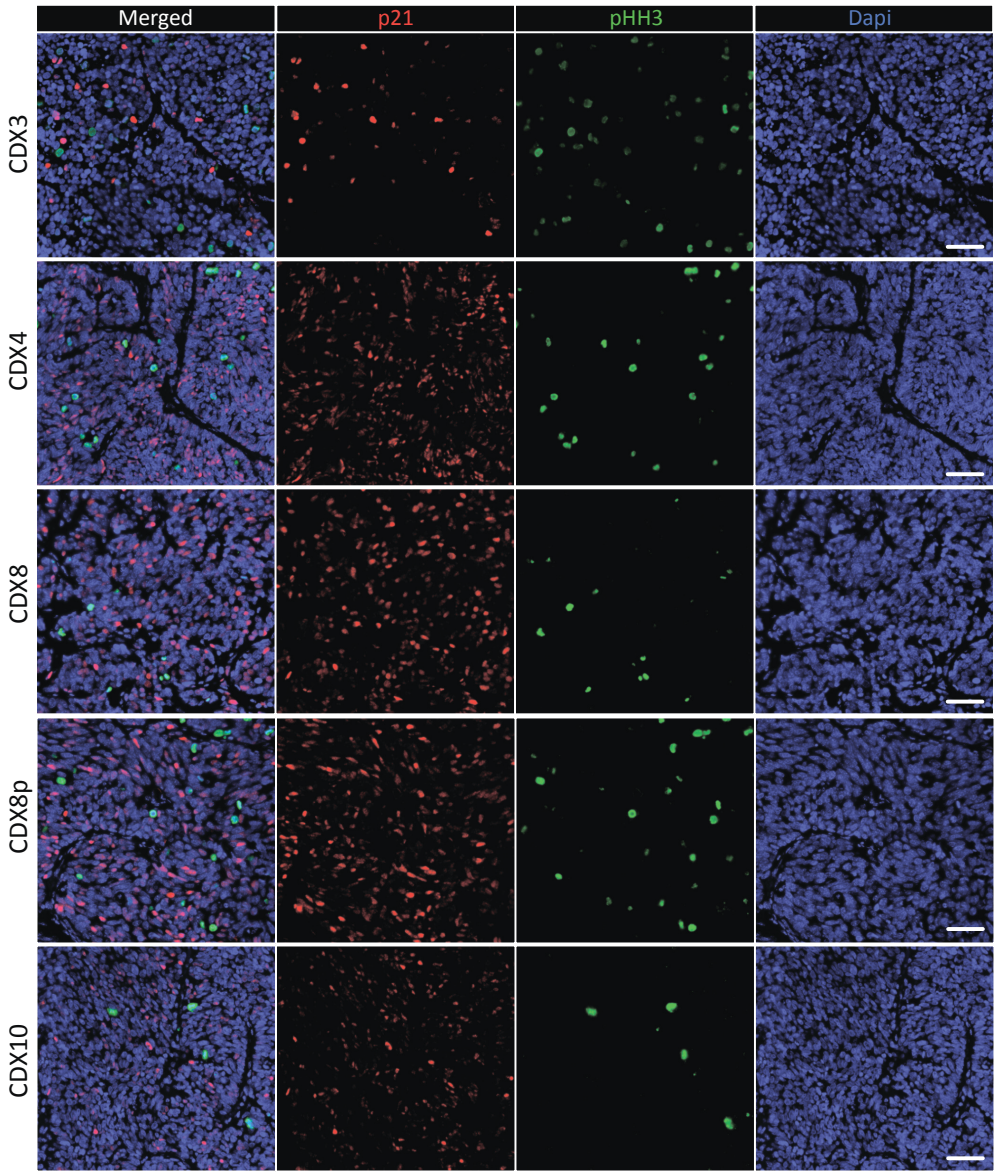

Appendix Figure 7 related to Figure 67. A. Representative images of p21 and pHH3 staining on the stated CDX. Scale bar = 50 µm.

A

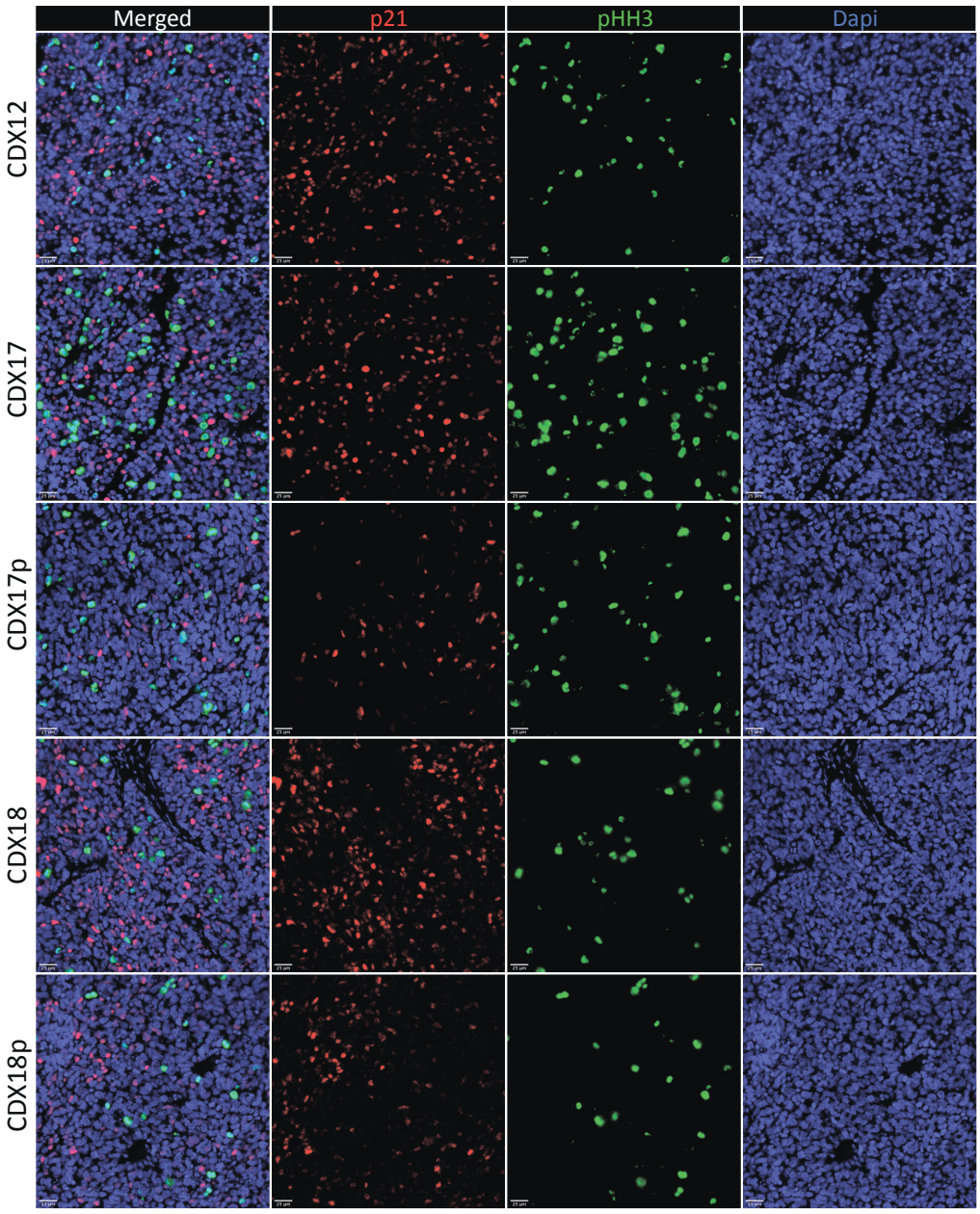

Appendix Figure 8 related to Figure 70. A. Representative images of p21 and pHH3 staining on the stated CDX. Scale bar = 50 µm.

A

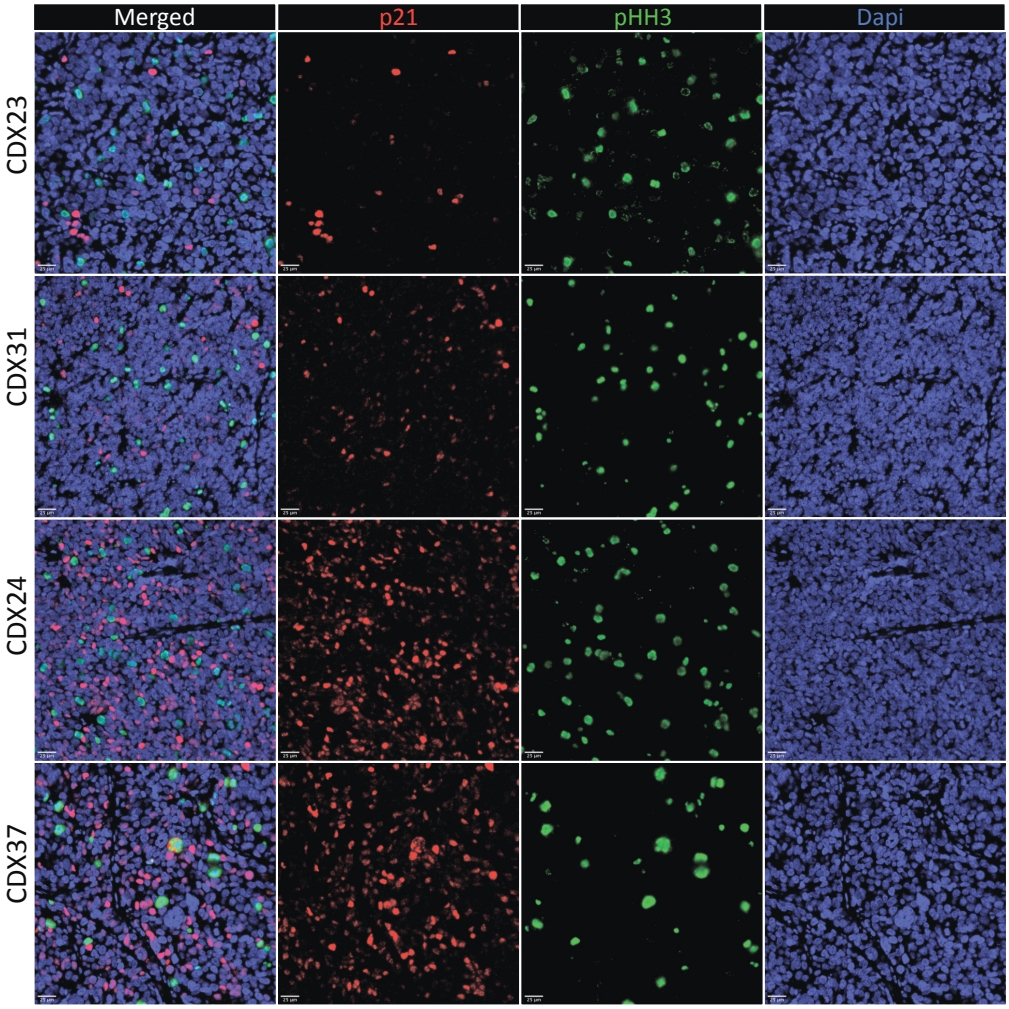

Appendix Figure 8.1 related to Figure 70. A. Representative images of p21 and pHH3 staining on the stated CDX. Scale bar = 50 µm.

A

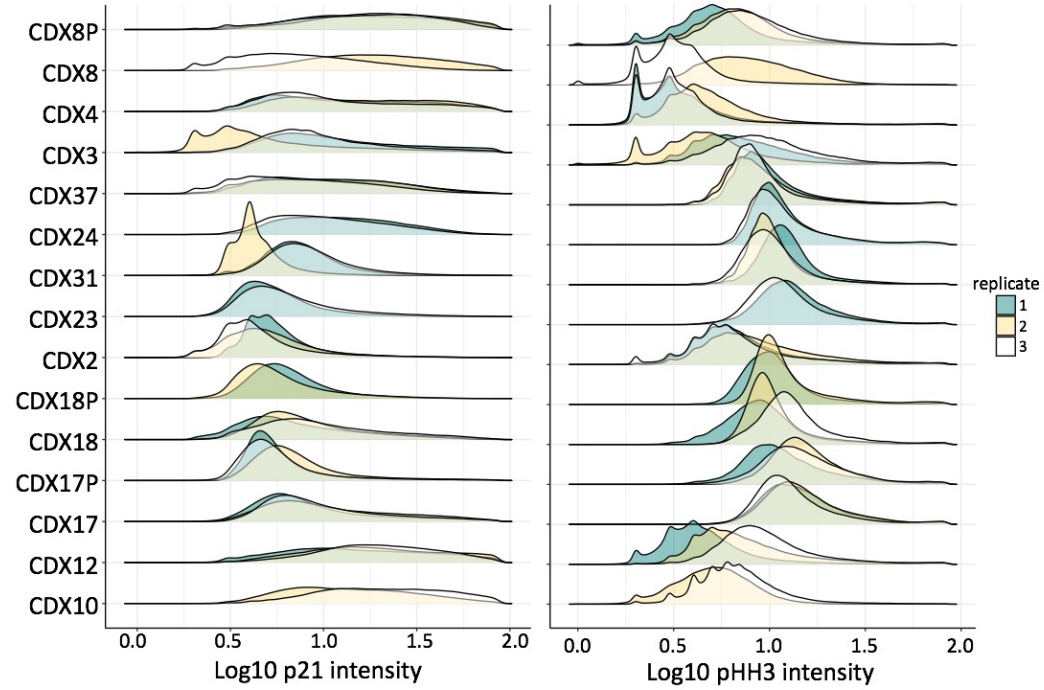

Appendix Figure 9 related to Figure 71. A. Distribution of p21 and pHH3 intensities in all CDX tested. Each distribution represent one replicate.

A

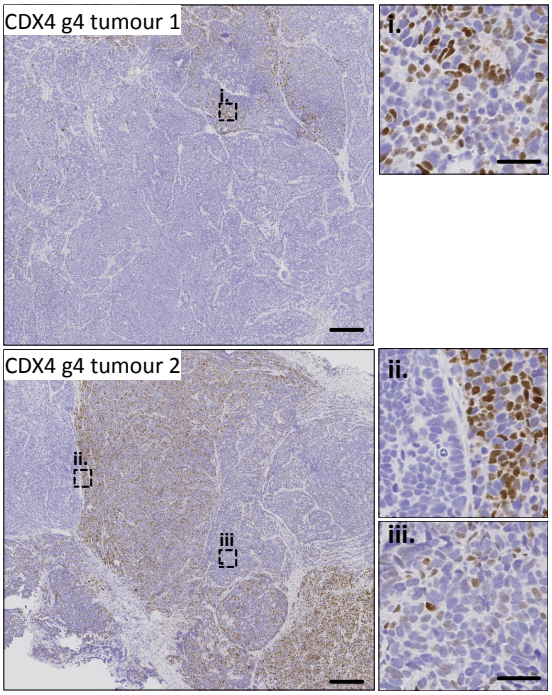

Appendix Figure 10 related to Figure 73. A. Representative images of CDX4 tumours infected with guide 4. Dotted squares delineate the region highlighted on the right hand side of the figure. Scale bar for the low magnification images is 250 µm, while for the high magnification images is 50 µm. g4: guide 4.

Bibliography

Aagaard, L., and Rossi, J.J. (2007). RNAi Therapeutics: Principles, Prospects and Challenges. Adv. Drug Deliv. Rev. *59*, 75–86.

Aarts, M., Sharpe, R., Garcia-Murillas, I., Gevensleben, H., Hurd, M.S., Shumway, S.D., Toniatti, C., Ashworth, A., and Turner, N.C. (2012). Forced Mitotic Entry of S-Phase Cells as a Therapeutic Strategy Induced by Inhibition of WEE1. Cancer Discov. *2*, 524–539.

Abbas, T., and Dutta, A. (2009). p21 in cancer: intricate networks and multiple activities. Nat. Rev. Cancer *9*, 400–414.

Adachi, N., Suzuki, H., Iiizumi, S., and Koyama, H. (2003). Hypersensitivity of Nonhomologous DNA End-joining Mutants to VP-16 and ICRF-193 IMPLICATIONS FOR THE REPAIR OF TOPOISOMERASE II-MEDIATED DNA DAMAGE. J. Biol. Chem. *278*, 35897–35902.

Aebi, S., Kurdi-Haidar, B., Gordon, R., Cenni, B., Zheng, H., Fink, D., Christen, R.D., Boland, C.R., Koi, M., Fishel, R., et al. (1996). Loss of DNA Mismatch Repair in Acquired Resistance to Cisplatin. Cancer Res. *56*, 3087–3090.

Aguilera, A., and García-Muse, T. (2013). Causes of Genome Instability. Annu. Rev. Genet. *47*, 1–32.

Akbari, M.R., Tonin, P., Foulkes, W.D., Ghadirian, P., Tischkowitz, M., and Narod, S.A. (2010). RAD51C germline mutations in breast and ovarian cancer patients. Breast Cancer Res. *12*, 404.

Alexandrov, L.B., Nik-Zainal, S., Wedge, D.C., Aparicio, S.A.J.R., Behjati, S., Biankin, A.V., Bignell, G.R., Bolli, N., Borg, A., Børresen-Dale, A.-L., et al. (2013). Signatures of mutational processes in human cancer. Nature *500*, 415–421.

Alexandrov, L.B., Ju, Y.S., Haase, K., Loo, P.V., Martincorena, I., Nik-Zainal, S., Totoki, Y., Fujimoto, A., Nakagawa, H., Shibata, T., et al. (2016). Mutational signatures associated with tobacco smoking in human cancer. Science *354*, 618–622.

Alix-Panabières, C., and Pantel, K. (2016). Clinical Applications of Circulating Tumor Cells and Circulating Tumor DNA as Liquid Biopsy. Cancer Discov. *6*, 479–491.

Allard, W.J., Matera, J., Miller, M.C., Repollet, M., Connelly, M.C., Rao, C., Tibbe, A.G.J., Uhr, J.W., and Terstappen, L.W.M.M. (2004). Tumor Cells Circulate in the Peripheral Blood of All Major Carcinomas but not in Healthy Subjects or Patients With Nonmalignant Diseases. Clin. Cancer Res. *10*, 6897–6904.

Al-Lazikani, B., Banerji, U., and Workman, P. (2012). Combinatorial drug therapy for cancer in the post-genomic era. Nat. Biotechnol. *30*, 679–692.

Allen, M., Poggiali, D., Whitaker, K., Marshall, T.R., and Kievit, R.A. (2019). Raincloud plots: a multi-platform tool for robust data visualization. Wellcome Open Res. *4*, 63.

Alvarado-Luna, G., and Morales-Espinosa, D. (2016). Treatment for small cell lung cancer, where are we now?—a review. Transl. Lung Cancer Res. *5*, 26-38–38.

Alvino, G.M., Collingwood, D., Murphy, J.M., Delrow, J., Brewer, B.J., and Raghuraman, M.K. (2007). Replication in Hydroxyurea: It's a Matter of Time. Mol. Cell. Biol. *27*, 6396–6406.

Amin, M.B., Greene, F.L., Edge, S.B., Compton, C.C., Gershenwald, J.E., Brookland, R.K., Meyer, L., Gress, D.M., Byrd, D.R., and Winchester, D.P. (2017). The Eighth Edition AJCC Cancer Staging Manual: Continuing to build a bridge from a population-based to a more "personalized" approach to cancer staging. CA. Cancer J. Clin. *67*, 93–99.

Anantha, R.W., Vassin, V.M., and Borowiec, J.A. (2007). Sequential and Synergistic Modification of Human RPA Stimulates Chromosomal DNA Repair. J. Biol. Chem. *282*, 35910–35923.

Antonia, S.J., López-Martin, J.A., Bendell, J., Ott, P.A., Taylor, M., Eder, J.P., Jäger, D., Pietanza, M.C., Le, D.T., de Braud, F., et al. (2016). Nivolumab alone and nivolumab plus ipilimumab in recurrent small-cell lung cancer (CheckMate 032): a multicentre, open-label, phase 1/2 trial. Lancet Oncol. *17*, 883–895.

Asano, F., Aoe, M., Ohsaki, Y., Okada, Y., Sasada, S., Sato, S., Suzuki, E., Senba, H., Fujino, S., and Ohmori, K. (2012). Deaths and complications associated with respiratory endoscopy: A survey by the Japan Society for Respiratory Endoscopy in 2010. Respirology *17*, 478–485.

Atrafi, F., Groen, H.J.M., Byers, L.A., Garralda, E., Lolkema, M.P., Sangha, R.S., Viteri, S., Chae, Y.K., Camidge, D.R., Gabrail, N.Y., et al. (2019). A Phase I Dose-Escalation Study of Veliparib Combined with Carboplatin and Etoposide in Patients with Extensive-Stage Small Cell Lung Cancer and Other Solid Tumors. Clin. Cancer Res. *25*, 496–505.

Augert, A., Zhang, Q., Bates, B., Cui, M., Wang, X., Wildey, G., Dowlati, A., and MacPherson, D. (2017). Small Cell Lung Cancer Exhibits Frequent Inactivating Mutations in the Histone Methyltransferase KMT2D/MLL2: CALGB 151111 (Alliance). J. Thorac. Oncol. *12*, 704–713.

Aupérin, A., Arriagada, R., Pignon, J.-P., Le Péchoux, C., Gregor, A., Stephens, R.J., Kristjansen, P.E.G., Johnson, B.E., Ueoka, H., Wagner, H., et al. (1999). Prophylactic Cranial Irradiation for Patients with Small-Cell Lung Cancer in Complete Remission. N. Engl. J. Med. *341*, 476–484.

Azarova, A.M., Lyu, Y.L., Lin, C.-P., Tsai, Y.-C., Lau, J.Y.-N., Wang, J.C., and Liu, L.F. (2007). Roles of DNA topoisomerase II isozymes in chemotherapy and secondary malignancies. Proc. Natl. Acad. Sci. *104*, 11014–11019.

Azzopardi, J.G. (1959). Oat-cell carcinoma of the bronchus. J. Pathol. Bacteriol. *78*, 513–519.

Bae, I.H., Kang, S.W., Yoon, S.H., and Um, H.-D. (2006). Cellular components involved in the cell death induced by cisplatin in the absence of p53 activation. Oncol. Rep. *15*, 1175–1180.

Bankhead, P., Loughrey, M.B., Fernández, J.A., Dombrowski, Y., McArt, D.G., Dunne, P.D., McQuaid, S., Gray, R.T., Murray, L.J., Coleman, H.G., et al. (2017). QuPath: Open source software for digital pathology image analysis. Sci. Rep. *7*, 16878.

Bauer, T.M., Jones, S.F., Greenlees, C., Cook, C., Mugundu, G.M., Jewsbury, P.J., Pierce, A.J., O'Connor, M.J., Johnson, M.L., Beck, J.T., et al. (2016). Abstract CT013: A phase Ib, open-label, multicenter study to assess the safety, tolerability, pharmacokinetics, and antitumor activity of AZD1775 monotherapy in patients with advanced solid tumors: initial findings. Cancer Res. *76*, CT013–CT013.

Beasley, M.B., Brambilla, E., and Travis, W.D. (2005). The 2004 World Health Organization classification of lung tumors. Semin. Roentgenol. *40*, 90–97.

Beck, H., Nähse-Kumpf, V., Larsen, M.S.Y., O'Hanlon, K.A., Patzke, S., Holmberg, C., Mejlvang, J., Groth, A., Nielsen, O., Syljuåsen, R.G., et al. (2012). Cyclin-Dependent Kinase Suppression by WEE1 Kinase Protects the Genome through Control of Replication Initiation and Nucleotide Consumption. Mol. Cell. Biol. *32*, 4226–4236.

Belani, C.P., Dahlberg, S.E., Rudin, C.M., Fleisher, M., Chen, H.X., Takebe, N., Ramalingam, S.S., and Schiller, J.H. (2013). Three-arm randomized phase II study of cisplatin and etoposide (CE) versus CE with either vismodegib (V) or cixutumumab (Cx) for patients with extensive stage-small cell lung cancer (ES-SCLC) (ECOG 1508). J. Clin. Oncol. *31*, 7508–7508.

Belizário, J.E. (2009). Immunodeficient Mouse Models: An Overview. Open Immunol. J. *2*.

Benaglia, T., Chauveau, D., Hunter, D.R., and Young, D. (2009). **mixtools** : An *R* Package for Analyzing Finite Mixture Models. J. Stat. Softw. *32*.

Ben-David, U., Ha, G., Tseng, Y.-Y., Greenwald, N.F., Oh, C., Shih, J., McFarland, J.M., Wong, B., Boehm, J.S., Beroukhim, R., et al. (2017). Patient-derived xenografts undergo mouse-specific tumor evolution. Nat. Genet. *49*, 1567–1575.

Ben-Ezra, J.M., Kornstein, M.J., Grimes, M.M., and Krystal, G. (1994). Small cell carcinomas of the lung express the Bcl-2 protein. Am. J. Pathol. *145*, 1036–1040.

Bensch, K.G., Corrin, B., Pariente, R., and Spencer, H. (1968). Oat-cell carcinoma of the lung. Its origin and relationship to bronchial carcinoid. Cancer *22*, 1163–1172.

Bertotti, A., Migliardi, G., Galimi, F., Sassi, F., Torti, D., Isella, C., Corà, D., Nicolantonio, F.D., Buscarino, M., Petti, C., et al. (2011). A Molecularly Annotated Platform of Patient-Derived Xenografts ("Xenopatients") Identifies HER2 as an Effective Therapeutic Target in Cetuximab-Resistant Colorectal Cancer. Cancer Discov. *1*, 508–523.

Bindra, R.S., Goglia, A.G., Jasin, M., and Powell, S.N. (2013). Development of an assay to measure mutagenic non-homologous end-joining repair activity in mammalian cells. Nucleic Acids Res. *41*, e115–e115.

Biswas, A.K., and Johnson, D.G. (2012). Transcriptional and Nontranscriptional Functions of E2F1 in Response to DNA Damage. Cancer Res. *72*, 13–17.

Biswas, S.K., Huang, J., Persaud, S., and Basu, A. (2004). Down-regulation of Bcl-2 is associated with cisplatin resistance in human small cell lung cancer H69 cells. Mol. Cancer Ther. *3*, 327–334.

Blackford, A.N., and Jackson, S.P. (2017). ATM, ATR, and DNA-PK: The Trinity at the Heart of the DNA Damage Response. Mol. Cell *66*, 801–817.

Blackhall, F.H., Pintilie, M., Michael, M., Leighl, N., Feld, R., Tsao, M.-S., and Shepherd, F.A. (2003). Expression and Prognostic Significance of Kit, Protein Kinase B, and Mitogen-activated Protein Kinase in Patients with Small Cell Lung Cancer. Clin. Cancer Res. *9*, 2241–2247.

Bobrow, M.N., Harris, T.D., Shaughnessy, K.J., and Litt, G.J. (1989). Catalyzed reporter deposition, a novel method of signal amplification application to immunoassays. J. Immunol. Methods *125*, 279–285.

Bobrow, M.N., Shaughnessy, K.J., and Litt, G.J. (1991). Catalyzed reporter deposition, a novel method of signal amplification: II. Application to membrane immunoassays. J. Immunol. Methods *137*, 103–112.

Bono, J. de, Ramanathan, R.K., Mina, L., Chugh, R., Glaspy, J., Rafii, S., Kaye, S., Sachdev, J., Heymach, J., Smith, D.C., et al. (2017). Phase I, Dose-Escalation, Two-Part Trial of the PARP Inhibitor Talazoparib in Patients with Advanced Germline BRCA1/2 Mutations and Selected Sporadic Cancers. Cancer Discov. *7*, 620–629.

Borges, M., Linnoila, R.I., Velde, H.J.K. van de, Chen, H., Nelkin, B.D., Mabry, M., Baylin, S.B., and Ball, D.W. (1997). An achaete-scute homologue essential for neuroendocrine differentiation in the lung. Nature *386*, 852.

Borromeo, M.D., Savage, T.K., Kollipara, R.K., He, M., Augustyn, A., Osborne, J.K., Girard, L., Minna, J.D., Gazdar, A.F., Cobb, M.H., et al. (2016). ASCL1 and NEUROD1 Reveal Heterogeneity in Pulmonary Neuroendocrine Tumors and Regulate Distinct Genetic Programs. Cell Rep. *16*, 1259–1272.

Böttger, F., Semenova, E.A., Song, J.-Y., Ferone, G., Vliet, J. van der, Cozijnsen, M., Bhaskaran, R., Bombardelli, L., Piersma, S.R., Pham, T.V., et al. (2019). Tumor Heterogeneity Underlies Differential Cisplatin Sensitivity in Mouse Models of Small-Cell Lung Cancer. Cell Rep. *27*, 3345-3358.e4.

Boyle, E.I., Weng, S., Gollub, J., Jin, H., Botstein, D., Cherry, J.M., and Sherlock, G. (2004). GO::TermFinder—open source software for accessing Gene Ontology information and finding significantly enriched Gene Ontology terms associated with

a list of genes. Bioinformatics *20*, 3710–3715.

Branzei, D., and Foiani, M. (2008). Regulation of DNA repair throughout the cell cycle. Nat. Rev. Mol. Cell Biol. *9*, 297–308.

Bray, F., Ferlay, J., Soerjomataram, I., Siegel, R.L., Torre, L.A., and Jemal, A. (2018). Global cancer statistics 2018: GLOBOCAN estimates of incidence and mortality worldwide for 36 cancers in 185 countries. CA. Cancer J. Clin. *68*, 394–424.

Bretones, G., Delgado, M.D., and León, J. (2015). Myc and cell cycle control. Biochim. Biophys. Acta BBA - Gene Regul. Mech. *1849*, 506–516.

Broers, J.L., Carney, D.N., Rot, M.K., Schaart, G., Lane, E.B., Vooijs, G.P., and Ramaekers, F.C. (1986). Intermediate filament proteins in classic and variant types of small cell lung carcinoma cell lines: a biochemical and immunochemical analysis using a panel of monoclonal and polyclonal antibodies. J. Cell Sci. *83*, 37–60.

Buchbinder, E.I., and Desai, A. (2016). CTLA-4 and PD-1 Pathways. Am. J. Clin. Oncol. *39*, 98–106.

Buisson, R., Dion-Côté, A.-M., Coulombe, Y., Launay, H., Cai, H., Stasiak, A.Z., Stasiak, A., Xia, B., and Masson, J.-Y. (2010). Cooperation of breast cancer proteins PALB2 and piccolo BRCA2 in stimulating homologous recombination. Nat. Struct. Mol. Biol. *17*, 1247–1254.

Buisson, R., Boisvert, J.L., Benes, C.H., and Zou, L. (2015). Distinct but Concerted Roles of ATR, DNA-PK, and Chk1 in Countering Replication Stress during S Phase. Mol. Cell *59*, 1011–1024.

Burris, H.A., Wang, J.S.-Z., Johnson, M.L., Falchook, G.S., Jones, S.F., Strickland, D.K., Greenlees, C., Brugger, W., Charlton, J., Pease, E., et al. (2017). A phase I, open-label, first-time-in-patient dose escalation and expansion study to assess the safety, tolerability, and pharmacokinetics of nanoparticle encapsulated Aurora B kinase inhibitor AZD2811 in patients with advanced solid tumours. J. Clin. Oncol. *35*, TPS2608–TPS2608.

Byers, L.A., and Rudin, C.M. (2015). Small cell lung cancer: Where do we go from here? Cancer *121*, 664–672.

Byers, L.A., Wang, J., Nilsson, M.B., Fujimoto, J., Saintigny, P., Yordy, J., Giri, U., Peyton, M., Fan, Y.H., Diao, L., et al. (2012). Proteomic Profiling Identifies Dysregulated Pathways in Small Cell Lung Cancer and Novel Therapeutic Targets Including PARP1. Cancer Discov. *2*, 798–811.

Cañadas, I., Rojo, F., Taus, Á., Arpí, O., Arumí-Uría, M., Pijuan, L., Menéndez, S., Zazo, S., Dómine, M., Salido, M., et al. (2014). Targeting Epithelial-to-Mesenchymal Transition with Met Inhibitors Reverts Chemoresistance in Small Cell Lung Cancer. Clin. Cancer Res. *20*, 938–950.

Canitrot, Y., Bichat, F., Cole, S.P.C., Deeley, R.G., Gerlach, J.H., Bastian, G., Arvelo, F., and Poupon, M.-F. (1998). Multidrug resistance genes (MRP) and MDR1 expression in small cell lung cancer xenografts: relationship with response to chemotherapy. Cancer Lett. *130*, 133–141.

Capasso, M., Devoto, M., Hou, C., Asgharzadeh, S., Glessner, J.T., Attiyeh, E.F., Mosse, Y.P., Kim, C., Diskin, S.J., Cole, K.A., et al. (2009). Common variations in *BARD1* influence susceptibility to high-risk neuroblastoma. Nat. Genet. *41*, 718–723.

Carbone, D.P., Morgensztern, D., Le Moulec, S., Santana-Davila, R., Ready, N., Hann, C.L., Glisson, B.S., Dowlati, A., Rudin, C.M., Lally, S., et al. (2018). Efficacy and safety of rovalpituzumab tesirine in patients With DLL3-expressing, ≥ 3rd line small cell lung cancer: Results from the phase 2 TRINITY study. J. Clin. Oncol. *36*, 8507–8507.

Cardnell, R.J., Feng, Y., Diao, L., Fan, Y.-H., Masrorpour, F., Wang, J., Shen, Y., Mills, G.B., Minna, J.D., Heymach, J.V., et al. (2013). Proteomic Markers of DNA Repair and PI3K Pathway Activation Predict Response to the PARP Inhibitor BMN 673 in Small Cell Lung Cancer. Clin. Cancer Res. *19*, 6322–6328.

Cardnell, R.J., Feng, Y., Mukherjee, S., Diao, L., Tong, P., Stewart, C.A., Masrorpour, F., Fan, Y., Nilsson, M., Shen, Y., et al. (2016). Activation of the PI3K/mTOR Pathway following PARP Inhibition in Small Cell Lung Cancer. PLOS ONE *11*, e0152584.

Carmena, M., and Earnshaw, W.C. (2003). The cellular geography of Aurora kinases. Nat. Rev. Mol. Cell Biol. *4*, 842.

Carney, D.N., Gazdar, A.F., Bepler, G., Guccion, J.G., Marangos, P.J., Moody, T.W., Zweig, M.H., and Minna, J.D. (1985). Establishment and Identification of Small Cell Lung Cancer Cell Lines Having Classic and Variant Features. Cancer Res. *45*, 2913–2923.

Carter, L., Rothwell, D.G., Mesquita, B., Smowton, C., Leong, H.S., Fernandez-Gutierrez, F., Li, Y., Burt, D.J., Antonello, J., Morrow, C.J., et al. (2017). Molecular analysis of circulating tumor cells identifies distinct copy-number profiles in patients with chemosensitive and chemorefractory small-cell lung cancer. Nat. Med. *23*, 114–119.

Castroviejo-Bermejo, M., Cruz, C., Llop-Guevara, A., Gutiérrez-Enríquez, S., Ducy, M., Ibrahim, Y.H., Gris-Oliver, A., Pellegrino, B., Bruna, A., Guzmán, M., et al. (2018). A RAD51 assay feasible in routine tumor samples calls PARP inhibitor response beyond BRCA mutation. EMBO Mol. Med. *10*, e9172.

Ceppi, P., Longo, M., Volante, M., Novello, S., Cappia, S., Bacillo, E., Selvaggi, G., Saviozzi, S., Calogero, R., Papotti, M., et al. (2008). Excision Repair Cross Complementing-1 and Topoisomerase IIα Gene Expression in Small-Cell Lung Cancer Patients Treated with Platinum and Etoposide: A Retrospective Study. J. Thorac. Oncol. *3*, 583–589.

Chae, Y.K., Pan, A.P., Davis, A.A., Patel, S.P., Carneiro, B.A., Kurzrock, R., and Giles,

F.J. (2017). Path toward Precision Oncology: Review of Targeted Therapy Studies and Tools to Aid in Defining “Actionability” of a Molecular Lesion and Patient Management Support. Mol. Cancer Ther. *16*, 2645–2655.

Chalishazar, M.D., Wait, S.J., Huang, F., Ireland, A.S., Mukhopadhyay, A., Lee, Y., Schuman, S., Guthrie, M.R., Berrett, K., Vahrenkamp, J., et al. (2019). MYC-driven small cell lung cancer is metabolically distinct and vulnerable to arginine depletion. Clin. Cancer Res. clincanres.4140.2018.

Champoux, J.J. (2001). DNA Topoisomerases: Structure, Function, and Mechanism. Annu. Rev. Biochem. *70*, 369–413.

Chang, H.H.Y., Pannunzio, N.R., Adachi, N., and Lieber, M.R. (2017). Non-homologous DNA end joining and alternative pathways to double-strand break repair. Nat. Rev. Mol. Cell Biol. *18*, 495–506.

Chen, H.H.W., Yan, J.-J., Chen, W.-C., Kuo, M.T., Lai, Y.-H., Lai, W.-W., Liu, H.-S., and Su, W.-C. (2012). Predictive and prognostic value of human copper transporter 1 (hCtr1) in patients with stage III non-small-cell lung cancer receiving first-line platinum-based doublet chemotherapy. Lung Cancer Amst. Neth. *75*, 228–234.

Chen, S., Lee, B., Lee, A.Y.-F., Modzelewski, A.J., and He, L. (2016). Highly Efficient Mouse Genome Editing by CRISPR Ribonucleoprotein Electroporation of Zygotes. J. Biol. Chem. *291*, 14457–14467.

Christensen, C.L., Kwiatkowski, N., Abraham, B.J., Carretero, J., Al-Shahrour, F., Zhang, T., Chipumuro, E., Herter-Sprie, G.S., Akbay, E.A., Altabef, A., et al. (2014). Targeting Transcriptional Addictions in Small Cell Lung Cancer with a Covalent CDK7 Inhibitor. Cancer Cell *26*, 909–922.

Cogliano, V.J., Baan, R., Straif, K., Grosse, Y., Lauby-Secretan, B., El Ghissassi, F., Bouvard, V., Benbrahim-Tallaa, L., Guha, N., Freeman, C., et al. (2011). Preventable Exposures Associated With Human Cancers. JNCI J. Natl. Cancer Inst. *103*, 1827–1839.

Collins, A.R. (2004). The Comet Assay for DNA Damage and Repair: Principles, Applications, and Limitations. Mol. Biotechnol. *26*, 249–261.

Cong, L., Ran, F.A., Cox, D., Lin, S., Barretto, R., Habib, N., Hsu, P.D., Wu, X., Jiang, W., Marraffini, L.A., et al. (2013). Multiplex Genome Engineering Using CRISPR/Cas Systems. Science *339*, 819–823.

Conway, J.R., Lex, A., and Gehlenborg, N. (2017). UpSetR: an R package for the visualization of intersecting sets and their properties. Bioinformatics *33*, 2938–2940.

Coschi, C.H., Ishak, C.A., Gallo, D., Marshall, A., Talluri, S., Wang, J., Cecchini, M.J., Martens, A.L., Percy, V., Welch, I., et al. (2014). Haploinsufficiency of an RB–E2F1–Condensin II Complex Leads to Aberrant Replication and Aneuploidy. Cancer Discov. *4*, 840–853.

Coste, F., Malinge, J.-M., Serre, L., Leng, M., Zelwer, C., Shepard, W., and Roth, M. (1999). Crystal structure of a double-stranded DNA containing a cisplatin interstrand cross-link at 1.63 Å resolution: Hydration at the platinated site. Nucleic Acids Res. *27*, 1837–1846.

Cruz, C., Castroviejo-Bermejo, M., Gutiérrez-Enríquez, S., Llop-Guevara, A., Ibrahim, Y.H., Gris-Oliver, A., Bonache, S., Morancho, B., Bruna, A., Rueda, O.M., et al. (2018). RAD51 foci as a functional biomarker of homologous recombination repair and PARP inhibitor resistance in germline BRCA-mutated breast cancer. Ann. Oncol. *29*, 1203–1210.

Cui, M., Augert, A., Rongione, M., Conkrite, K., Parazzoli, S., Nikitin, A.Y., Ingolia, N., and MacPherson, D. (2014). PTEN Is a Potent Suppressor of Small Cell Lung Cancer. Mol. Cancer Res. *12*, 654–659.

Cuneo, K.C., Morgan, M.A., Davis, M.A., Parcels, L.A., Parcels, J., Karnak, D., Ryan, C., Liu, N., Maybaum, J., and Lawrence, T.S. (2016). Wee1 Kinase Inhibitor AZD1775 Radiosensitizes Hepatocellular Carcinoma Regardless of TP53 Mutational Status Through Induction of Replication Stress. Int. J. Radiat. Oncol. *95*, 782–790.

Cuttitta, F., Carney, D.N., Mulshine, J., Moody, T.W., Fedorko, J., Fischler, A., and Minna, J.D. (1985). Bombesin-like peptides can function as autocrine growth factors in human small-cell lung cancer. Nature *316*, 823–826.

Dabholkar, M., Vionnet, J., Bostick-Bruton, F., Yu, J.J., and Reed, E. (1994). Messenger RNA levels of XPAC and ERCC1 in ovarian cancer tissue correlate with response to platinum-based chemotherapy. J. Clin. Invest. *94*, 703–708.

Damia, G., Filiberti, L., Vikhanskaya, F., Carrassa, L., Taya, Y., D'incalci, M., and Broggini, M. (2001). Cisplatinum and Taxol Induce Different Patterns of p53 Phosphorylation. Neoplasia N. Y. N *3*, 10–16.

D'Amico, D., Carbone, D., Mitsudomi, T., Nau, M., Fedorko, J., Russell, E., Johnson, B., Buchhagen, D., Bodner, S., and Phelps, R. (1992). High frequency of somatically acquired p53 mutations in small-cell lung cancer cell lines and tumors. Oncogene *7*, 339–346.

Dang, C.V. (2012). MYC on the Path to Cancer. Cell *149*, 22–35.

Daniel, D.B., Rudin, C.M., Hart, L., Spigel, D.R., Edelman, M.J., Goldschmidt, J., Bordoni, R., Glisson, B., Burns, T.F., Dowlati, A., et al. (2017). 1530PDResults of a randomized, placebo-controlled, phase 2 study of tarextumab (TRXT, anti-Notch2/3) in combination with etoposide and platinum (EP) in patients (pts) with untreated extensive-stage small-cell lung cancer (ED-SCLC). Ann. Oncol. *28*.

Daniel, V.C., Marchionni, L., Hierman, J.S., Rhodes, J.T., Devereux, W.L., Rudin, C.M., Yung, R., Parmigiani, G., Dorsch, M., Peacock, C.D., et al. (2009). A Primary Xenograft Model of Small-Cell Lung Cancer Reveals Irreversible Changes in Gene Expression Imposed by Culture In vitro. Cancer Res. *69*, 3364–3373.

Dao, D., Fraser, A.N., Hung, J., Ljosa, V., Singh, S., and Carpenter, A.E. (2016). CellProfiler Analyst: interactive data exploration, analysis and classification of large biological image sets. Bioinforma. Oxf. Engl. *32*, 3210–3212.

Davisson, M.T. (1997). Rules and guidelines for genetic nomenclature in mice: excerpted version. Transgenic Res. *6*, 309–319.

Day, C.-P., Merlino, G., and Van Dyke, T. (2015). Preclinical Mouse Cancer Models: A Maze of Opportunities and Challenges. Cell *163*, 39–53.

DeRose, Y.S., Wang, G., Lin, Y.-C., Bernard, P.S., Buys, S.S., Ebbert, M.T.W., Factor, R., Matsen, C., Milash, B.A., Nelson, E., et al. (2011). Tumor grafts derived from women with breast cancer authentically reflect tumor pathology, growth, metastasis and disease outcomes. Nat. Med. *17*, 1514–1520.

Dessauer, C.W., Chen-Goodspeed, M., and Chen, J. (2002). Mechanism of Gαi-mediated Inhibition of Type V Adenylyl Cyclase. J. Biol. Chem. *277*, 28823–28829.

Dev, H., Chiang, T.-W.W., Lescale, C., Krijger, I. de, Martin, A.G., Pilger, D., Coates, J., Sczaniecka-Clift, M., Wei, W., Ostermaier, M., et al. (2018). Shieldin complex promotes DNA end-joining and counters homologous recombination in BRCA1-null cells. Nat. Cell Biol. *20*, 954–965.

Dhillon, A.S., Hagan, S., Rath, O., and Kolch, W. (2007). MAP kinase signalling pathways in cancer. Oncogene *26*, 3279–3290.

Dingemans, A.-M.C., Witlox, M.A., Stallaert, R.A.L.M., Valk, P. van der, Postmus, P.E., and Giaccone, G. (1999). Expression of DNA Topoisomerase IIα and Topoisomerase IIβ Genes Predicts Survival and Response to Chemotherapy in Patients with Small Cell Lung Cancer. Clin. Cancer Res. *5*, 2048–2058.

Do, K., Doroshow, J.H., and Kummar, S. (2013). Wee1 kinase as a target for cancer therapy. Cell Cycle *12*, 3348–3353.

Dobbelstein, M., and Sørensen, C.S. (2015). Exploiting replicative stress to treat cancer. Nat. Rev. Drug Discov. *14*, 405–423.

Doerr, F., George, J., Schmitt, A., Beleggia, F., Rehkämper, T., Hermann, S., Walter, V., Weber, J.-P., Thomas, R.K., Wittersheim, M., et al. (2017). Targeting a non-oncogene addiction to the ATR/CHK1 axis for the treatment of small cell lung cancer. Sci. Rep. *7*, 15511.

Domínguez-Kelly, R., Martín, Y., Koundrioukoff, S., Tanenbaum, M.E., Smits, V.A.J., Medema, R.H., Debatisse, M., and Freire, R. (2011). Wee1 controls genomic stability during replication by regulating the Mus81-Eme1 endonuclease. J. Cell Biol. *194*, 567–579.

Dominguez-Sola, D., Ying, C.Y., Grandori, C., Ruggiero, L., Chen, B., Li, M., Galloway, D.A., Gu, W., Gautier, J., and Dalla-Favera, R. (2007). Non-transcriptional control of

DNA replication by c-Myc. Nature *448*, 445–451.

Dong, X., Guan, J., English, J.C., Flint, J., Yee, J., Evans, K., Murray, N., MacAulay, C., Ng, R.T., Gout, P.W., et al. (2010). Patient-Derived First Generation Xenografts of Non–Small Cell Lung Cancers: Promising Tools for Predicting Drug Responses for Personalized Chemotherapy. Clin. Cancer Res. *16*, 1442–1451.

Dooley, A.L., Winslow, M.M., Chiang, D.Y., Banerji, S., Stransky, N., Dayton, T.L., Snyder, E.L., Senna, S., Whittaker, C.A., Bronson, R.T., et al. (2011). Nuclear factor I/B is an oncogene in small cell lung cancer. Genes Dev. *25*, 1470–1475.

Dowlati, A., Lipka, M.B., McColl, K., Dabir, S., Behtaj, M., Kresak, A., Miron, A., Yang, M., Sharma, N., Fu, P., et al. (2016). Clinical correlation of extensive-stage small-cell lung cancer genomics. Ann. Oncol. *27*, 642–647.

Downward, J. (2004). PI 3-kinase, Akt and cell survival. Semin. Cell Dev. Biol. *15*, 177–182.

Drapkin, B.J., George, J., Christensen, C.L., Mino-Kenudson, M., Dries, R., Sundaresan, T., Phat, S., Myers, D.T., Zhong, J., Igo, P., et al. (2018). Genomic and Functional Fidelity of Small Cell Lung Cancer Patient-Derived Xenografts. Cancer Discov. *8*, 600–615.

Druker, B.J., Talpaz, M., Resta, D.J., Peng, B., Buchdunger, E., Ford, J.M., Lydon, N.B., Kantarjian, H., Capdeville, R., Ohno-Jones, S., et al. (2001). Efficacy and Safety of a Specific Inhibitor of the BCR-ABL Tyrosine Kinase in Chronic Myeloid Leukemia. N. Engl. J. Med. *344*, 1031–1037.

Du, Y., Yamaguchi, H., Wei, Y., Hsu, J.L., Wang, H.-L., Hsu, Y.-H., Lin, W.-C., Yu, W.-H., Leonard, P.G., Lee Iv, G.R., et al. (2016). Blocking c-Met–mediated PARP1 phosphorylation enhances anti-tumor effects of PARP inhibitors. Nat. Med. *22*, 194–201.

Duda, H., Arter, M., Gloggnitzer, J., Teloni, F., Wild, P., Blanco, M.G., Altmeyer, M., and Matos, J. (2016). A Mechanism for Controlled Breakage of Under-replicated Chromosomes during Mitosis. Dev. Cell *39*, 740–755.

Dyson, N.J. (2016). RB1: a prototype tumor suppressor and an enigma. Genes Dev. *30*, 1492–1502.

Eapen, G.A., Shah, A.M., Lei, X., Jimenez, C.A., Morice, R.C., Yarmus, L., Filner, J., Ray, C., Michaud, G., Greenhill, S.R., et al. (2013). Complications, Consequences, and Practice Patterns of Endobronchial Ultrasound-Guided Transbronchial Needle Aspiration: Results of the AQuIRE Registry. Chest *143*, 1044–1053.

Edlich, F. (2018). BCL-2 proteins and apoptosis: Recent insights and unknowns. Biochem. Biophys. Res. Commun. *500*, 26–34.

Edwards, S.L., Brough, R., Lord, C.J., Natrajan, R., Vatcheva, R., Levine, D.A., Boyd, J.,

Reis-Filho, J.S., and Ashworth, A. (2008). Resistance to therapy caused by intragenic deletion in BRCA2. Nature *451*, 1111–1115.

El-Brolosy, M.A., Kontarakis, Z., Rossi, A., Kuenne, C., Günther, S., Fukuda, N., Kikhi, K., Boezio, G.L.M., Takacs, C.M., Lai, S.-L., et al. (2019). Genetic compensation triggered by mutant mRNA degradation. Nature *568*, 193–197.

El-Khateeb, M., Appleton, T.G., Gahan, L.R., Charles, B.G., Berners-Price, S.J., and Bolton, A.-M. (1999). Reactions of cisplatin hydrolytes with methionine, cysteine, and plasma ultrafiltrate studied by a combination of HPLC and NMR techniques. J. Inorg. Biochem. *77*, 13–21.

Ertel, A., Verghese, A., Byers, S.W., Ochs, M., and Tozeren, A. (2006). Pathway-specific differences between tumor cell lines and normal and tumor tissue cells. Mol. Cancer *5*, 55.

Ettinger, D.S., Jotte, R., Lorigan, P., Gupta, V., Garbo, L., Alemany, C., Conkling, P., Spigel, D.R., Dudek, A.Z., Shah, C., et al. (2010). Phase II Study of Amrubicin As Second-Line Therapy in Patients With Platinum-Refractory Small-Cell Lung Cancer. J. Clin. Oncol. *28*, 2598–2603.

Evans, W.K., Shepherd, F.A., Feld, R., Osoba, D., Dang, P., and Deboer, G. (1985). VP-16 and cisplatin as first-line therapy for small-cell lung cancer. J. Clin. Oncol. *3*, 1471–1477.

Faber, A.C., Farago, A.F., Costa, C., Dastur, A., Gomez-Caraballo, M., Robbins, R., Wagner, B.L., Rideout, W.M., Jakubik, C.T., Ham, J., et al. (2015). Assessment of ABT-263 activity across a cancer cell line collection leads to a potent combination therapy for small-cell lung cancer. Proc. Natl. Acad. Sci. *112*, E1288–E1296.

Fang, Y., McGrail, D.J., Sun, C., Labrie, M., Chen, X., Zhang, D., Ju, Z., Vellano, C.P., Lu, Y., Li, Y., et al. (2019). Sequential Therapy with PARP and WEE1 Inhibitors Minimizes Toxicity while Maintaining Efficacy. Cancer Cell *35*, 851-867.e7.

Farago, A.F., and Keane, F.K. (2018). Current standards for clinical management of small cell lung cancer. Transl. Lung Cancer Res. *7*, 69-79–79.

Farago, A.F., Drapkin, B.J., Charles, A., Yeap, B.Y., Heist, R.S., Azzoli, C.G., Jackman, D.M., Marcoux, J.P., Barbie, D.A., Myers, D.T., et al. (2018). Safety and efficacy of combination olaparib (O) and temozolomide (T) in small cell lung cancer (SCLC). J. Clin. Oncol. *36*, 8571–8571.

Farago, A.F., Yeap, B.Y., Stanzione, M., Hung, Y.P., Heist, R.S., Marcoux, J.P., Zhong, J., Rangachari, D., Barbie, D.A., Phat, S., et al. (2019). Combination Olaparib and Temozolomide in Relapsed Small-Cell Lung Cancer. Cancer Discov. *9*, 1372–1387.

Feng, S., Zhao, Y., Xu, Y., Ning, S., Huo, W., Hou, M., Gao, G., Ji, J., Guo, R., and Xu, D. (2016). Ewing Tumor-associated Antigen 1 Interacts with Replication Protein A to Promote Restart of Stalled Replication Forks. J. Biol. Chem. *291*, 21956–21962.

Fichtner, I., Rolff, J., Soong, R., Hoffmann, J., Hammer, S., Sommer, A., Becker, M., and Merk, J. (2008). Establishment of Patient-Derived Non–Small Cell Lung Cancer Xenografts as Models for the Identification of Predictive Biomarkers. Clin. Cancer Res. *14*, 6456–6468.

Fok, J.H.L., Ramos-Montoya, A., Vazquez-Chantada, M., Wijnhoven, P.W.G., Follia, V., James, N., Farrington, P.M., Karmokar, A., Willis, S.E., Cairns, J., et al. (2019). AZD7648 is a potent and selective DNA-PK inhibitor that enhances radiation, chemotherapy and olaparib activity. Nat. Commun. *10*, 1–15.

Foucquier, J., and Guedj, M. (2015). Analysis of drug combinations: current methodological landscape. Pharmacol. Res. Perspect. *3*.

Foy, V., Schenk, M.W., Baker, K., Gomes, F., Lallo, A., Frese, K.K., Forster, M., Dive, C., and Blackhall, F. (2017). Targeting DNA damage in SCLC. Lung Cancer *114*, 12–22.

Fruman, D.A., and Rommel, C. (2014). PI3K and cancer: lessons, challenges and opportunities. Nat. Rev. Drug Discov. *13*, 140–156.

Fu, Y., Foden, J.A., Khayter, C., Maeder, M.L., Reyon, D., Joung, J.K., and Sander, J.D. (2013). High-frequency off-target mutagenesis induced by CRISPR-Cas nucleases in human cells. Nat. Biotechnol. *31*, 822–826.

Furuse, K., Kubota, K., Kawahara, M., Takada, M., Kimura, I., Fujii, M., Ohta, M., Hasegawa, K., Yoshida, K., Nakajima, S., et al. (1996). Phase II Study of Vinorelbine in Heavily Previously Treated Small Cell Lung Cancer. Oncology *53*, 169–172.

Gad, H., Koolmeister, T., Jemth, A.-S., Eshtad, S., Jacques, S.A., Ström, C.E., Svensson, L.M., Schultz, N., Lundbäck, T., Einarsdottir, B.O., et al. (2014). MTH1 inhibition eradicates cancer by preventing sanitation of the dNTP pool. Nature *508*, 215–221.

Gadagkar, S.R., and Call, G.B. (2015). Computational tools for fitting the Hill equation to dose–response curves. J. Pharmacol. Toxicol. Methods *71*, 68–76.

Gadgeel, S.M., Pennell, N.A., Fidler, M.J., Halmos, B., Bonomi, P., Stevenson, J., Schneider, B., Sukari, A., Ventimiglia, J., Chen, W., et al. (2018). Phase II Study of Maintenance Pembrolizumab in Patients with Extensive-Stage Small Cell Lung Cancer (SCLC). J. Thorac. Oncol. *13*, 1393–1399.

Galanos, P., Vougas, K., Walter, D., Polyzos, A., Maya-Mendoza, A., Haagensen, E.J., Kokkalis, A., Roumelioti, F.-M., Gagos, S., Tzetis, M., et al. (2016). Chronic p53-independent p21 expression causes genomic instability by deregulating replication licensing. Nat. Cell Biol. *18*, 777–789.

Galluzzi, L., Senovilla, L., Vitale, I., Michels, J., Martins, I., Kepp, O., Castedo, M., and Kroemer, G. (2012). Molecular mechanisms of cisplatin resistance. Oncogene *31*, 1869–1883.

Gannon, J. v., Greaves, R., Iggo, R., and Lane, D. p. (1990). Activating mutations in p53

produce a common conformational effect. A monoclonal antibody specific for the mutant form. EMBO J. *9*, 1595–1602.

Gao, H., Korn, J.M., Ferretti, S., Monahan, J.E., Wang, Y., Singh, M., Zhang, C., Schnell, C., Yang, G., Zhang, Y., et al. (2015). High-throughput screening using patient-derived tumor xenografts to predict clinical trial drug response. Nat. Med. *21*, 1318–1325.

Garderen, C.J.V., and Houte, L.P.A.V. (1994). The Solution Structure of a DNA Duplex Containing the cis -Pt(NH3)2[d(-GTG-)-N 7(G), N 7(G)] Adduct, as Determined with High-Field NMR and Molecular Mechanics/Dynamics. Eur. J. Biochem. *225*, 1169–1179.

Gardner, E.E., Connis, N., Poirier, J.T., Cope, L., Dobromilskaya, I., Gallia, G.L., Rudin, C.M., and Hann, C.L. (2014). Rapamycin Rescues ABT-737 Efficacy in Small Cell Lung Cancer. Cancer Res. *74*, 2846–2856.

Gardner, E.E., Lok, B.H., Schneeberger, V.E., Desmeules, P., Miles, L.A., Arnold, P.K., Ni, A., Khodos, I., de Stanchina, E., Nguyen, T., et al. (2017). Chemosensitive Relapse in Small Cell Lung Cancer Proceeds through an EZH2-SLFN11 Axis. Cancer Cell *31*, 286–299.

Gazdar, A.F., and Minna, J.D. (1996). NCI series of cell lines: An historical perspective. J. Cell. Biochem. *63*, 1–11.

Gazdar, A.F., and Oie, H.K. (1986). Cell culture methods for human lung cancer. Cancer Genet. Cytogenet. *19*, 5–10.

Gazdar, A.F., Carney, D.N., Russell, E.K., Sims, H.L., Baylin, S.B., Bunn, P.A., Guccion, J.G., and Minna, J.D. (1980). Establishment of Continuous, Clonable Cultures of Small-Cell Carcinoma of the Lung Which Have Amine Precursor Uptake and Decarboxylation Cell Properties. Cancer Res. *40*, 3502–3507.

Gazdar, A.F., Carney, D.N., Nau, M.M., and Minna, J.D. (1985). Characterization of Variant Subclasses of Cell Lines Derived from Small Cell Lung Cancer Having Distinctive Biochemical, Morphological, and Growth Properties. Cancer Res. *45*, 2924–2930.

Gazdar, A.F., Girard, L., Lockwood, W.W., Lam, W.L., and Minna, J.D. (2010). Lung Cancer Cell Lines as Tools for Biomedical Discovery and Research. JNCI J. Natl. Cancer Inst. *102*, 1310–1321.

Gazdar, A.F., Savage, T.K., Johnson, J.E., Berns, A., Sage, J., Linnoila, R.I., MacPherson, D., McFadden, D.G., Farago, A., Jacks, T., et al. (2015). The Comparative Pathology of Genetically Engineered Mouse Models for Neuroendocrine Carcinomas of the Lung. J. Thorac. Oncol. *10*, 553–564.

Gazdar, A.F., Bunn, P.A., and Minna, J.D. (2017). Small-cell lung cancer: what we know, what we need to know and the path forward. Nat. Rev. Cancer *17*, 725–737.

Geenen, J.J.J., and Schellens, J.H.M. (2017). Molecular Pathways: Targeting the Protein Kinase Wee1 in Cancer. Clin. Cancer Res. *23*, 4540–4544.

Gelasco, A., and Lippard, S.J. (1998). NMR Solution Structure of a DNA Dodecamer Duplex Containing a cis-Diammineplatinum(II) d(GpG) Intrastrand Cross-Link, the Major Adduct of the Anticancer Drug Cisplatin. Biochemistry *37*, 9230–9239.

Georgakilas, A.G., Martin, O.A., and Bonner, W.M. (2017). p21: A Two-Faced Genome Guardian. Trends Mol. Med. *23*, 310–319.

George, J., Lim, J.S., Jang, S.J., Cun, Y., Ozretić, L., Kong, G., Leenders, F., Lu, X., Fernández-Cuesta, L., Bosco, G., et al. (2015). Comprehensive genomic profiles of small cell lung cancer. Nature *524*, 47–53.

Gerbe, F., Sidot, E., Smyth, D.J., Ohmoto, M., Matsumoto, I., Dardalhon, V., Cesses, P., Garnier, L., Pouzolles, M., Brulin, B., et al. (2016). Intestinal epithelial tuft cells initiate type 2 mucosal immunity to helminth parasites. Nature *529*, 226–230.

Giaccone, G., Ferrati, P., Donadio, M., Testore, F., and Calciati, A. (1987). Reinduction chemotherapy in small cell lung cancer. Eur. J. Cancer Clin. Oncol. *23*, 1697–1699.

Giard, D.J., Aaronson, S.A., Todaro, G.J., Arnstein, P., Kersey, J.H., Dosik, H., and Parks, W.P. (1973). In Vitro Cultivation of Human Tumors: Establishment of Cell Lines Derived From a Series of Solid Tumors. JNCI J. Natl. Cancer Inst. *51*, 1417–1423.

Gilbert, L.A., and Hemann, M.T. (2010). DNA Damage-Mediated Induction of a Chemoresistant Niche. Cell *143*, 355–366.

Gillet, J.-P., Calcagno, A.M., Varma, S., Marino, M., Green, L.J., Vora, M.I., Patel, C., Orina, J.N., Eliseeva, T.A., Singal, V., et al. (2011). Redefining the relevance of established cancer cell lines to the study of mechanisms of clinical anti-cancer drug resistance. Proc. Natl. Acad. Sci. U. S. A. *108*, 18708–18713.

Glisson, B., Besse, B., Dols, M.C., Dubey, S., Schupp, M., Jain, R., Jiang, Y., Menon, H., Nackaerts, K., Orlov, S., et al. (2017). A Randomized, Placebo-Controlled, Phase 1b/2 Study of Rilotumumab or Ganitumab in Combination With Platinum-Based Chemotherapy as First-Line Treatment for Extensive-Stage Small-Cell Lung Cancer. Clin. Lung Cancer *18*, 615-625.e8.

Glover, T.W., Wilson, T.E., and Arlt, M.F. (2017). Fragile sites in cancer: more than meets the eye. Nat. Rev. Cancer *17*, 489–501.

Gong, J., Costanzo, A., Yang, H.-Q., Melino, G., Kaelin, W.G., Levrero, M., and Wang, J.Y.J. (1999). The tyrosine kinase c-Abl regulates p73 in apoptotic response to cisplatin-induced DNA damage. Nature *399*, 806.

Gong, X., Du, J., Parsons, S.H., Merzoug, F.F., Webster, Y., Iversen, P.W., Chio, L.-C., Horn, R.D.V., Lin, X., Blosser, W., et al. (2019). Aurora A Kinase Inhibition Is Synthetic Lethal with Loss of the RB1 Tumor Suppressor Gene. Cancer Discov. *9*, 248–263.

Gontan, C., de Munck, A., Vermeij, M., Grosveld, F., Tibboel, D., and Rottier, R. (2008). Sox2 is important for two crucial processes in lung development: Branching morphogenesis and epithelial cell differentiation. Dev. Biol. *317*, 296–309.

González-Martín, A., Pothuri, B., Vergote, I., DePont Christensen, R., Graybill, W., Mirza, M.R., McCormick, C., Lorusso, D., Hoskins, P., Freyer, G., et al. (2019). Niraparib in Patients with Newly Diagnosed Advanced Ovarian Cancer. N. Engl. J. Med. *0*, null.

Goodman, M.F., and Woodgate, R. (2013). Translesion DNA Polymerases. Cold Spring Harb. Perspect. Biol. *5*.

Grandori, C., and Eisenman, R.N. (1997). Myc target genes. Trends Biochem. Sci. *22*, 177–181.

Gray, K.A., Daugherty, L.C., Gordon, S.M., Seal, R.L., Wright, M.W., and Bruford, E.A. (2013). Genenames.org: the HGNC resources in 2013. Nucleic Acids Res. *41*, D545–D552.

Gu, Z., Eils, R., and Schlesner, M. (2016). Complex heatmaps reveal patterns and correlations in multidimensional genomic data. Bioinformatics *32*, 2847–2849.

Guo, L., Zhou, Y., Sun, Y., and Zhang, F. (2010). Non-receptor tyrosine kinase Etk regulation of drug resistance in small-cell lung cancer. Eur. J. Cancer *46*, 636–641.

Gyori, B.M., Venkatachalam, G., Thiagarajan, P.S., Hsu, D., and Clement, M.-V. (2014). OpenComet: An automated tool for comet assay image analysis. Redox Biol. *2*, 457–465.

Haahr, P., Hoffmann, S., Tollenaere, M.A.X., Ho, T., Toledo, L.I., Mann, M., Bekker-Jensen, S., Räschle, M., and Mailand, N. (2016). Activation of the ATR kinase by the RPA-binding protein ETAA1. Nat. Cell Biol. *18*, 1196–1207.

Hainaut, P., and Pfeifer, G.P. (2001). Patterns of p53 G→T transversions in lung cancers reflect the primary mutagenic signature of DNA-damage by tobacco smoke. Carcinogenesis *22*, 367–374.

Halazonetis, T.D., Gorgoulis, V.G., and Bartek, J. (2008). An Oncogene-Induced DNA Damage Model for Cancer Development. Science *319*, 1352–1355.

Hamilton, E., Falchook, G.S., Wang, J.S., Fu, S., Oza, A., Karen, S., Imedio, E.R., Kumar, S., Ottesen, L., Mugundu, G.M., et al. (2019). Abstract CT025: Phase Ib study of adavosertib in combination with olaparib in patients with refractory solid tumors: Dose escalation. Cancer Res. *79*, CT025–CT025.

Hampp, S., Kiessling, T., Buechle, K., Mansilla, S.F., Thomale, J., Rall, M., Ahn, J., Pospiech, H., Gottifredi, V., and Wiesmüller, L. (2016). DNA damage tolerance pathway involving DNA polymerase ι and the tumor suppressor p53 regulates DNA replication fork progression. Proc. Natl. Acad. Sci. *113*, E4311–E4319.

Hanahan, D., and Weinberg, R.A. (2011). Hallmarks of Cancer: The Next Generation. Cell *144*, 646–674.

Hang, B. (2010). Formation and Repair of Tobacco Carcinogen-Derived Bulky DNA Adducts. J. Nucleic Acids *2010*.

Hann, C.L., Daniel, V.C., Sugar, E.A., Dobromilskaya, I., Murphy, S.C., Cope, L., Lin, X., Hierman, J.S., Wilburn, D.L., Watkins, D.N., et al. (2008). Therapeutic Efficacy of ABT-737, a Selective Inhibitor of BCL-2, in Small Cell Lung Cancer. Cancer Res. *68*, 2321–2328.

Hansen, K.D., Timp, W., Bravo, H.C., Sabunciyan, S., Langmead, B., McDonald, O.G., Wen, B., Wu, H., Liu, Y., Diep, D., et al. (2011). Increased methylation variation in epigenetic domains across cancer types. Nat. Genet. *43*, 768–775.

Hansen, L.T., Lundin, C., Spang-Thomsen, M., Petersen, L.N., and Helleday, T. (2003). The role of RAD51 in etoposide (VP16) resistance in small cell lung cancer. Int. J. Cancer *105*, 472–479.

Harbour, J.W., Lai, S.L., Whang-Peng, J., Gazdar, A.F., Minna, J.D., and Kaye, F.J. (1988). Abnormalities in structure and expression of the human retinoblastoma gene in SCLC. Science *241*, 353–357.

Harper, J.V. (2005). Synchronization of Cell Populations in G1/S and G2/M Phases of the Cell Cycle. In Cell Cycle Control: Mechanisms and Protocols, T. Humphrey, and G. Brooks, eds. (Totowa, NJ: Humana Press), pp. 157–166.

Hartmann, T.N., Burger, J.A., Glodek, A., Fujii, N., and Burger, M. (2005). CXCR4 chemokine receptor and integrin signaling co-operate in mediating adhesion and chemoresistance in small cell lung cancer (SCLC) cells. Oncogene *24*, 4462.

Hauge, S., Macurek, L., and Syljuåsen, R.G. (2019). p21 limits S phase DNA damage caused by the Wee1 inhibitor MK1775. Cell Cycle *18*, 834–847.

He, L., Kulesskiy, E., Saarela, J., Turunen, L., Wennerberg, K., Aittokallio, T., and Tang, J. (2018). Methods for High-throughput Drug Combination Screening and Synergy Scoring. In Cancer Systems Biology: Methods and Protocols, L. von Stechow, ed. (New York, NY: Springer), pp. 351–398.

Heeke, A.L., Pishvaian, M.J., Lynce, F., Xiu, J., Brody, J.R., Chen, W.-J., Baker, T.M., Marshall, J.L., and Isaacs, C. (2018). Prevalence of Homologous Recombination–Related Gene Mutations Across Multiple Cancer Types. JCO Precis. Oncol.

Helfrich, B.A., Kim, J., Gao, D., Chan, D.C., Zhang, Z., Tan, A.-C., and Bunn, P.A. (2016). Barasertib (AZD1152), a Small Molecule Aurora B Inhibitor, Inhibits the Growth of SCLC Cell Lines In Vitro and In Vivo. Mol. Cancer Ther. *15*, 2314–2322.

Helin, K., Holm, K., Niebuhr, A., Eiberg, H., Tommerup, N., Hougaard, S., Poulsen, H.S., Spang-Thomsen, M., and Nørgaard, P. (1997). Loss of the retinoblastoma protein-

related p130 protein in small cell lung carcinoma. Proc. Natl. Acad. Sci. U. S. A. *94*, 6933–6938.

Hemström, T.H., Sandström, M., and Zhivotovsky, B. (2006). Inhibitors of the PI3-kinase/Akt pathway induce mitotic catastrophe in non-small cell lung cancer cells. Int. J. Cancer *119*, 1028–1038.

Hernando, E., Nahlé, Z., Juan, G., Diaz-Rodriguez, E., Alaminos, M., Hemann, M., Michel, L., Mittal, V., Gerald, W., Benezra, R., et al. (2004). Rb inactivation promotes genomic instability by uncoupling cell cycle progression from mitotic control. Nature *430*, 797.

Hiatt, J.B., and MacPherson, D. (2019). Delivering a STINGing Blow to Small Cell Lung Cancer via Synergistic Inhibition of DNA-Damage Response and Immune-Checkpoint Pathways. Cancer Discov. *9*, 584–586.

Hidalgo, M., Bruckheimer, E., Rajeshkumar, N.V., Garrido-Laguna, I., Oliveira, E.D., Rubio-Viqueira, B., Strawn, S., Wick, M.J., Martell, J., and Sidransky, D. (2011). A Pilot Clinical Study of Treatment Guided by Personalized Tumorgrafts in Patients with Advanced Cancer. Mol. Cancer Ther. *10*, 1311–1316.

Hidalgo, M., Amant, F., Biankin, A.V., Budinská, E., Byrne, A.T., Caldas, C., Clarke, R.B., Jong, S. de, Jonkers, J., Mælandsmo, G.M., et al. (2014). Patient-Derived Xenograft Models: An Emerging Platform for Translational Cancer Research. Cancer Discov. *4*, 998–1013.

Hill, S.J., Decker, B., Roberts, E.A., Horowitz, N.S., Muto, M.G., Worley, M.J., Feltmate, C.M., Nucci, M.R., Swisher, E.M., Nguyen, H., et al. (2018). Prediction of DNA Repair Inhibitor Response in Short-Term Patient-Derived Ovarian Cancer Organoids. Cancer Discov. *8*, 1404–1421.

Hirai, H., Iwasawa, Y., Okada, M., Arai, T., Nishibata, T., Kobayashi, M., Kimura, T., Kaneko, N., Ohtani, J., Yamanaka, K., et al. (2009). Small-molecule inhibition of Wee1 kinase by MK-1775 selectively sensitizes p53-deficient tumor cells to DNA-damaging agents. Mol. Cancer Ther. *8*, 2992–3000.

Hirose, Y., Katayama, M., Mirzoeva, O.K., Berger, M.S., and Pieper, R.O. (2005). Akt Activation Suppresses Chk2-Mediated, Methylating Agent–Induced G2 Arrest and Protects from Temozolomide-Induced Mitotic Catastrophe and Cellular Senescence. Cancer Res. *65*, 4861–4869.

Hnisz, D., Abraham, B.J., Lee, T.I., Lau, A., Saint-André, V., Sigova, A.A., Hoke, H.A., and Young, R.A. (2013). Super-Enhancers in the Control of Cell Identity and Disease. Cell *155*, 934–947.

Hodgkinson, C.L., Morrow, C.J., Li, Y., Metcalf, R.L., Rothwell, D.G., Trapani, F., Polanski, R., Burt, D.J., Simpson, K.L., Morris, K., et al. (2014). Tumorigenicity and genetic profiling of circulating tumor cells in small-cell lung cancer. Nat. Med. *20*, 897–903.

Hodkinson, P.S., Elliott, T., Wong, W.S., Rintoul, R.C., Mackinnon, A.C., Haslett, C., and Sethi, T. (2006). ECM overrides DNA damage-induced cell cycle arrest and apoptosis in small-cell lung cancer cells through β 1 integrin-dependent activation of PI3-kinase. Cell Death Differ. *13*, 1776.

Holzer, A.K., and Howell, S.B. (2006). The Internalization and Degradation of Human Copper Transporter 1 following Cisplatin Exposure. Cancer Res. *66*, 10944–10952.

Holzer, A.K., Katano, K., Klomp, L.W.J., and Howell, S.B. (2004). Cisplatin Rapidly Down-regulates Its Own Influx Transporter hCTR1 in Cultured Human Ovarian Carcinoma Cells. Clin. Cancer Res. *10*, 6744–6749.

Hook, K.E., Garza, S.J., Lira, M.E., Ching, K.A., Lee, N.V., Cao, J., Yuan, J., Ye, J., Ozeck, M., Shi, S.T., et al. (2012). An Integrated Genomic Approach to Identify Predictive Biomarkers of Response to the Aurora Kinase Inhibitor PF-03814735. Mol. Cancer Ther. *11*, 710–719.

Horn, L., Mansfield, A.S., Szczęsna, A., Havel, L., Krzakowski, M., Hochmair, M.J., Huemer, F., Losonczy, G., Johnson, M.L., Nishio, M., et al. (2018). First-Line Atezolizumab plus Chemotherapy in Extensive-Stage Small-Cell Lung Cancer. N. Engl. J. Med. *379*, 2220–2229.

Hou, J.-M., Greystoke, A., Lancashire, L., Cummings, J., Ward, T., Board, R., Amir, E., Hughes, S., Krebs, M., Hughes, A., et al. (2009). Evaluation of Circulating Tumor Cells and Serological Cell Death Biomarkers in Small Cell Lung Cancer Patients Undergoing Chemotherapy. Am. J. Pathol. *175*, 808–816.

Hou, J.-M., Krebs, M.G., Lancashire, L., Sloane, R., Backen, A., Swain, R.K., Priest, L.J.C., Greystoke, A., Zhou, C., Morris, K., et al. (2012). Clinical Significance and Molecular Characteristics of Circulating Tumor Cells and Circulating Tumor Microemboli in Patients With Small-Cell Lung Cancer. J. Clin. Oncol. *30*, 525–532.

Hsia, T.-C., Lin, C.-C., Wang, J.-J., Ho, S.-T., and Kao, A. (2002). Relationship Between Chemotherapy Response of Small Cell Lung Cancer and P-glycoprotein or Multidrug Resistance-Related Protein Expression. Lung *180*, 173–179.

Huang, F., Ni, M., Chalishazar, M.D., Huffman, K.E., Kim, J., Cai, L., Shi, X., Cai, F., Zacharias, L.G., Ireland, A.S., et al. (2018a). Inosine Monophosphate Dehydrogenase Dependence in a Subset of Small Cell Lung Cancers. Cell Metab. *28*, 369-382.e5.

Huang, J.C., Zamble, D.B., Reardon, J.T., Lippard, S.J., and Sancar, A. (1994). HMG-domain proteins specifically inhibit the repair of the major DNA adduct of the anticancer drug cisplatin by human excision nuclease. Proc. Natl. Acad. Sci. U. S. A. *91*, 10394–10398.

Huang, Y.-H., Klingbeil, O., He, X.-Y., Wu, X.S., Arun, G., Lu, B., Somerville, T.D.D., Milazzo, J.P., Wilkinson, J.E., Demerdash, O.E., et al. (2018b). POU2F3 is a master regulator of a tuft cell-like variant of small cell lung cancer. Genes Dev. *32*, 915–928.

Hubaux, R., Thu, K.L., Coe, B.P., MacAulay, C., Lam, S., and Lam, W.L. (2013). EZH2 promotes E2F driven SCLC tumorigenesis through modulation of apoptosis and cell cycle regulation. J. Thorac. Oncol. Off. Publ. Int. Assoc. Study Lung Cancer *8*, 1102–1106.

Huijbers, I.J., Ali, R.B., Pritchard, C., Cozijnsen, M., Kwon, M.-C., Proost, N., Song, J.-Y., Vries, H. de, Badhai, J., Sutherland, K., et al. (2014). Rapid target gene validation in complex cancer mouse models using re-derived embryonic stem cells. EMBO Mol. Med. *6*, 212–225.

Hustedt, N., and Durocher, D. (2017). The control of DNA repair by the cell cycle. Nat. Cell Biol. *19*, 1–9.

Ikegaki, N., Katsumata, M., Minna, J., and Tsujimoto, Y. (1994). Expression of bcl-2 in Small Cell Lung Carcinoma Cells. Cancer Res. *54*, 6–8.

Imamura, T., Izumi, H., Nagatani, G., Ise, T., Nomoto, M., Iwamoto, Y., and Kohno, K. (2001). Interaction with p53 Enhances Binding of Cisplatin-modified DNA by High Mobility Group 1 Protein. J. Biol. Chem. *276*, 7534–7540.

Ito, T., Udaka, N., Yazawa, T., Okudela, K., Hayashi, H., Sudo, T., Guillemot, F., Kageyama, R., and Kitamura, H. (2000). Basic helix-loop-helix transcription factors regulate the neuroendocrine differentiation of fetal mouse pulmonary epithelium. Development *127*, 3913–3921.

Izumchenko, E., Paz, K., Ciznadija, D., Sloma, I., Katz, A., Vasquez-Dunddel, D., Ben-Zvi, I., Stebbing, J., McGuire, W., Harris, W., et al. (2017). Patient-derived xenografts effectively capture responses to oncology therapy in a heterogeneous cohort of patients with solid tumors. Ann. Oncol. *28*, 2595–2605.

Jahchan, N.S., Lim, J.S., Bola, B., Morris, K., Seitz, G., Tran, K.Q., Xu, L., Trapani, F., Morrow, C.J., Cristea, S., et al. (2016). Identification and Targeting of Long-Term Tumor-Propagating Cells in Small Cell Lung Cancer. Cell Rep. *16*, 644–656.

Jaiswal, S., Chao, M.P., Majeti, R., and Weissman, I.L. (2010). Macrophages as mediators of tumor immunosurveillance. Trends Immunol. *31*, 212–219.

Jaspers, J.E., Kersbergen, A., Boon, U., Sol, W., Deemter, L. van, Zander, S.A., Drost, R., Wientjens, E., Ji, J., Aly, A., et al. (2013). Loss of 53BP1 Causes PARP Inhibitor Resistance in Brca1-Mutated Mouse Mammary Tumors. Cancer Discov. *3*, 68–81.

Jia, S., Wildner, H., and Birchmeier, C. (2015). Insm1 controls the differentiation of pulmonary neuroendocrine cells by repressing Hes1. Dev. Biol. *408*, 90–98.

Jiang, S.-X., Sato, Y., Kuwao, S., and Kameya, T. (1995). Expression of bcl-2 oncogene protein is prevalent in small cell lung carcinomas. J. Pathol. *177*, 135–138.

Jiang, T., Collins, B.J., Jin, N., Watkins, D.N., Brock, M.V., Matsui, W., Nelkin, B.D., and Ball, D.W. (2009). Achaete-Scute Complex Homologue 1 Regulates Tumor-Initiating

Capacity in Human Small Cell Lung Cancer. Cancer Res. *69*, 845–854.

Jimeno, S., Fernández-Ávila, M.J., Cruz-García, A., Cepeda-García, C., Gómez-Cabello, D., and Huertas, P. (2015). Neddylation inhibits CtIP-mediated resection and regulates DNA double strand break repair pathway choice. Nucleic Acids Res. *43*, 987–999.

Johnson, B.E., Russell, E., Simmons, A.M., Phelps, R., Steinberg, S.M., Ihde, D.C., and Gazdar, A.F. (1996). MYC family DNA amplification in 126 tumor cell lines from patients with small cell lung cancer. J. Cell. Biochem. *63*, 210–217.

Johnson, J.I., Decker, S., Zaharevitz, D., Rubinstein, L.V., Venditti, J.M., Schepartz, S., Kalyandrug, S., Christian, M., Arbuck, S., Hollingshead, M., et al. (2001). Relationships between drug activity in NCI preclinical in vitro and in vivo models and early clinical trials. Br. J. Cancer *84*, 1424.

Jonkers, J., and Berns, A. (2002). Conditional mouse models of sporadic cancer. Nat. Rev. Cancer *2*, 251–265.

Jordan, P., and Carmo-Fonseca*, M. (2000). Molecular mechanisms involved in cisplatin cytotoxicity: Cell. Mol. Life Sci. *57*, 1229–1235.

Jotte, R., Conkling, P., Reynolds, C., Galsky, M.D., Klein, L., Fitzgibbons, J.F., McNally, R., Renschler, M.F., and Oliver, J.W. (2010). Randomized Phase II Trial of Single-Agent Amrubicin or Topotecan as Second-Line Treatment in Patients With Small-Cell Lung Cancer Sensitive to First-Line Platinum-Based Chemotherapy. J. Clin. Oncol. *29*, 287–293.

Joung, J., Konermann, S., Gootenberg, J.S., Abudayyeh, O.O., Platt, R.J., Brigham, M.D., Sanjana, N.E., and Zhang, F. (2017). Genome-scale CRISPR-Cas9 knockout and transcriptional activation screening. Nat. Protoc. *12*, 828–863.

Justilien, V., Walsh, M.P., Ali, S.A., Thompson, E.A., Murray, N.R., and Fields, A.P. (2014). The PRKCI and SOX2 Oncogenes Are Coamplified and Cooperate to Activate Hedgehog Signaling in Lung Squamous Cell Carcinoma. Cancer Cell *25*, 139–151.

Kalari, S., Jung, M., Kernstine, K.H., Takahashi, T., and Pfeifer, G.P. (2013). The DNA methylation landscape of small cell lung cancer suggests a differentiation defect of neuroendocrine cells. Oncogene *32*, 3559–3568.

Kalemkerian, G.P. (2011). Staging and imaging of small cell lung cancer. Cancer Imaging *11*, 253–258.

Kandoth, C., McLellan, M.D., Vandin, F., Ye, K., Niu, B., Lu, C., Xie, M., Zhang, Q., McMichael, J.F., Wyczalkowski, M.A., et al. (2013). Mutational landscape and significance across 12 major cancer types. Nature *502*, 333–339.

Karachaliou, N., Papadaki, C., Lagoudaki, E., Trypaki, M., Sfakianaki, M., Koutsopoulos, A., Mavroudis, D., Stathopoulos, E., Georgoulias, V., and Souglakos, J.

(2013). Predictive Value of BRCA1, ERCC1, ATP7B, PKM2, TOPOI, TOPO-IIA, TOPOIIB and C-MYC Genes in Patients with Small Cell Lung Cancer (SCLC) Who Received First Line Therapy with Cisplatin and Etoposide. PLoS ONE *8*.

Kartalou, M., and Essigmann, J.M. (2001). Recognition of cisplatin adducts by cellular proteins. Mutat. Res. Mol. Mech. Mutagen. *478*, 1–21.

Kasahara, K., Fujiwara, Y., Nishio, K., Ohmori, T., Sugimoto, Y., Komiya, K., Matsuda, T., and Saijo, N. (1991). Metallothionein Content Correlates with the Sensitivity of Human Small Cell Lung Cancer Cell Lines to Cisplatin. Cancer Res. *51*, 3237–3242.

Kawamura, T., Kawatani, M., Muroi, M., Kondoh, Y., Futamura, Y., Aono, H., Tanaka, M., Honda, K., and Osada, H. (2016). Proteomic profiling of small-molecule inhibitors reveals dispensability of MTH1 for cancer cell survival. Sci. Rep. *6*, 26521.

Kawasaki, M., Nakanishi, Y., Kuwano, K., Takayama, K., Kiyohara, C., and Hara, N. (1998). Immunohistochemically detected p53 and P-glycoprotein predict the response to chemotherapy in lung cancer. Eur. J. Cancer *34*, 1352–1357.

Kerrigan, D., Pommier, Y., and Kohn, K.W. (1987). Protein-linked DNA strand breaks produced by etoposide and teniposide in mouse L1210 and human VA-13 and HT-29 cell lines: relationship to cytotoxicity. NCI Monogr. Publ. Natl. Cancer Inst. 117–121.

Kersten, K., de Visser, K.E., van Miltenburg, M.H., and Jonkers, J. (2017). Genetically engineered mouse models in oncology research and cancer medicine. EMBO Mol. Med. *9*, 137–153.

Kettle, J.G., Alwan, H., Bista, M., Breed, J., Davies, N.L., Eckersley, K., Fillery, S., Foote, K.M., Goodwin, L., Jones, D.R., et al. (2016). Potent and Selective Inhibitors of MTH1 Probe Its Role in Cancer Cell Survival. J. Med. Chem. *59*, 2346–2361.

Khandelwal, G., Girotti, M.R., Smowton, C., Taylor, S., Wirth, C., Dynowski, M., Frese, K.K., Brady, G., Dive, C., Marais, R., et al. (2017). Next-Generation Sequencing Analysis and Algorithms for PDX and CDX Models. Mol. Cancer Res. MCR *15*, 1012–1016.

Kilkenny, C., Browne, W., Cuthill, I.C., Emerson, M., Altman, D.G., and NC3Rs Reporting Guidelines Working Group (2010). Animal research: reporting in vivo experiments: the ARRIVE guidelines. Br. J. Pharmacol. *160*, 1577–1579.

Kim, H., George, E., Ragland, R.L., Rafail, S., Zhang, R., Krepler, C., Morgan, M.A., Herlyn, M., Brown, E.J., and Simpkins, F. (2017). Targeting the ATR/CHK1 Axis with PARP Inhibition Results in Tumor Regression in BRCA-Mutant Ovarian Cancer Models. Clin. Cancer Res. *23*, 3097–3108.

Kim, M.P., Evans, D.B., Wang, H., Abbruzzese, J.L., Fleming, J.B., and Gallick, G.E. (2009). Generation of orthotopic and heterotopic human pancreatic cancer xenografts in immunodeficient mice. Nat. Protoc. *4*, 1670–1680.

Kim, T.M., Son, M.Y., Dodds, S., Hu, L., Luo, G., and Hasty, P. (2015). RECQL5 and BLM exhibit divergent functions in cells defective for the Fanconi anemia pathway. Nucleic Acids Res. *43*, 893–903.

Kim, Y.H., Girard, L., Giacomini, C.P., Wang, P., Hernandez-Boussard, T., Tibshirani, R., Minna, J.D., and Pollack, J.R. (2006). Combined microarray analysis of small cell lung cancer reveals altered apoptotic balance and distinct expression signatures of MYC family gene amplification. Oncogene *25*, 130.

Kinner, A., Wu, W., Staudt, C., and Iliakis, G. (2008). γ-H2AX in recognition and signaling of DNA double-strand breaks in the context of chromatin. Nucleic Acids Res. *36*, 5678–5694.

Knezevic, C.E., Wright, G., Remsing Rix, L.L., Kim, W., Kuenzi, B.M., Luo, Y., Watters, J.M., Koomen, J.M., Haura, E.B., Monteiro, A.N., et al. (2016). Proteome-wide Profiling of Clinical PARP Inhibitors Reveals Compound-Specific Secondary Targets. Cell Chem. Biol. *23*, 1490–1503.

Knox, R.J., Friedlos, F., Lydall, D.A., and Roberts, J.J. (1986). Mechanism of Cytotoxicity of Anticancer Platinum Drugs: Evidence That cis-Diamminedichloroplatinum(II) and cis-Diammine-(1,1-cyclobutanedicarboxylato)platinum(II) Differ Only in the Kinetics of Their Interaction with DNA. Cancer Res. *46*, 1972–1979.

Koinis, F., Kotsakis, A., and Georgoulias, V. (2016). Small cell lung cancer (SCLC): no treatment advances in recent years. Transl. Lung Cancer Res. *5*, 39-50–50.

Kolde R. (2019). pheatmap: Pretty Heatmaps.

Kolev, V.N., Wright, Q.G., Vidal, C.M., Ring, J.E., Shapiro, I.M., Ricono, J., Weaver, D.T., Padval, M.V., Pachter, J.A., and Xu, Q. (2015). PI3K/mTOR Dual Inhibitor VS-5584 Preferentially Targets Cancer Stem Cells. Cancer Res. *75*, 446–455.

Kondrashova, O., Nguyen, M., Shield-Artin, K., Tinker, A.V., Teng, N.N.H., Harrell, M.I., Kuiper, M.J., Ho, G.-Y., Barker, H., Jasin, M., et al. (2017). Secondary Somatic Mutations Restoring RAD51C and RAD51D Associated with Acquired Resistance to the PARP Inhibitor Rucaparib in High-Grade Ovarian Carcinoma. Cancer Discov. *7*, 984–998.

Kotsantis, P., Petermann, E., and Boulton, S.J. (2018). Mechanisms of Oncogene-Induced Replication Stress: Jigsaw Falling into Place. Cancer Discov. *8*, 537–555.

Krajewska, M., Heijink, A.M., Bisselink, Y.J.W.M., Seinstra, R.I., Silljé, H.H.W., de Vries, E.G.E., and van Vugt, M.A.T.M. (2013). Forced activation of Cdk1 via wee1 inhibition impairs homologous recombination. Oncogene *32*, 3001–3008.

Kraus, A.C., Ferber, I., Bachmann, S.-O., Specht, H., Wimmel, A., Gross, M.W., Schlegel, J., Suske, G., and Schuermann, M. (2002). In vitro chemo- and radio-resistance in small cell lung cancer correlates with cell adhesion and constitutive

activation of AKT and MAP kinase pathways. Oncogene *21*, 8683.

Krejci, L., Altmannova, V., Spirek, M., and Zhao, X. (2012). Homologous recombination and its regulation. Nucleic Acids Res. *40*, 5795–5818.

Krokan, H.E., and Bjørås, M. (2013). Base Excision Repair. Cold Spring Harb. Perspect. Biol. *5*, a012583.

Krug, L.M., Crapanzano, J.P., Azzoli, C.G., Miller, V.A., Rizvi, N., Gomez, J., Kris, M.G., Pizzo, B., Tyson, L., Dunne, M., et al. (2005). Imatinib mesylate lacks activity in small cell lung carcinoma expressing c-kit protein. Cancer *103*, 2128–2131.

Krystal, G.W., Sulanke, G., and Litz, J. (2002). Inhibition of Phosphatidylinositol 3-Kinase-Akt Signaling Blocks Growth, Promotes Apoptosis, and Enhances Sensitivity of Small Cell Lung Cancer Cells to Chemotherapy 1 This work was supported in part by a Merit Review Award from the Department of Veterans Affairs and a grant from the Virginia Commonwealth Health Research Board. 1. Mol. Cancer Ther. *1*, 913–922.

Kubo, A., Yoshikawa, A., Hirashima, T., Masuda, N., Takada, M., Takahara, J., Fukuoka, M., and Nakagawa, K. (1996). Point Mutations of the Topoisomerase IIα Gene in Patients with Small Cell Lung Cancer Treated with Etoposide. Cancer Res. *56*, 1232–1236.

Kwon, M., Proost, N., Song, J.-Y., Sutherland, K.D., Zevenhoven, J., and Berns, A. (2015). Paracrine signaling between tumor subclones of mouse SCLC: a critical role of ETS transcription factor Pea3 in facilitating metastasis. Genes Dev. *29*, 1587–1592.

Lallo, A., Frese, K.K., Morrow, C.J., Sloane, R., Gulati, S., Schenk, M.W., Trapani, F., Simms, N., Galvin, M., Brown, S., et al. (2018). The Combination of the PARP Inhibitor Olaparib and the WEE1 Inhibitor AZD1775 as a New Therapeutic Option for Small Cell Lung Cancer. Clin. Cancer Res. *24*, 5153–5164.

Lallo, A., Gulati, S., Schenk, M.W., Khandelwal, G., Berglund, U.W., Pateras, I.S., Chester, C.P.E., Pham, T.M., Kalderen, C., Frese, K.K., et al. (2019). Ex vivo culture of cells derived from circulating tumour cell xenograft to support small cell lung cancer research and experimental therapeutics. Br. J. Pharmacol. *176*, 436–450.

Lamprecht, M.R., Sabatini, D.M., and Carpenter, A.E. (2007). CellProfiler: free, versatile software for automated biological image analysis. BioTechniques *42*, 71–75.

Lazzari, C., Gregorc, V., Bulotta, A., Dottore, A., Altavilla, G., and Santarpia, M. (2018). Temozolomide in combination with either veliparib or placebo in patients with relapsed-sensitive or refractory small-cell lung cancer. Transl. Lung Cancer Res. *0*, S329-S333–S333.

Le Péchoux, C., Dunant, A., Senan, S., Wolfson, A., Quoix, E., Faivre-Finn, C., Ciuleanu, T., Arriagada, R., Jones, R., Wanders, R., et al. (2009). Standard-dose versus higher-dose prophylactic cranial irradiation (PCI) in patients with limited-stage small-cell lung cancer in complete remission after chemotherapy and thoracic radiotherapy

(PCI 99-01, EORTC 22003-08004, RTOG 0212, and IFCT 99-01): a randomised clinical trial. Lancet Oncol. *10*, 467–474.

Lee, H.W., Han, J.H., Kim, J.H., Lee, M.H., Jeong, S.H., Kang, S.Y., Choi, J.-H., Oh, Y.T., Park, K.J., Hwang, S.C., et al. (2008). Expression of excision repair cross-complementation group 1 protein predicts poor outcome in patients with small cell lung cancer. Lung Cancer *59*, 95–104.

Lenhart, R., Kirov, S., Desilva, H., Cao, J., Lei, M., Johnston, K., Peterson, R., Schweizer, L., Purandare, A., Ross-Macdonald, P., et al. (2015). Sensitivity of Small Cell Lung Cancer to BET Inhibition Is Mediated by Regulation of ASCL1 Gene Expression. Mol. Cancer Ther. *14*, 2167–2174.

Leonard, M., Hill, N., Bubulya, P., and Kadakia, M. (2013). The PTEN-Akt pathway impacts the integrity and composition of mitotic centrosomes. Cell Cycle *12*, 1406–1415.

Lewis, C.W., Bukhari, A.B., Xiao, E.J., Choi, W.-S., Smith, J.D., Homola, E., Mackey, J.R., Campbell, S.D., Gamper, A.M., and Chan, G.K. (2019). Upregulation of Myt1 promotes acquired resistance of cancer cells to Wee1 inhibition. Cancer Res. canres.1961.2019.

Lheureux, S., Bruce, J.P., Burnier, J.V., Karakasis, K., Shaw, P.A., Clarke, B.A., Yang, S.Y.C., Quevedo, R., Li, T., Dowar, M., et al. (2017). Somatic BRCA1/2 Recovery as a Resistance Mechanism After Exceptional Response to Poly (ADP-ribose) Polymerase Inhibition. J. Clin. Oncol. *35*, 1240–1249.

Li, G.-M. (2008). Mechanisms and functions of DNA mismatch repair. Cell Res. *18*, 85–98.

Li, H., Handsaker, B., Wysoker, A., Fennell, T., Ruan, J., Homer, N., Marth, G., Abecasis, G., Durbin, R., and 1000 Genome Project Data Processing Subgroup (2009). The Sequence Alignment/Map format and SAMtools. Bioinforma. Oxf. Engl. *25*, 2078–2079.

Li, L., Ng, S.R., Colón, C.I., Drapkin, B.J., Hsu, P.P., Li, Z., Nabel, C.S., Lewis, C.A., Romero, R., Mercer, K.L., et al. (2019). Identification of DHODH as a therapeutic target in small cell lung cancer. Sci. Transl. Med. *11*.

Liao, Y., Smyth, G.K., and Shi, W. (2013). The Subread aligner: fast, accurate and scalable read mapping by seed-and-vote. Nucleic Acids Res. *41*, e108.

Liau, B.B., Sievers, C., Donohue, L.K., Gillespie, S.M., Flavahan, W.A., Miller, T.E., Venteicher, A.S., Hebert, C.H., Carey, C.D., Rodig, S.J., et al. (2017). Adaptive Chromatin Remodeling Drives Glioblastoma Stem Cell Plasticity and Drug Tolerance. Cell Stem Cell *20*, 233-246.e7.

Lim, J.S., Ibaseta, A., Fischer, M.M., Cancilla, B., O'Young, G., Cristea, S., Luca, V.C., Yang, D., Jahchan, N.S., Hamard, C., et al. (2017). Intratumoural heterogeneity generated by Notch signalling promotes small-cell lung cancer. Nature *545*, 360–364.

Lin, A., Giuliano, C.J., Palladino, A., John, K.M., Abramowicz, C., Yuan, M.L., Sausville, E.L., Lukow, D.A., Liu, L., Chait, A.R., et al. (2019). Off-target toxicity is a common mechanism of action of cancer drugs undergoing clinical trials. Sci. Transl. Med. *11*.

Lin, C.-P., Ban, Y., Lyu, Y.L., and Liu, L.F. (2009). Proteasome-dependent Processing of Topoisomerase I-DNA Adducts into DNA Double Strand Breaks at Arrested Replication Forks. J. Biol. Chem. *284*, 28084–28092.

Linden, A.A.V., Baturin, D., Ford, J.B., Fosmire, S.P., Gardner, L., Korch, C., Reigan, P., and Porter, C.C. (2013). Inhibition of Wee1 Sensitizes Cancer Cells to Antimetabolite Chemotherapeutics In Vitro and In Vivo, Independent of p53 Functionality. Mol. Cancer Ther. *12*, 2675–2684.

Linnoila, R.I. (2006). Functional facets of the pulmonary neuroendocrine system. Lab. Investig. J. Tech. Methods Pathol. *86*, 425–444.

Little, C.D., Nau, M.M., Carney, D.N., Gazdar, A.F., and Minna, J.D. (1983). Amplification and expression of the c-myc oncogene in human lung cancer cell lines. Nature *306*, 194–196.

Liu, E., Lee, A.Y.-L., Chiba, T., Olson, E., Sun, P., and Wu, X. (2007). The ATR-mediated S phase checkpoint prevents rereplication in mammalian cells when licensing control is disrupted. J. Cell Biol. *179*, 643–657.

Liu, S., Opiyo, S.O., Manthey, K., Glanzer, J.G., Ashley, A.K., Amerin, C., Troksa, K., Shrivastav, M., Nickoloff, J.A., and Oakley, G.G. (2012). Distinct roles for DNA-PK, ATM and ATR in RPA phosphorylation and checkpoint activation in response to replication stress. Nucleic Acids Res. *40*, 10780–10794.

Lohmann, D., Pütz, B., Reich, U., Böhm, J., Präuer, H., and Höfler, H. (1993). Mutational spectrum of the p53 gene in human small-cell lung cancer and relationship to clinicopathological data. Am. J. Pathol. *142*, 907–915.

Lok, B.H., Gardner, E.E., Schneeberger, V.E., Ni, A., Desmeules, P., Rekhtman, N., Stanchina, E. de, Teicher, B.A., Riaz, N., Powell, S.N., et al. (2017). PARP Inhibitor Activity Correlates with SLFN11 Expression and Demonstrates Synergy with Temozolomide in Small Cell Lung Cancer. Clin. Cancer Res. *23*, 523–535.

Long, B.H., Musial, S.T., and Brattain, M.G. (1985). Single- and Double-Strand DNA Breakage and Repair in Human Lung Adenocarcinoma Cells Exposed to Etoposide and Teniposide. Cancer Res. *45*, 3106–3112.

Lopus, M., Oroudjev, E., Wilson, L., Wilhelm, S., Widdison, W., Chari, R., and Jordan, M.A. (2010). Maytansine and Cellular Metabolites of Antibody-Maytansinoid Conjugates Strongly Suppress Microtubule Dynamics by Binding to Microtubules. Mol. Cancer Ther. *9*, 2689–2699.

Lord, C.J., and Ashworth, A. (2016). BRCAness revisited. Nat. Rev. Cancer *16*, 110–

120.

Lord, C.J., and Ashworth, A. (2017). PARP inhibitors: Synthetic lethality in the clinic. Science *355*, 1152–1158.

Lord, C.J., Tutt, A.N.J., and Ashworth, A. (2015). Synthetic Lethality and Cancer Therapy: Lessons Learned from the Development of PARP Inhibitors. Annu. Rev. Med. *66*, 455–470.

Lord, R.V.N., Brabender, J., Gandara, D., Alberola, V., Camps, C., Domine, M., Cardenal, F., Sánchez, J.M., Gumerlock, P.H., Tarón, M., et al. (2002). Low ERCC1 Expression Correlates with Prolonged Survival after Cisplatin plus Gemcitabine Chemotherapy in Non-Small Cell Lung Cancer. Clin. Cancer Res. *8*, 2286–2291.

Love, M.I., Huber, W., and Anders, S. (2014). Moderated estimation of fold change and dispersion for RNA-seq data with DESeq2. Genome Biol. *15*, 550.

Lovén, J., Hoke, H.A., Lin, C.Y., Lau, A., Orlando, D.A., Vakoc, C.R., Bradner, J.E., Lee, T.I., and Young, R.A. (2013). Selective Inhibition of Tumor Oncogenes by Disruption of Super-Enhancers. Cell *153*, 320–334.

Lu, P., Takai, K., Weaver, V.M., and Werb, Z. (2011). Extracellular Matrix Degradation and Remodeling in Development and Disease. Cold Spring Harb. Perspect. Biol. *3*, a005058.

Lu, Y., Futtner, C., Rock, J.R., Xu, X., Whitworth, W., Hogan, B.L.M., and Onaitis, M.W. (2010). Evidence That SOX2 Overexpression Is Oncogenic in the Lung. PLOS ONE *5*, e11022.

Ma, T., Chen, Y., Zhang, F., Yang, C.-Y., Wang, S., and Yu, X. (2013). RNF111-dependent neddylation activates DNA damage-induced ubiquitination. Mol. Cell *49*, 897–907.

Ma, Y.-C., Huang, J., Ali, S., Lowry, W., and Huang, X.-Y. (2000). Src Tyrosine Kinase Is a Novel Direct Effector of G Proteins. Cell *102*, 635–646.

Macheret, M., and Halazonetis, T.D. (2018). Intragenic origins due to short G1 phases underlie oncogene-induced DNA replication stress. Nature *555*, 112–116.

Maechler M, Rousseeuw P, Struyf A, Hubert M, and Hornik K (2019). cluster: Cluster Analysis Basics and Extensions.

Malhotra, J., Malvezzi, M., Negri, E., Vecchia, C.L., and Boffetta, P. (2016). Risk factors for lung cancer worldwide. Eur. Respir. J. *48*, 889–902.

Mali, P., Yang, L., Esvelt, K.M., Aach, J., Guell, M., DiCarlo, J.E., Norville, J.E., and Church, G.M. (2013). RNA-Guided Human Genome Engineering via Cas9. Science *339*, 823–826.

Mannava, S., Grachtchouk, V., Wheeler, L.J., Im, M., Zhuang, D., Slavina, E.G.,

Mathews, C.K., Shewach, D.S., and Nikiforov, M.A. (2008). Direct role of nucleotide metabolism in C-MYC-dependent proliferation of melanoma cells. Cell Cycle *7*, 2392–2400.

Manning, A.L., Yazinski, S.A., Nicolay, B., Bryll, A., Zou, L., and Dyson, N.J. (2014a). Suppression of Genome Instability in pRB-Deficient Cells by Enhancement of Chromosome Cohesion. Mol. Cell *53*, 993–1004.

Manning, A.L., Benes, C., and Dyson, N.J. (2014b). Whole chromosome instability resulting from the synergistic effects of pRB and p53 inactivation. Oncogene *33*, 2487–2494.

Martínez, P., Fidalgo, P.A.S., and Felip, E. (2014). Ganitumab for the treatment of small-cell lung cancer. Expert Opin. Investig. Drugs *23*, 1423–1432.

Mascaux, C., Paesmans, M., Berghmans, T., Branle, F., Lafitte, J.J., Lemaître, F., Meert, A.P., Vermylen, P., and Sculier, J.P. (2000). A systematic review of the role of etoposide and cisplatin in the chemotherapy of small cell lung cancer with methodology assessment and meta-analysis. Lung Cancer *30*, 23–36.

Masters, G.A., Declerck, L., Blanke, C., Sandler, A., DeVore, R., Miller, K., and Johnson, D. (2003). Phase II Trial of Gemcitabine in Refractory or Relapsed Small-Cell Lung Cancer: Eastern Cooperative Oncology Group Trial 1597. J. Clin. Oncol. *21*, 1550–1555.

Masuda, N., Fukuoka, M., Kusunoki, Y., Matsui, K., Takifuji, N., Kudoh, S., Negoro, S., Nishioka, M., Nakagawa, K., and Takada, M. (1992). CPT-11: a new derivative of camptothecin for the treatment of refractory or relapsed small-cell lung cancer. J. Clin. Oncol. *10*, 1225–1229.

McCabe, N., Turner, N.C., Lord, C.J., Kluzek, K., Białkowska, A., Swift, S., Giavara, S., O'Connor, M.J., Tutt, A.N., Zdzienicka, M.Z., et al. (2006). Deficiency in the Repair of DNA Damage by Homologous Recombination and Sensitivity to Poly(ADP-Ribose) Polymerase Inhibition. Cancer Res. *66*, 8109–8115.

McColl, K., Wildey, G., Sakre, N., Lipka, M.B., Behtaj, M., Kresak, A., Chen, Y., Yang, M., Velcheti, V., Fu, P., et al. (2017). Reciprocal expression of INSM1 and YAP1 defines subgroups in small cell lung cancer. Oncotarget *8*, 73745–73756.

McCormick, A., Donoghue, P., Dixon, M., O'Sullivan, R., O'Donnell, R.L., Murray, J., Kaufmann, A., Curtin, N.J., and Edmondson, R.J. (2017). Ovarian Cancers Harbor Defects in Nonhomologous End Joining Resulting in Resistance to Rucaparib. Clin. Cancer Res. *23*, 2050–2060.

McFadden, D.G., Papagiannakopoulos, T., Taylor-Weiner, A., Stewart, C., Carter, S.L., Cibulskis, K., Bhutkar, A., McKenna, A., Dooley, A., Vernon, A., et al. (2014). Genetic and Clonal Dissection of Murine Small Cell Lung Carcinoma Progression by Genome Sequencing. Cell *156*, 1298–1311.

van Meerbeeck, J.P., Fennell, D.A., and De Ruysscher, D.K.M. (2011). Small-cell lung cancer. Lancet Lond. Engl. *378*, 1741–1755.

Meijer, C., Mulder, N.H., Hospers, G.A., Uges, D.R., and de Vries, E.G. (1990). The role of glutathione in resistance to cisplatin in a human small cell lung cancer cell line. Br. J. Cancer *62*, 72–77.

Melichar, B., Adenis, A., Lockhart, A.C., Bennouna, J., Dees, E.C., Kayaleh, O., Obermannova, R., DeMichele, A., Zatloukal, P., Zhang, B., et al. (2015). Safety and activity of alisertib, an investigational aurora kinase A inhibitor, in patients with breast cancer, small-cell lung cancer, non-small-cell lung cancer, head and neck squamous-cell carcinoma, and gastro-oesophageal adenocarcinoma: a five-arm phase 2 study. Lancet Oncol. *16*, 395–405.

Melino, G., Laurenzi, V.D., and Vousden, K.H. (2002). p73: Friend or foe in tumorigenesis. Nat. Rev. Cancer *2*, 605.

Metzger, R., Leichman, C.G., Danenberg, K.D., Danenberg, P.V., Lenz, H.J., Hayashi, K., Groshen, S., Salonga, D., Cohen, H., Laine, L., et al. (1998). ERCC1 mRNA levels complement thymidylate synthase mRNA levels in predicting response and survival for gastric cancer patients receiving combination cisplatin and fluorouracil chemotherapy. J. Clin. Oncol. Off. J. Am. Soc. Clin. Oncol. *16*, 309–316.

Meuwissen, R., Linn, S.C., Linnoila, R.I., Zevenhoven, J., Mooi, W.J., and Berns, A. (2003). Induction of small cell lung cancer by somatic inactivation of both Trp53 and Rb1 in a conditional mouse model. Cancer Cell *4*, 181–189.

Micke, P., Basrai, M., Faldum, A., Bittinger, F., Rönnstrand, L., Blaukat, A., Beeh, K.M., Oesch, F., Fischer, B., Buhl, R., et al. (2003). Characterization of c-kit Expression in Small Cell Lung Cancer: Prognostic and Therapeutic Implications. Clin. Cancer Res. *9*, 188–194.

Milroy, R. (1993). A randomised clinical study of verapamil in addition to combination chemotherapy in small cell lung cancer. West of Scotland Lung Cancer Research Group, and the Aberdeen Oncology Group. Br. J. Cancer *68*, 813–818.

Mistry, A.R., Felix, C.A., Whitmarsh, R.J., Mason, A., Reiter, A., Cassinat, B., Parry, A., Walz, C., Wiemels, J.L., Segal, M.R., et al. (2005). DNA Topoisomerase II in Therapy-Related Acute Promyelocytic Leukemia. N. Engl. J. Med. *352*, 1529–1538.

Mizuno, N., and Itoh, H. (2009). Functions and Regulatory Mechanisms of Gq-Signaling Pathways. Neurosignals *17*, 42–54.

Mollaoglu, G., Guthrie, M.R., Böhm, S., Brägelmann, J., Can, I., Ballieu, P.M., Marx, A., George, J., Heinen, C., Chalishazar, M.D., et al. (2017). MYC Drives Progression of Small Cell Lung Cancer to a Variant Neuroendocrine Subtype with Vulnerability to Aurora Kinase Inhibition. Cancer Cell *31*, 270–285.

Morimoto, M., Nishinakamura, R., Saga, Y., and Kopan, R. (2012). Different

assemblies of Notch receptors coordinate the distribution of the major bronchial Clara, ciliated and neuroendocrine cells. Dev. Camb. Engl. *139*, 4365–4373.

Mortlock, A.A., Foote, K.M., Heron, N.M., Jung, F.H., Pasquet, G., Lohmann, J.-J.M., Warin, N., Renaud, F., De Savi, C., Roberts, N.J., et al. (2007). Discovery, Synthesis, and in Vivo Activity of a New Class of Pyrazoloquinazolines as Selective Inhibitors of Aurora B Kinase. J. Med. Chem. *50*, 2213–2224.

Morton, C.L., and Houghton, P.J. (2007). Establishment of human tumor xenografts in immunodeficient mice. Nat. Protoc. *2*, 247–250.

Mouw, K.W., Goldberg, M.S., Konstantinopoulos, P.A., and D'Andrea, A.D. (2017). DNA Damage and Repair Biomarkers of Immunotherapy Response. Cancer Discov. *7*, 675–693.

Mu, Y., Lou, J., Srivastava, M., Zhao, B., Feng, X., Liu, T., Chen, J., and Huang, J. (2016). SLFN11 inhibits checkpoint maintenance and homologous recombination repair. EMBO Rep. *17*, 94–109.

Müerköster, S., Wegehenkel, K., Arlt, A., Witt, M., Sipos, B., Kruse, M.-L., Sebens, T., Klöppel, G., Kalthoff, H., Fölsch, U.R., et al. (2004). Tumor Stroma Interactions Induce Chemoresistance in Pancreatic Ductal Carcinoma Cells Involving Increased Secretion and Paracrine Effects of Nitric Oxide and Interleukin-1β. Cancer Res. *64*, 1331–1337.

Murai, F., Koinuma, D., Shinozaki-Ushiku, A., Fukayama, M., Miyaozono, K., and Ehata, S. (2015). EZH2 promotes progression of small cell lung cancer by suppressing the TGF-β-Smad-ASCL1 pathway. Cell Discov. *1*, 15026.

Murai, J., Huang, S.N., Das, B.B., Renaud, A., Zhang, Y., Doroshow, J.H., Ji, J., Takeda, S., and Pommier, Y. (2012). Trapping of PARP1 and PARP2 by Clinical PARP Inhibitors. Cancer Res. *72*, 5588–5599.

Murai, J., Zhang, Y., Morris, J., Ji, J., Takeda, S., Doroshow, J.H., and Pommier, Y. (2014a). Rationale for Poly(ADP-ribose) Polymerase (PARP) Inhibitors in Combination Therapy with Camptothecins or Temozolomide Based on PARP Trapping versus Catalytic Inhibition. J. Pharmacol. Exp. Ther. *349*, 408–416.

Murai, J., Huang, S.-Y.N., Renaud, A., Zhang, Y., Ji, J., Takeda, S., Morris, J., Teicher, B., Doroshow, J.H., and Pommier, Y. (2014b). Stereospecific PARP Trapping by BMN 673 and Comparison with Olaparib and Rucaparib. Mol. Cancer Ther. *13*, 433–443.

Murai, J., Feng, Y., Yu, G.K., Ru, Y., Tang, S.-W., Shen, Y., and Pommier, Y. (2016). Resistance to PARP inhibitors by SLFN11 inactivation can be overcome by ATR inhibition. Oncotarget *7*, 76534–76550.

Murai, J., Tang, S.-W., Leo, E., Baechler, S.A., Redon, C.E., Zhang, H., Al Abo, M., Rajapakse, V.N., Nakamura, E., Jenkins, L.M.M., et al. (2018). SLFN11 Blocks Stressed Replication Forks Independently of ATR. Mol. Cell *69*, 371-384.e6.

Nagel, R., Avelar, A.T., Aben, N., Proost, N., Ven, M. van de, Vliet, J. van der, Cozijnsen, M., Vries, H. de, Wessels, L.F.A., and Berns, A. (2019). Inhibition of the Replication Stress Response Is a Synthetic Vulnerability in SCLC That Acts Synergistically in Combination with Cisplatin. Mol. Cancer Ther. *18*, 762–770.

Naipal, K.A.T., Verkaik, N.S., Ameziane, N., Deurzen, C.H.M. van, Brugge, P. ter, Meijers, M., Sieuwerts, A.M., Martens, J.W., O'Connor, M.J., Vrieling, H., et al. (2014). Functional Ex Vivo Assay to Select Homologous Recombination–Deficient Breast Tumors for PARP Inhibitor Treatment. Clin. Cancer Res. *20*, 4816–4826.

Nakasone, E.S., Askautrud, H.A., Kees, T., Park, J.-H., Plaks, V., Ewald, A.J., Fein, M., Rasch, M.G., Tan, Y.-X., Qiu, J., et al. (2012). Imaging Tumor-Stroma Interactions during Chemotherapy Reveals Contributions of the Microenvironment to Resistance. Cancer Cell *21*, 488–503.

National Cancer Institute (2014). Scientific Framework for Small Cell Lung Cancer (SCLC). Available online: https://deainfo.nci.nih.gov/advisory/ctac/workgroup/SCLC/SCLC%20Congressional%20Response.pdf.

Nau, M.M., Brooks, B.J., Battey, J., Sausville, E., Gazdar, A.F., Kirsch, I.R., McBride, O.W., Bertness, V., Hollis, G.F., and Minna, J.D. (1985). L-myc, a new myc-related gene amplified and expressed in human small cell lung cancer. Nature *318*, 69–73.

Negrini, S., Gorgoulis, V.G., and Halazonetis, T.D. (2010). Genomic instability — an evolving hallmark of cancer. Nat. Rev. Mol. Cell Biol. *11*, 220–228.

Neptune, E.R., Podowski, M., Calvi, C., Cho, J.-H., Garcia, J.G.N., Tuder, R., Linnoila, R.I., Tsai, M.-J., and Dietz, H.C. (2008). Targeted Disruption of NeuroD, a Proneural Basic Helix-Loop-Helix Factor, Impairs Distal Lung Formation and Neuroendocrine Morphology in the Neonatal Lung. J. Biol. Chem. *283*, 21160–21169.

Newlands, E.S., Stevens, M.F.G., Wedge, S.R., Wheelhouse, R.T., and Brock, C. (1997). Temozolomide: a review of its discovery, chemical properties, pre-clinical development and clinical trials. Cancer Treat. Rev. *23*, 35–61.

Nitiss, J.L. (2009). Targeting DNA topoisomerase II in cancer chemotherapy. Nat. Rev. Cancer *9*, 338–350.

Nogueira, V., Park, Y., Chen, C.-C., Xu, P.-Z., Chen, M.-L., Tonic, I., Unterman, T., and Hay, N. (2008). Akt Determines Replicative Senescence and Oxidative or Oncogenic Premature Senescence and Sensitizes Cells to Oxidative Apoptosis. Cancer Cell *14*, 458–470.

Noordermeer, S.M., and Attikum, H. van (2019). PARP Inhibitor Resistance: A Tug-of-War in BRCA-Mutated Cells. Trends Cell Biol. *29*, 820–834.

O'Brien, M.E.R., Ciuleanu, T.-E., Tsekov, H., Shparyk, Y., Čučeviá, B., Juhasz, G., Thatcher, N., Ross, G.A., Dane, G.C., and Crofts, T. (2006). Phase III Trial Comparing

Supportive Care Alone With Supportive Care With Oral Topotecan in Patients With Relapsed Small-Cell Lung Cancer. J. Clin. Oncol. *24*, 5441–5447.

O'Connor, M.J. (2015). Targeting the DNA Damage Response in Cancer. Mol. Cell *60*, 547–560.

OED online (2019). model, n. and adj.

Olive, P.L., and Banáth, J.P. (2006). The comet assay: a method to measure DNA damage in individual cells. Nat. Protoc. *1*, 23–29.

Olson, E., Nievera, C.J., Klimovich, V., Fanning, E., and Wu, X. (2006). RPA2 Is a Direct Downstream Target for ATR to Regulate the S-phase Checkpoint. J. Biol. Chem. *281*, 39517–39533.

Oltersdorf, T., Elmore, S.W., Shoemaker, A.R., Armstrong, R.C., Augeri, D.J., Belli, B.A., Bruncko, M., Deckwerth, T.L., Dinges, J., Hajduk, P.J., et al. (2005). An inhibitor of Bcl-2 family proteins induces regression of solid tumours. Nature *435*, 677.

Osborne, J.K., Larsen, J.E., Shields, M.D., Gonzales, J.X., Shames, D.S., Sato, M., Kulkarni, A., Wistuba, I.I., Girard, L., Minna, J.D., et al. (2013). NeuroD1 regulates survival and migration of neuroendocrine lung carcinomas via signaling molecules TrkB and NCAM. Proc. Natl. Acad. Sci. *110*, 6524–6529.

Oser, M.G., Fonseca, R., Chakraborty, A.A., Brough, R., Spektor, A., Jennings, R.B., Flaifel, A., Novak, J.S., Gulati, A., Buss, E., et al. (2019). Cells Lacking the RB1 Tumor Suppressor Gene Are Hyperdependent on Aurora B Kinase for Survival. Cancer Discov. *9*, 230–247.

Oshita, F., Kameda, Y., Hamanaka, N., Saito, H., Yamada, K., Noda, K., and Mitsuda, A. (2004). High expression of integrin beta1 and p53 is a greater poor prognostic factor than clinical stage in small-cell lung cancer. Am. J. Clin. Oncol. *27*, 215–219.

Otsu, N. (1979). A Threshold Selection Method from Gray-Level Histograms. IEEE Trans. Syst. Man Cybern. *9*, 62–66.

Ouadah, Y., Rojas, E.R., Riordan, D.P., Capostagno, S., Kuo, C.S., and Krasnow, M.A. (2019). Rare Pulmonary Neuroendocrine Cells Are Stem Cells Regulated by Rb, p53, and Notch. Cell *179*, 403-416.e23.

Owonikoko, T., Nackaerts, K., Csoszi, T., Ostoros, G., Baik, C., Ullmann, C.D., Zagadailov, E., Sheldon-Waniga, E., Huebner, D., Leonard, E.J., et al. (2017). OA05.05 Randomized Phase 2 Study: Alisertib (MLN8237) or Placebo + Paclitaxel as Second-Line Therapy for Small-Cell Lung Cancer (SCLC). J. Thorac. Oncol. *12*, S261–S262.

Owonikoko, T.K., Behera, M., Chen, Z., Bhimani, C., Curran, W.J., Khuri, F.R., and Ramalingam, S.S. (2012). A Systematic Analysis of Efficacy of Second-Line Chemotherapy in Sensitive and Refractory Small-Cell Lung Cancer. J. Thorac. Oncol. *7*, 866–872.

Owonikoko, T.K., Dahlberg, S.E., Sica, G.L., Wagner, L.I., Wade, J.L., Srkalovic, G., Lash, B.W., Leach, J.W., Leal, T.B., Aggarwal, C., et al. (2018). Randomized Phase II Trial of Cisplatin and Etoposide in Combination With Veliparib or Placebo for Extensive-Stage Small-Cell Lung Cancer: ECOG-ACRIN 2511 Study. J. Clin. Oncol. *37*, 222–229.

Owonikoko, T.K., Kim, H.R., Govindan, R., Ready, N., Reck, M., Peters, S., Dakhil, S.R., Navarro, A., Rodriguez-Cid, J., Schenker, M., et al. (2019). LBA1_PRNivolumab (nivo) plus ipilimumab (ipi), nivo, or placebo (pbo) as maintenance therapy in patients (pts) with extensive disease small cell lung cancer (ED-SCLC) after first-line (1L) platinum-based chemotherapy (chemo): Results from the double-blind, randomized phase III CheckMate 451 study. Ann. Oncol. *30*.

Pace, A.M., Faure, M., and Bourne, H.R. (1995). Gi2-mediated activation of the MAP kinase cascade. Mol. Biol. Cell *6*, 1685–1695.

Palma, D.A., Warner, A., Louie, A.V., Senan, S., Slotman, B., and Rodrigues, G.B. (2016). Thoracic Radiotherapy for Extensive Stage Small-Cell Lung Cancer: A Meta-Analysis. Clin. Lung Cancer *17*, 239–244.

Palmer, A.C., and Sorger, P.K. (2017). Combination Cancer Therapy Can Confer Benefit via Patient-to-Patient Variability without Drug Additivity or Synergy. Cell *171*, 1678-1691.e13.

Pandya, K.J., Dahlberg, S., Hidalgo, M., Cohen, R.B., Lee, M.W., Schiller, J.H., and Johnson, D.H. (2007). A Randomized, Phase II Trial of Two Dose Levels of Temsirolimus (CCI-779) in Patients with Extensive-Stage Small-Cell Lung Cancer Who Have Responding or Stable Disease after Induction Chemotherapy: A Trial of the Eastern Cooperative Oncology Group (E1500). J. Thorac. Oncol. *2*, 1036–1041.

Pantel, K., and Speicher, M.R. (2016). The biology of circulating tumor cells. Oncogene *35*, 1216–1224.

Pardo, O.E., Wellbrock, C., Khanzada, U.K., Aubert, M., Arozarena, I., Davidson, S., Bowen, F., Parker, P.J., Filonenko, V.V., Gout, I.T., et al. (2006). FGF-2 protects small cell lung cancer cells from apoptosis through a complex involving PKCε, B-Raf and S6K2. EMBO J. *25*, 3078–3088.

Pardo, O.E., Latigo, J., Jeffery, R.E., Nye, E., Poulsom, R., Spencer-Dene, B., Lemoine, N.R., Stamp, G.W., Aboagye, E.O., and Seckl, M.J. (2009). The Fibroblast Growth Factor Receptor Inhibitor PD173074 Blocks Small Cell Lung Cancer Growth In vitro and In vivo. Cancer Res. *69*, 8645–8651.

Park, K.-S., Liang, M.-C., Raiser, D.M., Zamponi, R., Roach, R.R., Curtis, S.J., Walton, Z., Schaffer, B.E., Roake, C.M., Zmoos, A.-F., et al. (2011a). Characterization of the cell of origin for small cell lung cancer. Cell Cycle Georget. Tex *10*, 2806–2815.

Park, K.-S., Martelotto, L.G., Peifer, M., Sos, M.L., Karnezis, A.N., Mahjoub, M.R., Bernard, K., Conklin, J.F., Szczepny, A., Yuan, J., et al. (2011b). A crucial requirement for Hedgehog signaling in small cell lung cancer. Nat. Med. *17*, 1504–1508.

Parsels, L.A., Karnak, D., Parsels, J.D., Zhang, Q., Vélez-Padilla, J., Reichert, Z.R., Wahl, D.R., Maybaum, J., O'Connor, M.J., Lawrence, T.S., et al. (2018). PARP1 Trapping and DNA Replication Stress Enhance Radiosensitization with Combined WEE1 and PARP Inhibitors. Mol. Cancer Res. *16*, 222–232.

Pasqua, A.J.D., Goodisman, J., and Dabrowiak, J.C. (2012). Understanding how the platinum anticancer drug carboplatin works: From the bottle to the cell. Inorganica Chim. Acta *389*, 29–35.

Pastwa, E., Somiari, R.I., Malinowski, M., Somiari, S.B., and Winters, T.A. (2009). In vitro non-homologous DNA end joining assays—The 20th anniversary. Int. J. Biochem. Cell Biol. *41*, 1254–1260.

Pathology, <blockquote> Edwin Roger Parra Department of Translational Molecular, Center, T.U. of T.M.A.C., Houston, Texas, and USA </blockquote> (2018). Novel Platforms of Multiplexed Immunofluorescence for Study of Paraffin Tumor Tissues. *2*, 43–53.

von Pawel, J., Jotte, R., Spigel, D.R., O'Brien, M.E.R., Socinski, M.A., Mezger, J., Steins, M., Bosquée, L., Bubis, J., Nackaerts, K., et al. (2014). Randomized Phase III Trial of Amrubicin Versus Topotecan As Second-Line Treatment for Patients With Small-Cell Lung Cancer. J. Clin. Oncol. *32*, 4012–4019.

Peifer, M., Fernández-Cuesta, L., Sos, M.L., George, J., Seidel, D., Kasper, L.H., Plenker, D., Leenders, F., Sun, R., Zander, T., et al. (2012). Integrative genome analyses identify key somatic driver mutations of small-cell lung cancer. Nat. Genet. *44*, 1104–1110.

Peng, G., Chun-Jen Lin, C., Mo, W., Dai, H., Park, Y.-Y., Kim, S.M., Peng, Y., Mo, Q., Siwko, S., Hu, R., et al. (2014). Genome-wide transcriptome profiling of homologous recombination DNA repair. Nat. Commun. *5*, 3361.

Petrocchi, A., Leo, E., Reyna, N.J., Hamilton, M.M., Shi, X., Parker, C.A., Mseeh, F., Bardenhagen, J.P., Leonard, P., Cross, J.B., et al. (2016). Identification of potent and selective MTH1 inhibitors. Bioorg. Med. Chem. Lett. *26*, 1503–1507.

Pettitt, S.J., Krastev, D.B., Brandsma, I., Dréan, A., Song, F., Aleksandrov, R., Harrell, M.I., Menon, M., Brough, R., Campbell, J., et al. (2018). Genome-wide and high-density CRISPR-Cas9 screens identify point mutations in PARP1 causing PARP inhibitor resistance. Nat. Commun. *9*.

Pfeifer, G.P., Denissenko, M.F., Olivier, M., Tretyakova, N., Hecht, S.S., and Hainaut, P. (2002). Tobacco smoke carcinogens, DNA damage and p53 mutations in smoking-associated cancers. Oncogene *21*, 7435.

Pfister, S.X., Markkanen, E., Jiang, Y., Sarkar, S., Woodcock, M., Orlando, G., Mavrommati, I., Pai, C.-C., Zalmas, L.-P., Drobnitzky, N., et al. (2015). Inhibiting WEE1 Selectively Kills Histone H3K36me3-Deficient Cancers by dNTP Starvation. Cancer Cell *28*, 557–568.

Phelps, R.M., Johnson, B.E., Ihde, D.C., Gazdar, A.F., Carbone, D.P., McClintock, P.R., Linnoila, R.I., Matthews, M.J., Bunn Jr., P.A., Carney, D., et al. (1996). NCI-navy medical oncology branch cell line data base. J. Cell. Biochem. *63*, 32–91.

Pietanza, M.C., Kadota, K., Huberman, K., Sima, C.S., Fiore, J.J., Sumner, D.K., Travis, W.D., Heguy, A., Ginsberg, M.S., Holodny, A.I., et al. (2012). Phase II Trial of Temozolomide in Patients with Relapsed Sensitive or Refractory Small Cell Lung Cancer, with Assessment of Methylguanine-DNA Methyltransferase as a Potential Biomarker. Clin. Cancer Res. *18*, 1138–1145.

Pietanza, M.C., Litvak, A.M., Varghese, A.M., Krug, L.M., Fleisher, M., Teitcher, J.B., Holodny, A.I., Sima, C.S., Woo, K.M., Ng, K.K., et al. (2016). A phase I trial of the Hedgehog inhibitor, sonidegib (LDE225), in combination with etoposide and cisplatin for the initial treatment of extensive stage small cell lung cancer. Lung Cancer *99*, 23–30.

Pietanza, M.C., Waqar, S.N., Krug, L.M., Dowlati, A., Hann, C.L., Chiappori, A., Owonikoko, T.K., Woo, K.M., Cardnell, R.J., Fujimoto, J., et al. (2018). Randomized, Double-Blind, Phase II Study of Temozolomide in Combination With Either Veliparib or Placebo in Patients With Relapsed-Sensitive or Refractory Small-Cell Lung Cancer. J. Clin. Oncol. *36*, 2386–2394.

Pignon, J.-P., Arriagada, R., Ihde, D.C., Johnson, D.H., Perry, M.C., Souhami, R.L., Brodin, O., Joss, R.A., Kies, M.S., Lebeau, B., et al. (1992). A Meta-Analysis of Thoracic Radiotherapy for Small-Cell Lung Cancer. N. Engl. J. Med. *327*, 1618–1624.

Pilié, P.G., Tang, C., Mills, G.B., and Yap, T.A. (2019). State-of-the-art strategies for targeting the DNA damage response in cancer. Nat. Rev. Clin. Oncol. *16*, 81–104.

Pleasance, E.D., Stephens, P.J., O'Meara, S., McBride, D.J., Meynert, A., Jones, D., Lin, M.-L., Beare, D., Lau, K.W., Greenman, C., et al. (2010). A small-cell lung cancer genome with complex signatures of tobacco exposure. Nature *463*, 184–190.

Poirier, J.T., Dobromilskaya, I., Moriarty, W.F., Peacock, C.D., Hann, C.L., and Rudin, C.M. (2013). Selective tropism of Seneca Valley virus for variant subtype small cell lung cancer. J. Natl. Cancer Inst. *105*, 1059–1065.

Poirier, J.T., Gardner, E.E., Connis, N., Moreira, A.L., de Stanchina, E., Hann, C.L., and Rudin, C.M. (2015). DNA methylation in small cell lung cancer defines distinct disease subtypes and correlates with high expression of EZH2. Oncogene *34*, 5869–5878.

Polley, E., Kunkel, M., Evans, D., Silvers, T., Delosh, R., Laudeman, J., Ogle, C., Reinhart, R., Selby, M., Connelly, J., et al. (2016). Small Cell Lung Cancer Screen of Oncology Drugs, Investigational Agents, and Gene and microRNA Expression. JNCI J. Natl. Cancer Inst. *108*.

Pommier, Y., Barcelo, J.M., Rao, V.A., Sordet, O., Jobson, A.G., Thibaut, L., Miao, Z., Seiler, J.A., Zhang, H., Marchand, C., et al. (2006). Repair of Topoisomerase I-Mediated DNA Damage. In Progress in Nucleic Acid Research and Molecular Biology,

(Academic Press), pp. 179–229.

Pommier, Y., Leo, E., Zhang, H., and Marchand, C. (2010). DNA Topoisomerases and Their Poisoning by Anticancer and Antibacterial Drugs. Chem. Biol. *17*, 421–433.

Pommier, Y., Sun, Y., Huang, S.N., and Nitiss, J.L. (2016a). Roles of eukaryotic topoisomerases in transcription, replication and genomic stability. Nat. Rev. Mol. Cell Biol. *17*, 703–721.

Pommier, Y., O'Connor, M.J., and Bono, J. de (2016b). Laying a trap to kill cancer cells: PARP inhibitors and their mechanisms of action. Sci. Transl. Med. *8*, 362ps17-362ps17.

Potter, D.S., Galvin, M., Brown, S., Lallo, A., Hodgkinson, C.L., Blackhall, F., Morrow, C.J., and Dive, C. (2016). Inhibition of PI3K/BMX Cell Survival Pathway Sensitizes to BH3 Mimetics in SCLC. Mol. Cancer Ther. *15*, 1248–1260.

Poupon, M.F., Arvelo, F., Goguel, A.F., Bourgeois, Y., Jacrot, M., Hanania, N., Arriagada, R., and Chevalier, T.L. (1993). Response of Small-Cell Lung Cancer Xenografts to Chemotherapy: Multidrug Resistance and Direct Clinical Correlates. JNCI J. Natl. Cancer Inst. *85*, 2023–2029.

Pujol, J.-L., Carestia, and Daurès, J.-P. (2000). Is there a case for cisplatin in the treatment of small-cell lung cancer? A meta-analysis of randomized trials of a cisplatin-containing regimen versus a regimen without this alkylating agent. Br. J. Cancer *83*, 8.

Qi, L.S., Larson, M.H., Gilbert, L.A., Doudna, J.A., Weissman, J.S., Arkin, A.P., and Lim, W.A. (2013). Repurposing CRISPR as an RNA-Guided Platform for Sequence-Specific Control of Gene Expression. Cell *152*, 1173–1183.

Quinet, A., Carvajal-Maldonado, D., Lemacon, D., and Vindigni, A. (2017). Chapter Three - DNA Fiber Analysis: Mind the Gap! In Methods in Enzymology, B.F. Eichman, ed. (Academic Press), pp. 55–82.

R Core Team (2018). R: A language and environment for statistical computing. R Foundation for Statistical Computing.

Rackley, C.R., and Stripp, B.R. (2012). Building and maintaining the epithelium of the lung. J. Clin. Invest. *122*, 2724–2730.

Rajeshkumar, N.V., Oliveira, E.D., Ottenhof, N., Watters, J., Brooks, D., Demuth, T., Shumway, S.D., Mizuarai, S., Hirai, H., Maitra, A., et al. (2011). MK-1775, a Potent Wee1 Inhibitor, Synergizes with Gemcitabine to Achieve Tumor Regressions, Selectively in p53-Deficient Pancreatic Cancer Xenografts. Clin. Cancer Res. *17*, 2799–2806.

Ray Chaudhuri, A., and Nussenzweig, A. (2017). The multifaceted roles of PARP1 in DNA repair and chromatin remodelling. Nat. Rev. Mol. Cell Biol. *18*, 610–621.

Reck, Vicente D, C.T., Gettinger S, P.S., Horn L, A.-V.C., Pardo N, J.-V.O., Checg Y, Z.H., Shi M, W.J., Antonia SJ, N.K., Selvaggi G, B.C., and Chang H, S.D. (2018). Second-Line Nivolumab Is Not Superior to Chemotherapy in SCLC | ESMO.

Reck, M., Bondarenko, I., Luft, A., Serwatowski, P., Barlesi, F., Chacko, R., Sebastian, M., Lu, H., Cuillerot, J.-M., and Lynch, T.J. (2013). Ipilimumab in combination with paclitaxel and carboplatin as first-line therapy in extensive-disease-small-cell lung cancer: results from a randomized, double-blind, multicenter phase 2 trial. Ann. Oncol. *24*, 75–83.

Reck, M., Luft, A., Szczesna, A., Havel, L., Kim, S.-W., Akerley, W., Pietanza, M.C., Wu, Y., Zielinski, C., Thomas, M., et al. (2016). Phase III Randomized Trial of Ipilimumab Plus Etoposide and Platinum Versus Placebo Plus Etoposide and Platinum in Extensive-Stage Small-Cell Lung Cancer. J. Clin. Oncol. *34*, 3740–3748.

Resnitzky, D., Gossen, M., Bujard, H., and Reed, S.I. (1994). Acceleration of the G1/S phase transition by expression of cyclins D1 and E with an inducible system. Mol. Cell. Biol. *14*, 1669–1679.

Richmond, A., and Su, Y. (2008). Mouse xenograft models vs GEM models for human cancer therapeutics. Dis. Model. Mech. *1*, 78–82.

Ritchie, M.E., Phipson, B., Wu, D., Hu, Y., Law, C.W., Shi, W., and Smyth, G.K. (2015). limma powers differential expression analyses for RNA-sequencing and microarray studies. Nucleic Acids Res. *43*, e47.

Ritz, C., Baty, F., Streibig, J.C., and Gerhard, D. (2015). Dose-Response Analysis Using R. PloS One *10*, e0146021.

Robinson, J.T., Thorvaldsdóttir, H., Winckler, W., Guttman, M., Lander, E.S., Getz, G., and Mesirov, J.P. (2011). Integrative genomics viewer. Nat. Biotechnol. *29*, 24–26.

Robinson, J.T., Thorvaldsdóttir, H., Wenger, A.M., Zehir, A., and Mesirov, J.P. (2017). Variant Review with the Integrative Genomics Viewer. Cancer Res. *77*, e31–e34.

Roos, W.P., and Kaina, B. (2006). DNA damage-induced cell death by apoptosis. Trends Mol. Med. *12*, 440–450.

Rossi, A., Di Maio, M., Chiodini, P., Rudd, R.M., Okamoto, H., Skarlos, D.V., Früh, M., Qian, W., Tamura, T., Samantas, E., et al. (2012). Carboplatin- or Cisplatin-Based Chemotherapy in First-Line Treatment of Small-Cell Lung Cancer: The COCIS Meta-Analysis of Individual Patient Data. J. Clin. Oncol. *30*, 1692–1698.

Rottenberg, S., Jaspers, J.E., Kersbergen, A., Burg, E. van der, Nygren, A.O.H., Zander, S.A.L., Derksen, P.W.B., Bruin, M. de, Zevenhoven, J., Lau, A., et al. (2008). High sensitivity of BRCA1-deficient mammary tumors to the PARP inhibitor AZD2281 alone and in combination with platinum drugs. Proc. Natl. Acad. Sci. *105*, 17079–17084.

Rudin, C.M., Salgia, R., Wang, X., Hodgson, L.D., Masters, G.A., Green, M., and Vokes,

E.E. (2008). Randomized Phase II Study of Carboplatin and Etoposide With or Without the bcl-2 Antisense Oligonucleotide Oblimersen for Extensive-Stage Small-Cell Lung Cancer: CALGB 30103. J. Clin. Oncol. Off. J. Am. Soc. Clin. Oncol. *26*, 870–876.

Rudin, C.M., Durinck, S., Stawiski, E.W., Poirier, J.T., Modrusan, Z., Shames, D.S., Bergbower, E.A., Guan, Y., Shin, J., Guillory, J., et al. (2012a). Comprehensive genomic analysis identifies SOX2 as a frequently amplified gene in small-cell lung cancer. Nat. Genet. *44*, 1111–1116.

Rudin, C.M., Hann, C.L., Garon, E.B., Oliveira, M.R. de, Bonomi, P.D., Camidge, D.R., Chu, Q., Giaccone, G., Khaira, D., Ramalingam, S.S., et al. (2012b). Phase II Study of Single-Agent Navitoclax (ABT-263) and Biomarker Correlates in Patients with Relapsed Small Cell Lung Cancer. Clin. Cancer Res. *18*, 3163–3169.

Rudin, C.M., Pietanza, M.C., Bauer, T.M., Ready, N., Morgensztern, D., Glisson, B.S., Byers, L.A., Johnson, M.L., Burris, H.A., Robert, F., et al. (2017). Rovalpituzumab tesirine, a DLL3-targeted antibody-drug conjugate, in recurrent small-cell lung cancer: a first-in-human, first-in-class, open-label, phase 1 study. Lancet Oncol. *18*, 42–51.

Rudin, C.M., Poirier, J.T., Byers, L.A., Dive, C., Dowlati, A., George, J., Heymach, J.V., Johnson, J.E., Lehman, J.M., MacPherson, D., et al. (2019). Molecular subtypes of small cell lung cancer: a synthesis of human and mouse model data. Nat. Rev. Cancer *19*, 289.

Ruotsalainen, T., Joensuu, H., Mattson, K., and Salven, P. (2002). High Pretreatment Serum Concentration of Basic Fibroblast Growth Factor Is a Predictor of Poor Prognosis in Small Cell Lung Cancer. Cancer Epidemiol. Prev. Biomark. *11*, 1492–1495.

Russel W.M.S., and Burch R.L. (1959). The Principles of Humane Experimental Technique.

Sabari, J.K., Lok, B.H., Laird, J.H., Poirier, J.T., and Rudin, C.M. (2017). Unravelling the biology of SCLC: implications for therapy. Nat. Rev. Clin. Oncol. *14*, 549–561.

Saito, Y., Nagae, G., Motoi, N., Miyauchi, E., Ninomiya, H., Uehara, H., Mun, M., Okumura, S., Ohyanagi, F., Nishio, M., et al. (2016). Prognostic significance of CpG island methylator phenotype in surgically resected small cell lung carcinoma. Cancer Sci. *107*, 320–325.

Sale, J.E. (2013). Translesion DNA Synthesis and Mutagenesis in Eukaryotes. Cold Spring Harb. Perspect. Biol. *5*, a012708.

Salic, A., and Mitchison, T.J. (2008). A chemical method for fast and sensitive detection of DNA synthesis in vivo. Proc. Natl. Acad. Sci. *105*, 2415–2420.

Salphati, L., Pang, J., Plise, E.G., Chou, B., Halladay, J.S., Olivero, A.G., Rudewicz, P.J., Tian, Q., Wong, S., and Zhang, X. (2011). Preclinical pharmacokinetics of the novel PI3K inhibitor GDC-0941 and prediction of its pharmacokinetics and efficacy in

human. Xenobiotica *41*, 1088–1099.

Sanjana, N.E., Shalem, O., and Zhang, F. (2014). Improved vectors and genome-wide libraries for CRISPR screening. Nat. Methods *11*, 783–784.

Sartorius, U.A., and Krammer, P.H. (2002). Upregulation of bcl-2 is involved in the mediation of chemotherapy resistance in human small cell lung cancer cell lines. Int. J. Cancer *97*, 584–592.

Sato, T., Kaneda, A., Tsuji, S., Isagawa, T., Yamamoto, S., Fujita, T., Yamanaka, R., Tanaka, Y., Nukiwa, T., Marquez, V.E., et al. (2013). PRC2 overexpression and PRC2-target gene repression relating to poorer prognosis in small cell lung cancer. Sci. Rep. *3*, 1911.

Saunders, L.R., Bankovich, A.J., Anderson, W.C., Aujay, M.A., Bheddah, S., Black, K., Desai, R., Escarpe, P.A., Hampl, J., Laysang, A., et al. (2015). A DLL3-targeted antibody-drug conjugate eradicates high-grade pulmonary neuroendocrine tumor-initiating cells in vivo. Sci. Transl. Med. *7*, 302ra136-302ra136.

Schaffer, B.E., Park, K.-S., Yiu, G., Conklin, J.F., Lin, C., Burkhart, D.L., Karnezis, A.N., Sweet-Cordero, E.A., and Sage, J. (2010). Loss of p130 Accelerates Tumor Development in a Mouse Model for Human Small-Cell Lung Carcinoma. Cancer Res. *70*, 3877–3883.

Schärer, O.D. (2013). Nucleotide Excision Repair in Eukaryotes. Cold Spring Harb. Perspect. Biol. *5*.

Schiewer, M.J., Mandigo, A.C., Gordon, N., Huang, F., Gaur, S., de Leeuw, R., Zhao, S.G., Evans, J., Han, S., Parsons, T., et al. (2018). PARP-1 regulates DNA repair factor availability. EMBO Mol. Med. *10*, e8816.

Schneider, B.J., Kalemkerian, G.P., Ramnath, N., Kraut, M.J., Wozniak, A.J., Worden, F.P., Ruckdeschel, J.C., Zhang, X., Chen, W., and Gadgeel, S.M. (2010). Phase II Trial of Imatinib Maintenance Therapy After Irinotecan and Cisplatin in Patients With c-Kit–Positive, Extensive-Stage Small-Cell Lung Cancer. Clin. Lung Cancer *11*, 223–227.

Schöffski, P., Besse, B., Gauler, T., de Jonge, M.J.A., Scambia, G., Santoro, A., Davite, C., Jannuzzo, M.G., Petroccione, A., and Delord, J.-P. (2015). Efficacy and safety of biweekly i.v. administrations of the Aurora kinase inhibitor danusertib hydrochloride in independent cohorts of patients with advanced or metastatic breast, ovarian, colorectal, pancreatic, small-cell and non-small-cell lung cancer: a multi-tumour, multi-institutional phase II study. Ann. Oncol. *26*, 598–607.

Schreiber, R.D., Old, L.J., and Smyth, M.J. (2011). Cancer Immunoediting: Integrating Immunity's Roles in Cancer Suppression and Promotion. Science *331*, 1565–1570.

Schultheis, A.M., Bos, M., Schmitz, K., Wilsberg, L., Binot, E., Wolf, J., Büttner, R., and Schildhaus, H.-U. (2014). *Fibroblast growth factor receptor 1 (FGFR1)* amplification is a potential therapeutic target in small-cell lung cancer. Mod. Pathol. *27*, 214–221.

Semenova, E.A., Kwon, M., Monkhorst, K., Song, J.-Y., Bhaskaran, R., Krijgsman, O., Kuilman, T., Peters, D., Buikhuisen, W.A., Smit, E.F., et al. (2016). Transcription Factor NFIB Is a Driver of Small Cell Lung Cancer Progression in Mice and Marks Metastatic Disease in Patients. Cell Rep. *16*, 631–643.

Sen, T., Tong, P., Stewart, C.A., Cristea, S., Valliani, A., Shames, D.S., Redwood, A.B., Fan, Y.H., Li, L., Glisson, B.S., et al. (2017a). CHK1 Inhibition in Small-Cell Lung Cancer Produces Single-Agent Activity in Biomarker-Defined Disease Subsets and Combination Activity with Cisplatin or Olaparib. Cancer Res. *77*, 3870–3884.

Sen, T., Tong, P., Diao, L., Li, L., Fan, Y., Hoff, J., Heymach, J.V., Wang, J., and Byers, L.A. (2017b). Targeting AXL and mTOR Pathway Overcomes Primary and Acquired Resistance to WEE1 Inhibition in Small-Cell Lung Cancer. Clin. Cancer Res. *23*, 6239–6253.

Sen, T., Gay, C.M., and Byers, L.A. (2018). Targeting DNA damage repair in small cell lung cancer and the biomarker landscape. Transl. Lung Cancer Res. *7*, 50–68.

Sen, T., Della Corte, C.M., Milutinovic, S., Cardnell, R.J., Diao, L., Ramkumar, K., Gay, C.M., Stewart, C.A., Fan, Y., Shen, L., et al. (2019a). Combination treatment of the oral CHK1 inhibitor, SRA737 and low dose gemcitabine, enhances the effect of PD-L1 blockade by modulating the immune microenvironment in small cell lung cancer. J. Thorac. Oncol.

Sen, T., Rodriguez, B.L., Chen, L., Corte, C.M.D., Morikawa, N., Fujimoto, J., Cristea, S., Nguyen, T., Diao, L., Li, L., et al. (2019b). Targeting DNA Damage Response Promotes Antitumor Immunity through STING-Mediated T-cell Activation in Small Cell Lung Cancer. Cancer Discov. *9*, 646–661.

Sereno, M., Sereno, M., Cejas, P., Cejas, P., Moreno, V., Moreno, V., Belda-Iniesta, C., Belda-Iniesta, C., López, R., López, R., et al. (2012). ERCC1 and topoisomerase I expression in small cell lung cancer: Prognostic and predictive implications. Int. J. Oncol. *40*, 2104–2110.

Sergushichev, A.A. (2016). An algorithm for fast preranked gene set enrichment analysis using cumulative statistic calculation. BioRxiv 060012.

Sharma, S.V., Lee, D.Y., Li, B., Quinlan, M.P., Takahashi, F., Maheswaran, S., McDermott, U., Azizian, N., Zou, L., Fischbach, M.A., et al. (2010). A Chromatin-Mediated Reversible Drug-Tolerant State in Cancer Cell Subpopulations. Cell *141*, 69–80.

Shepherd, F.A., Evans, W.K., Feld, R., Young, V., Patterson, G.A., Ginsberg, R., and Johansen, E. (1988). Adjuvant chemotherapy following surgical resection for small-cell carcinoma of the lung. J. Clin. Oncol. *6*, 832–838.

Shimizu, E., Coxon, A., Otterson, G.A., Steinberg, S.M., Kratzke, R.A., Kim, Y.W., Fedorko, J., Oie, H., Johnson, B.E., and Mulshine, J.L. (1994). RB protein status and clinical correlation from 171 cell lines representing lung cancer, extrapulmonary

small cell carcinoma, and mesothelioma. Oncogene *9*, 2441–2448.

Shoemaker, R.H. (2006). The NCI60 human tumour cell line anticancer drug screen. Nat. Rev. Cancer *6*, 813.

Shoemaker, A.R., Mitten, M.J., Adickes, J., Ackler, S., Refici, M., Ferguson, D., Oleksijew, A., O'Connor, J.M., Wang, B., Frost, D.J., et al. (2008). Activity of the Bcl-2 Family Inhibitor ABT-263 in a Panel of Small Cell Lung Cancer Xenograft Models. Clin. Cancer Res. *14*, 3268–3277.

Siddik, Z.H. (2003). Cisplatin: mode of cytotoxic action and molecular basis of resistance. Oncogene *22*, 7265.

Simbulan-Rosenthal, C.M., Rosenthal, D.S., Luo, R., Samara, R., Espinoza, L.A., Hassa, P.O., Hottiger, M.O., and Smulson, M.E. (2003). PARP-1 binds E2F-1 independently of its DNA binding and catalytic domains, and acts as a novel coactivator of E2F-1-mediated transcription during re-entry of quiescent cells into S phase. Oncogene *22*, 8460.

Simms, E., Gazdar, A.F., Abrams, P.G., and Minna, J.D. (1980). Growth of Human Small Cell (Oat Cell) Carcinoma of the Lung in Serum-free Growth Factor-Supplemented Medium. *40*, 9.

Simon, J.A., and Lange, C.A. (2008). Roles of the EZH2 histone methyltransferase in cancer epigenetics. Mutat. Res. Mol. Mech. Mutagen. *647*, 21–29.

Simpson, K.L., Stoney, R., Frese, K.K., Simms, N., Rowe, W., Booth, L., Morgan, D., Dynowski, M., Trapani, F., Catozzi, A., et al. (2019). (under revision) A Biobank of Small Cell Lung Cancer CDX Models Elucidates Inter- and Intra-tumoural Phenotypic Heterogeneity. Nature Cancer.

Singh, M., Lima, A., Molina, R., Hamilton, P., Clermont, A.C., Devasthali, V., Thompson, J.D., Cheng, J.H., Bou Reslan, H., Ho, C.C.K., et al. (2010). Assessing therapeutic responses in *Kras* mutant cancers using genetically engineered mouse models. Nat. Biotechnol. *28*, 585–593.

Siravegna, G., Marsoni, S., Siena, S., and Bardelli, A. (2017). Integrating liquid biopsies into the management of cancer. Nat. Rev. Clin. Oncol. *14*, 531–548.

Smit, E.F., Fokkema, E., Biesma, B., Groen, H.J., Snoek, W., and Postmus, P.E. (1998). A phase II study of paclitaxel in heavily pretreated patients with small-cell lung cancer. Br. J. Cancer *77*, 347–351.

Smith, J., Mun Tho, L., Xu, N., and A. Gillespie, D. (2010). Chapter 3 - The ATM–Chk2 and ATR–Chk1 Pathways in DNA Damage Signaling and Cancer. In Advances in Cancer Research, G.F. Vande Woude, and G. Klein, eds. (Academic Press), pp. 73–112.

Smyth, J.F., Smith, I.E., Sessa, C., Schoffski, P., Wanders, J., Franklin, H., and Kaye, S.B. (1994). Activity of docetaxel (Taxotere) in small cell lung cancer. The Early Clinical

Trials Group of the EORTC. Eur. J. Cancer Oxf. Engl. 1990 *30A*, 1058–1060.

Socinski, M.A., Kaye, F.J., Spigel, D.R., Kudrik, F.J., Ponce, S., Ellis, P.M., Majem, M., Lorigan, P., Gandhi, L., Gutierrez, M.E., et al. (2017). Phase 1/2 Study of the CD56-Targeting Antibody-Drug Conjugate Lorvotuzumab Mertansine (IMGN901) in Combination With Carboplatin/Etoposide in Small-Cell Lung Cancer Patients With Extensive-Stage Disease. Clin. Lung Cancer *18*, 68-76.e2.

Song, H., Yao, E., Lin, C., Gacayan, R., Chen, M.-H., and Chuang, P.-T. (2012). Functional characterization of pulmonary neuroendocrine cells in lung development, injury, and tumorigenesis. Proc. Natl. Acad. Sci. U. S. A. *109*, 17531–17536.

Song, I.-S., Savaraj, N., Siddik, Z.H., Liu, P., Wei, Y., Wu, C.J., and Kuo, M.T. (2004). Role of human copper transporter Ctr1 in the transport of platinum-based antitumor agents in cisplatin-sensitive and cisplatin-resistant cells. Mol. Cancer Ther. *3*, 1543–1549.

Sos, M.L., Dietlein, F., Peifer, M., Schöttle, J., Balke-Want, H., Müller, C., Koker, M., Richters, A., Heynck, S., Malchers, F., et al. (2012). A framework for identification of actionable cancer genome dependencies in small cell lung cancer. Proc. Natl. Acad. Sci. *109*, 17034–17039.

Spigel, D.R., Hainsworth, J.D., Simons, L., Meng, C., Burris, H.A., Yardley, D.A., Grapski, R., Schreeder, M., Mallidi, P.V., and Greco, F.A. (2007). Irinotecan, Carboplatin, and Imatinib in Untreated Extensive-Stage Small-Cell Lung Cancer: A Phase II Trial of the Minnie Pearl Cancer Research Network. J. Thorac. Oncol. *2*, 854–861.

Srinivasan, S.V., Dominguez-Sola, D., Wang, L.C., Hyrien, O., and Gautier, J. (2013). Cdc45 Is a Critical Effector of Myc-Dependent DNA Replication Stress. Cell Rep. *3*, 1629–1639.

Staker, B.L., Hjerrild, K., Feese, M.D., Behnke, C.A., Burgin, A.B., and Stewart, L. (2002). The mechanism of topoisomerase I poisoning by a camptothecin analog. Proc. Natl. Acad. Sci. *99*, 15387–15392.

Steele-Perkins, G., Plachez, C., Butz, K.G., Yang, G., Bachurski, C.J., Kinsman, S.L., Litwack, E.D., Richards, L.J., and Gronostajski, R.M. (2005). The Transcription Factor Gene Nfib Is Essential for both Lung Maturation and Brain Development. Mol. Cell. Biol. *25*, 685–698.

Stein, W.D., Litman, T., Fojo, T., and Bates, S.E. (2004). A Serial Analysis of Gene Expression (SAGE) Database Analysis of Chemosensitivity: Comparing Solid Tumors with Cell Lines and Comparing Solid Tumors from Different Tissue Origins. Cancer Res. *64*, 2805–2816.

Stengel, K.R., Thangavel, C., Solomon, D.A., Angus, S.P., Zheng, Y., and Knudsen, E.S. (2009). Retinoblastoma/p107/p130 Pocket Proteins. J. Biol. Chem. *284*, 19265–19271.

Stewart, D.J. (2010). Tumor and host factors that may limit efficacy of chemotherapy in non-small cell and small cell lung cancer. Crit. Rev. Oncol. Hematol. *75*, 173–234.

Stewart, C.A., Tong, P., Cardnell, R.J., Sen, T., Li, L., Gay, C.M., Masrorpour, F., Fan, Y., Bara, R.O., Feng, Y., et al. (2017). Dynamic variations in epithelial-to-mesenchymal transition (EMT), ATM, and SLFN11 govern response to PARP inhibitors and cisplatin in small cell lung cancer. Oncotarget *8*, 28575–28587.

Su, K.-Y., Chen, H.-Y., Li, K.-C., Kuo, M.-L., Yang, J.C.-H., Chan, W.-K., Ho, B.-C., Chang, G.-C., Shih, J.-Y., Yu, S.-L., et al. (2012). Pretreatment Epidermal Growth Factor Receptor (EGFR) T790M Mutation Predicts Shorter EGFR Tyrosine Kinase Inhibitor Response Duration in Patients With Non–Small-Cell Lung Cancer. J. Clin. Oncol. *30*, 433–440.

Su, Z., Wang, Z., Ni, X., Duan, J., Gao, Y., Zhuo, M., Li, R., Zhao, J., Ma, Q., Bai, H., et al. (2019). Inferring the Evolution and Progression of Small-Cell Lung Cancer by Single-Cell Sequencing of Circulating Tumor Cells. Clin. Cancer Res. clincanres.3571.2018.

Subramanian, A., Tamayo, P., Mootha, V.K., Mukherjee, S., Ebert, B.L., Gillette, M.A., Paulovich, A., Pomeroy, S.L., Golub, T.R., Lander, E.S., et al. (2005). Gene set enrichment analysis: A knowledge-based approach for interpreting genome-wide expression profiles. Proc. Natl. Acad. Sci. *102*, 15545–15550.

Sun, Z., Chen, J., Aakre, J., Marks, R.S., Garces, Y.Y., Jiang, R., Idowu, O., Cunningham, J.M., Liu, Y., Pankratz, V.S., et al. (2010). Genetic variation in glutathione metabolism and DNA repair genes predicts survival of small-cell lung cancer patients. Ann. Oncol. *21*, 2011–2016.

Sundstrøm, S., Bremnes, R.M., Kaasa, S., Aasebø, U., Hatlevoll, R., Dahle, R., Boye, N., Wang, M., Vigander, T., Vilsvik, J., et al. (2002). Cisplatin and Etoposide Regimen Is Superior to Cyclophosphamide, Epirubicin, and Vincristine Regimen in Small-Cell Lung Cancer: Results From a Randomized Phase III Trial With 5 Years' Follow-Up. J. Clin. Oncol. *20*, 4665–4672.

Sutherland, K.D., and Berns, A. (2010). Cell of origin of lung cancer. Mol. Oncol. *4*, 397–403.

Svensson, L.M., Jemth, A.-S., Desroses, M., Loseva, O., Helleday, T., Högbom, M., and Stenmark, P. (2011). Crystal structure of human MTH1 and the 8-oxo-dGMP product complex. FEBS Lett. *585*, 2617–2621.

TAHOE Trial (2017). Study Comparing Rovalpituzumab Tesirine Versus Topotecan in Subjects With Advanced or Metastatic Small Cell Lung Cancer With High Levels of Delta-like Protein 3 (DLL3) and Who Have First Disease Progression During or Following Front-line Platinum-based Chemotherapy (TAHOE) - NCT03061812.

Takahashi, T., Nau, M.M., Chiba, I., Birrer, M.J., Rosenberg, R.K., Vinocour, M., Levitt, M., Pass, H., Gazdar, A.F., and Minna, J.D. (1989). p53: a frequent target for genetic

abnormalities in lung cancer. Science *246*, 491–494.

Takahashi, T., Yamanaka, T., Seto, T., Harada, H., Nokihara, H., Saka, H., Nishio, M., Kaneda, H., Takayama, K., Ishimoto, O., et al. (2017). Prophylactic cranial irradiation versus observation in patients with extensive-disease small-cell lung cancer: a multicentre, randomised, open-label, phase 3 trial. Lancet Oncol. *18*, 663–671.

Tarhini, A., Kotsakis, A., Gooding, W., Shuai, Y., Petro, D., Friedland, D., Belani, C.P., Dacic, S., and Argiris, A. (2010). Phase II Study of Everolimus (RAD001) in Previously Treated Small Cell Lung Cancer. Clin. Cancer Res. *16*, 5900–5907.

Técher, H., Koundrioukoff, S., Azar, D., Wilhelm, T., Carignon, S., Brison, O., Debatisse, M., and Le Tallec, B. (2013). Replication Dynamics: Biases and Robustness of DNA Fiber Analysis. J. Mol. Biol. *425*, 4845–4855.

Thomas, A., and Pommier, Y. (2016). Small cell lung cancer: Time to revisit DNA-damaging chemotherapy. Sci. Transl. Med. *8*, 346fs12-346fs12.

Thomas, A., Vilimas, R., Trindade, C., Erwin-Cohen, R., Roper, N., Xi, L., Krishnasamy, V., Levy, E., Mammen, A., Nichols, S., et al. (2019). Durvalumab in Combination with Olaparib in Patients with Relapsed SCLC: Results from a Phase II Study. J. Thorac. Oncol. *14*, 1447–1457.

Toledo, L., Neelsen, K.J., and Lukas, J. (2017). Replication Catastrophe: When a Checkpoint Fails because of Exhaustion. Mol. Cell *66*, 735–749.

Toledo, L.I., Altmeyer, M., Rask, M.-B., Lukas, C., Larsen, D.H., Povlsen, L.K., Bekker-Jensen, S., Mailand, N., Bartek, J., and Lukas, J. (2013). ATR Prohibits Replication Catastrophe by Preventing Global Exhaustion of RPA. Cell *155*, 1088–1103.

Travis, W.D., Brambilla, E., Müller-Hermelink, H.K., and Harris, C.C. (2004). Pathology and Genetics of Tumours of the Lung, Pleura, Thymus and Heart.

Travis, W.D., Brambilla, E., Nicholson, A.G., Yatabe, Y., Austin, J.H.M., Beasley, M.B., Chirieac, L.R., Dacic, S., Duhig, E., Flieder, D.B., et al. (2015). The 2015 World Health Organization Classification of Lung Tumors: Impact of Genetic, Clinical and Radiologic Advances Since the 2004 Classification. J. Thorac. Oncol. Off. Publ. Int. Assoc. Study Lung Cancer *10*, 1243–1260.

Triller, N., Korošec, P., Kern, I., Košnik, M., and Debeljak, A. (2006). Multidrug resistance in small cell lung cancer: Expression of P-glycoprotein, multidrug resistance protein 1 and lung resistance protein in chemo-naive patients and in relapsed disease. Lung Cancer *54*, 235–240.

Tripathi, S.C., Fahrmann, J.F., Celiktas, M., Aguilar, M., Marini, K.D., Jolly, M.K., Katayama, H., Wang, H., Murage, E.N., Dennison, J.B., et al. (2017). MCAM Mediates Chemoresistance in Small-Cell Lung Cancer via the PI3K/AKT/SOX2 Signaling Pathway. Cancer Res. *77*, 4414–4425.

Tse, C., Shoemaker, A.R., Adickes, J., Anderson, M.G., Chen, J., Jin, S., Johnson, E.F., Marsh, K.C., Mitten, M.J., Nimmer, P., et al. (2008). ABT-263: A Potent and Orally Bioavailable Bcl-2 Family Inhibitor. Cancer Res. *68*, 3421–3428.

Tsurutani, J., West, K.A., Sayyah, J., Gills, J.J., and Dennis, P.A. (2005). Inhibition of the Phosphatidylinositol 3-Kinase/Akt/Mammalian Target of Rapamycin Pathway but not the MEK/ERK Pathway Attenuates Laminin-Mediated Small Cell Lung Cancer Cellular Survival and Resistance to Imatinib Mesylate or Chemotherapy. Cancer Res. *65*, 8423–8432.

Tsuzuki, T., Nakatsu, Y., and Nakabeppu, Y. (2007). Significance of error-avoiding mechanisms for oxidative DNA damage in carcinogenesis. Cancer Sci. *98*, 465–470.

Umemura, S., Mimaki, S., Makinoshima, H., Tada, S., Ishii, G., Ohmatsu, H., Niho, S., Yoh, K., Matsumoto, S., Takahashi, A., et al. (2014). Therapeutic Priority of the PI3K/AKT/mTOR Pathway in Small Cell Lung Cancers as Revealed by a Comprehensive Genomic Analysis. J. Thorac. Oncol. *9*, 1324–1331.

U.S. Food and Drug Administration (2019). FDA approves atezolizumab for extensive-stage small cell lung cancer. FDA.

Vafa, O., Wade, M., Kern, S., Beeche, M., Pandita, T.K., Hampton, G.M., and Wahl, G.M. (2002). c-Myc Can Induce DNA Damage, Increase Reactive Oxygen Species, and Mitigate p53 Function: A Mechanism for Oncogene-Induced Genetic Instability. Mol. Cell *9*, 1031–1044.

Vassin, V.M., Anantha, R.W., Sokolova, E., Kanner, S., and Borowiec, J.A. (2009). Human RPA phosphorylation by ATR stimulates DNA synthesis and prevents ssDNA accumulation during DNA-replication stress. J. Cell Sci. *122*, 4070–4080.

Vernardis, S.I., Terzoudis, K., Panoskaltsis, N., and Mantalaris, A. (2017). Human embryonic and induced pluripotent stem cells maintain phenotype but alter their metabolism after exposure to ROCK inhibitor. Sci. Rep. *7*.

Vignard, J., Mirey, G., and Salles, B. (2013). Ionizing-radiation induced DNA double-strand breaks: A direct and indirect lighting up. Radiother. Oncol. *108*, 362–369.

Vincent, M., Evans, B., and Smith, I. (1988). First-line chemotherapy rechallenge after relapse in small cell lung cancer. Cancer Chemother. Pharmacol. *21*, 45–48.

Vousden, K.H., and Lane, D.P. (2007). p53 in health and disease. Nat. Rev. Mol. Cell Biol. *8*, 275–283.

Wahlberg, E., Karlberg, T., Kouznetsova, E., Markova, N., Macchiarulo, A., Thorsell, A.-G., Pol, E., Frostell, Å., Ekblad, T., Öncü, D., et al. (2012). Family-wide chemical profiling and structural analysis of PARP and tankyrase inhibitors. Nat. Biotechnol. *30*, 283–288.

Wakuda, K., Kenmotsu, H., Naito, T., Akamatsu, H., Ono, A., Shukuya, T., Nakamura,

Y., Tsuya, A., Murakami, H., Takahashi, T., et al. (2012). Efficacy of rechallenge chemotherapy in patients with sensitive relapsed small cell lung cancer. J. Clin. Oncol. *30*, 7088–7088.

Wang, J.C. (2002). Cellular roles of DNA topoisomerases: a molecular perspective. Nat. Rev. Mol. Cell Biol. *3*, 430.

Wang, D., and Lippard, S.J. (2005). Cellular processing of platinum anticancer drugs. Nat. Rev. Drug Discov. *4*, 307–320.

Wang, K., Singh, D., Zeng, Z., Coleman, S.J., Huang, Y., Savich, G.L., He, X., Mieczkowski, P., Grimm, S.A., Perou, C.M., et al. (2010). MapSplice: accurate mapping of RNA-seq reads for splice junction discovery. Nucleic Acids Res. *38*, e178.

Wang, W.-L., Healy, M.E., Sattler, M., Verma, S., Lin, J., Maulik, G., Stiles, C.D., Griffin, J.D., Johnson, B.E., and Salgia, R. (2000). Growth inhibition and modulation of kinase pathways of small cell lung cancer cell lines by the novel tyrosine kinase inhibitor STI 571. Oncogene *19*, 3521.

Warde, P., and Payne, D. (1992). Does thoracic irradiation improve survival and local control in limited-stage small-cell carcinoma of the lung? A meta-analysis. J. Clin. Oncol. *10*, 890–895.

Warpman Berglund, U., Sanjiv, K., Gad, H., Kalderén, C., Koolmeister, T., Pham, T., Gokturk, C., Jafari, R., Maddalo, G., Seashore-Ludlow, B., et al. (2016). Validation and development of MTH1 inhibitors for treatment of cancer. Ann. Oncol. *27*, 2275–2283.

Watanabe, K., Ueno, M., Kamiya, D., Nishiyama, A., Matsumura, M., Wataya, T., Takahashi, J.B., Nishikawa, S., Nishikawa, S., Muguruma, K., et al. (2007). A ROCK inhibitor permits survival of dissociated human embryonic stem cells. Nat. Biotechnol. *25*, 681–686.

Watanabe, Y., Koi, M., Hemmi, H., Hoshai, H., and Noda, K. (2001). A change in microsatellite instability caused by cisplatin-based chemotherapy of ovarian cancer. Br. J. Cancer *85*, 1064.

Watkins, D.N., Berman, D.M., Burkholder, S.G., Wang, B., Beachy, P.A., and Baylin, S.B. (2003). Hedgehog signalling within airway epithelial progenitors and in small-cell lung cancer. Nature *422*, 313.

Weinberg, R.A. (1995). The retinoblastoma protein and cell cycle control. Cell *81*, 323–330.

Weinstein, Z.B., Bender, A., and Cokol, M. (2017). Prediction of synergistic drug combinations. Curr. Opin. Syst. Biol. *4*, 24–28.

Weis, W.I., and Kobilka, B.K. (2018). The Molecular Basis of G Protein–Coupled Receptor Activation. Annu. Rev. Biochem. *87*, 897–919.

Weiskopf, K., Jahchan, N.S., Schnorr, P.J., Cristea, S., Ring, A.M., Maute, R.L., Volkmer, A.K., Volkmer, J.-P., Liu, J., Lim, J.S., et al. (2016). CD47-blocking immunotherapies stimulate macrophage-mediated destruction of small-cell lung cancer. J. Clin. Invest. *126*, 2610–2620.

Welsh, C., Day, R., McGurk, C., Masters, J.R.W., Wood, R.D., and Köberle, B. (2004). Reduced levels of XPA, ERCC1 and XPF DNA repair proteins in testis tumor cell lines. Int. J. Cancer *110*, 352–361.

Whang-Peng, J., Kao-Shan, C.S., Lee, E.C., Bunn, P.A., Carney, D.N., Gazdar, A.F., and Minna, J.D. (1982). Specific chromosome defect associated with human small-cell lung cancer; deletion 3p(14-23). Science *215*, 181–182.

Whiteman, K.R., Johnson, H.A., Mayo, M.F., Audette, C.A., Carrigan, C.N., LaBelle, A., Zukerberg, L., Lambert, J.M., and Lutz, R.J. (2014). Lorvotuzumab mertansine, a CD56-targeting antibody-drug conjugate with potent antitumor activity against small cell lung cancer in human xenograft models. MAbs *6*, 556–566.

Wickham, H. (2009). ggplot2: Elegant Graphics for Data Analysis (New York: Springer-Verlag).

Widmann, C., Gibson, S., and Johnson, G.L. (1998). Caspase-dependent Cleavage of Signaling Proteins during Apoptosis A TURN-OFF MECHANISM FOR ANTI-APOPTOTIC SIGNALS. J. Biol. Chem. *273*, 7141–7147.

Williams, A.B., and Schumacher, B. (2016). p53 in the DNA-Damage-Repair Process. Cold Spring Harb. Perspect. Med. *6*, a026070.

Willmore, E., Frank, A.J., Padget, K., Tilby, M.J., and Austin, C.A. (1998). Etoposide Targets Topoisomerase IIα and IIβ in Leukemic Cells: Isoform-Specific Cleavable Complexes Visualized and QuantifiedIn Situ by a Novel Immunofluorescence Technique. Mol. Pharmacol. *54*, 78–85.

Wistuba, I.I., and Gazdar, A.F. (2006). Lung Cancer Preneoplasia. Annu. Rev. Pathol. Mech. Dis. *1*, 331–348.

Wistuba, I.I., Berry, J., Behrens, C., Maitra, A., Shivapurkar, N., Milchgrub, S., Mackay, B., Minna, J.D., and Gazdar, A.F. (2000). Molecular Changes in the Bronchial Epithelium of Patients with Small Cell Lung Cancer. Clin. Cancer Res. *6*, 2604–2610.

Woll, P., Gaunt, P., Steele, N., Ahmed, S., Mulatero, C., Shah, R., Danson, S., Hodgkinson, E., James, K., Watkins, B., et al. (2017). P1.07-015 STOMP: A UK National Cancer Research Network Randomised, Double Blind, Multicentre Phase II Trial of Olaparib as Maintenance Therapy in SCLC: Topic: Drug Treatment Alone and in Combination with Radiotherapy. J. Thorac. Oncol. *12*, S704–S705.

Wood, D.E., Kazerooni, E.A., Baum, S.L., Eapen, G.A., Ettinger, D.S., Hou, L., Jackman, D.M., Klippenstein, D., Kumar, R., Lackner, R.P., et al. (2018). Lung Cancer Screening, Version 3.2018, NCCN Clinical Practice Guidelines in Oncology. J. Natl. Compr. Canc.

Netw. *16*, 412–441.

Wood, L., Palmer, M., Hewitt, J., Urtasun, R., Bruera, E., Rapp, E., and Thaell, J.F. (1998). Results of a phase III, double-blind, placebo-controlled trial of megestrol acetate modulation of P-glycoprotein-mediated drug resistance in the first-line management of small-cell lung carcinoma. Br. J. Cancer *77*, 627–631.

Wright, G., Golubeva, V., Remsing Rix, L.L., Berndt, N., Luo, Y., Ward, G.A., Gray, J.E., Schonbrunn, E., Lawrence, H.R., Monteiro, A.N.A., et al. (2017). Dual Targeting of WEE1 and PLK1 by AZD1775 Elicits Single Agent Cellular Anticancer Activity. ACS Chem. Biol. *12*, 1883–1892.

Wu, N., Jia, D., Ibrahim, A.H., Bachurski, C.J., Gronostajski, R.M., and MacPherson, D. (2016). NFIB overexpression cooperates with Rb/p53 deletion to promote small cell lung cancer. Oncotarget *7*, 57514–57524.

Wynes, M.W., Hinz, T.K., Gao, D., Martini, M., Marek, L.A., Ware, K.E., Edwards, M.G., Böhm, D., Perner, S., Helfrich, B.A., et al. (2014). FGFR1 mRNA and Protein Expression, not Gene Copy Number, Predict FGFR TKI Sensitivity across All Lung Cancer Histologies. Clin. Cancer Res. *20*, 3299–3309.

Xie, M., Yen, Y., Owonikoko, T.K., Ramalingam, S.S., Khuri, F.R., Curran, W.J., Doetsch, P.W., and Deng, X. (2014). Bcl2 Induces DNA Replication Stress by Inhibiting Ribonucleotide Reductase. Cancer Res. *74*, 212–223.

Xu, G., Chapman, J.R., Brandsma, I., Yuan, J., Mistrik, M., Bouwman, P., Bartkova, J., Gogola, E., Warmerdam, D., Barazas, M., et al. (2015). REV7 counteracts DNA double-strand break resection and affects PARP inhibition. Nature *521*, 541–544.

Yadav, B., Wennerberg, K., Aittokallio, T., and Tang, J. (2015). Searching for Drug Synergy in Complex Dose–Response Landscapes Using an Interaction Potency Model. Comput. Struct. Biotechnol. J. *13*, 504–513.

Yamaguchi, T., Yamashita, J., Ohmoto, M., Aoudé, I., Ogura, T., Luo, W., Bachmanov, A.A., Lin, W., Matsumoto, I., and Hirota, J. (2014). Skn-1a/Pou2f3 is required for the generation of Trpm5-expressing microvillous cells in the mouse main olfactory epithelium. BMC Neurosci. *15*, 13.

Yamashita, J., Ohmoto, M., Yamaguchi, T., Matsumoto, I., and Hirota, J. (2017). Skn-1a/Pou2f3 functions as a master regulator to generate Trpm5-expressing chemosensory cells in mice. PloS One *12*, e0189340.

Yang, C.-F.J., Chan, D.Y., Speicher, P.J., Gulack, B.C., Wang, X., Hartwig, M.G., Onaitis, M.W., Tong, B.C., D'Amico, T.A., Berry, M.F., et al. (2016). Role of Adjuvant Therapy in a Population-Based Cohort of Patients With Early-Stage Small-Cell Lung Cancer. J. Clin. Oncol. *34*, 1057–1064.

Yang, D., Denny, S.K., Greenside, P.G., Chaikovsky, A.C., Brady, J.J., Ouadah, Y., Granja, J.M., Jahchan, N.S., Lim, J.S., Kwok, S., et al. (2018). Intertumoral

Heterogeneity in SCLC Is Influenced by the Cell Type of Origin. Cancer Discov.

Yang, P., Ebbert, J.O., Sun, Z., and Weinshilboum, R.M. (2006). Role of the Glutathione Metabolic Pathway in Lung Cancer Treatment and Prognosis: A Review. J. Clin. Oncol. *24*, 1761–1769.

Yang, S.W., Burgin, A.B., Huizenga, B.N., Robertson, C.A., Yao, K.C., and Nash, H.A. (1996). A eukaryotic enzyme that can disjoin dead-end covalent complexes between DNA and type I topoisomerases. Proc. Natl. Acad. Sci. U. S. A. *93*, 11534–11539.

Yeh, J.-J., Hsu, N.-Y., Hsu, W.-H., Tsai, C.-H., Lin, C.-C., and Liang, J.-A. (2005). Comparison of Chemotherapy Response with P-Glycoprotein, Multidrug Resistance-Related Protein-1, and Lung Resistance-Related Protein Expression in Untreated Small Cell Lung Cancer. Lung *183*, 177–183.

Yoshimura, D., Sakumi, K., Ohno, M., Sakai, Y., Furuichi, M., Iwai, S., and Nakabeppu, Y. (2003). An Oxidized Purine Nucleoside Triphosphatase, MTH1, Suppresses Cell Death Caused by Oxidative Stress. J. Biol. Chem. *278*, 37965–37973.

Young, L.A., O'Connor, L.O., Renty, C. de, Veldman-Jones, M.H., Dorval, T., Wilson, Z., Jones, D.R., Lawson, D., Odedra, R., Maya-Mendoza, A., et al. (2019). Differential activity of ATR and WEE1 inhibitors in a highly sensitive subpopulation of DLBCL linked to replication stress. Cancer Res.

Yu, G., and He, Q.-Y. (2016). ReactomePA: an R/Bioconductor package for reactome pathway analysis and visualization. Mol. Biosyst. *12*, 477–479.

Yu, G., Wang, L.-G., Han, Y., and He, Q.-Y. (2012). clusterProfiler: an R Package for Comparing Biological Themes Among Gene Clusters. OMICS J. Integr. Biol. *16*, 284–287.

Zangemeister-Wittke, U., Schenker, T., Luedke, G.H., and Stahel, R.A. (1998). Synergistic cytotoxicity of bcl-2 antisense oligodeoxynucleotides and etoposide, doxorubicin and cisplatin on small-cell lung cancer cell lines. Br. J. Cancer *78*, 1035–1042.

Zhang, S., and Cui, W. (2014). Sox2, a key factor in the regulation of pluripotency and neural differentiation. World J. Stem Cells *6*, 305–311.

Zhang, W., and Liu, H.T. (2002). MAPK signal pathways in the regulation of cell proliferation in mammalian cells. Cell Res. *12*, 9.

Zhang, W., Girard, L., Zhang, Y.-A., Haruki, T., Papari-Zareei, M., Stastny, V., Ghayee, H.K., Pacak, K., Oliver, T.G., Minna, J.D., et al. (2018). Small cell lung cancer tumors and preclinical models display heterogeneity of neuroendocrine phenotypes. Transl. Lung Cancer Res. *7*, 32-49–49.

Zhao, B., Li, L., Lei, Q., and Guan, K.-L. (2010). The Hippo–YAP pathway in organ size control and tumorigenesis: an updated version. Genes Dev. *24*, 862–874.

Zhao, H., Chiaro, C.R., Zhang, L., Smith, P.B., Chan, C.Y., Pedley, A.M., Pugh, R.J., French, J.B., Patterson, A.D., and Benkovic, S.J. (2015). Quantitative Analysis of Purine Nucleotides Indicates That Purinosomes Increase de Novo Purine Biosynthesis. J. Biol. Chem. *290*, 6705–6713.

Zhou, B.-B.S., Zhang, H., Damelin, M., Geles, K.G., Grindley, J.C., and Dirks, P.B. (2009). Tumour-initiating cells: challenges and opportunities for anticancer drug discovery. Nat. Rev. Drug Discov. *8*, 806–823.

Zinn, R.L., Gardner, E.E., Marchionni, L., Murphy, S.C., Dobromilskaya, I., Hann, C.L., and Rudin, C.M. (2013). ERK Phosphorylation Is Predictive of Resistance to IGF-1R Inhibition in Small Cell Lung Cancer. Mol. Cancer Ther. *12*, 1131–1139.

Zou, L., and Elledge, S.J. (2003). Sensing DNA Damage Through ATRIP Recognition of RPA-ssDNA Complexes. Science *300*, 1542–1548.